LONG-TERM SHEAR INVESTIGATION OF POLYPROPYLENE FIBER-REINFORCED CONCRETE BEAMS

by

MICHAEL DANIELS

Presented to the Faculty of the Graduate School of

The University of Texas at Arlington in Partial Fulfillment

of the Requirements

for the Degree of

DOCTOR OF PHILOSOPHY

THE UNIVERSITY OF TEXAS AT ARLINGTON

May 2017

Acknowledgements

I would like to express my profound gratitude to Dr. Ali Abolmaali, supervising professor, for his constant support and mentoring with love and care throughout the course of this research. It has been my great pleasure and honor to have the opportunity to work with him. Appreciation is also extended to Dr. Yazdani, Dr. Ardekani, and Dr. Chan for their time, guidance, and helpful suggestions. Also, special thanks goes to Ehsan Navadeh for his tremendous efforts during this project.

Finally, I would like to give my heartfelt thanks to my parents for their support, encouragement, and endless love.

February 2, 2017

Abstract

LONG-TERM SHEAR INVESTIGATION OF

POLYPROPYLENE FIBER-REINFORCED

CONCRETE BEAMS

Michael Daniels, PhD

The University of Texas at Arlington, 2017

Supervising Professor: Ali Abolmaali

This study investigates the long-term influence of polypropylene fibers on the shear strength and failure behavior of longitudinally reinforced concrete beams, with or without stirrups, subjected to accelerated aging conditions. For this study, 32 large scale short beams with different volume fractions of polypropylene fibers were casted and tested in the Civil Engineering Laboratory Building (CELB) at the University of Texas at Arlington: (1) Control reinforced concrete beams (RC); (2) Reinforced concrete beams with minimum stirrups (RCS) according to ACI 318; (3) Synthetic fiber-reinforced concrete beams with V_f=0.5% (SNFRC 0.5%), which correspond to 7.67 lbs./yd^3 (4.55 kg/m^3)'; and (4) Synthetic fiber-reinforced concrete beams with V_f=0.75% (SNFRC 0.75%), which correspond to 11.5 lbs/yd^3 (6.82 kg/m^3). In addition, a total of 108 cylindrical specimens, 4 in. (102mm) in diameter and 8 in. (203mm) in height, were tested after 28 days, 1 month, 3 months, and 6 months after curing, and were subjected to accelerated aging conditions in an environmental chamber at 122˚F (100% relative humidity). Moreover, a total of 36 flexural beam specimens, 6 in. (152mm) wide and high were produced and tested at CELB.

A 3-D non-linear finite element model (FEM) with concrete damage plasticity (CDP) was considered to analyze the failure of the large-scale reinforced concrete beams.

All of the experimental large-scale beam results were verified using FEM software. The concrete constitutive law in tension and compression of the experimental data were found with inverse analysis and trial and error to model the shear behavior of the concrete beams. The concrete constitutive law in tension and compression, using FEM in 100 years, were developed to predict the long-term behavior of the concrete beams.

The essential modeling parameters for shear capacity of large-scale beams with different volume fractions of polypropylene fibers for regression analysis were identified. Finally, a shear design equation was developed for the concrete beams, with a different volume fraction of polypropylene fibers in 100 years.

Table of Contents

List of Illustrations

List of Tables

1 INTRODUCTION

Shear failure is catastrophic and occurs without warning. This failure mode is undesirable (ACI 318-14, 2014) due to the brittle nature of concrete, and design provisions ensure that flexural failure occurs prior to the brittle shear failure. Cracks provide a means for water to penetrate the concrete and ultimately cause the corrosion of the steel reinforcement, generally degrading the concrete. A conventional transverse reinforcement is often placed close to an element, which leads to honeycombing and poor quality concrete. Concrete is weak in tension and does not show post-cracking behavior.

Introducing synthetic fibers into the matrix improves the mechanical behavior of concrete after a crack occurs. According to ACI, the introduction of fibers into concrete can potentially enhance the structure's capability "to maintain its strength and integrity and provide its designed function over its intended service life" (ACI 544, 2002). According to Balaguru and Shah, the serviceability of concrete can be improved with the addition of fibers since they have the ability to control cracking and enhance the tensile strength of the matrix (Balaguru and Shah, 1992). This is of significant importance when trying to enhance the shear capacity of a structure since tensile stresses play a pivotal role in the shear failure mechanism.

The primary goal of this study was to enhance the service life of corrosion-free concrete structures through ductility and identification of long-term (i.e., 100 year life) strength and durability. To accomplish this goal, corrosion-free polypropylene fibers were introduced in different volume fractions to the matrix of concrete. The final goal was to develop tools to predict the long-term shear performance of synthetic fiber concrete beams.

1.1 Objectives

The primary objectives of this study were to: (1) study the effects of polypropylene fibers on the shear strength and failure behavior of longitudinally reinforced concrete beams without stirrups, under accelerated aging conditions, using experimental methods; (b) correlate the short-term data obtained from accelerated aging, such as high temperature, high humidity, and chemical exposure in an environmental chamber, to actual long-term data, using Arrhenius principles; and (c) verify the experimental results with finite element modeling simulation and analysis, using ABAQUS® software.

1.2 Scope and Limitations

The force and dimension limitations for the experimental testing are summarized as follows:

1- The specified compressive strength of concrete was limited to 5 ksi.

2- The size of the beams for structural testing was limited to width=10 in., depth= 15 in., and length = 6ft.

3- The size of the beams for material testing was 6 in. x 6 in. x 20 in. in accordance with the ASTM 1609 requirements.

4- All the specimens were exposed to harsh alkaline environment using saturated solution of calcium hydroxide with a pH of 12 for aging purposes in this study.

The following limitations were imposed on the parametric study:

1- The length of the beams varied from 6ft. to 30ft.

2- The shear span to depth ratio (a/d) varied from 1.8 to 3.0.

3- The tensile reinforcement ratio varied from 1.4% to 2.4%.

4- The fibers dosage was limited to a volume fraction of 0.75% due to workability issues.

5- The proposed shear design equation was limited to 100-year prediction.

1.3 Research Contribution

This research has the potential to greatly benefit the construction industry. The procedures contained herein can save labor time and costs, and provide a safer design through ductility and flexibility due to the potential elimination of the construction of shear stirrups, which is time consuming. Also, the publications resulting from this study will disseminate the information to academic communities and engineering design firms. Finally, ACI codes, and ASCE and AASHTO specifications can be developed to aid design engineers.

1.4 Outline for Dissertation

This dissertation is organized into eight chapters. Details of each chapter are described as follows:

Chapter 1 – Introduction: This chapter explains the nature of concrete in tension and why fibers have been introduced to the concrete mixture.

Chapter 2 – Literature Review: This chapter presents the background of fiber-reinforced concrete and accelerated aging methods, based on the Arrhenius equation, to quickly determine the long-term strength of material.

Chapter 3 – Experimental Program: This chapter presents the design and fabrication of large-scale beam specimens, test set-ups and procedures, curing and aging of all of the specimens in this study.

Chapter 4 – Experimental Results and Analysis: This chapter presents the failure mode and mechanism of large-scale beams, load-deflection response of large-scale and small flexural beams, load-strain response, displacement-strain response, and compressive and tensile strength of cylinder specimens.

Chapter 5 – Analytical Studies: This chapter presents the long-term prediction of specimens based on the Arrhenius Principle and the design life of the specimens (i.e. 100 years).

Chapter 6 – Development of Three-Dimensional Finite-Element Model: This chapter presents a 3-D non-linear finite element model (FEM), developed by using Abaqus, with concrete damage plasticity (CDP) to analyze the failure of reinforced concrete beams specimens.

Chapter 7 – Parametric Study: The essential parameters for shear capacity of concrete beams, including volume fraction of polypropylene fibers (V_f), shear span to depth ratio (a/d), width of beam (b), and compression strength of concrete in 28 days (f'_c) are discussed in this chapter.

Chapter 8 – Summary and Conclusions: The findings of this research are summarized and the conclusions are presented.

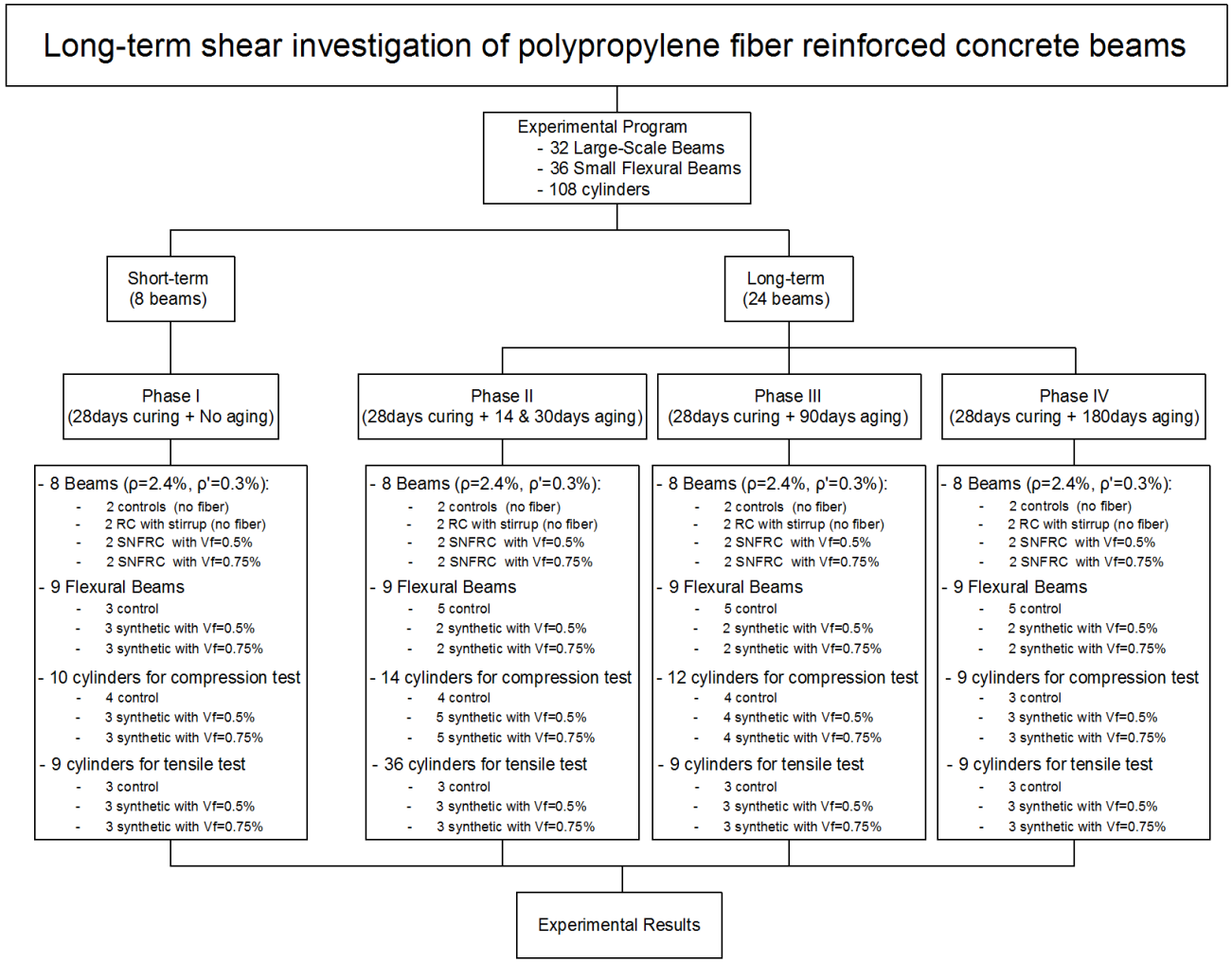

Figure 1 Framework of the conducted research

Table 1 Research program details

Phase	Beam No.	Beam Type	V_f (%)			Stirrups	Accelerated aging at 50°C (122°F), days			
			0	0.5	0.75		0	30	90	180
I	1	Control RC	✓	–	–	–	✓	–	–	–
	2									
	3	RCS	✓	–	–	✓		–	–	–
	4									
	5	SNFRC 0.5%	–	✓	–	–		–	–	–
	6									
	7	SNFRC 0.75%	–	–	✓	–		–	–	–
	8									
II	9	Control RC	✓	–	–	–	–	✓	–	–
	10									
	11	RCS	✓	–	–	✓	–		–	–
	12									
	13	SNFRC 0.5%	–	✓	–	–	–		–	–
	14									
	15	SNFRC 0.75%	–	–	✓	–	–		–	–
	16									
III	17	Control RC	✓	–	–	–	–	–	✓	–
	18									
	19	RCS	✓	–	–	✓	–	–		–
	20									
	21	SNFRC 0.5%	–	✓	–	–	–	–		–
	22									
	23	SNFRC 0.75%	–	–	✓	–	–	–		–
	24									
IV	25	Control RC	✓	–	–	–	–	–	–	✓
	26									
	27	RCS	✓	–	–	✓	–	–	–	
	28									
	29	SNFRC 0.5%	–	✓	–	–	–	–	–	
	30									
	31	SNFRC 0.75%	–	–	✓	–	–	–	–	
	32									

2 LITERATURE REVIEW

Research on the use of fibers in structural material dates back to 1910 when wire segments, nails, and metal chips were mixed into concrete in an attempt to improve its strength (Naaman, 1985). Initial efforts were made in the 1960s to evaluate the potential of steel fibers as reinforcement (Romualdi and Batson, 1963). Since then, considerable resources have been invested in researching the application of fiber to concrete. The primary focus has been steel fiber-reinforced concrete (SFRC), which resulted in promoting the use of SFRC for modern day industry purposes. A comprehensive database of all of the studies performed on SFRC included approximately 192 beams, which supported the application of steel fibers as an alternative to minimum transverse shear reinforcement for beams exposed to shear forces ranging from $0.085.\sqrt{f'_c}.b.w.d$ to $0.17.\sqrt{f'_c}.b.w.d$. As a result, the research was incorporated by the ACI building code requirements for structural concrete, permitting the application of SFRC according to Section 11 (ACI 318, 2008). The introduction of fibers leads to a slump loss, which is greater when a higher volume of fibers is used. Therefore, the ACI strongly recommends that the ASTM C995 standard test measures for evaluating the workability of a fiber reinforced mix be followed. Steel fiber-reinforced concrete demonstrates improved post-crack performance due to increased resistance to pullout from the concrete matrix. The improvement is notable in cases of fibers with hooked ends, roughed up surfaces, and crimped fibers, where the pullout resistance effect proves the post-crack performance (ACI 544, 2002). Application of steel fibers into concrete does not require modification of current construction materials used for casting, and the labor used for placing reinforcing bars is eliminated as a result. Steel fibers have demonstrated an increase in compressive strength, tensile strength, shear and torsion capacity, flexural capacity, and fatigue strength. These results contributed to the adoption of steel fibers by the ACI Building Requirements Code, and hence its application

for industrial purposes in the construction of tunnel linings, rock slope stabilization, etc. However, the potential of the advantages of fibrous content exceeds its current use, and much more research is required. Unfortunately, with all of its proven advantages, steel fibers do not address the corrosion issue in concrete's structural failures. Structural concrete reinforced with steel has always been prone to deterioration through corrosion of the steel. For instance, corrosion of steel in bridges has a direct cost of more than 13.6 billion dollars annually (NACE, 2012). In addition, updating deficient existing bridges will cost tax payers up to 20.5 billion dollars annually according to the Federal Highway Administration (FHWA, 2010). Corrosion is known as the leading factor in degradation of bridges, which are an important part of the transportation infrastructure (NACE, 2012). Steel fibers do not address the susceptibility of concrete to corrosion which is of great importance. Laboratory and field testing of cracked steel fiber reinforced concrete by George Hoff, showed that steel fiber concrete is prone to corrosion and is a source of significant structural damage (Hoff, 1987). As a result, there is a need for other fibrous materials which can significantly enhance concrete's structural properties but are not susceptible to corrosion and deterioration. Macro-synthetic polypropylene fibers have shown promising potential in recent studies.

Few research studies have been performed on the shear behavior of synthetic fibers because of the lack of availability of high quality synthetic fibers which could improve the capability of concrete. However, with the emergence of polypropylene synthetic fibers, which are manufactured with the intent of advancing the structural capabilities of concrete, the concept of inexpensive, fiber-reinforced concrete with a good performance becomes plausible. The improvement of concrete properties such as compressive strength, crack resistance, elastic modulus, tensile strength, durability, and extended service life can provide substantial advances in structural materials.

One of the initial efforts, in 1992, of studying the behavior of synthetic fiber-reinforced concrete showed an increase in the ultimate strength due to the increased capacity of resisting tensile forces along diagonal cracks. The study aimed to investigate the effect of fiber reinforcement on the strength and failure mode of longitudinally reinforced beams, without stirrups, subjected to shear and bending. The authors claimed that the fibers were more efficient as shear reinforcement when the shear-span ratio increased, supposedly due to the insignificant effect of the fibers on arch action versus their high impact on beam action. Additionally, a high percentage increase in shear strength and initial shear crack stress increase were reported. The results of the study conducted by V. Li, et al. were probably due to the increased resistance to propagation of dowel cracks, resulting from a larger volume of synthetic fibers.

Later in 2000, Noghabai's study showed that fibers improve the resistance of tensile cracks in both the web and tension zone of the specimen, which leads to stress redistribution. The study concluded that fiber reinforcement enhances the toughness and stiffness of beams (Noghabai, 2000). Similarly, 12 reinforced concrete beams with different volume fractions were tested in 2002 by Kwak, et al. with variable shear span-depth ratios. The study used 0.5% and 0.75% fiber reinforcement ratios and showed nominal stress at shear cracking, and the ultimate shear strength and compressive strength increased with increased fiber volume. In addition, the study showed that the failure mode changed from shear to flexure as the fiber dosage was increased (Kwak, et al., 2002). Another study on the shear behavior of steel fiber-reinforced concrete beams reported a 5% to 50% increase in shear strength of beams with 1% to 1.5% reinforcement ratios (Hwang, et al, 2013). Likewise, an experimental study in 2011 on 12 beams under four-point loading showed that the addition of fiber increased the shear capacity by 30% and also increased the ductility of the specimens (Kang, et al., 2011). Similarly, Cho and Kim tested 30 steel-fiber-

reinforced concrete beams loaded in shear and reported improvements in shear resistance, stiffness, cracking, ultimate load capacity, and ductility (Cho and Kim, 2003). Narayan and Darwish tested 49 beams under concentrated loads in a simply supported setup where 10 beams were reinforced with conventional stirrups and 33 beams used steel fibers as shear reinforcement. Using various volume fractions, fiber aspect ratios, and shear-span depth ratios, the test results showed an increased first crack shear strength with respect to the crack-arrest mechanism of fibers. The authors showed that steel fibers with a volume fraction of 1% improved shear strength in the same manner as conventional stirrups (Narayanan and Darwish, 1987). The compilation of numerous experiments such as the previously mentioned studies led to the adoption of steel fibers by the Building Code Requirements Design Code. Consequently, a study in 2006 on synthetic-fiber-reinforced concrete beams showed a linear increase in shear strength of specimens with respect to the increase in volume fraction of fibers. The study reported significant improvements in ductility and shear load resistance (Majzadeh, et al., 2006). Furthermore, an experimental program on synthetic-fiber-reinforced self-consolidating concrete conducted by Greenough presented that 1% reinforcement yields a significant increase in shear capacity of specimens (Greenough, 2008). Cifuentes and his colleagues conducted a comprehensive experimental study investigating the effect of polypropylene fibers on the fracture behavior of fiber-reinforced concrete of various strengths. The study included three-point bending tests on 88 notched small beams and reported enhanced mechanical properties with significant improvement of fracture behavior and ductility. The fibers influenced the elastic modulus of the concrete, improved its compressive strength, and showed a high resistance mechanism against pullout of the fibers (Cifuentes, et al., 2013). Furthermore, a research study reported that polypropylene fibers increase the load-bearing capacity of specimens and need relatively higher energy for their extraction during failure, which affects the pullout

phenomena and leads to a ductile performance of the specimens (Di Maida, et al., 2015). Subsequently, a 1997 study on shear behavior of fiber-reinforced concrete beams reported an increase in tensile strength and ductility, modulus of elasticity, and significant improvement of shear strength as a result of using polypropylene synthetic fibers for reinforcement (Furlan and Hanai, 1997). One considerable study on polypropylene fibers was conducted by Sahoo et al. on the flexural behavior of seven full-scale beams. They reported a considerable increase in the tensile strength of the concrete and displacement ductility of the beam specimens. The results also showed an increase in ultimate bending resistance of beams and a better post-crack residual strength response, resulting from multiple cracks related to the fiber-bridging action (Sahoo, et al., 2014). The development of macro-synthetic fibers has significantly enhanced the overall performance of concrete structures such as slabs-on-ground versus conventional concrete slabs (Roesler, et al., 2004). There has been growing research and investment in the use of high modulus synthetic fibers in beams, indicating that structural engineers realize their potential benefits. In addition, further studies on macro-synthetic fibers showed better bonding between the fibers and the concrete mix due to the higher modulus of elasticity of the fibers. One of the most significant recent tests using macro-synthetic fibers was by Altoubat et al., where 12 large-scale beams were tested to determine the shear strength and failure behavior of longitudinally reinforced concrete beams without transverse reinforcement. The experiment used short beams and slender beams with macro-synthetic fiber dosages of 0.5, 0.75, and 1.0% volume. The results showed that the introduction of macro-synthetic fibers to the concrete mix improved initial shear cracking strength by 30%, while also increasing the ultimate shear strength of the reinforced beams by at least 28% (Altoubat, et al., 2009). Furthermore, the results showed a variation in the cracking pattern and a significant change in the mode of failure. Shear failures are notorious for their undesirable

sudden brittle failure type. However, beams with macro-synthetic fibers are known to alter this and demonstrate gradual shear crack development up to the supports, ultimately exhibiting a ductile behavior and a failure mode changed to a flexural shear cracking rather than a web-shear cracking. This advocates an improved arch action in macro-synthetic reinforced concrete beams. It is notable that a higher deflection capacity due to the ductile behavior of the material and a higher strain capacity due to an effective distribution of stresses along the cracks were reported in the aforementioned study. In addition, the beams reinforced with macro-synthetic fibers showed a slight load decline after the initial diagonal crack and went on to resist a higher load until other shear cracks formed with higher deflection. This increase in deflection (up to 138%) was more significant in the short beams. This shows improvement in ductility of the beams, along with higher resistance to shear force and change of failure type from very brittle to somewhat ductile

The addition of macro-synthetic fibers resulted in increased ultimate shear strength. Consequently, the shape of the load-deflection graph presented in this study shows promising improvement to global structural response, as well as depicting the result of adding fibers to the concrete mix. The failure in control beams occurred with a single diagonal crack, whereas the failure in fiber-reinforced beams occurred with multiple shear cracks which extended to the support. This shows enhanced arch action and, therefore, improved shear strength. Meanwhile, macro-synthetic fibers changed failure mode from web-shear cracking, which normally occurs in conventionally reinforced concrete beams, to flexural shear cracking. Furthermore, the results showed improved strain capacity with delayed crack propagation and diagonal crack widening. This strain data showed that the structures resisted higher forces after the initial diagonal crack and continued to distribute stresses. Although the results from the research were based on macro-synthetic fibers and presented a promising potential for application of these fibers to concrete, the volume of

research done at this time is not adequate for the building requirements specifications to adopt macro-synthetic fibers. Therefore, this doctoral research project involves comprehensive detailed testing and analysis of numerous concrete beams and their accompanying material properties, providing substantial quality, reliable data. In addition to analyzing the mechanical properties of synthetic-fiber-reinforced concrete, the main goal of this research is to evaluate the effects of harsh environmental surroundings on synthetic-fiber-reinforced concrete beams, providing an accurate means of determining the service life of these structures.

2.1 Long-term Prediction based on Arrhenius Principle

The deterioration process of a material, using the accelerated aging method, aids in determining the service life of structures built using this material. As a result, short-term accelerated performance of artificially aged specimens is employed to mimic the long-term performance of the structures.

Temperature plays a pivotal role in this procedure. A higher storage temperature, which increases the rate of the water-cement hydration reaction, is the principal means of accelerating concrete's aging process. A common method for accelerating the aging of any material with a chemically driven degradation method is the process of thermal aging. This is based on the knowledge that higher temperatures result in a quicker occurrence of chemical reactions. The concept is based on using the Arrhenius equation (2) to find the activation energy of the chemical reaction (Arrhenius, 1889).

According to the Arrhenius equation, reaction rates are temperature dependent:

K_t = Rate Constant

E = Activation Energy of chemical reaction

R = Universal Gas Constant (8.314 J/K-mol)

T = Temperature (Kelvin)

A = Constant or Frequency Factor

Plotting the tensile strength (psi) versus aged period (days) of a tested specimen provides an exponential function:

where:

F_t is the final strength after “t” days of aging

F_0 is the initial strength of the specimen

r is the rate constant of the exponential curve

Rate constant K_t of the Arrhenius Equations is determined using the exponential function curve

Plotting $\ln(K_t)$ versus (1/T) produces a linear plot known as the Arrhenius plot, in which the activation energy is the slope divided by the universal gas constant. The temperature sensitivity of a reaction is indicated by its activation energy (E). A higher activation energy value means more energy is required to initiate a reaction. The ratio of rate constants (K_t) of specimens is subject to different aging temperatures, as determined by equation (1):

$$\ln(\frac{K_2}{K_1}) = \frac{-E}{R} \cdot \left(\frac{1}{T_2} - \frac{1}{T_1}\right) \quad (1)$$

Activation energy is determined by equation (2):

$$E = \frac{-\mathrm{R}}{\left(\frac{1}{T_2} - \frac{1}{T_1}\right)} \cdot \ln(\frac{K_2}{K_1}) \quad (2)$$

The hydration of cement in concrete is a time-dependent process, and accelerated aging can be used to accelerate subsequent degradation of the material. Cement hydration and the reaction of supplementary cement materials lead to development of internal microstructures in concrete. The resultant microstructural skeleton formation progresses in

development with respect to the growing resultant hydrates. Considering the fact that the cement hydration is a chemical reaction, its rate is dominated by two variables: temperature and concentration of reactants. As a result, the rate of formation of internal microstructure is controlled by the concrete's temperature. In addition, temperature has the capability to physically or chemically change the microstructure. This method is used to predict the mechanical properties of concrete in a very short time, long before the 28-day strength is achieved. Performing tests 28 days after casting concrete is not feasible in the industry; thus these accelerated aging methods provide avenues for forecasting the health of concrete in a shorter period of time (Abdun-Nur, 1978). Similarly, acceleration of the degradation process is applicable to concrete produced today to predict whether it can stand the test of time if exposed to environmental conditions. The accelerated aging procedure is designed to accelerate the mechanics that take place under normal exposure conditions. The American Standard for Testing and Materials, (ASTM), implements these methods widely for research purposes (Pinto, et. al., 2002).

Structural research studies have previously attempted to implement these methods as a means for forecasting future behavior of structural materials. For instance, Proctor et al., in 1982, used accelerated aging methods based on the Arrhenius equation to determine the long-term strength of material in a short time. The study found that immersing the concrete specimens for one day at 50°C in water is equivalent to 101 days of exposure to natural environmental conditions. Using the same methods, equivalent time and temperature for up to 4.5 years were determined (Proctor et. al., 1982). It is noteworthy that there has been only one prior research using aging methods for determining structural behavior of fiber-reinforced concrete. The research used the accelerated aging process to determine the long-term durability by studying flexural toughness of 4x4x14 inch specimens. Khajuria stored limewater-immersed specimens at 120 degrees Fahrenheit

with the intent of accelerating the fiber deterioration process (Khajuria, 1991). The results showed lower toughness indices after being exposed to alkaline conditions, leading the researchers to claim that fibers did not deteriorate and that they maintained bonding within the concrete matrix, providing crack resistance. It is important to emphasize that the aforementioned study only used one testing procedure, ASTM C1018, on a limited number of relatively small concrete specimens. One can naturally argue that relying on the flexural toughness of small specimens, although valuable, may not provide viable results for studying the durability of polypropylene-fiber-reinforced concrete in the long run. Additionally, previously manufactured polypropylene fibers did not demonstrate the qualities of the fibers that are produced today. The ASTM committee discontinued the testing guideline, C1018, used in the previously mentioned study in May 2006. Consequently, there is no ground for assessing the durability of macro-synthetic polypropylene-fiber-reinforced concrete simply because there is no previous testing or available data in this regard. As previously mentioned, researchers have paid substantial attention to studying macro-synthetic fibers, and efforts in this regard have added to growing literature. However, the long-term aging effects of this material have not been yet studied and, therefore, the vast volume of data presented through this research provides ample grounds for analyzing the performance of synthetic fibers in the long run.

3 EXPERIMENTAL PROGRAM

3.1 General

The effects of span-to-depth ratios (a/d) on the shear strength of beams without stirrups are shown in Figure 2 and Figure 3 (Wight and Macgregor, 2012).

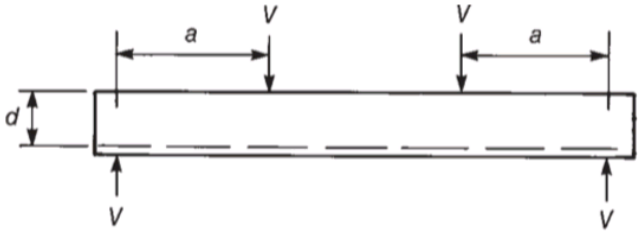

Figure 2 Typical photo of shear span to depth ratio (Wight and Macgregor, 2012)

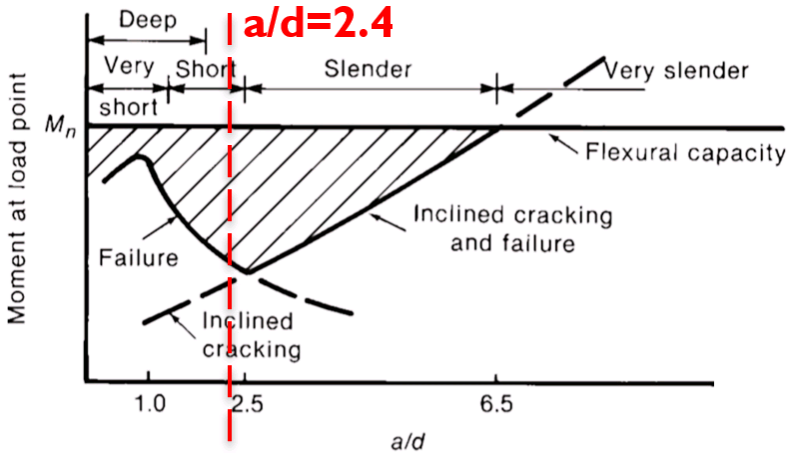

Figure 3 Moment at cracking and failure (Wight and Macgregor, 2012)

In this study, span-to-depth ratios (a/d) approximately equal to 2.4 were considered for all of the specimens which fall into the category of short beams. As shown in Figure 4, the possibility of the shear failure mode is higher than the possibility of the flexural failure for the span-to-depth ratio of 2.4.

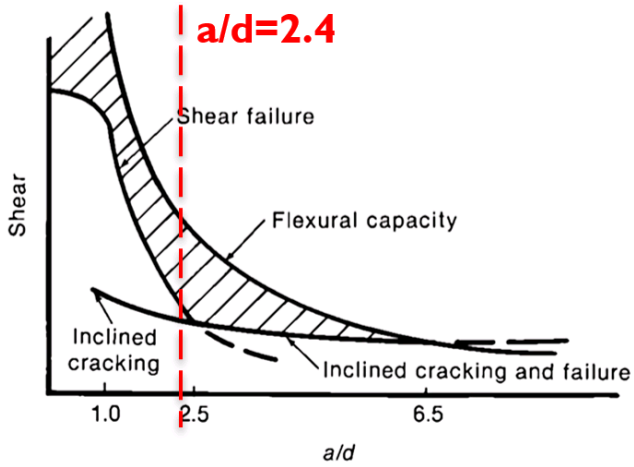

Figure 4 Shear at cracking and failure (Wight and Macgregor, 2012)

3.2 Material Properties of Polypropylene Fibers

Rust-proof, alkali-resistant MasterFiber MAC Matrix fibers were used to replace temperature, shrinkage, and welded-wire reinforcement. The performance characteristics of the fibers are summarized in Table 2.

Table 2 Physical properties of polypropylene fibers used in this study (BASF Corporation)

Specific Gravity	0.91
Melting Point	320 °F (160 °C)
Ignition Point	1094 °F (590 °C)
Absorption	Nil
Alkali Resistance	Excellent
Tensile Strength	85 ksi (585 MPa)
Length	2.1 in. (54 mm)
Aspect Ratio	67
Fiber Type	Embossed
Material	100% virgin polypropylene
Chemical Resistance	Excellent

Advantages of macro fibers, according to the BASF Corporation, include saving time and labor cost due to elimination of stirrups construction, which is time consuming; they are corrosion-free and highly chemical resistant; and they improve the crack resistance of concrete. The disadvantages are their poor UV and thermal stability and high thermal expansion coefficient, which is difficult to work with at high temperatures.

3.3 Fabrication of Test Specimens

3.3.1 Design of Beam Specimens

All of the beam specimens had a height of 15 in., length of 6 ft., span-to-depth ratio (a/d) approximately equal to 2.4, and reinforcement ratio of 2.4%, and were designed to fail in shear first, then flexure. The design calculations of the beams in Mathcad are summarized in Appendix M. Stirrups were placed in half span only to ensure that the failure would occur in the other span without stirrups or with minimum stirrups. Therefore, the span with minimum stirrups or without stirrups was monitored to reduce the number of steel and concrete strain gages. Also, bent bars with adequate extension, according to ACI 25.4, were used to prevent the anchorage failure. Configuration of large-scale beam specimens and their cross section details are shown in Figure 5.

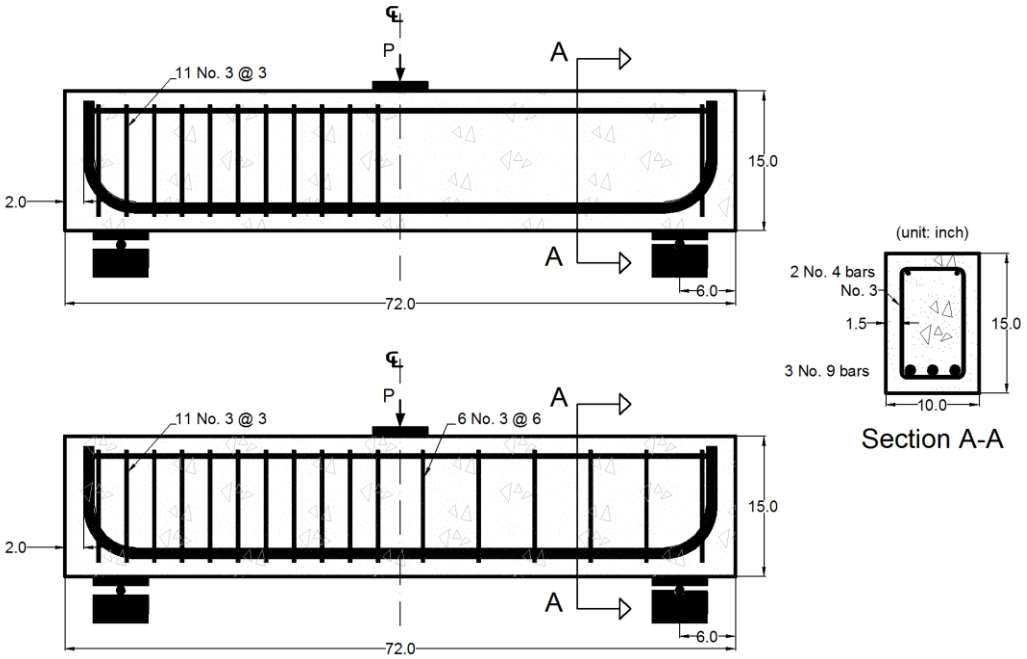

Figure 5 Configuration of large-scale beam specimens

3.3.2 Test Specimens

A total of 16 formworks for large-scale beams and one big formwork for 12 small flexural beams were built, as shown in Figure 6. All of the formworks were oiled twice, one day and two days prior to casting, to avoid the possibility of the concrete sticking to the formworks, thereby making it easier to de-mold the specimens after casting. The molds were used only twice to avoid any delamination of formworks.

Figure 6 Typical photo of formworks used in this study

The details of the reinforced concrete beams (RC), reinforced concrete beams with minimum stirrups (RCS), synthetic fiber-reinforced concrete beams with V_f=0.5% (SNFRC 0.5%), and synthetic fiber-reinforced concrete beams with V_f=0.75% (SNFRC 0.75%) are shown in Figure 7.

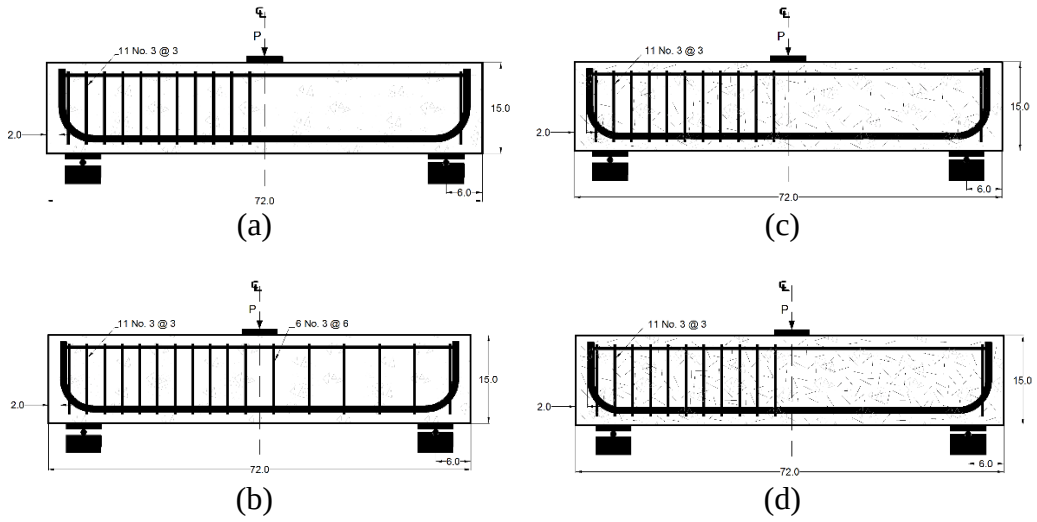

Figure 7 Details of large-scale specimen in inches; (a) Reinforced Concrete beam (RC), (b) Reinforced concrete beam with minimum stirrups (RCS), (c) Synthetic fiber-reinforced concrete beam with V_f=0.5% (SNFRC 0.5%), and (d) Synthetic fiber-reinforced concrete beam with V_f=0.75% (SNFRC 0.75%)

3.3.2.1 Steel Strain Gages

The steel rebars were ground, using an Air Die grinder, to create a flat, smooth surface for installing the strain gage, as shown in Figure 8. Since the threading on rebars is complementary to steel-concrete bonding, grinding away a substantial amount of threading might affect the bonding features. Therefore, only a very minimal amount of the thread was ground. Once a smooth steel surface was available, the surface was prepared and the strain gage was installed per Instruction Bulletin B-129 and B-137 of Micro-Measurements' precision group (manufacturer).

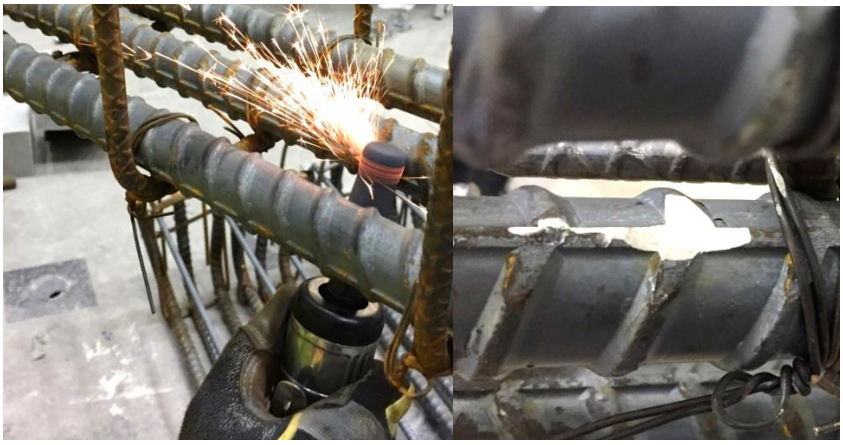

Figure 8 Typical photo of grinding the surface of the rebars with an Air Die Grinder

A strong bond between the installed strain gage and the surface of interest is required for the proper transmission of surface strains to the gage. Surface preparation included the following 5 steps:

(1) Degreasing

(2) Abrading

(3) Burnishing of Layout Lines

(4) Conditioning

(5) Neutralizing

Performing the above mentioned steps required standard materials such as CSM-Degreaser, Silicon Carbide Paper 320 and 400 grit, Neutralizer 5A, M-Prep Conditioner A, cotton-tip applicators, and a 4H pencil. A clear, smooth glass surface was used to align the tape over the strain gage prior to placing it on the surface of interest, as shown in Figure 9.

Figure 9 Typical photo of surface preparation for placement of steel strain gages

The steel surface was initially degreased using CSM-degreaser and a gauze sponge was used to clean the surface. Next, the surface was dry abraded using 320 grit silicon carbide paper, and wet abrasion was performed by flooding the surface and abrading. using 320 grit paper, followed by 400 grit silicon carbide paper.

Figure 10 Typical photo of surface preparation of steel strain gages

A 4H pencil was used to burnish layout lines onto the surface. These straight lines were solely meant to provide alignment while placing the gage in future stages, as shown in Figure 11.

Figure 11 Typical photo of alignment of steel strain gage preparation with a 4H pencil

The cotton-tip applicators were used along with M-Prep Conditioner-A, and the surface was properly conditioned and then wiped clean with a gauze sponge. Finally, M-Prep Neutralizer 5A was used to regulate the pH of the surface area so that proper bonding occurred between the gage and the area of contact. The final step was the application of the neutralizer and scrubbing the area with cotton-tip applicators. Once the surface was ready, the strain gage was installed within 30 minutes to ensure that the surface did not lose bonding properties during the surface preparation.

The materials that were used to install the strain gages on the surface included PCT Tape, M-Bond 200 Adhesive, M-Bond Neutralizer-5A, M-Bond 200 Catalyst, gauze sponge, tweezers, and a smooth glass surface. Initially the tweezers and glass surface were cleaned with M-bond Neutralizer-5A and a gauze sponge. It was important to make sure that the alkalinity of the surfaces, where the strain gage was installed, was between 7.0 to 7.5 pH, which is the specified alkalinity specified by the manufacturer for the adhesive. Therefore, a liberal amount of Neutrlizer-5A was used in the final surface preparation process, while cleaning the glass surface and the tweezers. The gage was then removed from its envelope. using the tweezers, and was placed bonding side down

on the chemically clean glass surface. A 4-6 inch piece of PCT-2M tape was placed on top of the gage, which was used to carry the gage from the glass surface to the steel surface.

The tape was lifted at a shallow angle to ensure that the wiring terminal was not disconnected. The gage was then aligned with the burnished layout lines and placed on the steel surface.

The tape was lifted at a shallow angle once again until the gage and the terminal were free. The tape was then placed back upon itself so that the bonding side of the strain gage was exposed. The gage was then coated with a very thin layer of the M-Bond 200 catalyst, which restricted the absorption of moisture by uncured adhesive, as shown in Figure 12.

Figure 12 Typical photo of strain gage installation with M-Bond 200 catalyst

After the catalyst was dry (approximately one minute), a drop M-Bond 200 adhesive was placed on the steel surface, right beside the tape. The gage was then carefully flipped back onto the steel surface, and the tape was wiped onto the steel surface with a gauze sponge so that the adhesive was spread evenly under the gage. Firm thumb pressure was then exerted onto the gage. The ambient temperature was set below 70 degrees fahrenheit to ensure proper curing of the adhesive.

A twisting action was applied while lifting the thumb, and after a few minutes, the tape could be removed at a shallow angle. Extra care was taken to make sure that the tape did not damage the soldered terminals on the gage. The health of the strain gage was then checked, using an ohm meter. The ohm resistance shown on the ohm meter device should be the same resistance specified by the gage manufactrurer to ensure that the strain gages are not faulty.

Figure 13 Typical photo of testing the resistance of steel strain gages

Since strain gages installed on steel bars will be subjected to challenging circumstances, necessary precautions must be taken to ensure they are well protected and will be healthy at the time of casting the specimens. The strain gages and the surrounding area were initially coated with a 0.02 inch coat of M-Coat C, a thick noncorrosive transparent silicone rubber film with good electrical properties. M-Coat C has a -75 to 550 Fahrenheit degree operating temperature range, which met our experiment demands. The coat provides protection against corrosion, chemicals, and water. After 24 hours of curring at 75˚F, the next layer of coating was placed on top of the gage.

The second protective coating layer was Vishay Precision Group's M-Coat B, an air-drying solvent-thinned nitrile rubber flexible coating. This product has an operating temperature range of -320 to 300 Fahrenheit and requires 24 hours of curing at room temperature. The coating on the installed strain gage is shown in Figure 14.

Figure 14 Typical photo of M-Coat B on the steel strain gages

Likewise, necessary precautions must be taken to protect the vinyl-coated strain gage wires since considerable lengths of a gage wire will be embedded in the concrete beam and are, therefore, subjected to challenging concrete casting and curing procedures. If no protection is provided, the wires might be either physically damaged during concrete casting or short circuited upon any contact with any liquids. The vinyl coated wires have microscopic pores on them which makes them prone to damage through liquid penetration. To address this issue, the strain gage wire was passed through a 0.17 inch thick polyethylene tube, which provided excellent physical and chemical protection. Furthermore, to prevent any fluid or debris penetration into the tube during and after concrete casting, the tube's end which meets the strain gage was protected with two layers of coating. First, an extra thick rubber insulating moisture-sealing 3M electrical tape was placed at the top of the strain gage and tube, covering both the strain gage assembly and the tube's end. (Figure 15.)

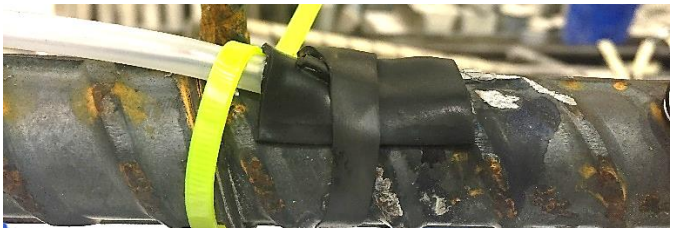

Figure 15 Typical photo of steel strain gage protected with a polyethylene tube

Finally, Gardner Bender's liquid electric tape was applied on top of the whole assembly, as shown in Figure 16. This tape provides resistance to chemicals, solvents, saltwater, and other fluids by forming a solid, waterproof, UV-resistant, dielectic seal.

Figure 16 Typical photo of steel strain gage protected with a liquid electric tape

The four layers of coatings, along with the polyethylene tubing, provided considerable protection to the strain gage assembly. Furthurmore, the tubing was aligned and tied so that it would exit the beam at the far end to avoid being on the load path of simply supported beam specimens.

Figure 17 Typical photo of steel strain gage installation

A total of 256 encapsulated constantan steel strain gages (C2A-06-125LW-350) with pre-attached, ready-to-use cables, a gage length of 0.125 in. and overall length of 0.238 in. from Micro Measurement Laboratories were installed on the surface of the rebars. A total of seven steel strain gages were installed for the beams, with half-span stirrups to monitor the steel strains in the middle of the beam where flexural is critical, and also on the path of shear failure, which was assumed to be from the edge of the support plate to the edge of the load plate (Figure 18). Eleven (11) strain gages were installed on the rebars of the reinforced concrete beams with minimum stirrups (RCS) to monitor the steel strain in the middle of the beam, as well as the path of shear failure, which was assumed to be from the edge of the support plate to the edge of the load plate. The steel strain gages for the RCS speciments are shown in Figure 19. The designation that was used for the location of the steel strain gages represents the intersection of the grids; for example, strain gage M2 denotes that it is located at the intersection of grid M and grid 2.

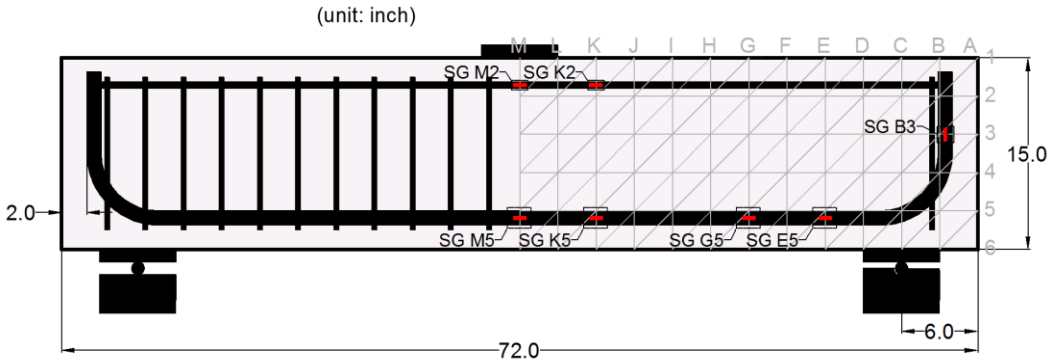

Figure 18 Typical location and orientation of steel strain gages on rebars in RC Control and SNFRC beams (All phases)

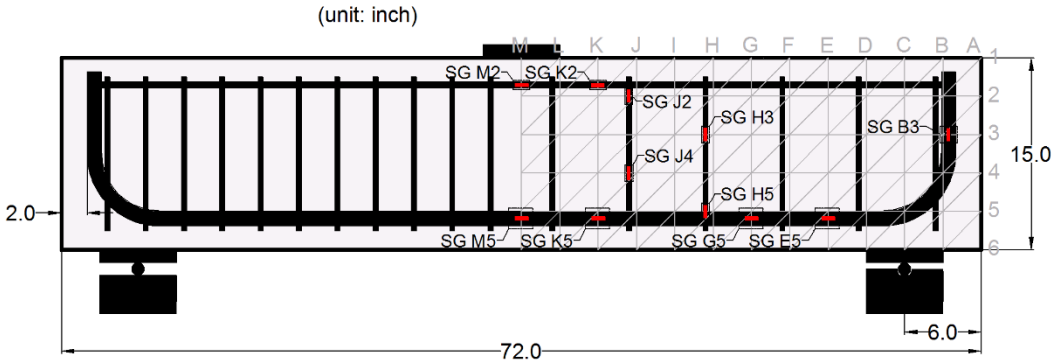

Figure 19 Typical location and orientation of steel strain gages on rebars in RCS beams (All phases)

3.3.2.2 Concrete Strain Gages (Rosette strain gages)

According to Micro Measurement (manufacture), a rosette strain gage refers to an arrangement of two or more closely placed gage grids that are aligned in a certain orientation to measure the normal strains in different directions on a test surface. The application of a rosette strain gage is particularly crucial in experimental stress analysis when the determination of principal strains and stresses due to a state of biaxial stress is of special interest. Implementation of these gages aids in determining both the direction and the magnitude of strain on a test surface. Rosette strain gages are produced in a variety of alignments and orientations, Three basic forms are Tee Rosettes, Rectangular

Rosettes, and Delta Rosettes. Tee Rosette gages are two perpendicular grids, as shown in Figure 20 (a). Rectangular Rosette gages have three grids, and the first and third grids are oriented at 45 degrees with respect to the second grid, which is oriented perpendicularly, as shown in Figure 20 (b). Similarly, Delta Rosettes have three grids, with each grid at a 60-degree orientation from the previous grid, as shown in Figure 20 (c). The rosette gages are available in a variety of gage lengths. Selection of a rosette type for experimental testing purposes is based on application limitations, testing conditions, and testing objectives. The active length of each grid within a rosette is commonly referred to as the “gage length.”

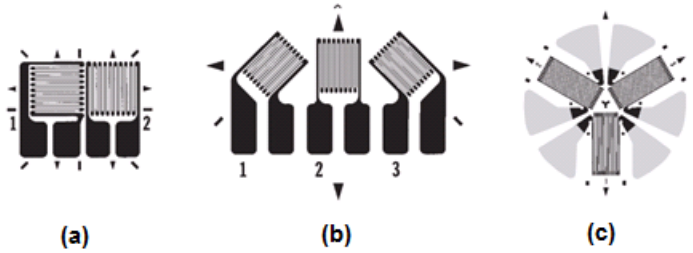

Figure 20 Typical photo of Rosette strain gages: (a) Tee (b) Rectangular (c) Delta

The application of rosette strain gages is fundamental to obtaining principal strains and stresses when testing a structural member subject to a biaxial state of stress, and proper selection of the type of rosette to be used is critical to obtaining accurate and reliable data. Apart from basic parameters which must be considered while selecting a strain gage type (gage length, temperature compensation, backing material, strain-sensitive alloy, etc.), two other criteria are particularly important in selecting a rosette strain gage, type of rosette (Delta, Rectangular or Tee), and construction type (single-plane or stacked).

When the direction of the principal strains is known, the Tee rosettes should be

used. It is very important that no extraneous stresses such as axial or bending stress are present since the existence of these stresses affects the direction of the principal

axes. Tee rosettes may not yield accurate results if they are used on geometrically irregular surfaces with imperfections, since these imperfections modify the principal directions. Therefore, if there is any hint of uncertainty as to the principal directions, a delta or rectangular rosette is a more reliable choice. Moreover, since there is very little difference between delta and rectangular rosettes based on the functionality, the selection is usually governed by practical considerations. Stacked rosettes are manufactured by assembling and laminating three properly oriented gages, as shown in Figure 21(b). Planar rosettes have each gage lying in a single plane, as shown in Figure 21(a).

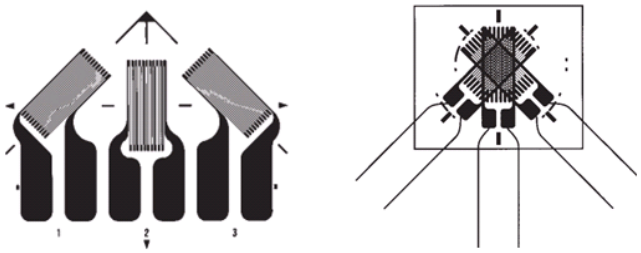

(a) (b)

Figure 21 Typical photo of rosette strain gages: (a) planar (b) stacked

Flexibility, low reinforcement effect, and higher heat dissipation are the advantages of the planar rosette strain gages. However, they have the disadvantage of covering a larger surface area. This is critical for situations where a limited surface is available or considered. In addition, if the testing surface includes a steep stress gradient, each gage element within a planar rosette assembly may be subject to a different strain field and/or magnitude. The stacked rosette, however, has three grids measuring the same point of a test surface and covers a smaller surface, yielding measurements of strain at a single point. Considering all the governing parameters and selection criteria mentioned by the manufacturer, general purpose stacked rosette strain gages C2A-06-125WW-350 were selected for installation on the concrete surface of the large-scale beams, as shown in

Figure 22. The selected rosette gages were encapsulated constantan gages with pre-attached ready-to-use cables, a ±3 % strain range and a –60° to +150°F temperature range.

Figure 22 Typical photo of general purpose stacked rosette strain gage used on the surface of concrete beams in this study

Labeling each individual grid in a particular sequence is of significant importance for correctly interpreting the obtained measurements, and failure to follow the correct numbering methods would lead to erroneous principal strain interpretations. Therefore, it is important to mention that all of these considerations were taken into account when deciding on a numbering sequence for individual grids to ensure that the numbering sequence is correlated to the derived data-reduction relationships. Achieving the objective of obtaining principal stresses is comprised of three steps:

(i) Measurement of concrete's surface strains by installing rosette gages

(ii) Calculation of the attained surface strains to the principal strains

(iii) Transformation of the principal strains to the principal stresses

Strain transformation formulas are used for calculating the principal strain measurements from rosette strain gages. The normal strain in any orientation is expressed in terms of the angle from the principal axis to the direction of a given strain and the principal strain. Cracks in concrete occur when the maximum principal tensile stress reaches the tensile stress of concrete, which is calculated by testing the small flexural beams, according to ASTM 1609.

The designation of the stacked concrete strain gages, for instance K2-1, denotes that the strain gage is located at the intersection of grid K and grid 2 and has an orientation of 1, as shown in Figure 23. The load-strain response and displacement-strain response of all the large-scale beams are shown in Appendix G.

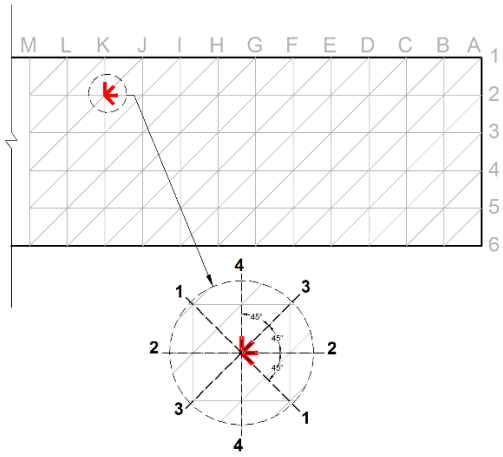

Figure 23 Typical concrete strain orientation on the surface of concrete beams

The location of all of the concrete strain gages that were installed prior to testing for each phase are shown in figures 24 to 26. It's noteworthy that the strain gages were installed randomly on the load path of the span, without transverse reinforcement, to capture the cracks and to study the overall behavior of the beam.

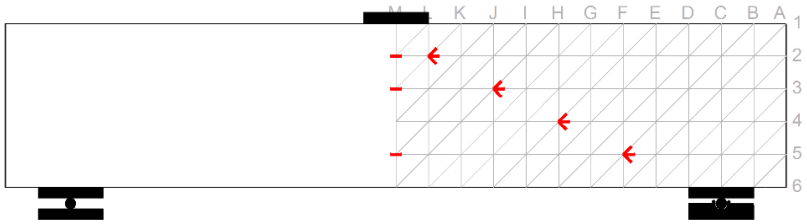

Figure 24 Location and orientation of concrete strain gages on the surface of all the large-scale beams in Phase 1 and Phase 4

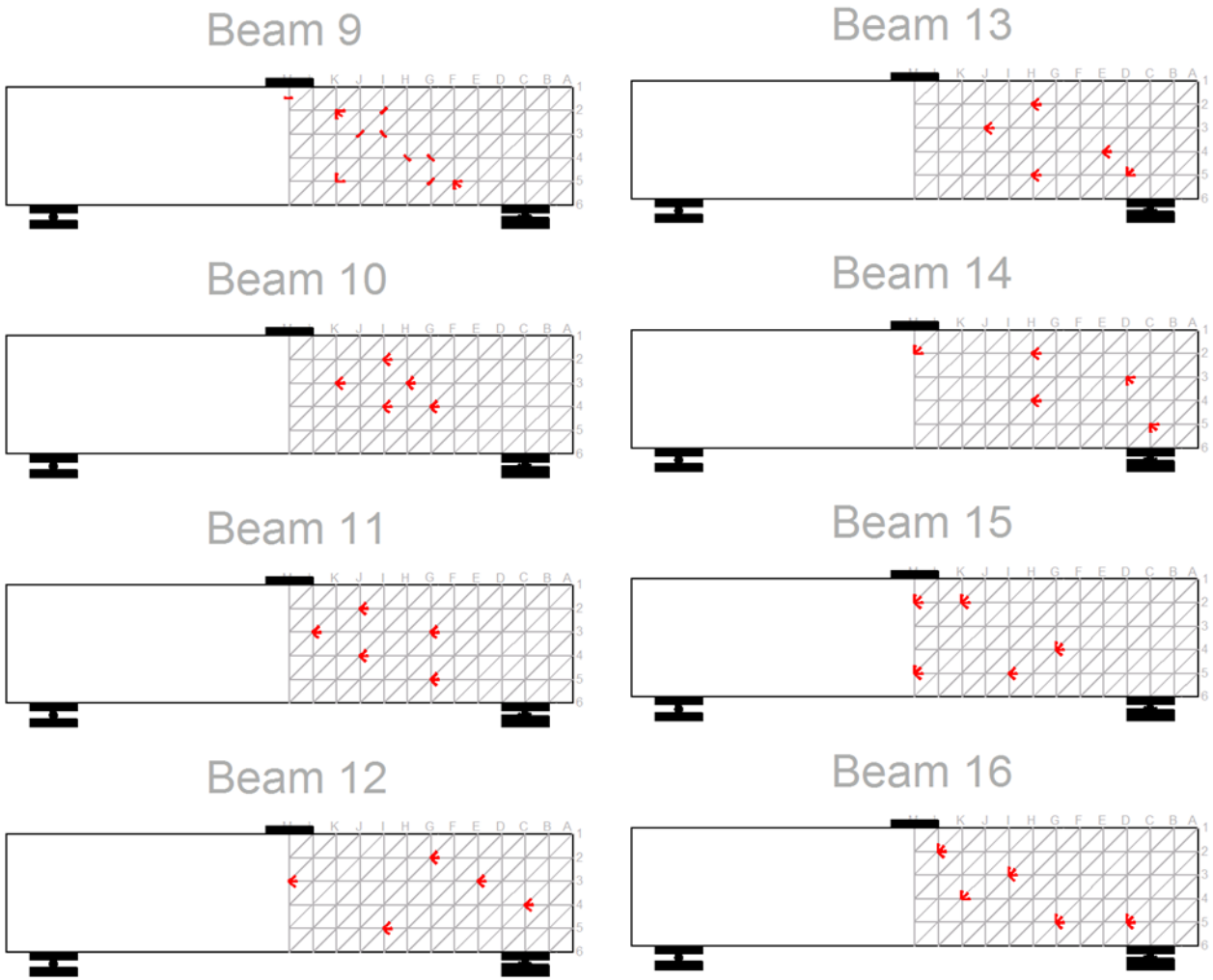

Figure 25 location and orientation of concrete strain gages on the surface of all the large-scale beams in Phase 2

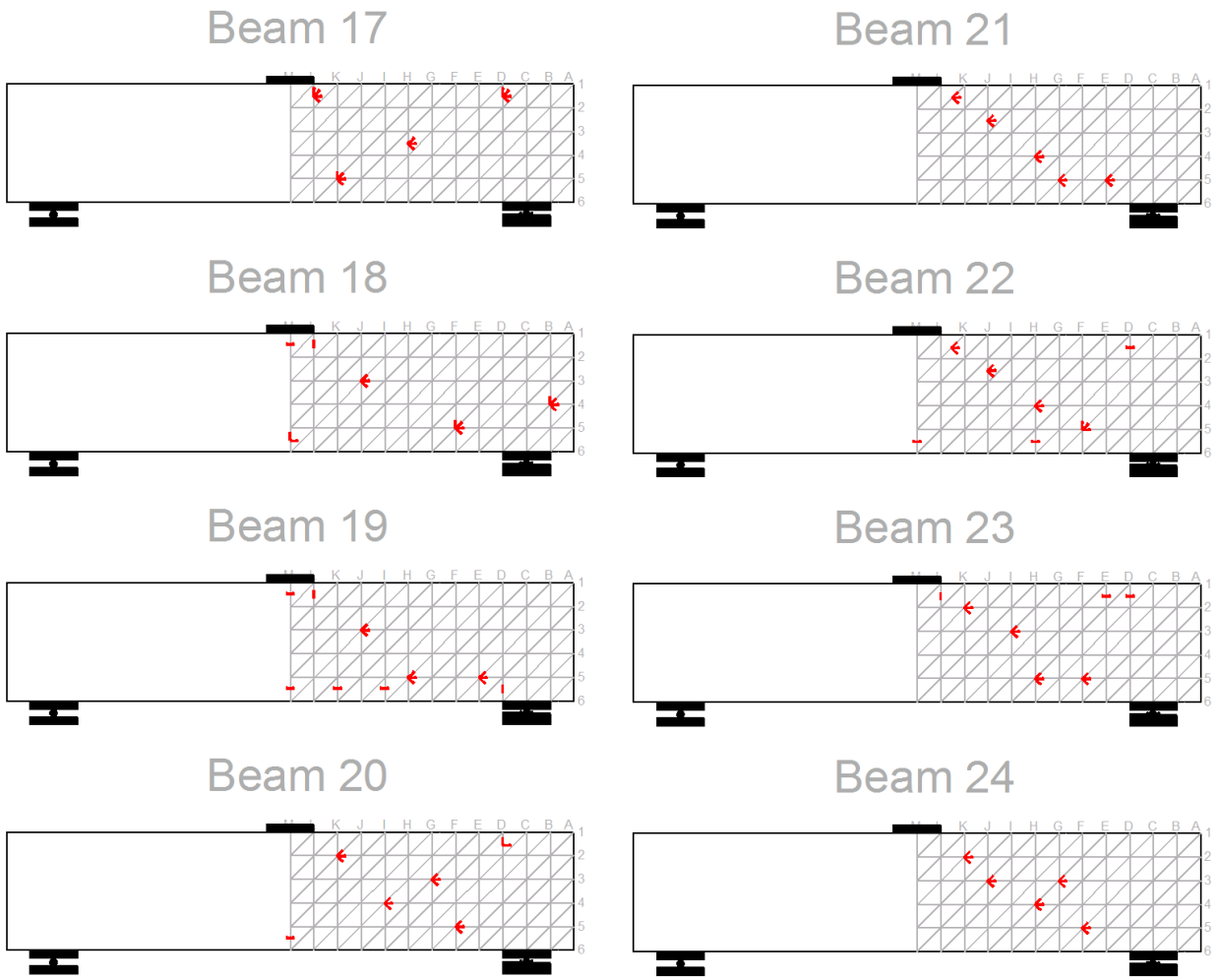

Figure 26 Location and orientation of concrete strain gages on the surface of all the large-scale beams in Phase 3

3.3.2.3 Concrete Casting

After grinding, surface preparation, steel strain gage installation, coating, and tubing, the steel cage was placed inside the formwork and was finally ready for concrete casting, as shown in Figure 27.

Figure 27 Typical photo of formworks ready for casting

All concrete specimens (32 large-scale beams, 36 flexural beams, and 108 cylinders) were casted in two days within the same week. The identical large-scale beams were casted in order to increase the reliability of the experimental results. During the first stage, a total of 16 large-scale beams (eight control RCs and eight RCS), 18 flexural beams, and 36 cylinders were casted. The first stage did not include the involvement of fibers in the mix, but polypropylene fibers were added to the mix during casting in the second stage. The second stage of casting included the other 16 large-scale beams (eight SNFRC 0.5% and eight SNFRC0 0.75%), 18 flexural beams, and 72 cylinders.

A volumetric concrete mixer was used for the concrete casting. The mixer contained concrete ingredient materials and water, which were mixed on the truck upon arrival at the Civil Engineering Laboratory Building (CELB). The mixer was capable of measuring the raw materials, using volume, and then blending the concrete mixture, using an auger with water. The process initiated with a batch metering system that measured the volume of raw materials before they entered the mixing chamber. Once the truck was loaded with the volumes of concrete ingredients at the plant and arrived at the job site, the truck began mixing the ingredients according to required concrete strength requirements, as shown in Figure 28.

Figure 28 Typical photo of concrete casting at the CELB, UTA

Four cubic yards of concrete with a strength of 5,000 psi and slump of 7.0 to 8.0 inches were delivered to the CELB at the University of Texas at Arlington (UTA) for the two stages of casting. Superplasticizers were used with polypropylene fiber mixes to increase the desired workability. A slump test was performed, using a slump cone that was 12 inches high, with an 8-inch bottom diameter, and 4-inch top diameter. The cone was placed on the floor and filled with fresh concrete up to one-third of the height initially, and then tamped 25 times with a standard rod. The process was repeated twice more, then the concrete was leveled flat to the top cone. The cone was then carefully lifted vertically. The concrete then subsided, and the height of this subsidence, known as the slump, was then measured. The measured slump of the ordered concrete is illustrated in Figure 29. The slump test procedure and the cone used for this experiment followed ASTM's C-143 standard.

Figure 29 Typical photo of measuring slump of concrete during casting

After casting all 6 large-scale beams, the formworks were demolded for casting the other 16 large-scale beams, as shown in Figure 30.

Figure 30 Typical photo of demolded formworks ready for second stage of casting

Plain concrete and synthetic-fiber-reinforced concrete (SNFRC) batches with fiber volume fractions of 0.5% and 0.75% are shown in Figure 31.

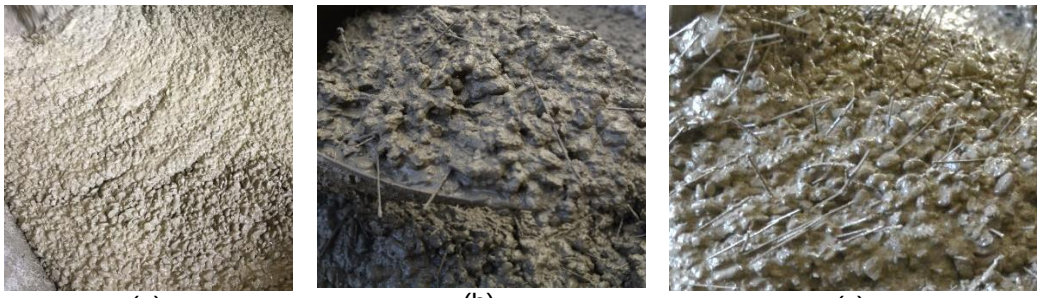

(a) (b) (c)

Figure 31 Typical photo of (a) plain concrete, (b) 0.5% SNFRC (c) 0.75% SNFRC

The concrete mix design of the delivered concrete is summarized in Table 3.

Simultaneously, 108 cylinders were casted according to ASTM C39 and ASTM C496, and 36 beams were casted according to ASTM C1609, accompanying the 32 large-scale beams.

Table 3 Details of mix design of concrete in this study

Source	Description	ASTM	SG	Abs.Vol. (CF)	Admix. Oz.	SSD Wt. (lbs)
CCI	Type I/II/Pozzoslag Blend	C-1157	2.85	3.7		658
Trinity Materials	Pea Gravel	C-33	2.65	11		1819
Trinity Materials	Concrete Sand	C-33	2.66	6.71		1114
Dallas	City Water	C-1602	1	3.93		245
Sika	6100	C-494	1.02	0.04	39	3
Euclid	Air 30	C-260	1		7.92	1
	Air			1.62		
f'_c	5000 psi @ 28d			27	TOTAL	3840
Slump	7.00 to 8.00 inch	Designed Unit Weight		142.22		
Specified Air	0.00 to 0.00	Designed W/C Ratio		0.37		
Designed Air	6.00%	Designed Volume		27.00		

Freshly poured concrete beams were vibrated to remove voids within the specimens, as shown in Figure 32. The first stage casting of all 16 large-scale beams and the small flexural beam specimens, which were later used for material properties testing, are shown in Figure 33.

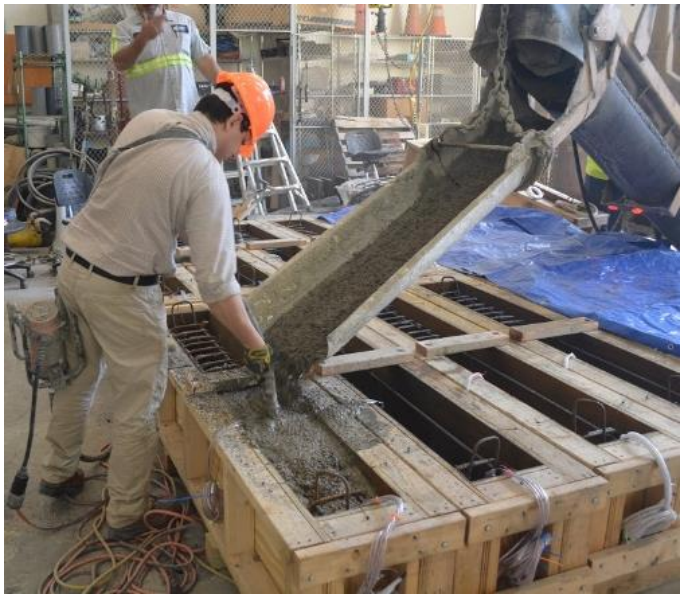

Figure 32 Typical photo of vibration of large-scale beams

Figure 33 Typical photo of casted large-scale beams

Finally, after casting, all of the specimens were covered with polyethylene sheets to prevent evaporation of the water from the surface of the concrete specimens.

3.4 Curing and aging of the specimens

Once concrete casting was completed, the specimens were then covered with polyethylene sheets to prevent moisture loss. The casted specimens were then demolded and transported into the curing room to cure for 28 days.

Three large-scale tubs and four small-scale tubs were then built in the curing room. Each large-scale tub was used to hold eight large-scale concrete beams fully immersed in a chemical solution. Each tub was 96 inches long, 40 inches deep, and 64 inches wide, and held approximately 225 gallons of liquid. The self-weight of the 8 large beams combined was around 8,000 pounds. These tubs were built using concrete masonry units and were braced to withstand lateral displacement of the walls due to the combined resultant force imposed by the liquid. The total resultant force exerted from 8 large-scale beams and liquid on the floor was approximately 12.5 kips. The walls were thoroughly braced, and grouts were used during the construction of each tub. Furthermore, since any leakage from these tubs was potentially hazardous and a safety concern, adequate measures were taken to ensure that no leakage would occur during accelerated aging of the specimens. Hence, the floor of each tub was made from an ASTM Standard high-strength bedding mix, and the liquid was held by a custom made polyvinyl-chloride pan liner (PVC). These highly flexible pan liners are known in the industry for their excellent waterproofing and are used for construction of shower tubs. The PVC pan liner has a high temperature tolerance and provides a waterproofing membrane. This material complies with the plastic flexible concealed water-containment membranes standard of ASTM D4551.

The large-scale beams were transported with two pallet jacks (Figure 34) to the curing room and were placed on top of a wooden panel and then wrapped with a PVC pan liner (Figure 35).

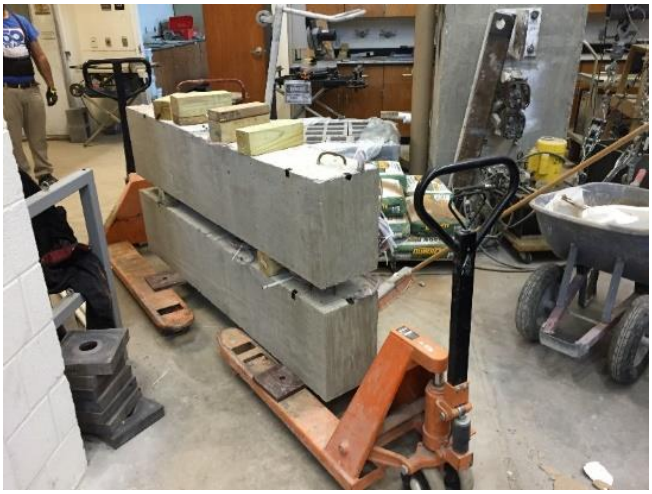

Figure 34 Typical photo of transportation of large-scale beams with two pallet jacks to the curing room

Figure 35 Typical photo of eight large-scale beams wrapped with PVC pan liner

After that, the walls of the tub were constructed around the beams, using grouted CMUs, and the tubs were adequately braced by using timber, ratchets, and steel wires to hold the walls together. The tubs were each fully filled with water, as shown in Figure 36. The temperature of the curing room was kept constant at 50°C (122°F) for a period of six months.

Figure 36 Typical photo of tubs for large-scale beams

Finally, a controlled dosage of a calcium hydroxide chemical compound was added to the water, raising the pH of the solution to the desired level of around 12. $Ca(OH)_2$, a colorless crystal powder, when mixed with water, produces limewater, a saturated solution of calcium hydroxide. Hydroxyl anions are released into water once the chemical dissolves and are capable of raising the pH up to 12.5. Consequently, an 80-inch long, 25-inch wide and 16-inch deep tub was constructed for immersion of small-scale material test specimens into 140 gallons of liquid solution. The small-scale tub was divided into two sub sections,

where each provided different temperatures. The first tub provided an ambient temperature, 50°C (122°F), and the second tub provided a high temperature by using two immersion heaters to heat the liquid to raise the temperature of the specimens to 70°C (158°F). Two different temperatures were employed for using the Arrhenius principle to find the activation energy of the chemical reaction of the concrete with varying volume fractions of polypropylene fibers.

Figure 37 Photograph of concrete cylinders and flexural beams

3.5 Test Set-Up and Procedure

3.5.1 Testing Machines

A 400 kips load-controlled universal compression testing machine, as shown in Figure 38, was used for testing the 32 large-scale beams. The 810 Materials Test System (MTS) machine with a load capacity of 50 kips was used to test the small flexural beam specimens. In addition, a 500 kips compression machine was used to obtain the compressive strength of the cylinders, and a 60 kips compression machine was used for conducting splitting tensile tests on cylindrical specimens.

Figure 38 Typical photo of Universal Testing Machine with a capacity of 400 kips

Large-scale beams were set up in a simply supported condition under the 400 kips compression machine. The machine has a lower plate which gradually moves up, while the upper crosshead is fixed and uses a built-in load cell to monitor the loading rate. Two 10 ft. I-shaped steel beams were placed side by side on the lower plate, centered and aligned in both directions to spread the displacement from the machine plate to the supports, as shown in Figure 39.

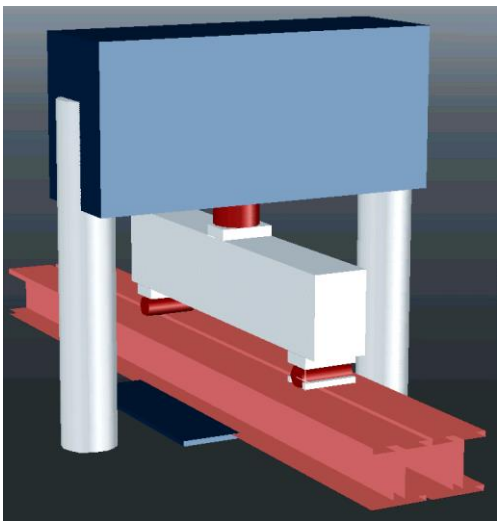

Figure 39 Typical photo of instrumentation of large-scale beams

Steel plates and rollers were used to set up the supports on each end. The left support was set up as a roller which allows lateral translation, and the right support was set up as a pin with no lateral translation. Each large-scale beam was perfectly aligned and centered to ensure that the load was applied at the exact center of the beam. The top of the beams were grouted, steel plates were placed on top of the beam to spread the loading, and a load cell was placed on top of the plates. A monotonic load was then applied at a constant rate of 2.2 kips/minute while the load cell recorded the applied load constantly. In addition, two linear variable differential transformers (LVDT), capable of showing up to 2 inches of net deflection, were used to measure the beam's mid-span and quarter-span deflections, as shown in Figure 40. Displacements at two locations were monitored for all the specimens to compare with results from Abaqus software.

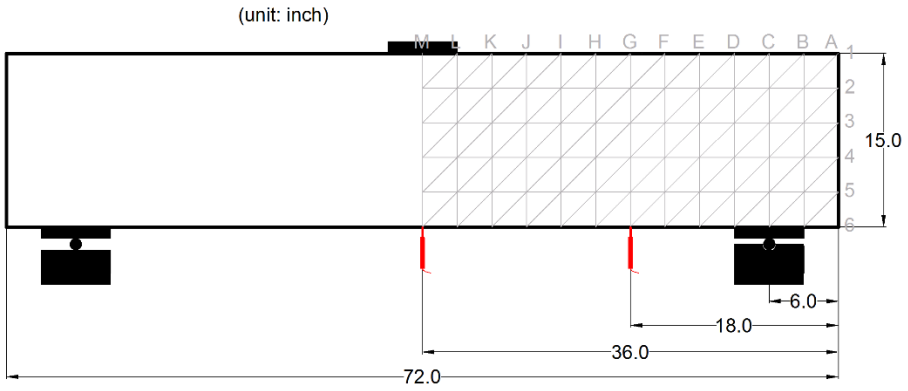

Figure 40 Typical location of LVDTs in all the large-scale beams

Each LVDT was clamped to the steel girder under the beam and then connected to the concrete beam through a very light steel plate that was attached under the concrete beam. The LVDTs and the load cells were calibrated by the manufacturer before the start of the testing phase. Furthermore, data acquisition scanners were used to record the data with a rate of 5 scans per second. Three scanners were used for each test, each scanner having 20 channels available; therefore, 60 channels were made available by setting up a network series of scanners together, using relay wires. The scanners have the capability

of acquiring test data within 1 millisecond at a 0.02 second scan intervals, resulting in accurate and reliable test results being obtained. Input channels in a single scanner were scanned consecutively at 0.04-ms and were stored in the RAM within a 1-ms window (vishaypg.com, 2016). Sensor connectors are responsible for transferring data from the surface and embedded strain gages, load cells, and LVDTs. These connectors were manually calibrated, set up, and then connected to the back of each scanner. Strain gage cards have built-in bridge completion for quarter and half bridges. After the setup was completed, the scanner was connected to a laptop using a “PC5101B PCMCIA” interface adapter. The laptop was equipped with StrainSmart, software, which records all the incoming data from the sensors connected to the scanners. Since different strain gages were used on steel and concrete, the resistance and variabilities in strain gage properties were defined for each test separately by the StrainSmart software. The assembly provided a complete data system for stress analysis.

Figure 41 Typical photo of data acquisition in this study

Similarly, small-scale beams were tested in accordance with the ASTM's Standard Test Method for Flexural Performance of Fiber-Reinforced Concrete, ASTM 1609. This involved setting up the 6-inch by 6-inch by 20-inch beam in a standard size fixture which

tightly held the beam. The fixture's predominant application was to hold the LVDTs while being securely fixed to the beam, which resulted in recording the mid-span deflection of the beam while the machine was moving up. Two flexure beam test standard iron-made crossheads were initially mounted to the MTS machine, as shown in Figure 42. The top hydraulic wedge was fixed, while the bottom hydraulic wedge moved upward, with a constant displacement rate. The support conditions for this test are roller and pin support. Two LVDTs were used, one on the back face of the beam and the other on the front face of the beam. The average deflection of the LVDTs was taken at the center of the beam; the deflection was recorded up to 1/150th of the span. The loading rate used for this experiment was 0.004 inch per minute, according to ASTM 1609.

The LVDTs were then connected to the scanner through sensor connectors, and the Vishay scanner transmitted recorded data to a laptop via an interface adapter. The MTS-Flex test scanner, which scanned the applied live load and the displacement of the hydraulic wedges, transmitted this data to the Vishay scanner via two high voltage cables.

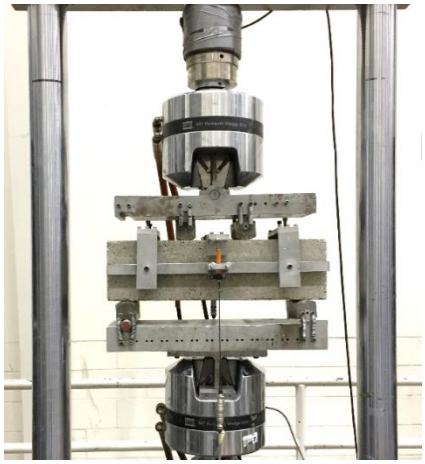

Figure 42 Typical photo of MTS machine

The cylinders were tested in a similar manner. A jig held two LVDTs while being tightly screwed to the cylinder, and the LVDT measured the displacement in the middle 5.5 inches of the cylinder. According to ASTM C39, the load rate for a 4-inch by 8-inch cylinder

is around 400 lbs./sec. The specifications mentioned in the standard test method for determining the compressive strength of cylinder specimens were closely followed in performing the test. After the jig was attached to the cylinder, the specimen was then placed under the 500 kips compression machine, a load cell was placed on top of the cylinder, and the LVDTs were mounted onto the jig, as shown in Figure 43. A continuous axial load of 35 psi/sec was applied, and the load cell and the LVDTs transmitted data to the scanner via sensor connectors. The load-deflection data was recorded and transmitted to the laptop via an interface adapter, using StrainSmart software, as shown in Figure 44.

Figure 43 Typical photo of a 500 kip compression machine for compressive cylinders

Figure 44 Typical photo of data acquisition for compressive cylinders

Similarly, the splitting tensile strength of cylinders was conducted according to ASTM's C469 specifications, using a load controlled compression machine with a load capacity of 60 kips, as shown in Figure 45. A diametric compressive force was applied along the length of the specimen at a constant loading rate of 100 to 200 psi/minute until failure occurred in tension since the loaded area was under tri-axial compression. The maximum load achieved at the failure was recorded and used in calculating the splitting tensile strength of specimens.

Figure 45 Typical photo of splitting test for cylinders

4 EXPERIMENTAL RESULTS AND ANALYSIS

4.1 Large-Scale Beams

The comparison of the shear strength of all of the large-scale beams is shown graphically in Figure 46. The shear strength is half of the ultimate load applied at the center of the concrete beams. The RCS beams with minimum stirrups increased the shear capacity by 31%, compared with the control beams, which was the greatest increase among all the specimens. SNFRC beams with a volume fraction of 0.75% increased the shear capacity by 29% compared to the control beams and can be considered as an alternate replacement for the specimens with minimum stirrups. In this study, the color blue represents the specimens without fiber, orange represents specimens with 0.5% synthetic fiber, red represents the specimens with 0.75%, and green represents the large-scale beams with minimum stirrups.

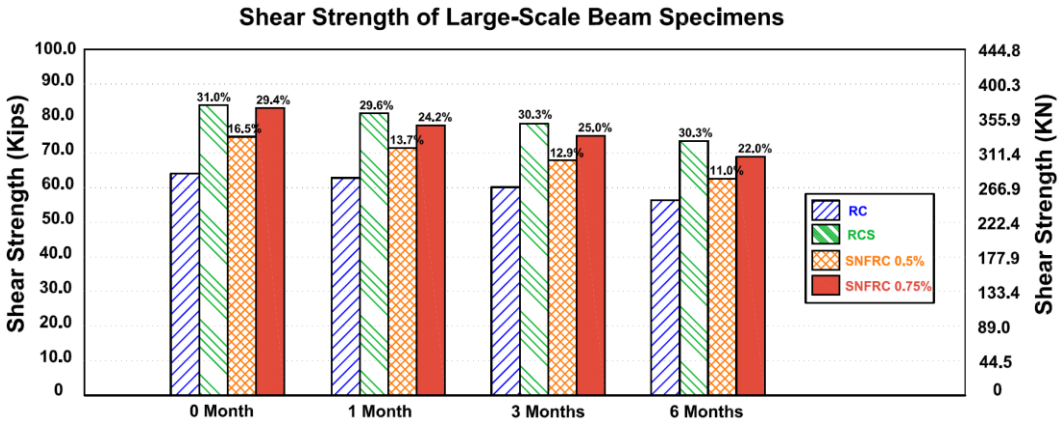

Figure 46 Shear strength comparison of large-scale beams subjected to 1 month, 3 months, and 6 months of accelerated aging

Shear strength degradation of all the large-scale beams is shown in Figure 47. More degradation over time was observed for higher volume fractions of polypropylene fibers.

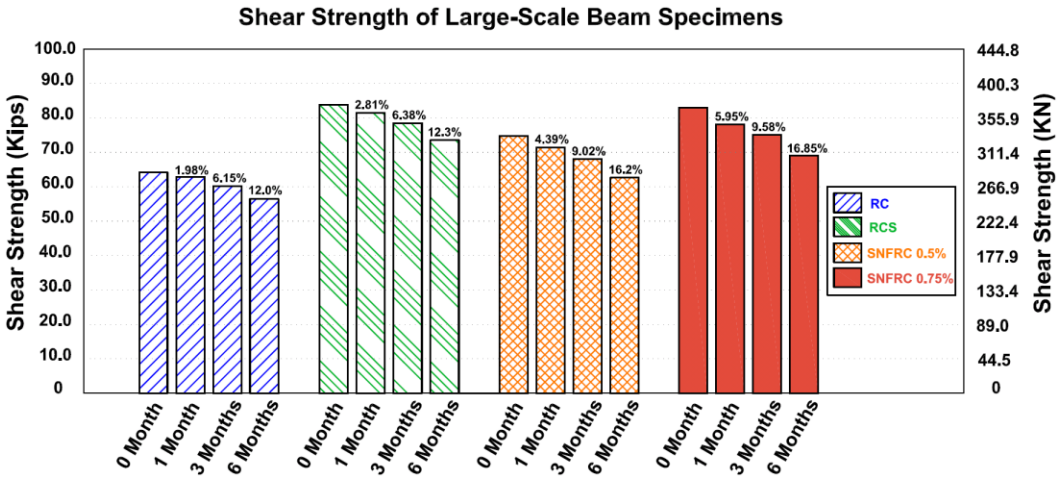

Figure 47 Degradation of shear strength of large-scale beams subjected to 1 month, 3 months, and 6 months of accelerated aging

The degradation of the shear strength of the RC control beams and RCS beams with minimum stirrups were similar. The SNFRC beams with a volume fraction of 0.75% were degraded, and a reduction in shear strength of 16.8% was observed after being subjected to accelerating aging conditions for 6 months. This was considered the highest reduction of shear strength among all the other specimens. It was concluded that the higher volume fraction of fibers results in more shear strength degradation over time. On the other hand, the shear capacity of specimen increases initially with a higher volume fraction of fibers mixed into the body of concrete. There was no corrosion or rust for the rebars embedded in concrete due to the adequate cover for the rebars. The failure load and shear capacity of all of the large-scale beams are summarized in Table 4. The shear stresses were calculated by half of the applied load (shear load) by the product of beam effective depth and beam width $\left(\frac{.5\ V_u}{b\ .\ d}\right)$.

Table 4 Failure load and shear capacity of all of the large-scale beams in this study

Phase	BM#	BM Type	Failure Load (Kips)	Shear Strength (Kips)	Shear Stress (psi)	Ave. Shear Strength (Kips)
I (No Aging, 28 Days Curing)	1	RC	123.8	61.9	410	64.1
	2	RC	132.8	66.4	440	
	3	RCS	166.9	83.4	550	83.8
	4	RCS	168.5	84.3	550	
	5	SNFRC 0.5%	147.1	73.5	480	74.7
	6	SNFRC 0.5%	151.9	76.0	500	
	7	SNFRC 0.75%	164.3	82.1	540	83.0
	8	SNFRC 0.75%	167.8	83.9	550	
II (1month Aging)	9	RC	128.3	64.2	420	62.9
	10	RC	123.2	61.6	400	
	11	RCS	163.9	81.9	540	81.5
	12	RCS	162.1	81.0	530	
	13	SNFRC 0.5%	144.2	72.1	470	71.5
	14	SNFRC 0.5%	141.6	70.8	460	
	15	SNFRC 0.75%	161.0	80.5	530	78.1
	16	SNFRC 0.75%	151.3	75.6	500	
III (3months Aging)	17	RC	122.9	61.4	400	60.2
	18	RC	118.0	59.0	390	
	19	RCS	158.8	79.4	520	78.5
	20	RCS	155.2	77.6	510	
	21	SNFRC 0.5%	136.6	68.3	450	68.0
	22	SNFRC 0.5%	135.5	67.7	440	
	23	SNFRC 0.75%	148.9	74.5	490	75.1
	24	SNFRC 0.75%	151.3	75.7	500	
IV (6 months of aging)	25	RC	121.3	60.6	400	56.4
	26	RC	104.5	52.3	340	
	27	RCS	145.3	72.7	480	73.6
	28	RCS	148.9	74.4	490	
	29	SNFRC 0.5%	132.3	66.2	430	62.6
	30	SNFRC 0.5%	118.2	59.1	390	
	31	SNFRC 0.75%	133.0	66.5	440	69.0
	32	SNFRC 0.75%	143.1	71.5	470	

The load-deflection response of RC beam #1, without aging, at quarter-length and mid-length of the beam is shown in Figure 48. Graphs for all the 32 large-scale beams are shown in Appendix E.

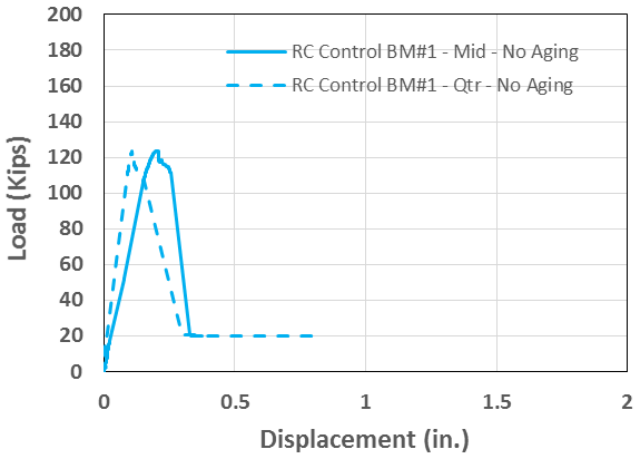

Figure 48 Load-deflection response at quarter and mid-span for RC beam #1 without aging

The exponential trend lines or regression lines for the shear strength degradation of all of the large-scale beams subjected to 0 month, 1 month, 3 months, and 6 months of accelerated aging conditions are shown in Figure 49. The SNFRC 0.75% concrete beams have the sharpest curve, which translates into more degradation over time.

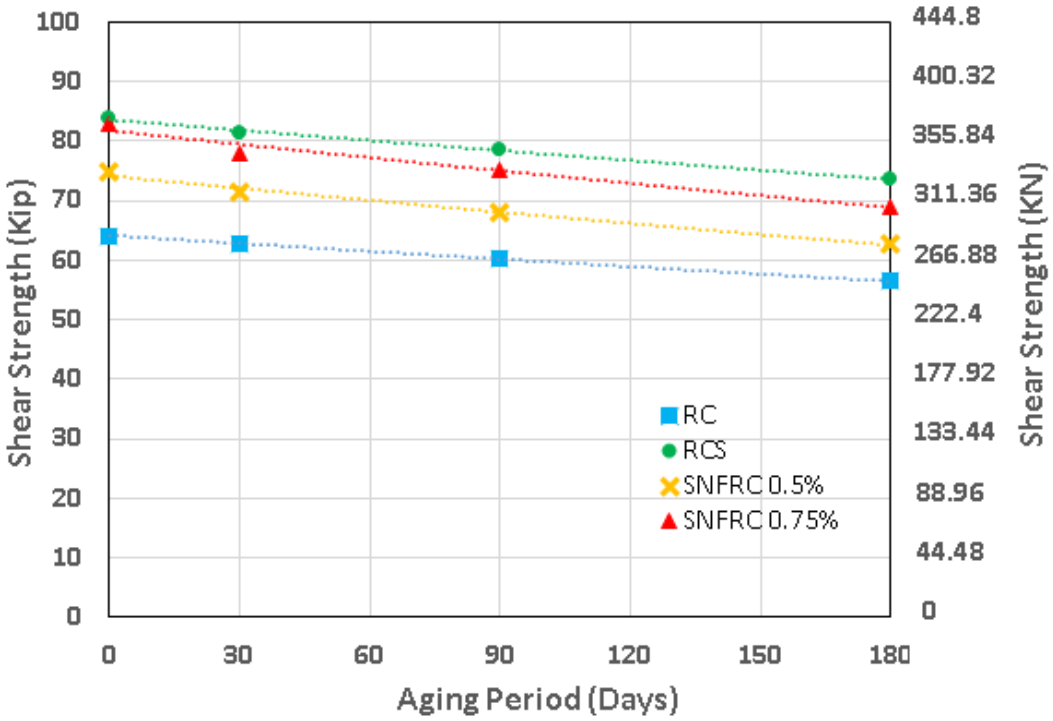

Figure 49 Shear strength degradation curve of large-scale beams subjected to 0 day, 30 days, 90 days, and 180 days of accelerated aging

The shear load-deflection response of the large-scale beams subjected to 0 month, 1 month, 3 months, and 6 months of accelerated aging for RC control beams, RCS with minimum stirrups, SNFRC 0.5%, and SNFRC 0.75% are shown in Figure 50. The failure of the RC control beams without fibers was more brittle than that of the beams with fibers. A sudden sharp drop in the graph was observed after the load reached the ultimate load, which indicates the shear failure of the specimens. The beams with synthetic fibers showed a gradual increase in the slope of the graph after the ultimate load; this behavior was observed only in the beams with synthetic fibers.

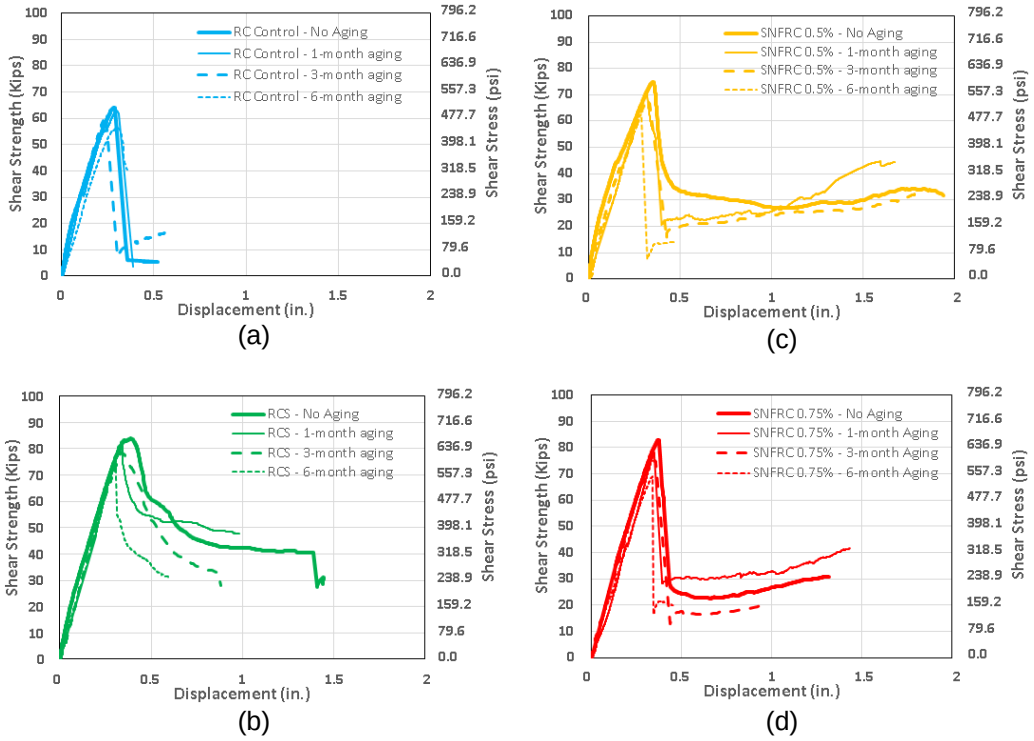

Figure 50 Shear load-deflection response of the large-scale beams subjected to 0 month, 1 month, 3 months, and 6 months of accelerated aging for beams: (a) RC Control, (b) RCS with minimum stirrups, (c) SNFRC 0.5%, and (d) SNFRC 0.75%

As illustrated in Figure 51, the addition of fibers to the concrete can increase the post strength of the beams after shear failure occurs. A very brittle and sudden failure was observed in the RC control beams, and this failure mode was improved to a ductile mode by the introduction of fibers. The shear load-deflection response of all of the large-scale beams in varying phases of accelerated aging and 100 years in actual weathering are shown in this figure.

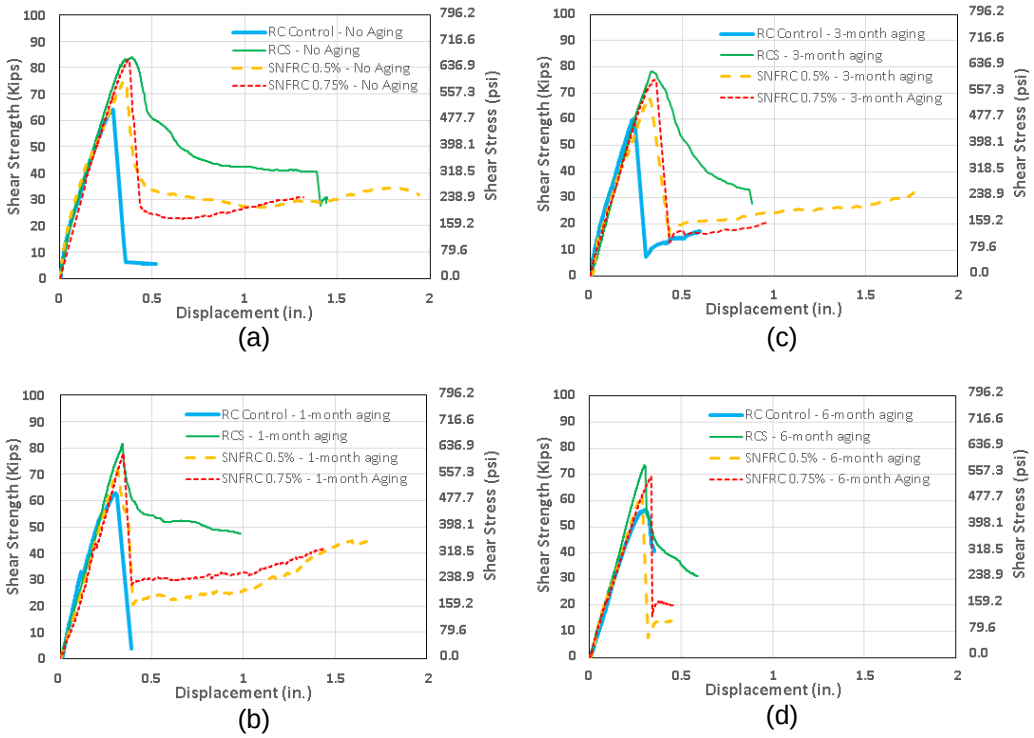

Figure 51 Shear load-deflection response of the all of the large-scale beams: (a) Phase 1, without aging; (b) Phase 2, 1 month of aging; (c) Phase 3, 3 months of aging; and (d) Phase 4, 6 months of aging

4.1.1 Failure Mode and Mechanism

All of the 32 large-scale beams failed in shear; no single failure was observed in flexure. The initial crack in the large scale specimens occurred within the middle 15 inches of the beams' centerline, which was a shear-flexural cracking. The pattern and propagations of all of the visible cracks were precisely monitored during the testing of all of the specimens.

The crack pattern for the RC control beam in Phase 1 is shown in Figure 52. The crack pattern and crack propagation of all 32 large-scale beams are shown in appendix A.

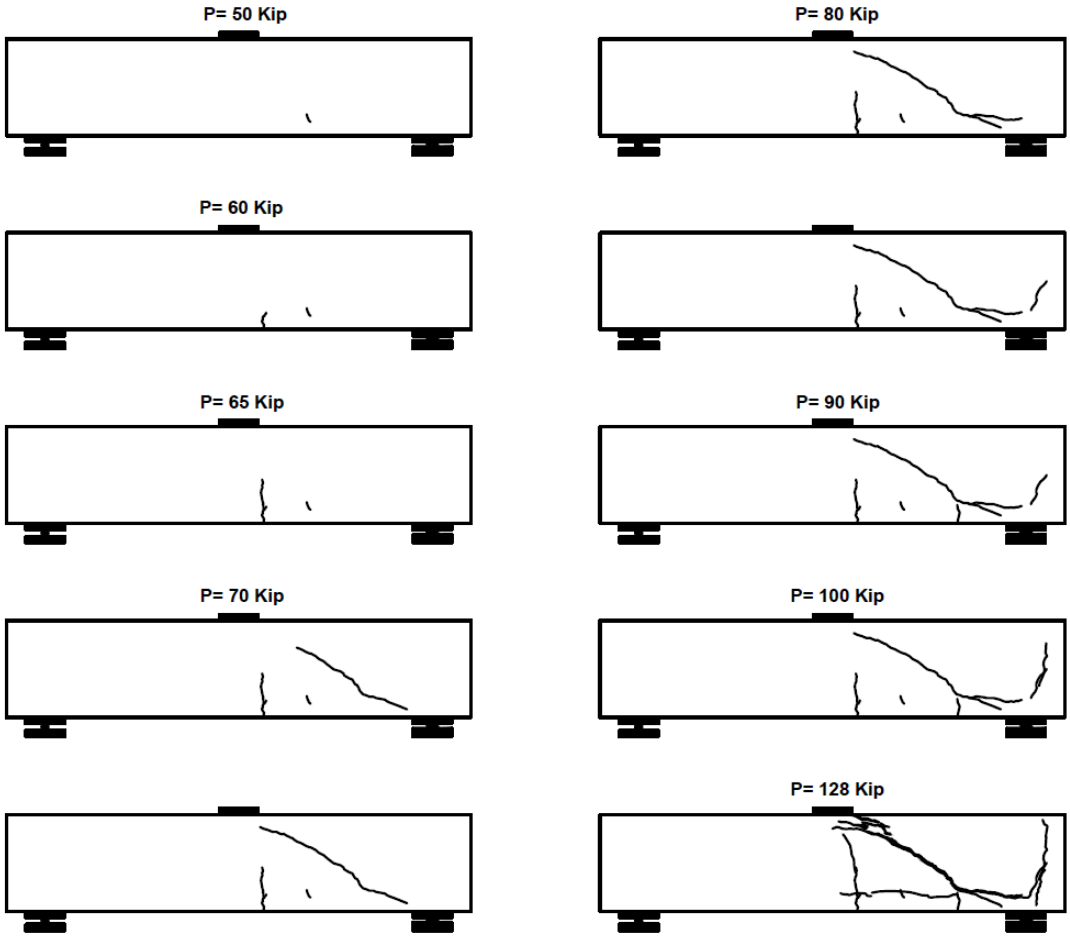

Figure 52 Crack pattern for RC beam #1

It was observed that the first crack in the majority of the beams started at the mid-span and then propagated towards the end supports. As the load was increased, the flexural cracks started to incline as shear-flexural cracks, which are commonly referred to as diagonal cracks. RC control beams failed with a single diagonal crack, while SNFRC beams failed with multiple cracks and concrete crushing in the compression zone. The difference in fiber reinforcement was clearly evident during testing, as the SNFRC beams did not fail after the first major diagonal crack and went on to resist higher loads with higher deflections. SNFRC beams showed ductile behavior, especially with a volume fraction of

0.75%. Moreover, it was observed that the diagonal cracks in the RC control beams were steeper, whereas diagonal cracks in RCS and SNFRC beams were relatively flatter. This shows a similar crack behavior between fiber-reinforced and conventional shear stirrups. In general, the crack at failure was larger in the RC and RCS beams, whereas the crack widths in the SNFRC beams were relatively smaller. This is due to a phenomena known as fiber-bridging, where fibers create a bridge and resist the separation of two splitting surfaces. The fibers resist principal stresses once inclined cracks start to open up until they are pulled out or broken. Figure 53 shows the bridging of fibers in the SNFRC beam after failure.

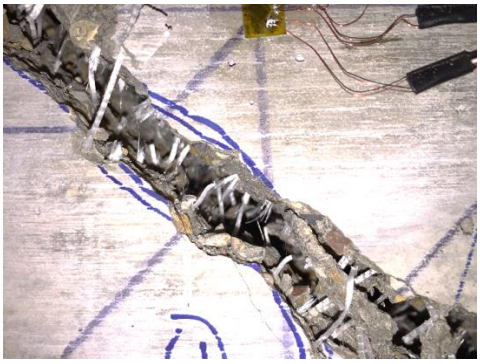

Figure 53 Typical photo of bridging the crack by using polypropylene fibers in the large-scale beam specimens

In addition, the RC control beams failed due an abrupt brittle web-shear crack. The introduction of macro-synthetic fibers into the concrete mixture altered the mode of failure from web-shear cracking to a more flexure-shear cracking. In RC control beams, where web-shear cracking was the failure mode because the tensile strength of the concrete could not resist the maximum shear, stress and failure occurred very suddenly. However, flexure-shear failure occurred in SNFRC beams. The cracks started in the mid-span and gradually inclined towards the edge of the loading plate and extended towards the edge of the support plate. In addition, failures in RC beams were explosive, whereas failures in

SNFRC beams were non-explosive and gradual. In the case of beams with stirrups, the diagonal cracking was extreme; on the other hand, fibers in the SNFRC beams prevented shear failure. Moreover, SNFRC beams failed with more than one diagonal crack, which indicated the redistribution of forces.

A photo of the typical RC control beam at failure is shown in Figure 54, and the rest of the beams are shown in Appendix J.

Figure 54 Typical photo of RC control beam at failure

The crack width of the RC control beam at failure was measured using image processing, as shown in Figure 55. The crack widths of all of the specimens in inches are graphically shown in Appendix D.

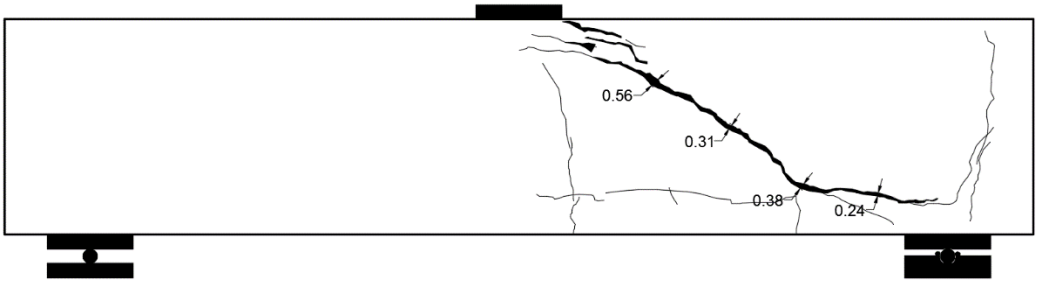

Figure 55 Crack pattern at failure for RC beam #1

4.1.2 Strains in Concrete

The rosette strain gages recorded the strain on the surface of the concrete during testing, and the results up to failure are shown in Figure 56 for RC control beams in Phase 1. The load-strain responses of all 32 large-scale beams are shown in Appendix I.

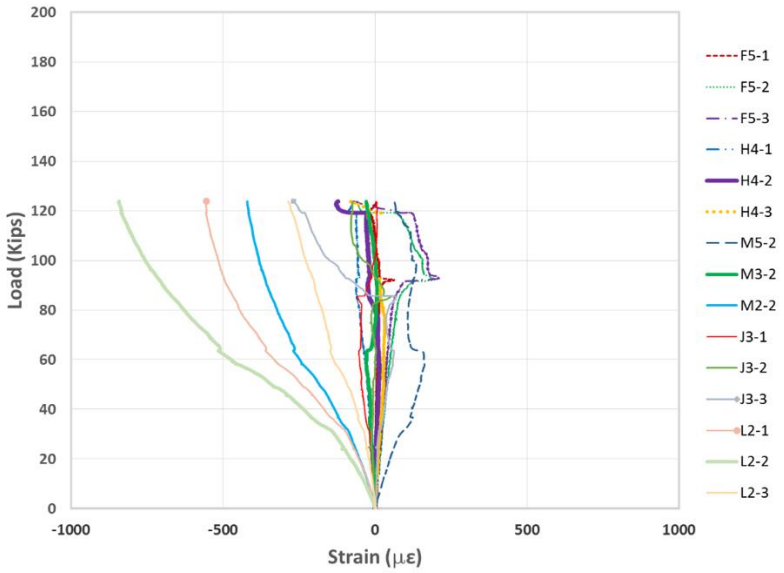

Figure 56 Load-strain response for RC beam #1 without aging

Maximum principal strain (ε_p), minimum principal strain (ε_Q), and shear strain (γ) of the rosette gages in this study were calculated by the following formulas:

$$\frac{\varepsilon_P + \varepsilon_Q}{2} + \frac{\varepsilon_P - \varepsilon_Q}{2} . \cos(2 . \theta) = \varepsilon_1$$

$$\frac{\varepsilon_P + \varepsilon_Q}{2} + \frac{\varepsilon_P - \varepsilon_Q}{2} . \cos(2 . (\theta + 45\ \text{deg})) = \varepsilon_2$$

$$\frac{\varepsilon_P + \varepsilon_Q}{2} + \frac{\varepsilon_P - \varepsilon_Q}{2} . \cos(2 . (\theta + 90\ \text{deg})) = \varepsilon_3$$

$$\gamma = |\varepsilon_P - \varepsilon_Q|$$

For example, for RC control beam No. 1, the calculation for the location of F5 is shown below:

ε_1=41.34με, ε_2=131.12με, ε_3=98.93με

$$\begin{bmatrix} \varepsilon_p \\ \varepsilon_Q \\ \theta \end{bmatrix} := \text{find}(\varepsilon_p, \varepsilon_Q, \theta) = \begin{bmatrix} 137.6 \\ 2.7 \\ 2.1 \end{bmatrix}$$

θ = 2.1 radian = 122.36 degree

$\theta_{p,max}$ = -122.36 degree

$\theta_{p,min}$ = 57.64 degree

$\theta_{p,\gamma}$ = -32.36 degree

$\gamma = |\varepsilon_p| - |\varepsilon_Q| = 134.88\ \mu\varepsilon$

$$y\_dir1 := \frac{\varepsilon_p - \varepsilon_Q}{2} \cdot \sin(2 \cdot \theta) = -13.5$$

$$y\_dir2 := \frac{\varepsilon_p - \varepsilon_Q}{2} \cdot \sin(2 \cdot (\theta + 45\ deg)) = -36.78$$

$$y\_dir3 := \frac{\varepsilon_p - \varepsilon_Q}{2} \cdot \sin(2 \cdot (\theta + 90\ deg)) = 13.5$$

The Mohr's circles of the stacked rosette strain gages are shown in Figure 57 for the three orientations of the strains.

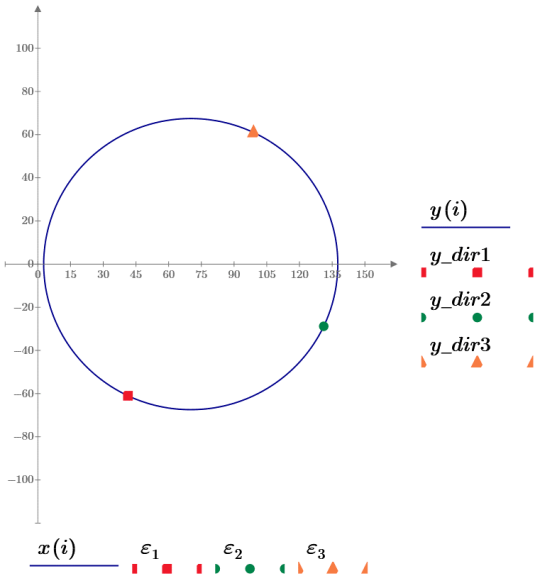

Figure 57 Mohr's circle for stacked rosette concrete strain gages in RC control beam #1, location F5

Maximum principal strain (ε_p), minimum principal strain (ε_Q), and shear strain (γ) of the rosette gages are shown tabulated in Appendix B. As shown in Figure 58 and according to ASTM 1609, the ratio of the principal strain to the cracking tensile strain, (ε_p / ε_t), is very close to 1 (average=1.01, standard deviation=0.08). This leads to the conclusion that once the principal strain reaches the maximum cracking tensile, concrete cracks.

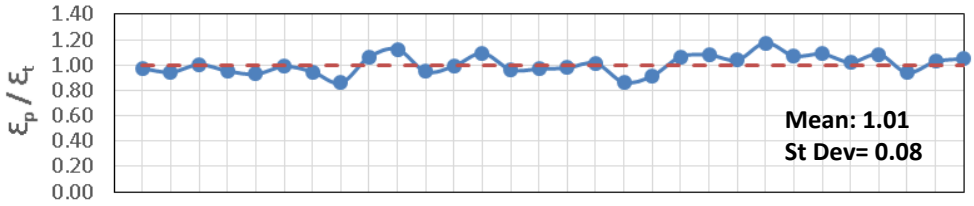

Figure 58 ε_p / ε_t ratio for the concrete rosette strain gages specified in Table 9

The maximum and minimum principal strain orientations of the concrete strain gages are shown in Figure 59. As shown, the maximum principal strain was perpendicular to the crack orientation for the cracks that occurred adjacent to the strain gages. In other words, cracks occur when the maximum principal strains reach the tensile strength of concrete. All the rest of the results are shown in Appendix C.

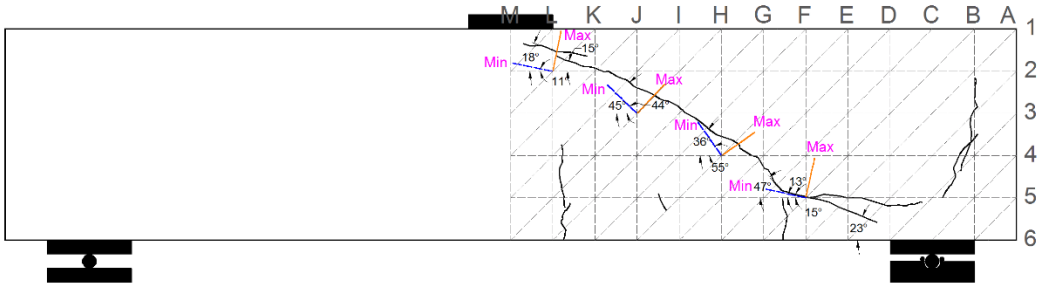

Figure 59 Maximum and minimum principal strain orientations for RC beam #1

4.1.3 Strain in Steel Rebars

The strain gages recorded the strains of the top and bottom longitudinal bars at 6 inch intervals in the half span only. The strain on the surface of the rebars embedded in the large-scale beams in the middle of the span (M5) was recorded less than 0.002 under

ultimate load for all of the specimens, showing that the longitudinal bars were not yielded. On the other hand, high strains were monitored for the steel strain gages installed on the stirrups, and some of the gages reached strain of 0.15 after failure, showing that the stirrups were yielded. The load-strain response for RC control beam #1 without aging is shown in Figure 60. All of the steel strains of the beam specimens are plotted in Appendix H.

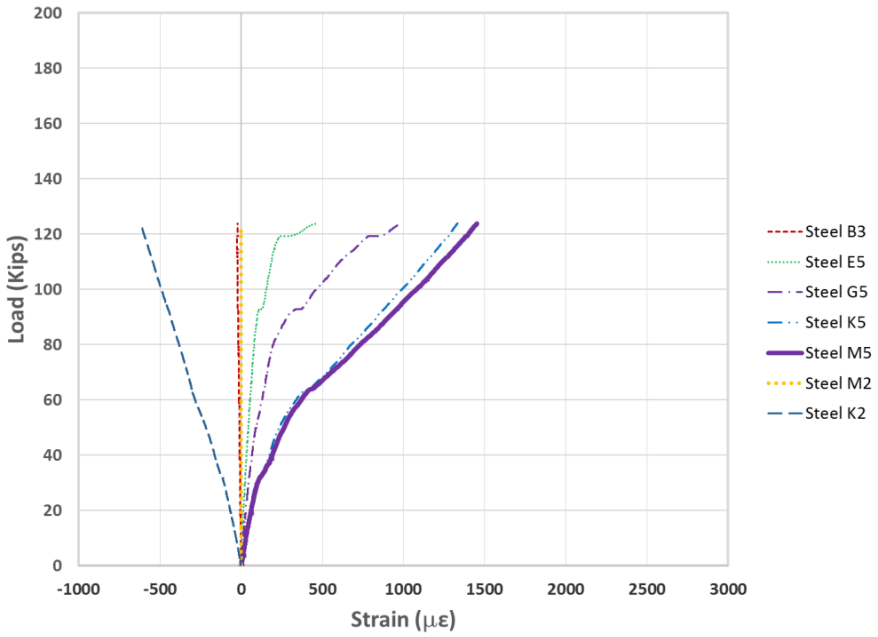

Figure 60 Load-strain response for RC control beam #1 without aging (Phase 1)

4.2 Tensile Strength of the Cylinder Specimens

The splitting tensile strength of the cylinder specimens with different volume fractions of polypropylene fibers and subjected to accelerated aging with different temperatures is summarized in Table 5. (Per ASTM C469.)

Table 5 Details of tensile strength of all the cylinder specimens in this study

Temperature	Aging Period	Specimen Type	Tensile Strength (psi)			Average Tensile Strength (psi)
20°C (68°F)	No Aging (28 Days Curing)	Plain Conc.	525.0	534.3	522.9	527.4
		0.5% SNFRC	562.5	601.0	582.5	582.0
		0.75% SNFRC	715.4	629.9	727.8	691.0
50°C (122°F)	14 Days	Plain Conc.	520.8	518.8	521.2	520.3
		0.5% SNFRC	575.9	552.1	585.6	571.2
		0.75% SNFRC	654.9	699.7	678.1	677.6
	30 Days	Plain Conc.	516.5	520.1	515.3	517.3
		0.5% SNFRC	565.2	571.7	558.7	565.2
		0.75% SNFRC	637.5	679.2	670.8	662.5
	90 Days	Plain Conc.	488.7	478.1	490.0	485.6
		0.5% SNFRC	556.6	498.0	532.5	529.0
		0.75% SNFRC	545.7	680.8	650.6	625.7
	180 Days	Plain Conc.	603.0	362.9	420.9	462.3
		0.5% SNFRC	539.7	463.5	482.0	495.1
		0.75% SNFRC	519.1	605.5	624.3	583.0
70°C (158°F)	14 Days	Plain Conc.	464.4	449.6	452.2	455.4
		0.5% SNFRC	484.8	464.3	497.7	482.3
		0.75% SNFRC	576.5	569.9	563.4	569.9
	30 Days	Plain Conc.	387.0	384.8	405.1	392.3
		0.5% SNFRC	404.2	385.3	399.1	396.2
		0.75% SNFRC	477.5	482.8	411.6	457.3

Comparison of tensile strength of concrete cylinder specimens subjected to 0 day, 14 days, 1 month, 3 months, and 6 months of accelerated aging at 50°C (122°F)

The splitting tensile strength of concrete cylinder specimens subjected to 0 day, 14 days, 1 month, 3 months, and 6 months of accelerated aging at 50°C (122°F) with varying volume fraction of polypropylene fibers is compared in Figure 61. The SNFRC 0.5%

and SNFRC 0.75% specimens increased the tensile strength of plain concrete after 28 days of curing by 10.3% and 31.0%, respectively. The efficiency of the fibers decreased as the aging period increased.

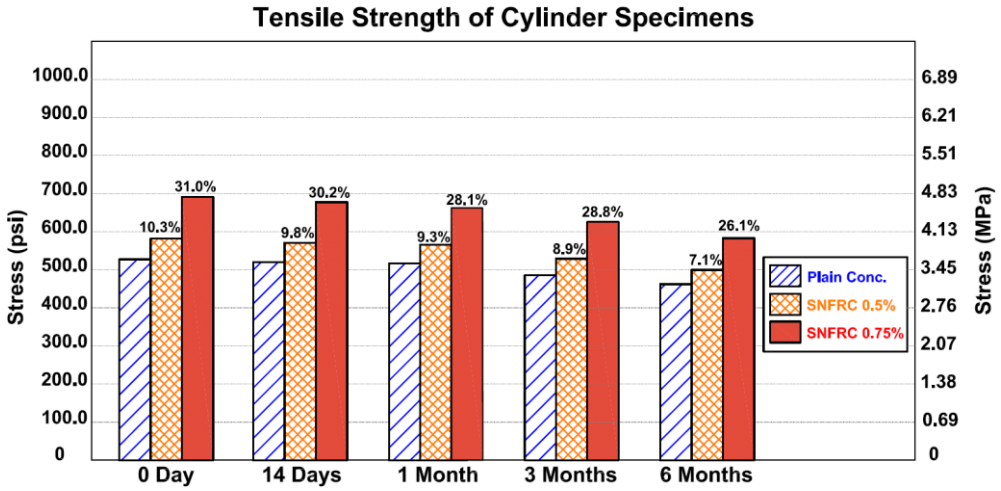

Figure 61 Comparison of tensile strength of concrete cylinder specimens subjected to 0 day, 14 days, 1 month, 3 months, and 6 months of accelerated aging at 50°C (122°F)

The tensile strength degradation of the concrete cylinder specimens subjected to 14 days, 1 month, 3 months, and 6 months of accelerated aging at 50°C (122°F) is shown in Figure 62. As more fibers were added to concrete, more degradation over time was observed. On the other hand, the addition of fibers initially increased the strength of the specimens. In summary, it is more beneficial to consider 0.75% volume fraction of fibers than 0.5%.

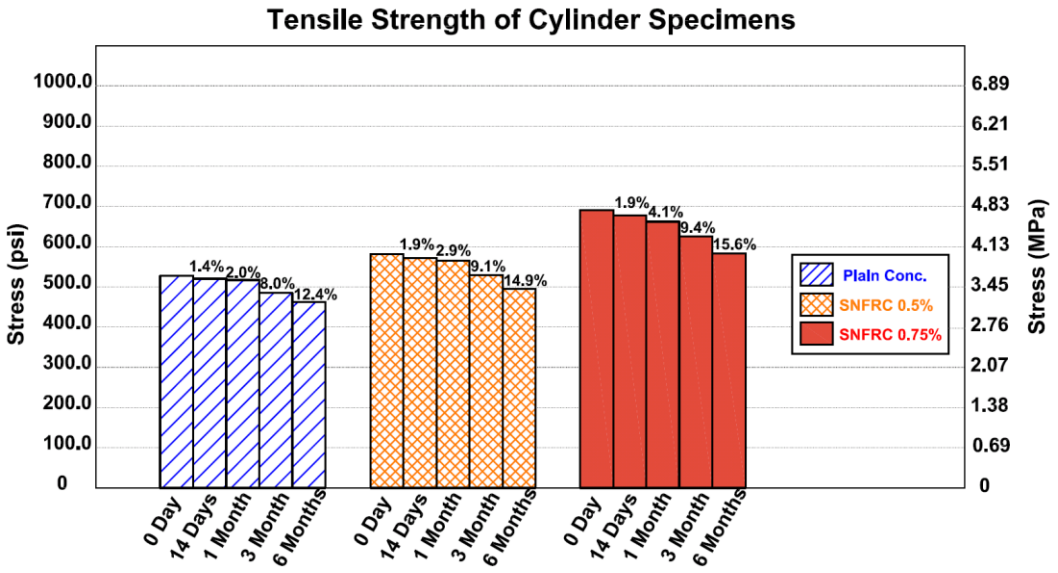

Figure 62 Tensile strength degradation of the concrete cylinder specimens subjected to 14 days, 1 month, 3 months, and 6 months of accelerated aging at 50°C (122°F)

The tensile strength of concrete cylinder specimens subjected to 0 day, 14 days, and 30 days of accelerated aging at 70°C (158°F) are compared graphically in Figure 63. The cylinder specimens were aged at this temperature in two periods, 14 days and 30 days. Due to the high temperature of the tub, a very large amount of water evaporated daily; therefore, the tub was inspected regularly. Also, the circuit breaker in the curing room tripped frequently due to the high wattage consumption of the immersion heaters, so it had to be monitored. The tensile strength degradation of the concrete cylinder specimens subjected to 0 day, 14 days, and 30 days of accelerated aging at 70°C (158°F) is shown in Figure 64. It was found that the rate of the degradation at this temperature was much higher than the rate of degradation at 50°C (122°F), proving that temperature plays a vital role in degradation of the specimens.

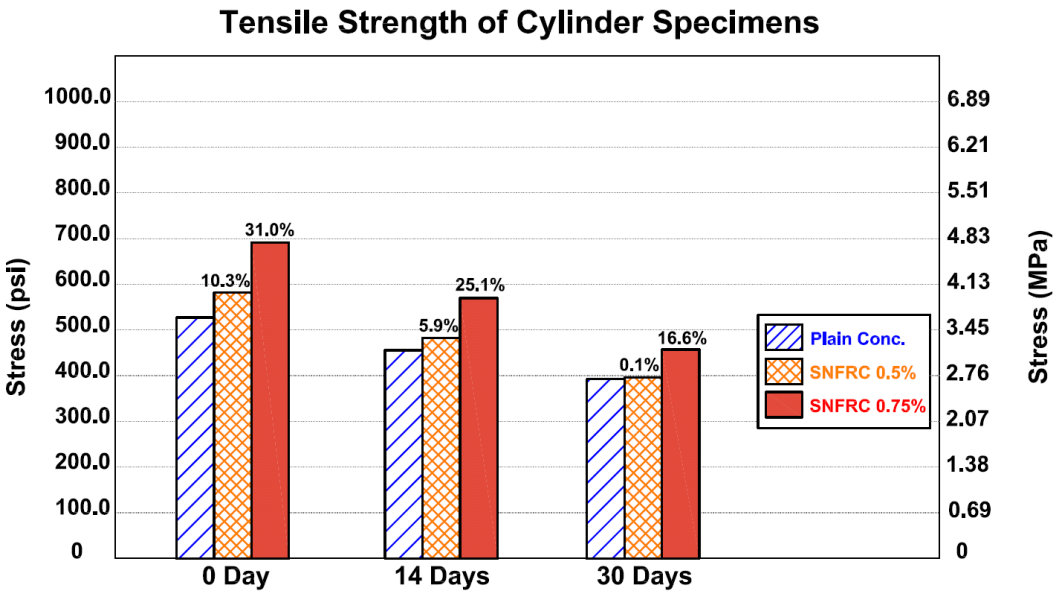

Figure 63 Comparison of tensile strength of concrete cylinder specimens subjected to 0 day, 14 days, and 30 days of accelerated aging at 70°C (158°F)

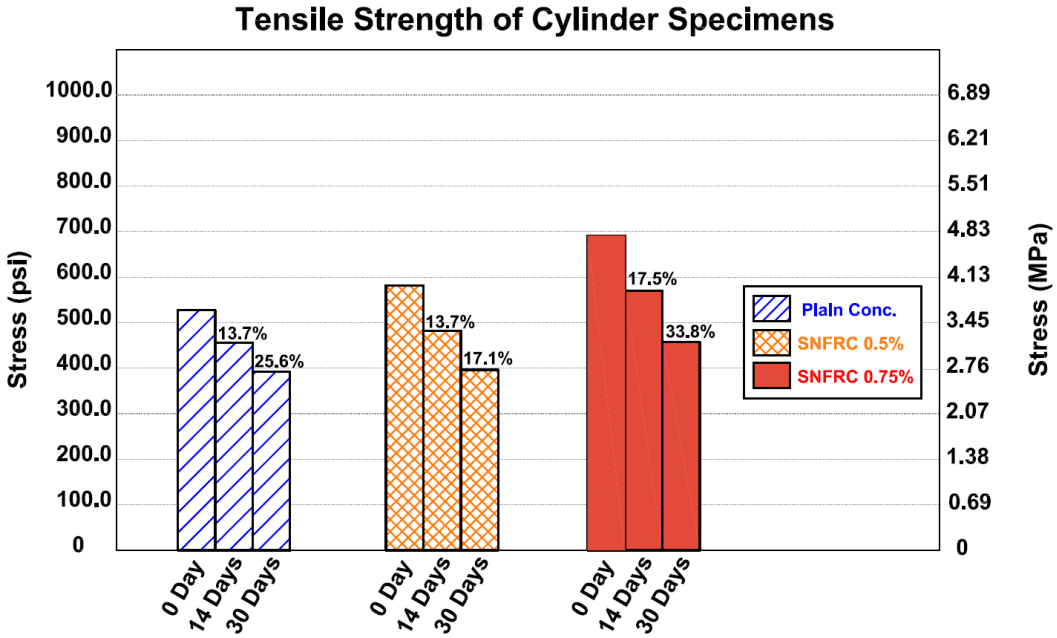

Figure 64 Tensile Strength degradation of the concrete cylinder specimens subjected to 0-day, 14 days, and 30 days of accelerated aging at 70°C (158°F)

4.3 Compressive Strength of the Cylinder Specimens

The compressive strength of all of the cylinder specimens with different volume fractions of polypropylene fibers and subjected to accelerated aging at 50°C (122°F) is summarized in Table 6.

Table 6 Compressive strength of all the cylinder specimens in this study

Aging Period	Specimen Type	Compressive Strength (ksi)					Average Compressive Strength (ksi)
Phase I (No Aging, 28 Days Curing)	Plain Conc.	4.96	5.01	4.85	4.92	_	4.94
	SNFRC 0.5%	5.56	5.16	5.42	_	_	5.38
	SNFRC 0.75%	5.59	5.65	5.35	_	_	5.53
PHASE II (1 month aging)	Plain Conc.	4.77	4.80	4.93	4.97	_	4.87
	SNFRC 0.5%	5.30	5.17	5.03	5.10	5.43	5.21
	SNFRC 0.75%	5.16	5.10	5.56	5.34	5.39	5.31
PHASE III (3 months aging)	Plain Conc.	4.73	4.93	4.99	4.45	_	4.77
	SNFRC 0.5%	5.01	4.80	5.00	4.83	_	4.91
	SNFRC 0.75%	4.95	5.00	5.09	5.01	_	5.01
PHASE IV (6 months aging)	Plain Conc.	4.51	4.71	4.59	_	_	4.60
	SNFRC 0.5%	4.36	4.69	4.90	_	_	4.65
	SNFRC 0.75%	4.65	4.55	4.88	_	_	4.69

The specimens with volume fractions of 0.75% and 0.5% increased the compressive strength of the 28-day cured concrete by 12.0% and 8.9%, respectively, compared to the control specimens. As the specimens were subjected to more aging, the strength increase was reduced to 4.7% and 1.1% for the specimens with a volume fraction of 0.75% and 0.5%, respectively, as shown in Figure 65.

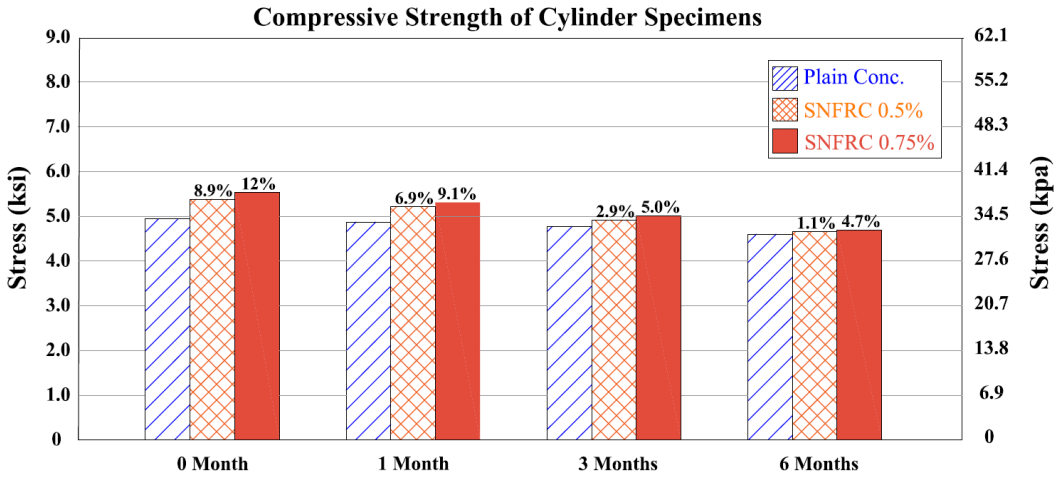

Figure 65 Comparison of compressive strength of concrete cylinder specimens subjected to 0-month, 1 month, 3 months, and 6 months of accelerated aging

The compressive strength degradation of the specimens with varying volume fractions and subjected to different accelerated aging periods is shown in Figure 66. The specimens with higher volume fractions of fibers were subjected to more degradation, and specimens without fibers showed the least reduction of strength.

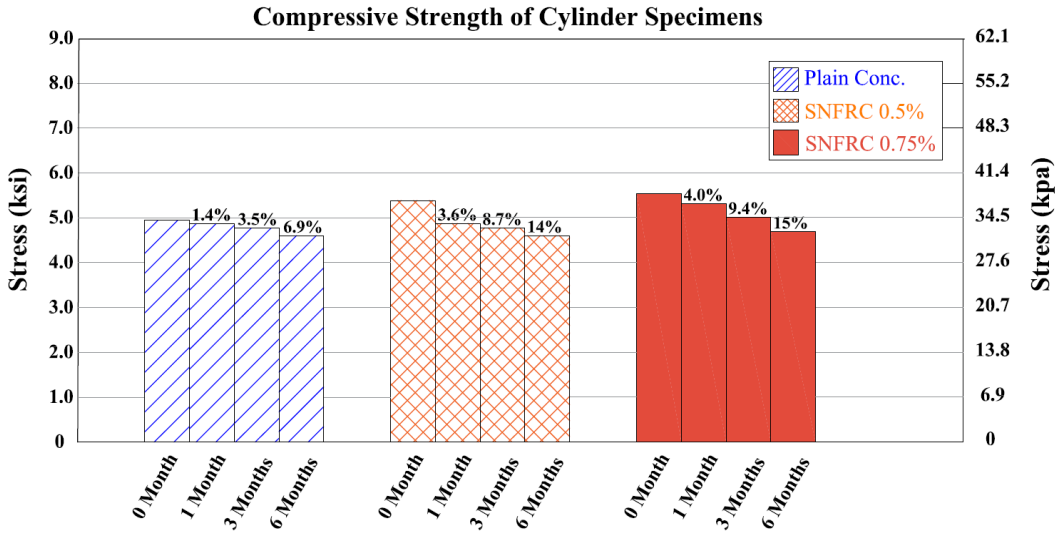

Figure 66 Compressive strength degradation of the concrete cylinder specimens subjected to 1 month, 3 months and 6 months of accelerated aging

Compressive strength-strain response of average plain concrete cylinders subjected to 0-month, 1 month, 3 months and 6 months of accelerated aging for the specimens, with varying volume fractions, is shown in Figure 67. The modulus of E_c=4,189,411 was found for all of the specimens with different volume fractions of polypropylene. The difference between the modulus of elasticity of specimens was insignificant (less than 1%) since the volume fraction of fibers was negligible (0.0075 volume of concrete). The compressive stress-strain response of all of the concrete cylinders in this study are plotted in Appendix N.

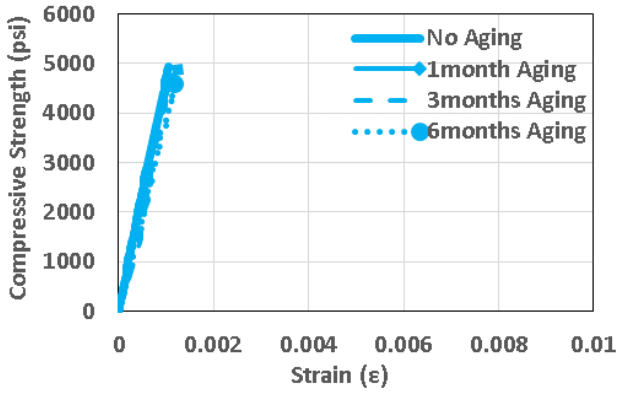

(a)

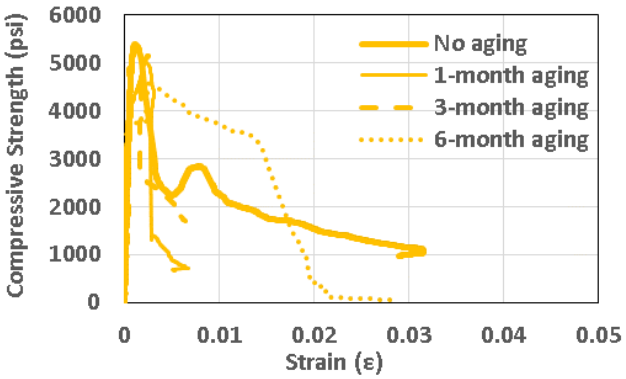

(b)

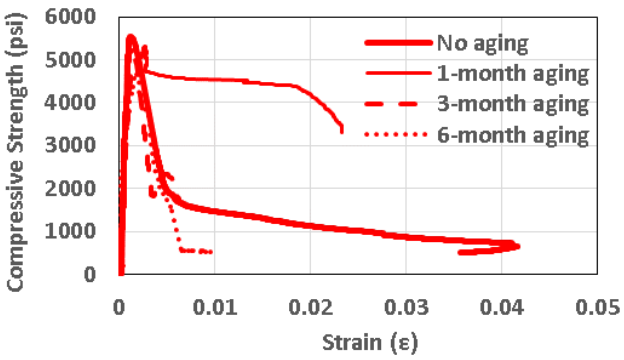

(c)

Figure 67 Compressive strength-strain response of average plain concrete cylinders subjected to 0 month, 1 month, 3 months, and 6 months of accelerated aging for the specimens with: (a) V_f =0, plain; (b) V_f =0.5% SNFRC; (c) V_f =0.75% SNFRC

4.4 Tensile Strength of Flexural Specimens

The tensile strength of the flexural beam (modulus of rupture) specimens were calculated according to ASTM 1609 (equation 3):

$$f = \frac{P \,.\, L}{b \,.\, d^2} \tag{3}$$

Where:

f: strength (psi)

P: the first-peak load (lbs)

L: the span length of the beam, which was 18 inches in this study

b: the width of the beam, which was 6 inches in this study

d: the depth of the beam, which was 6 inches in this study

The tensile strength (modulus of rupture) of all the flexural beams were calculated and were summarized in the Table 7.

Table 7 Flexural results of beam specimens

Aging Period	Specimen Type	Tensile Strength (psi)	Average Tensile Strength (psi)
PHASE I (No aging, 28 Days Curing)	Plain Conc.	765.01	752.0
		750.30	
		740.70	
	0.5% SNFRC	810.90	812.2
		795.12	
		830.53	
	0.75% SNFRC	936.70	940.8
		944.22	
		941.50	
PHASE II (1 month aging)	Plain Conc.	722.21	728.9
		735.75	
		731.88	
		728.58	
		726.00	
	0.5% SNFRC	766.22	772.4
		778.50	
	0.75% SNFRC	879.08	874.1
		869.17	
PHASE III (3 months aging)	Plain Conc.	709.98	696.2
		714.92	
		701.17	
		696.67	
		658.33	
	0.5% SNFRC	761.04	759.5
		757.98	
	0.75% SNFRC	819.52	821.6
		823.67	
PHASE IV (6 months aging)	Plain Conc.	638.42	640.0
		635.33	
		657.75	
		634.25	
		634.00	
	0.5% SNFRC	679.77	672.9
		666.10	
	0.75% SNFRC	765.92	770.3
		774.67	

The specimens with volume fractions of 0.75% and 0.5% increased the flexural strength of the 28-day cured concrete by 25.0% and 8.0%, respectively, compared to the control specimens. As the specimens were subjected to more aging, the strength increase was reduced to 20% and 5% for the specimens with a volume fraction of 0.75% and 0.5%, respectively, as shown in Figure 68.

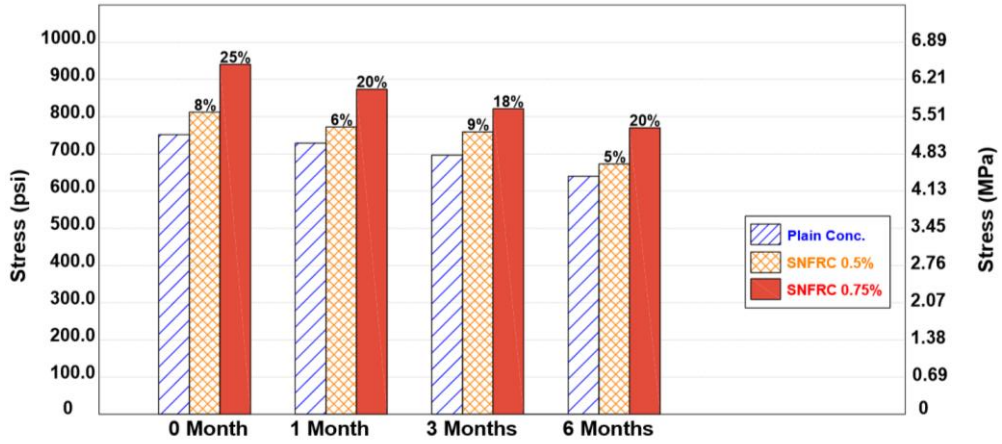

Figure 68 Comparison of tensile strength of flexural beams subjected to 1 month, 3 months, and 6 months of accelerated aging

The flexural strength degradation of the specimens with varying volume fractions of fibers and subjected to different accelerated aging periods is shown in Figure 69. The specimens with a higher volume fraction of fibers (0.75%) were subjected to more degradation, and specimens without fibers (control) showed the least reduction of strength. All of the load-deflection responses of small-scale flexural beams are summarized in Appendix O.

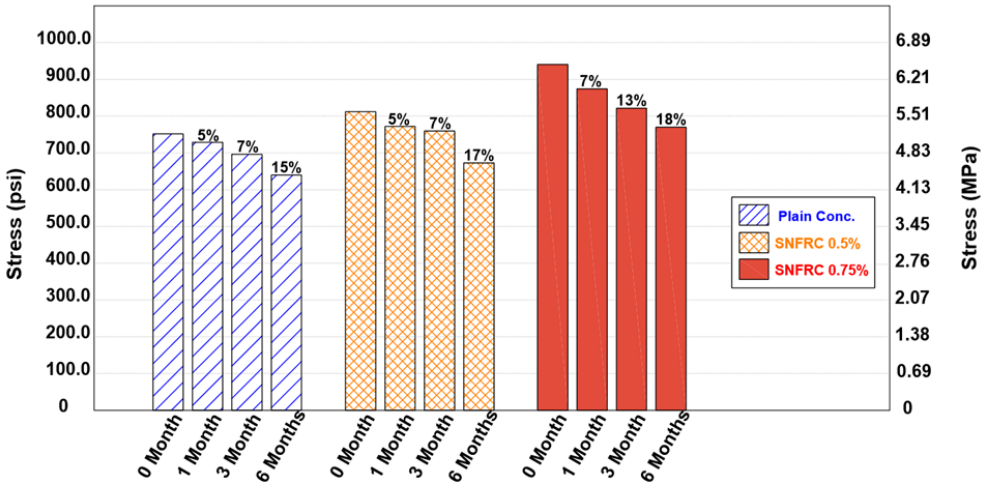

Figure 69 Degradation of tensile strength of flexural beams subjected to 1 month, 3 months, and 6 months of accelerated aging

The load-deflection response of average plain flexural beams subjected to 0 month, 1 month, 3 months, and 6 months of accelerated aging for the specimens with varying volume fractions of fibers is plotted in Figure 70. The failure in specimens without fibers was very sudden and brittle. Introduction of fibers to the concrete increased the modulus of rupture and ductility of concrete. The post-strength behavior after failure was observed in the specimens with fibers. Also, the fibers bridged the cracks and prevented the cracks from widening.

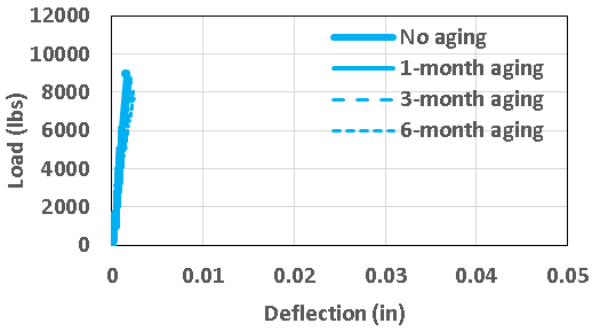

(a)

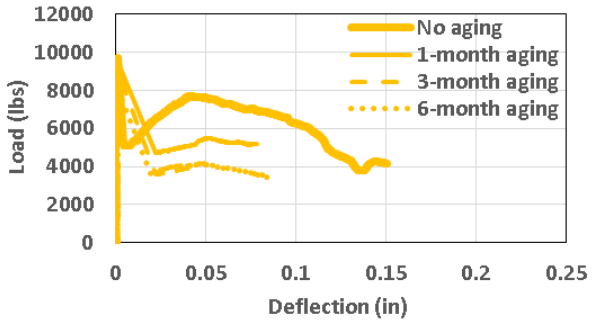

(b)

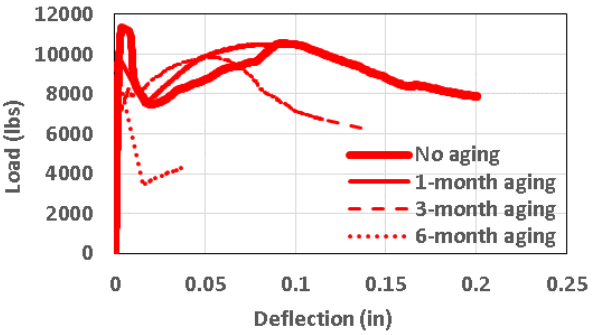

(c)

Figure 70 Load-deflection response of average plain flexural beams subjected to 0 month, 1 month, 3 months, and 6 months of accelerated aging for the specimens with: (a) V_f =0, plain; (b) V_f =0.5% SNFRC; (c) V_f =0.75% SNFRC

The load-deflection responses of all of the concrete flexural beams are plotted in Appendix O.

5 ANALATYCAL STUDIES

5.1 Long-term prediction of specimens based on the Arrhenius Principle

The concrete cylinder specimens with 50°C (122°F) were subjected to up to 6 months of accelerated aging, and the cylinder specimens with 70°C (158°F) were subjected to up to 1 month of accelerated aging to find the activation energy of the specimens to predict the long-term strength of concrete with synthetic fibers. The tensile strength of plain concrete cylinders subjected to accelerated aging conditions up to 6 months is shown in Figure 71.

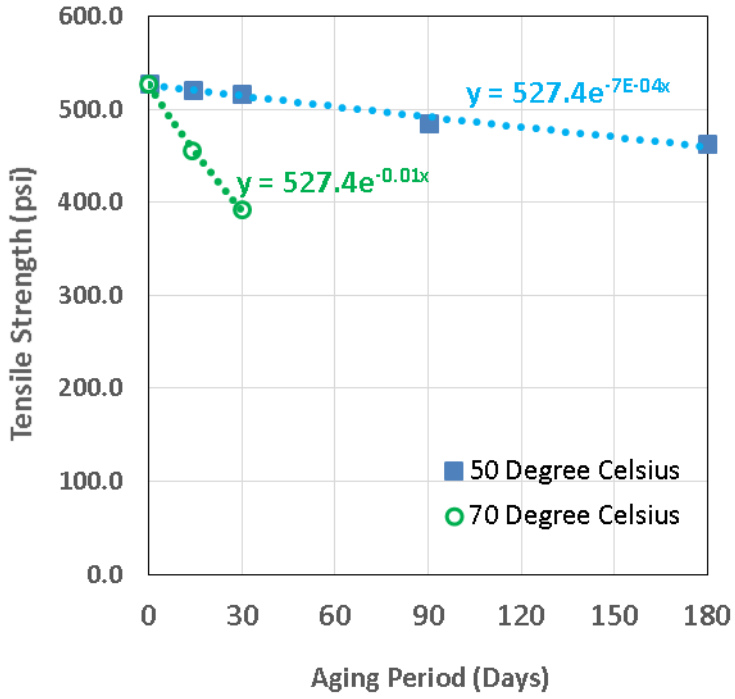

Figure 71 Tensile strength of plain concrete cylinders subjected to accelerated aging conditions

The activation energy calculation of the plain concrete is as follows:

$R = 0.008314$

$T_1 = 273 + 50 = 323$

$T_2 = 273 + 70 = 343$

$T_3 = 273 + 20 = 293$

$K_1 = \frac{-1}{180} \cdot \ln\left(\frac{462.3}{527.4}\right) = 7.319 \cdot 10^{-4}$

$K_2 = \frac{-1}{30} \cdot \ln\left(\frac{392.3}{527.4}\right) = 0.01$

$E_a = \frac{-R \cdot \ln\left(\frac{K_2}{K_1}\right)}{\frac{1}{T_2} - \frac{1}{T_1}} = 119.8 \ \frac{KJ}{Mol}$

$K_3 = K_2 \cdot e^{\frac{-E_a}{R} \cdot \left(\frac{1}{T_3} - \frac{1}{T_2}\right)} = 7.602 \cdot 10^{-6}$

One day of accelarated aging at 50 degree celsius is equivalent to $\frac{K_1}{K_3} = 96$ days at 20 degree celsius, which is the Mean Annual Temperature (M.A.T)

One day of accelarated aging at 70 degree celsius is equivalent to $\frac{K_2}{K_3} = 1315$ days at 20 degree celsius, which is the Mean Annual Temperature (M.A.T.)

One month of accelarated aging at 70 degree celsius is equivalent to $\frac{30 \cdot \frac{K_2}{K_3}}{365} = 107$ years.

Tensile strength after 100 years in psi is: $F_{100years} = 527.4 \cdot e^{-K_3 \cdot 36500} = 399.6$

Degradation in percentage after 100 years is: $100 - \frac{F_{100years}}{527.4} \cdot 100 = 24.23\ \%$

$\frac{N}{t} = e^{-\frac{E_a}{R} \cdot \left(\frac{1}{T_3} - \frac{1}{T}\right)} = e^{49.175 - \frac{14408}{T}}$

All the rest of the calculations for SNFRC 0.5% and SNFRC 0.75% are summarized in Appendix K.

The tensile strength of concrete cylinders subjected to 14 days, 1 month, 3 months, and 6 months of accelerated aging at temperatures 50 degree Celsius and 70 degree Celsius is shown in Figure 72.

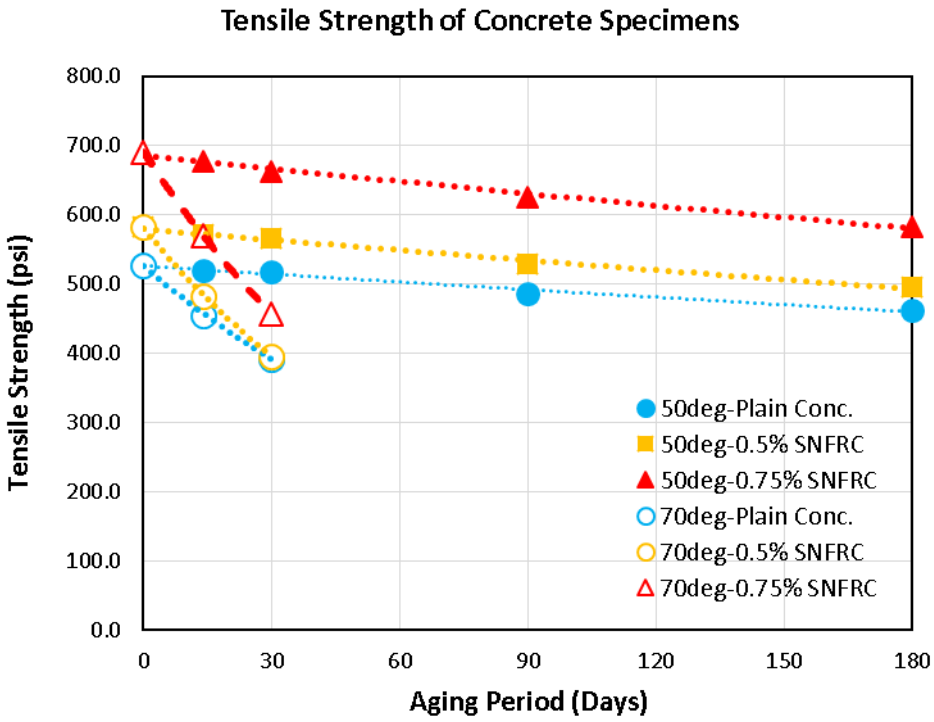

Figure 72 Tensile strength of concrete cylinders subjected to 14 days, 1 month, 3 months, and 6 months of accelerated aging at different temperatures

Strength degradation comparison of cylinders versus large-scale beams at 50°C is shown in Figure 73. It was concluded that the rate of degradation of shear strength of large-scale beams was in good agreement with the rate of degradation of tensile strength of the cylinder specimens.

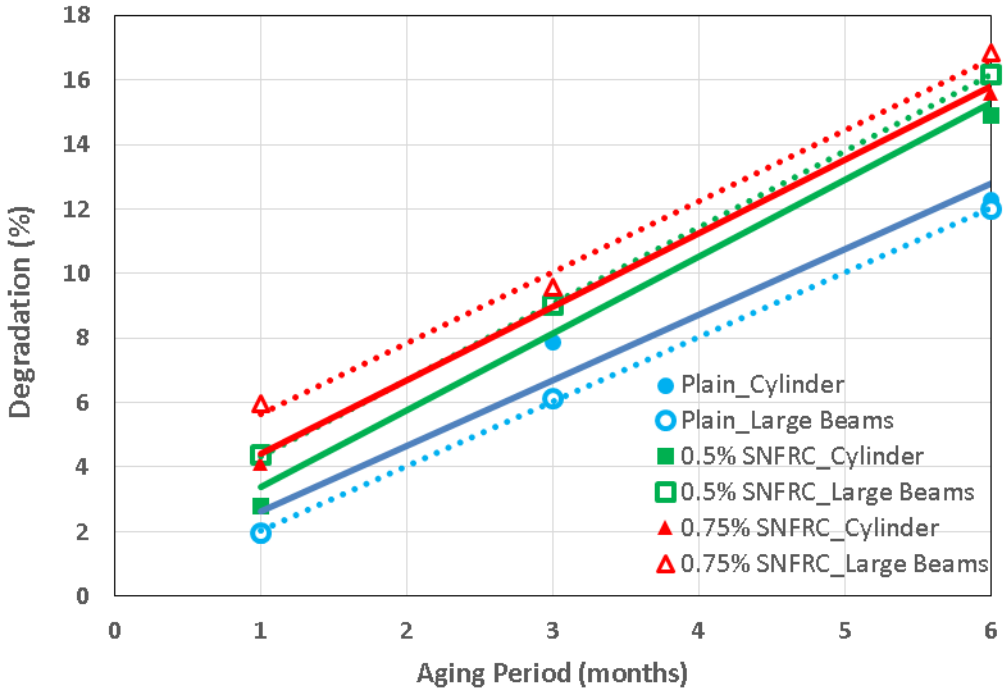

Figure 73 Strength degradation comparison of cylinders versus large-scale beams at 50°C

The predicted life for the tensile strength of the cylinder specimens and design shear strength of large-scale beams at 20°C up to 100 years are shown in Figure 74 and Figure 75, respectively.

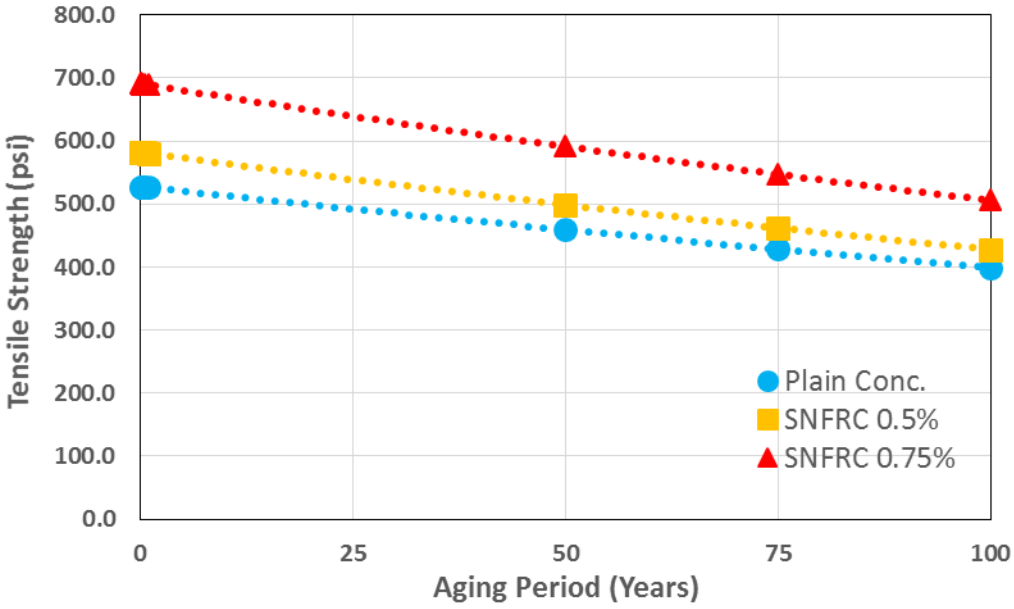

Figure 74 Predicted life for the tensile strength of cylinder specimens at 20°C in years

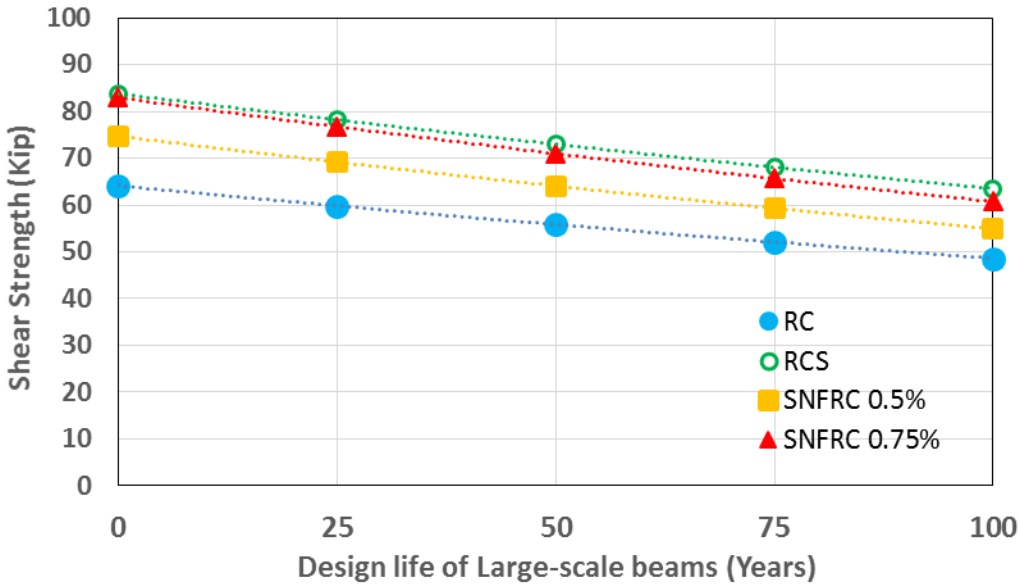

Figure 75 Design life for the shear strength of large-scale beams at 20°C in years

6 DEVELOPMENT OF THREE-DIMENSIONAL FINITE ELEMENT MODEL

6.1 Modeling and Analysis

This chapter explains the numerical analyses performed, using Abaqus v6.12, to verify the experimental data and predict the short-term and long-term shear capacity of large-scale concrete beams with different volume fractions of polypropylene fibers. A 3-D non-linear finite element model (FEM) with Concrete Damage Plasticity (CDP) was considered for analyzing the failure of the large-scale reinforced concrete beams. In the concrete damage plasticity approach, the two main failure mechanisms are tensile cracking and compressive crushing of the concrete.

Concrete constitute laws in tension and compression are shown in Figure 76 and Figure 77, where σ_{t0} is the ultimate tensile stress, σ_{c0} is the initial yielding compressive stress, σ_{c0} is the ultimate compressive stress, E_0 is the initial (undamaged) modulus of the concrete, and d_t and d_c are degradation factors of the elastic stiffness in tension and compression, respectively.

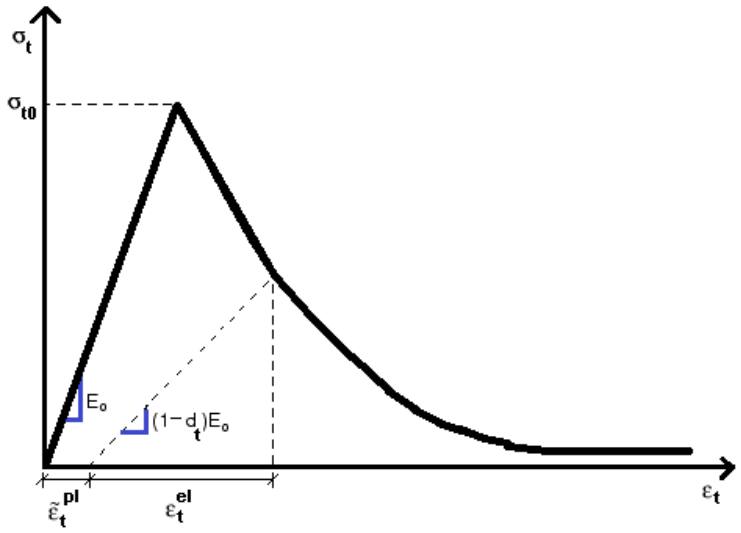

Figure 76 Stress-strain response of concrete to uniaxial loading in tension

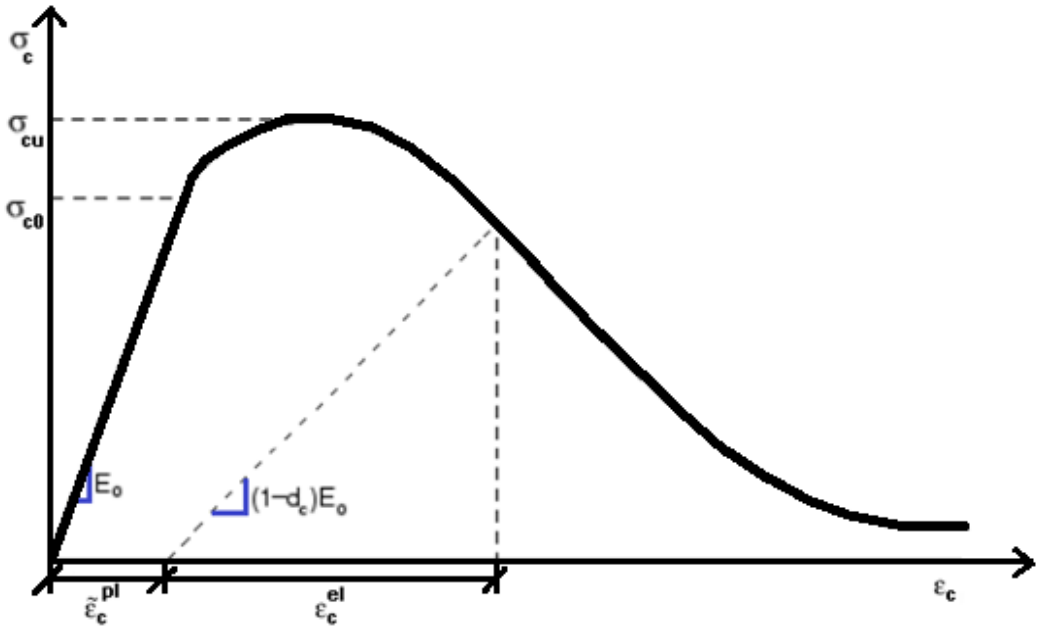

Figure 77 Stress-strain response of concrete to uniaxial loading in compression

The stress-strain relations under uniaxial tension and compression loading are given by equations (4) and (5):

$$\sigma_t = (1 - d_t)E_0\left(\varepsilon_t - \tilde{\varepsilon}_t^{pl}\right) \tag{4}$$

$$\sigma_c = (1 - d_c)E_0\left(\varepsilon_c - \tilde{\varepsilon}_c^{pl}\right) \tag{5}$$

The effective tensile and compressive stresses are given by equations (6) and (7):

$$\tilde{\sigma}_t = \frac{\sigma_t}{(1 - d_t)} = E_0\left(\varepsilon_t - \tilde{\varepsilon}_t^{pl}\right) \tag{6}$$

$$\tilde{\sigma}_c = \frac{\sigma_c}{(1 - d_c)} = E_0\left(\varepsilon_c - \tilde{\varepsilon}_c^{pl}\right) \tag{7}$$

The elastic modulus reduction is defined as:

$$E = (1 - d)E_0 \tag{8}$$

Concrete with the following properties was assigned to the large-scale beams: mass density of 0.00022483 pci, which is equivalent to weight density of 2,400 kg/m^3 (0.00022483 pci x 32.17405 ft./s^2 x 12 in/ft. x 27,679.9 kg/m^3/pci= 2,400 kg/m^3); Modulus of Elasticity (E_c) of 4,189,411pci (28,885 Mpa) for concrete with and without polypropylene fibers; and Poisson's ratio of 0.2. The parameters of the CDP model are summarized in Table 8.

Table 8 Details of parameters of CDP model

Dilation Angle	Eccentricity	fb0/fc0	K	Viscosity Parameter
30	0.1	1.16	0.667	0.0001

According to the Abaqus manual, eccentricity is the rate at which the function approaches the asymptote. (The flow potential tends to a straight line as the eccentricity tends to zero.) The dilation angle is measured in the p-q plane (first and second stress invariants) at high confining pressure, and it determines the shape of the flow potential. The higher the dilation angle value in the CDP model is, the stiffer the load-deflection response of the concrete structure is. The fb0/fc0 is defined as the ratio of equibiaxial compressive yield stress to initial uniaxial compressive yield stress. The parameter K is the ratio of the second stress invariant on the tensile meridian to compressive meridian at initial yield, based on full triaxial laboratory tests of concrete, and it determines the shape of the loading surface in the deviatoric plane. The viscosity parameter close to zero is usually considered to avoid any instability and to obtain converged results.

Steel with the following properties was assigned to the rebars embedded in large-scale beams: mass density of 0.000734456 pci, which is equivalent to weight density of 7,850kg/m^3 (0.000734456 pci x 32.17405 ft./s^2 x 12 in/ft. x 27,679.9 kg/m^3/pci = 7,850kg/m^3); Modulus of Elasticity (E_s) of 29,000,000pci (199.9 Gpa); Poisson's ratio of

0.3; and yielding stress of 64,800 psi. An elastic, perfectly plastic bilinear model was used to simulate the steel bars, as shown in Figure 78.

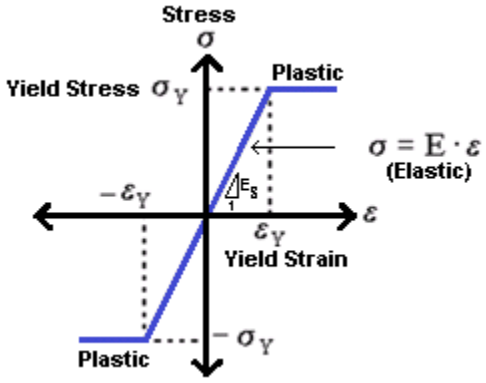

Figure 78 Stress-strain response of elastic, perfectly plastic steel bars

A high stiff 3-D deformable plate (2in. height x 10in. width x 72in. length), with a Modulus of Elasticity (E_s) of 300,000,000pci (2,068.4 Gpa), and Poisson's ratio of 0.3 was modeled, as shown in Figure 79, to simulate the two steel I-girders with stiffeners that were placed under the large-scale concrete beams during testing.

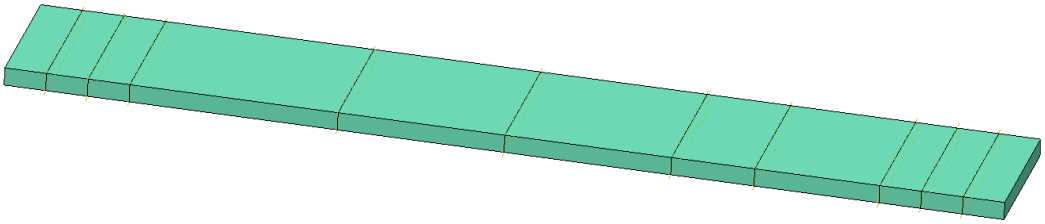

Figure 79 FEM model part for steel beam below concrete large-scale beams

A 3-D deformable steel plate (2in. height x 6in. width x 10in. length) with a Modulus of Elasticity (E_s) of 29,000,000pci (199.9 Gpa) and Poisson's ratio of 0.3 was modeled as shown in Figure 80 to simulate the plates that were placed under the load-cell and above the supports of the large-scale concrete beams during testing.

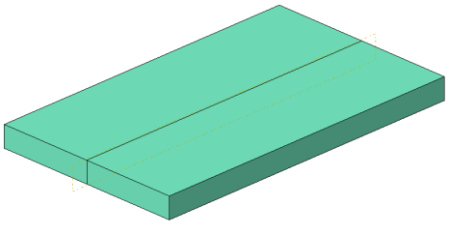

Figure 80 FEM model part for steel plate

A 3-D deformable, steel semi roller (2 in. diameter x 10 in. length), with a Modulus of Elasticity (E_s) of 29,000,000pci (199.9 Gpa) and Poisson's ratio of 0.3 was modeled as shown in Figure 81 to simulate the rollers that were placed under the support plates during testing of the large-scale beams.

Figure 81 FEM model part for semi roller

6.1.1 Element Type

A solid, homogeneous, 8-node linear brick, reduced integration (C3D8R) with hourglass control was selected to model the concrete beams, as shown in Figure 82.

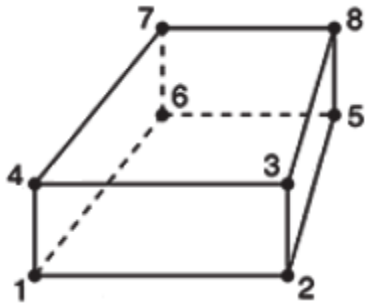

Figure 82 8-noded linear brick for isoparametric concrete elements

A 2-node linear 3-D truss (T3D2) was selected for the steel bars, as shown in Figure 83. Truss elements are slender structural members that cannot transmit moments.

Truss elements are solid, long, one-dimensional members that can only transmit the axial loads.

Figure 83 2-node linear 3-D truss (T3D2) for steel bar elements

A solid, homogeneous, 8-node linear brick, reduced integration (C3D8R) with hourglass control was selected to model the steel plates and steel beams.

A mesh sensitivity analysis was performed to make sure that the mesh was the right size so that it did not change the results significantly. The concrete elements were meshed at 1-inch intervals, as shown in Figure 84. A total number of 10,800 linear hexahedral elements with 12,848 nodes were analyzed for all the concrete beams.

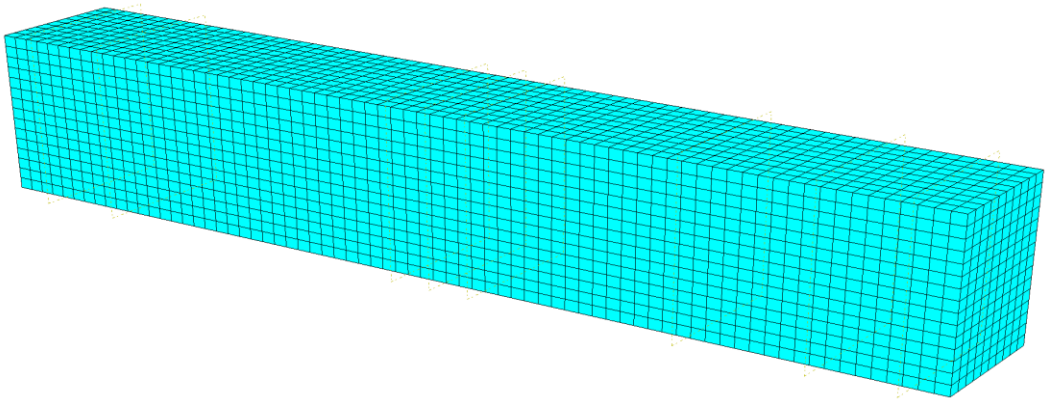

Figure 84 Typical mesh for the large-scale concrete beams

The semi rollers were meshed at 1-inch intervals, as shown in Figure 85. A total of 60 linear hexahedral elements with 121 nodes were analyzed for all the semi rollers.

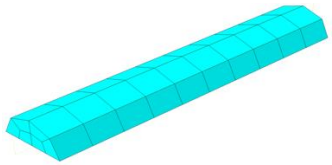

Figure 85 Typical mesh for the steel semi-roller supports

The steel plates were meshed at 1-inch intervals, as shown in Figure 86. A total of 60 linear hexahedral elements with 154 nodes were analyzed for all three steel plates.

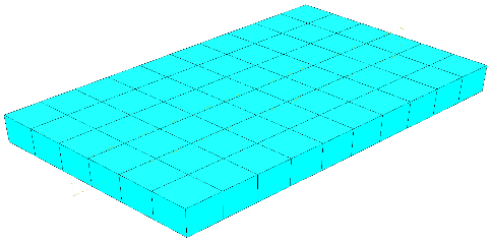

Figure 86 Typical mesh for the load and support steel plates

The compression rebars and tension-bent rebars were meshed at every 0.5 in. A total of 174 linear line elements with 175 nodes for the three tension-bent bars and a total of 136 linear line elements with 137 nodes for the two compression bars were analyzed in Abaqus.

6.1.2 Boundary Conditions and Applied Loads

The steel reinforcement was embedded in the concrete and was considered as a host region. The bottom of the semi rollers were tied to the top of steel beam, and the top of the semi rollers were tied to the bottom of the steel support plates. A surface-to-surface contact with a finite sliding, a friction coefficient of 0.45 for the tangential behavior, and hard contact for the normal behavior was defined for the contact between the load plate and top of the concrete beam. A surface-to-surface contact with a finite sliding, a frictionless contact for the tangential behavior, and hard contact for the normal behavior was defined for the contact between the left support and the bottom of the concrete beam to simulate the roller support. Also, a surface-to-surface contact with a finite sliding, a

friction coefficient of 0.45 for the tangential behavior, and hard contact for the normal behavior was defined for the contact between the pin support plate and the bottom of the concrete beam. For the top surface of the semi rollers and bottom of the support plates, a surface-to-surface contact with a finite sliding, a friction coefficient of 0.4 for the tangential behavior, and hard contact for the normal behavior was defined. The edges and centerline of the steel plate on the top center of the concrete beam was restrained, and no displacement was allowed (U_1= U_2= U_3=0), as shown in Figure 87.

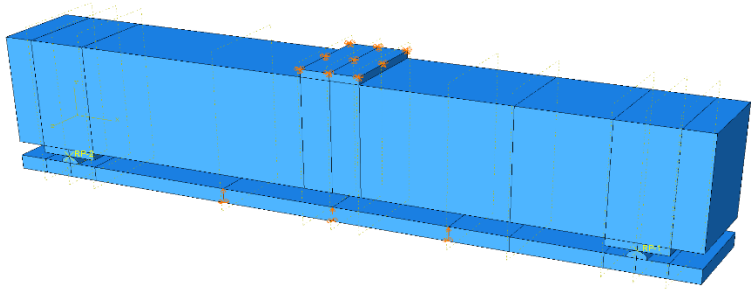

Figure 87 Configuration of the large-scale beam in the Abaqus software

The uniform displacement controlled load was applied through the bottom of the steel beam to simulate the actual laboratory testing of the large-scale beams. Three lines of the steel beam were constrained with the following displacements: U_1= U_3=0 and U_2=0.5.

6.2 Finite Element Results and Discussion

All of the large-scale beams were verified with the experimental data and inverse analysis. Trial and error for the concrete constitutive law in tension and compression was used to predict the behavior of the beams. The modulus of elasticity and compressive strength of specimens were obtained according to ASTM C39 and were used for the concrete constitutive law in compression. The tensile strength of the specimens was obtained according to ASTM 1609 and was used for the concrete constitutive law in tension. The inverse analysis with trial and error was performed on the concrete constitutive law until the load-deflection response of the large scale beams at mid-length

and quarter length of the beams verified the experimental results. Figure 88 illustrates the typical deformed shape of large-scale beams in Abaqus at failure in this study.

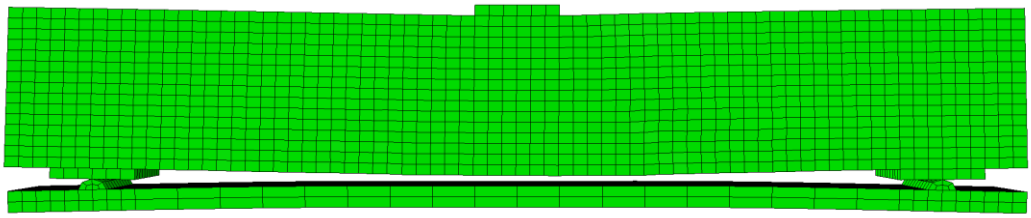

Figure 88 Deformed shape of large-scale beams in Abaqus at failure (Deformation scale factor: 3.0)

The maximum plastic strain (PE) contour of the concrete beams from FEM at failure is shown for the RC control beam in Figure 89. As shown in this figure, the plastic strain propagated from the edge of the load plate approximately 45 degree towards the tension rebars at the bottom of the beam and then along the bars toward the support.

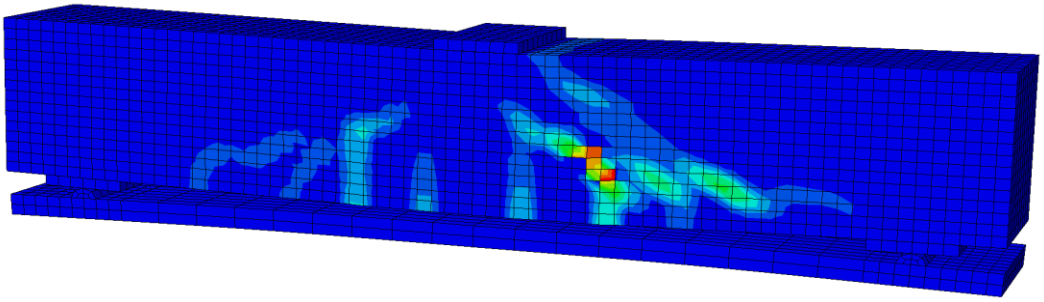

Figure 89 Maximum plastic strain (PE) contour of the concrete beams from FEM at failure

Tensile Damage (DAMAGET) and Compression Damage (DAMAGEC) were used in ABAQUS software to represent the crack location and crack formation. As shown in Figure 90, more tensile damage was observed in the elements of the span without transverse reinforcement. The tensile damage formed initially in the middle of beam hat represented the flexural crack, and then propagated from the web of the beam towards the edge of the load plate and support until failure occurred.

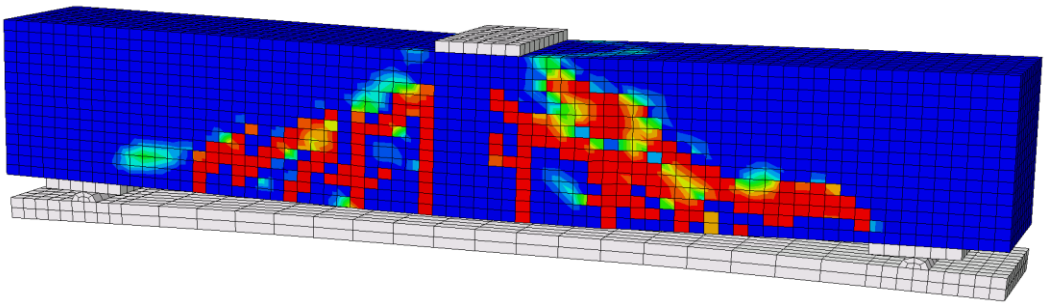

Figure 90 Location and formation of tensile crack lines from FEM analysis (DAMAGET)

The location and formation of crack lines from FEM in compression at failure (DAMAGEC) are shown in Figure 91. The compression damage formed initially at the edge of the load plate, where compression is maximum, and then propagated approximately 45 degrees towards the tension bars and along the bars towards the edge of the support.

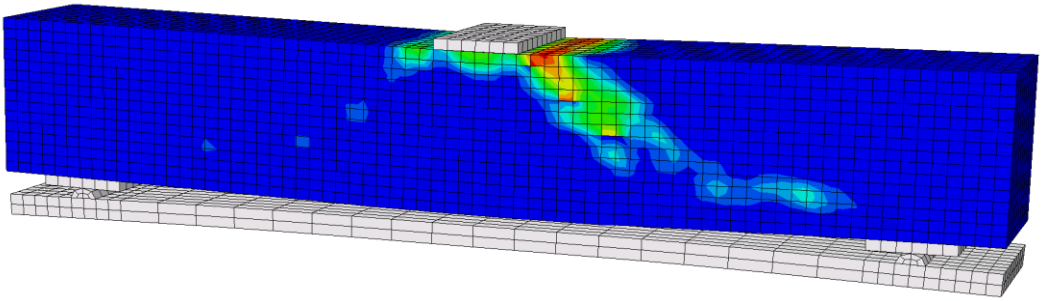

Figure 91 Location and formation of compressive crack lines from FEM analysis (DAMAGEC)

Figure 92, illustrates the Elastic Strain (E11) of steel bars embedded in concrete beams. As shown on the contour legend, the axial strain reached a maximum value of 0.001862 in the middle of the beam, where moment is maximum. Since the maximum strain was less than the yield strain of bars (ε_y=0.00207), the bars were not yielded. The compression bars at the top of the beam at the location of the load path experienced a large axial compression strain up to 0.003483, indicating that rebars at the top locally were yielded.

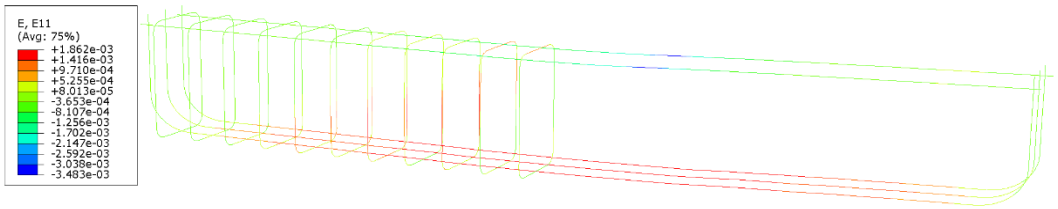

Figure 92 Elastic strain of steel bars embedded in concrete beams

Concrete constitutive law in tension subjected to 0 month, 1 month, 3 months, and 6 months of accelerated aging and large-scale beams with varying volume fractions of fibers after 100 years are shown in Figure 93. The concrete constitutive law in 100 years was attained by using inverse analysis to reach the tensile strength, according to ASTM 1609, and compression strength, according to ASTM C39, to reach the shear strength of the large-scale beams after 100 years of using Arrhenius principles. The inverse analysis leads to a very unique graph to obtain the long-term load-deflection response of the large-scale beams. Also, concrete constitutive law in compression subjected to 0 month, 1 month, 3 months, and 6 months of accelerated aging and after 100 years for the large-scale beams with varying volume fractions of fibers are shown in Figure 94. As shown in Figures 93 and 94, the maximum stress and maximum strain decreased due to degradation of concrete over time, and less ductility was found.

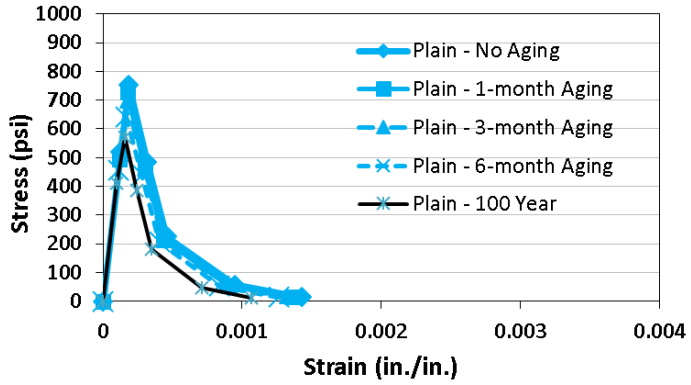

(a)

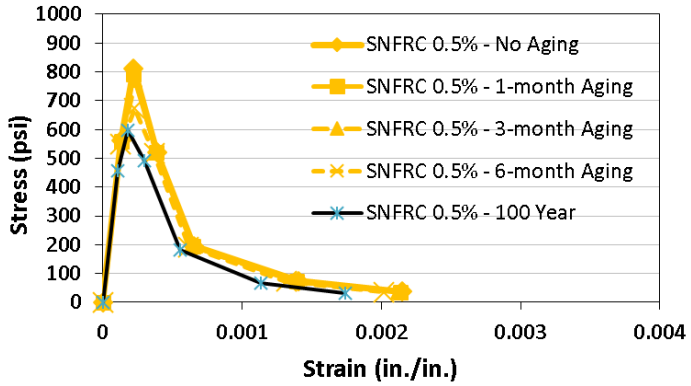

(b)

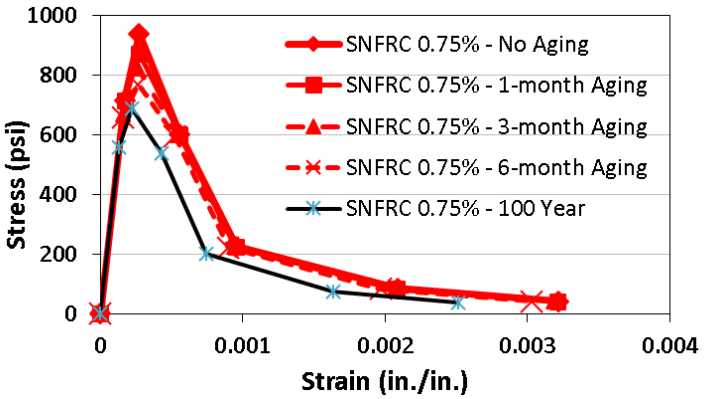

(c)

Figure 93 Concrete constitutive law in tension subjected to 0 month, 1 month, 3 months, and 6 months of accelerated aging and after 100 years for the large-scale beams with: (a) V_f =0, plain; (b) V_f =0.5% SNFRC; (c) V_f =0.75% SNFRC

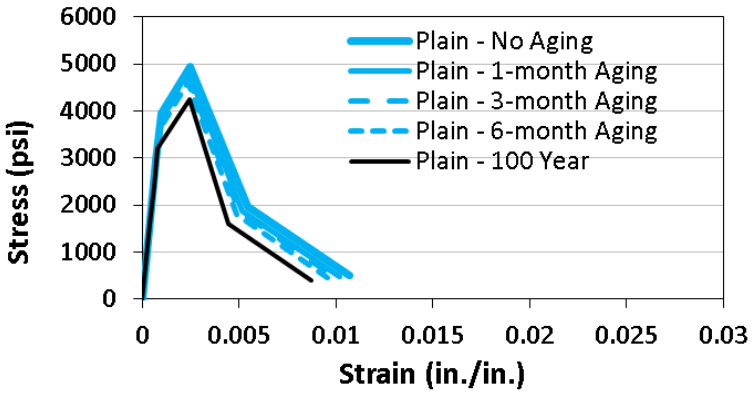

(a)

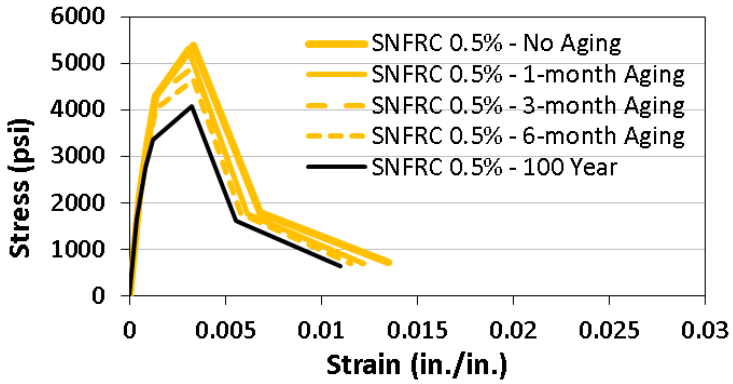

(b)

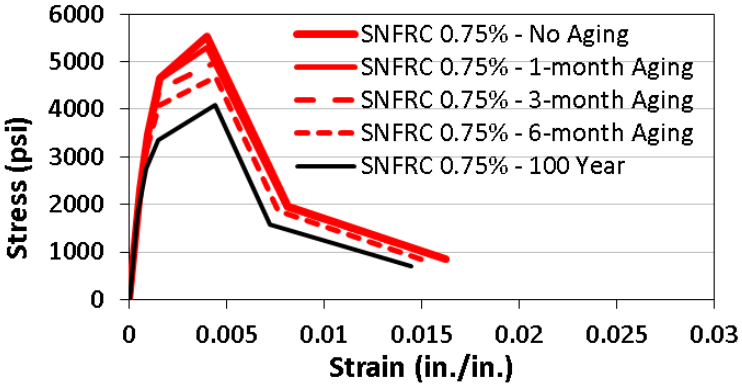

(c)

Figure 94 Concrete constitutive law in compression subjected to 0 month, 1 month, 3 months, and 6 months of accelerated aging and after 100 years for the large-scale beams with: (a) V_f =0, plain; (b) V_f =0.5% SNFRC; (c) V_f =0.75% SNFRC

The concrete constitutive law in tension and compression for all of the beams with varying aging periods and 100 years of being exposed to actual weathering are shown in Figure 95 and Figure 96. As the volume fraction of fibers was increased, the peak stress and peak strain were higher.

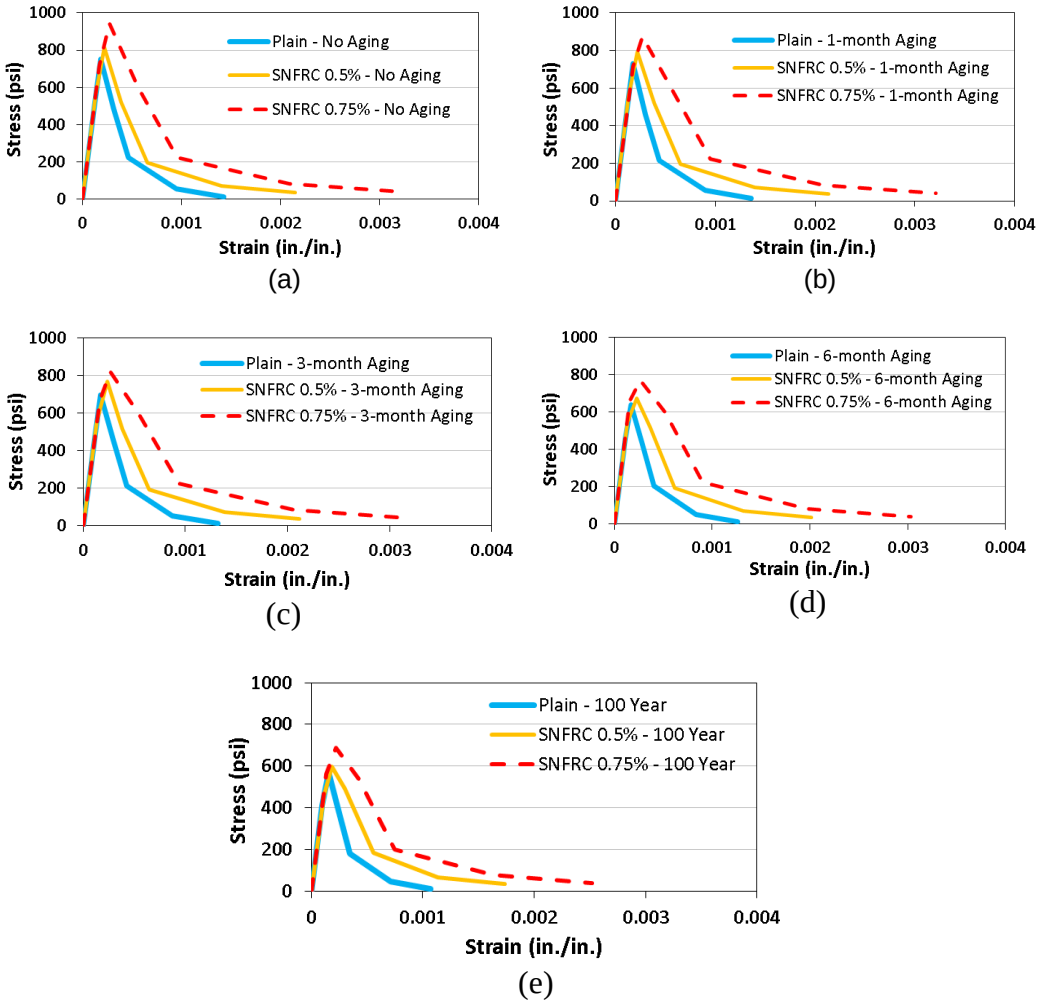

Figure 95 Concrete constitutive law in tension for all the beams: (a) without aging, Phase 1; (b) 1 month of aging, Phase 2; (c) 3 months of aging, Phase 3; (d) 6 months of aging, Phase 4; and (e) 100 years

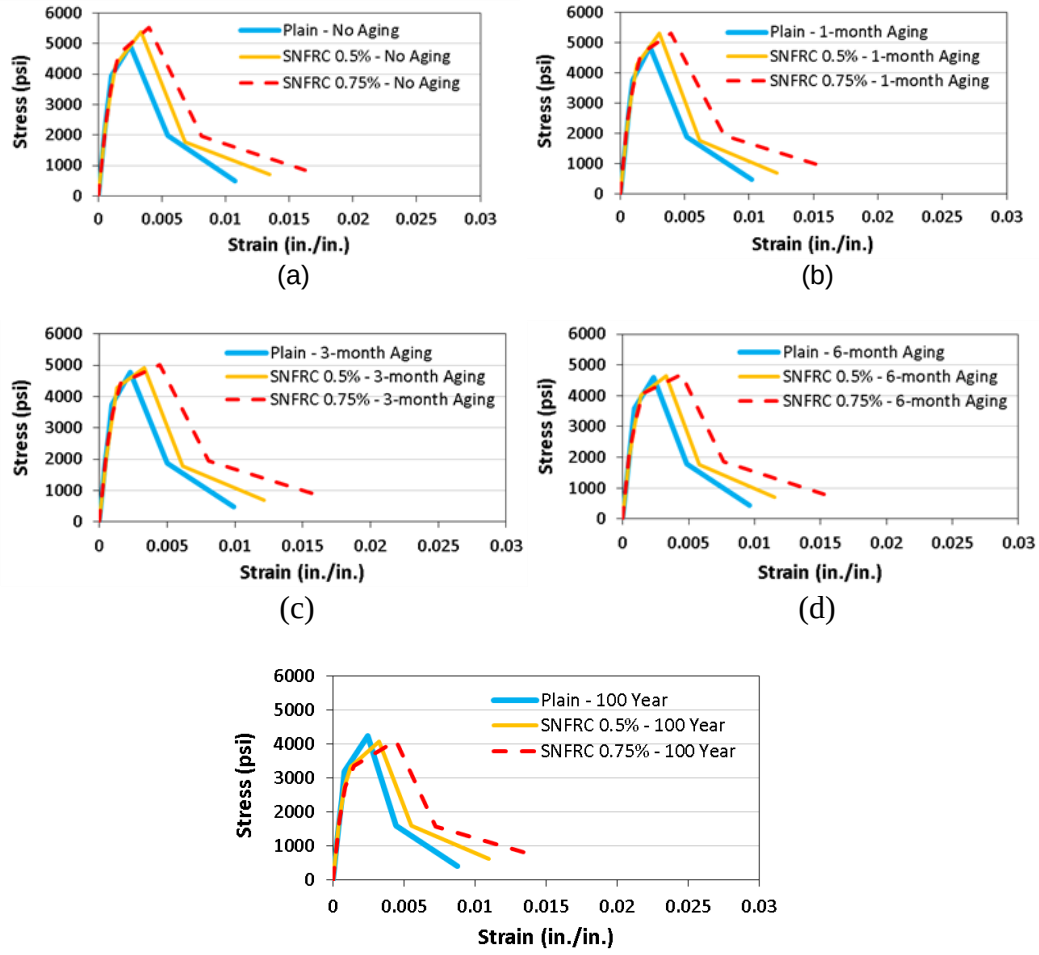

Figure 96 Concrete constitutive law in compression for all the beams: (a) without aging, Phase 1; (b) 1 month aging, Phase 2; (c) 3 months aging, Phase 3; (d) 6 months aging, Phase 4; and (e) 100 years

The load versus deflection response of RC control beams without aging was verified with FEM software, ABAQUS, as shown in Figure 97. The mid-length and quarter-length of the beams were monitored and verified with FEM to ensure that the FEM models predicted the behavior of the beams accurately. The concrete constitutive law in tension and compression for the RC control beams without aging in Phase 1 is shown in Figure 98

and Figure 99. The FEM verification of the rest of the beams is summarized in Appendix F.

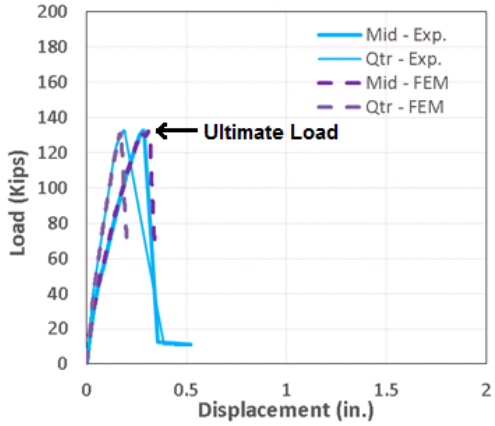

Figure 97 Load - deflection response of RC – Control beams without aging

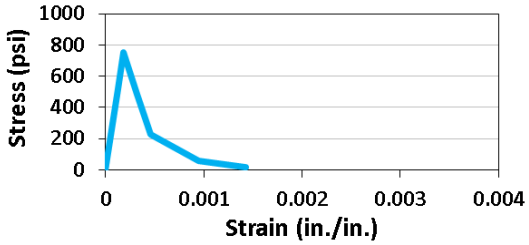

Figure 98 Concrete constitutive law in tension for RC – Control beams without aging

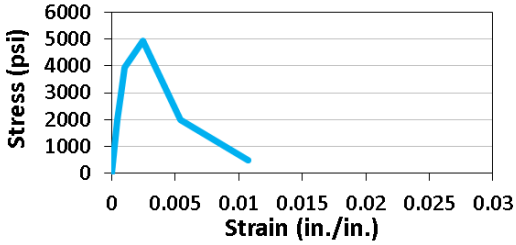

Figure 99 Concrete constitutive law in compression for RC – Control beams without aging

More FEM models were developed, as discussed in the next chapter, to develop a shear design equation. Simply supported beams with two support plates under the concrete beams were modeled in Abaqus. Constitutive law in tension and compression in 100 years were used in FEM without considering the steel beam and semi rollers under the concrete beam for the parametric study.

7 PARAMETRIC STUDY AND DESIGN EQUATION

The essential modeling parameters for shear capacity of large-scale beams with different volume fractions of polypropylene fibers for regression analysis were identified. The independent variables, including beam width (b), effective depth (d), volume fraction of polypropylene fibers (V_f), reinforcement ratio, and span-to-depth ratio are among the essential parameters which are included in this study. A total of 57 cases with three different lengths, 6 ft., 20 ft., and 30 ft., were investigated in Abaqus software to develop a long-term shear design equation for large-scale beams with polypropylene fibers. The configurations of all 57 beams in the parametric study are shown in Appendix L. The concrete constitutive law in tension and compression after 100 years in actual weathering, as discussed in the previous chapters, were used in Abaqus to predict the long-term shear strength of the beams after 100 years. The low, medium, and high value of each independent parameter was selected for the sensitivity analysis. For example, low, medium, and high values for the span-to-depth ratio represented deep beam, short beam and slender beam, respectively. The essential design parameters for the sensitivity study are summarized in Tables 9-11. Multiple linear regression (MLR) analysis was used, employing Excel data analysis to find the effects of each parameter on long-term shear strength of concrete with fibers.

Prior to the year 1900, the classic equation of (9) was used to compute the shear stresses:

$$v = \frac{V\,Q}{I\,b} \tag{9}$$

Where v is the unit horizontal shear stress at a distance y from the neutral axis, V is the vertical shear at the section, Q is the first moment part of the cross-sectional area at distance y from the neutral axis, with respect to the neutral axis, I is the moment of inertia

of the cross-sectional area with respect to the neutral axis and b is the width of the cross section at a distance y from the neutral axis.

Emil Mörsch in Germany in the early 1900s found that the tensile stress must exist on a plane of 45-degree if the pure shear stress exists. Also, he concluded that the ultimate nominal shear stress in beams without web reinforcement, according to equation (10) is to measure diagonal tension which is close to the tensile strength of concrete. He believed that the shear failure is a tensile phenomenon. In this classic shear stress equation, jd is the internal moment arm. Also, maximum allowable stress v, was limited to 64 psi for members without web reinforcement.

$$v = \frac{V}{b\ j\ d} \tag{10}$$

The Prussian code in 1907 allotted a shear stress of up to 64 psi based on equation (10) for a minimum concrete cube strength of 1500 psi. The excessive shear stresses up to 77 psi should be resisted by web reinforcement.

National Association of Cement Users (NACU) in 1908 stated that “the shearing strength of concrete, corresponding to a compressive strength of 2000 psi, shall be assumed at 200 psi”. Talbot in 1909 found that reinforcement percentage, length-to-depth ratio affects the shear and diagonal tension strength of beam without web reinforcement. However, he could not support his findings in mathematical terms.

The ACI reports in 1916 and 1917 suggested that the allowable shearing stress of 0.02f’c should be resisted by concrete with a maximum limit of 66 psi and web reinforcement can be used to resist excess shear up to a value of 0.075f’c.

ACI Standard Specification No. 23 of 1920 permitted the nominal shear stress of 0.03f’c for beams without web reinforcement, with special anchorage of longitudinal reinforcement.

ACI 318-51 specified at a maximum shear stress of 0.03f'c for all beams without shear reinforcement, a maximum limit of 0.12f'c for beams with web reinforcement. After five years, ACI 318-56 suggests the shear stress of 0.08f'c not exceeding 90 psi for beams without stirrups, and 240 psi with stirrups.

The 400 square foot warehouse roof collapsed without warning at Wilkins Air Force Depot in Shelby, Ohio, in 1955 due to the diagonal tension failure in a frame girder. The largest cracks occurred in the low moment regions. Moreover, less cracks were observed in frames with continuous top reinforcement and shear stirrups. As a result of failure experiences, the ACI 318-56 code was revised and the shear stress of 0.03f'c with a maximum value of 240 psi was considered for members without transverse reinforcement.

In the early 1950's, A. P. Clark introduced an expression to support Talbot's findings by a mathematical equation involving span-to-depth ratio, percentage of longitudinal reinforcement, and concrete strength. In the meantime, the University of Illinois developed theories based on the dimensionless ratio M/Vd, involving bending moment M, shear force V, and effective depth d.

This concept led to an empirical solution of shear and diagonal tension for design purposes. Numerous empirical design procedures were conducted to solve the shear and diagonal tension problems that have not been fundamentally solved.

Joint committee 326 (now 426) of the American Concrete Institute (ACI) and the American Society of Civil Engineers (ASCE) was established in 1950 to develop shear and diagonal tension formula for reinforced concrete members. A total of 440 tests on the beams without web reinforcement indicated that the shear capacity depends on the percentage of longitudinal reinforcement, the ratio M/Vd, and the compressive strength of concrete (f'_c). It was found that the location and inclination of diagonal tension crack is due

to excessive principal tensile stresses. A principal tensile stress at a point is given by equation (11)

Where f_t is the tensile bending stress and v is the shear stress. The tensile bending stress can be computed prior to the presence of tensile cracks. Therefore, it cannot be calculated based on the assumption of uncracked sections. In this approach, the tensile bending stress f_t is assumed to be proportional to the steel stress (equation 12)

$$f_t = C\,\frac{M}{n\,\rho\,j\,b\,d^2} = F_1\,\frac{M}{n\,\rho\,b\,d^2} \tag{12}$$

Where F_1 is constant and equal to $\frac{C}{j}$, and n is the modular ratio of steel to concrete (E_s/E_c). Also, it was assumed that the concrete shear stress (v) is proportional to the average shear stress of the cross section (equation 13). In this equation F_2 is a constant.

$$\nu = F_2\,\frac{V}{b\,d} \tag{13}$$

By substituting equations (11) and (12) into equation (10) can be rearranged to obtain equation (14)

$$\frac{V}{b\,d} = \frac{f_{t(max)}}{\frac{1}{2}F_1\,\frac{M}{n\,V\,\rho\,d} + \sqrt{\left(\frac{1}{2}F_1\,\frac{M}{n\,V\,\rho\,d}\right)^2 + {F_2}^2}} \tag{14}$$

Once the maximum tensile stress f_t (max) reaches the tensile strength of concrete (f'_t), diagonal tension crack occurs. The equation (14) can be rearranged to obtain equation (15)

$$\frac{V}{b\,d\,{f'}_t} = \frac{1}{C_1\frac{E_c}{E_s\,p}\,\frac{M}{V\,d} + \sqrt{\left(C_1\frac{E_c}{E_s\,p}\,\frac{M}{V\,d}\right)^2 + {C_2}^2}} \tag{15}$$

Where C_1 and C_2 are the new constants. It was assumed that f'_t and E_c are equals to a constant times $\sqrt{f'_c}$. A total of 194 beams are plotted in Figure 100. In this graph, $\frac{V}{b\,d\,\sqrt{f'_c}}$ and $\frac{M\sqrt{f'_c}}{P\,V\,d}$ represent the diagonal tension strength and properties of the considered section; respectively.

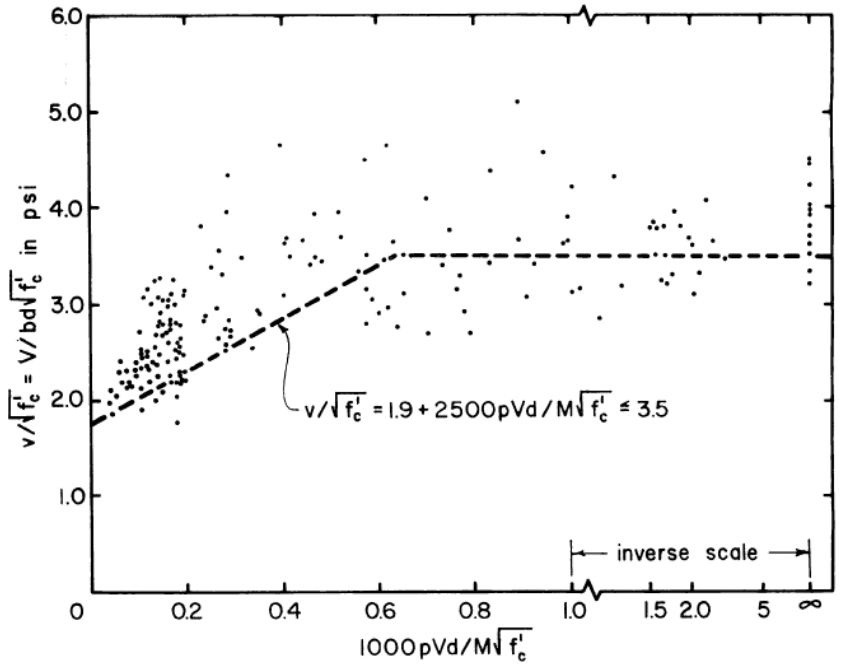

Figure 100 Derivation of ACI design equation (ACI-ASCE Committee 326 report, 1962)

Based on the trend of the test data in Figure (100), the shear strength of concrete (V_c) can be expressed in two straight lines and can be computed by equation (16):

$$V_c = \left(1.9\sqrt{f'_c} + 2500\,\rho_w\,\frac{V_U\,d}{M_U}\right) b_w\,d \;\leq 3.5\sqrt{f'_c}\;\;b_w\,d \qquad (16)$$

Where:

f'_c : Specified compressive strength of concrete

b: Web width

d: Beam depth from the center of longitudinal tension reinforcement to the extreme compression fiber of beam

ρ_w: Percentage of longitudinal reinforcement $(\frac{A_s}{b_w\, d})$

V_u : Factored shear force at considered section

M_u : Factored shear force and factored moment at considered section

For most design purposes, according to ACI 318 code the second part of equation (16) can be considered to be equal to $0.1\sqrt{f'_c}$, and therefore, design equation (17) can be simply used.

$$V_c = 2\sqrt{f'_c}\; b\; d \tag{17}$$

This ACI design equation does not address the effects of volume fraction of fibers and long-term shear strength of concrete. Therefore, the equation in this study was developed based on the current ACI code formula.

Table 9 Parametric study details of the 6 ft. large-scale beams

	Case	As ($in.^2$)	b (in.)	h (in.)	a (in.)	d (in.)	V_f (%)	a/d	ρ (%)	Length (ft.)
-High (As, 3#9) - Low (b,10) -Medium (a/d, 2.4)	1	3.0	10	15	30	12.6	0	2.4	2.4	6.0
	2						0.5			
	3						0.75			
Medium (As,2#10)	4	2.5					0		2.0	
	5						0.5			
	6						0.75			
Low (As,3#7)	7	1.8					0		1.4	
	8						0.5			
	9						0.75			
Medium (b=12.5)	10	3.0	12.5				0		1.9	
	11						0.5			
	12						0.75			
High (b=15)	13		15				0		1.6	
	14						0.5			
	15						0.75			

Table 10 Parametric study details of the 20-ft. large-scale beams

	Case	As ($in.^2$)	b (in.)	h (in.)	a (in.)	d (in.)	V_f (%)	a/d	ρ (%)	Length (ft.)
-High (As, 10#9) - Low (b,20) - Medium (a/d, 2.4)	16	10.0	18	27	55	22.9	0	2.4	2.4	20.0
	17						0.5			
	18						0.75			
Medium (As,10#8)	19	7.9					0		1.9	
	20						0.5			
	21						0.75			
Low (As,10#7)	22	6.0					0		1.5	
	23						0.5			
	24						0.75			
Medium (b=22)	25	10.0	22				0		2.0	
	26						0.5			
	27						0.75			
High (b=27)	28	10.0	27				0		1.6	
	29						0.5			
	30						0.75			
High (Slender,a/d=3.0)	31	10.0	18		68.7		0	3.0	2.4	
	32						0.5			
	33						0.75			
Low (Deep,a/d=1.8)	34				41.2		0	1.8		
	35						0.5			
	36						0.75			

Table 11 Parametric study details of the 30-ft. large-scale beams

	Case	As ($in.^2$)	b (in.)	h (in.)	a (in.)	d (in.)	V_f (%)	a/d	ρ (%)	Length (ft.)
-High (As, 18#9) - Low (b,24) -Medium (a/d, 2.4)	37	18.0	24	36	76.6	31.9	0	2.4	2.4	30.0
	38						0.5			
	39						0.75			
Medium (As,20#8)	40	15.8					0		2.1	
	41						0.5			
	42						0.75			
Low (As,1 8#7)	43	10.8					0		1.4	
	44						0.5			
	45						0.75			
Medium (b=30)	46	18.0	30				0		1.9	
	47						0.5			
	48						0.75			
High (b=36)	49	18.0	36				0		1.6	
	50						0.5			
	51						0.75			
High (Slender,a/d=3.0)	52	18.0	24		95.7		0	3.0	2.4	
	53						0.5			
	54						0.75			
Low (Deep,a/d=1.8)	55				57.4		0	1.8		
	56						0.5			
	57						0.75			

The coefficient of determination, $R^{2,}$ was used to measure the accurateness of the data to the regression fit. The closer R^2 is to 1, the more reliable the data is assumed to be. As illustrated in Figure 101, there is a perfect linear correlation (R^2=0.92) in the shear strength of beams with an increase in the volume fraction of polypropylene fibers.

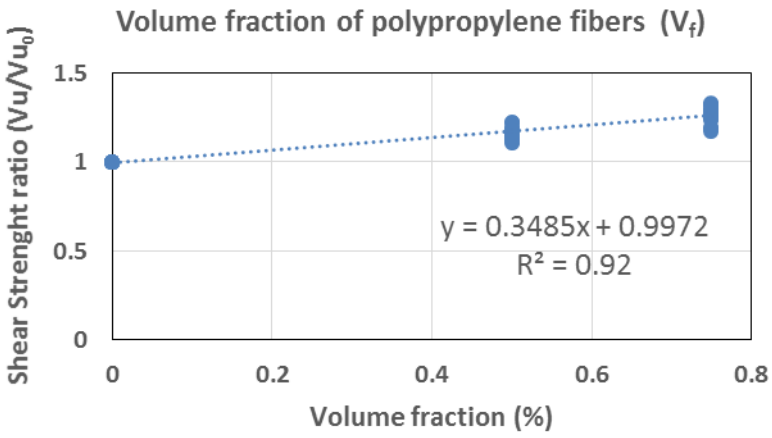

Figure 101 Sensitivity analysis of volume fraction of fibers to shear strength

A perfect relationship (R^2=0.96) between the span-to-depth ratio (a/d) and the shear strength of the beams was observed, as shown in Figure 102. As the span-to-depth ratio increased, the shear strength linearly decreased.

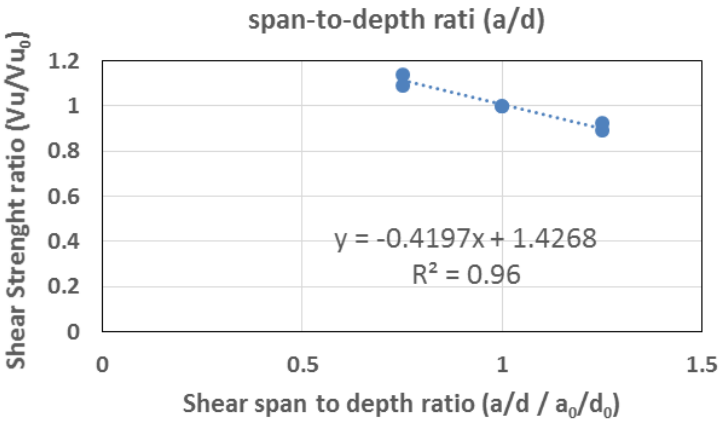

Figure 102 Sensitivity analysis of span-to-depth ratio to shear strength

Moreover, a perfect relationship (R^2=0.94) exists between the width ratio and the shear strength of the beams, as shown in Figure 103.

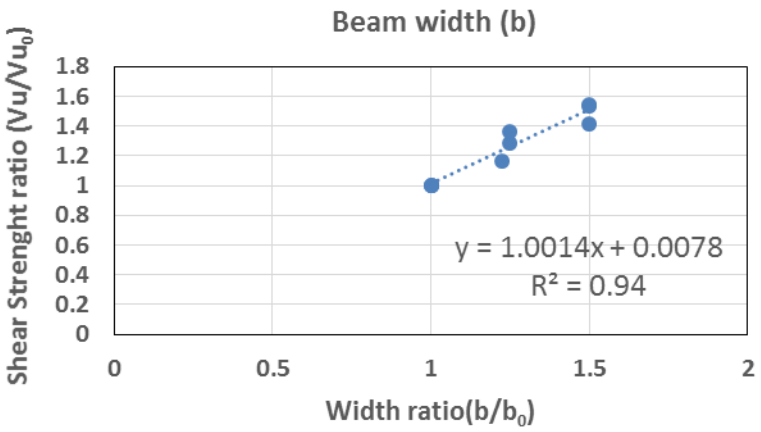

Figure 103 Sensitivity analysis of beam width to shear strength

The sensitivity analysis showed that the reinforcement ratio was negligible and didn't affect the shear strength significantly (Figure 104).

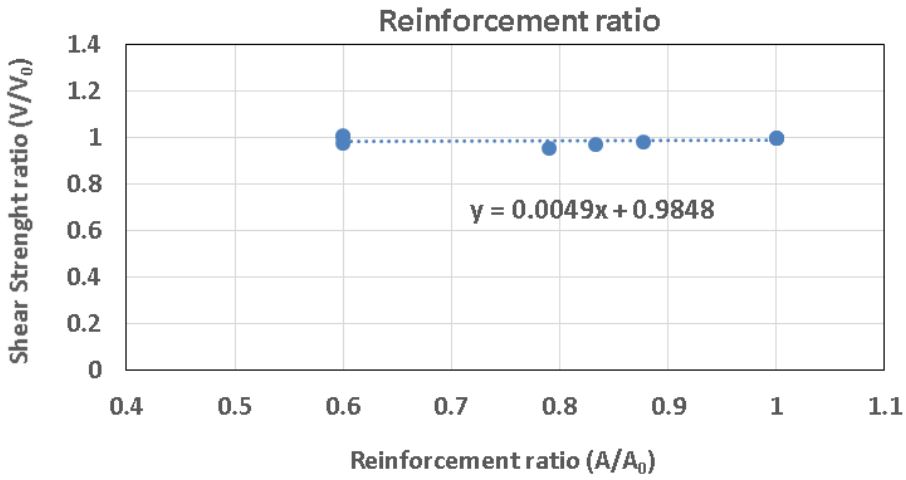

Figure 104 Sensitivity analysis of reinforcement ratio to shear strength

A simple formula was developed to predict the long-term (100 years) shear strength of concrete beams with a different volume fractions of polypropylene fibers (equation 18)

$$V_u = 5.6\left(1 + 0.35\,V_f(\%)\right).\sqrt{f'_c}.b.d.\left(1.4 - .17\,\frac{a}{d}\right) \qquad (18)$$

Where:

V_u: Long-term (100 years) shear prediction of polypropylene fiber-reinforced concrete beams with a compressive strength of 5 ksi at 28 days in this study.

V_f: Volume fraction of polypropylene fibers ($0 \leq V_f \leq 0.75\%$)

A_s : Longitudinal reinforcement area

b: Width of beam

$\frac{a}{d}$: span-to-depth ratio

Figure 105 shows the ratio of predicted and experimental shear strength with different volume fractions of fibers in this parametric study, with a mean and standard deviation for the predicted and experimental strength ratio of 1.01 and 0.04, respectively. The red dash in the figure indicates the ratio of predicted and experimental strength ratio equal to one.

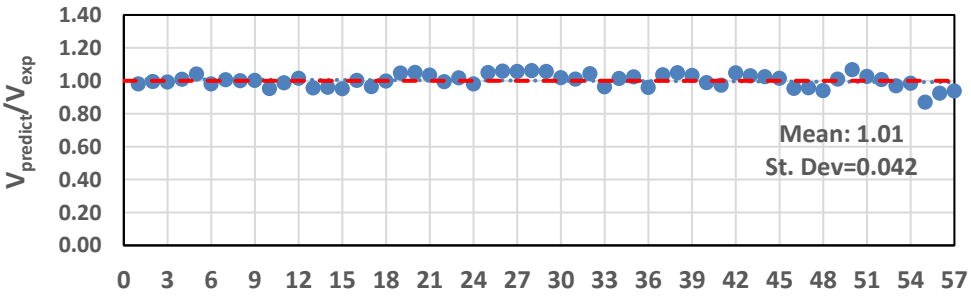

Figure 105 Evaluation of shear strength ratio of proposed equation and FEM

The results of the proposed formula for the shear strength of large-scale specimens in sensitivity analysis using Abaqus is summarized in Table 12.

Table 12 Summary of proposed formula for the shear strength of large-scale specimens in sensitivity analysis using Abaqus

Case	V_{FEM} (lbs)	$V_{Predict}$ (lbs)	$\frac{V_{Predict}}{V_{FEM}}$
1	51,400	50,392	0.98
2	59,498	59,161	0.99
3	64,057	63,545	0.99
4	49,978	50,392	1.01
5	56,839	59,161	1.04
6	64,845	63,545	0.98
7	50,139	50,392	1.01
8	59,158	59,161	1.00
9	63,432	63,545	1.00
10	66,191	62,990	0.95
11	74,918	73,951	0.99
12	78,350	79,431	1.01
13	79,053	75,589	0.96
14	92,492	88,741	0.96
15	100,223	95,317	0.95
16	164,570	164,855	1.00
17	200,888	193,540	0.96
18	208,370	207,882	1.00
19	157,506	164,855	1.05
20	184,282	193,540	1.05
21	201,083	207,882	1.03
22	165,853	164,855	0.99
23	190,233	193,540	1.02
24	212,126	207,882	0.98
25	192,012	201,490	1.05
26	223,695	236,549	1.06
27	240,526	254,078	1.06
28	233,167	247,283	1.06
29	274,830	290,310	1.06
30	306,242	311,823	1.02
31	146,385	147,717	1.01
32	166,379	173,419	1.04
33	193,593	186,271	0.96
34	179,555	181,994	1.01
35	208,959	213,660	1.02
36	239,441	229,494	0.96
37	295,606	306,194	1.04
38	342,903	359,471	1.05
39	374,225	386,110	1.03
40	309,818	306,194	0.99
41	369,674	359,471	0.97
42	368,834	386,110	1.05
43	297,424	306,194	1.03
44	350,961	359,471	1.02
45	380,703	386,110	1.01
46	401,512	382,742	0.95
47	469,641	449,339	0.96
48	513,936	482,638	0.94
49	455,247	459,291	1.01
50	505,708	539,207	1.07
51	564,506	579,165	1.03
52	272,504	274,362	1.01
53	332,691	322,101	0.97
54	351,530	345,970	0.98
55	389,018	338,026	0.87
56	429,784	396,842	0.92
57	454,573	426,251	0.94

8 SUMMARY AND CONCLUSIONS

8.1 Summary

The long-term behavior of polypropylene fibers on the shear strength and failure behavior of longitudinally reinforced concrete beams, with and without stirrups and subjected to accelerated aging conditions up to 6 months, were investigated. Accelerated aging methods of raising the pH of the saturated solution of calcium hydroxide to 12 with two constant temperatures of 50°C (122°F) and 70°C (158°F), based on Arrhenius principle, were used to find the long-term strength of material in a short time. The effects of introducing corrosion-free polypropylene fibers into the body of concrete were also studied.

A 3-D non-linear finite element modeling (FEM) with Concrete Damage Plasticity (CDP) was used to analyze the failure of the large-scale reinforced concrete beams. All of the experimental large-scale beam results were verified using FEM software. The concrete constitutive law in tension and compression, using FEM in 100 years, was developed to predict the long-term behavior of concrete beams. The correlation of main failure mechanisms in shear and crack occurrence to principal strains was investigated in this study.

The essential modeling parameters for shear capacity of large-scale beams with different volume fractions of polypropylene fibers for regression analysis were identified. Finally, a simple formula was developed to predict the long-term (100 years) shear strength of concrete beams with different volume fractions of polypropylene fibers.

8.2 Conclusion Remarks

The conclusions can be summarized as follows:

- The results revealed that the use of polypropylene fibers with volume fractions of 0.5% and 0.75% in the large-scale beam specimens can increase the shear strength of the beams by 16% and 29%, respectively.

- The tensile strength and shear strength degradation of concrete with volume fractions of 0%, 0.5%, and 0.75% were found to be 24.2%, 26.5% and 26.8%, respectively, after 100 years of actual weathering, while this degradation was found to be 13.0%, 14.3%, and 14.4%, respectively, after 50 years of actual weathering. The compressive strength degradation of concrete with volume fractions of 0%, 0.5%, and 0.75% was found to be 14.2%, 24.2% and 26.1%, respectively, after 100 years of actual weathering, while this degradation was found to be 7.3%, 12.9%, and 14.0%, respectively after 50 years of actual weathering.

- The addition of 0.75% polypropylene fibers can increase the shear capacity of concrete beams without stirrups by 29%, while using minimum conventional stirrups can increase the shear capacity of concrete beams by 31%. Fibers with a volume fraction of 0.75% can be considered as a replacement for the specimens with the minimum stirrups if 2% strength reduction is acceptable.

- The results showed that the use of polypropylene fibers with a volume fraction of 0.5% and 0.75% can increase the compressive strength of the cylinder specimens by 8.9% and 12%, respectively, at 28 days.

- A 3-D nonlinear FEM model was developed to predict the behavior of large-scale beams subjected to the different periods of accelerated aging conditions, with less than 1% error.

- FEM models were developed to predict the long-term shear behavior of the concrete beams with different volume fractions of fibers simulated to real-time weathering of 100 years.
- The tensile cracking is the main failure mechanisms in shear, and it was verified that cracks in concrete occur when the maximum principal tensile stress reaches the tensile stress of concrete, which is calculated by testing the small flexural beams according to ASTM 1609.
- The long-term shear design equation in 100 years was developed for different volume fractions of polypropylene fibers to enhance the service life of corrosion-free structures.
- Temperature plays a vital role on the degradation of the concrete specimens.
- The modulus of elasticity was approximated and found to be the same for all of the specimens with different volume fractions of polypropylene. The difference between the modulus of elasticity of specimens was insignificant (less than 1%) since the volume fraction of fibers was negligible (0.0075 volume of concrete).
- It was concluded that the rate of degradation of the shear strength of large-scale beams was in good agreement with the rate of degradation of tensile strength of the cylinder specimens.
- The sensitivity analysis showed that the reinforcement ratio is negligible and does not affect the shear strength significantly.
- The results showed that the use of polypropylene fibers with a volume fraction of 0.5% and 0.75% can increase the tensile strength of the cylinder specimens by 8% and 25%, respectively.

■ The specimens subjected to accelerated aging conditions such as high temperature, high humidity, and chemical exposure in the environmental chamber were correlated to actual long-term data, using Arrhenius principles.

■ The rate of degradation over time was higher for the specimens with higher volume fractions of polypropylene fibers.

■ There was no corrosion for the rebars embedded in concrete beams due to the adequate concrete cover.

■ Polypropylene fibers can bridge the cracks after failure and change the sudden, brittle, and explosive shear failure mode to the more desirable gradual failure.

■ Peak normalized shear stress of the SNFRC 0.5% and SNFRC 0.75% after 28-days of curing increased the shear stress of RC control beams from $6.01\sqrt{f'_c}$ (psi) to $6.86\sqrt{f'_c}$ and $7.71\sqrt{f'_c}$, respectively.

8.3 Suggested Future Studies

The following are suggestions for future studies:

■ The current study could be modified and conducted with a different compressive strengths of concrete since this study was focused on only the compressive strength of 5 ksi at 28 days.

■ A calcium hydroxide chemical compound was added to the water, raising the pH of the saturated solution to 12 to accelerate the aging of the concrete specimens. The effects of different levels of pH could be investigated in future studies. Higher temperatures could also be considered to find the effects of heat on the fibers.

■ Different span-to-depth ratios could be considered to study the shear behavior of deep or slender beams.

■ Dog-bone shape specimens could be casted to obtain the stress-strain response of concrete specimens in tension.

Appendix A

Crack Patterns and Propagation

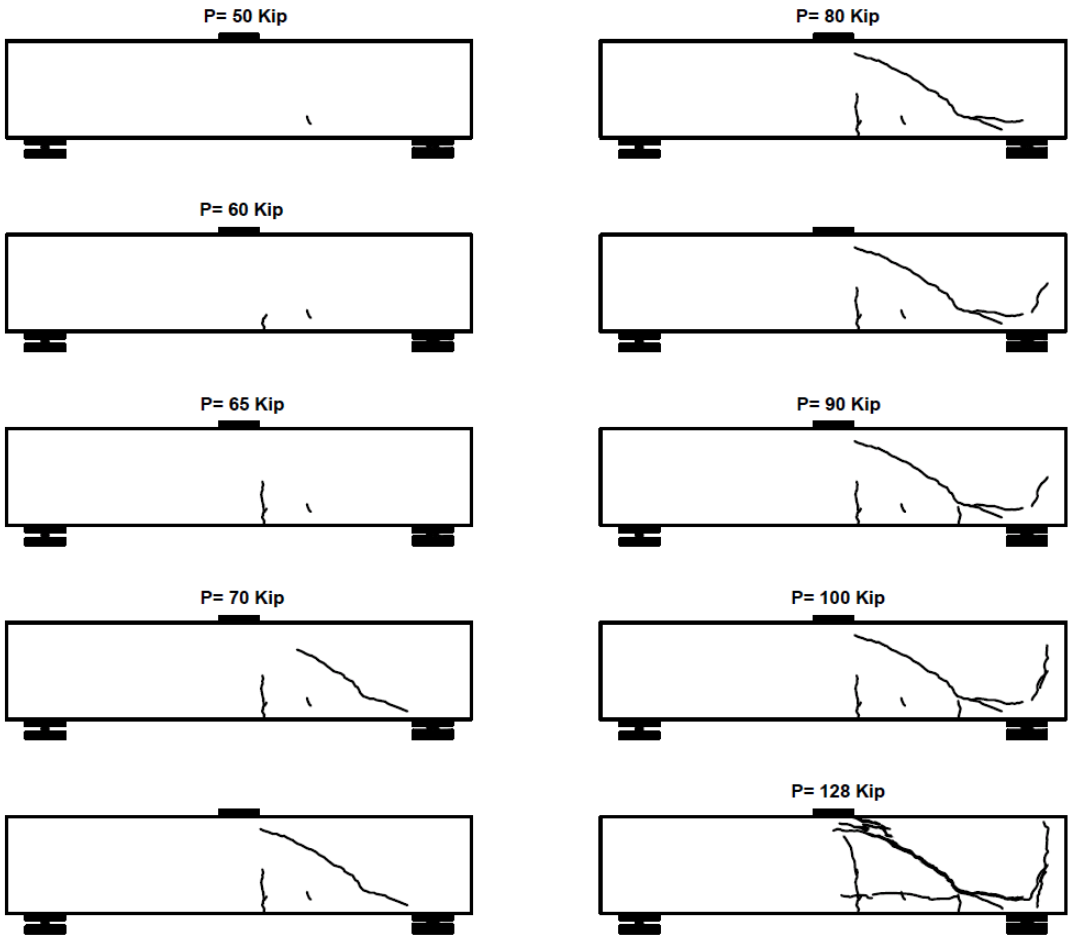

Figure 106 Crack pattern for RC beam #1

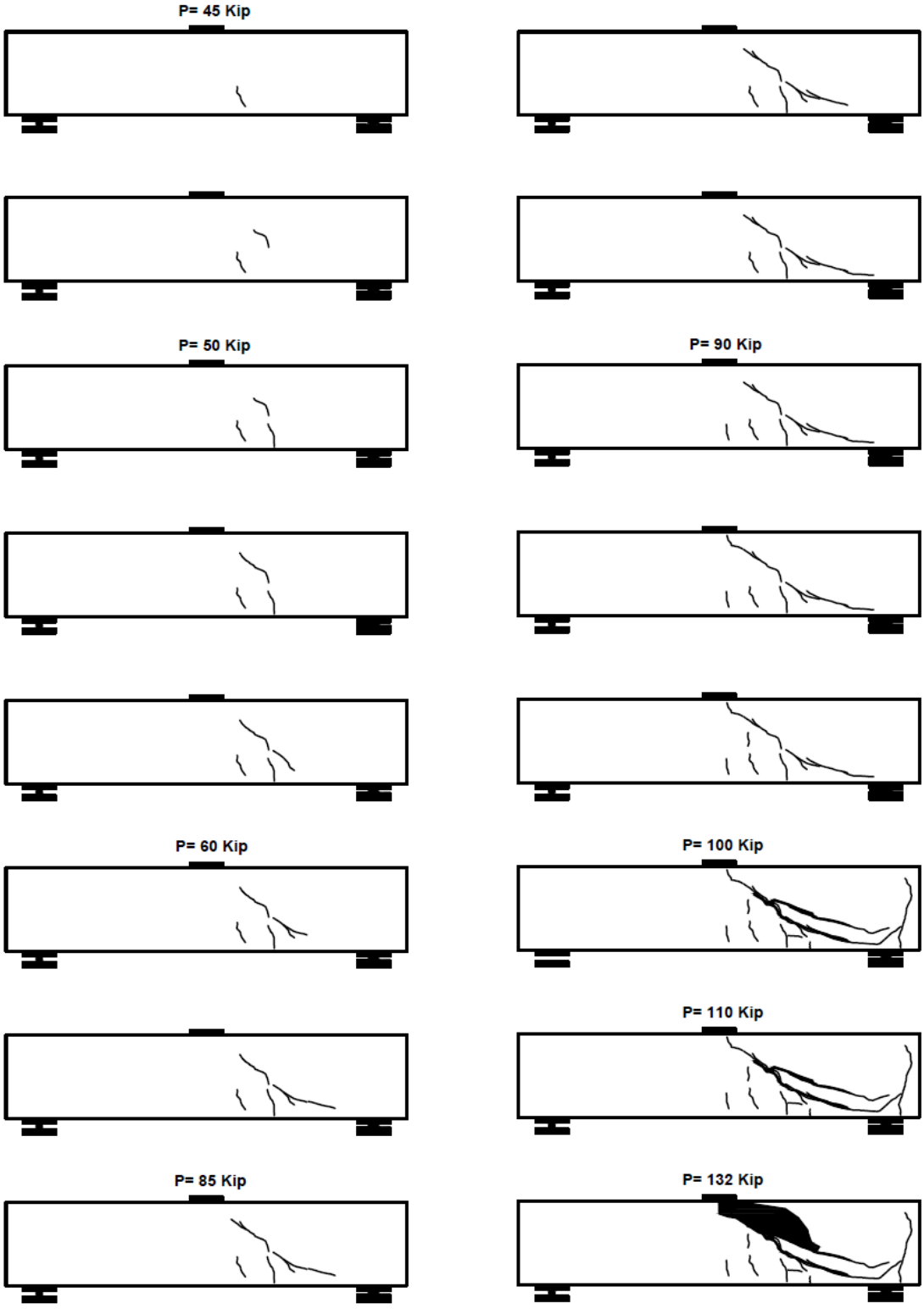

Figure 107 Crack pattern for RC beam #2

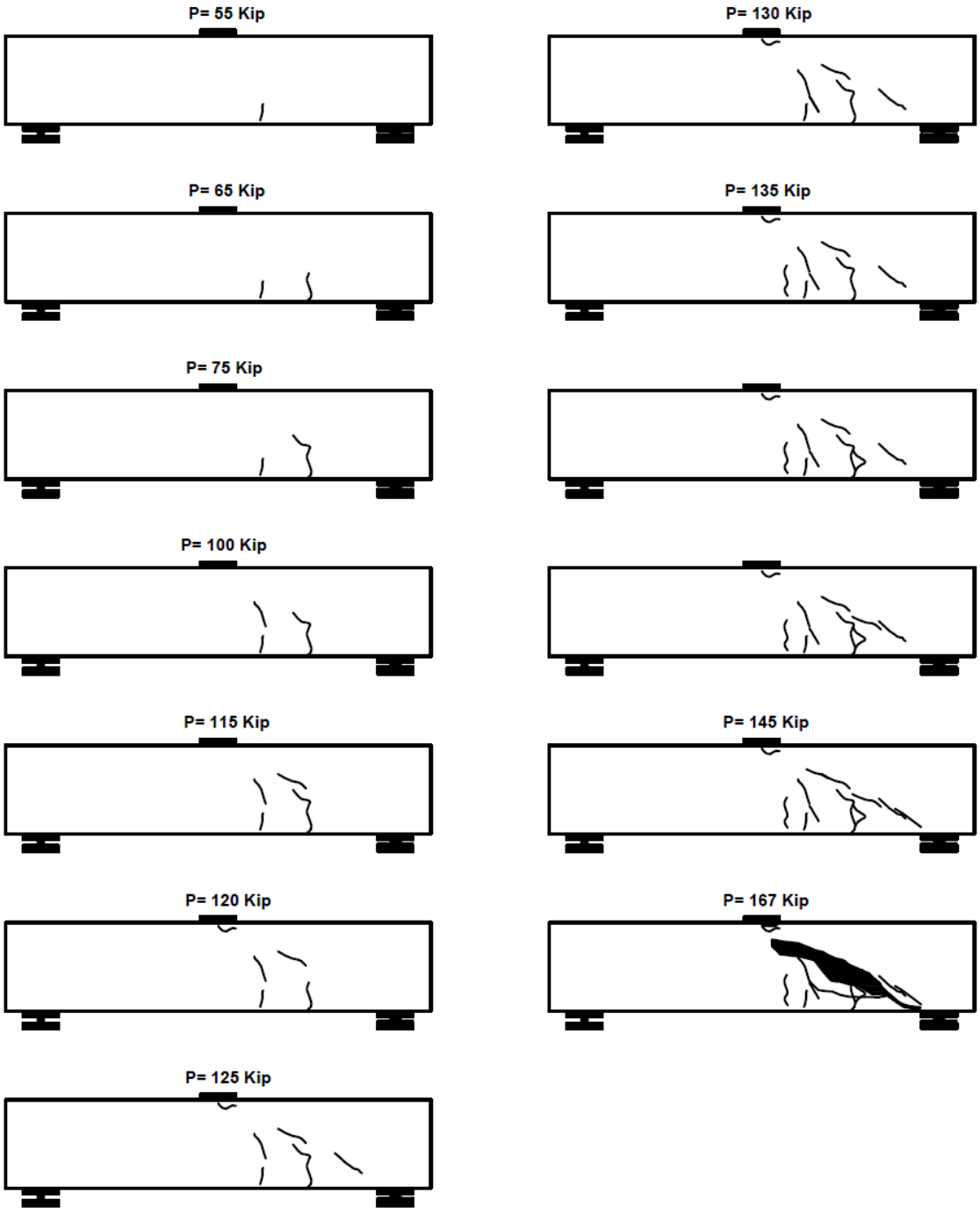

Figure 108 Crack pattern for RCS beam #3

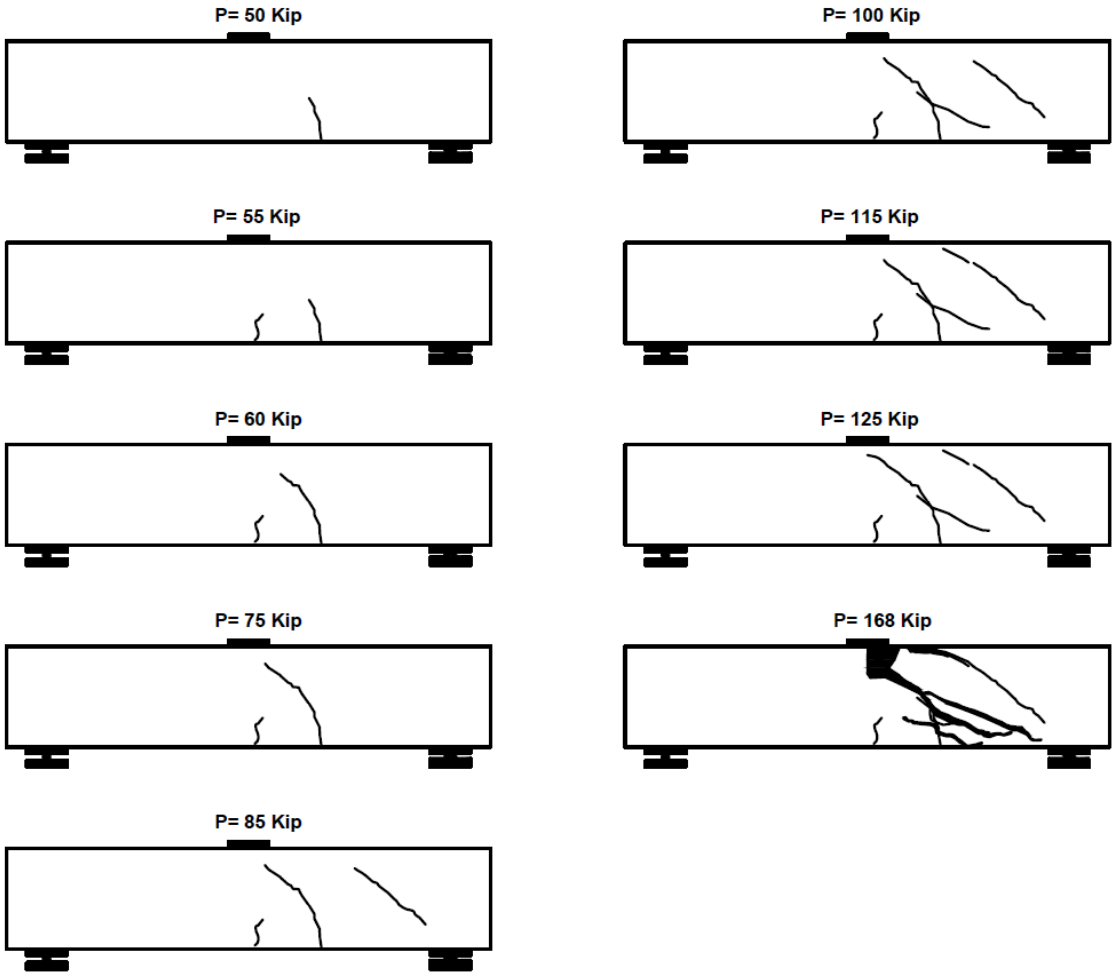

Figure 109 Crack pattern for RCS beam #4

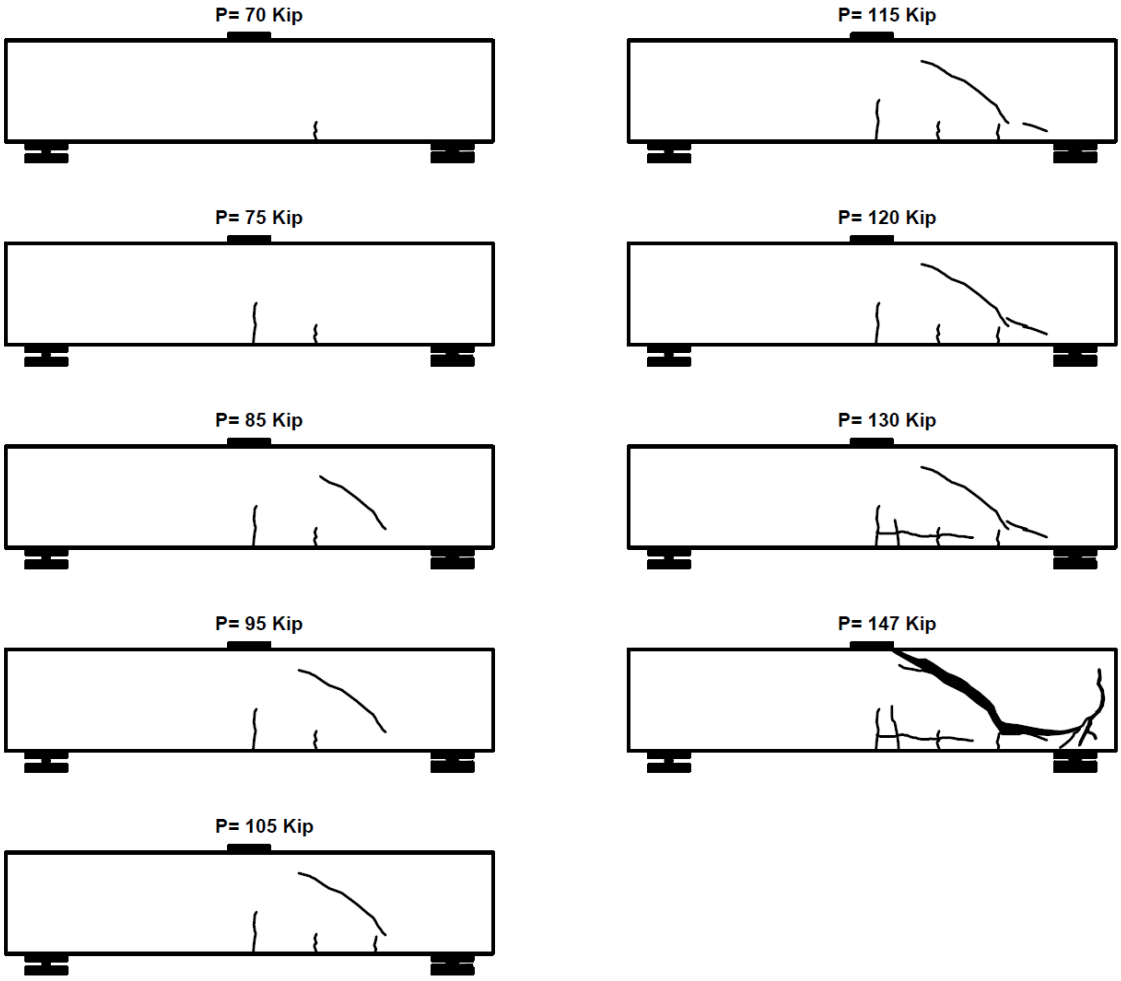

Figure 110 Crack pattern for SNFRC 0.5% beam #5

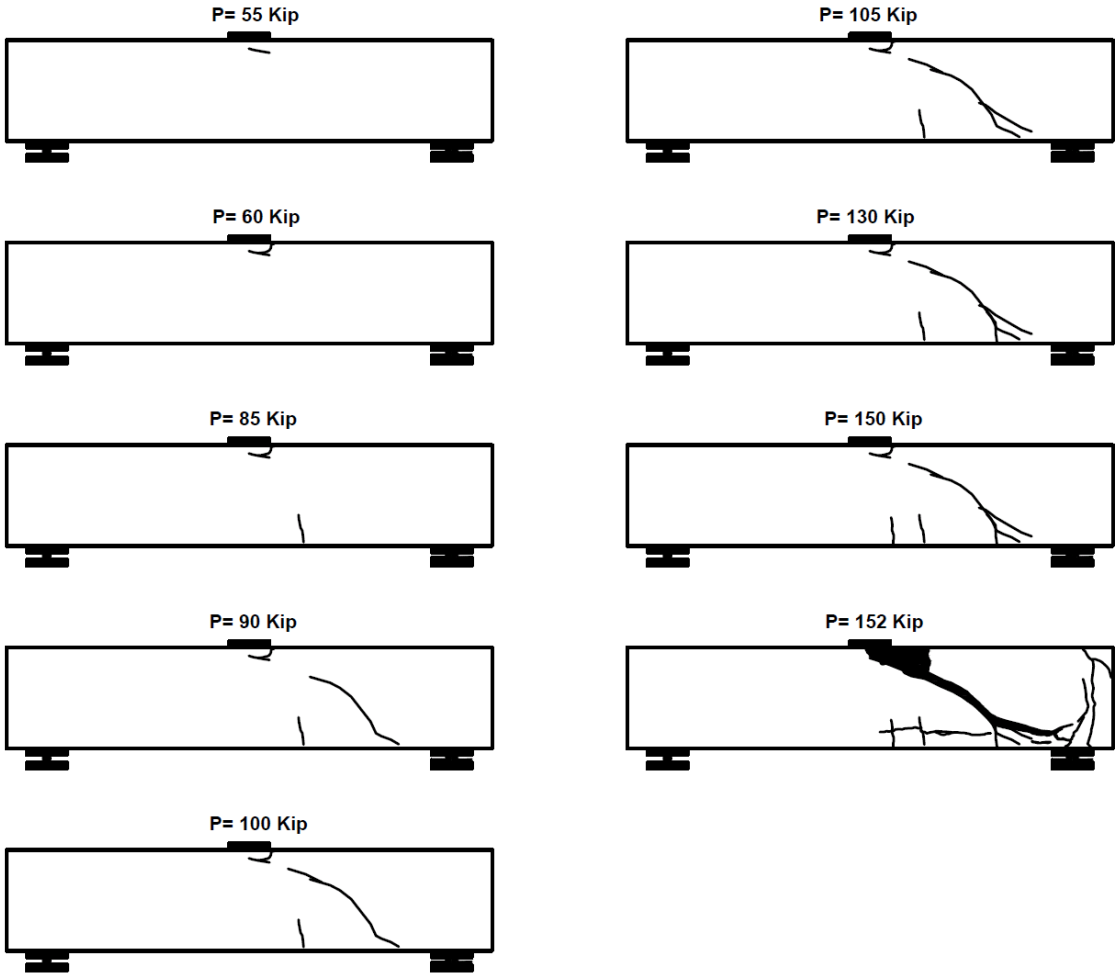

Figure 111 Crack pattern for SNFRC 0.5% beam #6

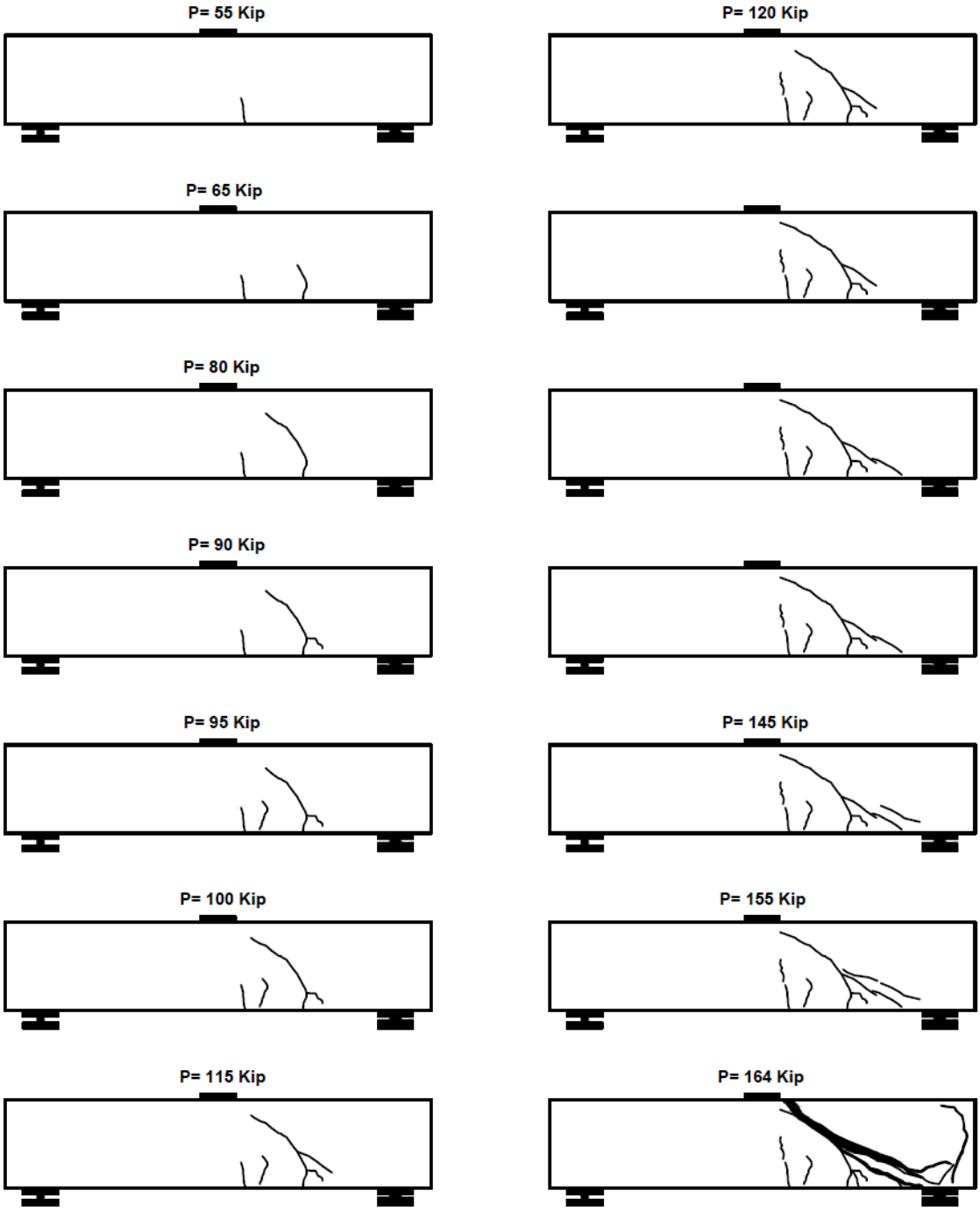

Figure 112 Crack pattern for SNFRC 0.75% beam #7

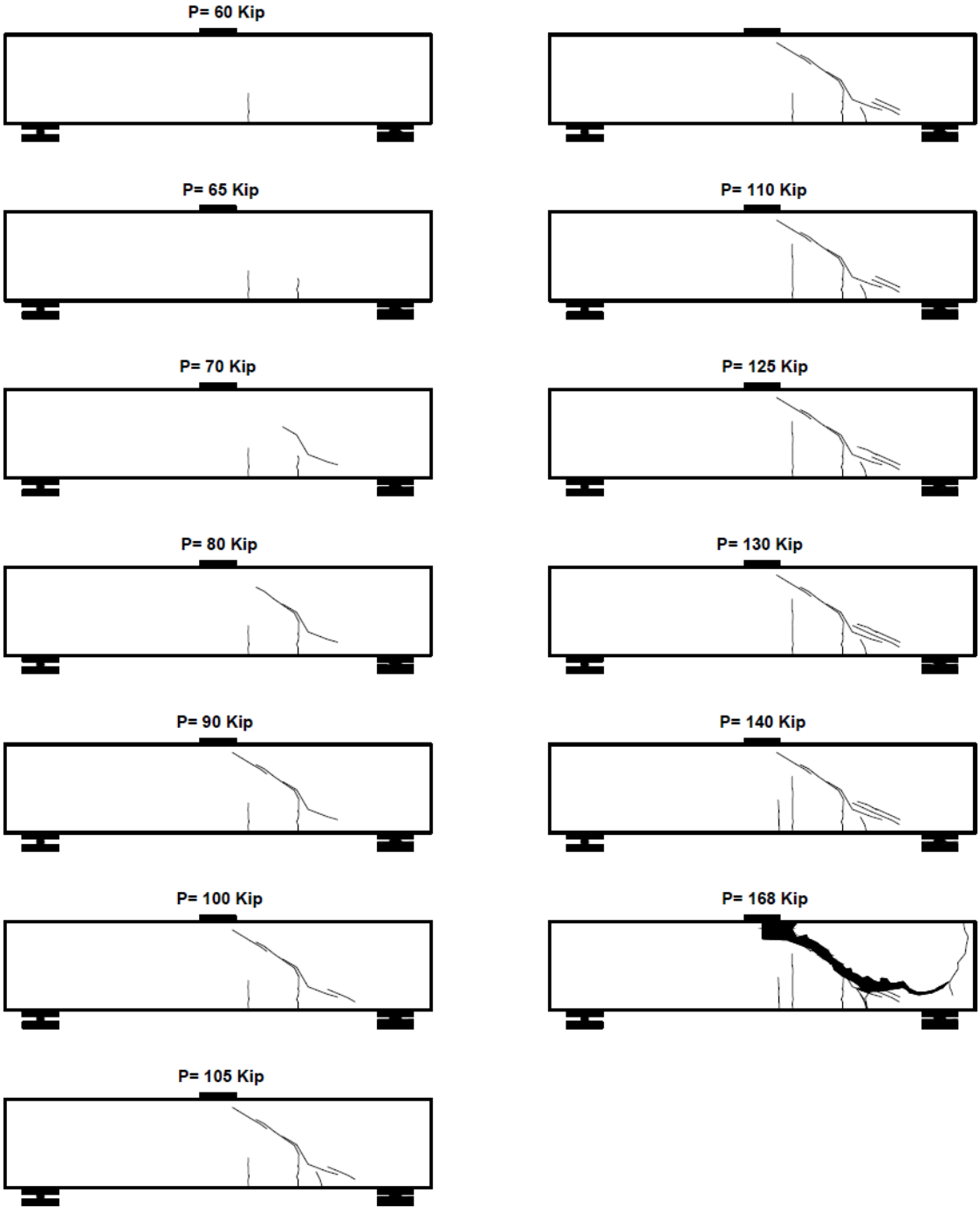

Figure 113 Crack pattern for SNFRC 0.75% beam #8

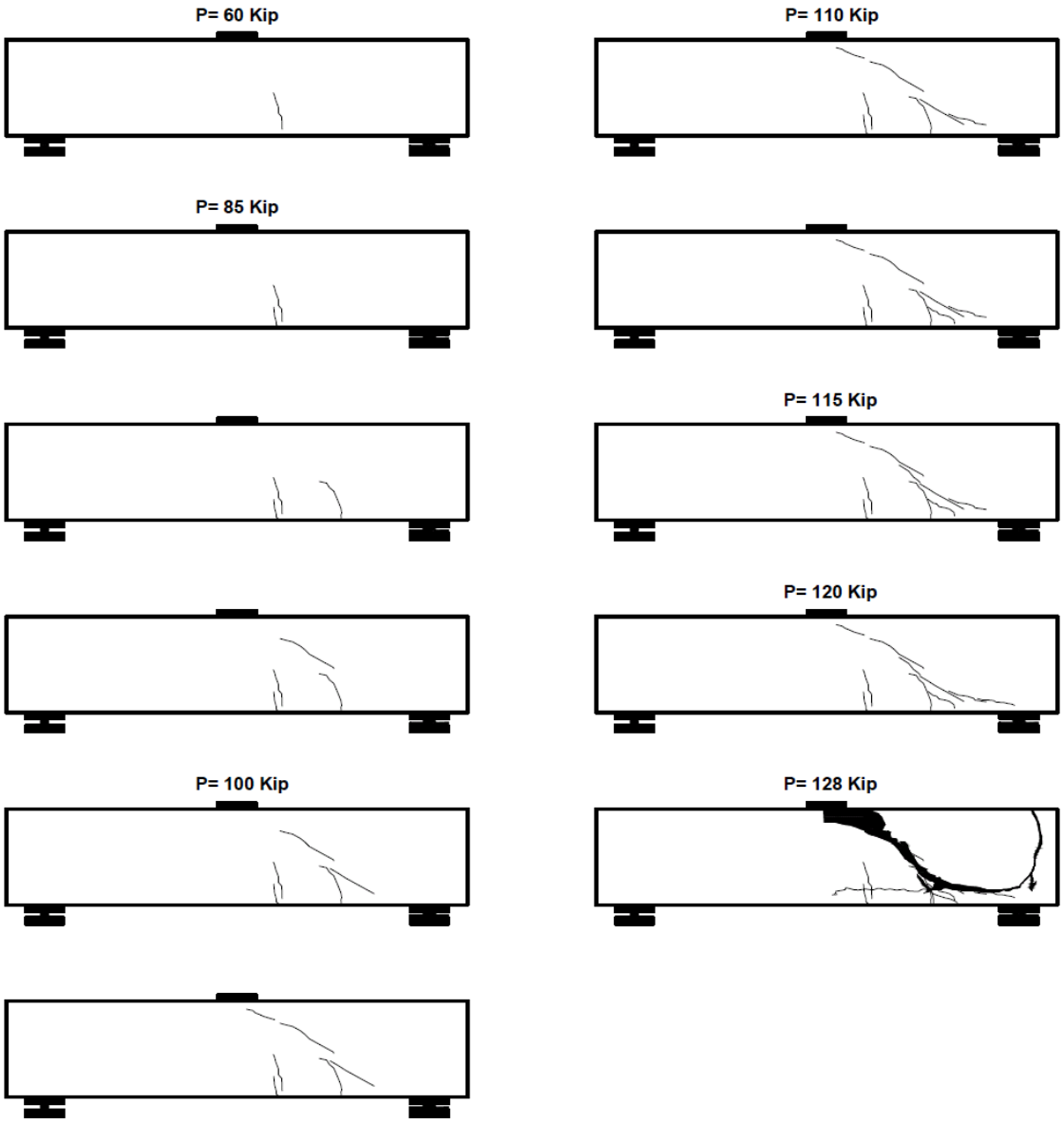

Figure 114 Crack pattern for RC beam #9

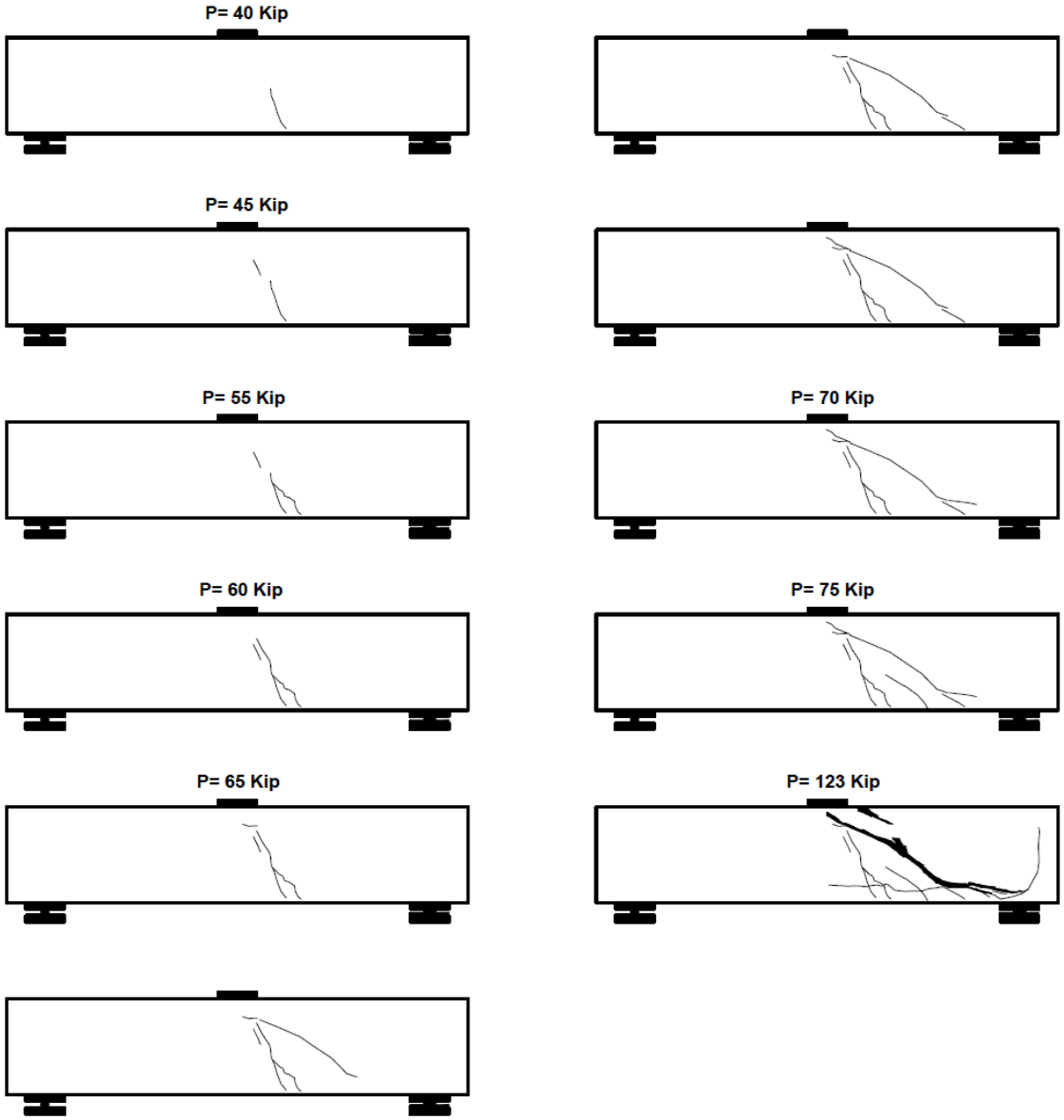

Figure 115 Crack pattern for RC beam #10

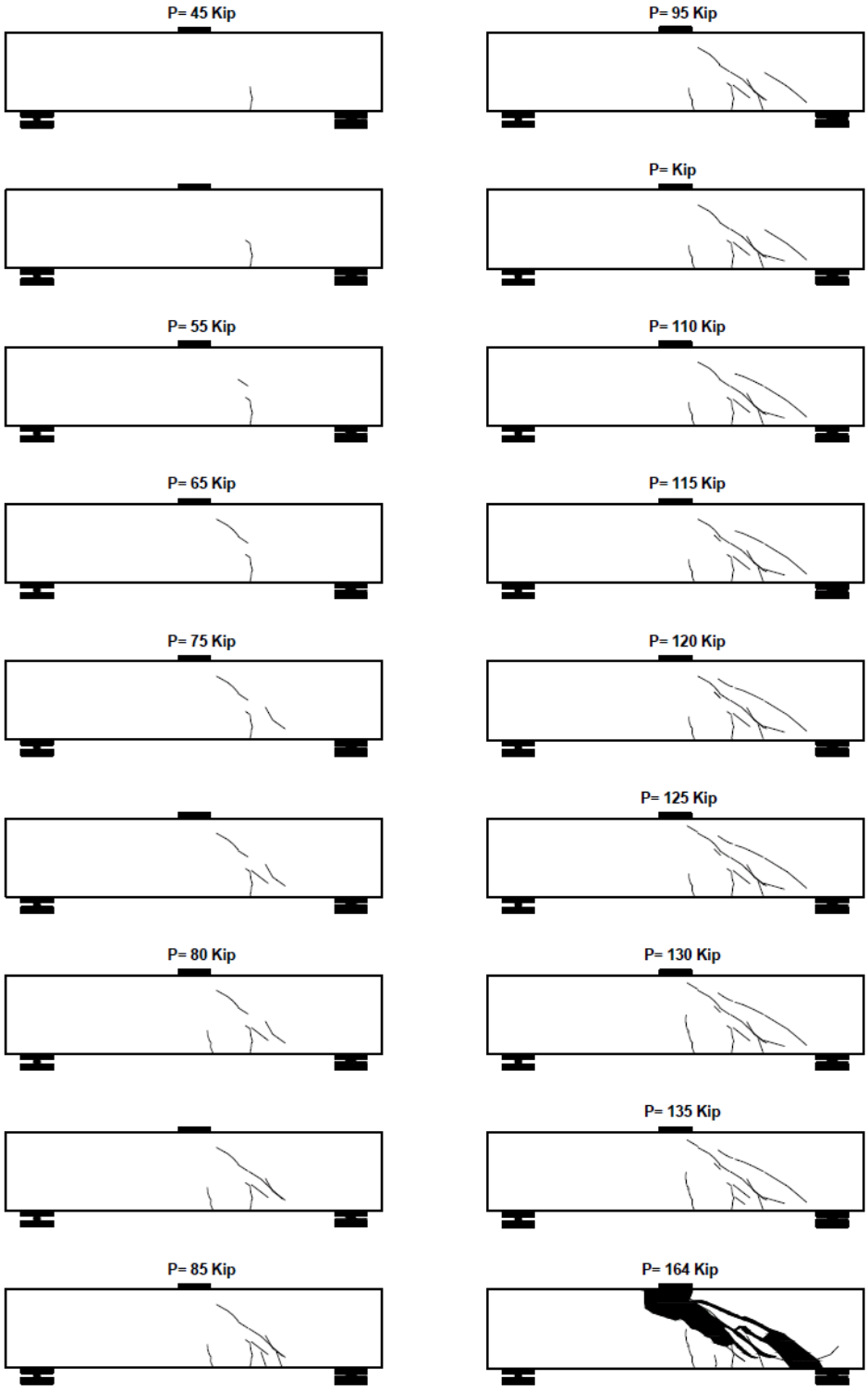

Figure 116 Crack pattern for RCS beam #11

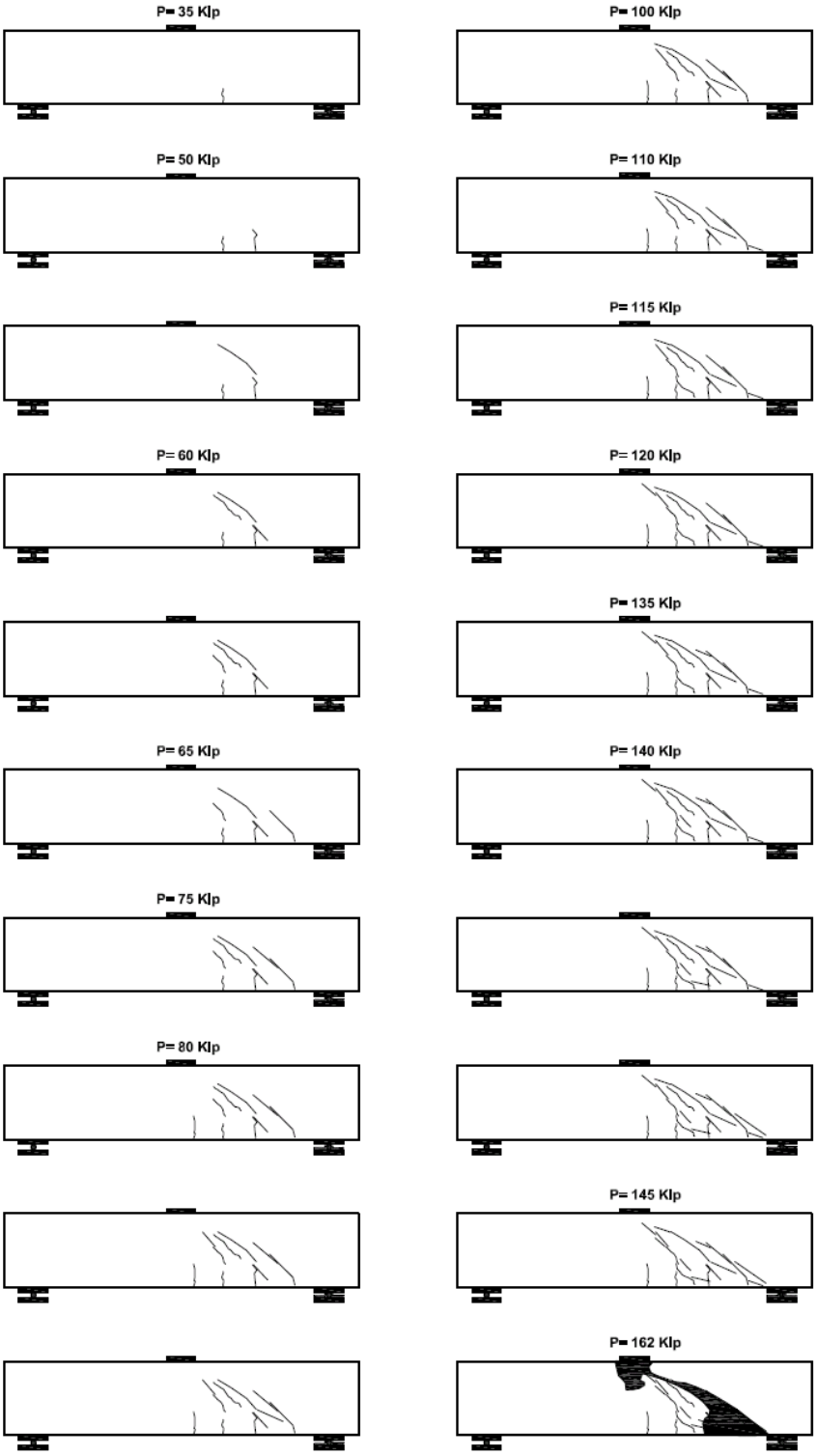

Figure 117 Crack pattern for RCS beam #12

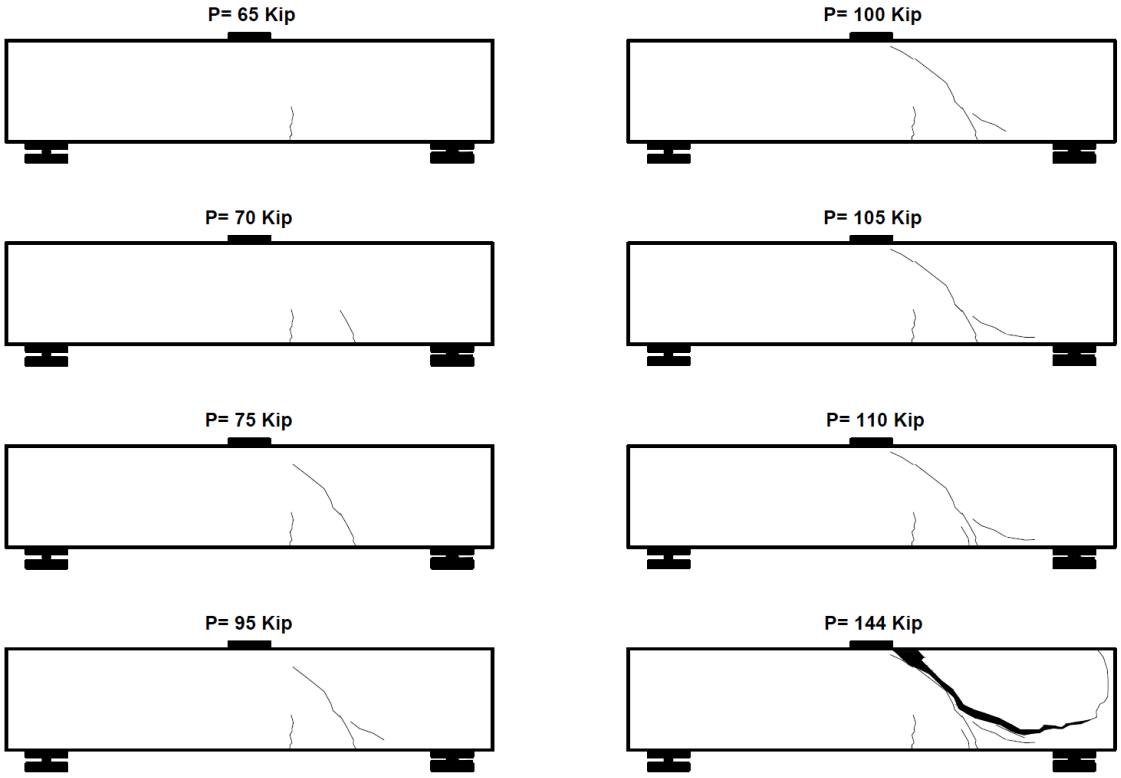

Figure 118 Crack pattern for SNFRC 0.5% beam #13

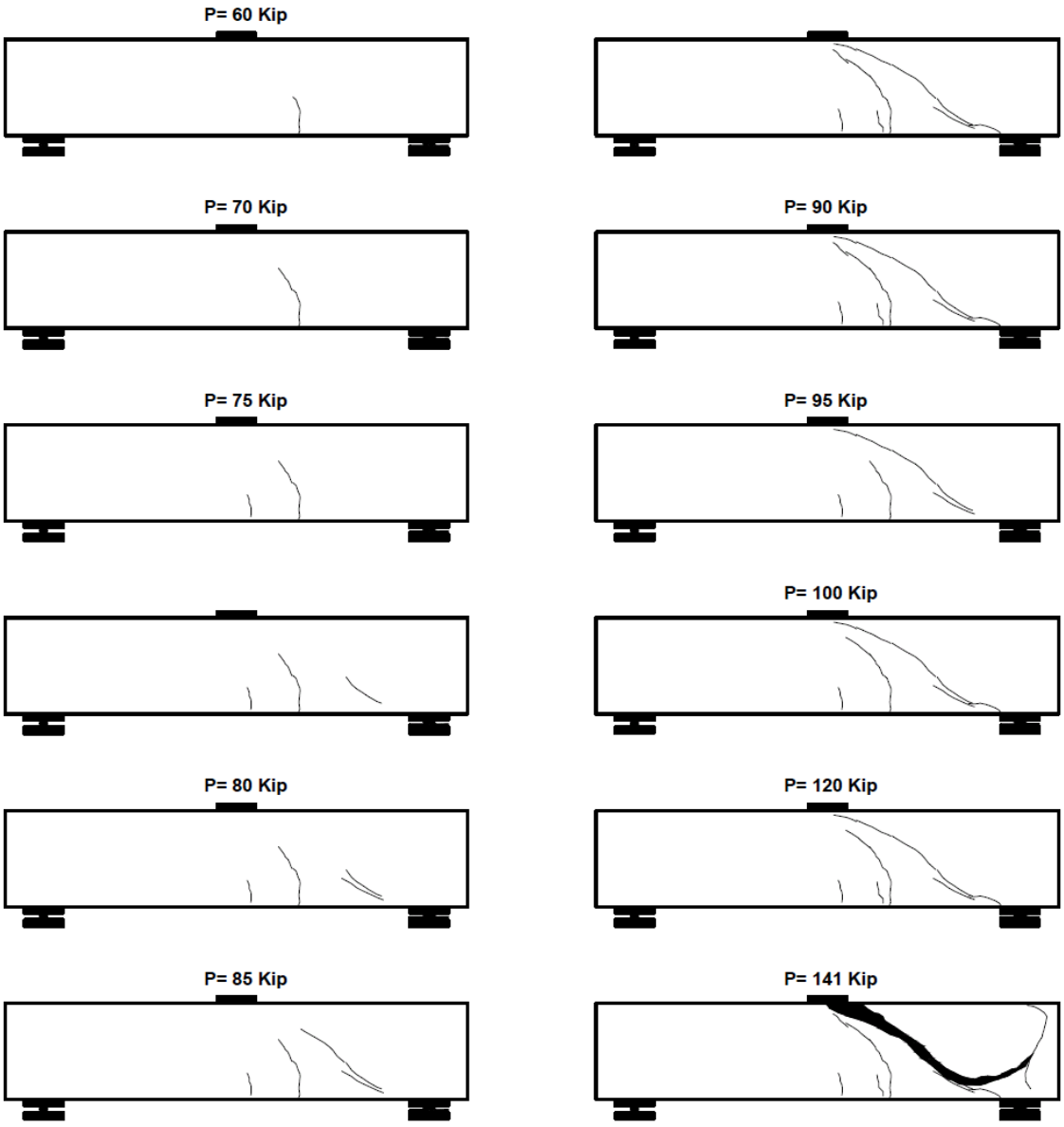

Figure 119 Crack pattern for SNFRC 0.5% beam #14

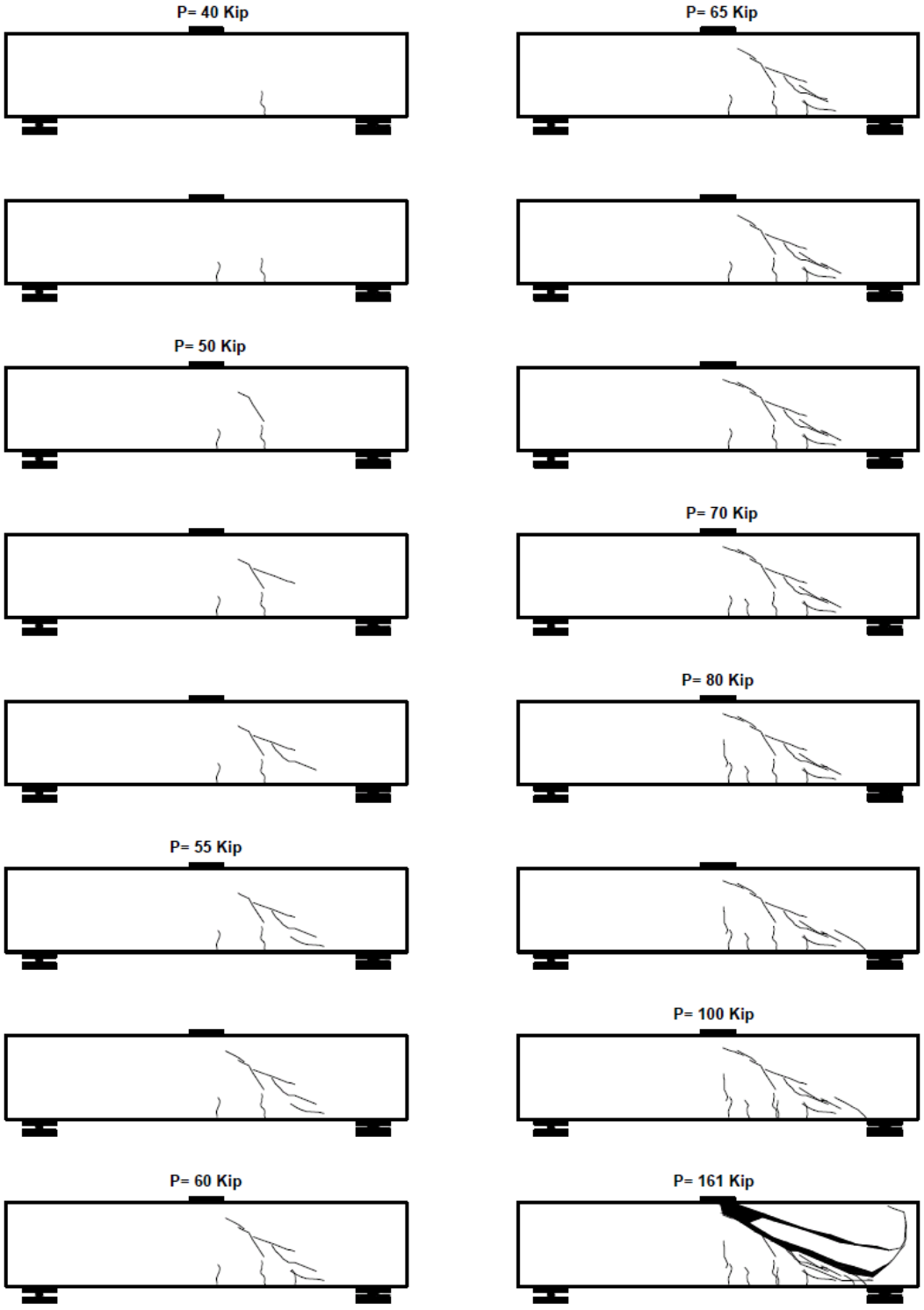

Figure 120 Crack pattern for SNFRC 0.75% beam #15

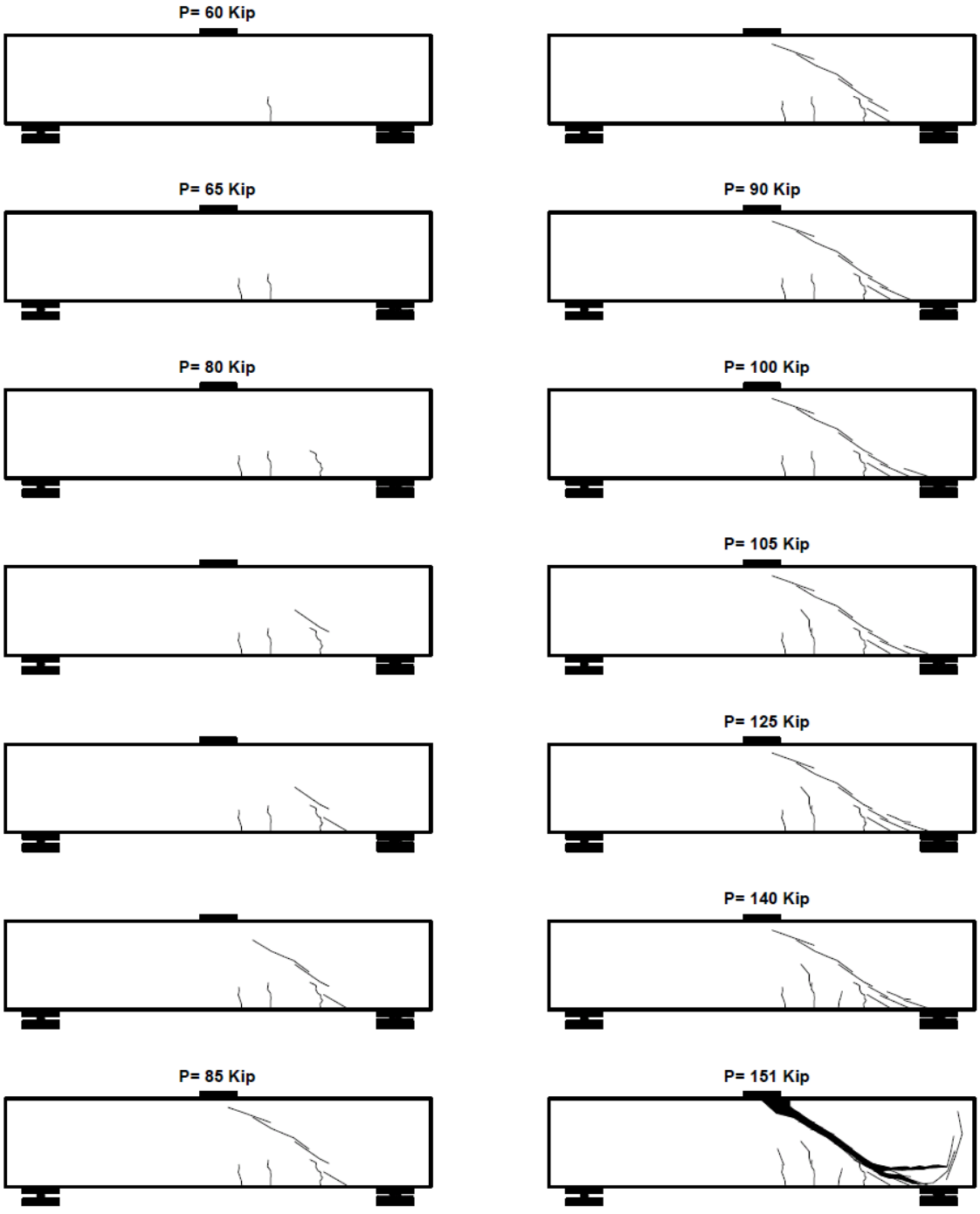

Figure 121 Crack pattern for SNFRC 0.75% beam #16

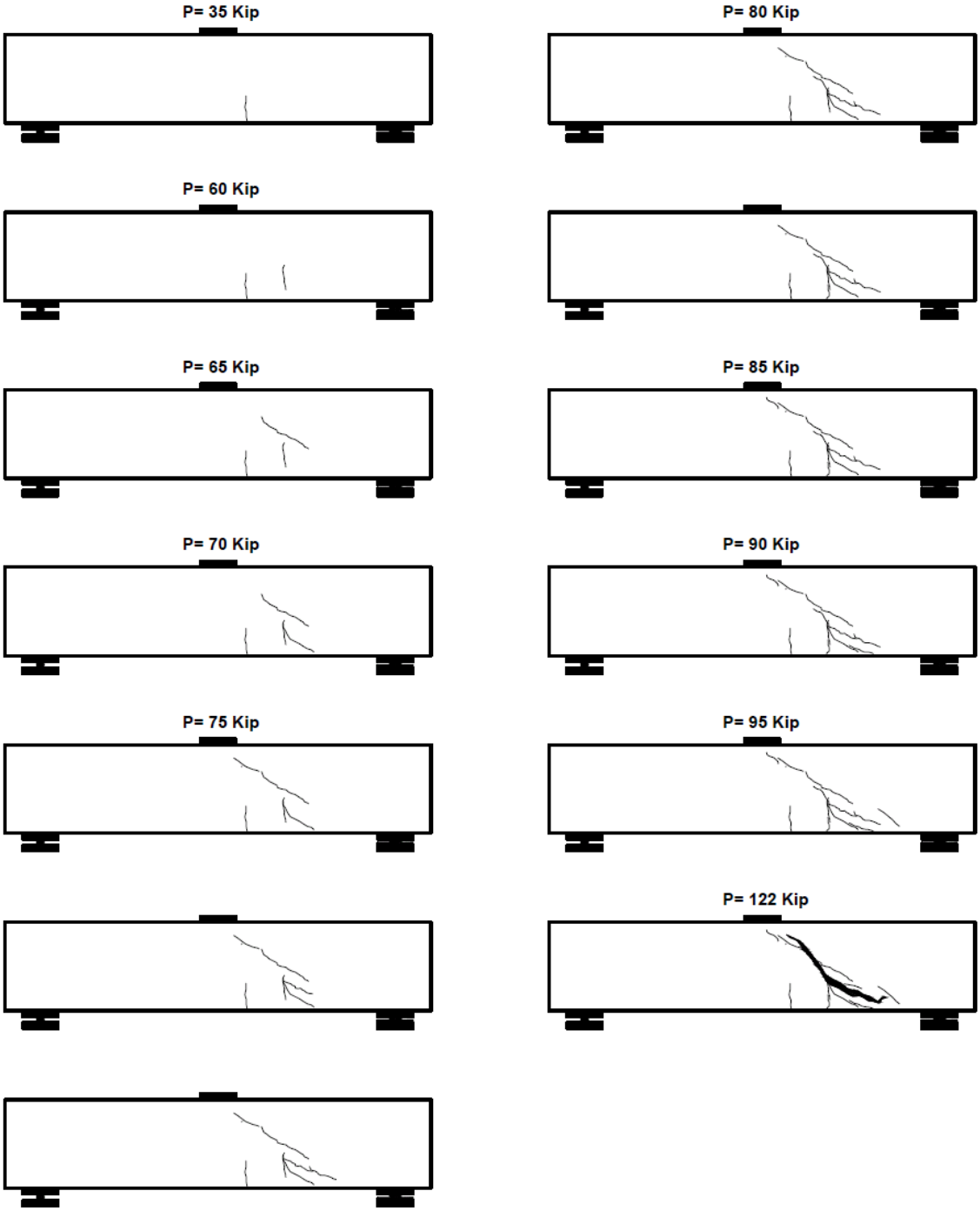

Figure 122 Crack pattern for RC beam #17

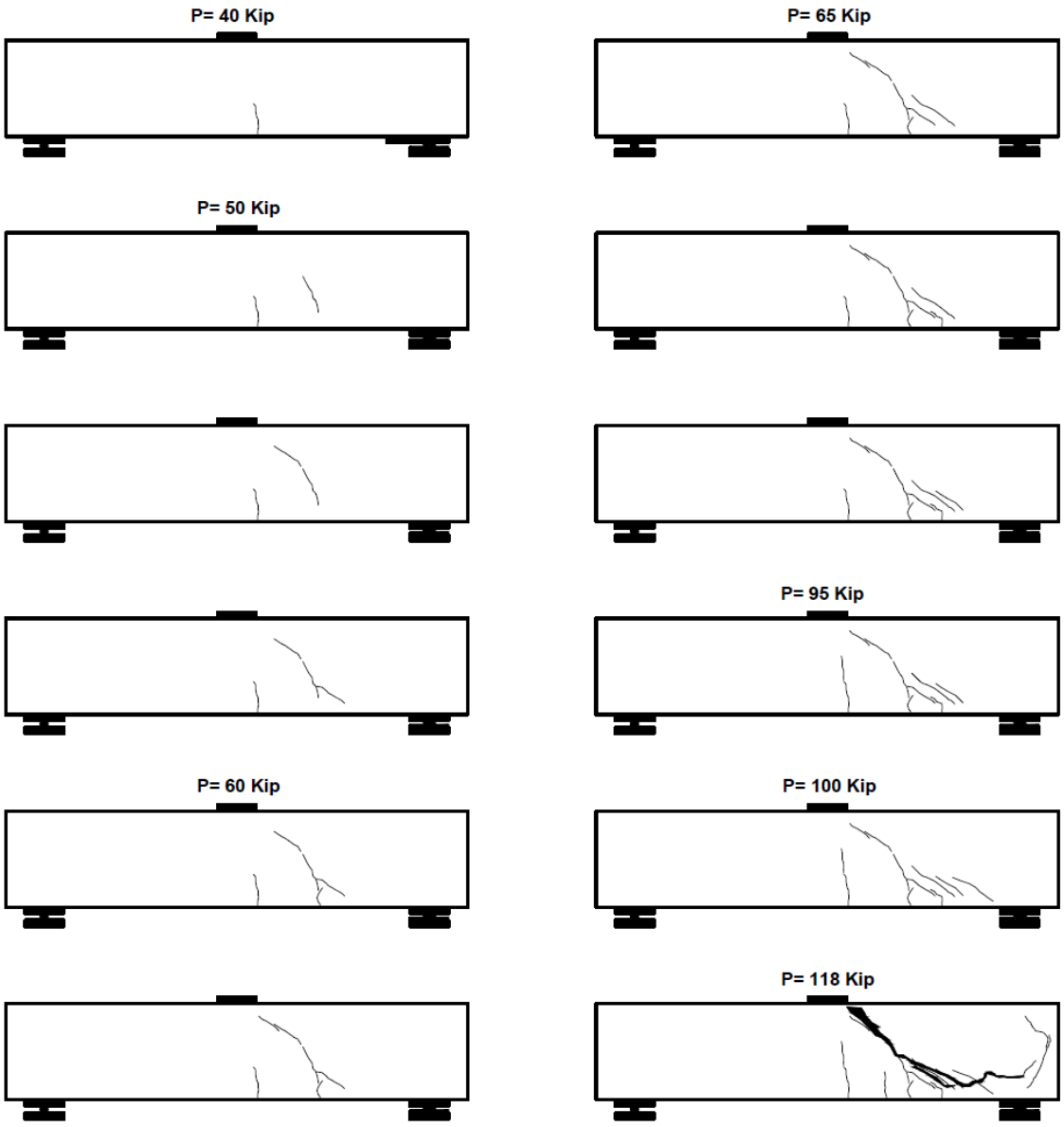

Figure 123 Crack pattern for RC beam #18

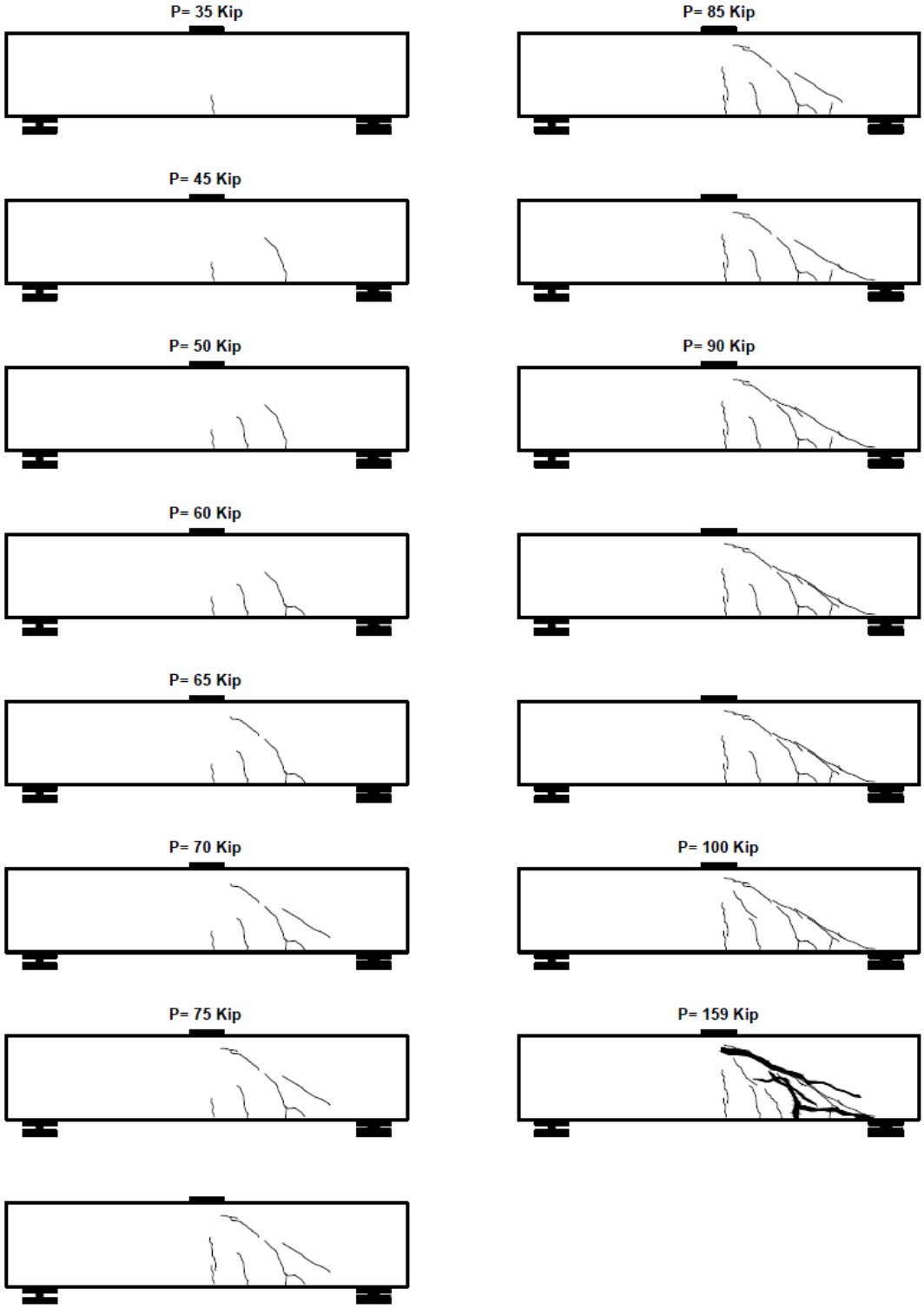

Figure 124 Crack pattern for RCS beam #19

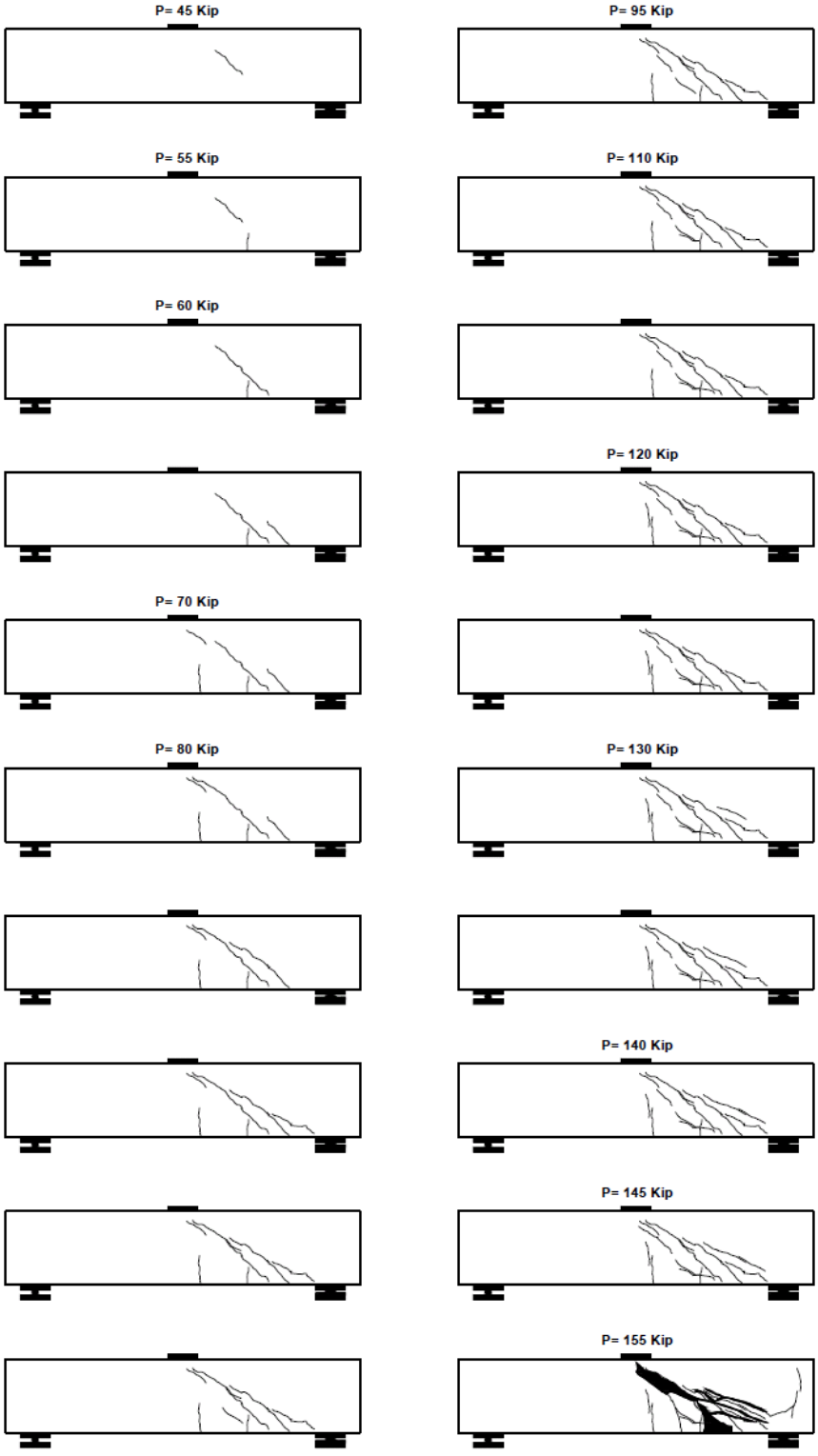

Figure 125 Crack pattern for RCS beam #20

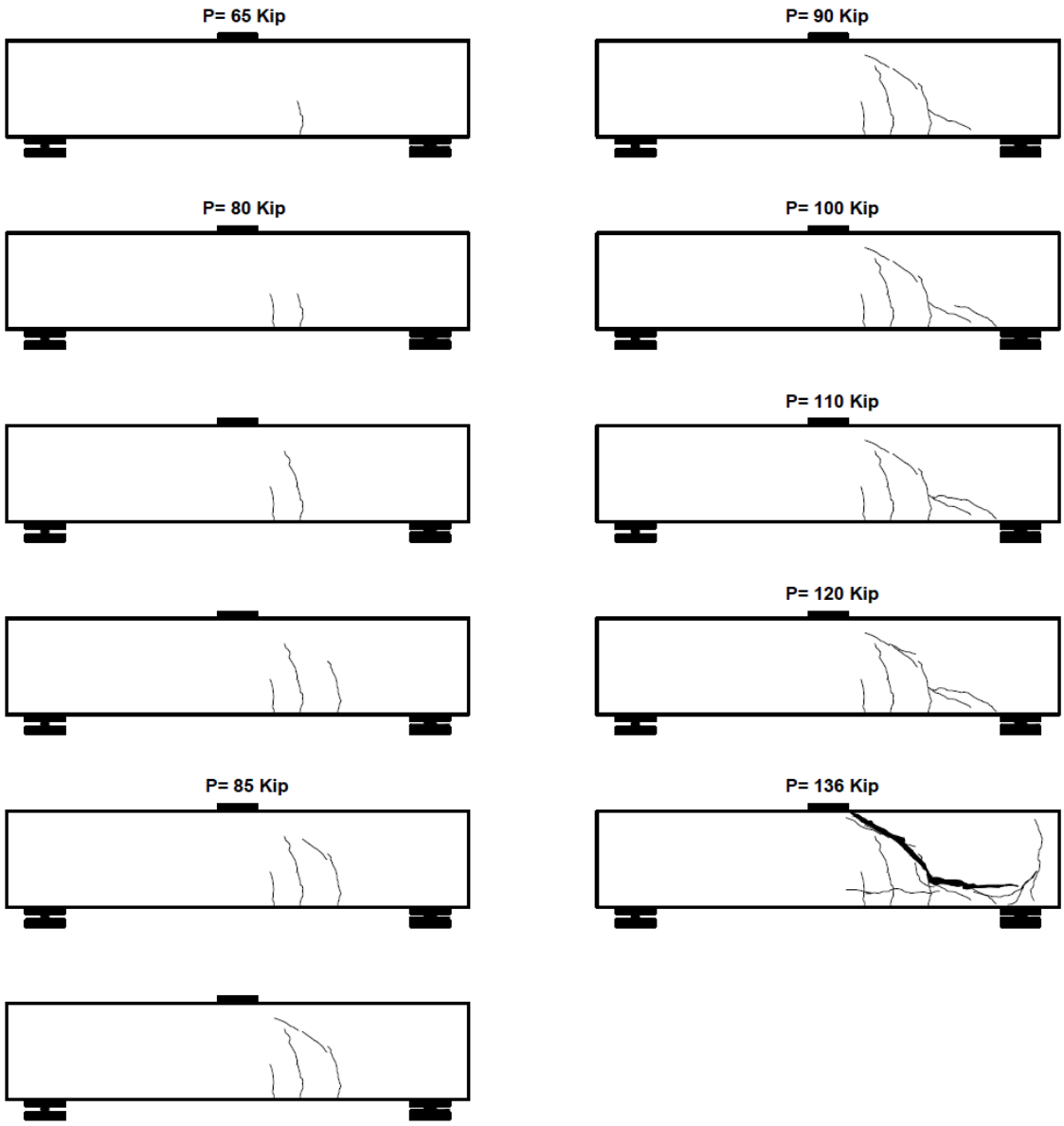

Figure 126 Crack pattern for SNFRC 0.5% beam #21

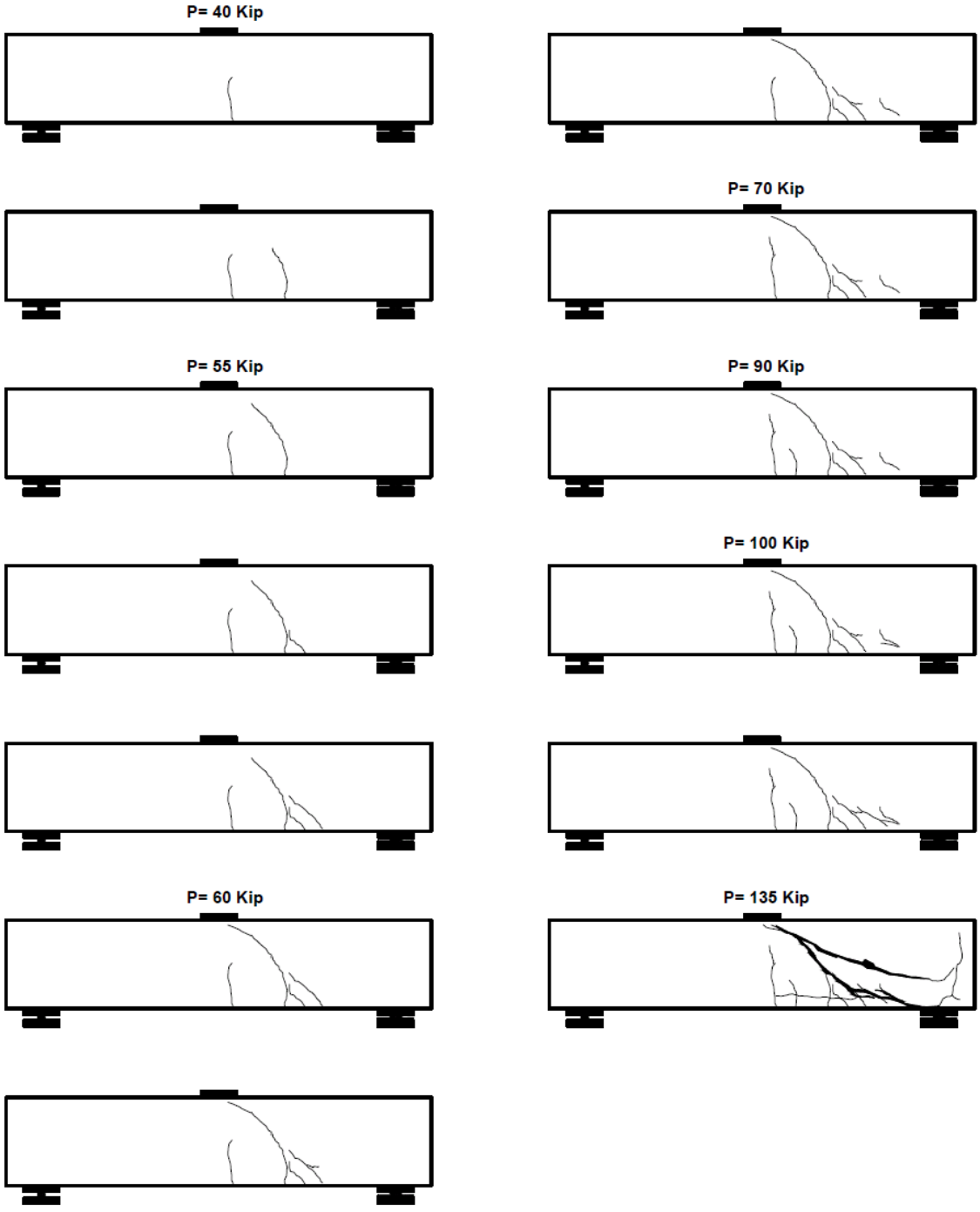

Figure 127 Crack pattern for SNFRC 0.5% beam #22

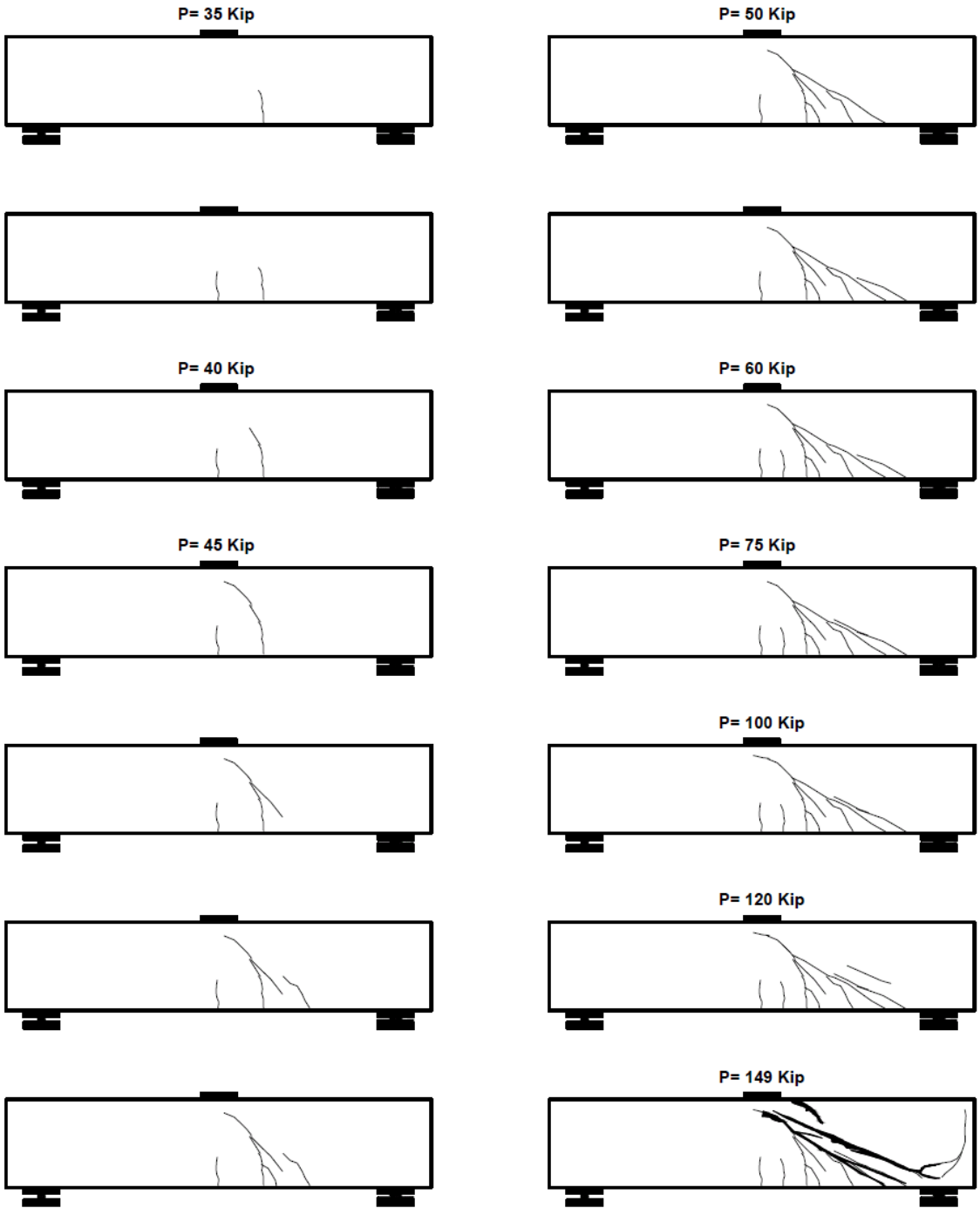

Figure 128 Crack pattern for SNFRC 0.75% beam #23

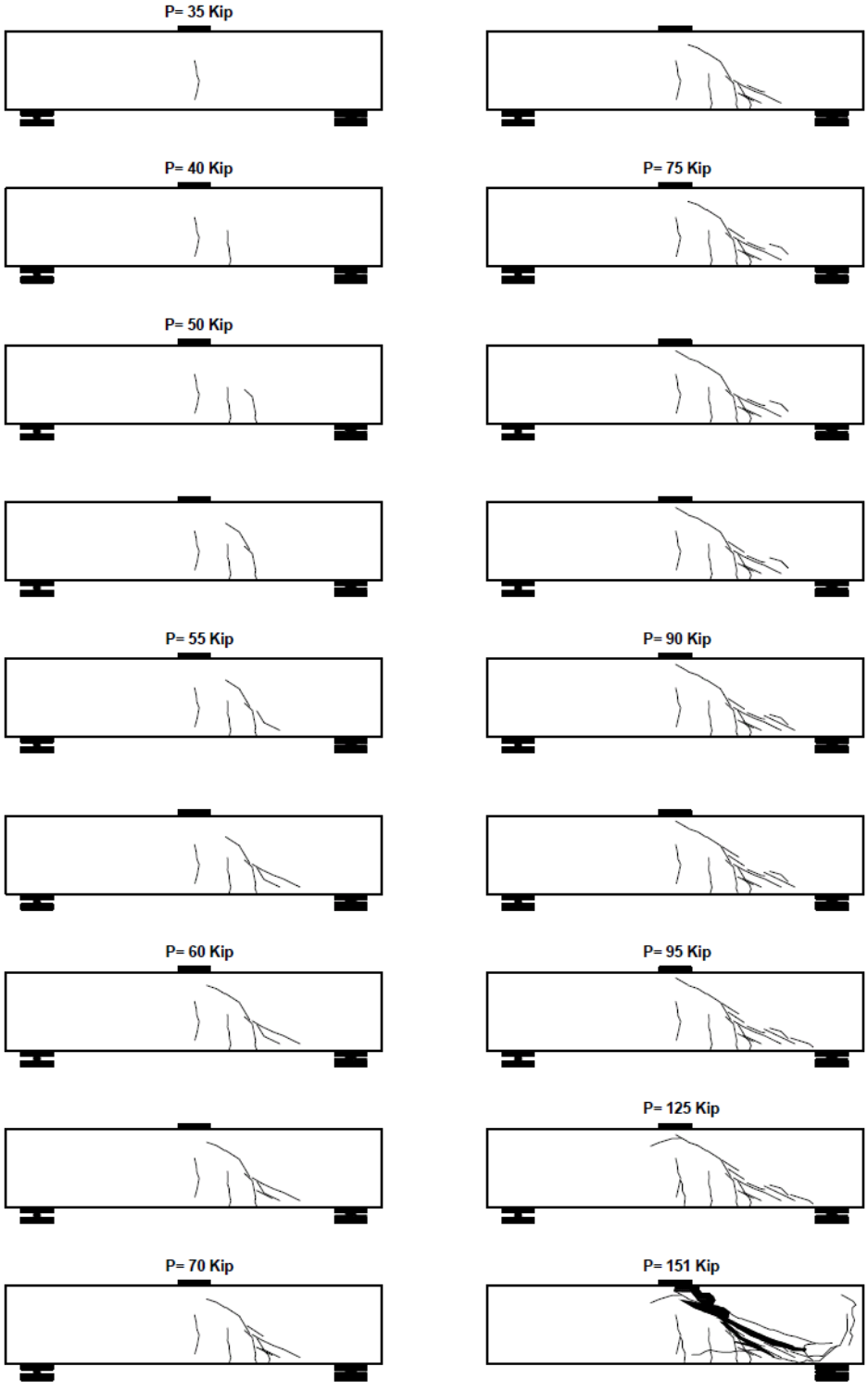

Figure 129 Crack pattern for SNFRC 0.75% beam #24

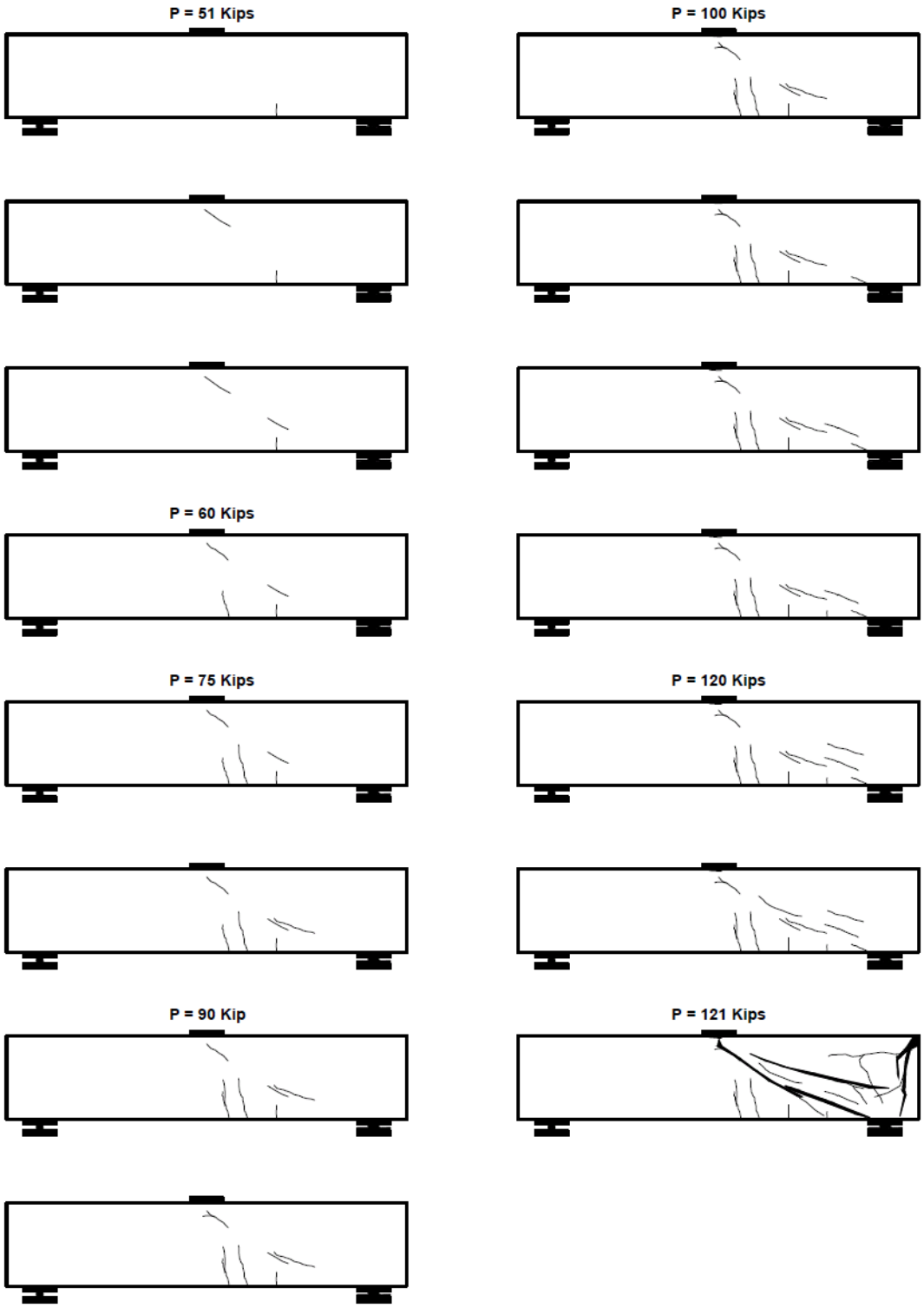

Figure 130 Crack pattern for RC beam #25

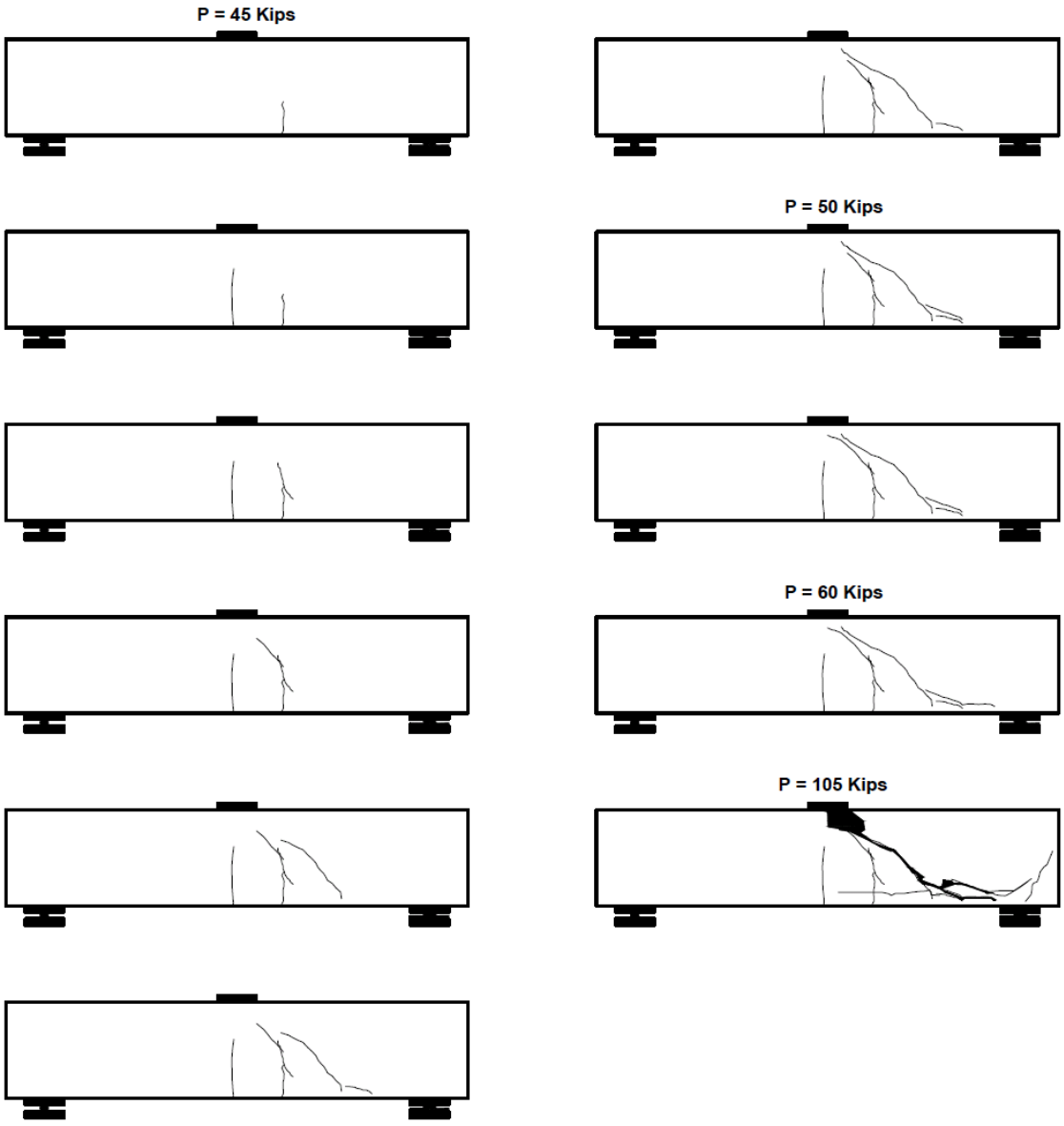

Figure 131 Crack pattern for RC beam #26

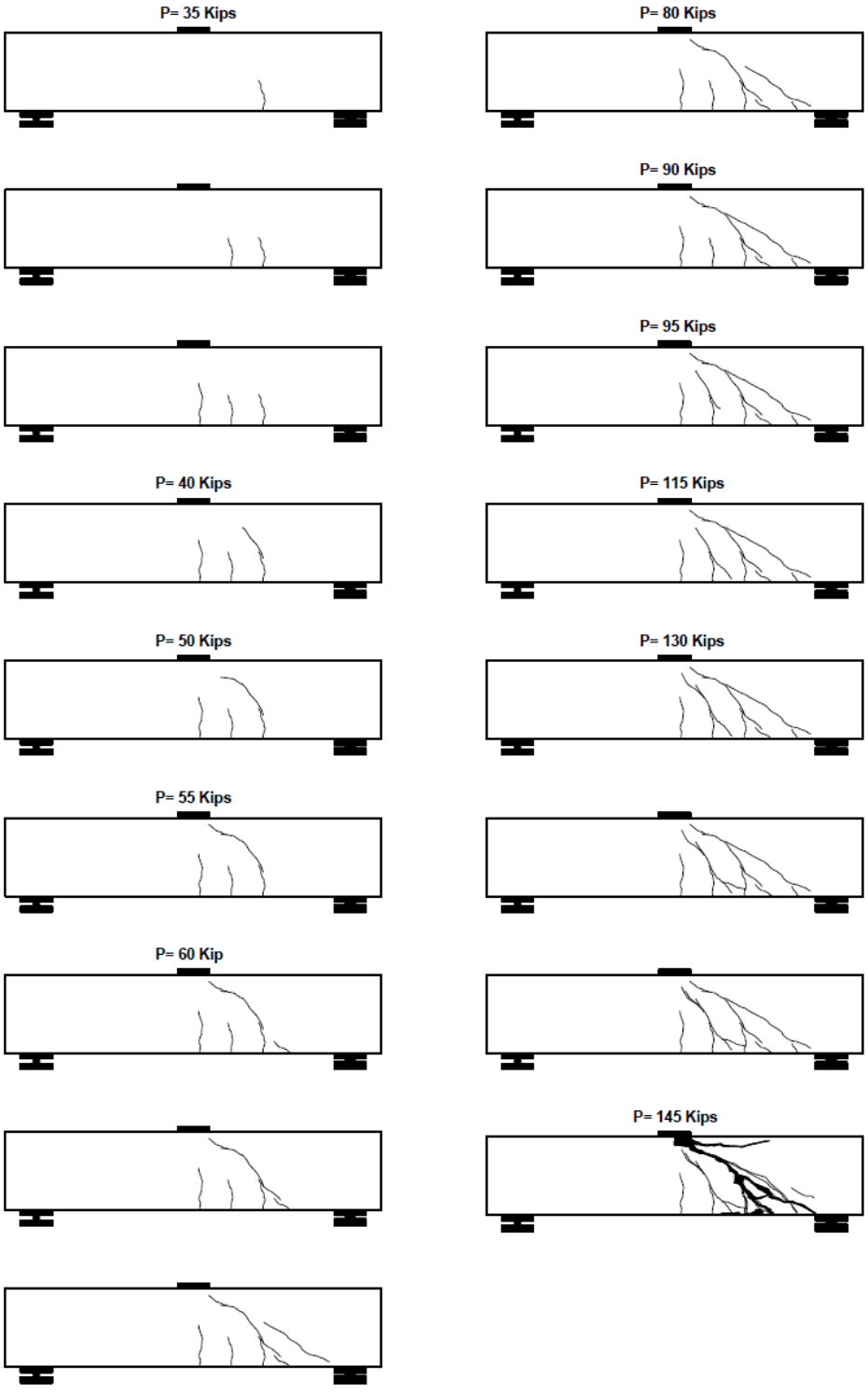

Figure 132 Crack pattern for RCS beam #27

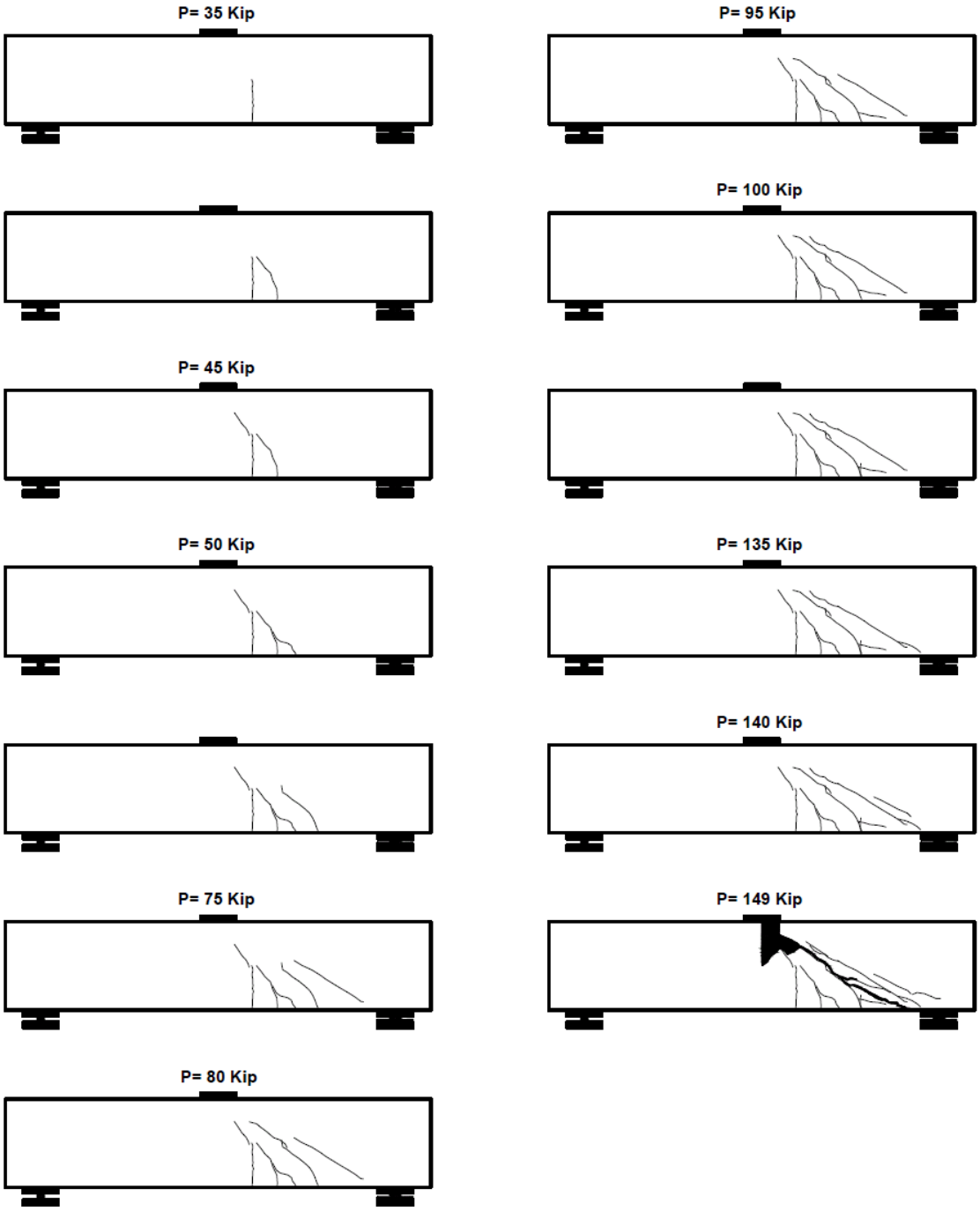

Figure 133 Crack pattern for RCS beam #28

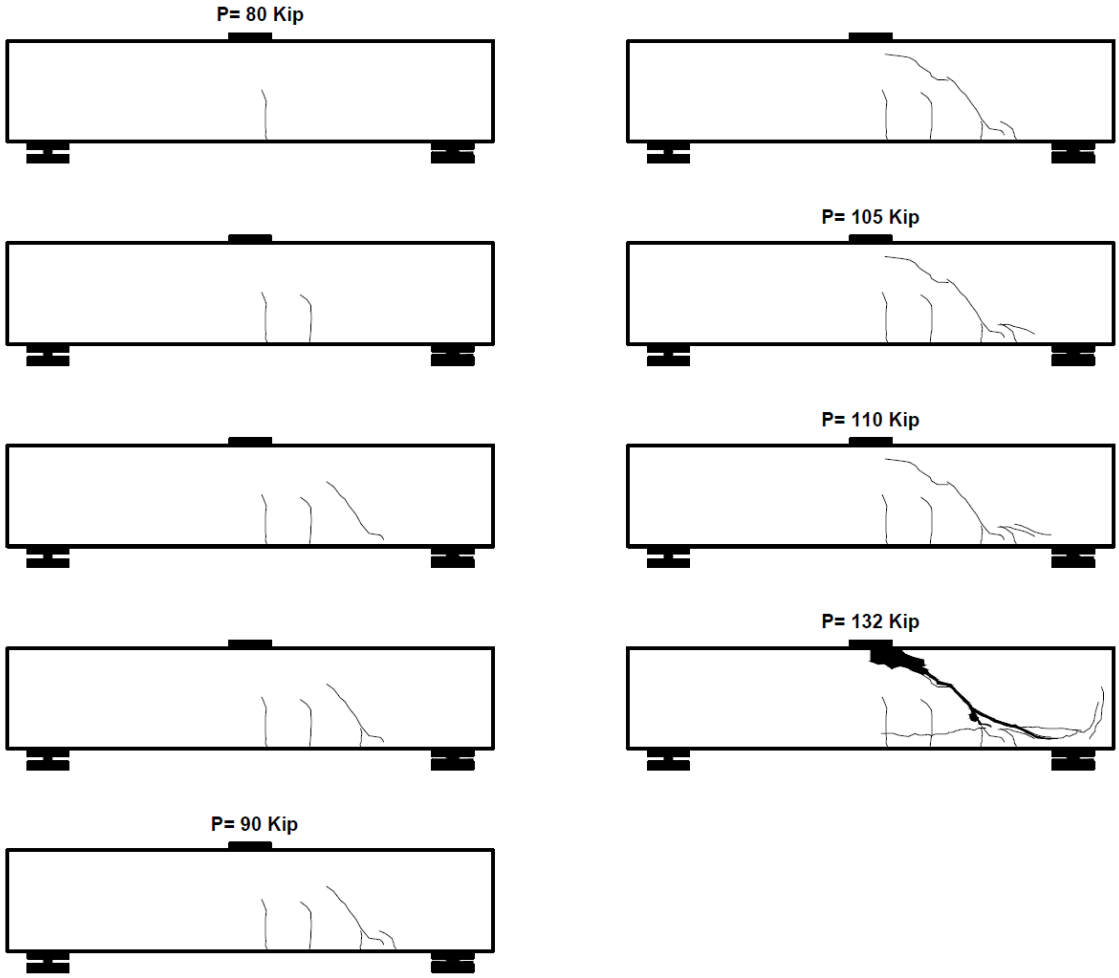

Figure 134 Crack pattern for SNFRC 0.5% beam #29

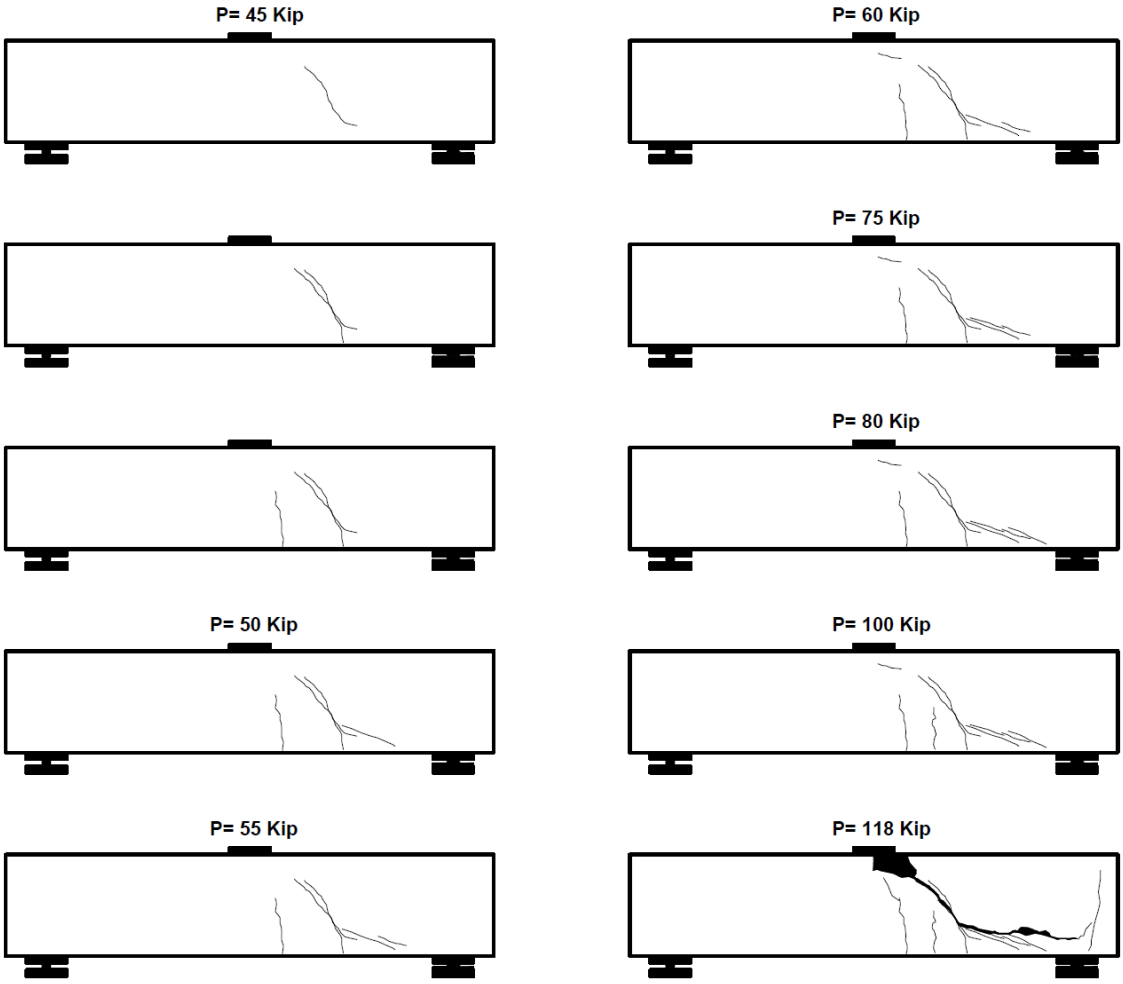

Figure 135 Crack pattern for SNFRC 0.5% beam #30

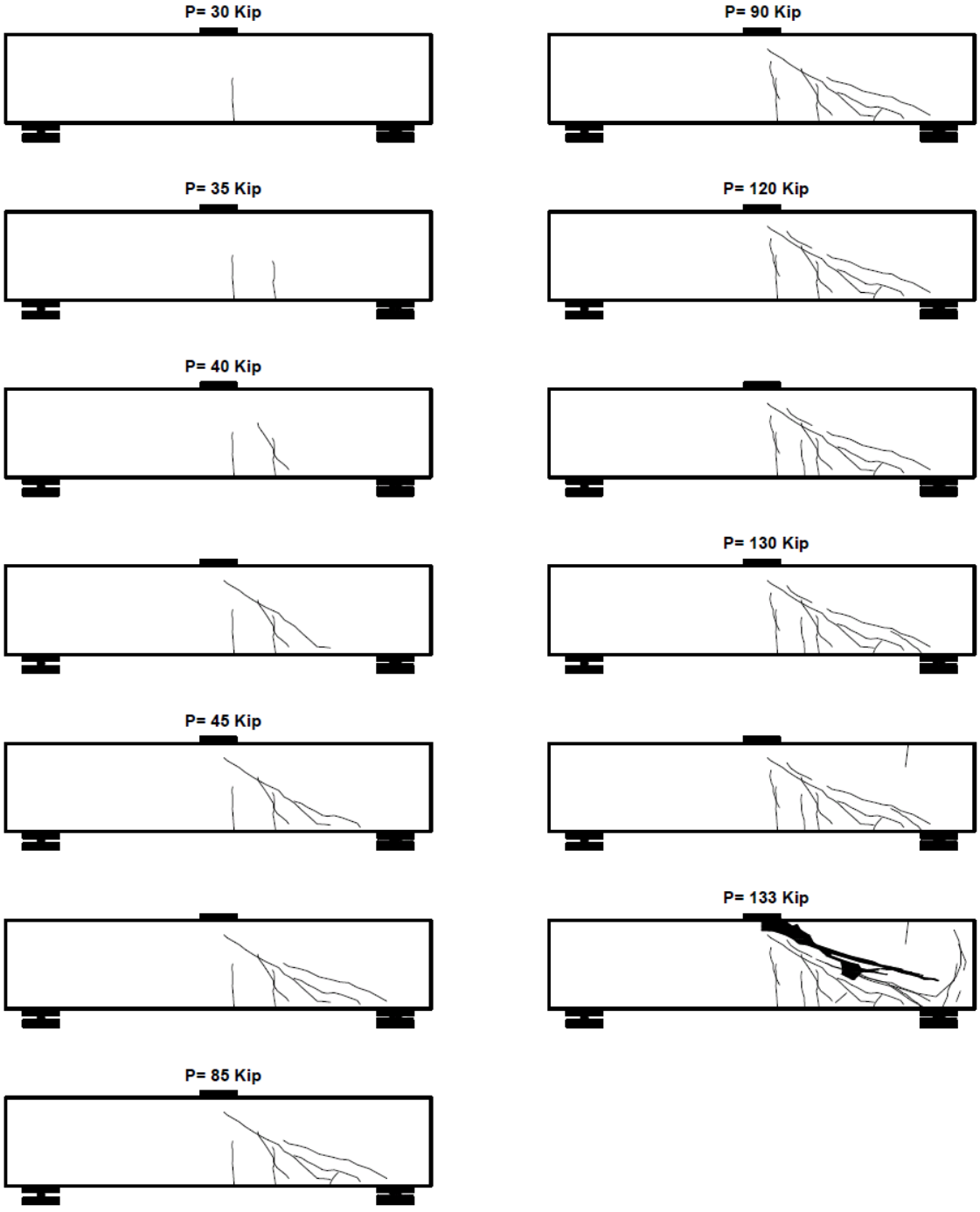

Figure 136 Crack pattern for SNFRC 0.75% beam #31

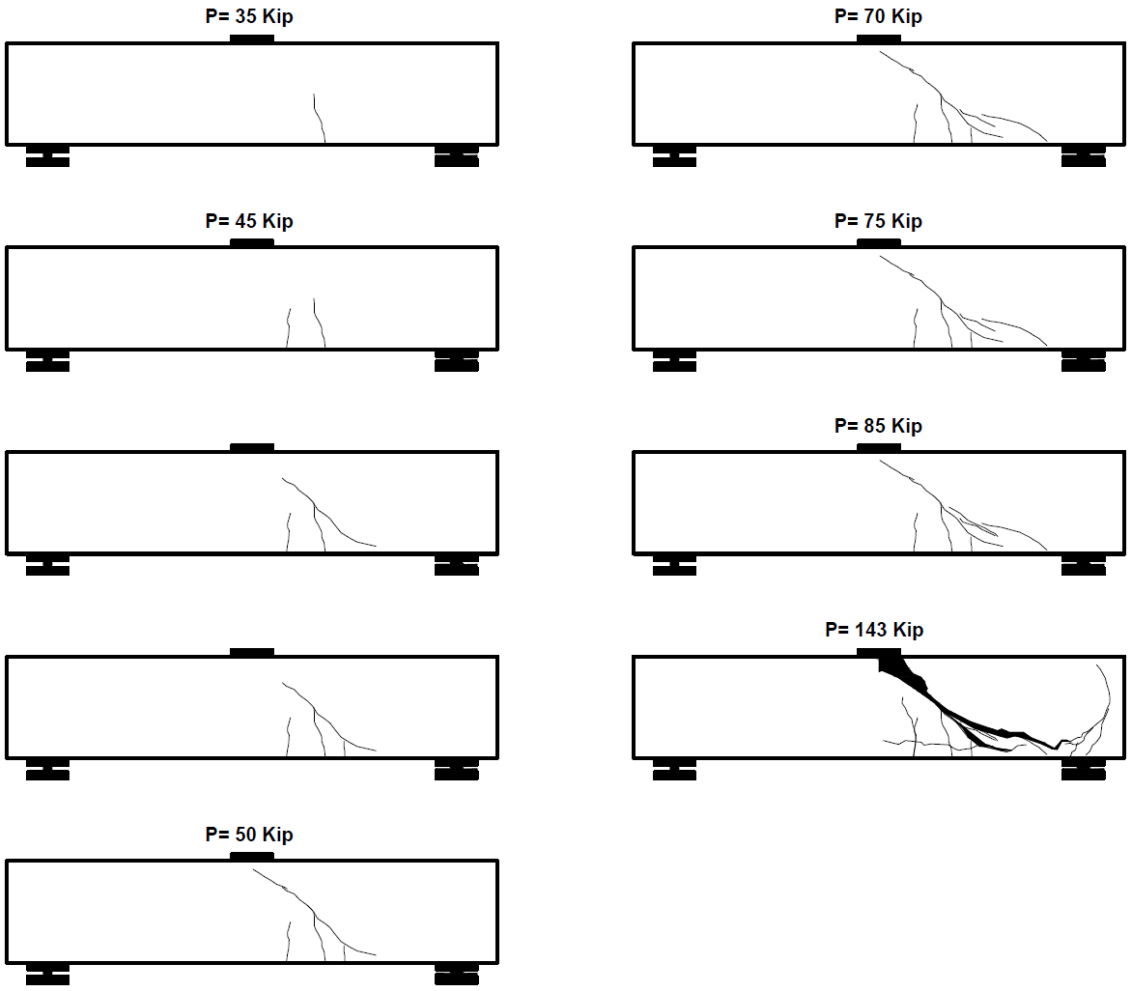

Figure 137 Crack pattern for SNFRC 0.75% beam #32

Appendix B

Concrete Principal Strain Calculation

Table 13 Details of principal strains of large-scale beam specimens without accelerated aging in this study (Phase 1)

BM No.	Beam Type	Location of Conc. SGs	ε_1 (με)	ε_2 (με)	ε_3 (με)	ε_P (με)	ε_Q (με)	γ (με)	σ_t (psi)	ε_t(με)	ε_p / ε_t
1	RC (V_f=0)	F5	52.5	166.5	125.6	174.8	3.4	171.3	752.0	179.5	0.97
2	RC (V_f=0)	J3	-902.0	-581.4	133.2	169.4	-938.2	1107.6	752.0	179.5	0.94
3	RCS (V_f=0)	F5	-163.5	85.4	157.6	180.3	-186.2	366.5	752.0	179.5	1.00
4	RCS (V_f=0)	L2	-364.0	-188.3	157.6	171.1	-377.6	548.7	752.0	179.5	0.95
5	SNFRC 0.5%	F5	-171.6	-212.5	94.1	180.0	-257.5	437.6	812.2	193.9	0.93
6	SNFRC 0.5%	F5	-41.0	-62.6	138.6	191.9	-94.3	286.2	812.2	193.9	0.99
7	SNFRC 0.75%	H4	-165.7	-79.9	190.2	212.6	-188.1	400.7	940.8	224.6	0.95
8	SNFRC 0.75%	F5	-60.9	188.8	24.7	193.2	-229.3	422.5	940.8	224.6	0.86
8	SNFRC 0.75%	H4	-273.5	-196.2	191.7	238.8	-320.6	559.4	940.8	224.6	1.06

Table 14 Details of principal strains of large-scale beams subjected to 1 month and 3 months aging in this study (Phases 2 and 3)

BM No.	Beam Type	Location of Conc. SGs	ε_1 (με)	ε_2 (με)	ε_3 (με)	ε_P (με)	ε_Q (με)	γ (με)	σ_t (psi)	ε_t(με)	ε_p / ε_t
9	RC (V_f=0)	K2	-47.4	203.8	-38.5	203.0	-289.7	492.7	728.9	174.0	1.17
13	SNFRC 0.5%	H5	-57.1	-27.4	156.5	181.4	-82.0	263.4	772.4	184.4	0.98
16	SNFRC 0.75%	G5	-197.1	-298.6	76.9	214.9	-335.1	550.0	874.1	208.6	1.03
16	SNFRC 0.75%	I3	110.8	-163.2	-54.3	236.7	-180.2	416.9	874.1	208.6	1.13
18	RC (V_f=0)	F5	166.1	14.0	-151.8	166.2	-151.9	318.1	696.2	166.2	1.00
18	RC (V_f=0)	J3	-72.2	6.1	160.9	167.0	-78.3	245.3	696.2	166.2	1.00
19	RCS (Vf=0)	J3	-93.8	-277.8	-18.6	168.6	-281.0	449.6	696.2	166.2	1.01
20	RCS (Vf=0)	I4	85.3	-78.4	4.7	174.8	-84.8	259.6	696.2	166.2	1.05
21	SNFRC 0.5%	G5	155.4	8.4	-59.2	162.5	-66.3	228.8	759.5	181.3	0.90
23	SNFRC 0.75%	F5	-281.3	-137.2	171.6	186.1	-295.8	481.9	821.6	196.1	0.95
24	SNFRC 0.75%	H4	18.0	-91.4	101.7	216.8	-97.1	313.9	821.6	196.1	1.11

Table 15 Details of principal strains of large-scale beams subjected to 6 months accelerated aging in this study (Phase 4)

BM #	Beam Type	Location of Conc. SGs	ε_1 (με)	ε_2 (με)	ε_3 (με)	ε_P (με)	ε_Q (με)	γ (με)	σ_t (psi)	ε_t(με)	ε_p / ε_t
26	RC (Vf=0)	L2	107.4	0.3	60.8	171.1	-2.9	174.0	640.0	152.8	1.12
27	RCS (Vf=0)	H4	12.1	-362.0	-239.2	164.9	-392.0	556.9	640.0	152.8	1.08
28	RCS (Vf=0)	J3	-3.7	5.6	159.0	186.3	-31.0	217.3	640.0	152.8	1.22
29	SNFRC 0.5%	F5	-46.5	42.2	176.3	178.6	-48.8	227.4	672.9	160.6	1.11
29	SNFRC 0.5%	H4	-264.4	-590.7	-149.3	181.3	-595.0	776.3	672.9	160.6	1.13
30	SNFRC 0.5%	J3	30.3	-127.0	12.6	170.2	-127.3	297.5	672.9	160.6	1.06
30	SNFRC 0.5%	L2	-142.8	-31.3	174.0	180.8	-149.6	330.4	672.9	160.6	1.13
31	SNFRC 0.75%	L2	-456.4	-82.1	173.9	179.4	-461.9	641.3	770.3	183.9	0.98
32	SNFRC 0.75%	F5	-1913.3	-1060.0	178.6	196.2	-1930.9	2127.1	770.3	183.9	1.07
32	SNFRC 0.75%	L2	-182.5	-64.6	188.4	200.3	-194.4	394.7	770.3	183.9	1.09

Appendix C

Concrete Principal Strains

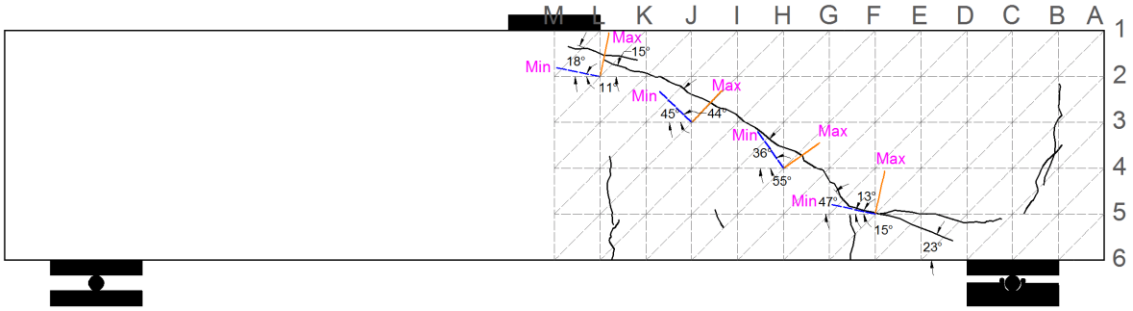

Figure 138 Maximum and minimum principal strain orientations for RC beam #1

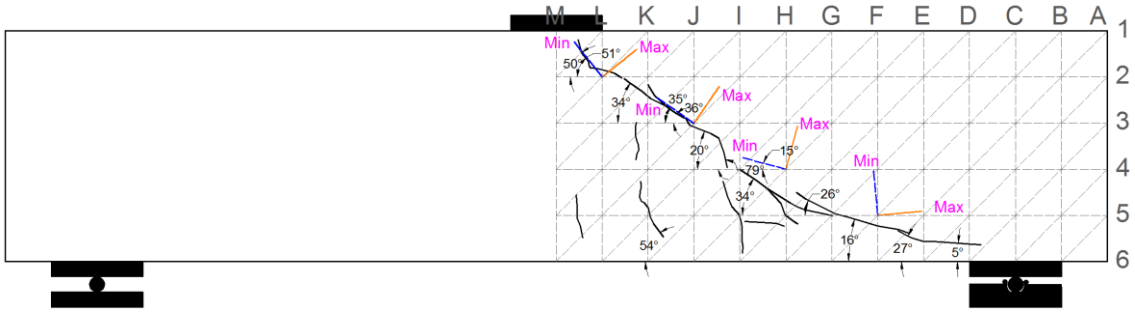

Figure 139 Maximum and minimum principal strain orientations for RC beam #2

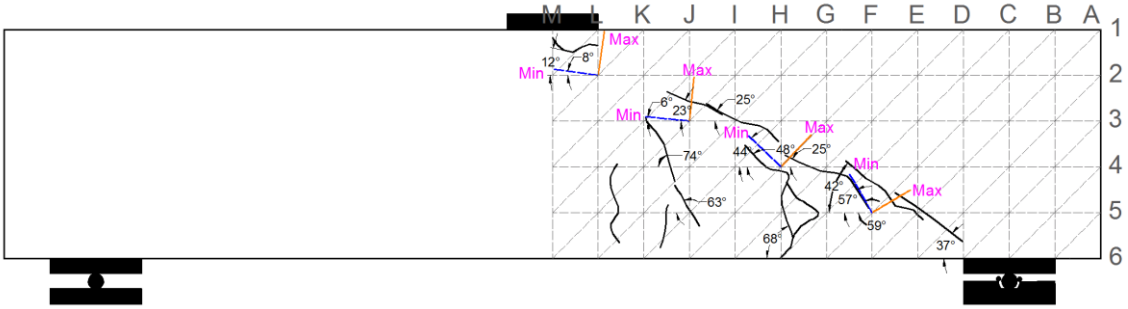

Figure 140 Maximum and minimum principal strain orientations for RCS beam #3

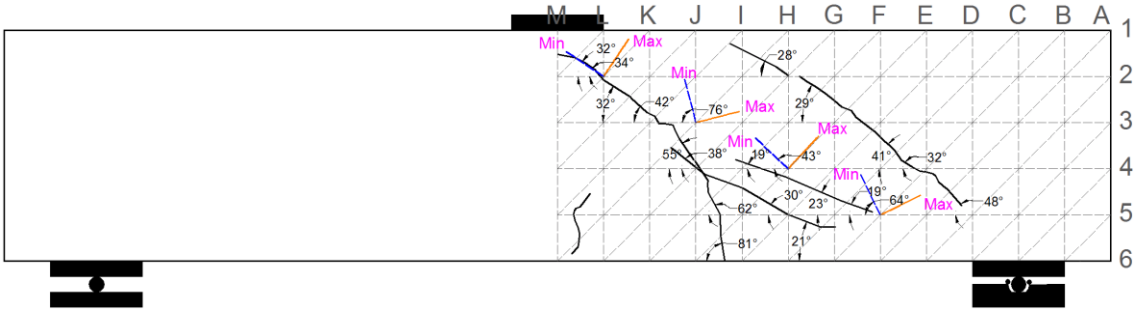

Figure 141 Maximum and minimum principal strain orientations for RCS beam #4

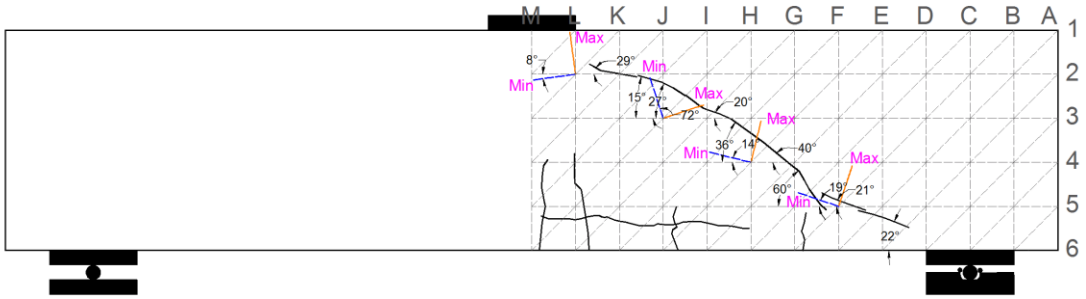

Figure 142 Maximum and minimum principal strain orientations for SNFRC 0.5% beam #5

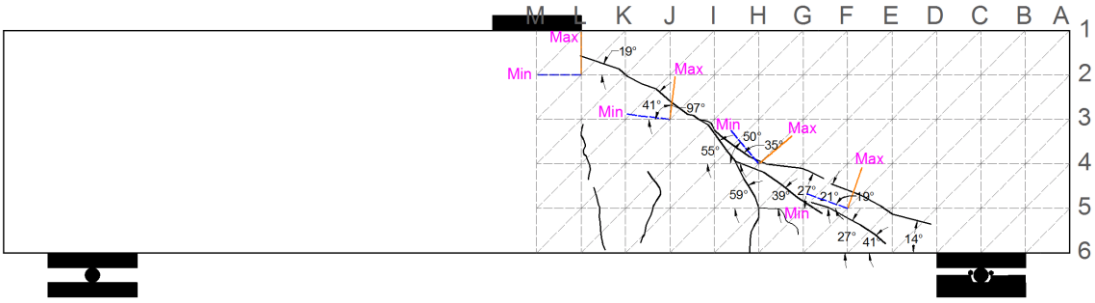

Figure 143 Maximum and minimum principal strain orientations for SNFRC 0.5% beam #6

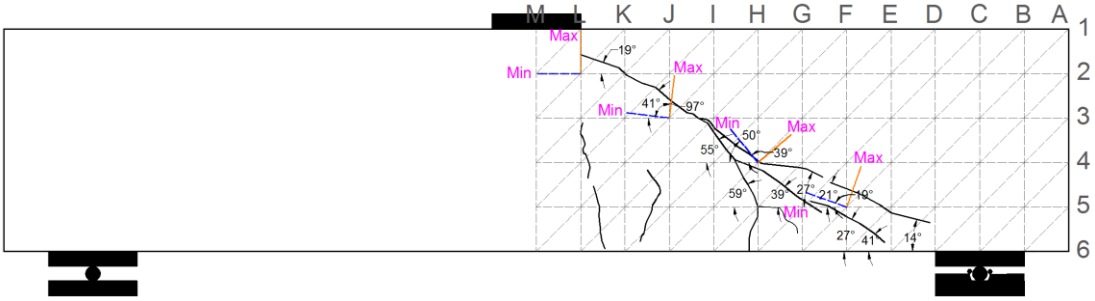

Figure 144 Maximum and minimum principal strain orientations for SNFRC 0.75% beam #7

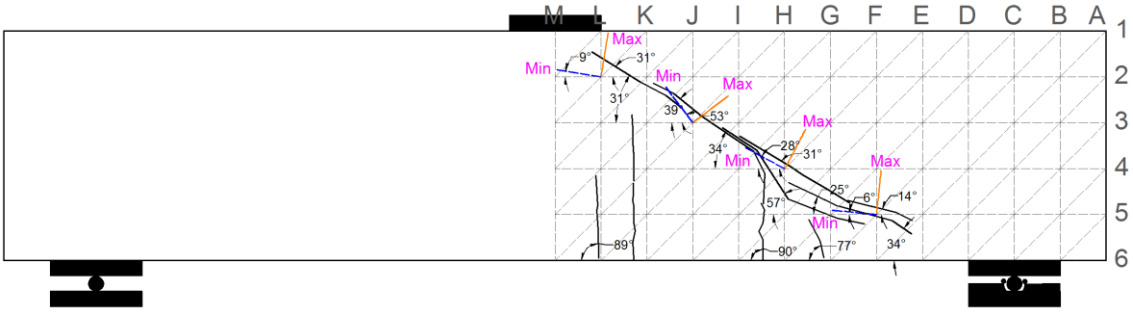

Figure 145 Maximum and minimum principal strain orientations for SNFRC 0.75% beam #8

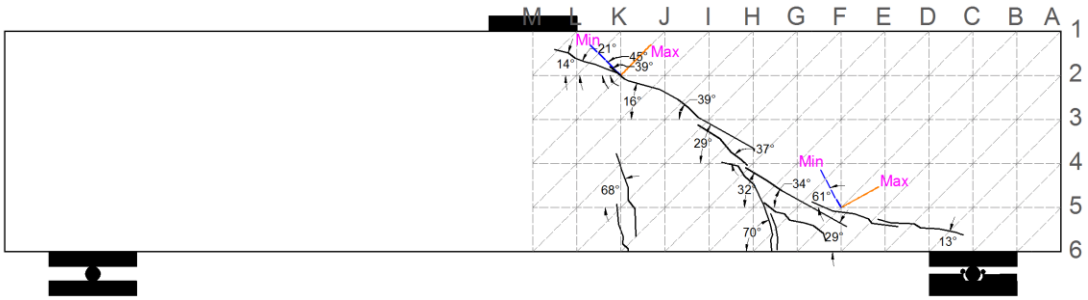

Figure 146 Maximum and minimum principal strain orientations for RC beam #9

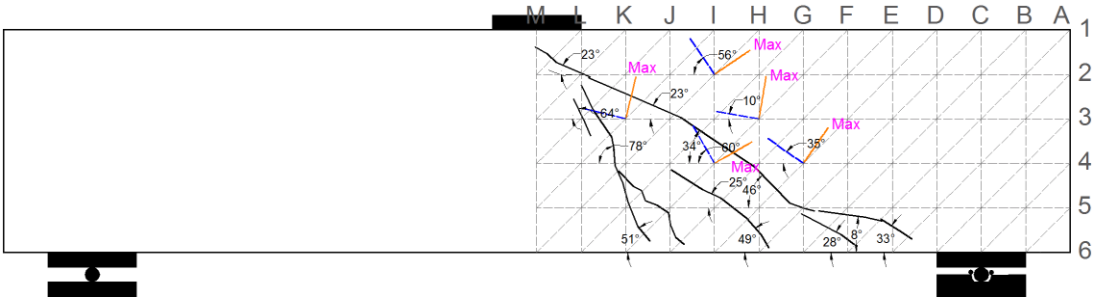

Figure 147 Maximum and minimum principal strain orientations for RC beam #10

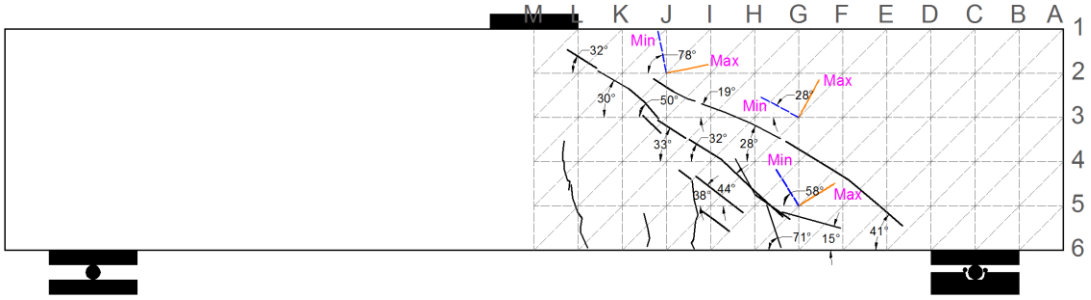

Figure Maximum and minimum principal strain orientations for RCS beam #11

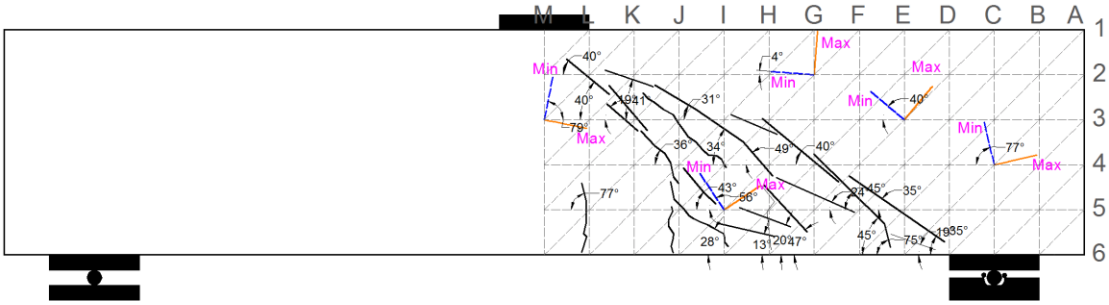

Figure 148 Maximum and minimum principal strain orientations for RCS beam #12

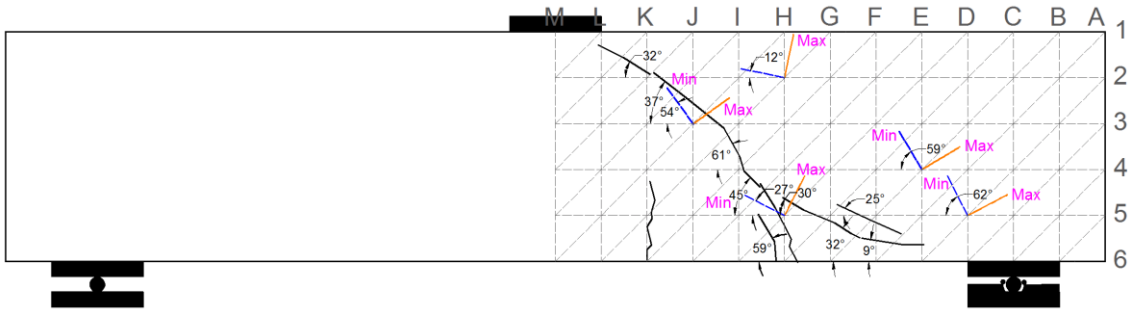

Figure Maximum and minimum principal strain orientations for SNFRC 0.5% beam #13

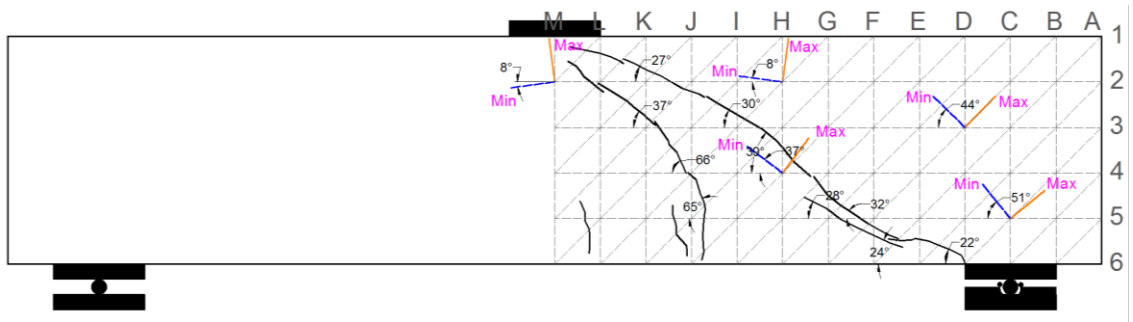

Figure 149 Maximum and minimum principal strain orientations for SNFRC 0.5% beam #14

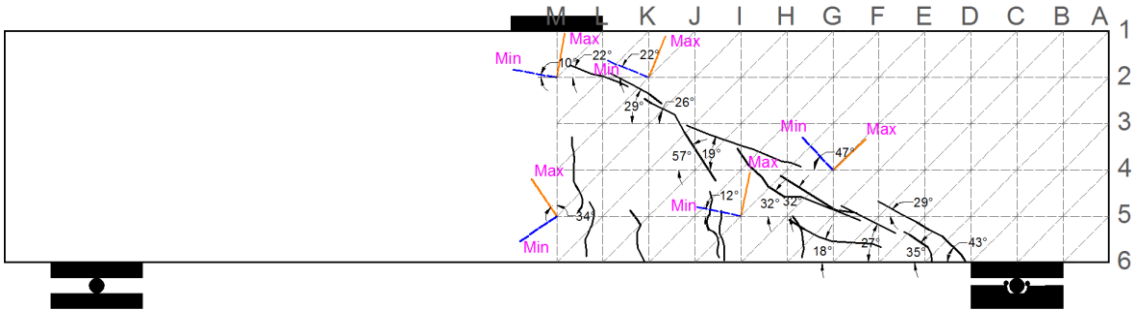

Figure Maximum and minimum principal strain orientations for SNFRC 0.75% beam #15

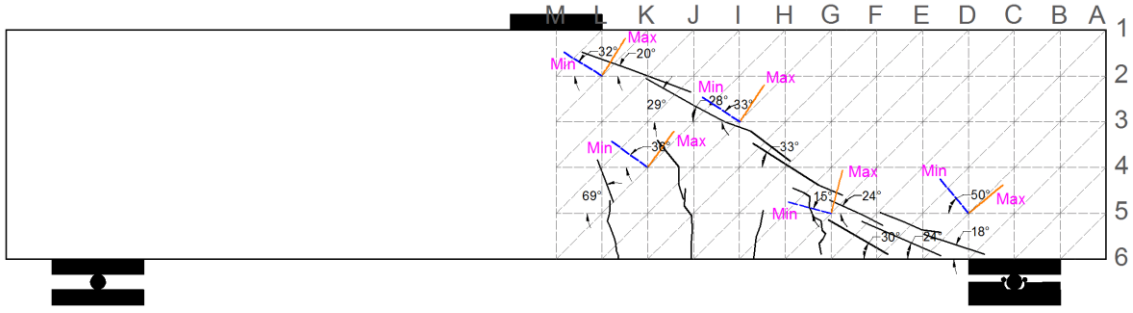

Figure 150 Maximum and minimum principal strain orientations for SNFRC 0.75% beam #16

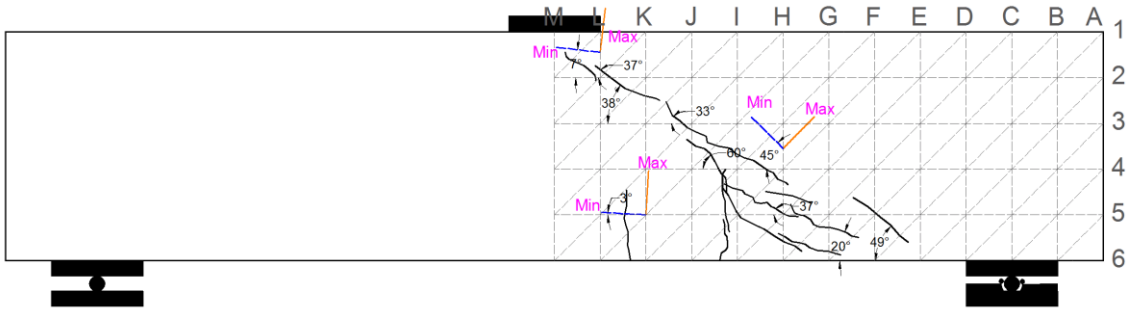

Figure 151 Maximum and minimum principal strain orientations for RC beam #17

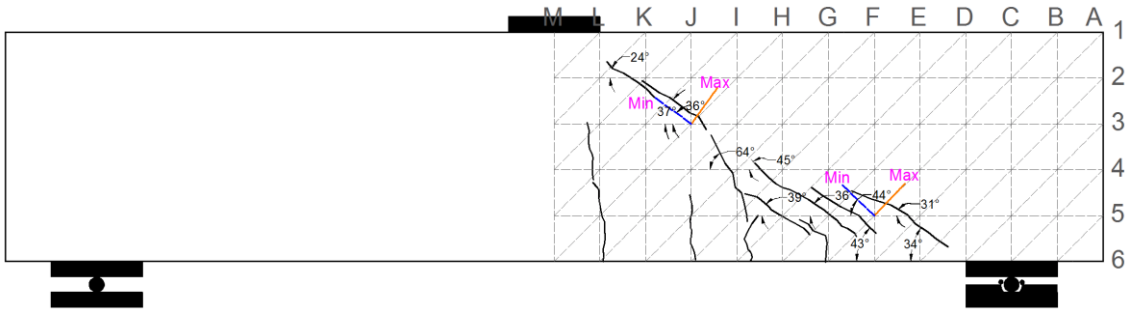

Figure 152 Maximum and minimum principal strain orientations for RC beam #18

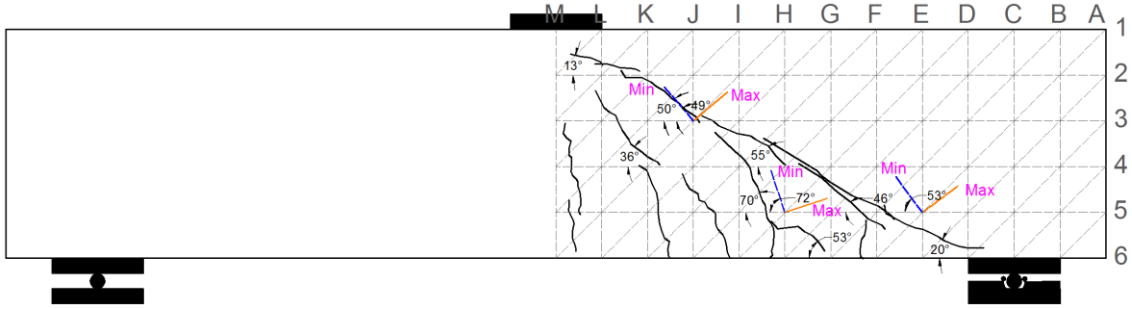

Figure 153 Maximum and minimum principal strain orientations for RCS beam #19

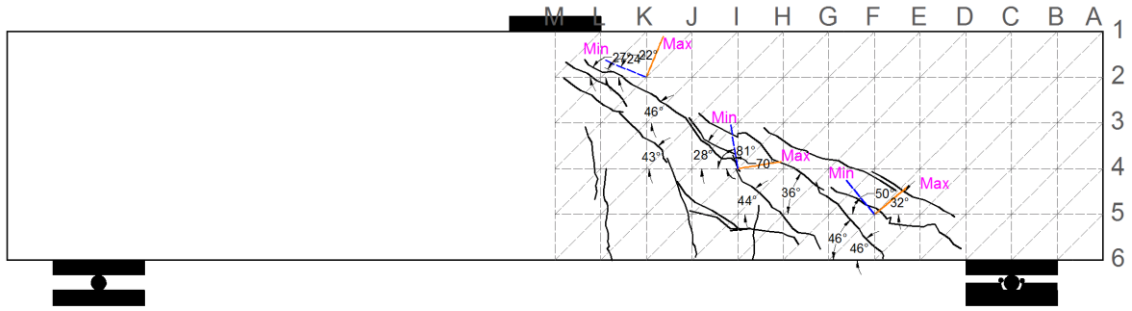

Figure 154 Maximum and minimum principal strain orientations for RCS beam #20

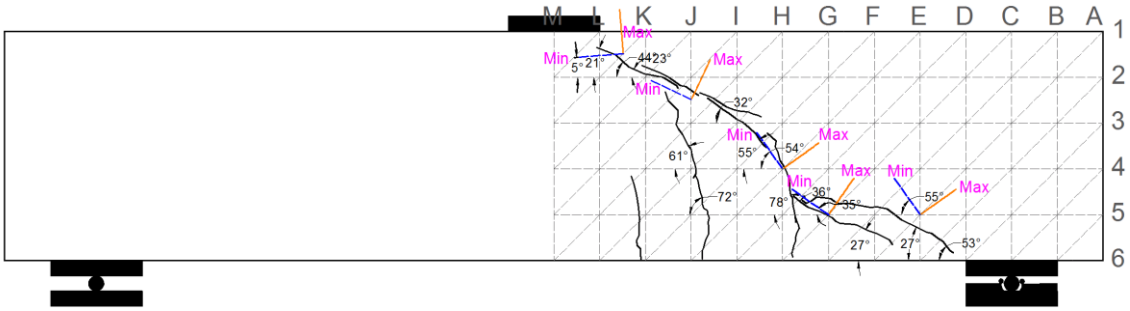

Figure 155 Maximum and minimum principal strain orientations for SNFRC 0.5% beam #21

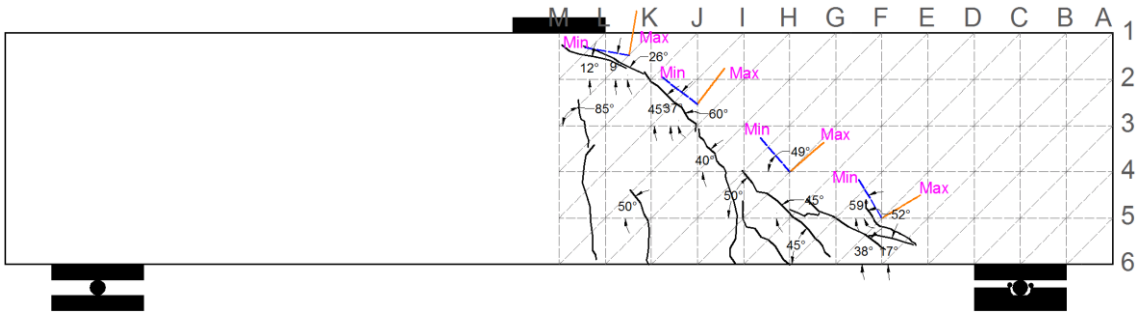

Figure 156 Maximum and minimum principal strain orientations for SNFRC 0.5% beam #22

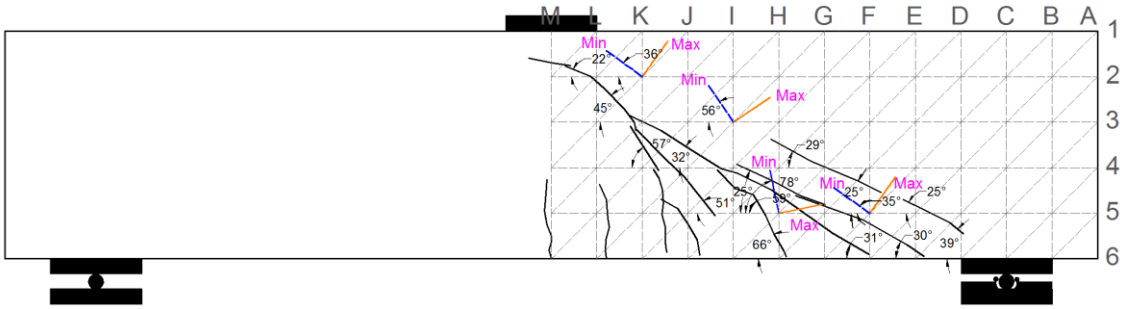

Figure 157 Maximum and minimum principal strain orientations for SNFRC 0.75% beam #23

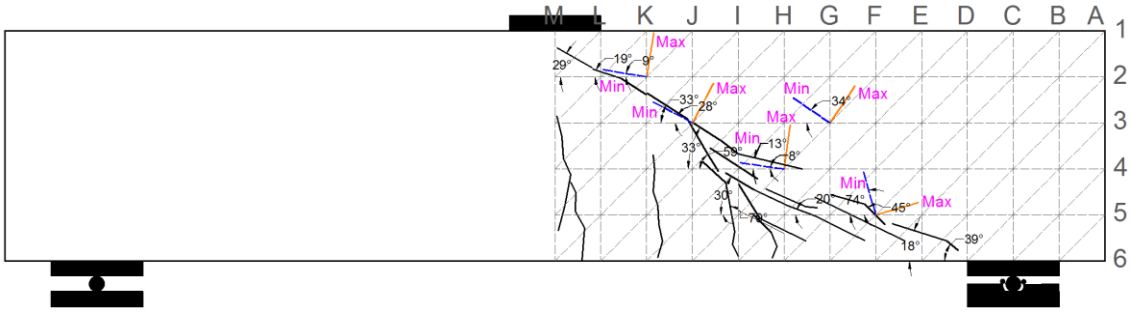

Figure 158 Maximum and minimum principal strain orientations for SNFRC 0.75% beam #24

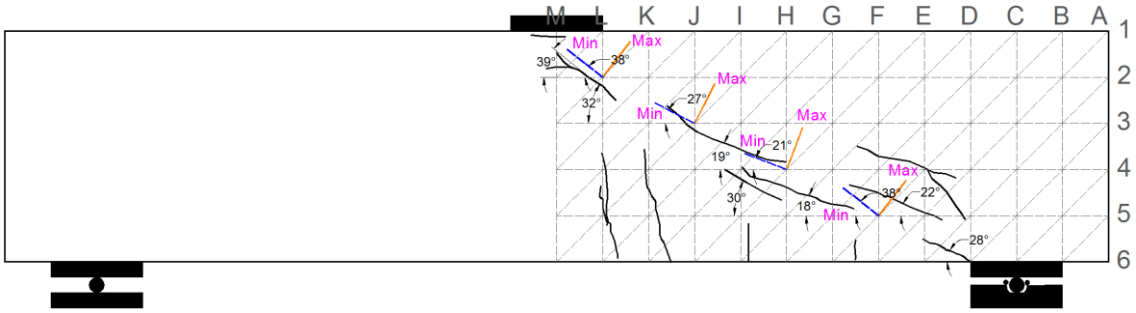

Figure 159 Maximum and minimum principal strain orientations for RC beam #25

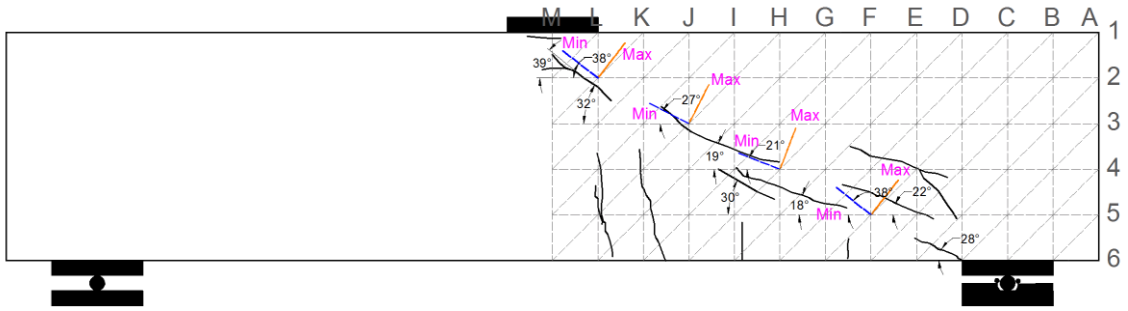

Figure 160 Maximum and minimum principal strain orientations for RC beam #26

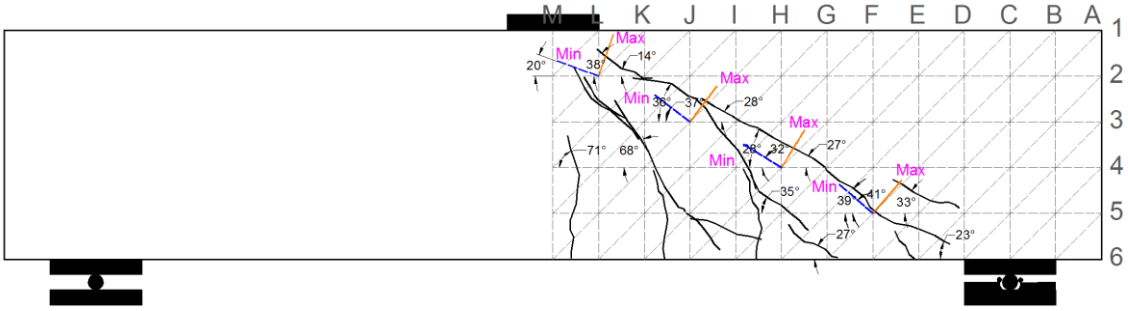

Figure 161 Maximum and minimum principal strain orientations for RCS beam #27

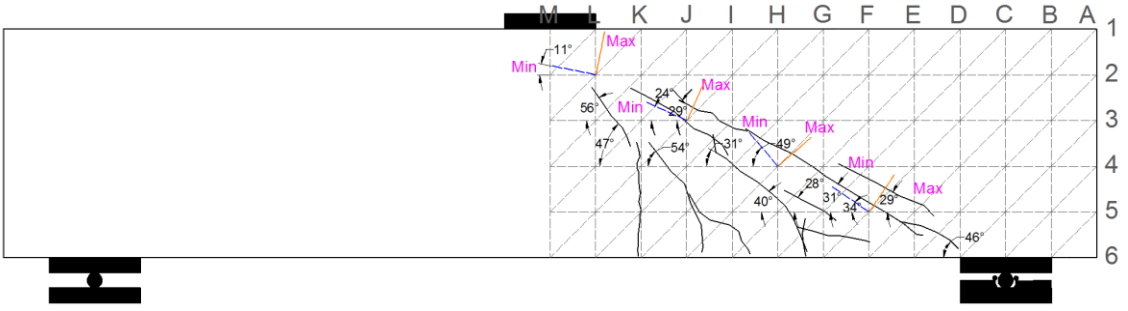

Figure 162 Maximum and minimum principal strain orientations for RCS beam #28

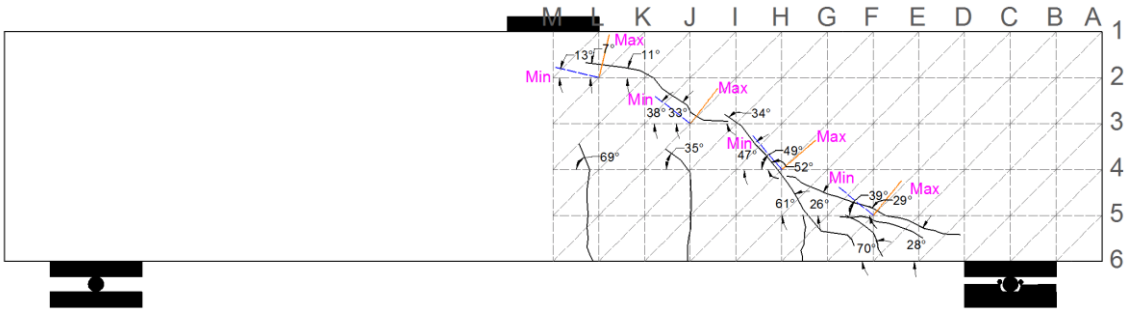

Figure 163 Maximum and minimum principal strain orientations for SNFRC 0.5% beam #29

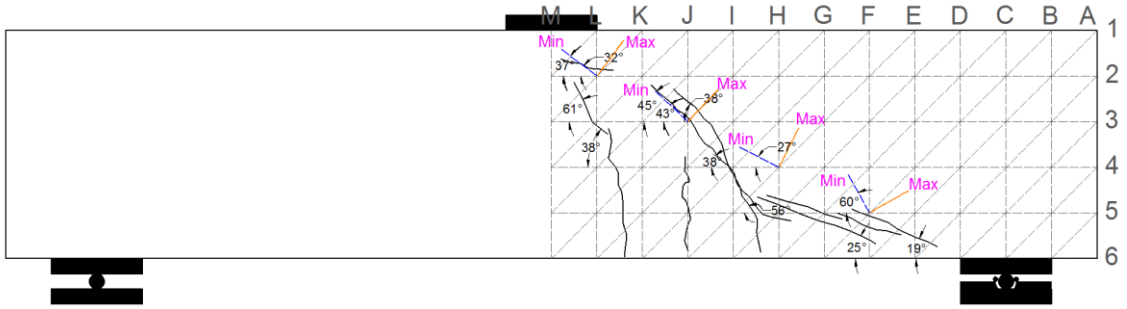

Figure 164 Maximum and minimum principal strain orientations for SNFRC 0.5% beam #30

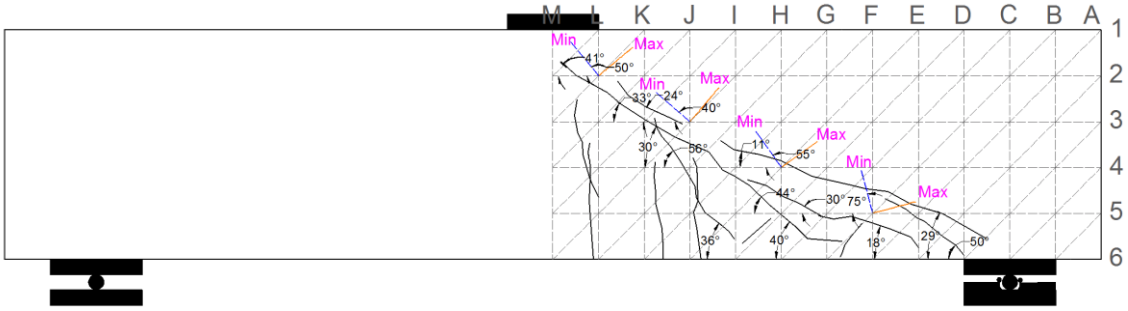

Figure 165 Maximum and minimum principal strain orientations for SNFRC 0.75% beam #31

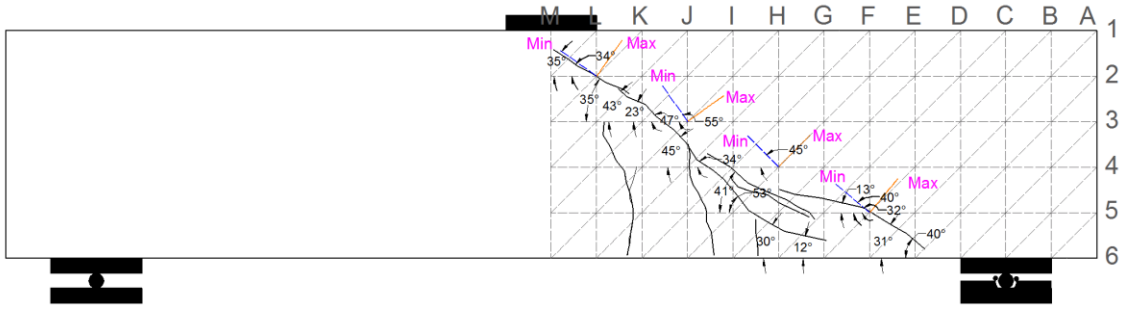

Figure 166 Maximum and minimum principal strain orientations for SNFRC 0.75% beam #32

Appendix D

Crack width at failure of the large-scale beams

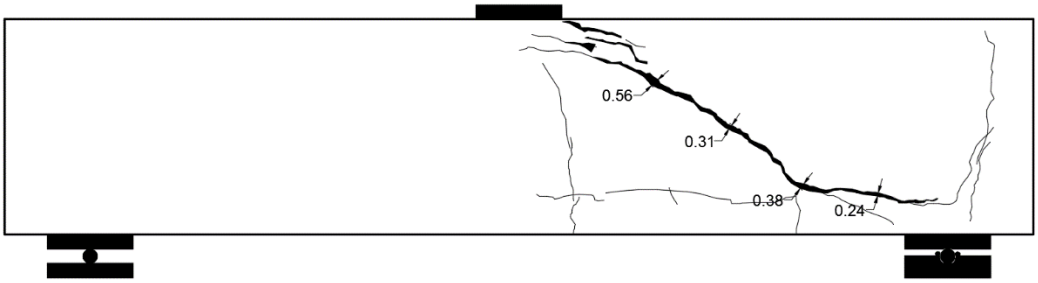

Figure 167 Crack pattern at failure for RC beam #1

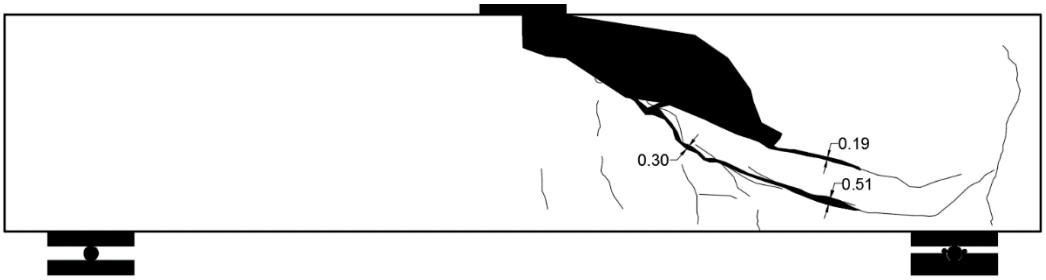

Figure 168 Crack pattern at failure for RC beam #2

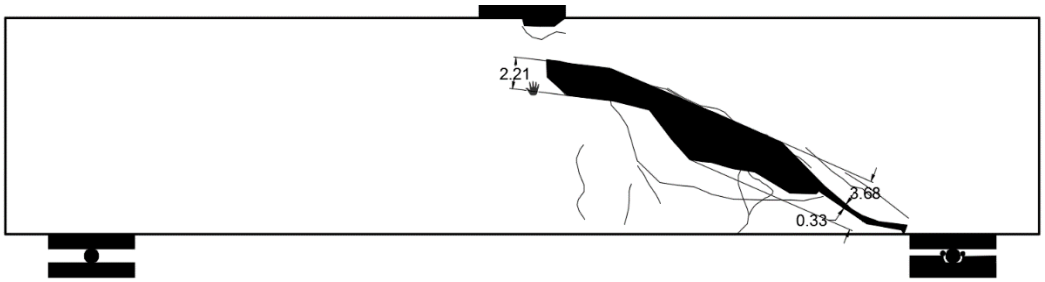

Figure 169 Crack pattern at failure for RCS beam #3

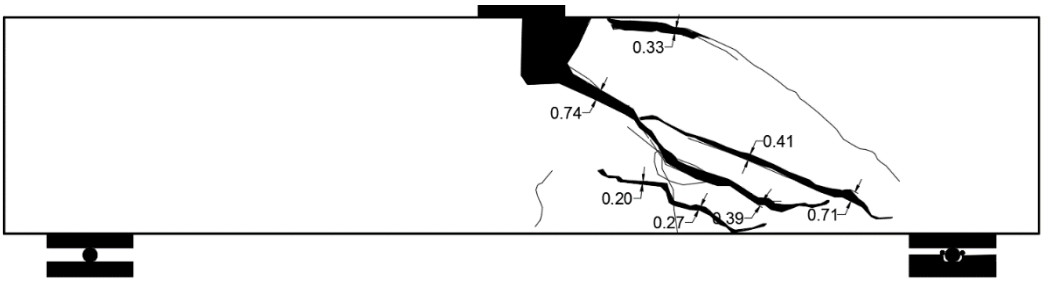

Figure 170 Crack pattern at failure for RCS beam #4

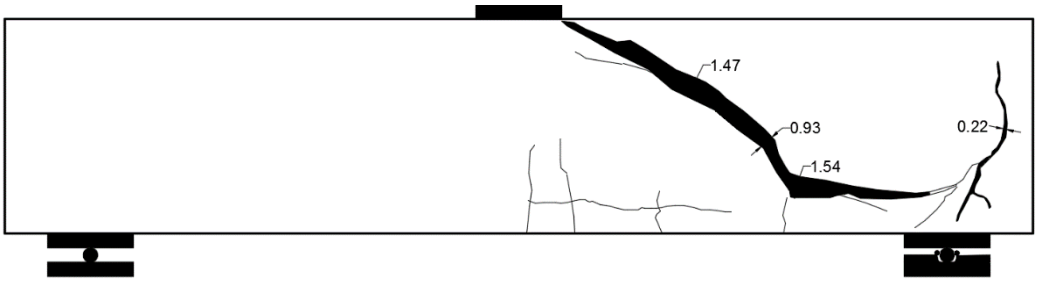

Figure 171 Crack pattern at failure for SNFRC 0.5% beam #5

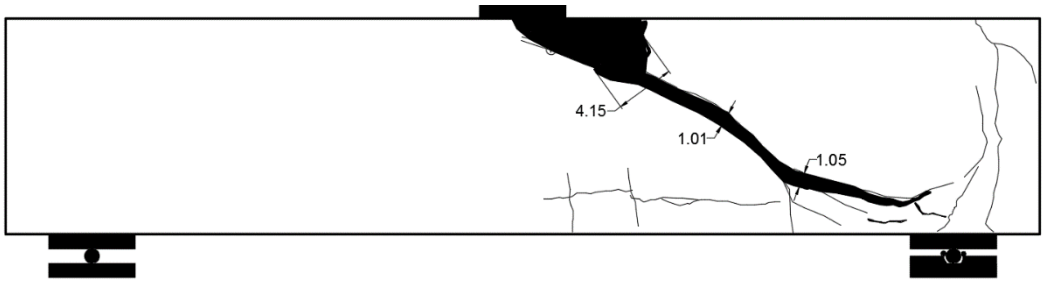

Figure 172 Crack pattern at failure for SNFRC 0.5% beam #6

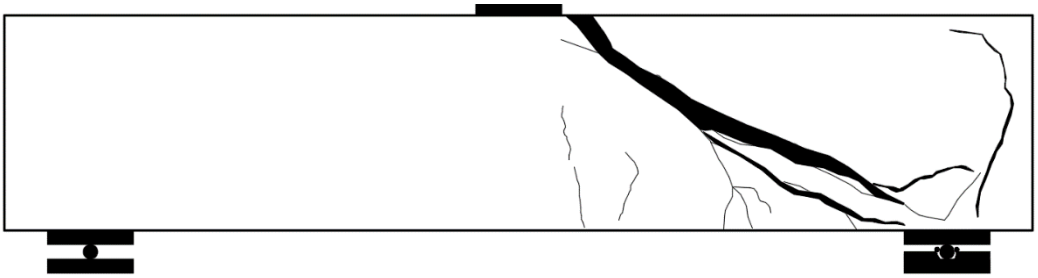

Figure 173 Crack pattern at failure for SNFRC 0.75% beam #7

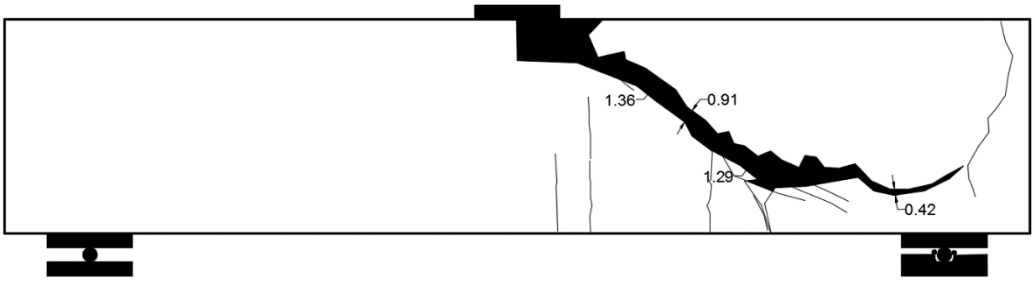

Figure 174 Crack pattern at failure for SNFRC 0.75% beam #8

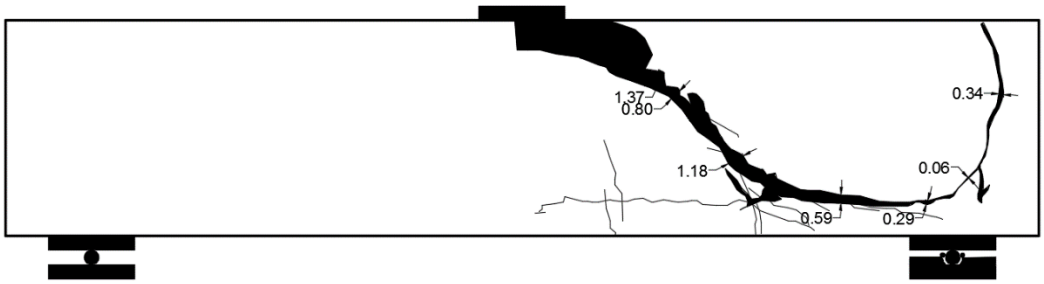

Figure 175 Crack pattern at failure for RC beam #9

Figure 176 Crack pattern at failure for RC beam #10

Figure 177 Crack pattern at failure for RCS beam #11

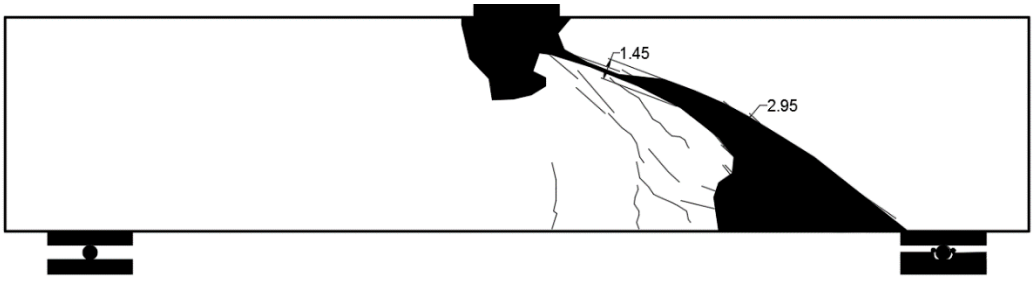

Figure 178 Crack pattern at failure for RCS beam #12

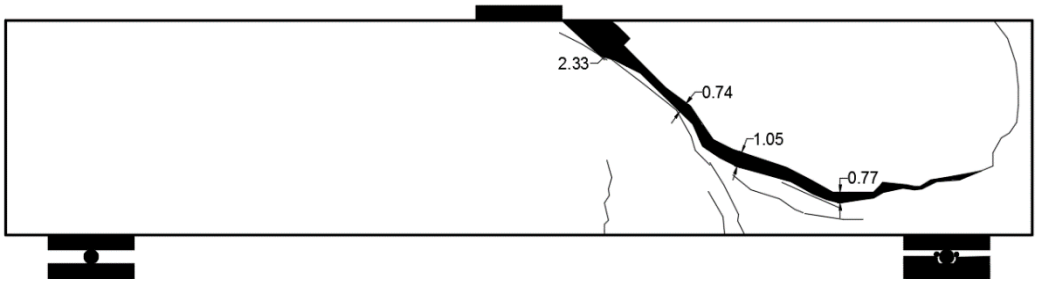

Figure 179 Crack pattern at failure for SNFRC 0.5% beam #13

Figure 180 Crack pattern at failure for SNFRC 0.5% beam #14

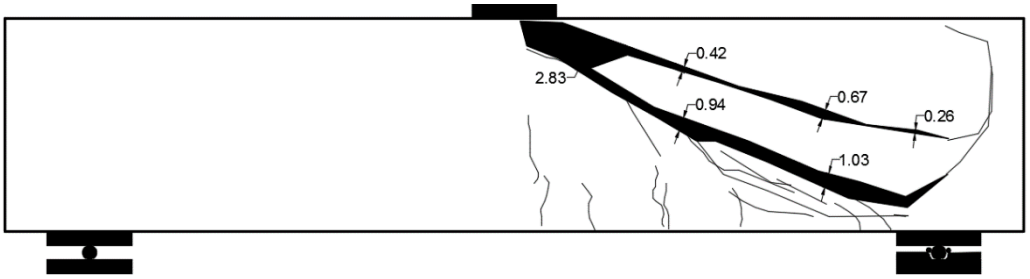

Figure 181 Crack pattern at failure for SNFRC 0.75% beam #15

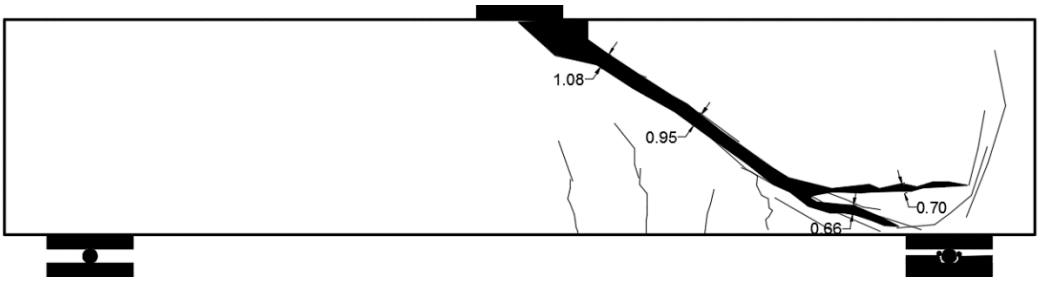

Figure 182 Crack pattern at failure for SNFRC 0.75% beam #16

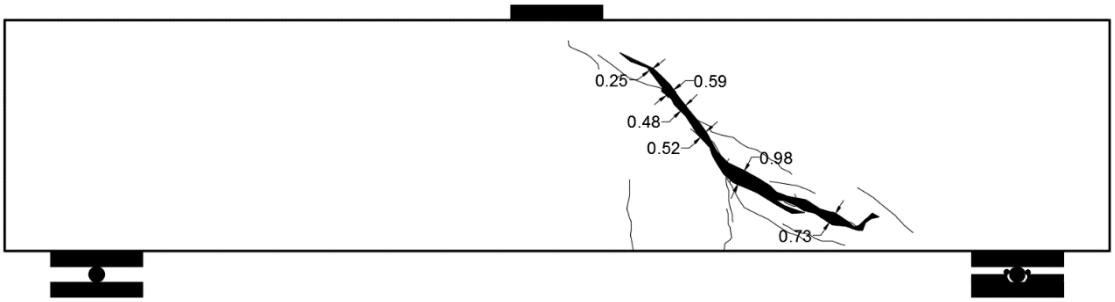

Figure 183 Crack pattern at failure for RC beam #17

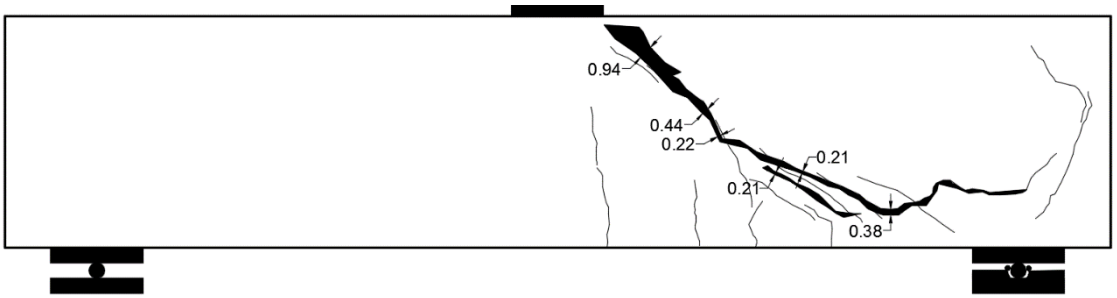

Figure 184 Crack pattern at failure for RC beam #18

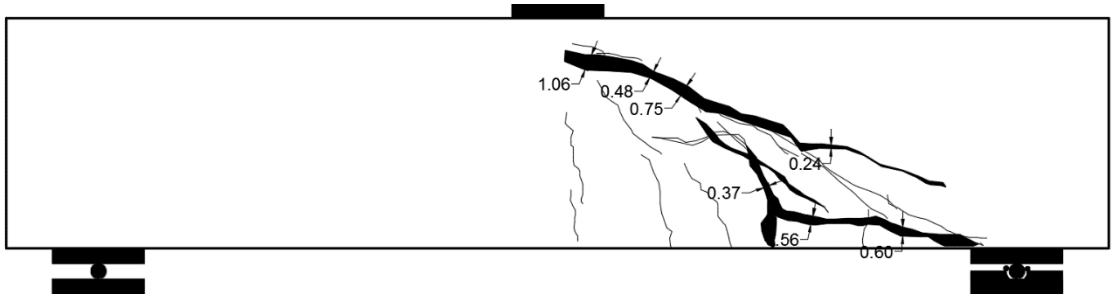

Figure 185 Crack pattern at failure for RCS beam #19

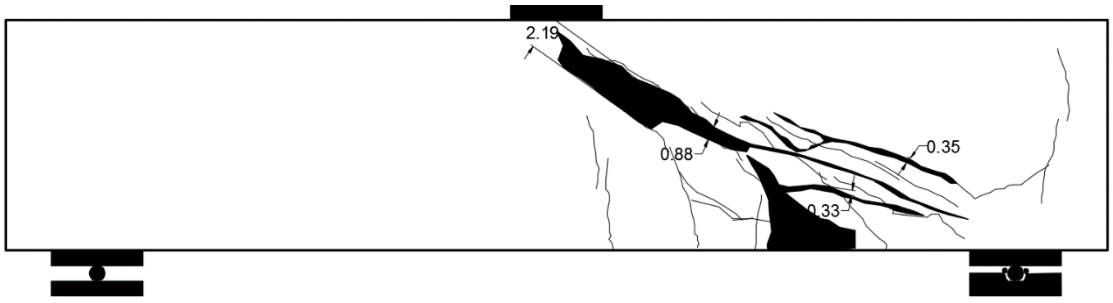

Figure 186 Crack pattern at failure for RCS beam #20

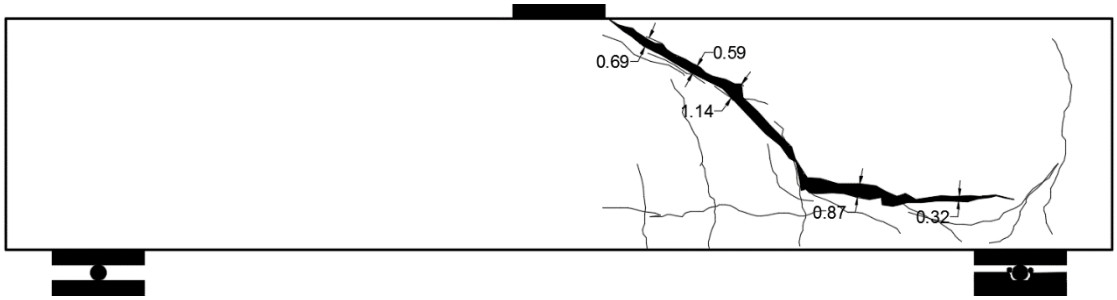

Figure 187 Crack pattern at failure for SNFRC 0.5% beam #21

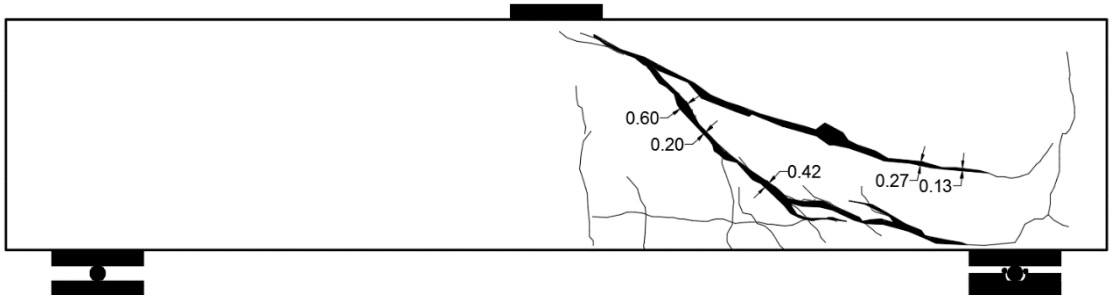

Figure 188 Crack pattern at failure for SNFRC 0.5% beam #22

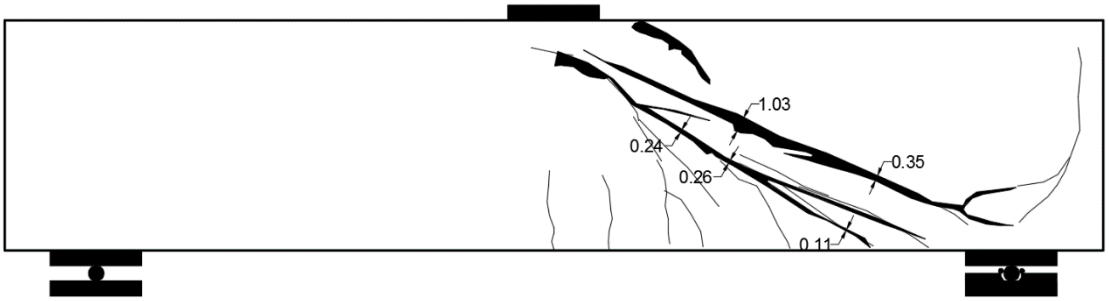

Figure 189 Crack pattern at failure for SNFRC 0.75% beam #23

Figure 190 Crack pattern at failure for SNFRC 0.75% beam #24

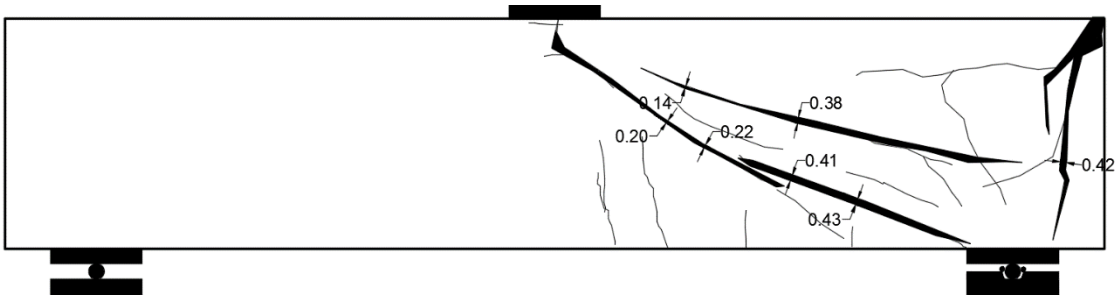

Figure 191 Crack pattern at failure for RC beam #25

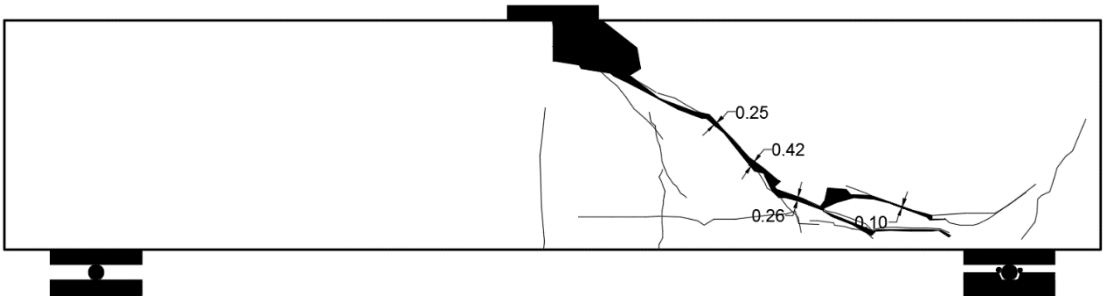

Figure 192 Crack pattern at failure for RC beam #26

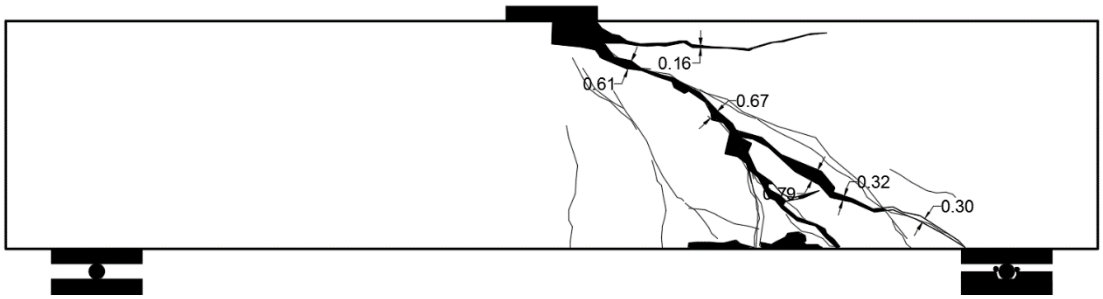

Figure 193 Crack pattern at failure for RCS beam #27

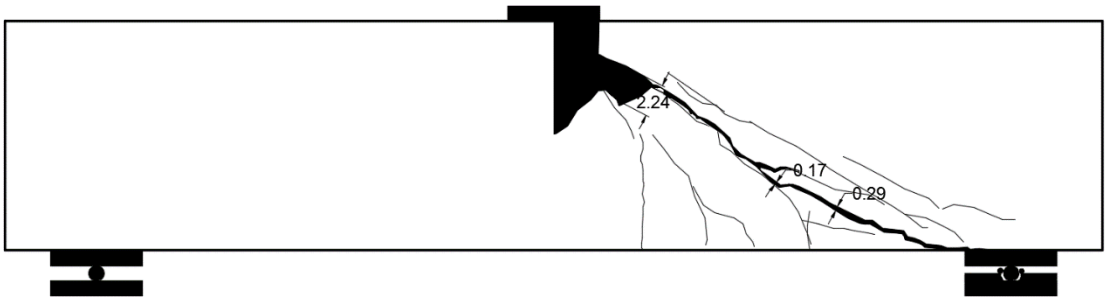

Figure 194 Crack pattern at failure for RCS beam #28

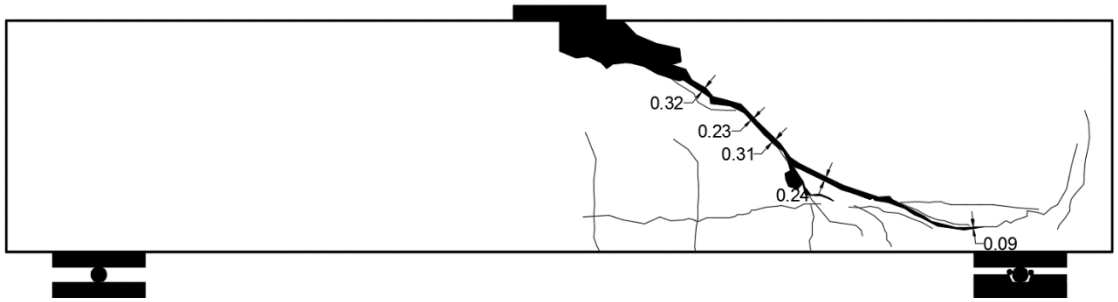

Figure 195 Crack pattern at failure for SNFRC 0.5% beam #29

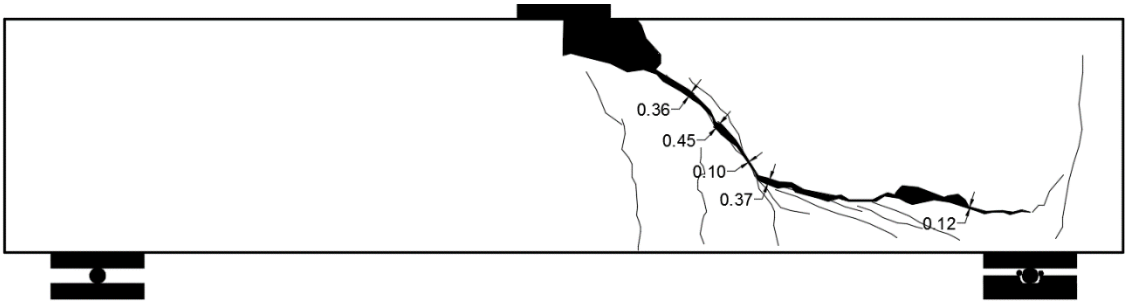

Figure 196 Crack pattern at failure for SNFRC 0.5% beam #30

Figure 197 Crack pattern at failure for SNFRC 0.75% beam #31

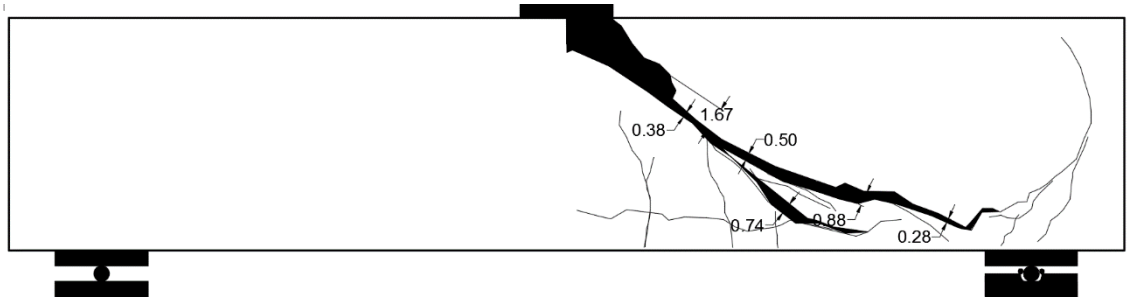

Figure 198 Crack pattern at failure for SNFRC 0.75% beam #32

Appendix E

Load-Deflection Response of large-scale beams

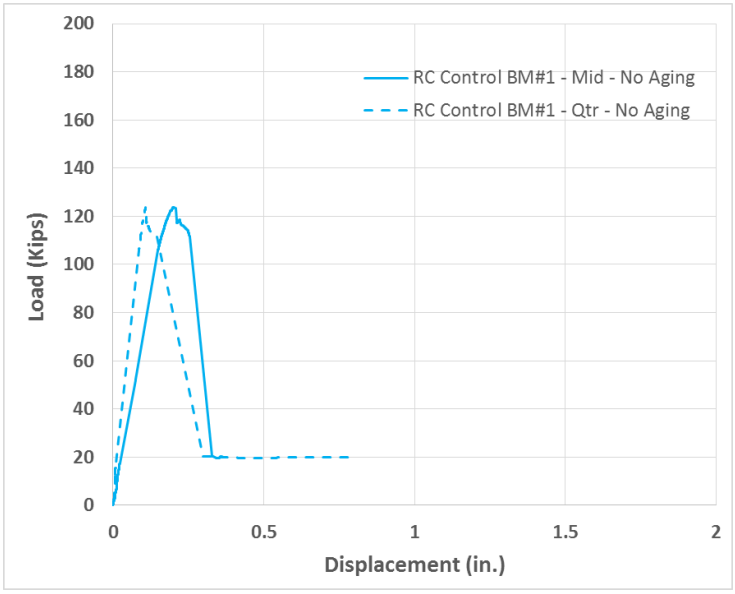

Figure 199 Load-deflection response at quarter and mid-span for RC beam #1 without aging

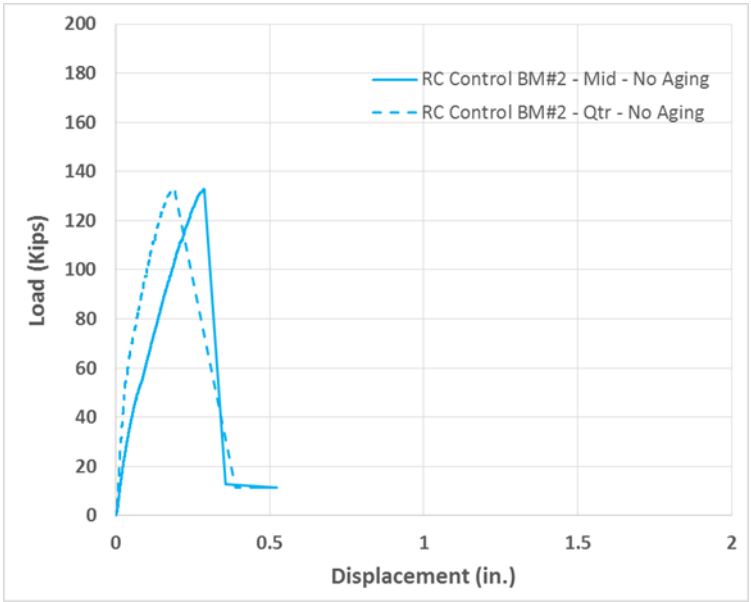

Figure 200 Load-deflection response at quarter and mid-span for RC beam #2 without aging

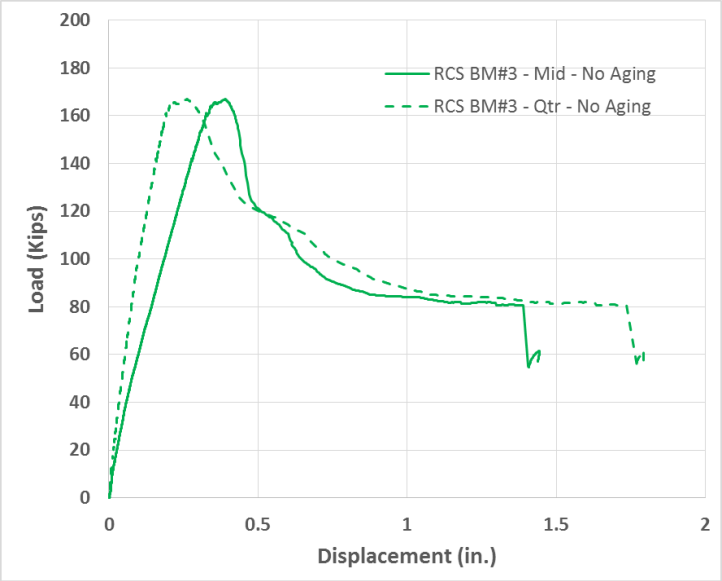

Figure 201 Load-deflection response at quarter and mid-span for RCS beam #3 without aging (Phase 1)

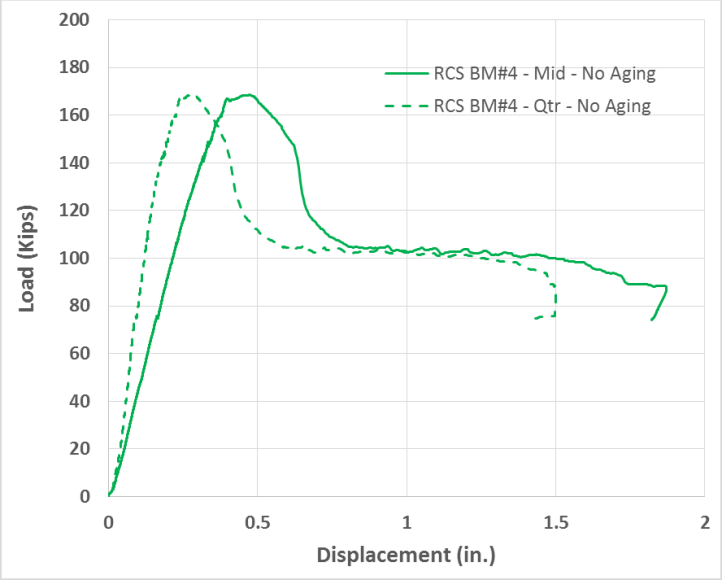

Figure 202 Load-deflection response at quarter and mid-span for RCS beam #4 without aging (Phase 1)

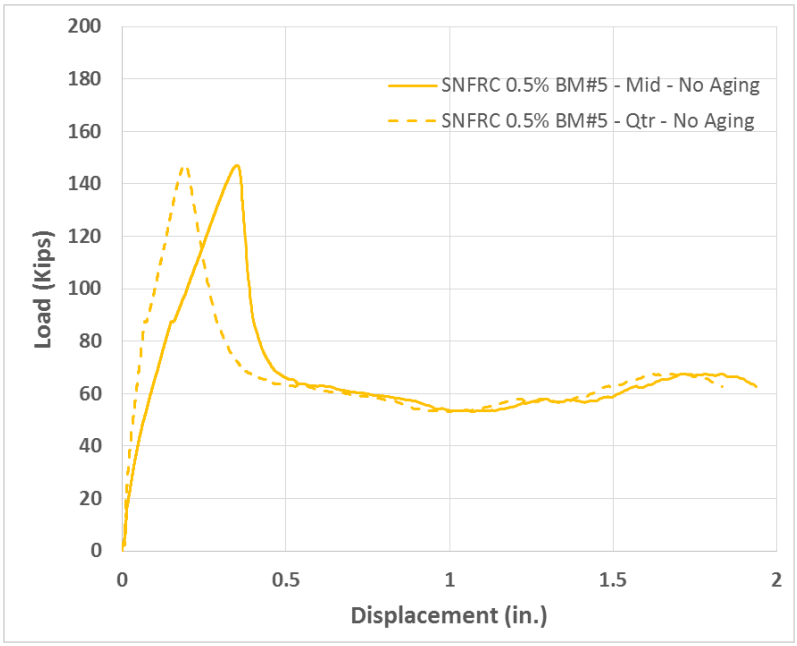

Figure 203 Load-deflection response at quarter and mid-span for SNFRC 0.5% beam #5 without aging (Phase 1)

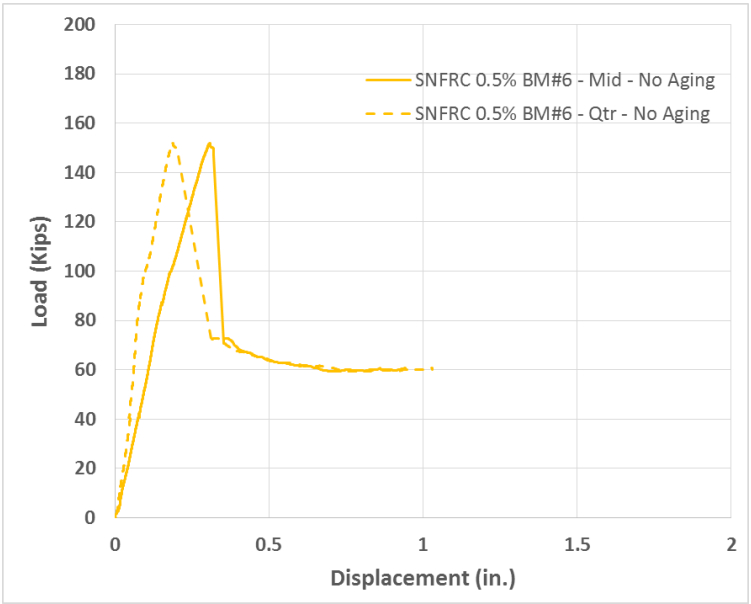

Figure 204 Load-deflection response at quarter and mid-span for SNFRC 0.5% beam #6 without aging (Phase 1)

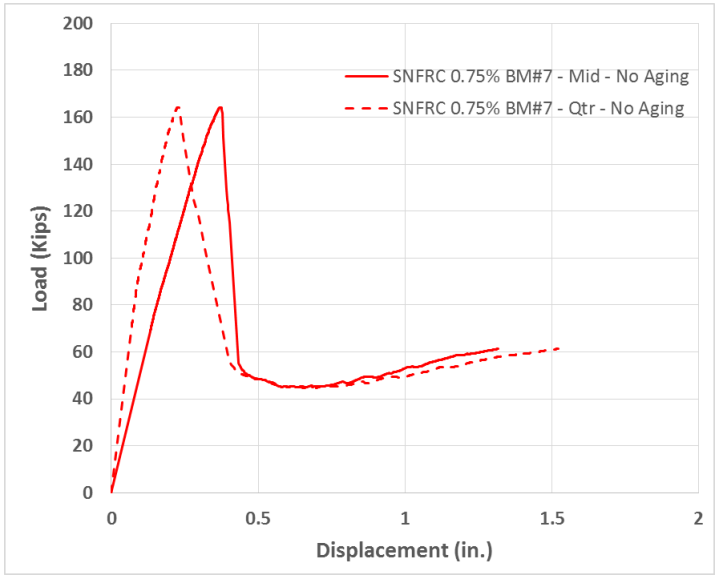

Figure 205 Load-deflection response at quarter and mid-span for SNFRC 0.75% beam #7 without aging (Phase 1)

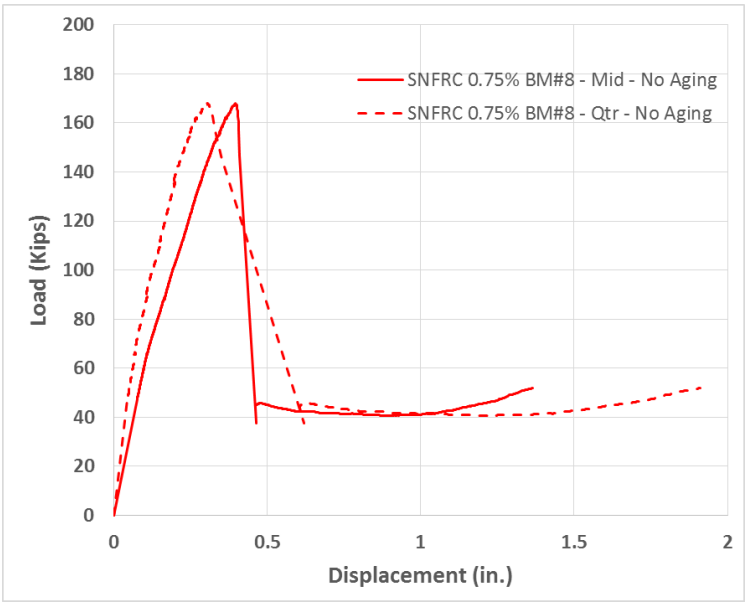

Figure 206 Load-deflection response at quarter and mid-span for SNFRC 0.75% beam #7 without aging (Phase 1)

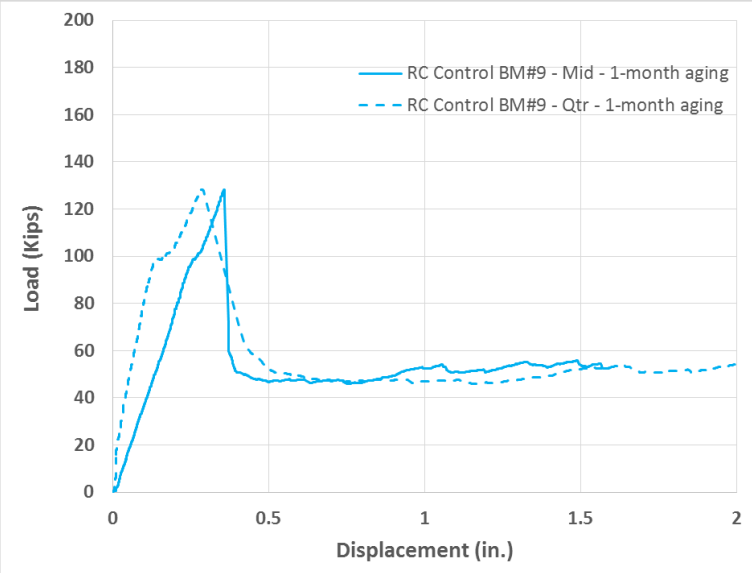

Figure 207 Load-deflection response at quarter and mid-span for RC beam #9 subjected to 1 month of aging (Phase 2)

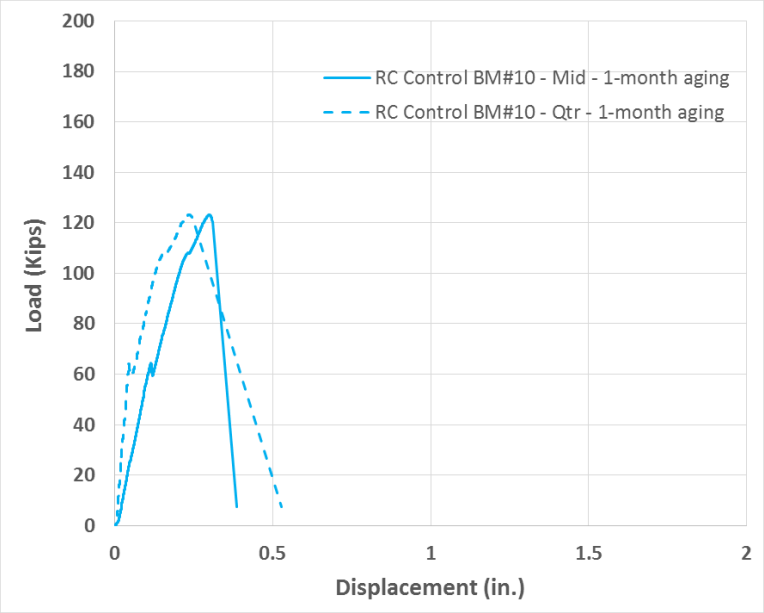

Figure 208 Load-deflection response at quarter and mid-span for RC beam #10 subjected to 1 month of aging (Phase 2)

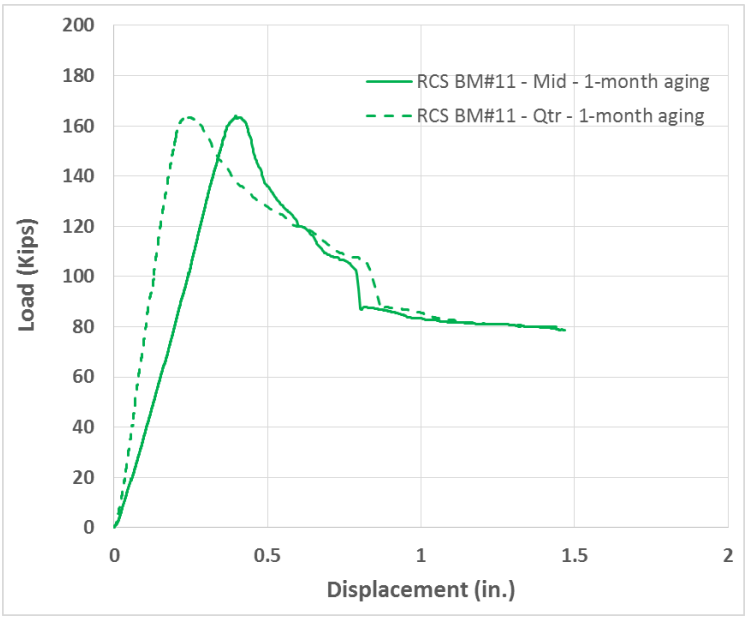

Figure 209 Load-deflection response at quarter and mid-span for RCS beam #11 subjected to 1 month of aging (Phase 2)

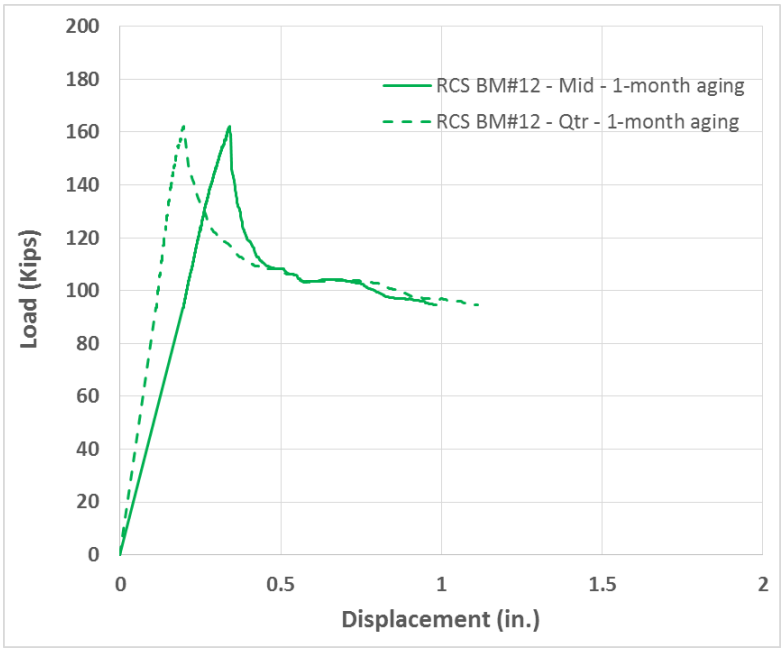

Figure 210 Load-deflection response at quarter and mid-span for RCS beam #12 subjected to 1 month of aging (Phase 2)

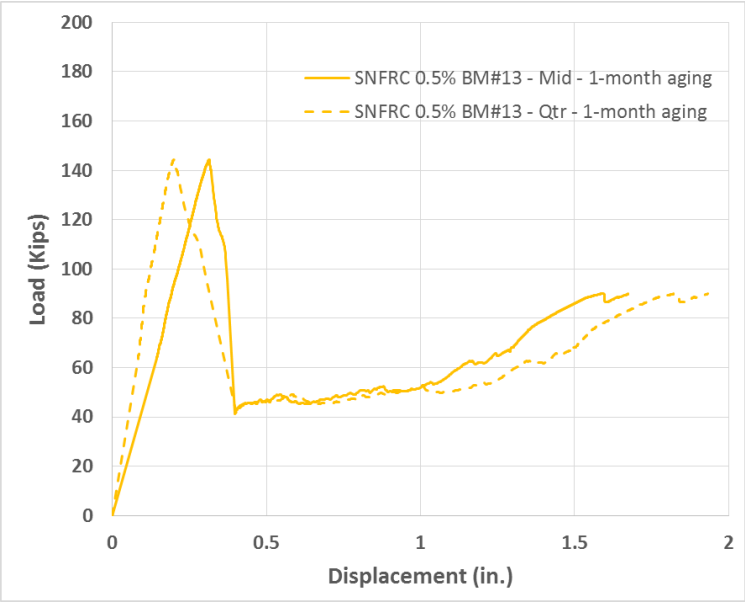

Figure 211 Load-deflection response at quarter and mid-span for SNFRC 0.5% beam #13 subjected to 1 month of aging (Phase 2)

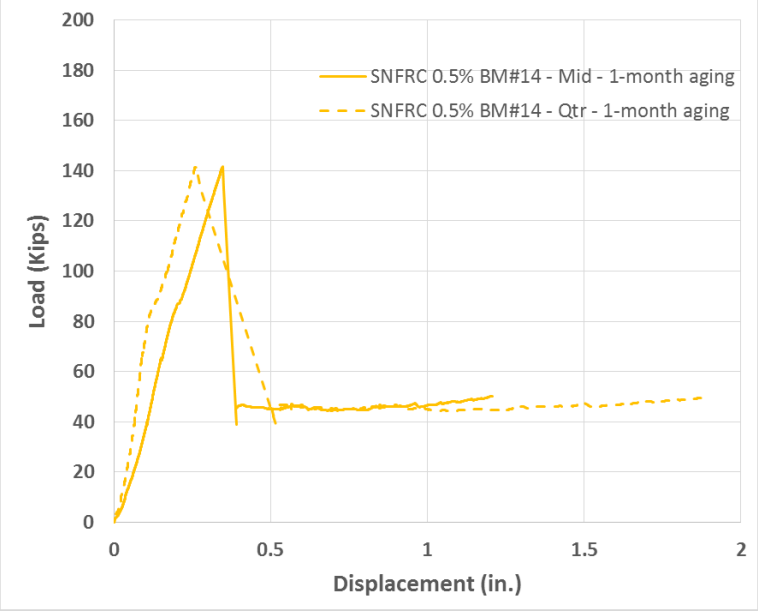

Figure 212 Load-deflection response at quarter and mid-span for SNFRC 0.5% beam #14 subjected to 1 month of aging (Phase 2)

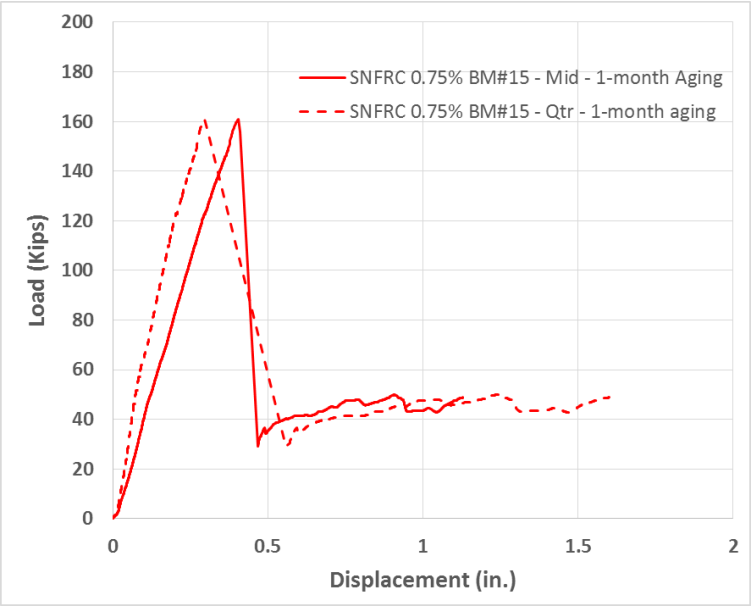

Figure 213 Load-deflection response at quarter and mid-span for SNFRC 0.75% beam #15 subjected to 1 month of aging (Phase 2)

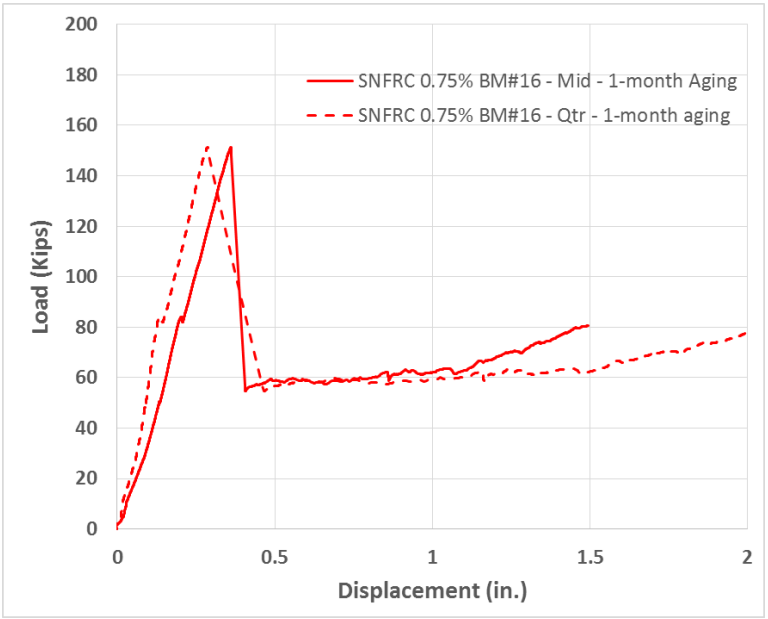

Figure 214 Load-deflection response at quarter and mid-span for SNFRC 0.75% beam #16 subjected to 1 month of aging (Phase 2)

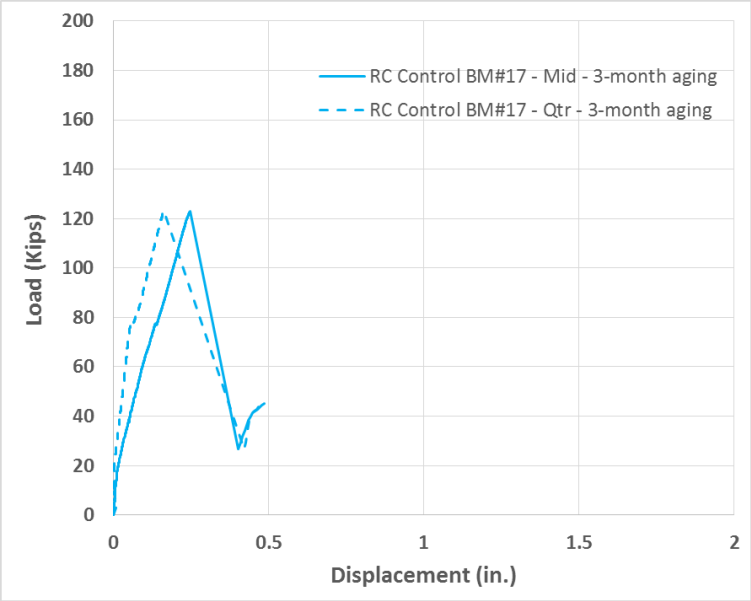

Figure 215 Load-deflection response at quarter and mid-span for RC beam #17 subjected to 3 months of aging (Phase 3)

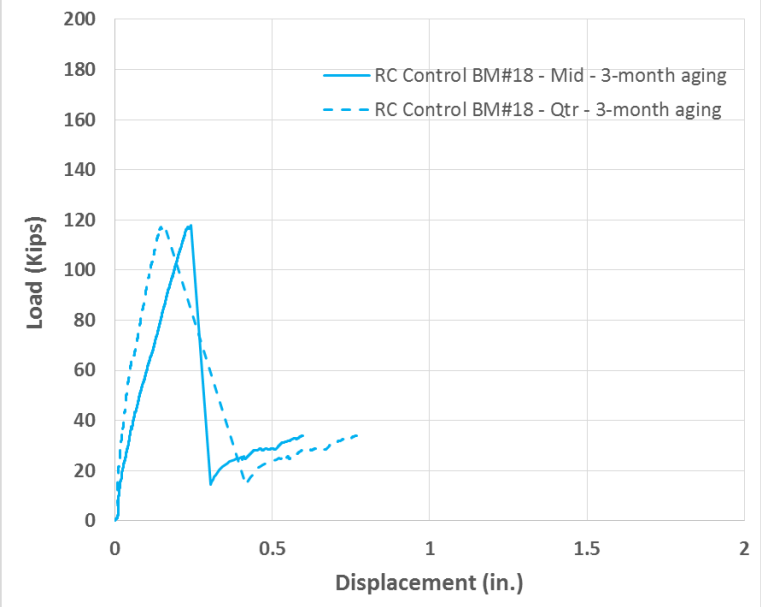

Figure 216 Load-deflection response at quarter and mid-span for RC beam #18 subjected to 3 months of aging (Phase 3)

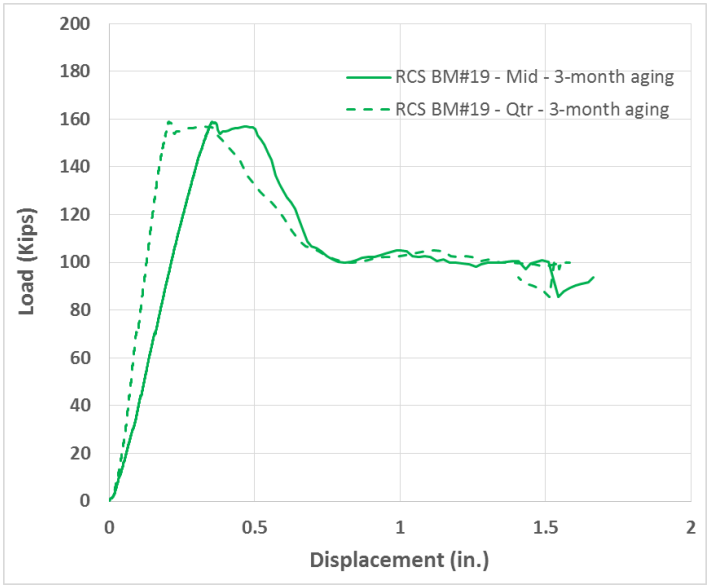

Figure 217 Load-deflection response at quarter and mid-span for RCS beam #19 subjected to 3 months of aging (Phase 3)

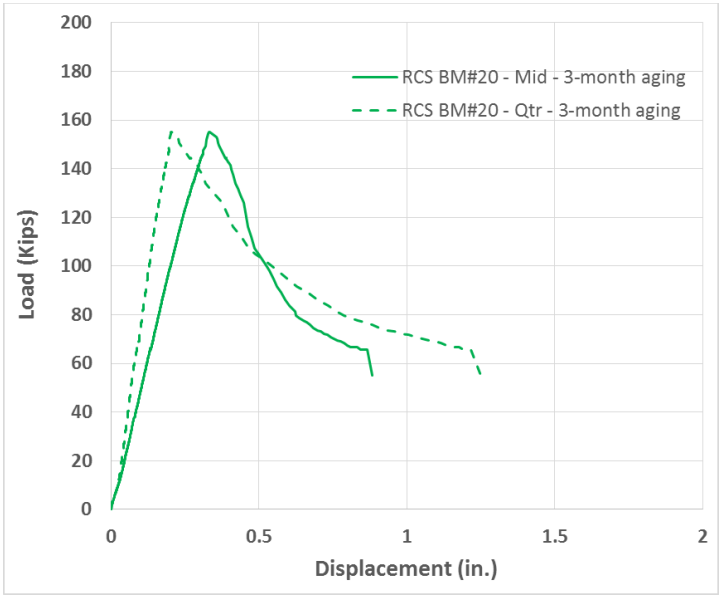

Figure 218 Load-deflection response at quarter and mid-span for RCS beam #20 subjected to 3 months of aging (Phase 3)

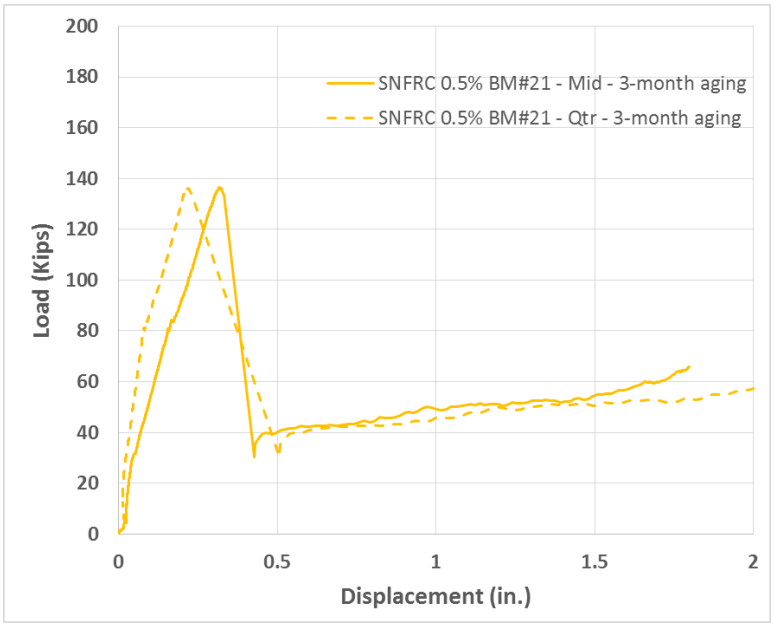

Figure 219 Load-deflection response at quarter and mid-span for SNFRC 0.5% beam #21 subjected to 3 months of aging (Phase 3)

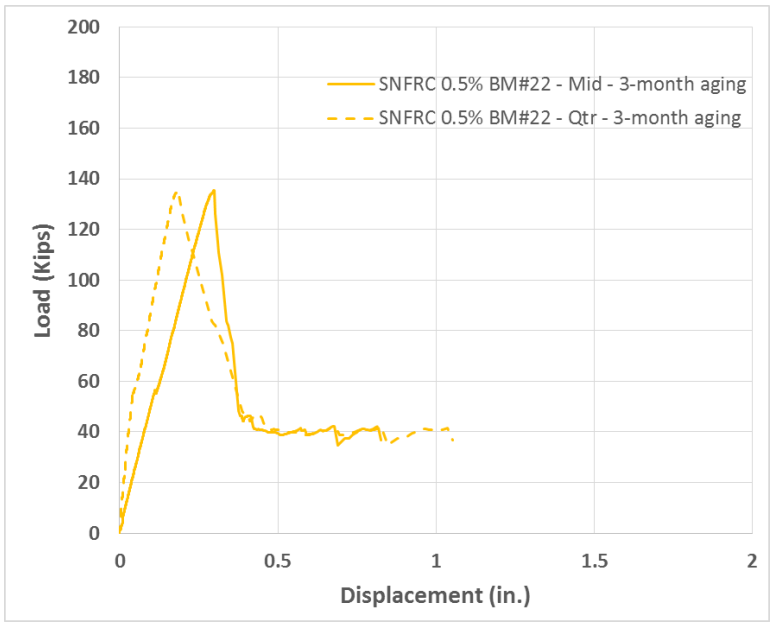

Figure 220 Load-deflection response at quarter and mid-span for SNFRC 0.5% beam #22 subjected to 3 months of aging (Phase 3)

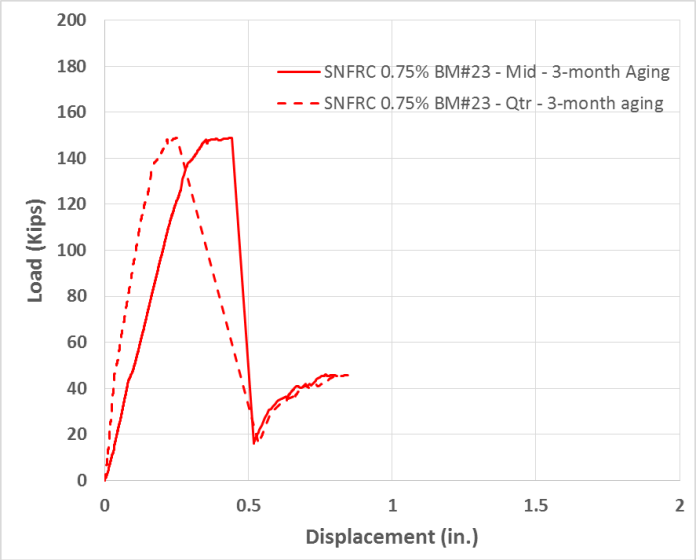

Figure 221 Load-deflection response at quarter and mid-span for SNFRC 0.75% beam #23 subjected to 3 months of aging (Phase 3)

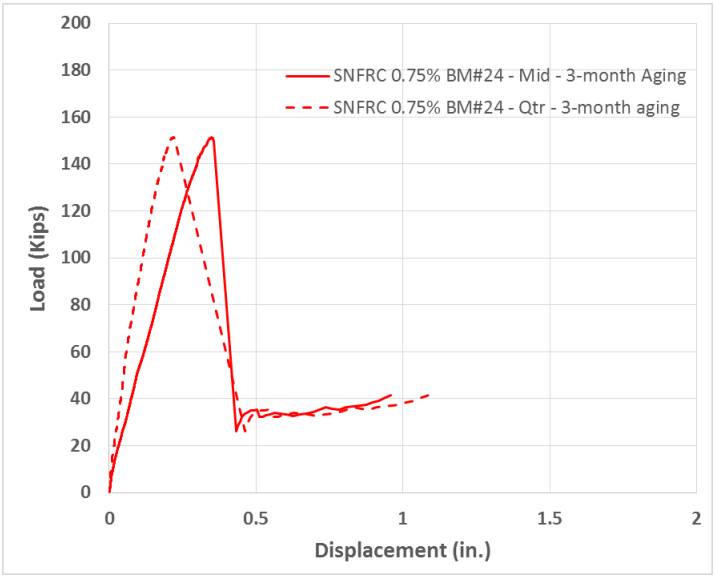

Figure 222 Load-deflection response at quarter and mid-span for SNFRC 0.75% beam #24 subjected to 3 months of aging (Phase 3)

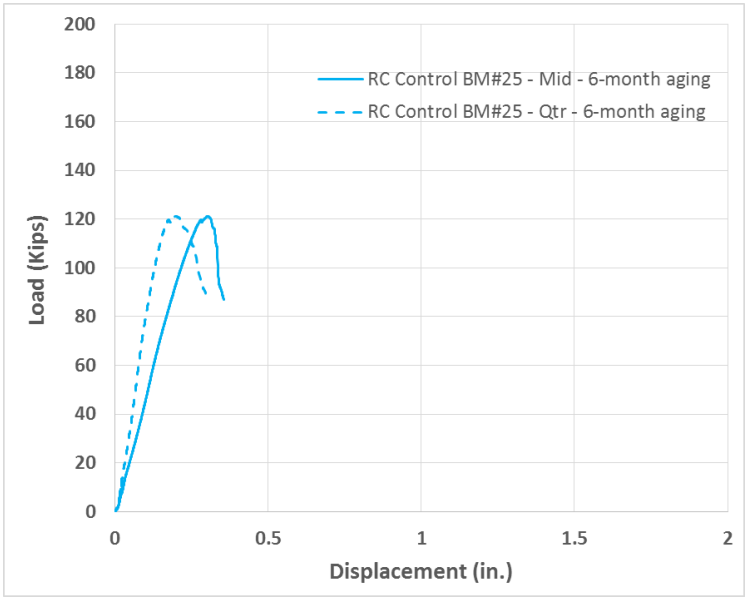

Figure 223 Load-deflection response at quarter and mid-span for RC beam #25 subjected to 6 months of aging (Phase 4)

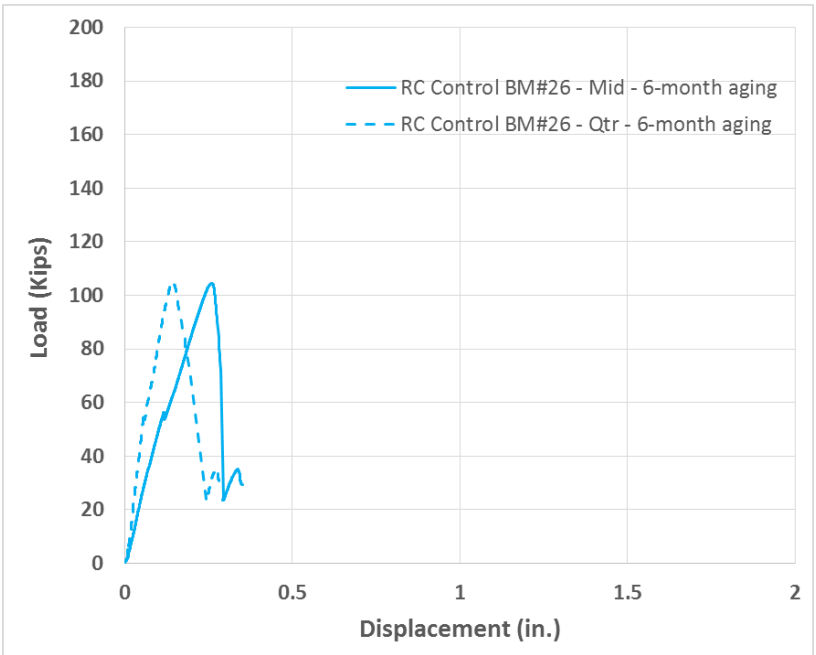

Figure 224 Load-deflection response at quarter and mid-span for RC beam #26 subjected to 6 months of aging (Phase 4)

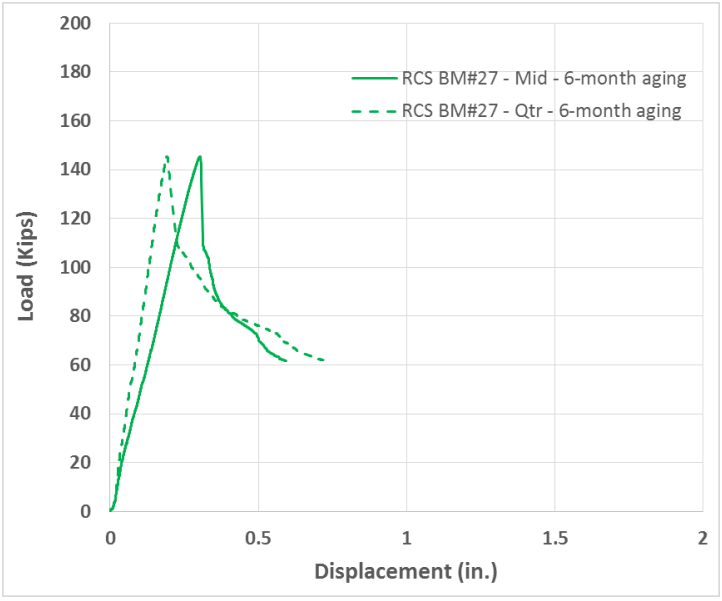

Figure 225 Load-deflection response at quarter and mid-span for RCS beam #27 subjected to 6 months of aging (Phase 4)

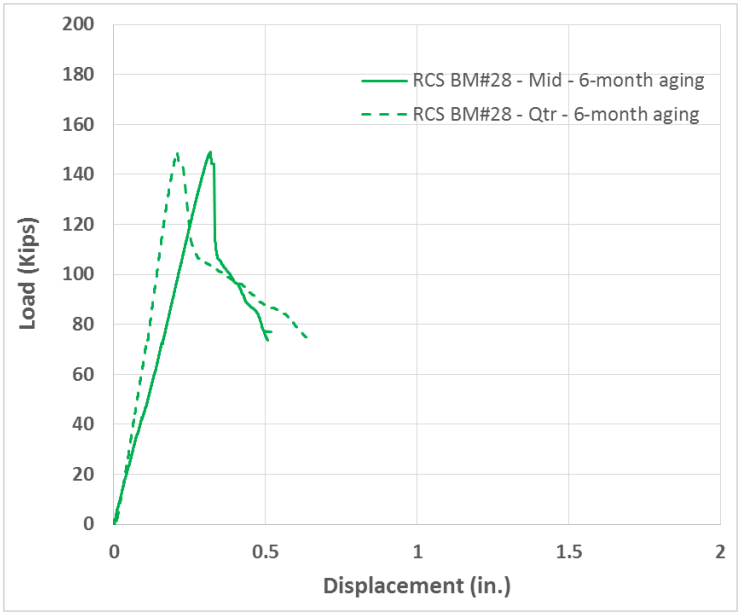

Figure 226 Load-deflection response at quarter and mid-span for RCS beam #28 subjected to 6 months of aging (Phase 4)

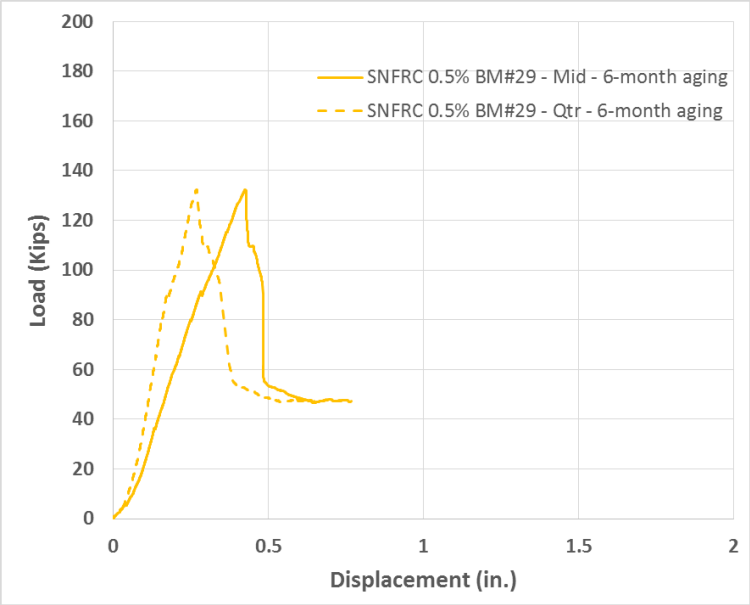

Figure 227 Load-deflection response at quarter and mid-span for SNFRC 0.5% beam #29 subjected to 6 months of aging (Phase 4)

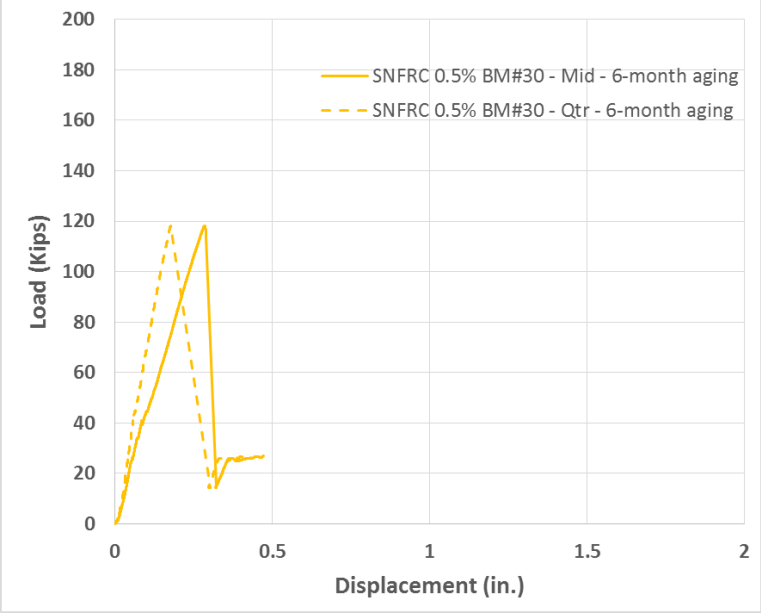

Figure 228 Load-deflection response at quarter and mid-span for SNFRC 0.5% beam #30 subjected to 6 months of aging (Phase 4)

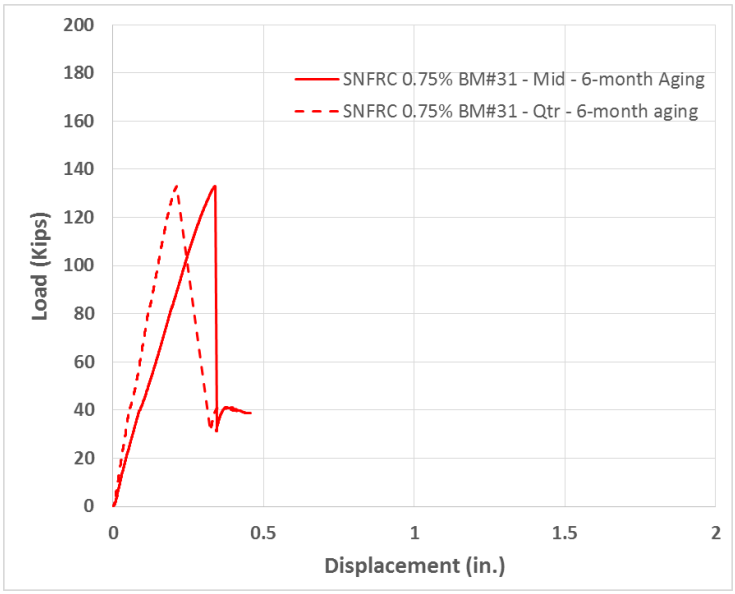

Figure 229 Load-deflection response at quarter and mid-span for SNFRC 0.75% beam #31 subjected to 6 months of aging (Phase 4)

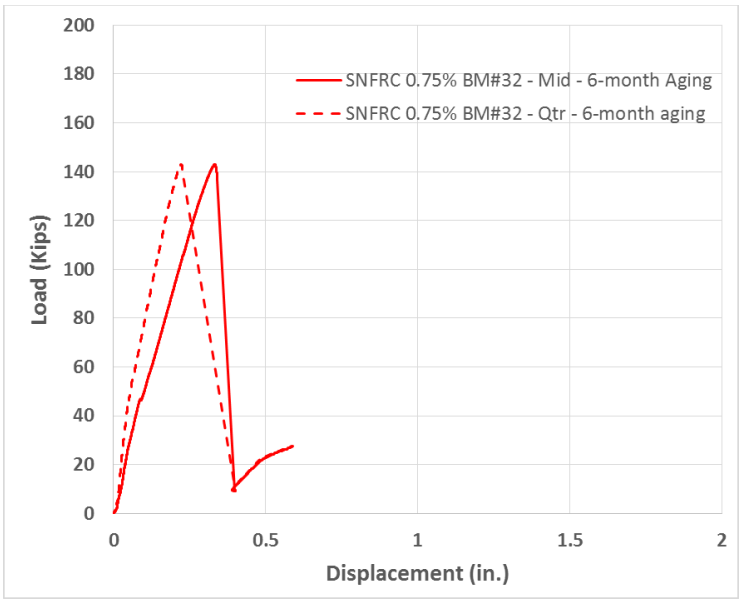

Figure 230 Load-deflection response at quarter and mid-span for SNFRC 0.75% beam #32 subjected to 6 months of aging (Phase 4)

Appendix F

Load-Deflection Response of large-scale beams with FEM

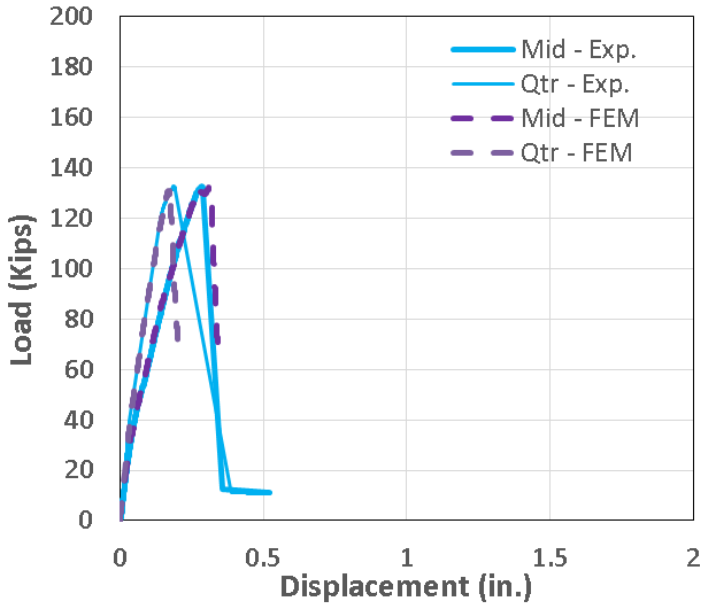

Figure 231 Load - deflection response of RC – Control beams without aging

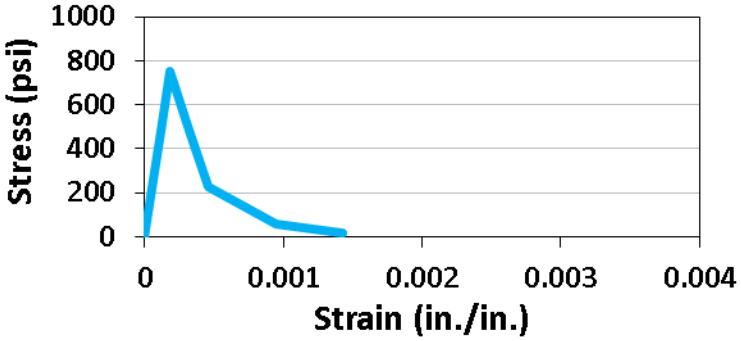

Figure 232 Concrete constitutive law in tension for RC – Control beams without aging

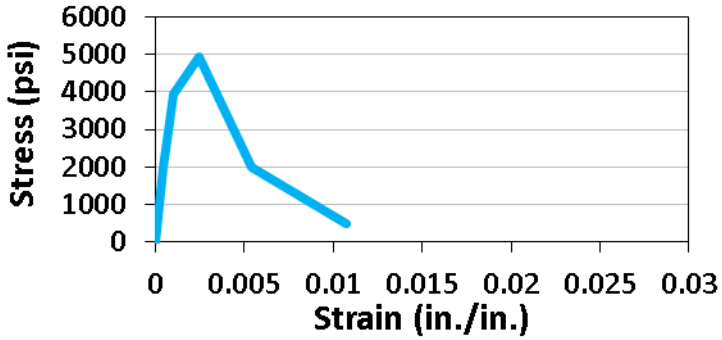

Figure 233 Concrete constitutive law in compression for RC – Control beams without aging

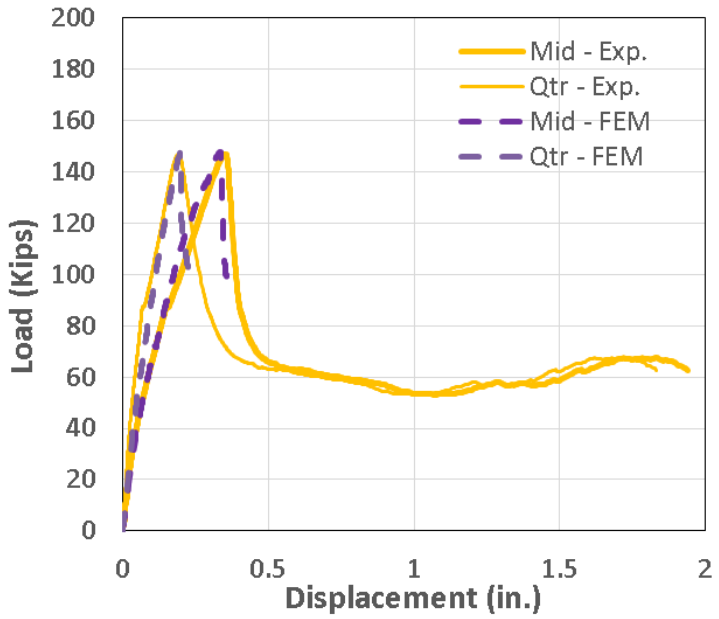

Figure 234 Load - deflection response of SNFRC 0.5% beams without aging

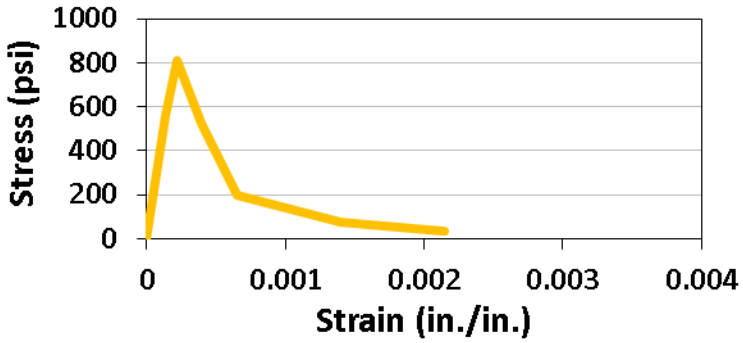

Figure 235 Concrete constitutive law in tension for SNFRC 0.5% beams without aging

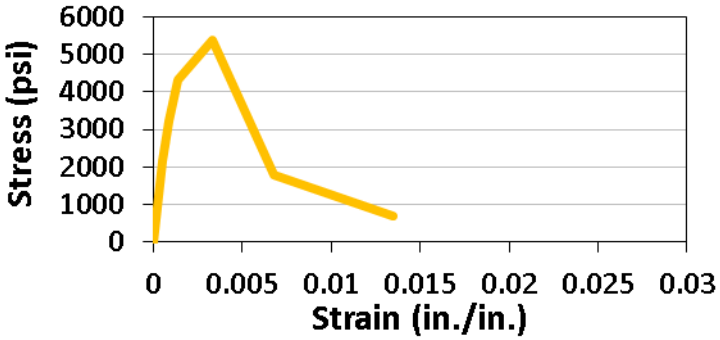

Figure 236 Concrete constitutive law in compression for SNFRC 0.5% beams without aging

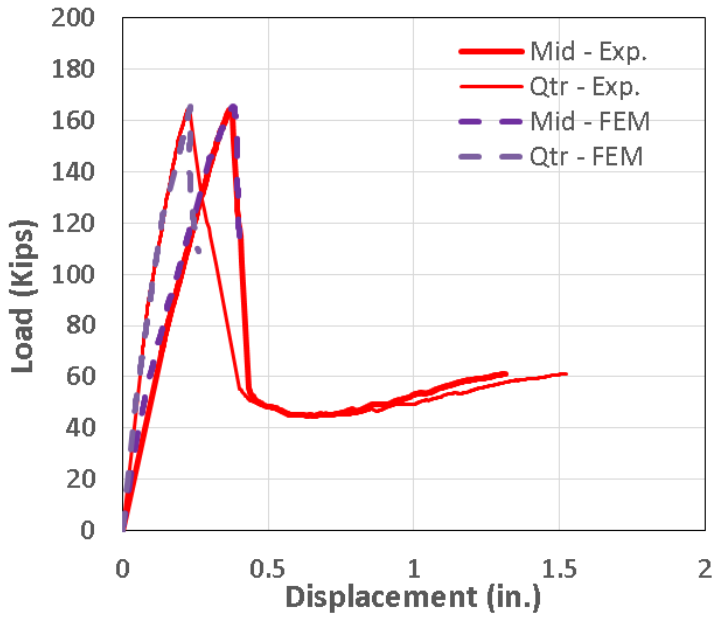

Figure 237 Load - deflection response of SNFRC 0.75% beams without aging

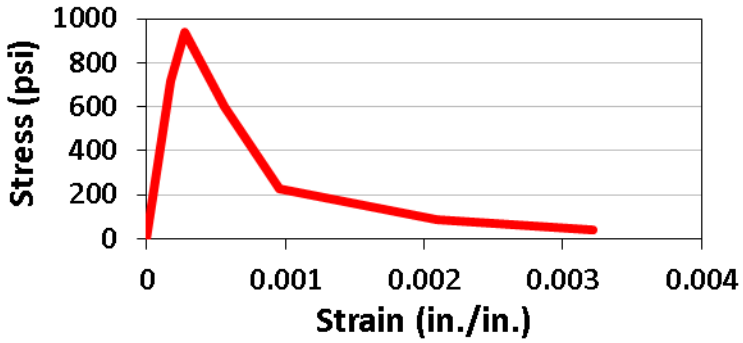

Figure 238 Concrete constitutive law in tension for SNFRC 0.75% beams without aging

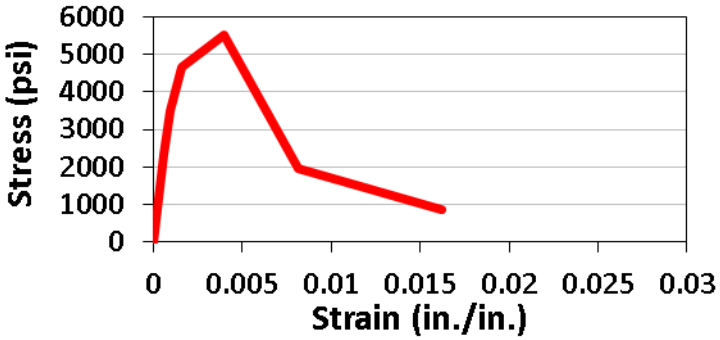

Figure 239 Concrete constitutive law in compression for SNFRC 0.75% beams without aging

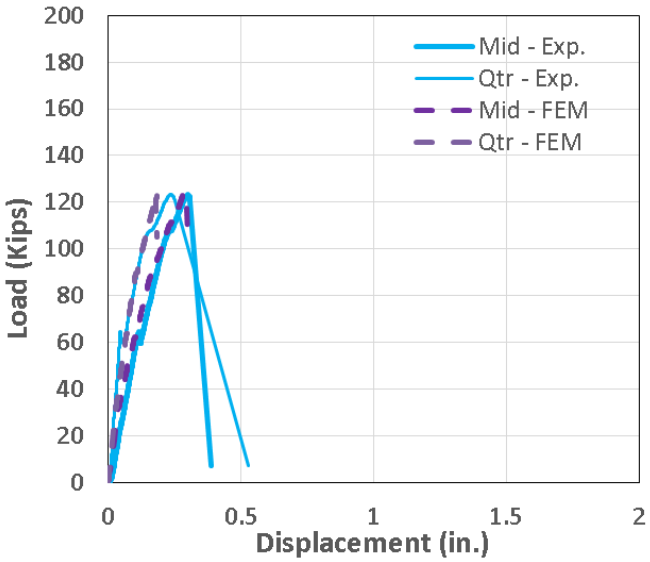

Figure 240 Load - deflection response of RC – Control beams subjected to 1 month of aging

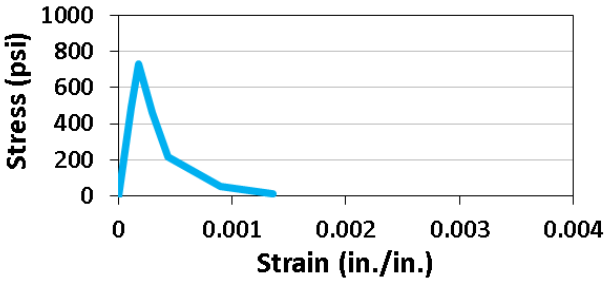

Figure 241 Concrete constitutive law in tension for RC – Control beams subjected to 1 month of aging

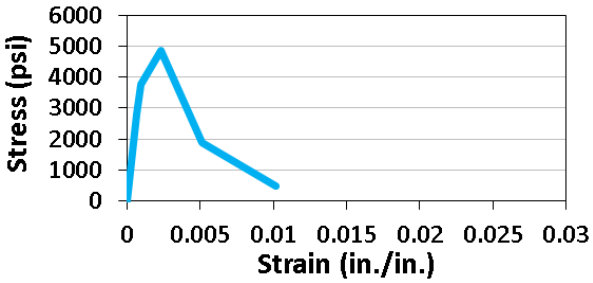

Figure 242 Concrete constitutive law in compression for RC – Control beams subjected to 1 month of aging

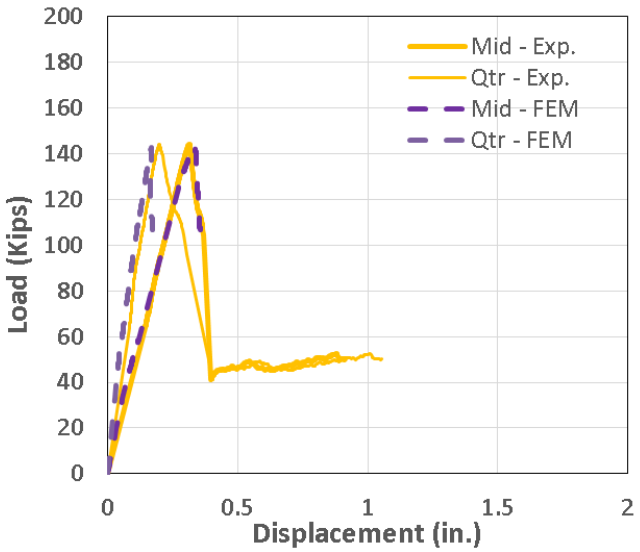

Figure 243 Load - deflection response of SNFRC 0.5% beams subjected to 1 month of aging

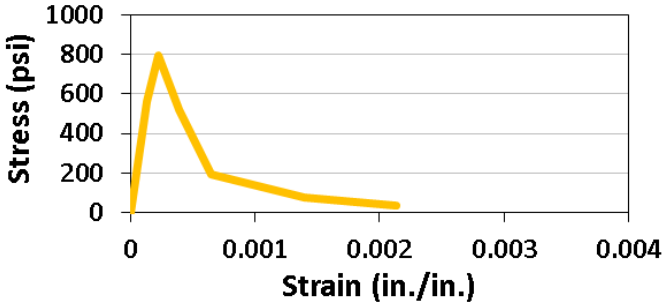

Figure 244 Concrete constitutive law in tension for SNFRC 0.5% beams subjected to 1 month of aging

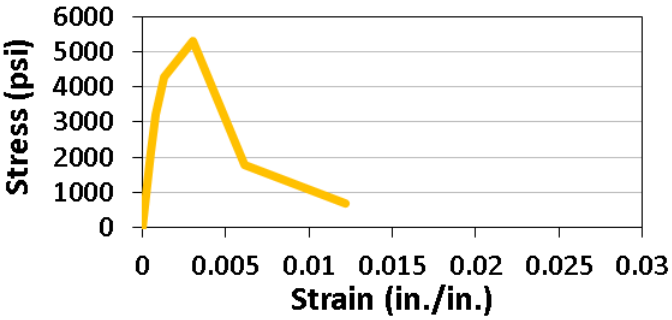

Figure 245 Compression - hardening of SNFRC 0.5% beams subjected to 1 month of aging

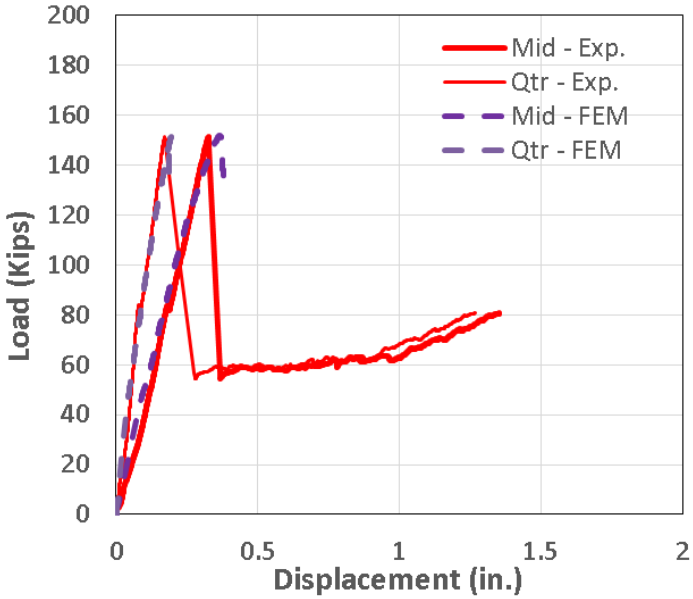

Figure 246 Load - deflection response of SNFRC 0.75% beams subjected to 1 month of aging

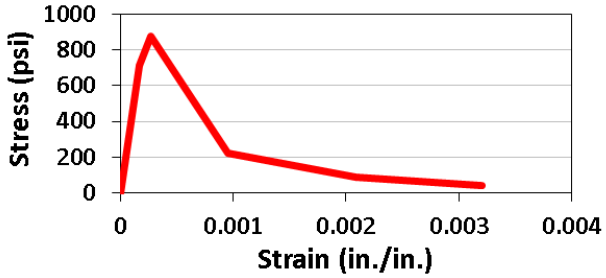

Figure 247 Concrete constitutive law in tension for SNFRC 0.75% beams subjected to 1 month of aging

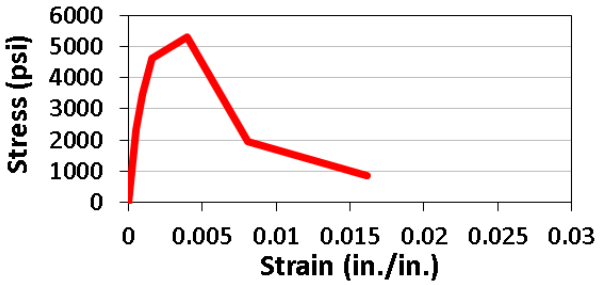

Figure 248 Concrete constitutive law in compression for SNFRC 0.75% beams subjected to 1 month of aging

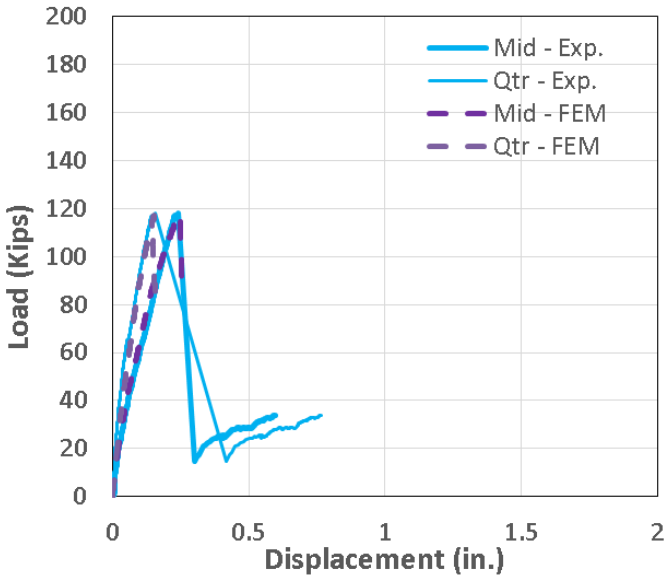

Figure 249 Load - deflection response of RC – Control beams subjected to 3 months of aging

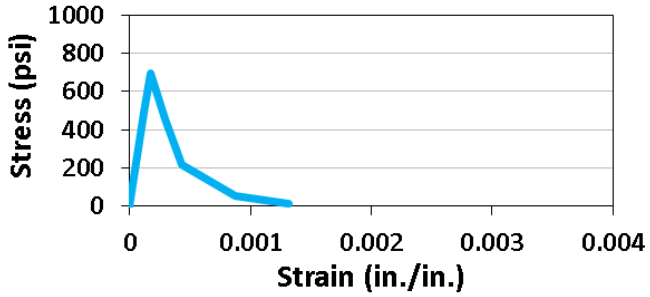

Figure 250 Concrete constitutive law in tension for RC – Control beams subjected to 3 months of aging

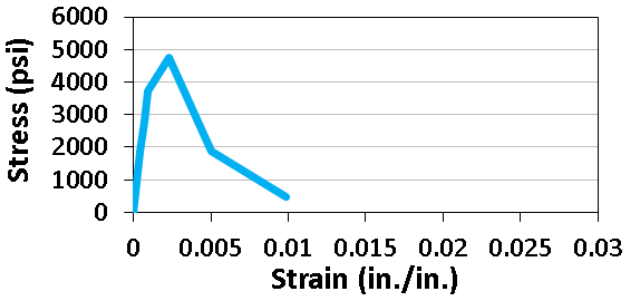

Figure 251 Concrete constitutive law in compression for RC – Control beams subjected to 3 months of aging

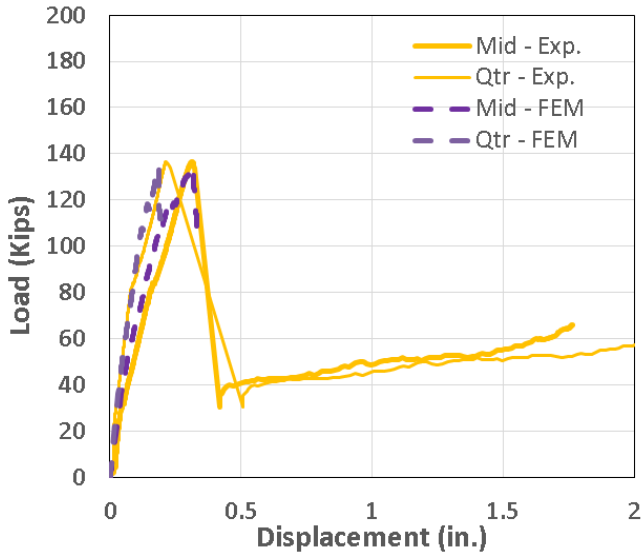

Figure 252 Load - deflection response of SNFRC 0.5% beams subjected to 3 months of aging

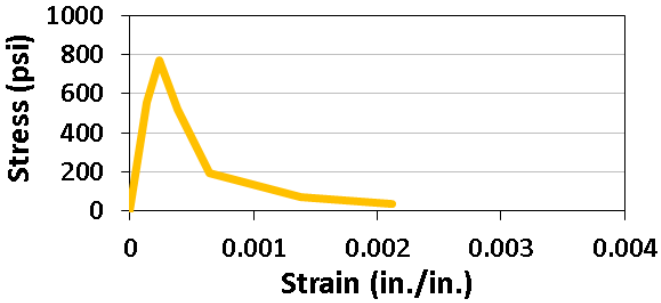

Figure 253 Concrete constitutive law in tension for SNFRC 0.5% beams subjected to 3 months of aging

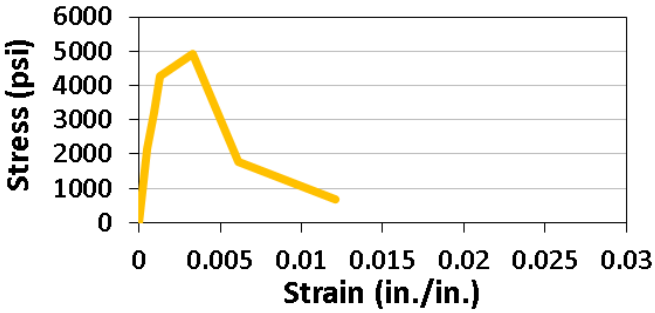

Figure 254 Concrete constitutive law in compression for SNFRC 0.5% beams subjected to 3 months of aging

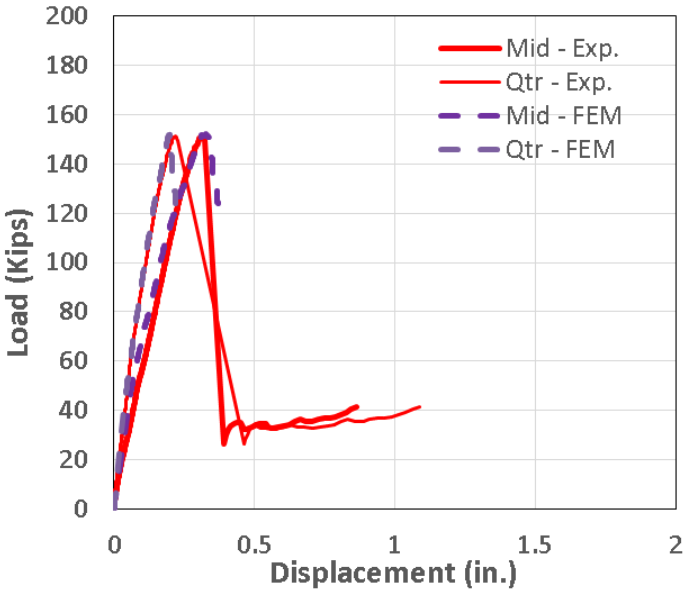

Figure 255 Load - deflection response of SNFRC 0.75% beams subjected to 3 months of aging

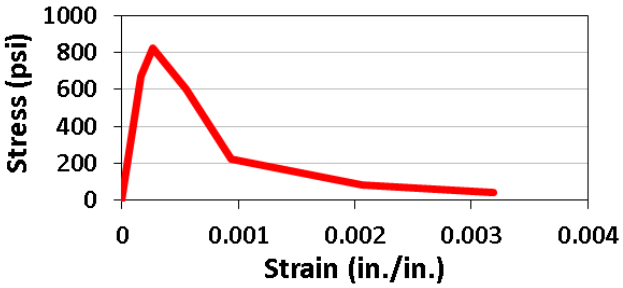

Figure 256 Concrete constitutive law in tension for 0.75% beams subjected to 3 months of aging

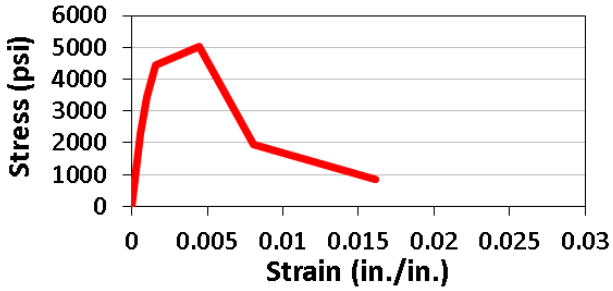

Figure 257 Concrete constitutive law in compression for SNFRC 0.75% beams subjected to 3 months of aging

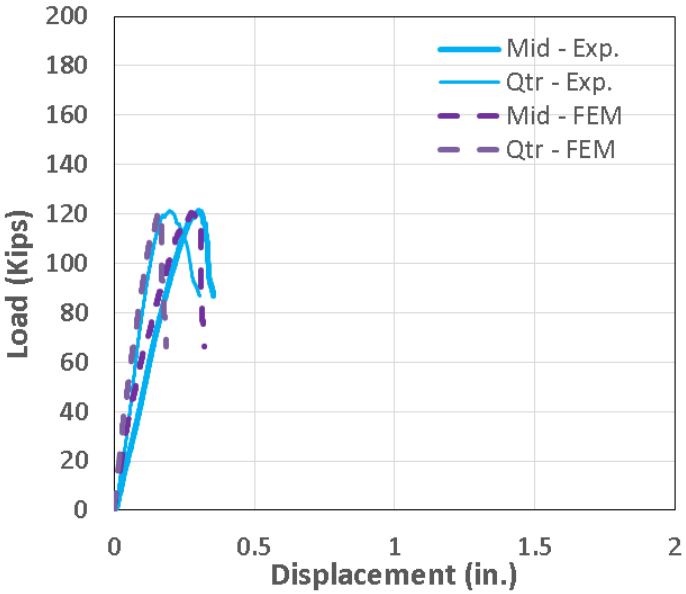

Figure 258 Load - deflection response of RC – Control beams subjected to 6 months of aging

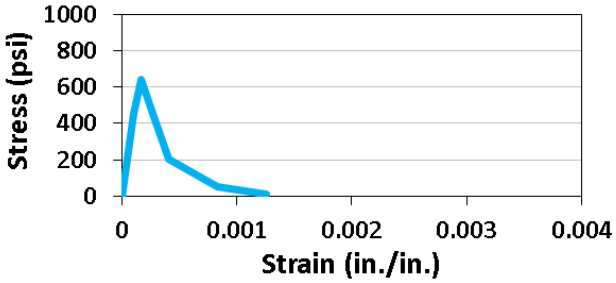

Figure 259 Concrete constitutive law in tension for RC – Control beams subjected to 6 months of aging

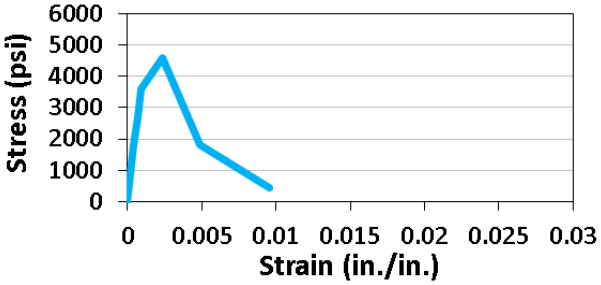

Figure 260 Concrete constitutive law in compression for RC – Control beams subjected to 6 months of aging

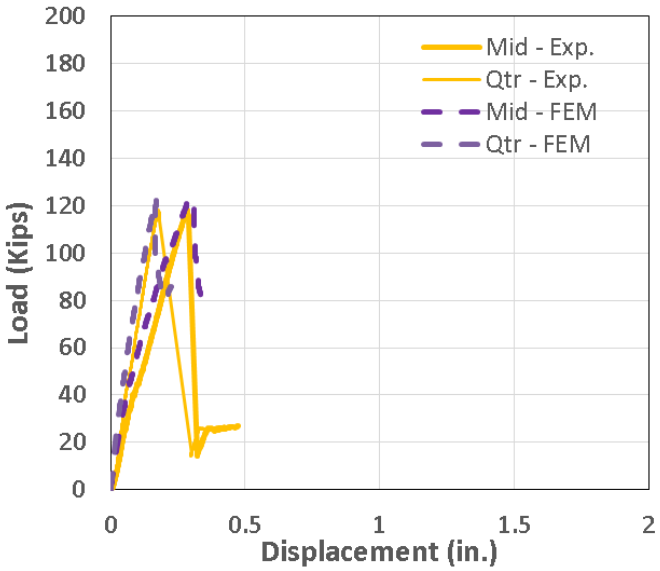

Figure 261 Load - deflection response of SNFRC 0.5% beams subjected to 6 months of aging

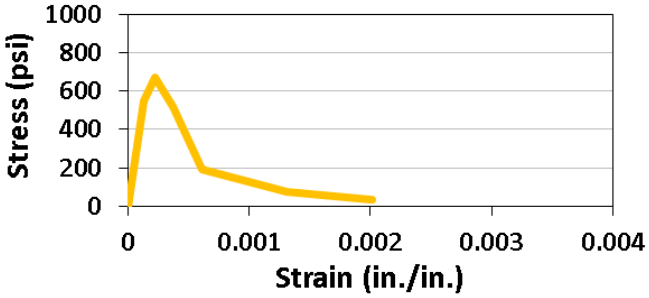

Figure 262 Concrete constitutive law in tension for SNFRC 0.5% beams subjected to 6 months of aging

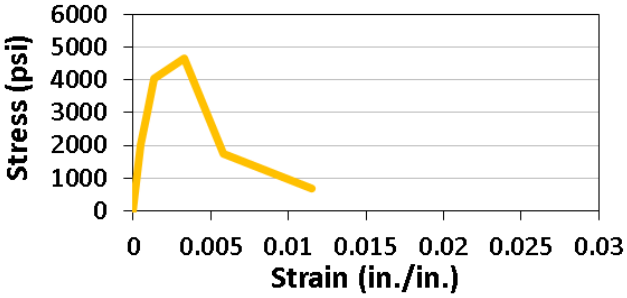

Figure 263 Concrete constitutive law in compression for SNFRC 0.5% beams subjected to 6 months of aging

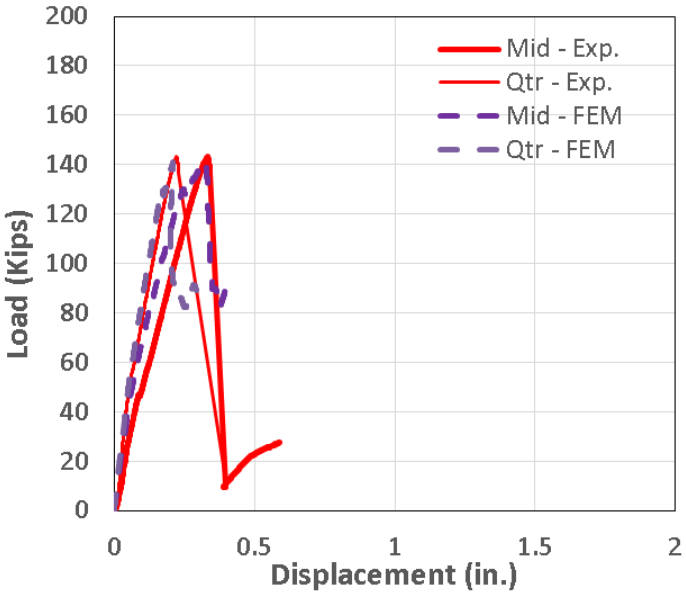

Figure 264 Load - deflection response of SNFRC 0.75% beams subjected to 6 months of aging

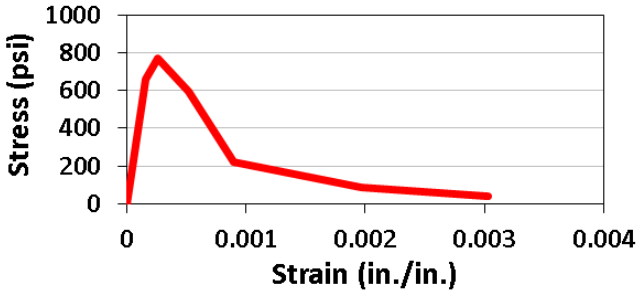

Figure 265 Concrete constitutive law in tension for SNFRC 0.75% beams subjected to 6 months of aging

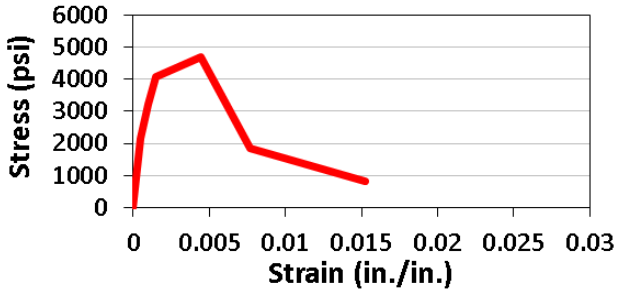

Figure 266 Concrete constitutive law in compression for SNFRC 0.75% beams subjected to 6 months of aging

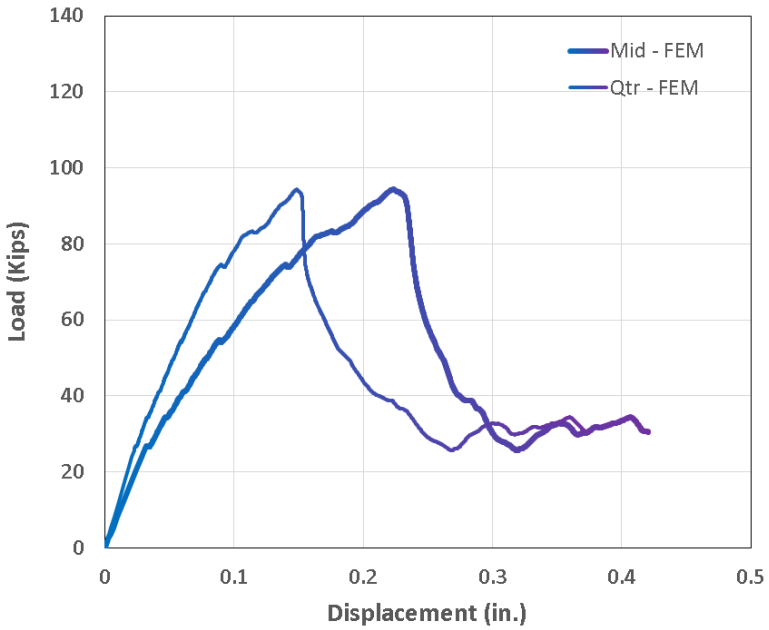

Figure 267 Load - deflection response of RC – Control beams after 100 Years

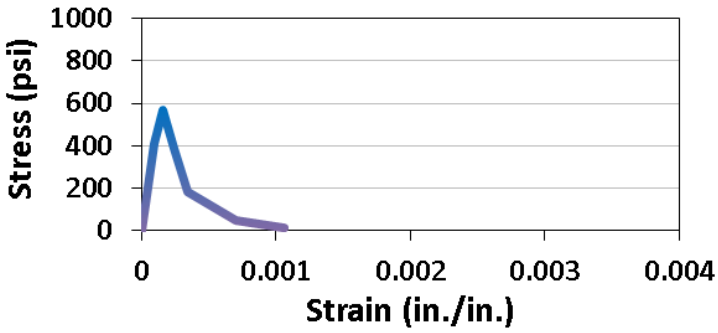

Figure 268 Concrete constitutive law in tension for RC – Control beams after 100 Years

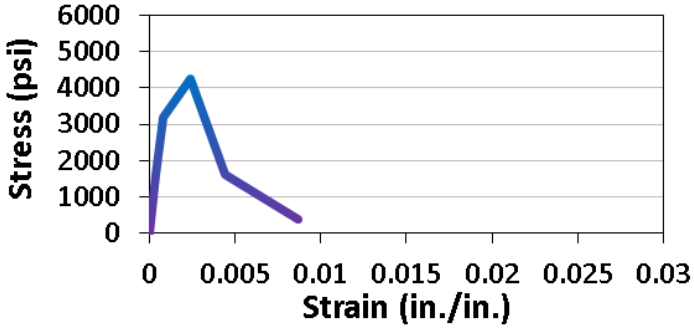

Figure 269 Concrete constitutive law in compression for RC – Control beams after 100 Years

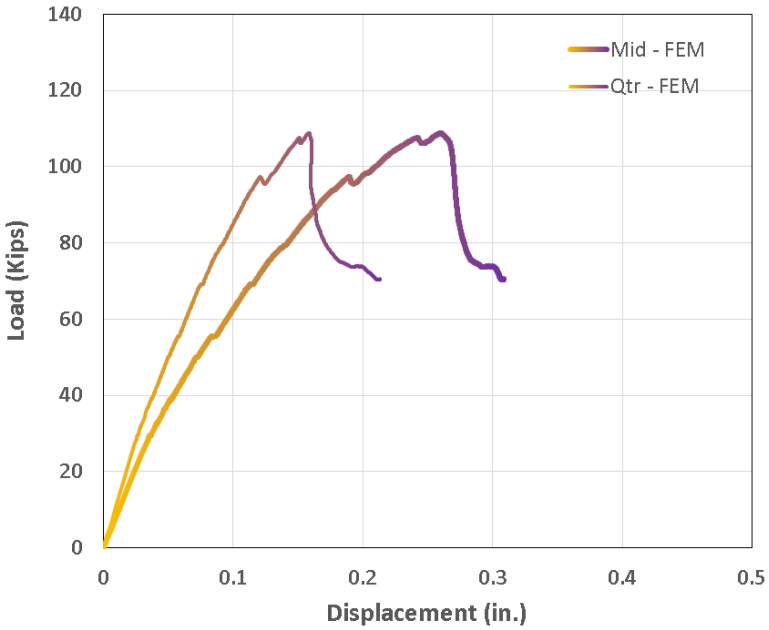

Figure 270 Load - deflection response of SNFRC 0.5% beams after 100 years

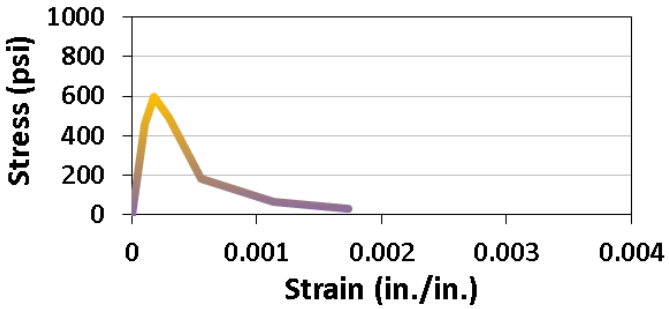

Figure 271 Concrete constitutive law in tension for SNFRC 0.5% beams after 100 Years

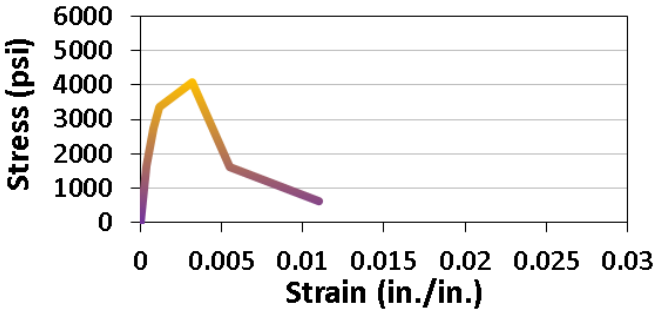

Figure 272 Concrete constitutive law in compression for SNFRC 0.5% beams after 100 Years

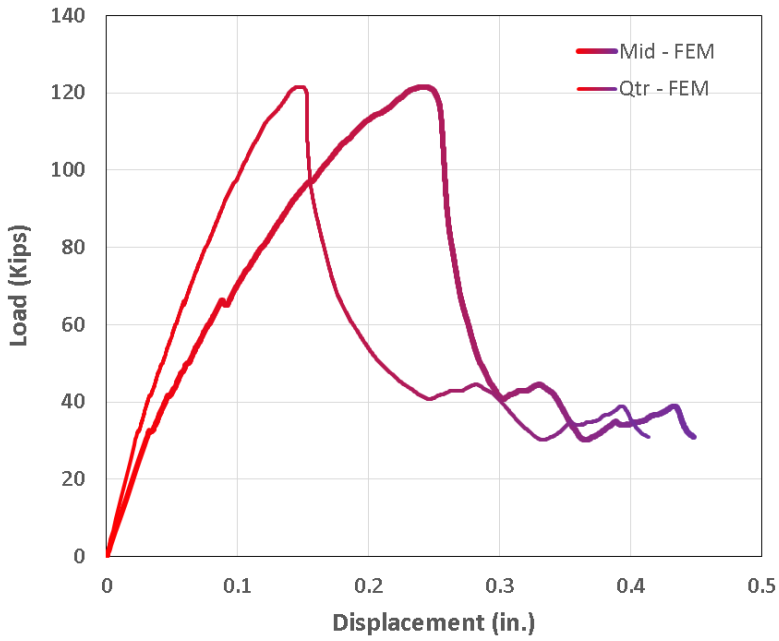

Figure 273 Load - deflection response of SNFRC 0.75% beams after 100 years

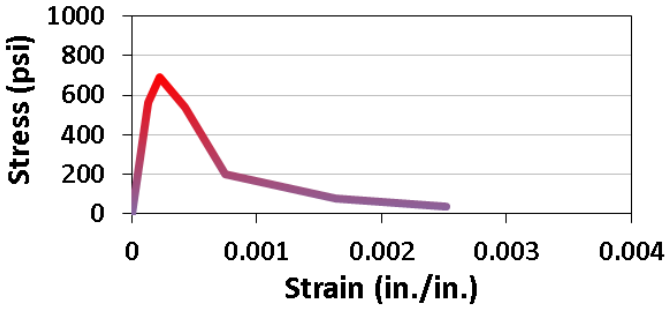

Figure 274 Concrete constitutive law in tension for SNFRC 0.75% beams after 100 Years

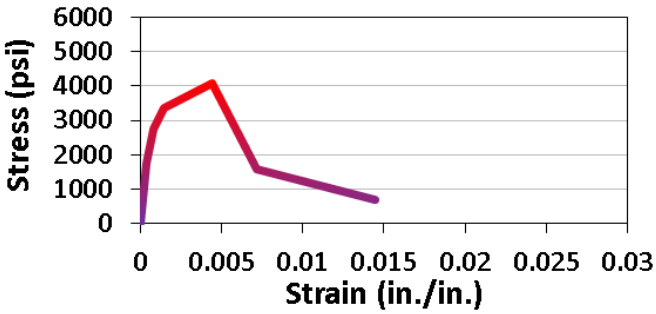

Figure 275 Concrete constitutive law in compression for SNFRC 0.75% beams after 100 Years

Appendix G

Load-Deflection Response of large-scale beams in parametric study

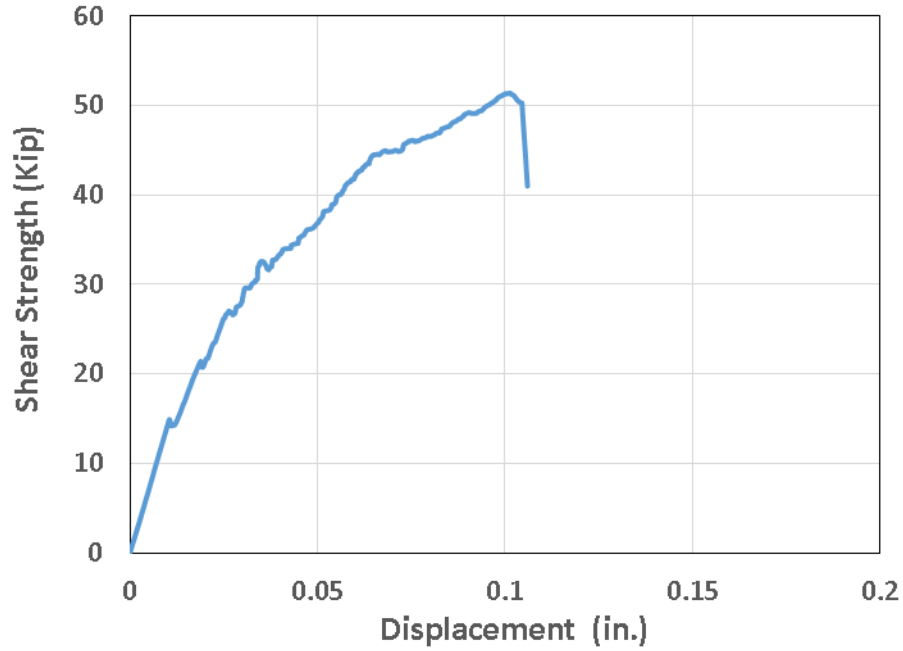

Figure 276 Load - deflection response of large-scale beam, P1

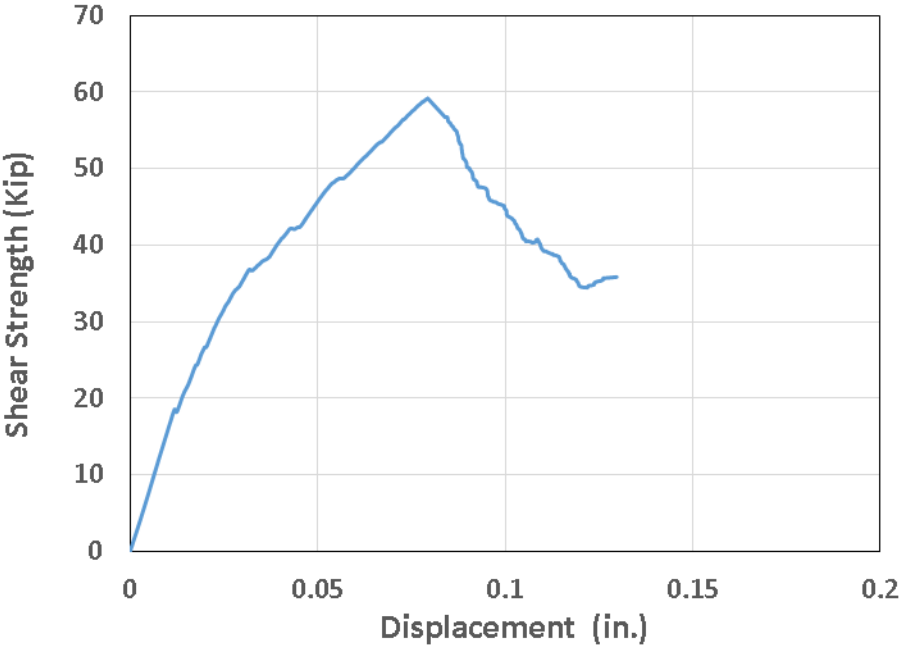

Figure 277 Load - deflection response of large-scale beam, P2

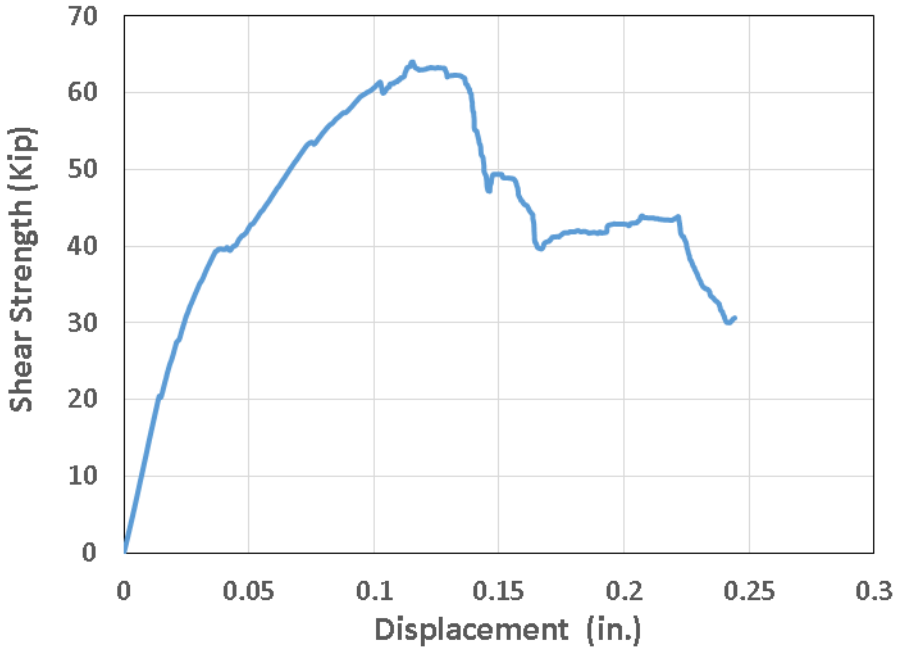

Figure 278 Load - deflection response of large-scale beam, P3

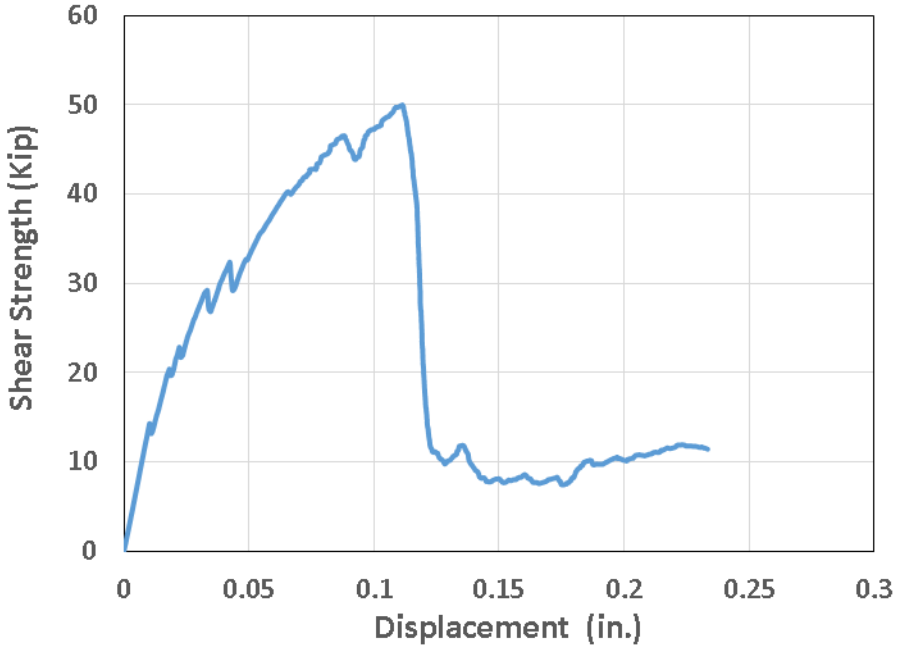

Figure 279 Load - deflection response of large-scale beam, P4

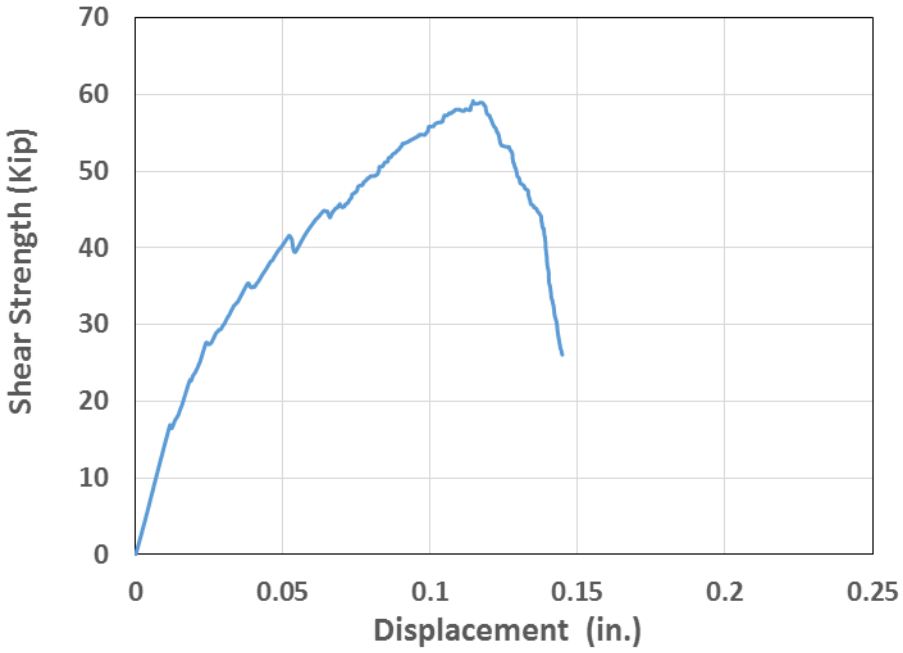

Figure 280 Load - deflection response of large-scale beam, P5

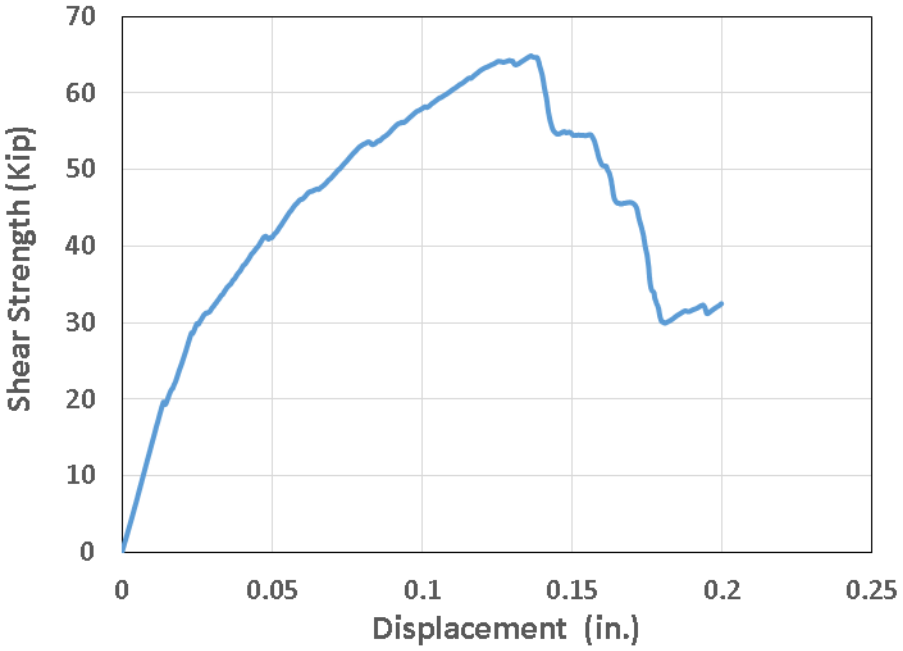

Figure 281 Load - deflection response of large-scale beam, P6

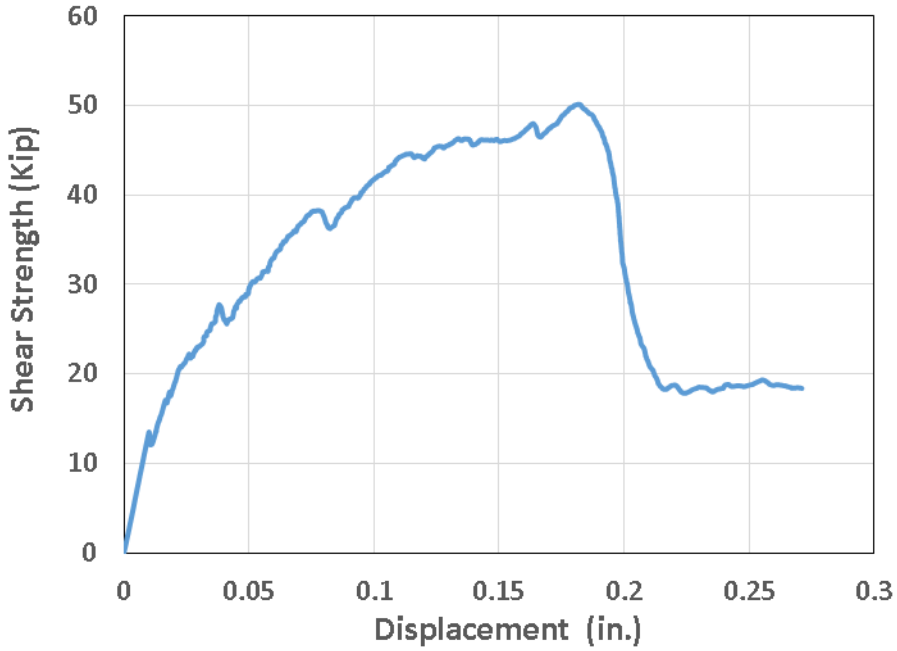

Figure 282 Load - deflection response of large-scale beam, P7

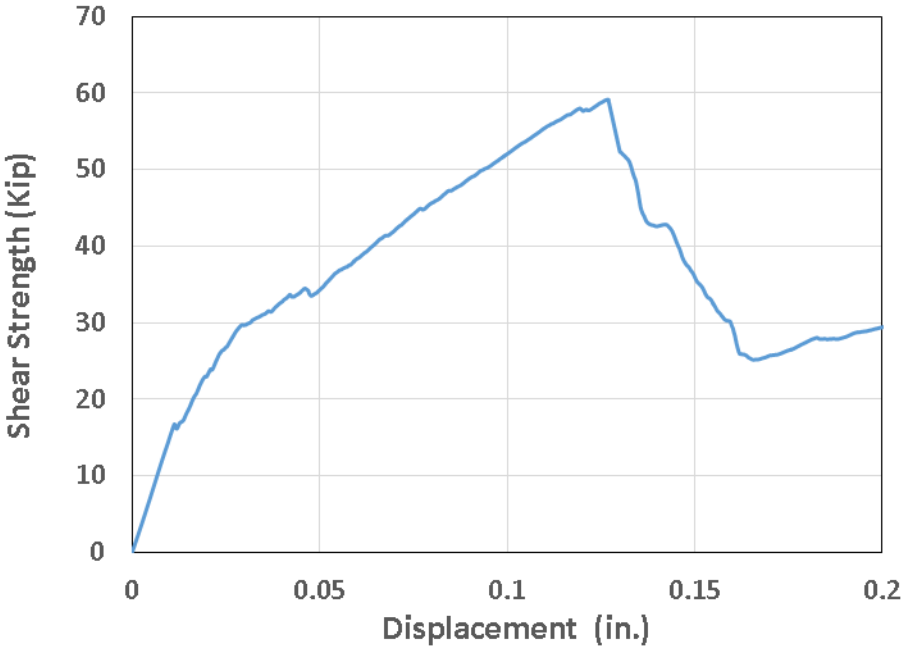

Figure 283 Load - deflection response of large-scale beam, P8

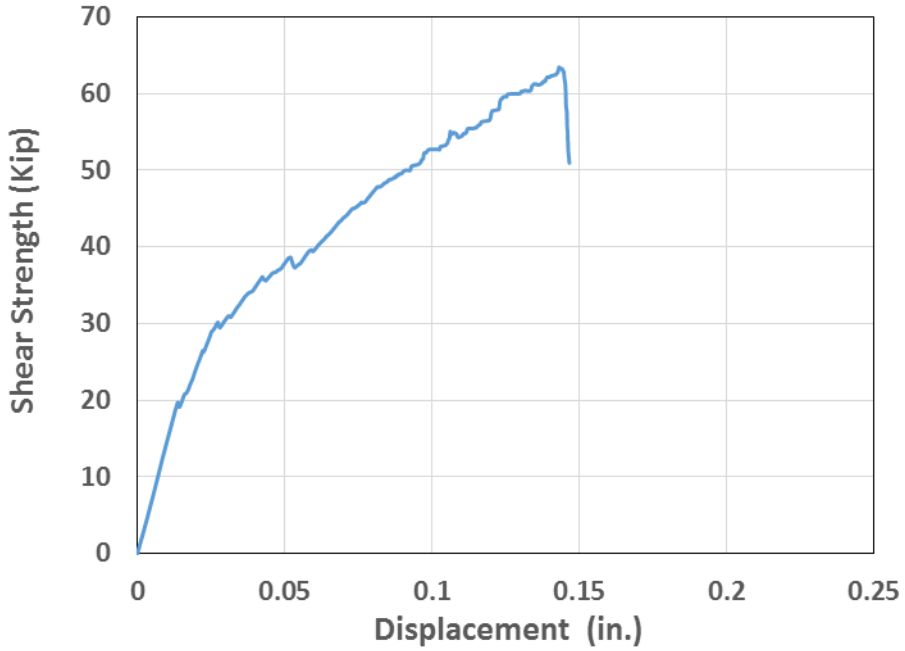

Figure 284 Load - deflection response of large-scale beam, P9

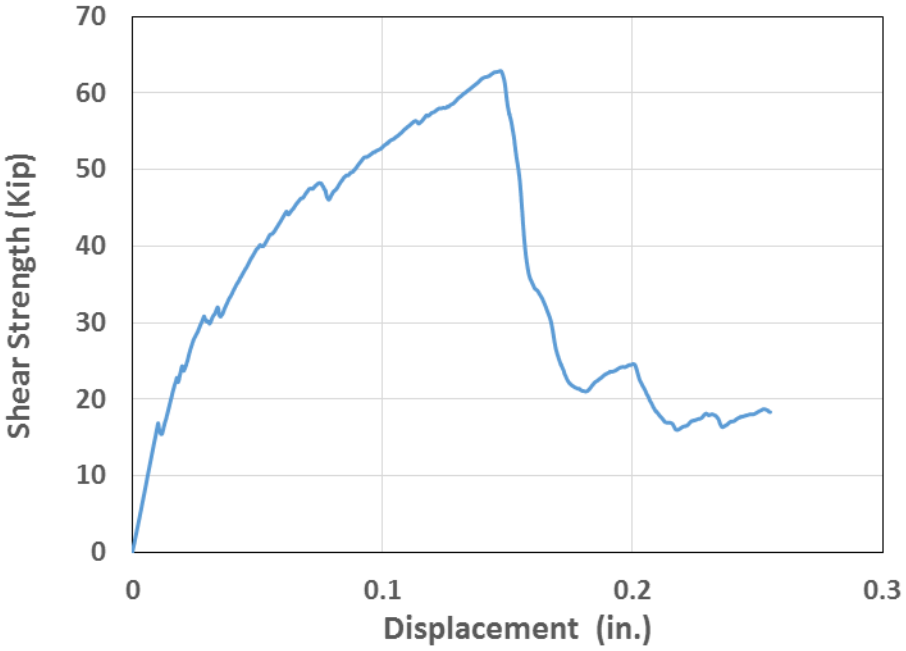

Figure 285 Load - deflection response of large-scale beam, P10

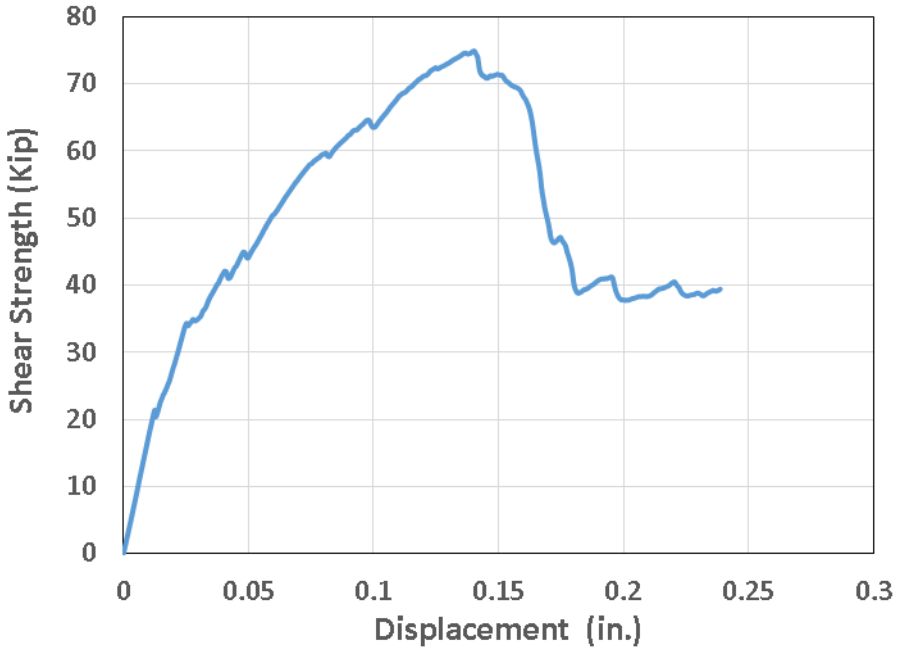

Figure 286 Load - deflection response of large-scale beam, P11

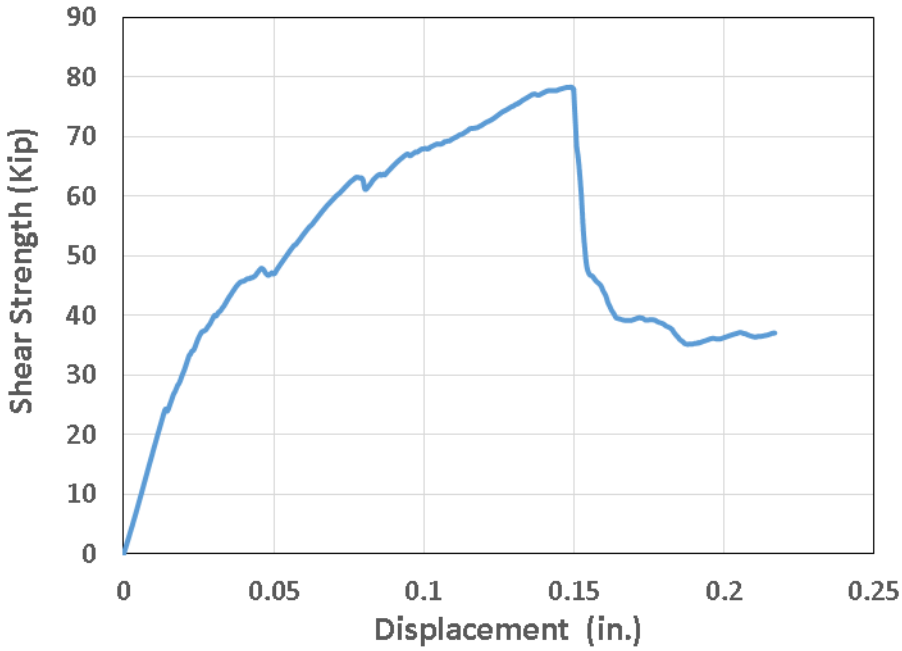

Figure 287 Load - deflection response of large-scale beam, P12

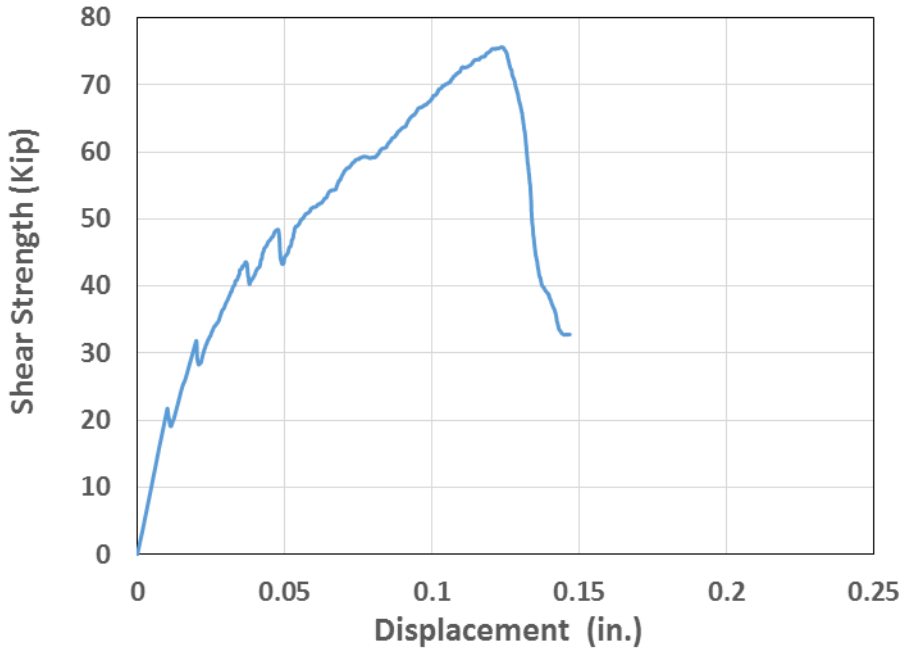

Figure 288 Load - deflection response of large-scale beam, P13

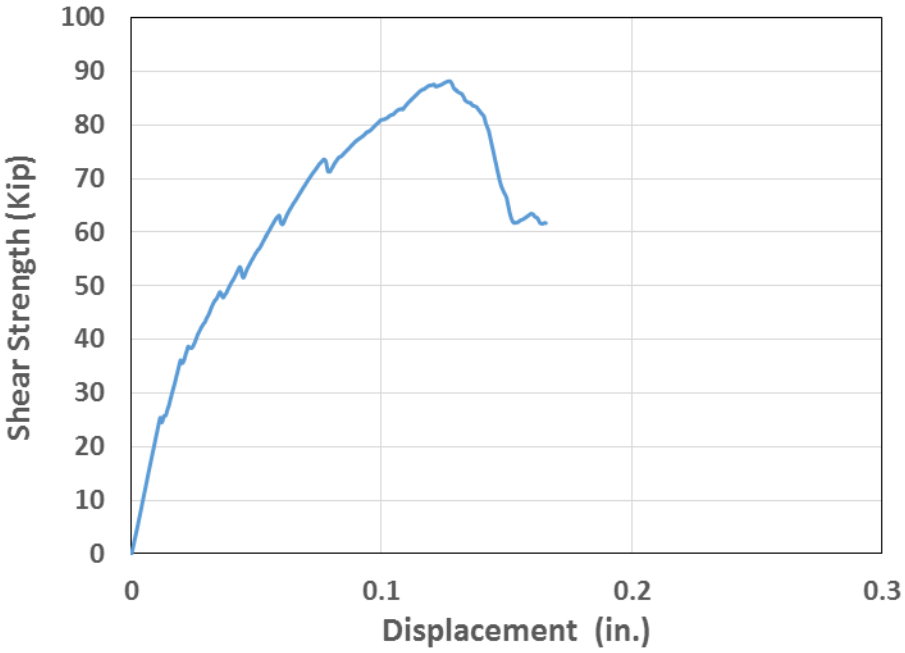

Figure 289 Load - deflection response of large-scale beam, P14

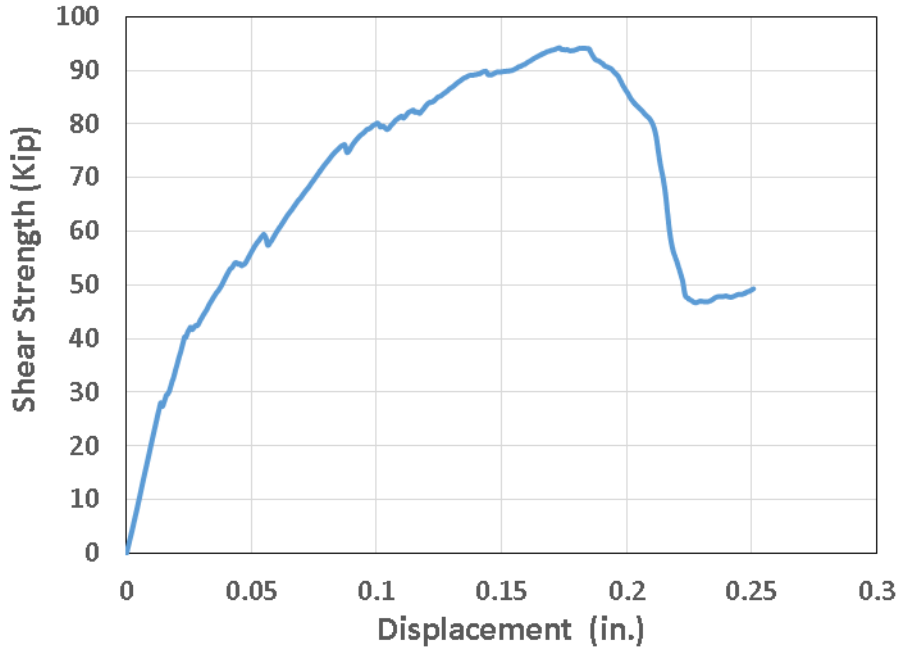

Figure 290 Load - deflection response of large-scale beam, P15

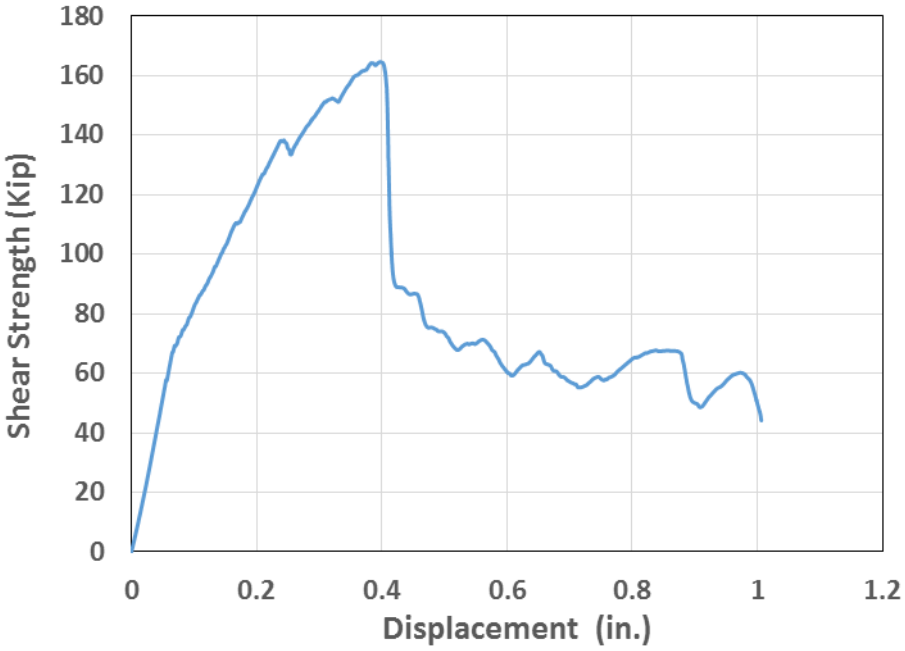

Figure 291 Load - deflection response of large-scale beam, P16

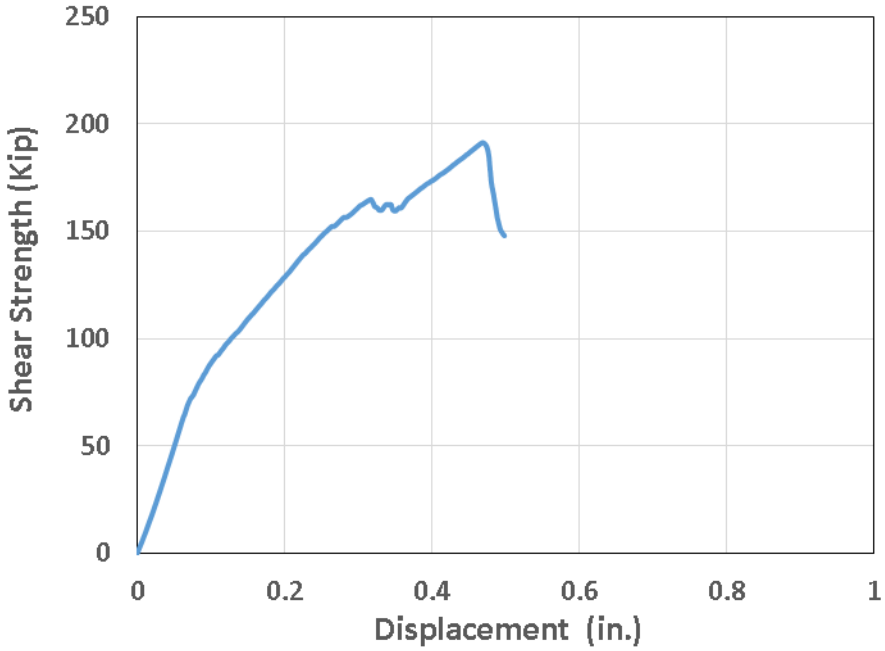

Figure 292 Load - deflection response of large-scale beam, P17

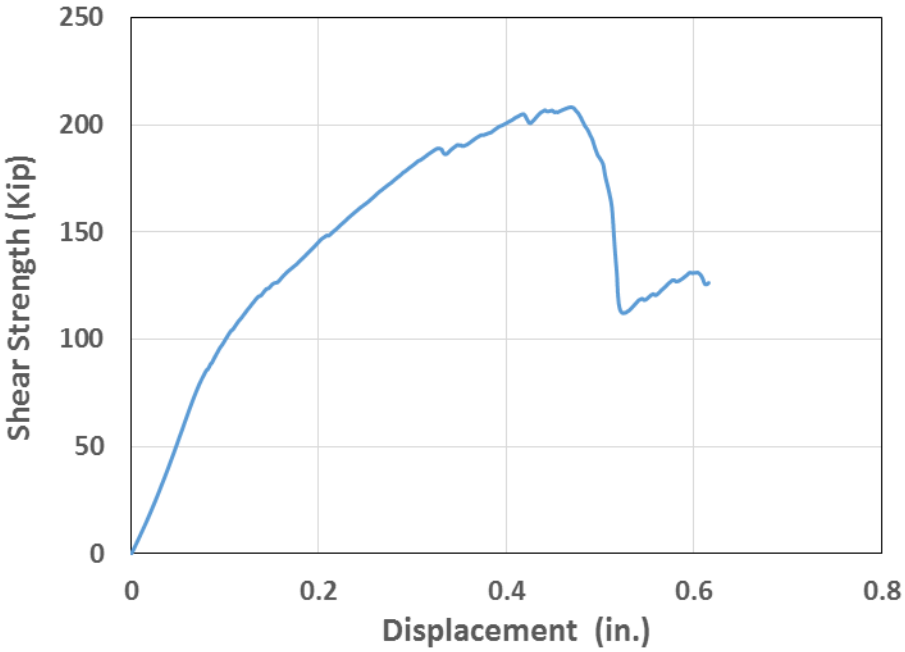

Figure 293 Load - deflection response of large-scale beam, P18

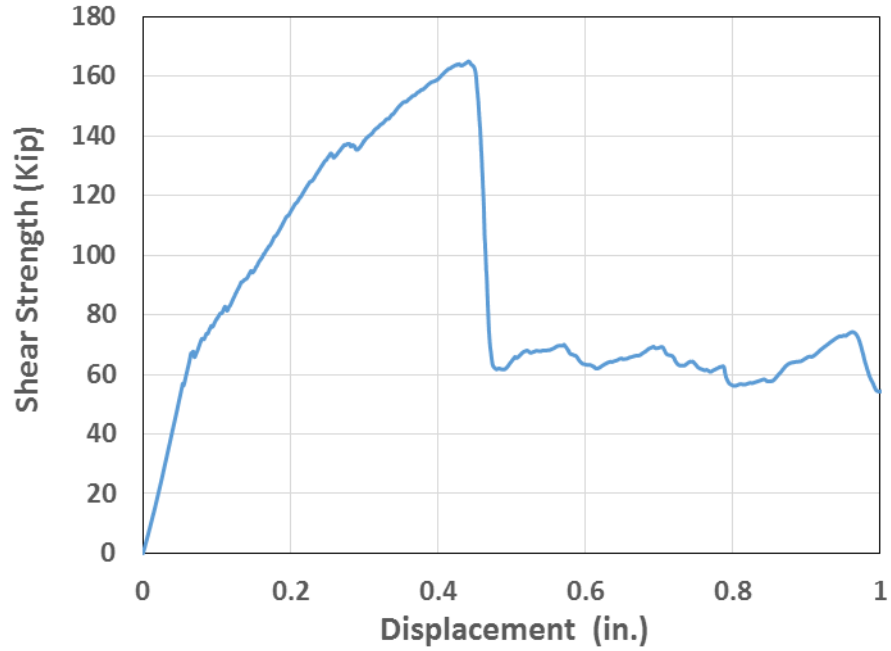

Figure 294 Load - deflection response of large-scale beam, P19

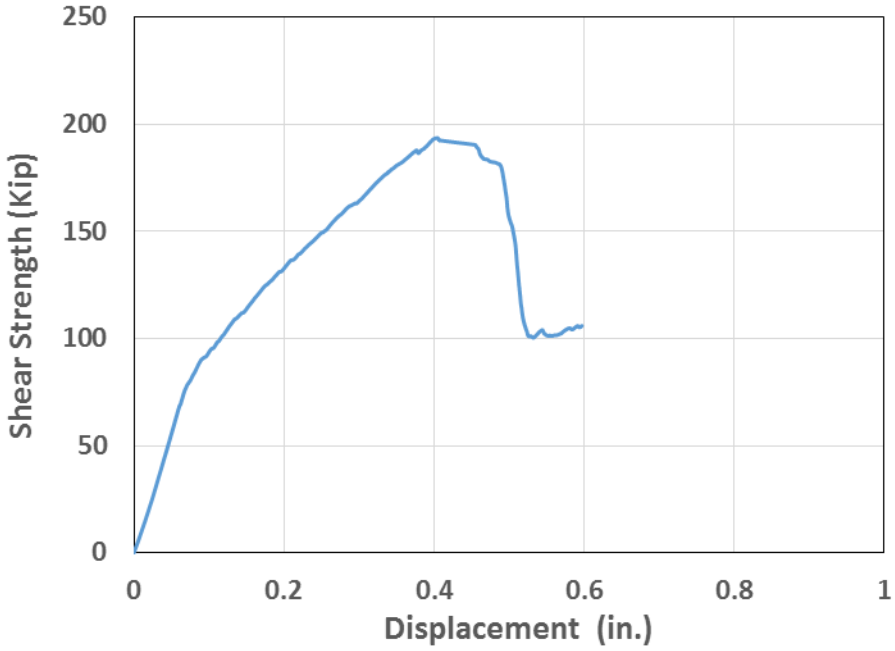

Figure 295 Load - deflection response of large-scale beam, P20

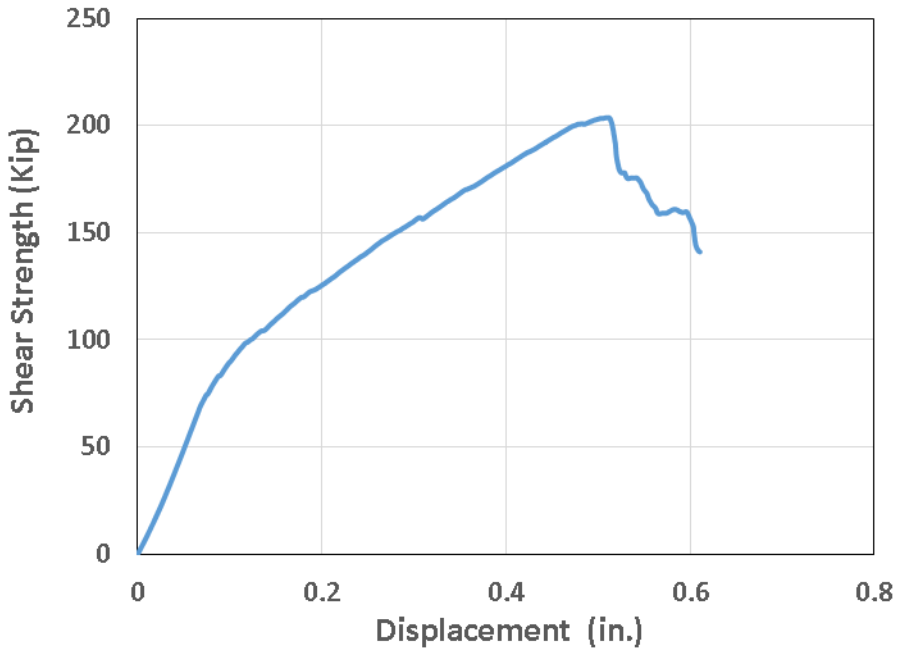

Figure 296 Load - deflection response of large-scale beam, P21

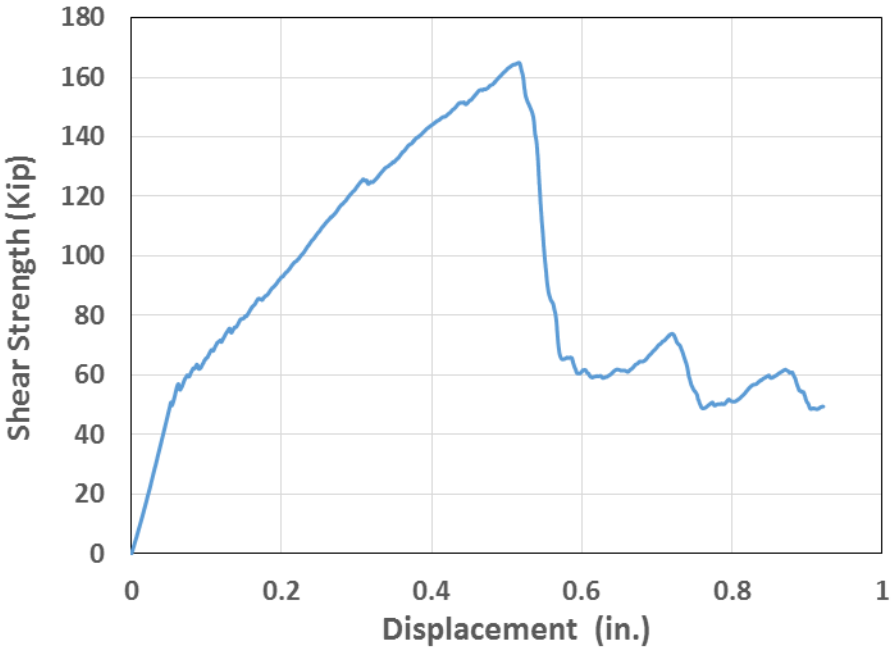

Figure 297 Load - deflection response of large-scale beam, P22

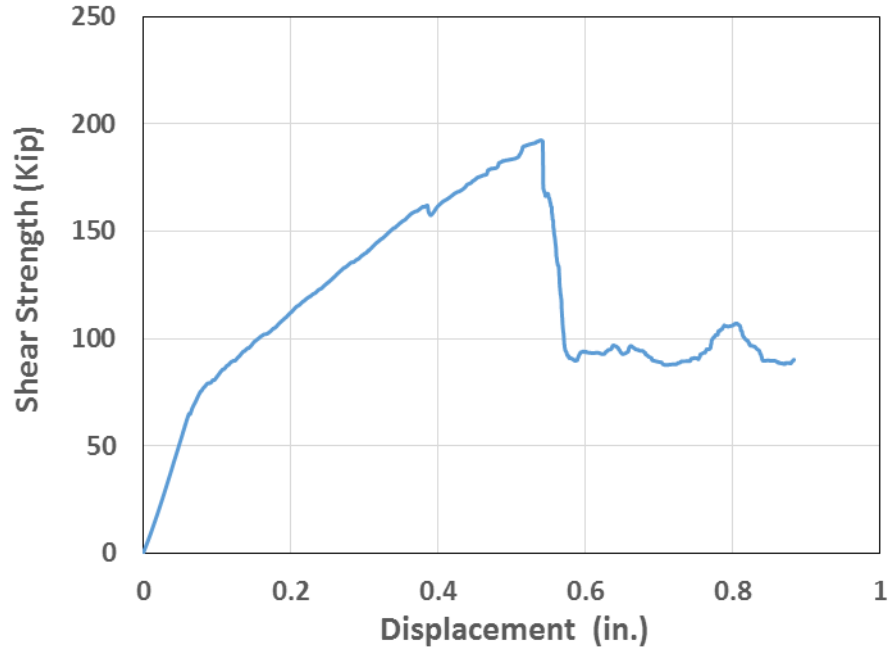

Figure 298 Load - deflection response of large-scale beam, P23

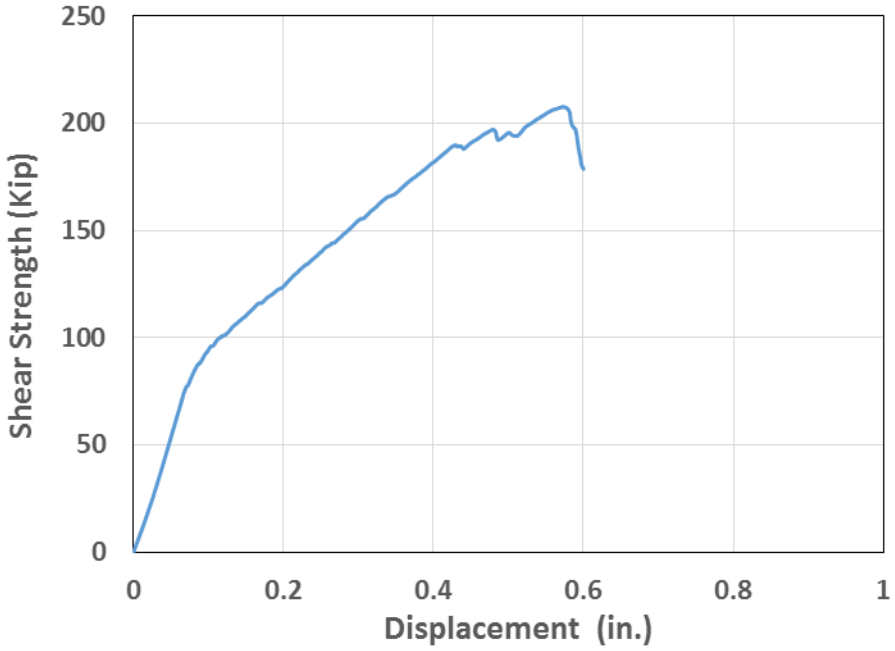

Figure 299 Load - deflection response of large-scale beam, P24

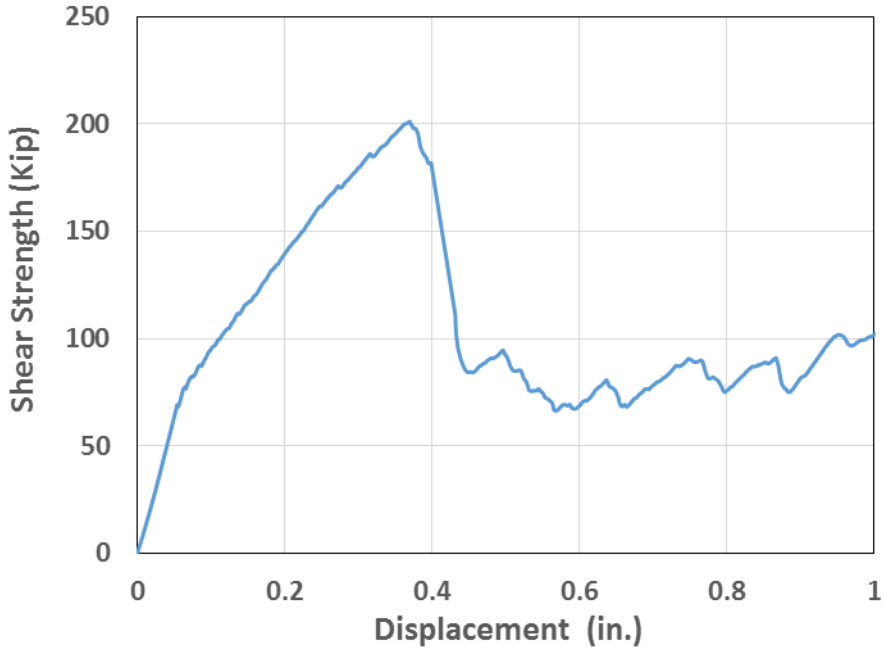

Figure 300 Load - deflection response of large-scale beam, P25

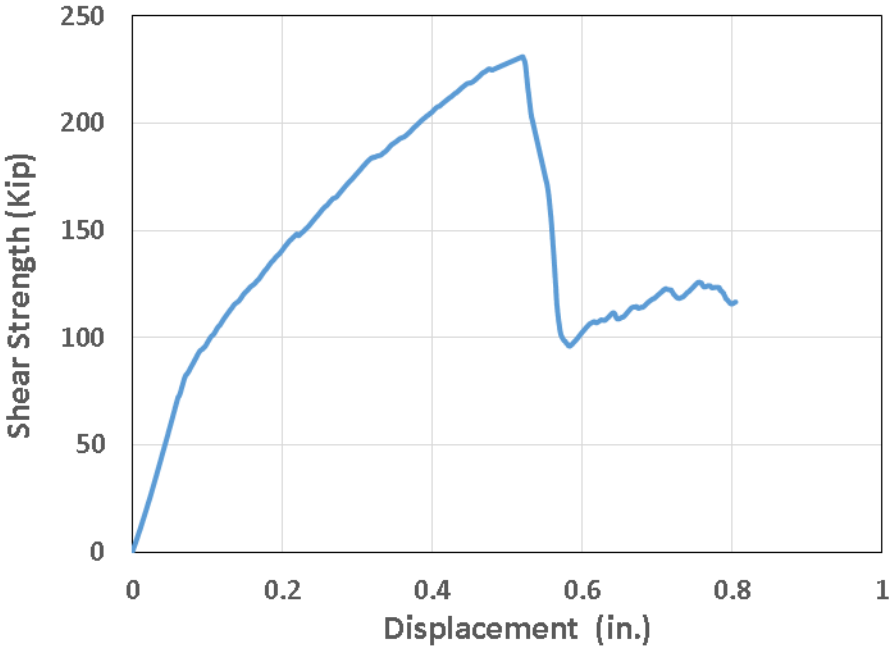

Figure 301 Load - deflection response of large-scale beam, P26

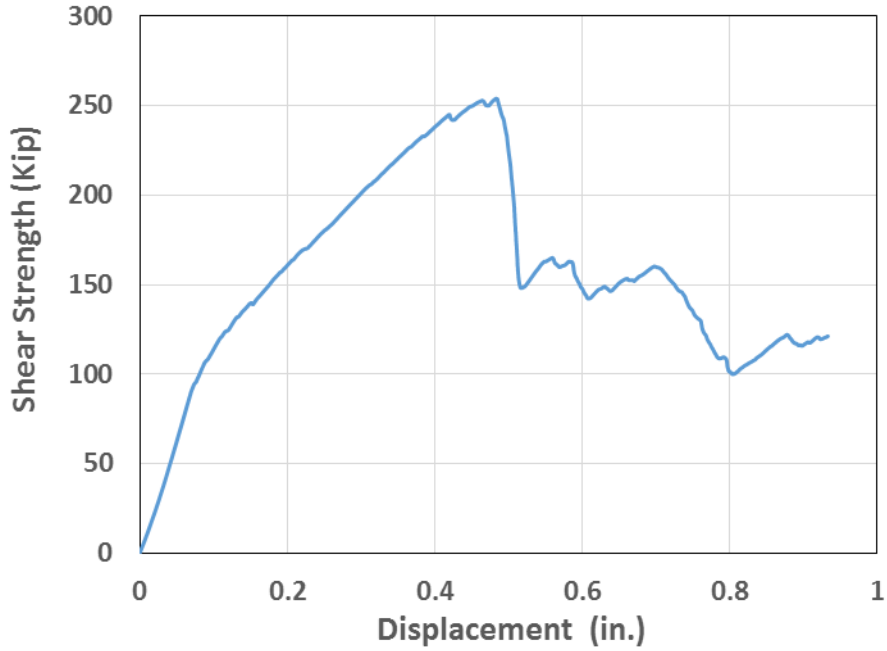

Figure 302 Load - deflection response of large-scale beam, P27

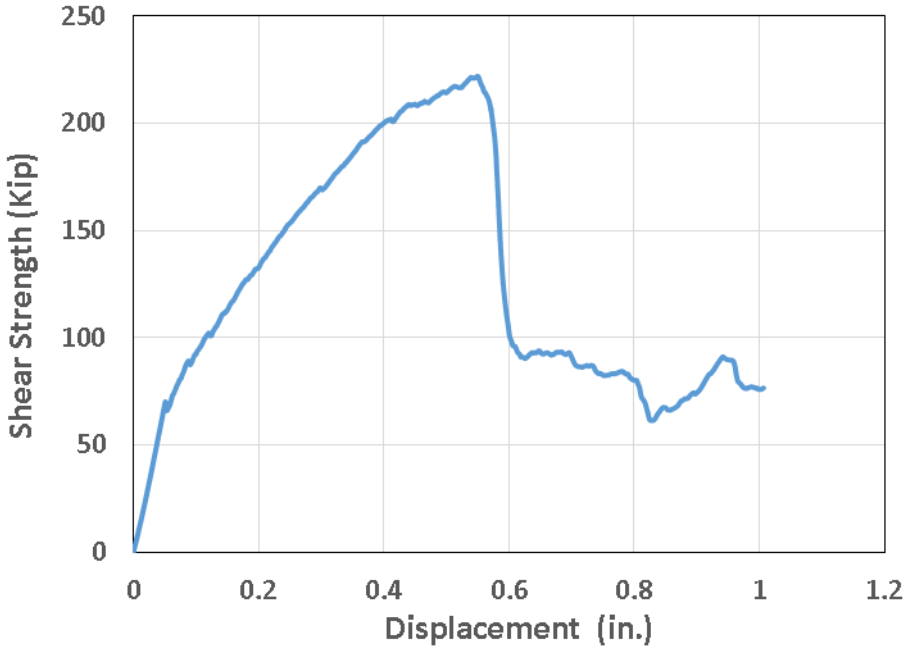

Figure 303 Load - deflection response of large-scale beam, P28

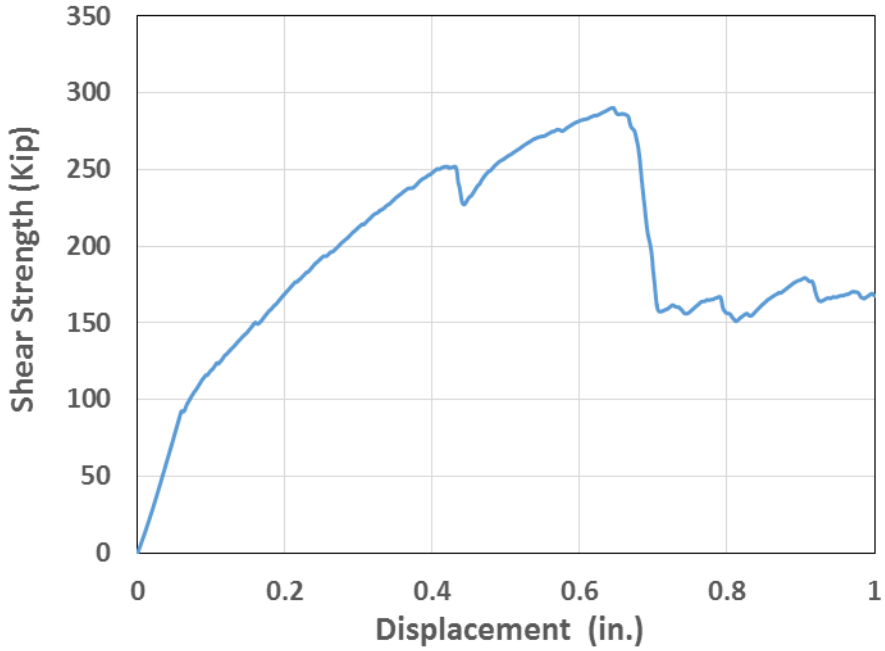

Figure 304 Load - deflection response of large-scale beam, P29

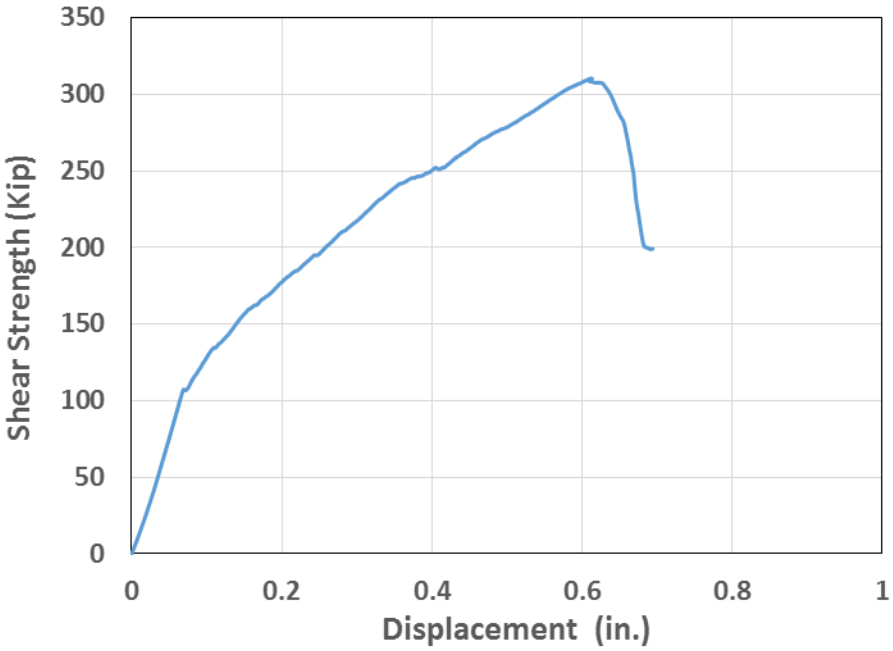

Figure 305 Load - deflection response of large-scale beam, P30

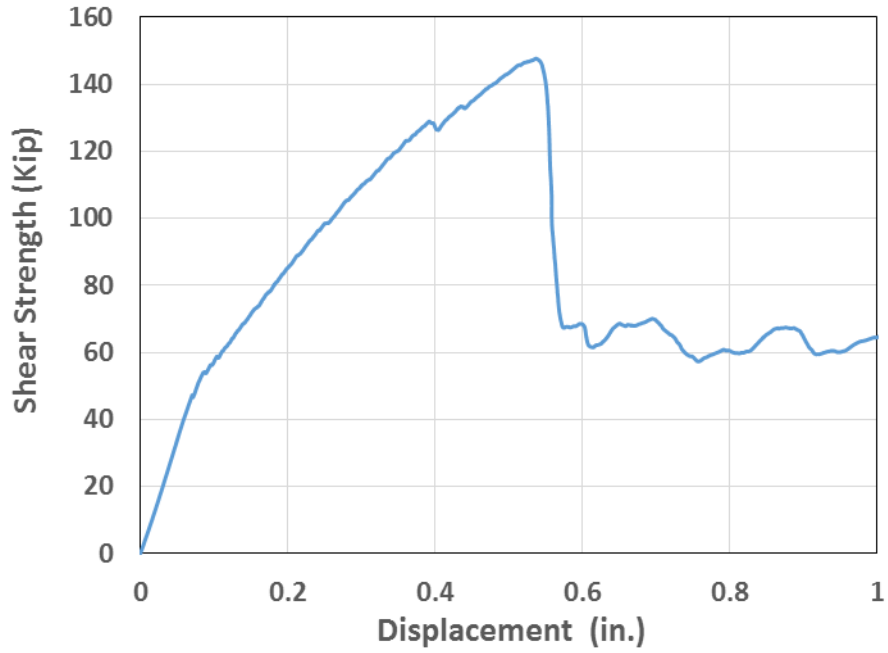

Figure 306 Load - deflection response of large-scale beam, P31

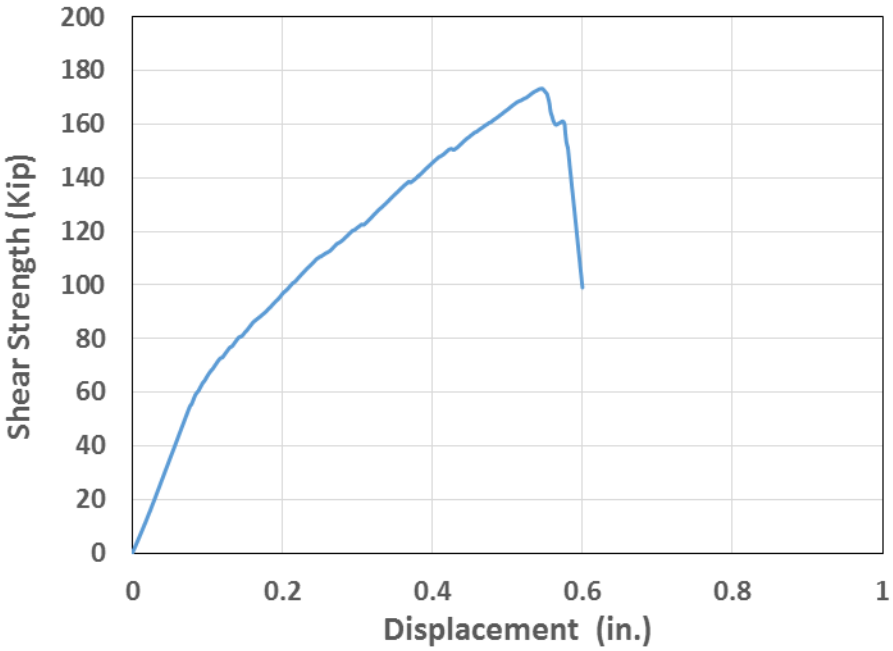

Figure 307 Load - deflection response of large-scale beam, P32

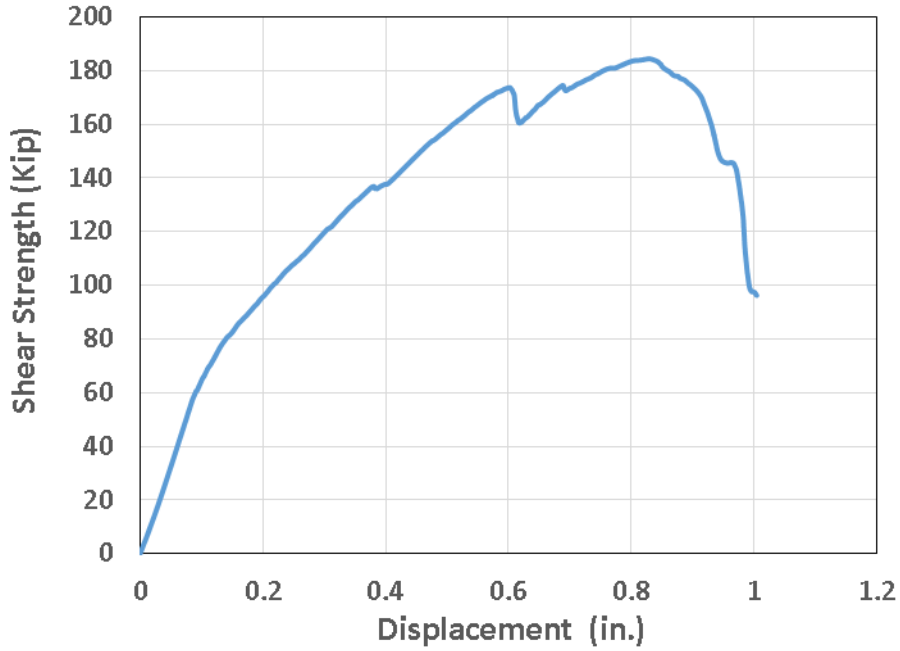

Figure 308 Load - deflection response of large-scale beam, P33

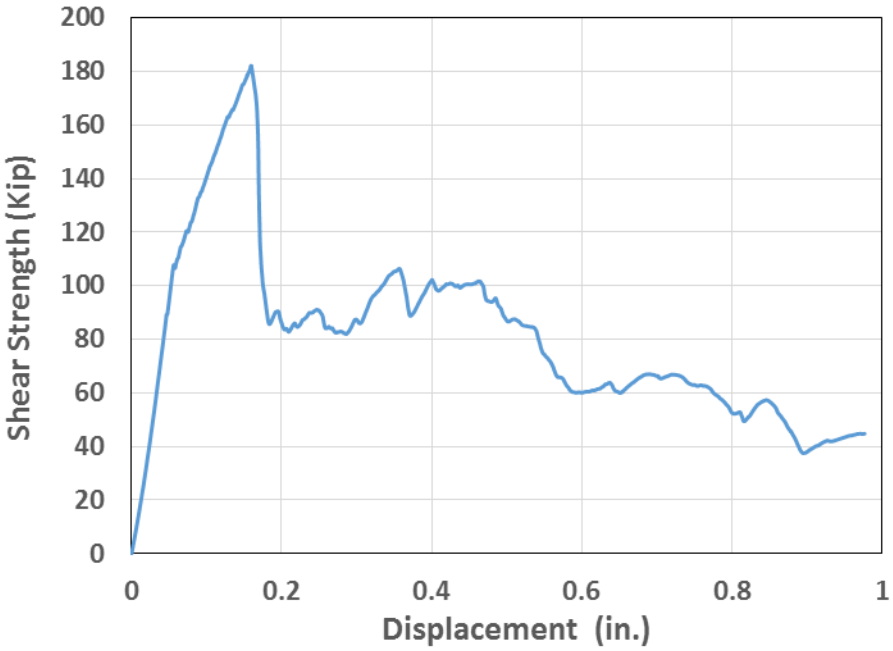

Figure 309 Load - deflection response of large-scale beam, P34

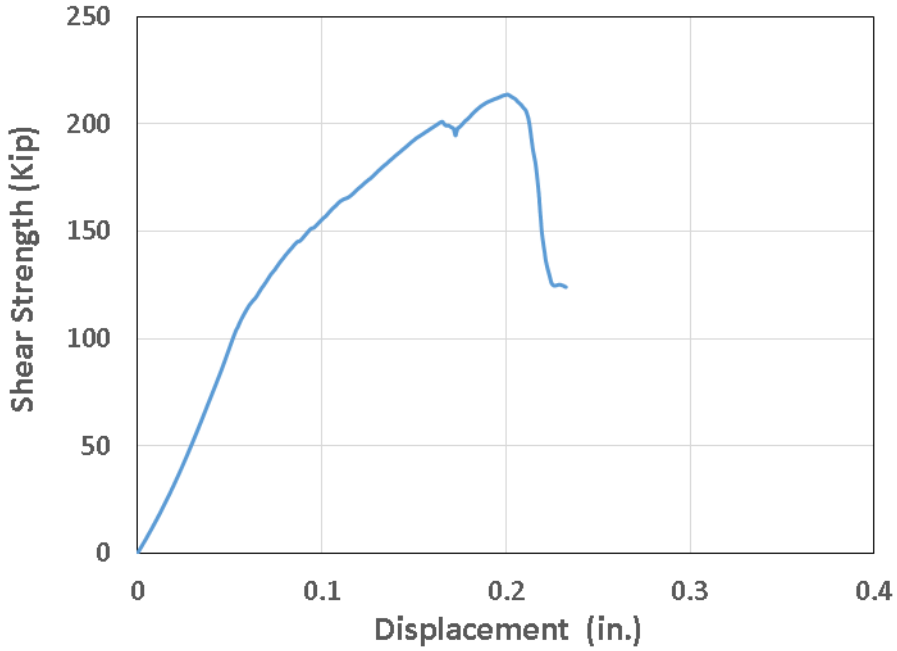

Figure 310 312 Load - deflection response of large-scale beam, P35

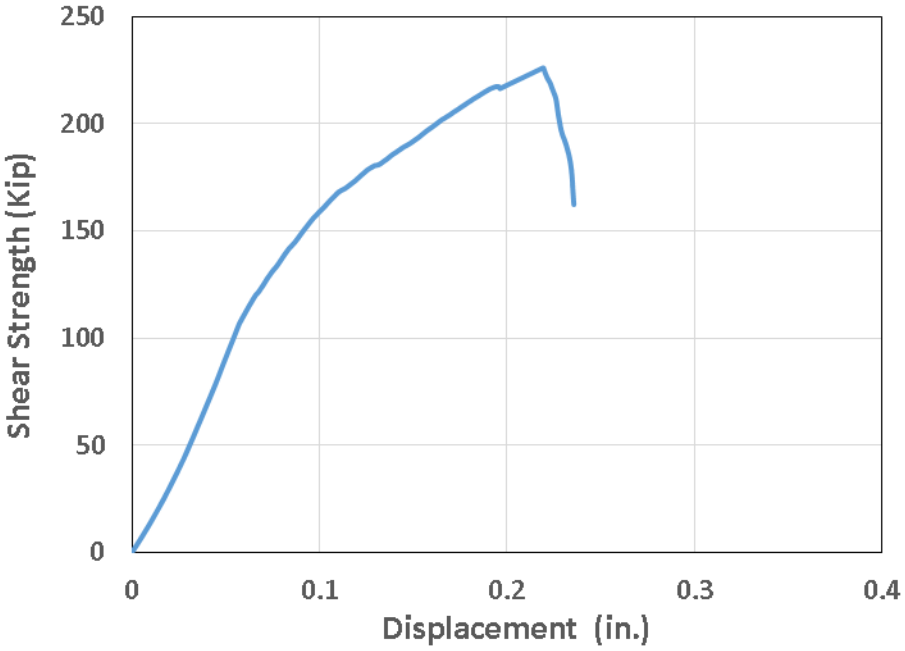

Figure 311 Load - deflection response of large-scale beam, P36

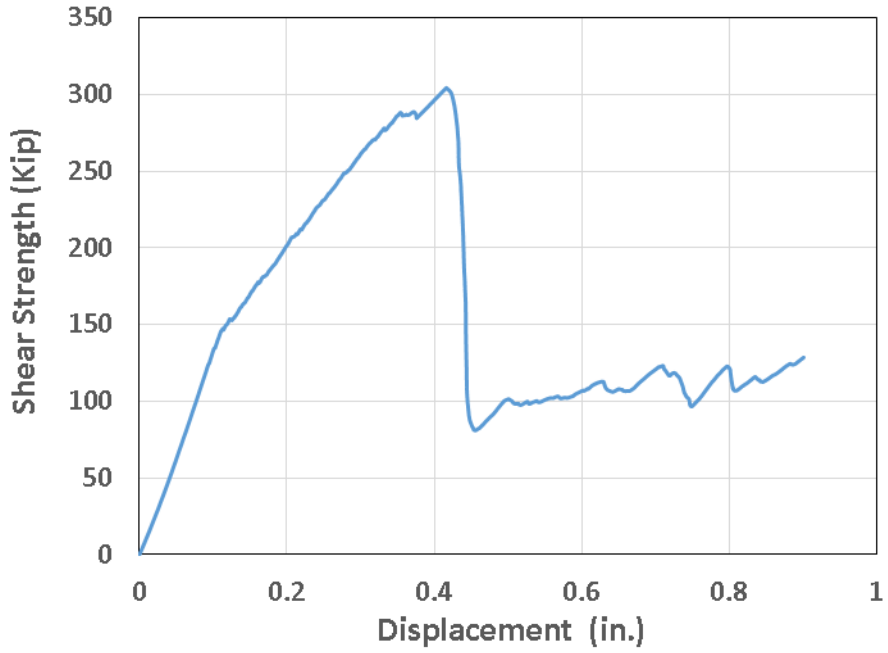

Figure 312 Load - deflection response of large-scale beam, P37

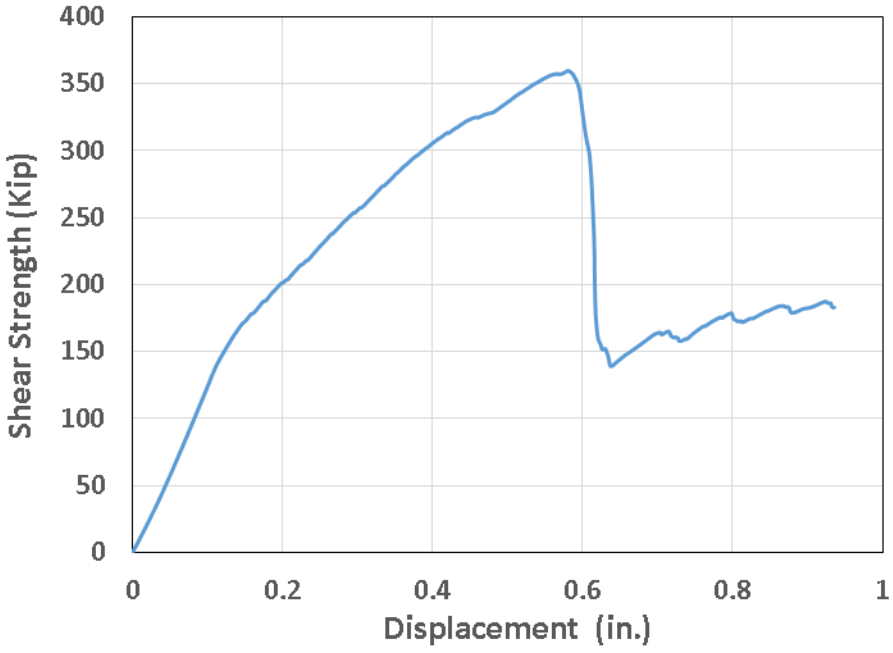

Figure 313 Load - deflection response of large-scale beam, P38

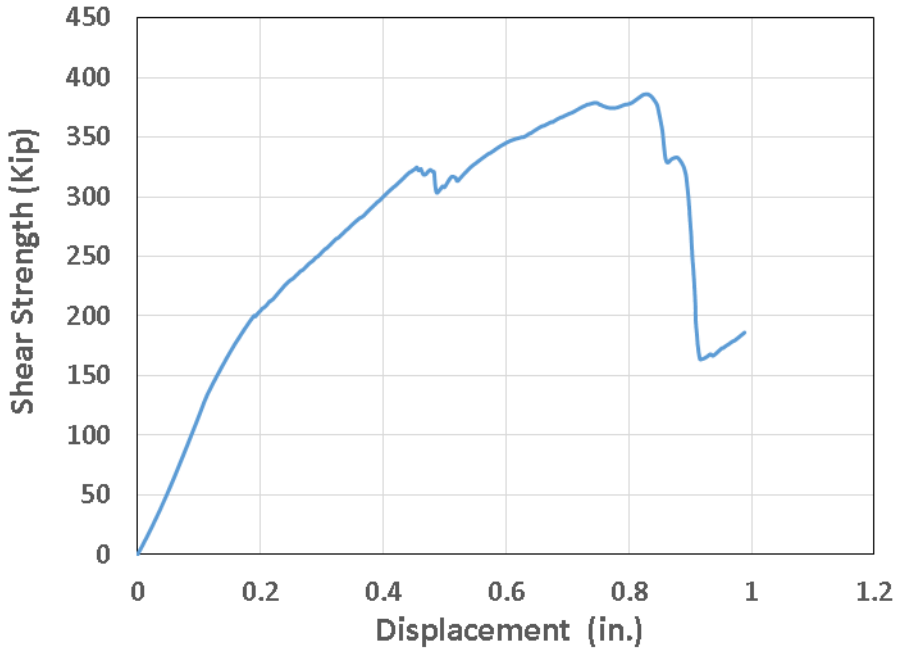

Figure 314 Load - deflection response of large-scale beam, P39

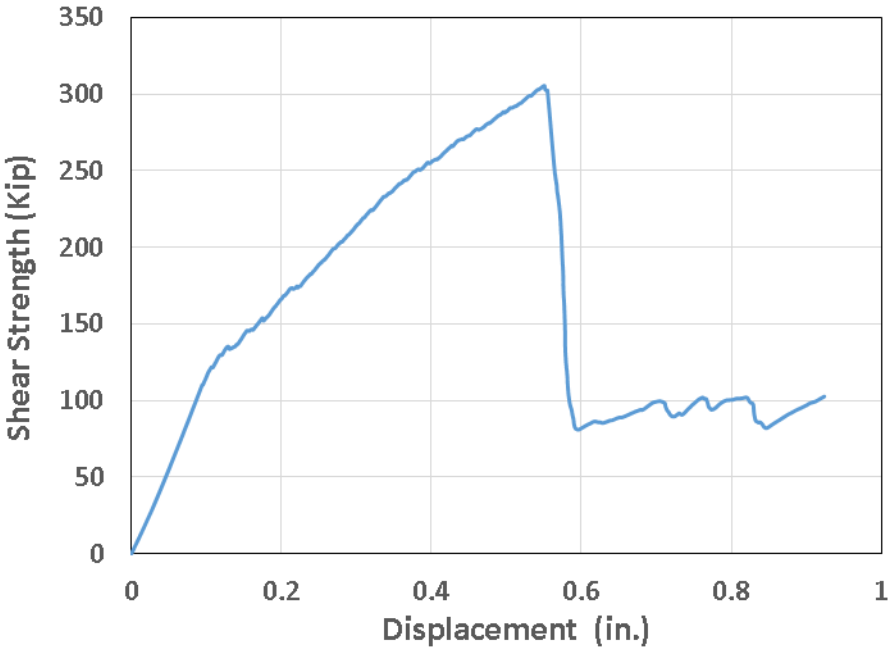

Figure 315 Load - deflection response of large-scale beam, P40

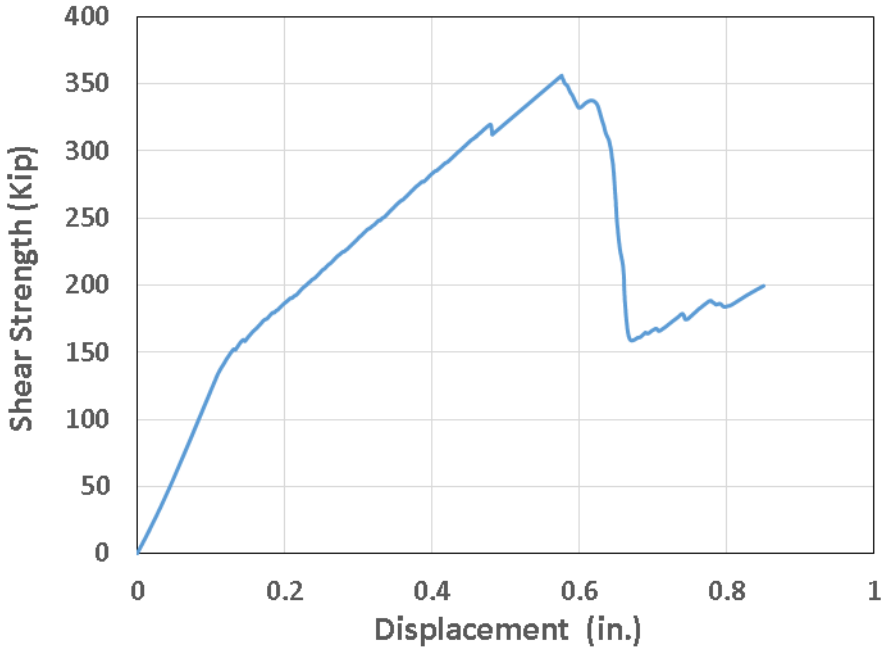

Figure 316 Load - deflection response of large-scale beam, P41

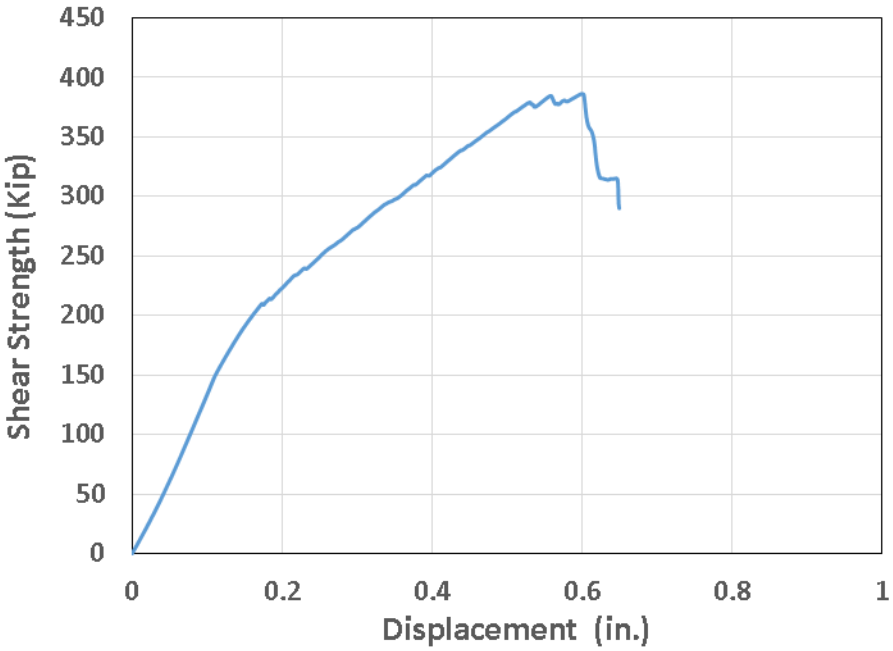

Figure 317 Load - deflection response of large-scale beam, P42

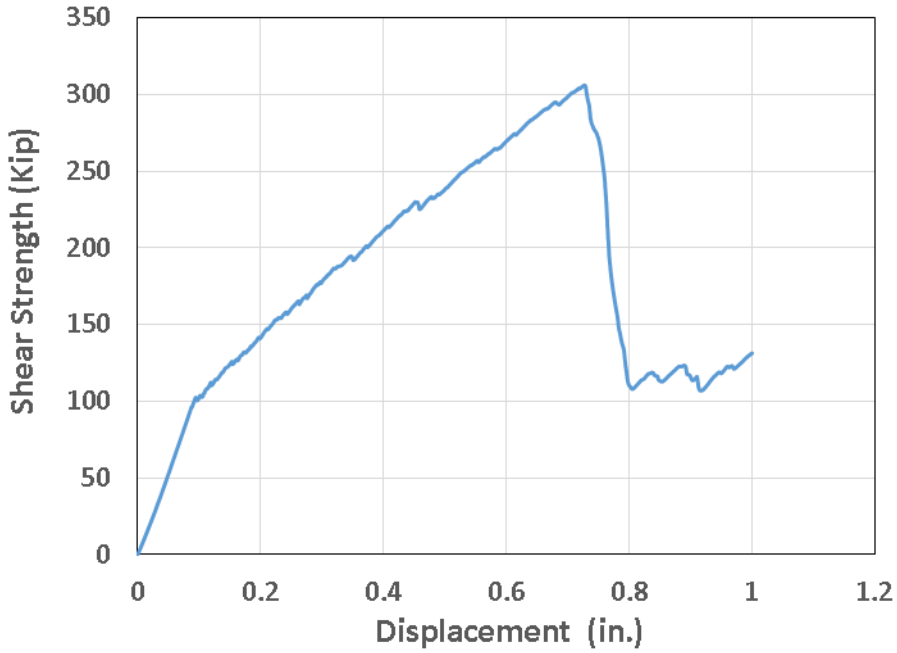

Figure 318 Load - deflection response of large-scale beam, P43

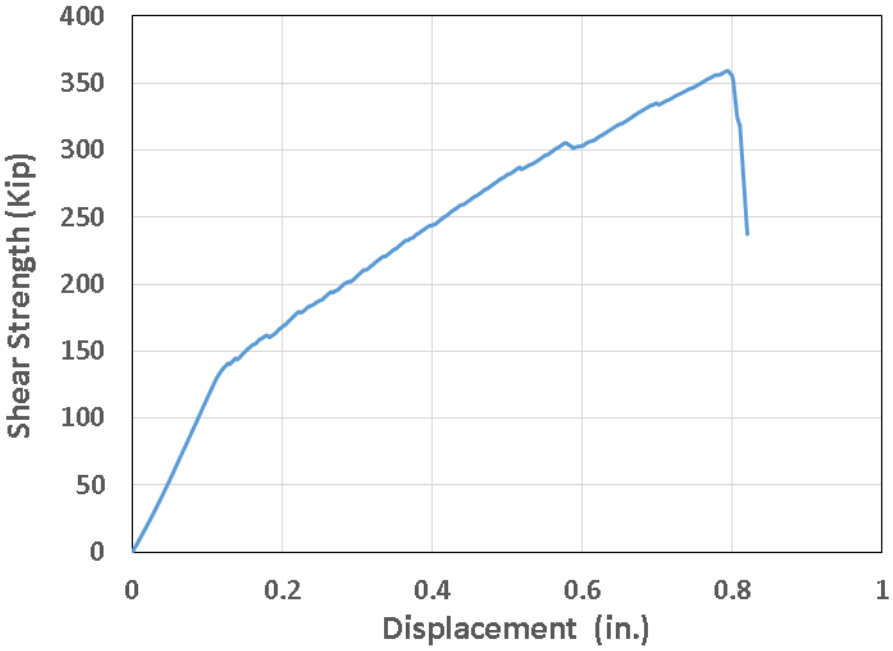

Figure 319 Load - deflection response of large-scale beam, P44

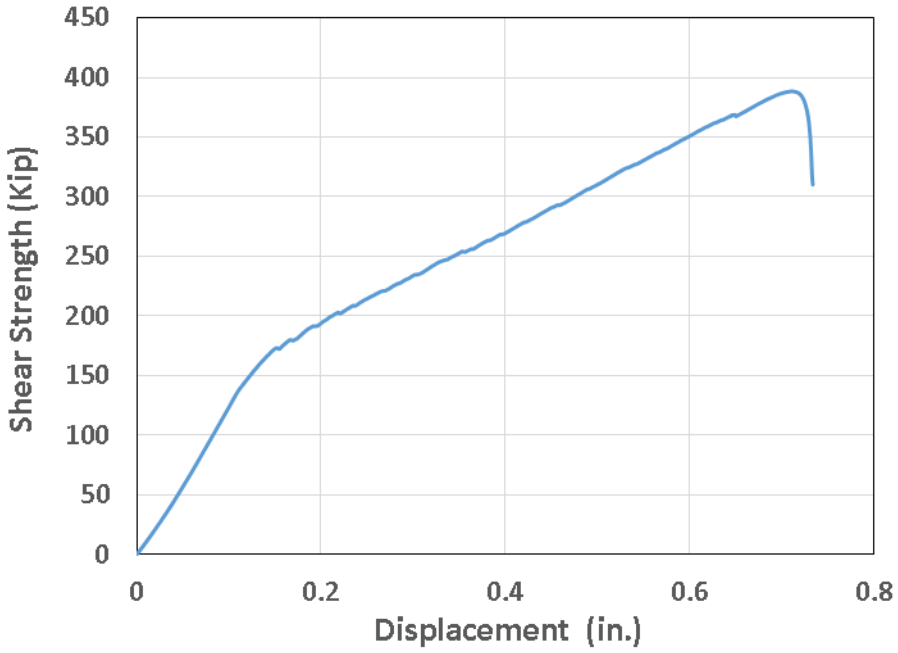

Figure 320 Load - deflection response of large-scale beam, P45

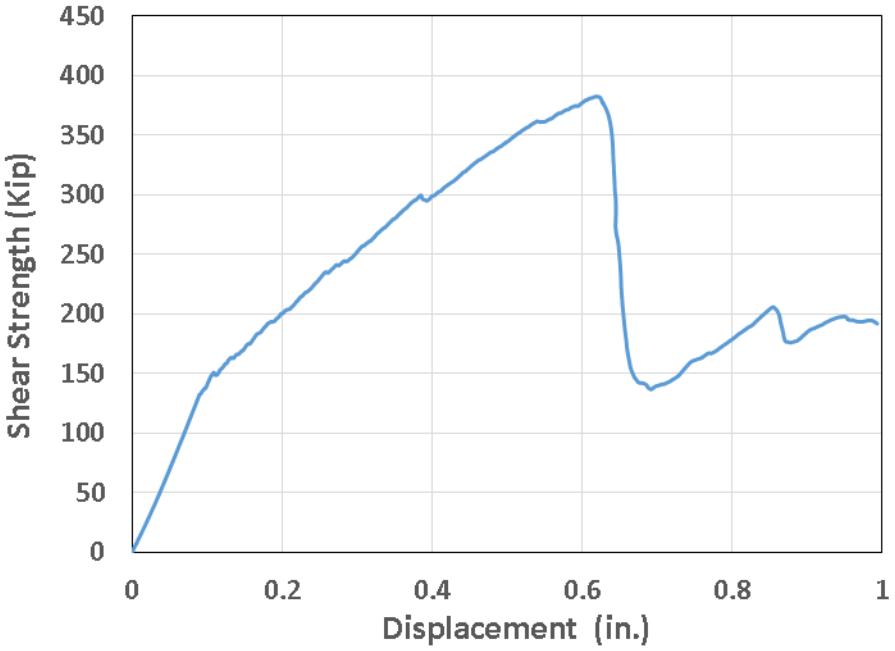

Figure 321 Load - deflection response of large-scale beam, P46

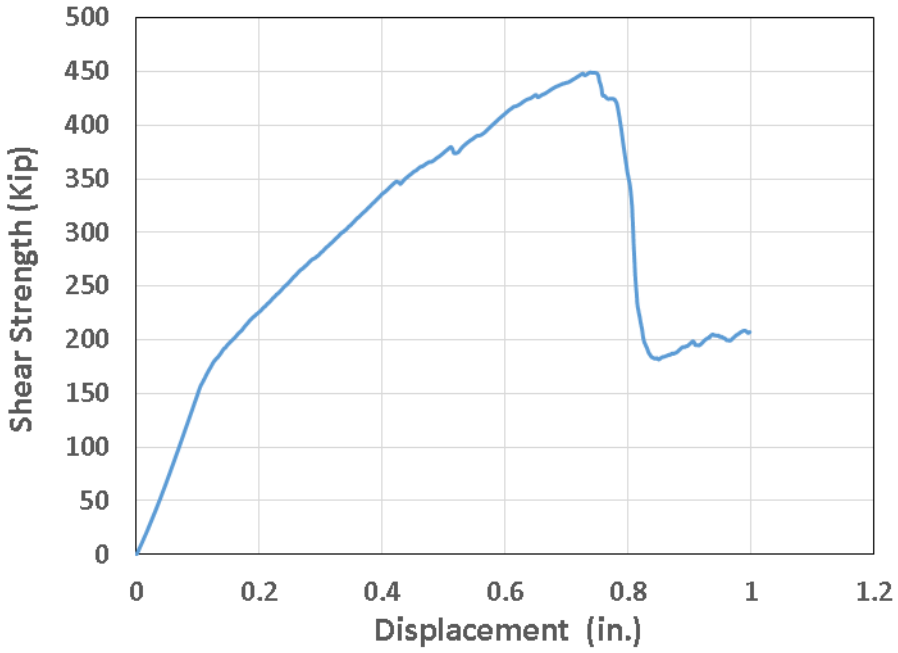

Figure 322 Load - deflection response of large-scale beam, P47

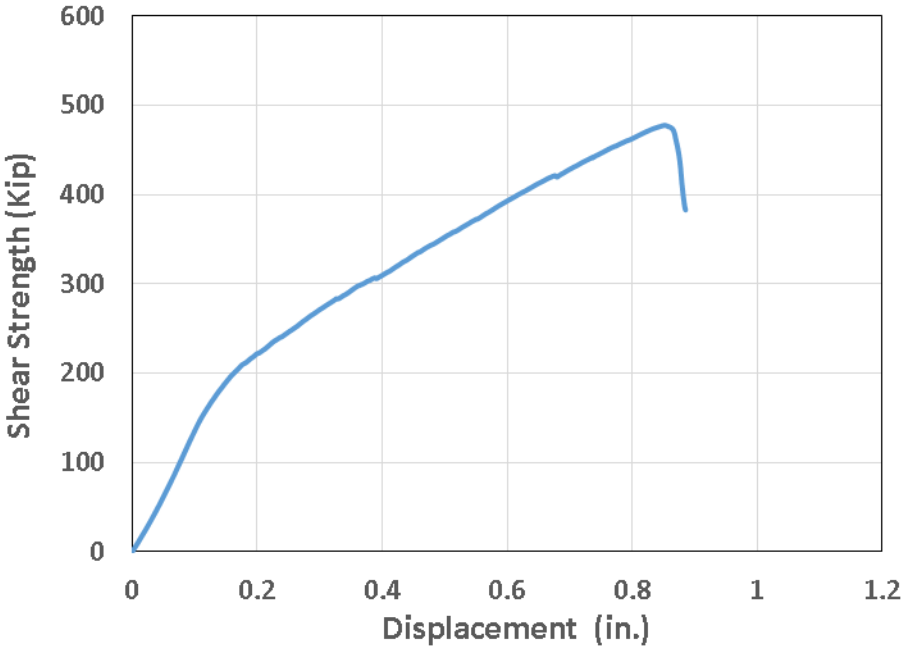

Figure 323 Load - deflection response of large-scale beam, P48

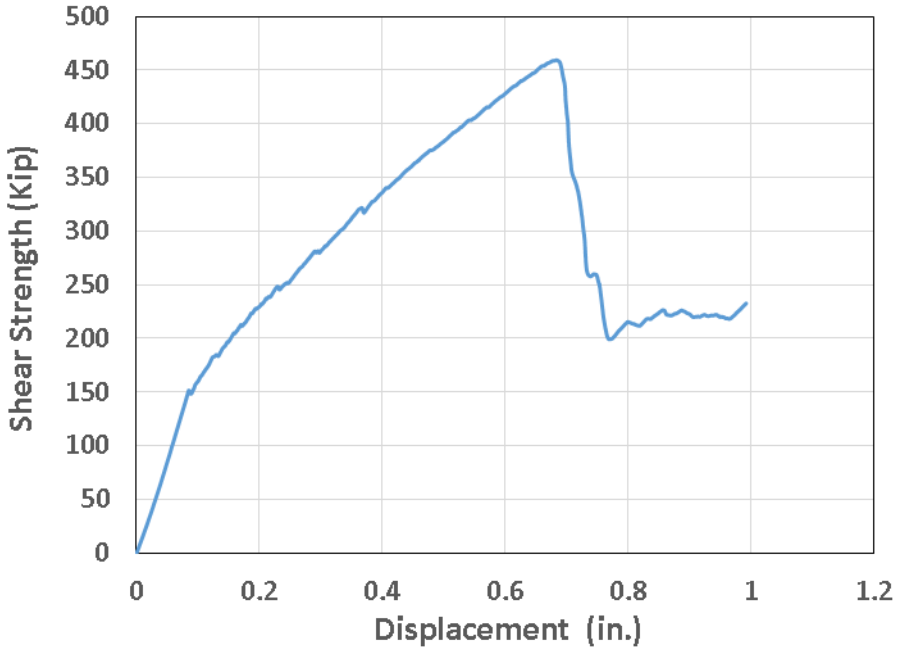

Figure 324 Load - deflection response of large-scale beam, P49

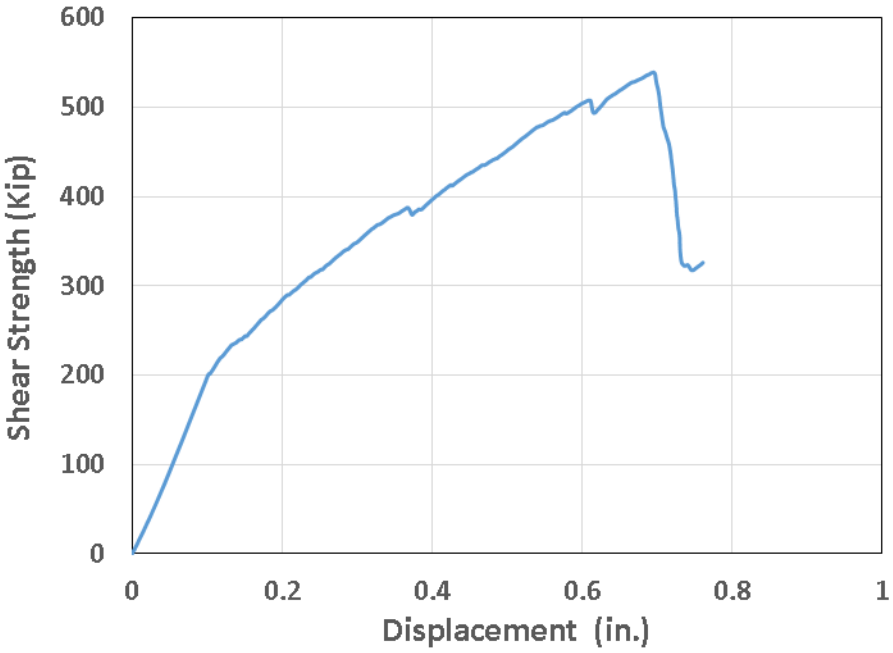

Figure 325 Load - deflection response of large-scale beam, P50

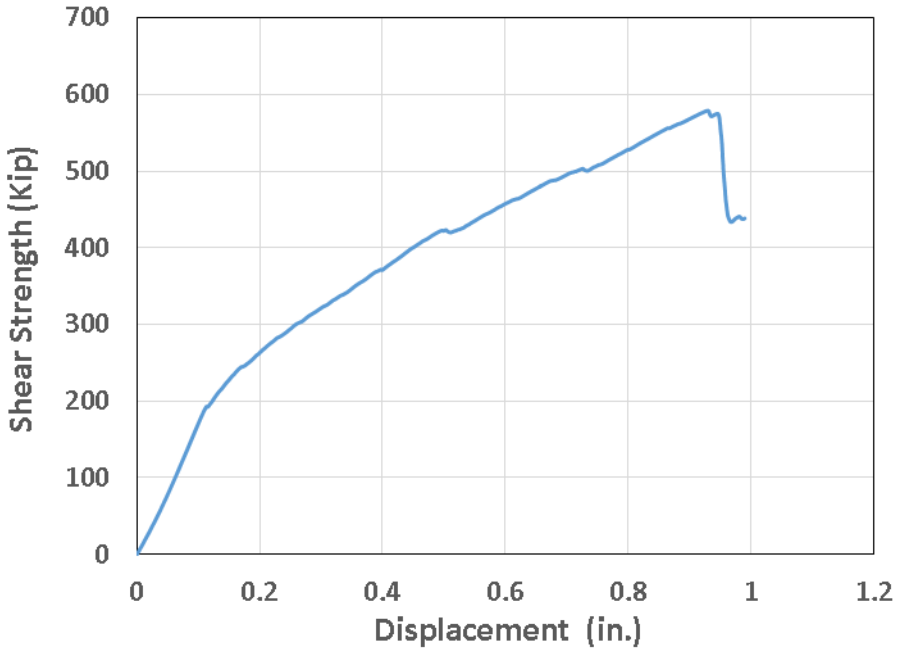

Figure 326 Load - deflection response of large-scale beam, P51

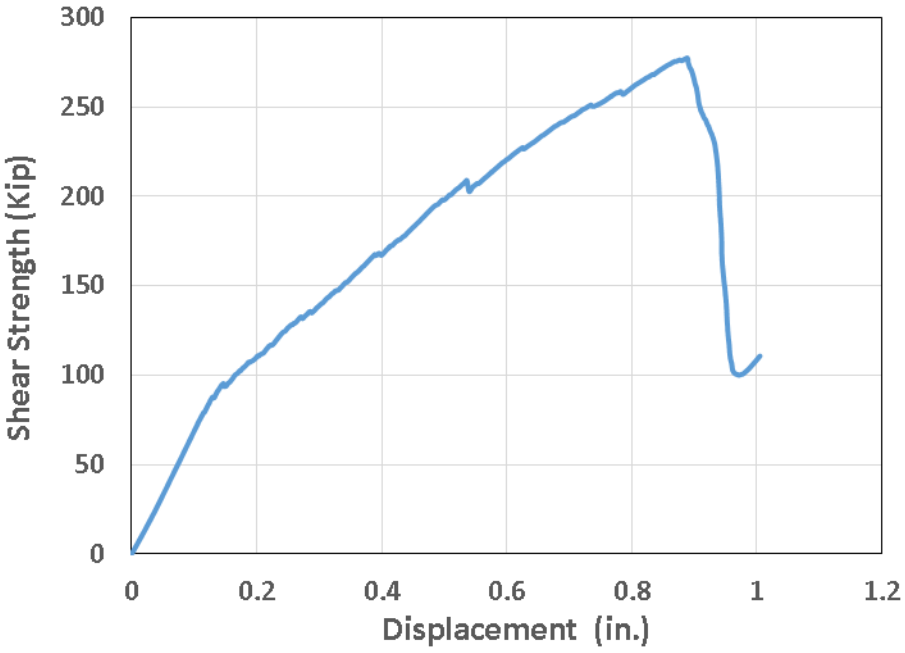

Figure 327 Load - deflection response of large-scale beam, P52

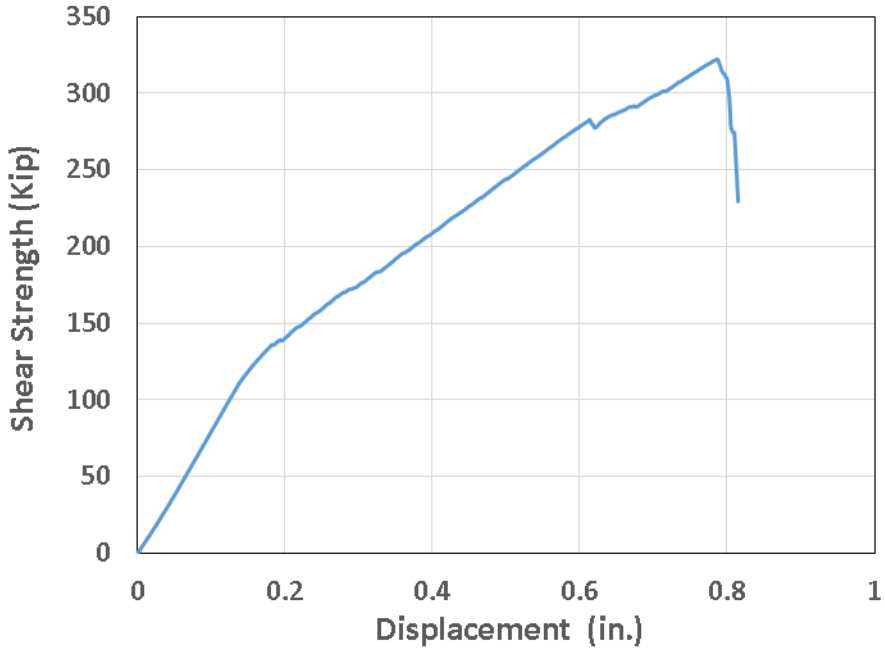

Figure 328 Load - deflection response of large-scale beam, P53

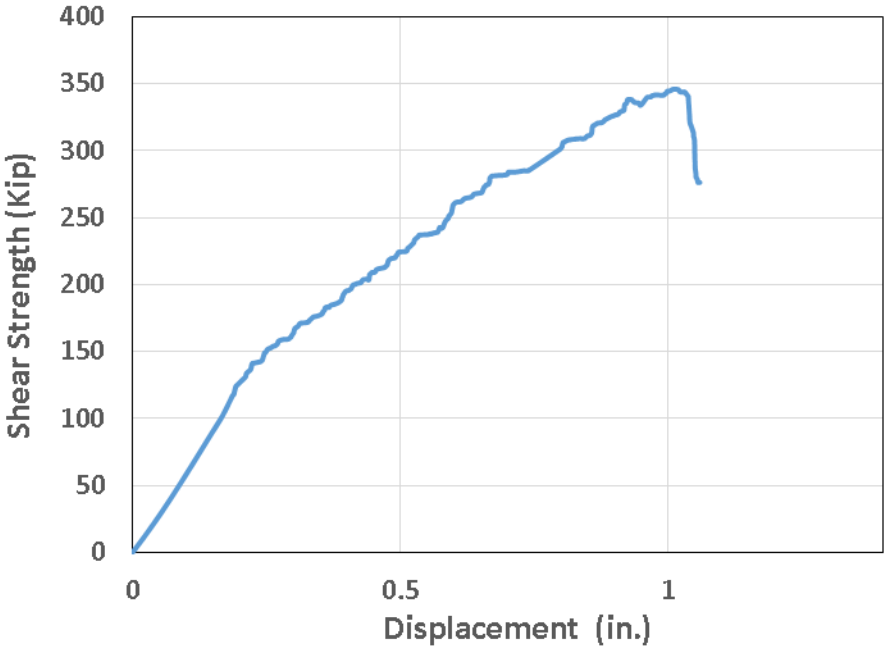

Figure 329 Load - deflection response of large-scale beam, P54

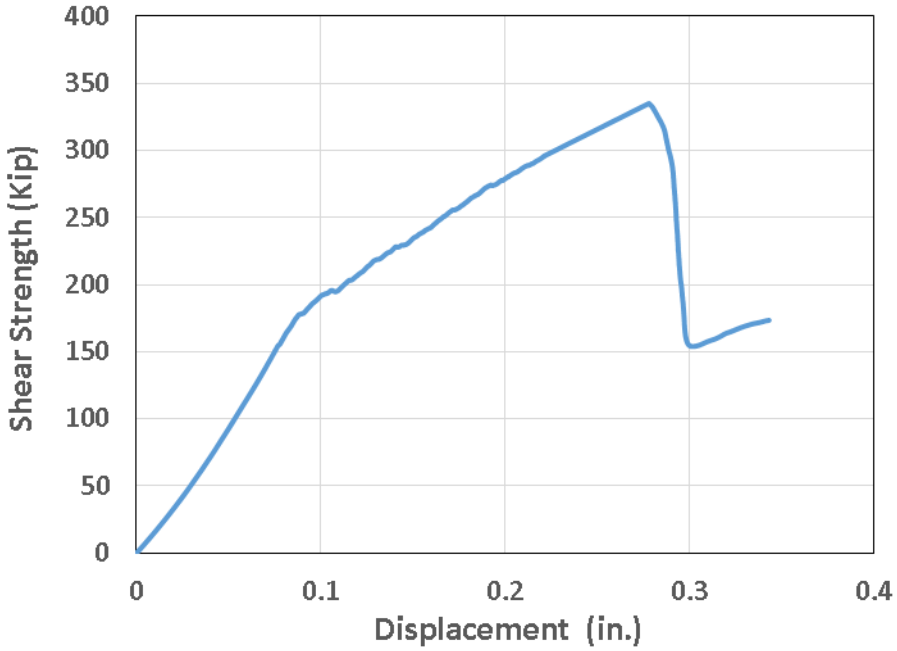

Figure 330 Load - deflection response of large-scale beam, P55

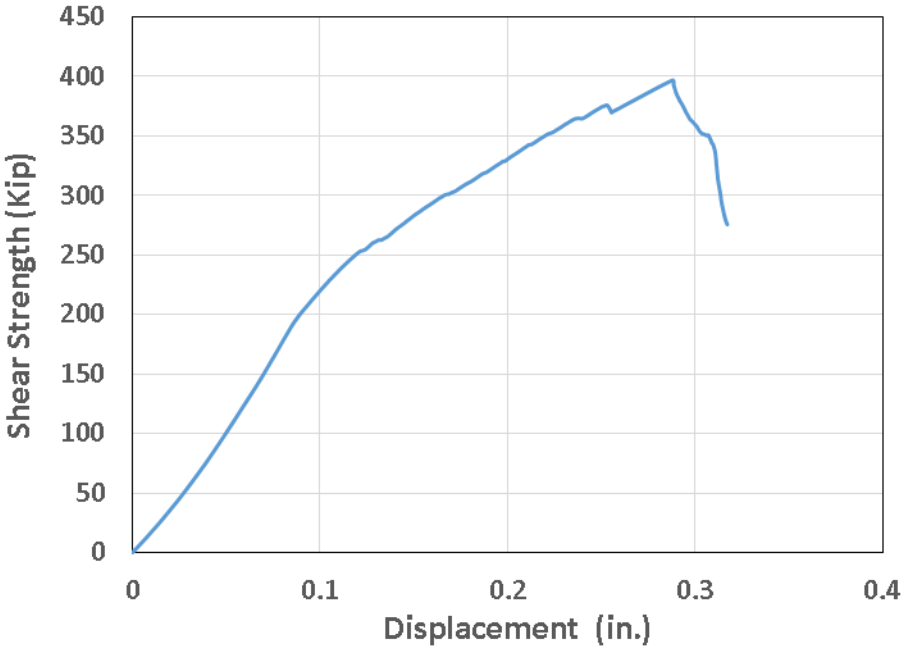

Figure 331 Load - deflection response of large-scale beam, P56

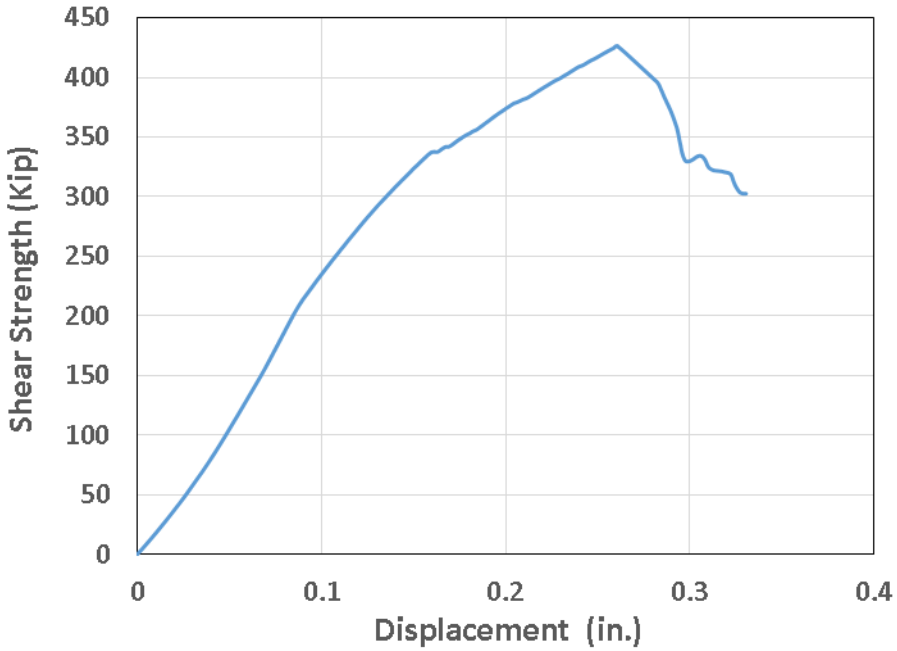

Figure 332 Load - deflection response of large-scale beam, P57

Appendix H

Steel Strain Gages

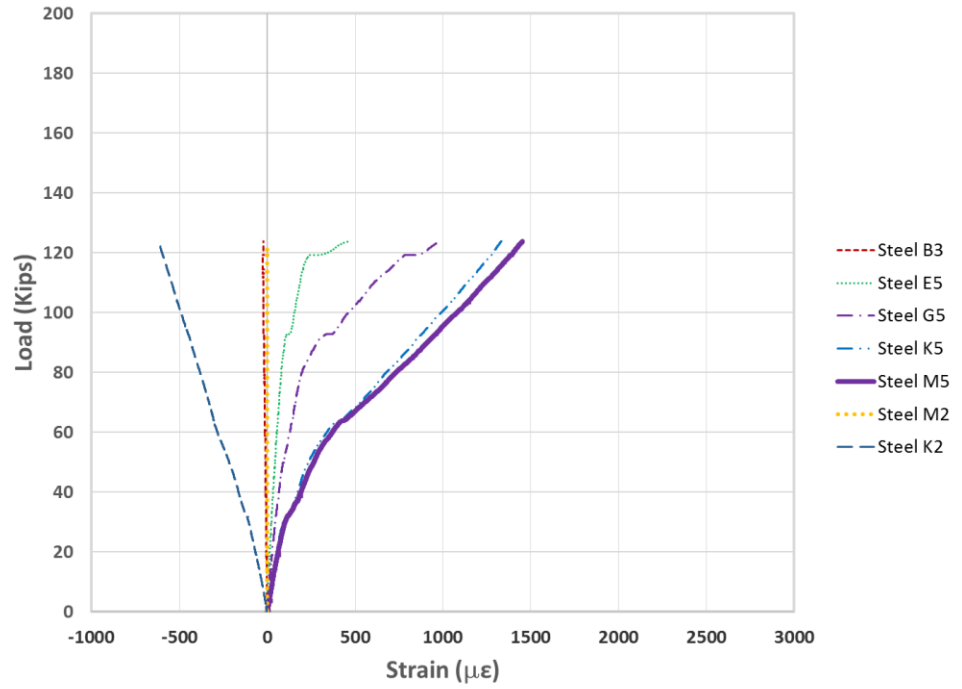

Figure 333 Load-strain response for RC control beam #1 without aging (Phase 1)

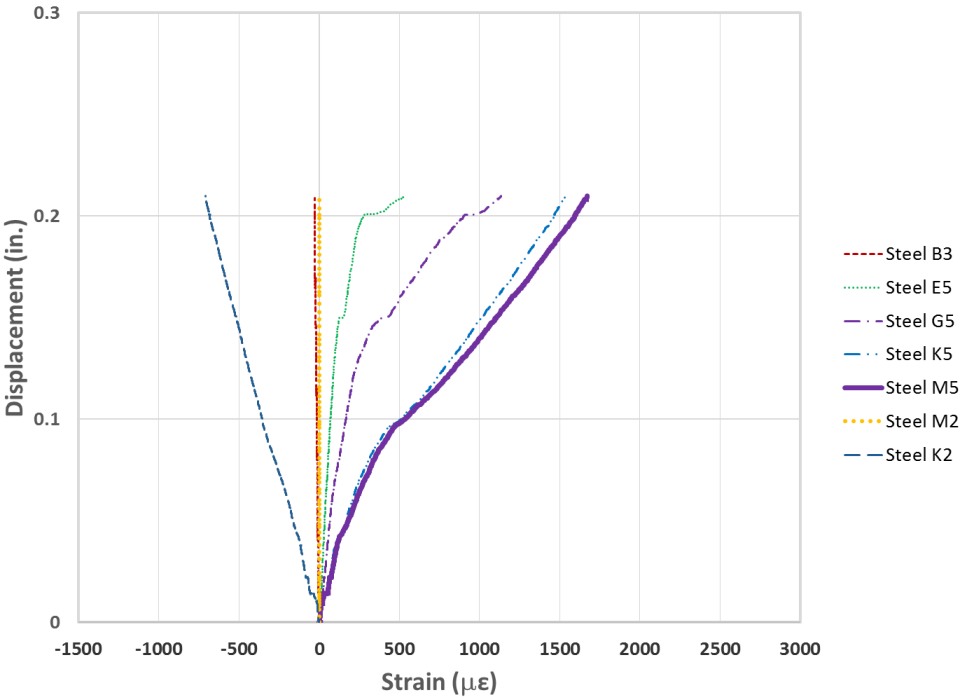

Figure 334 Displacement-strain response for RC control beam #1 without aging (Phase 1)

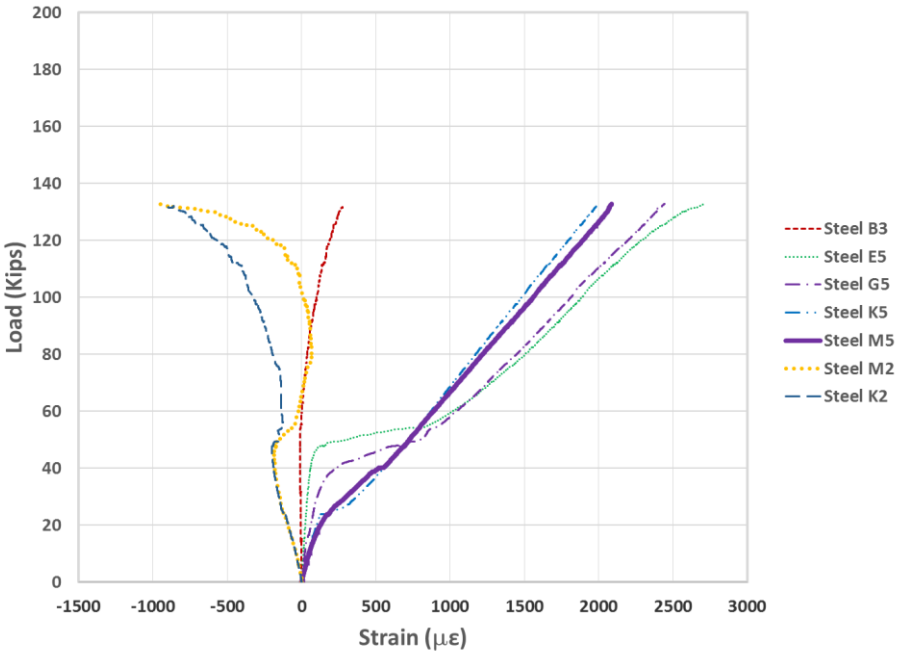

Figure 335 Load-strain response for RC control beam #2 without aging (Phase 1)

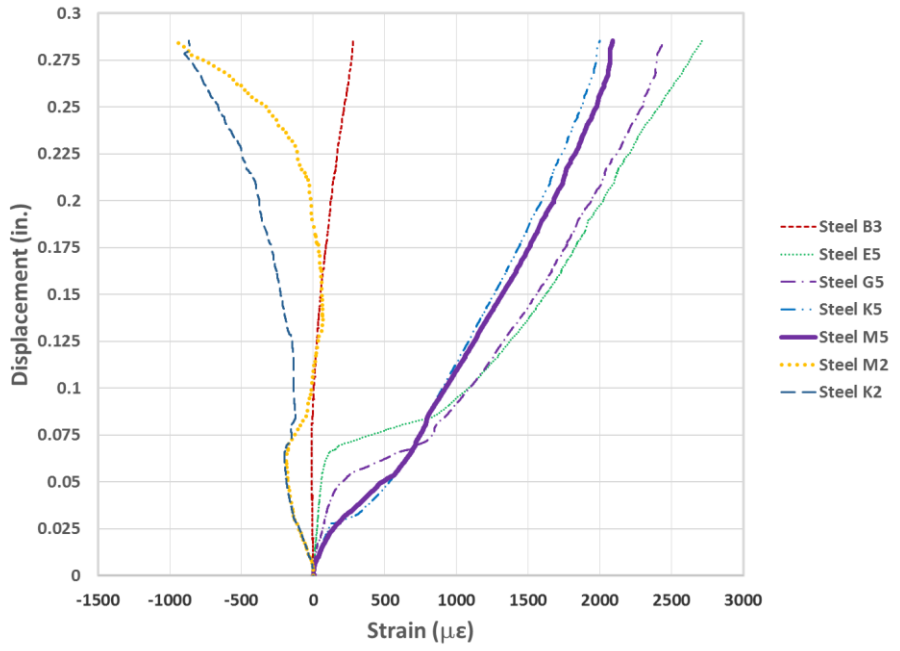

Figure 336 Displacement-strain response for RC control beam #2 without aging (Phase 1)

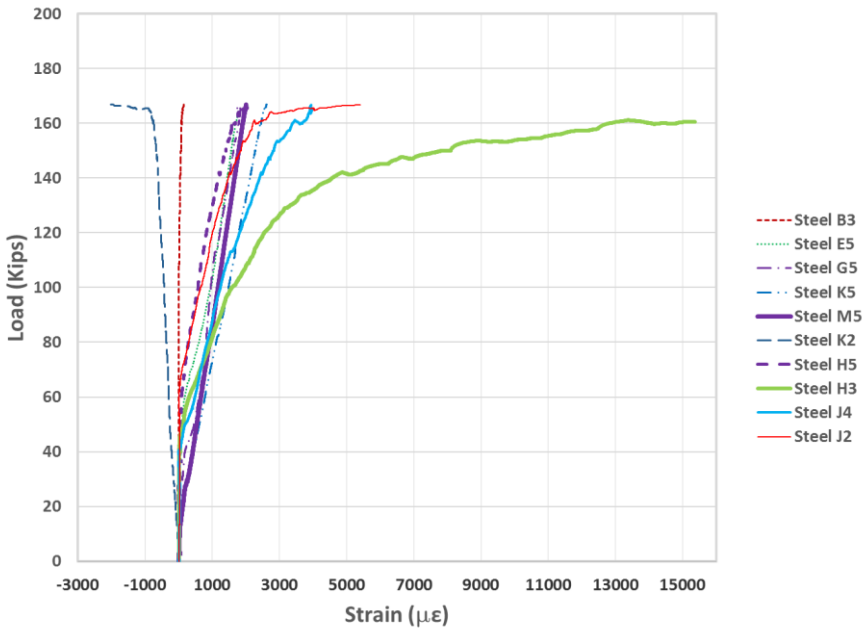

Figure 337 Load-strain response for RCS beam #3 without aging (Phase 1)

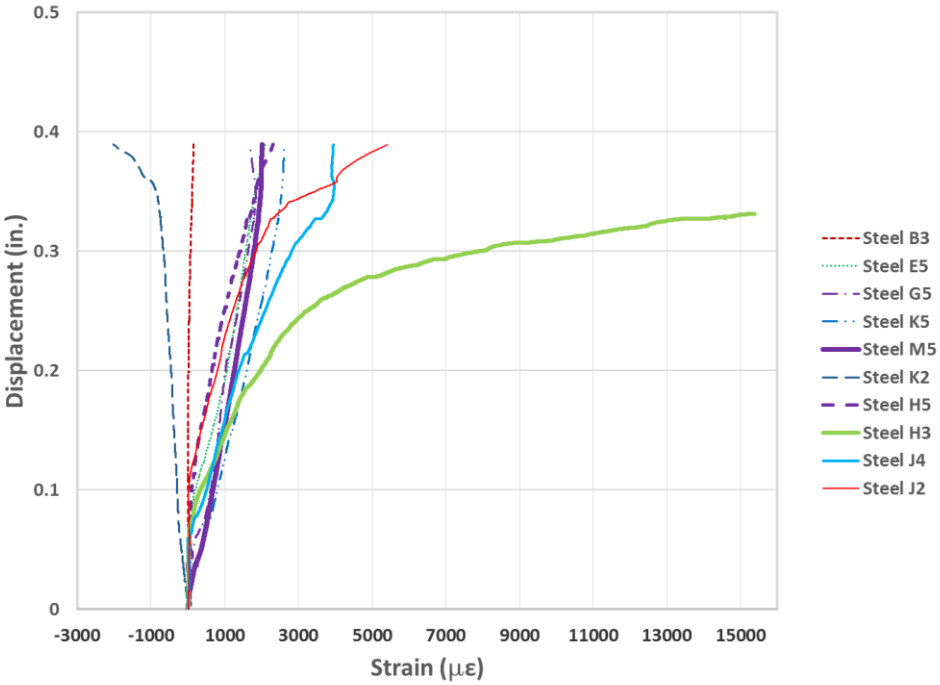

Figure 338 Displacement-strain response for RCS beam #3 without aging (Phase 1)

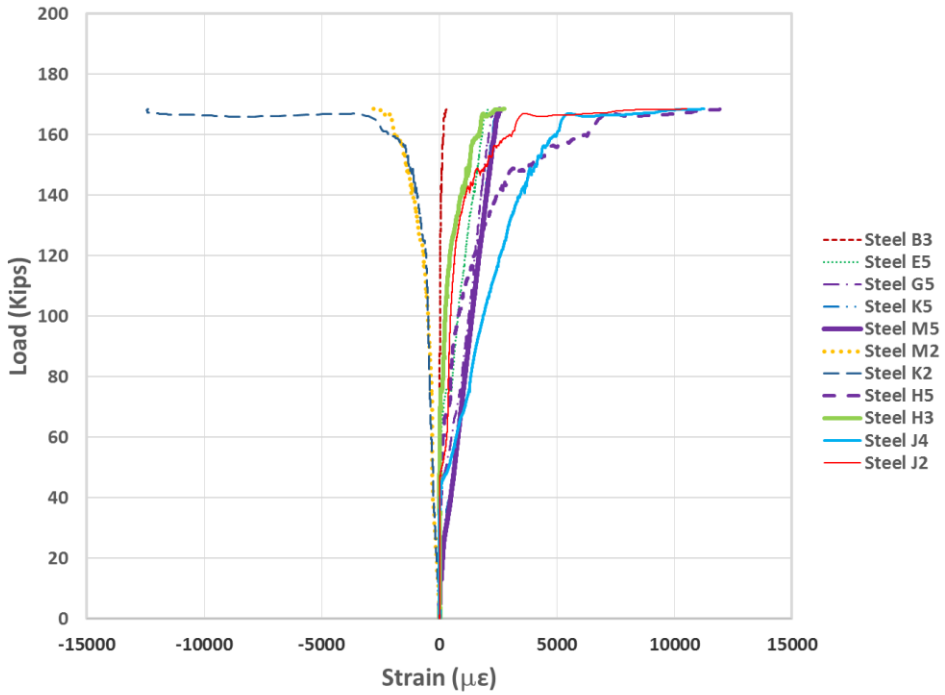

Figure 339 Load-strain response for RCS beam #4 without aging (Phase 1)

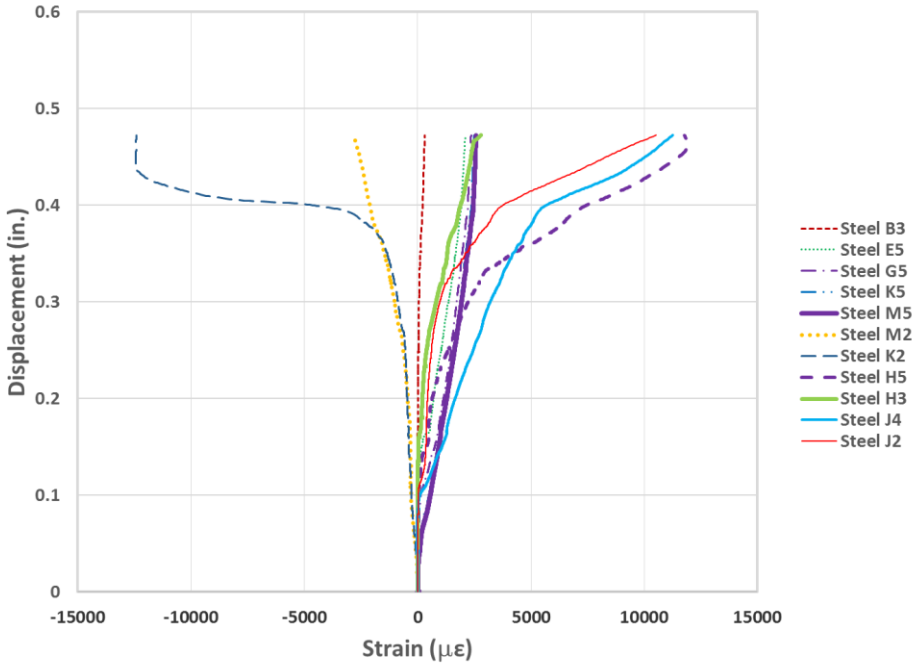

Figure 340 Displacement-strain response for RCS beam #4 without aging (Phase 1)

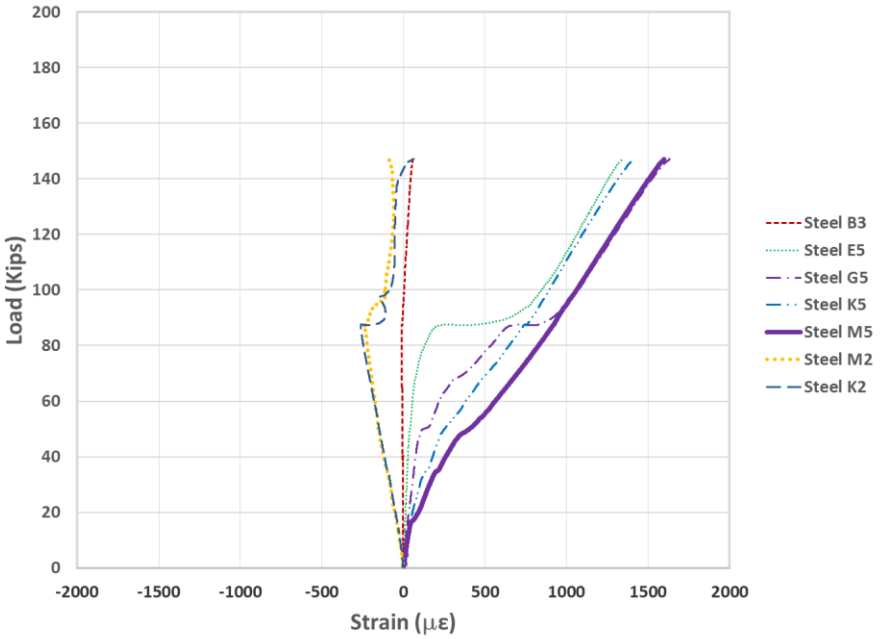

Figure 341 Load-strain response for SNFRC 0.5% beam #5 without aging (Phase 1)

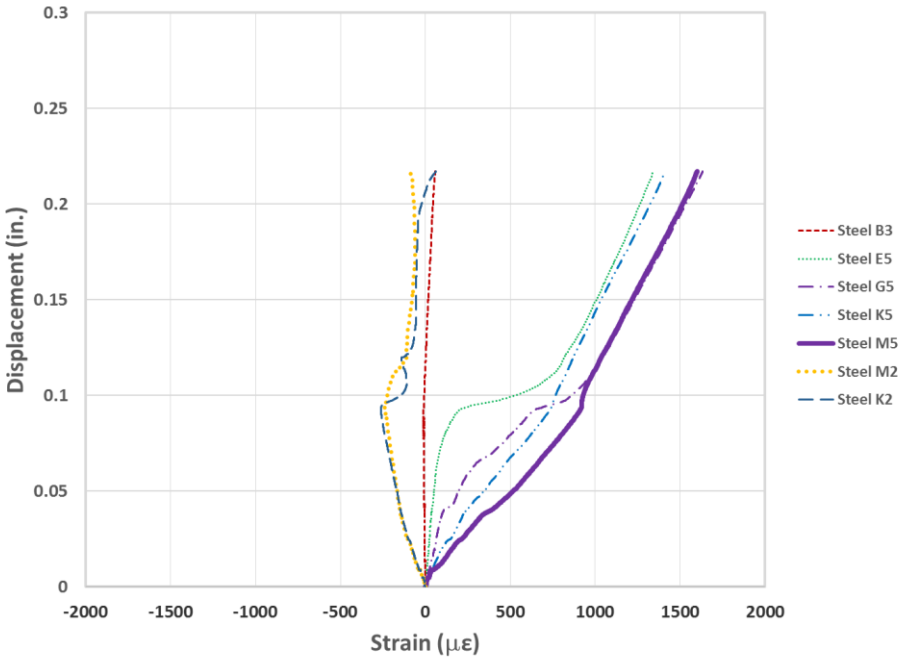

Figure 342 Displacement-strain response for SNFRC 0.5% beam #5 without aging (Phase 1)

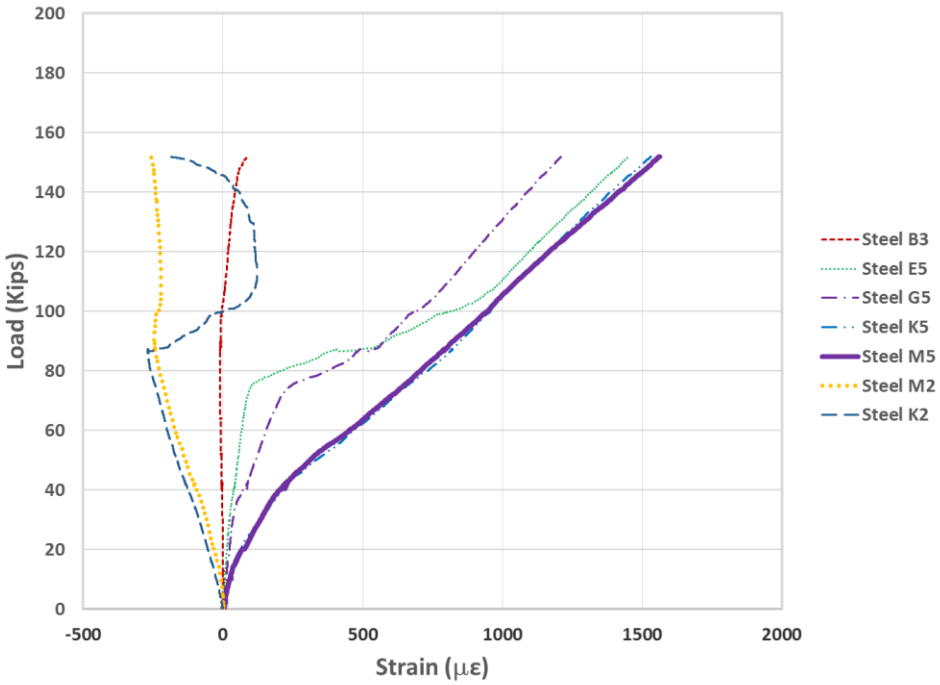

Figure 343 Load-strain response for SNFRC 0.5% beam #6 without aging (Phase 1)

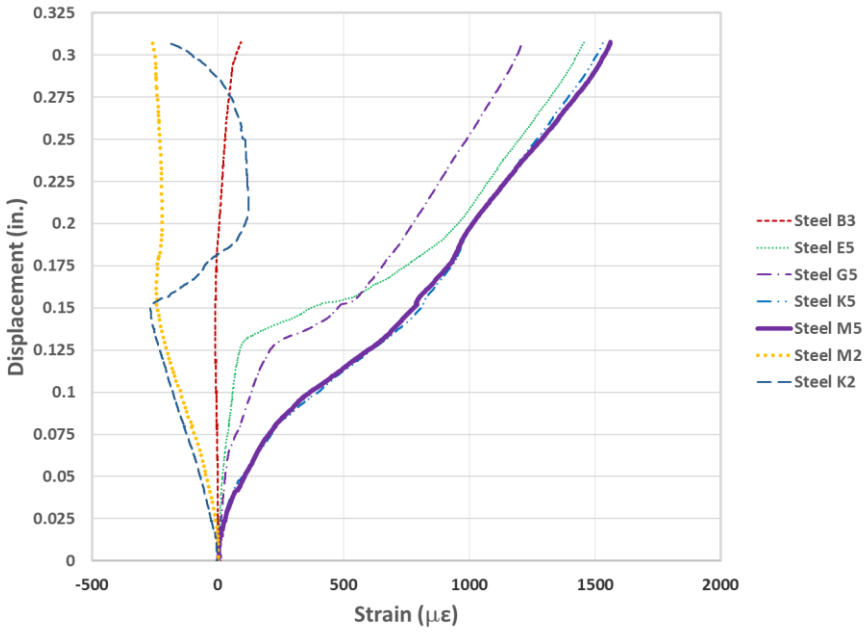

Figure 344 Displacement-strain response for SNFRC 0.5% beam #6 without aging (Phase 1)

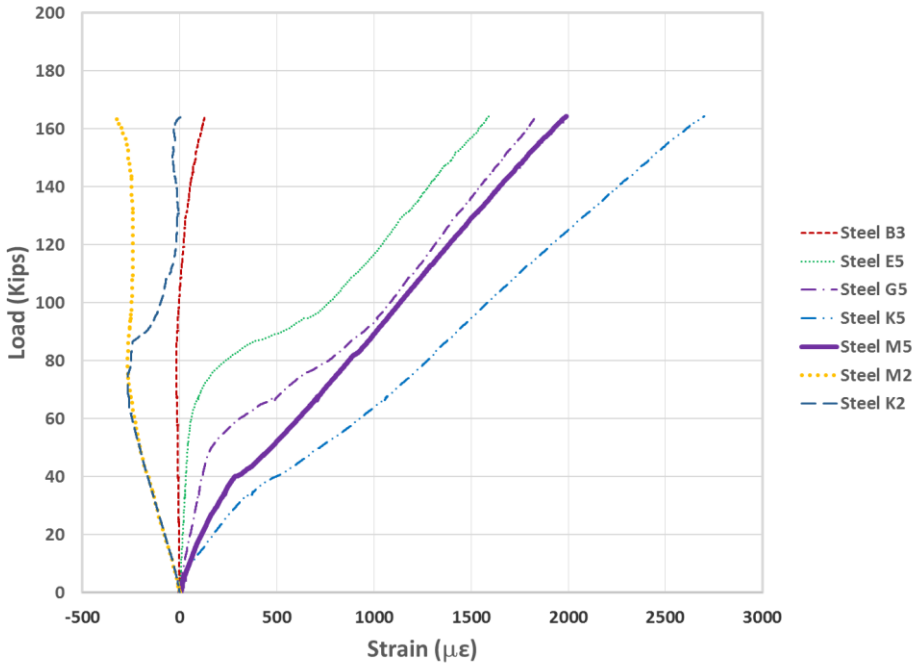

Figure 345 Load-strain response for SNFRC 0.75% beam #7 without aging (Phase 1)

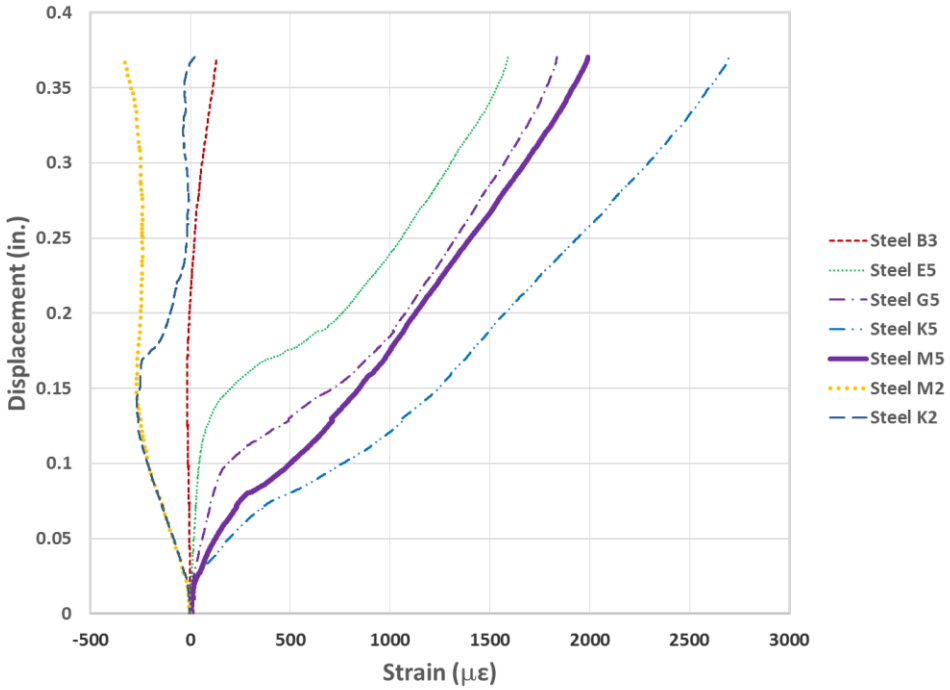

Figure 346 Displacement-strain response for SNFRC 0.75% beam #7 without aging (Phase 1)

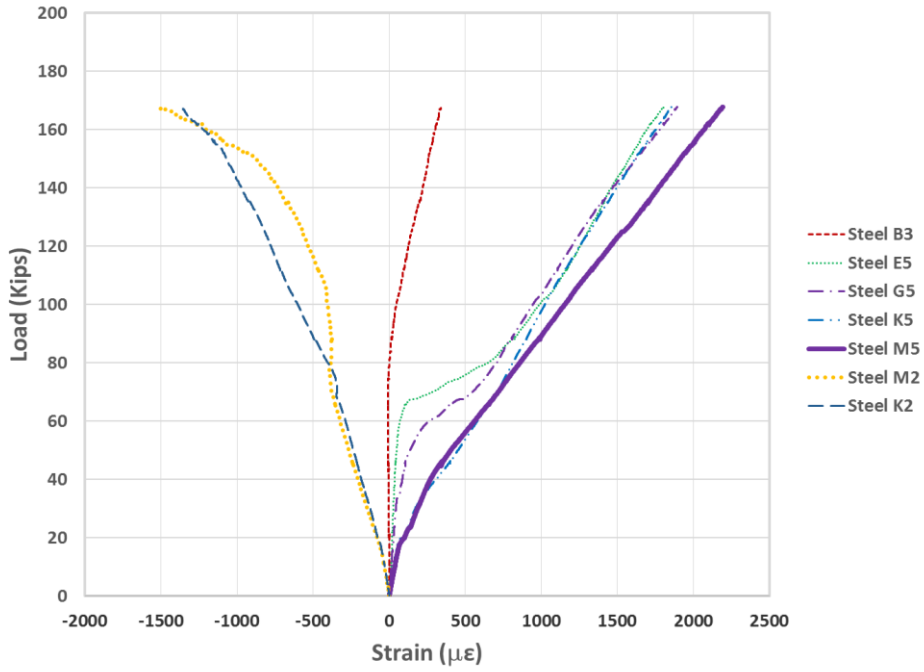

Figure 347 Load-strain response for SNFRC 0.75% beam #8 without aging (Phase 1)

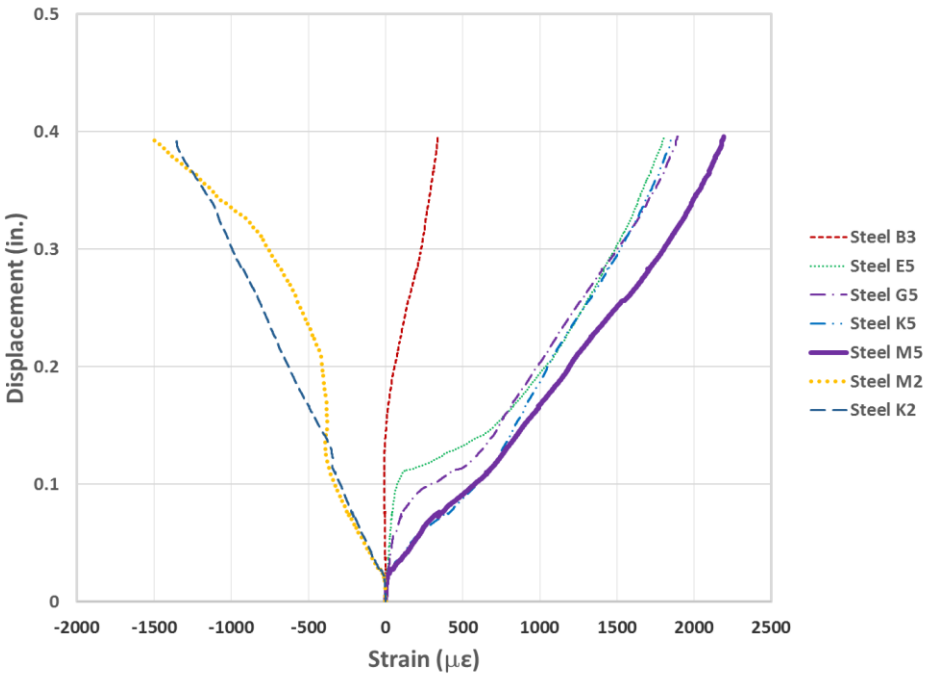

Figure 348 Displacement-strain response for SNFRC 0.75% beam #8 without aging (Phase 1)

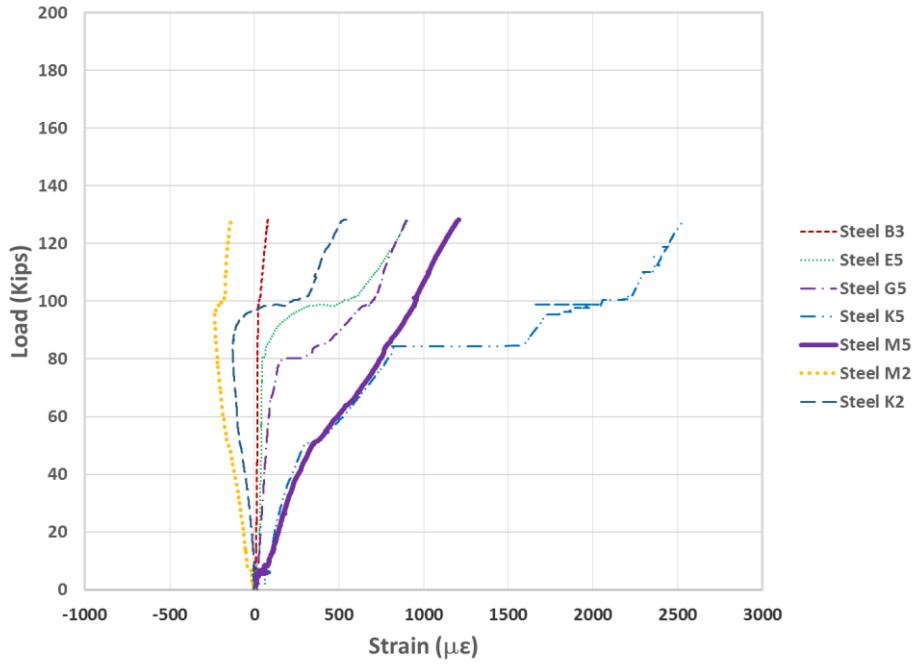

Figure 349 Load-strain response for RC control beam #9 subjected to 1-month aging (Phase 2)

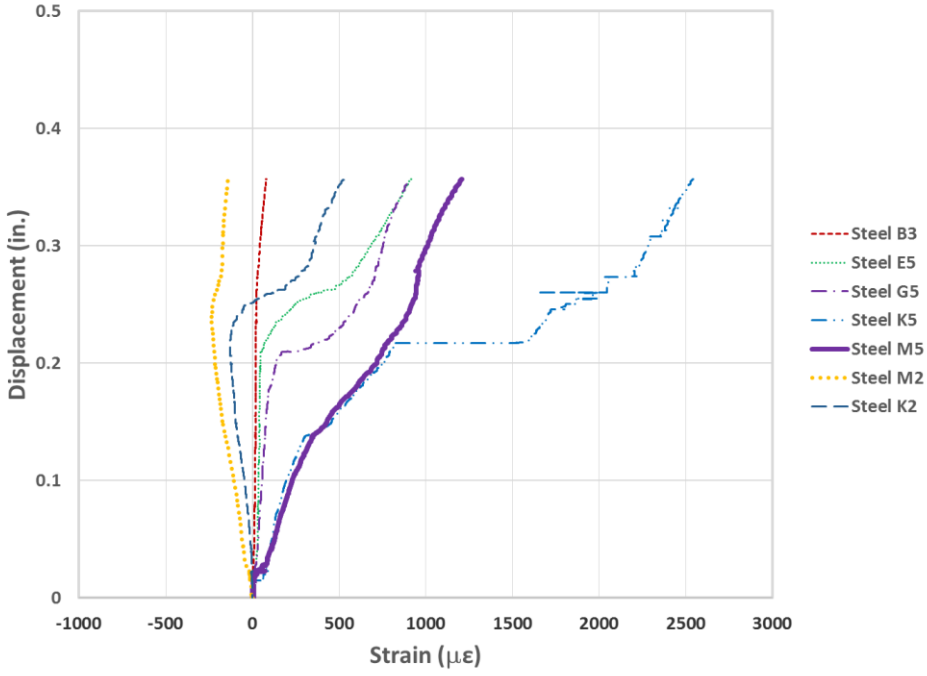

Figure 350 Displacement-strain response for RC control beam #9 subjected to 1-month aging (Phase 2)

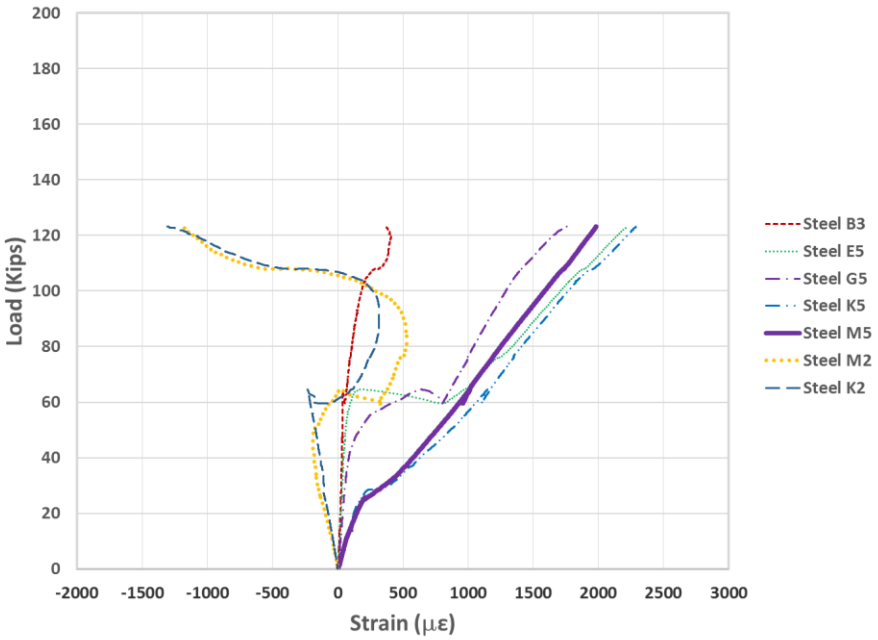

Figure 351 Load-strain response for RC control beam #10 subjected to 1-month aging (Phase 2)

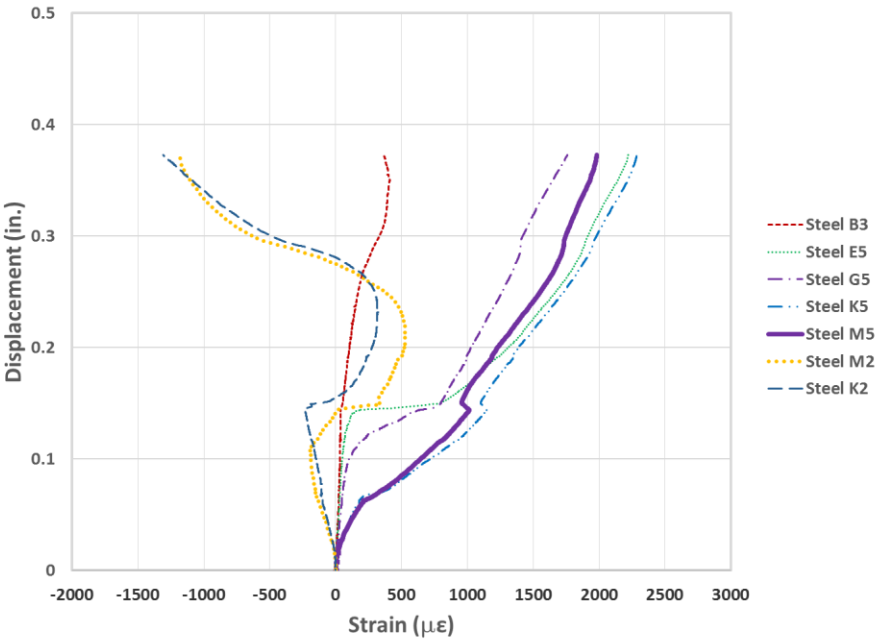

Figure 352 Displacement-strain response for RC beam #10 subjected to 1-month aging (Phase 2)

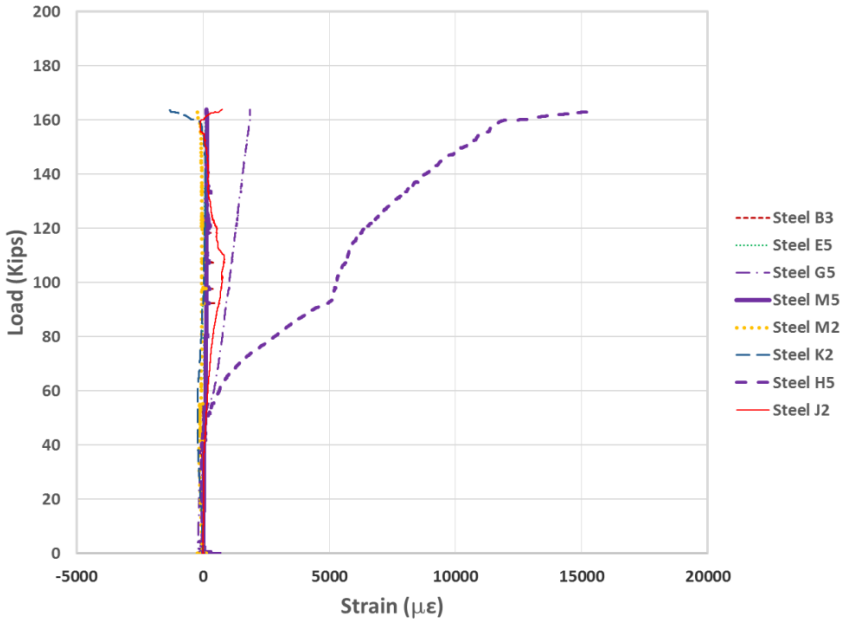

Figure 353 Load-strain response for RCS beam #11 subjected to 1-month aging (Phase 2)

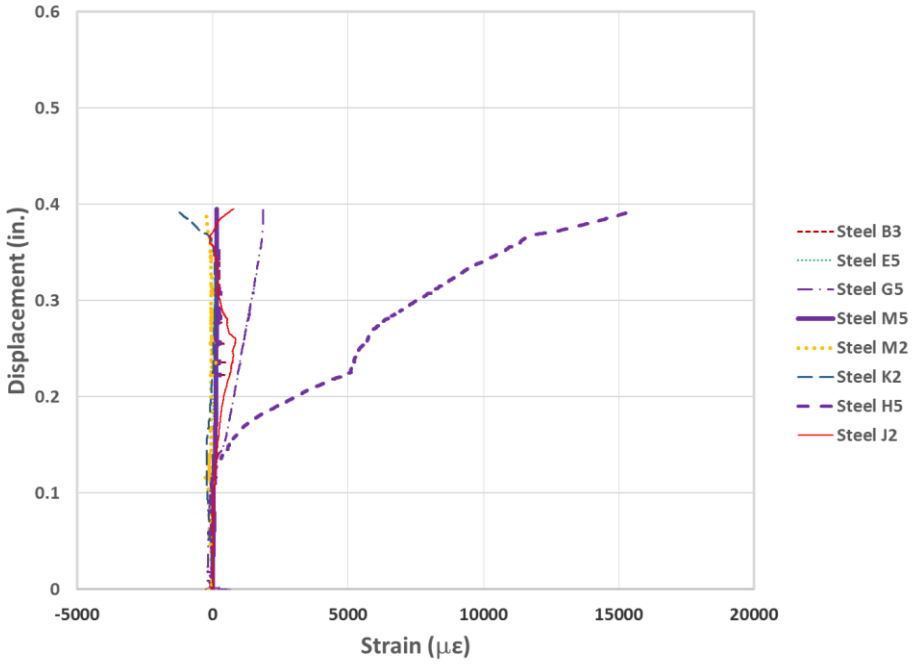

Figure 354 Displacement-strain response for RCS beam #11 subjected to 1-month aging (Phase 2)

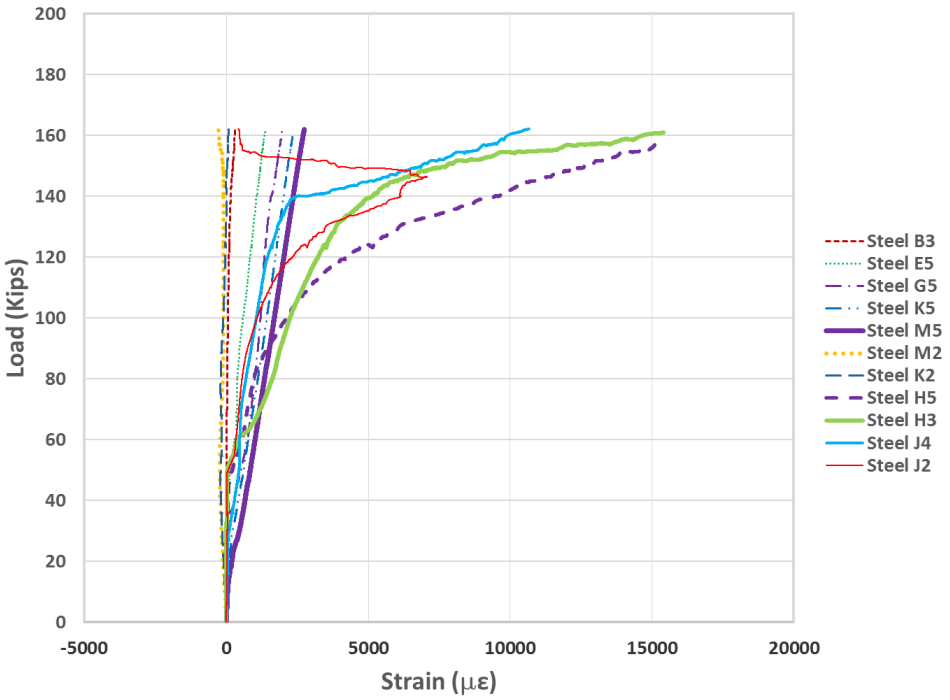

Figure 355 Load-strain response for RCS beam #12 subjected to 1-month aging (Phase 2)

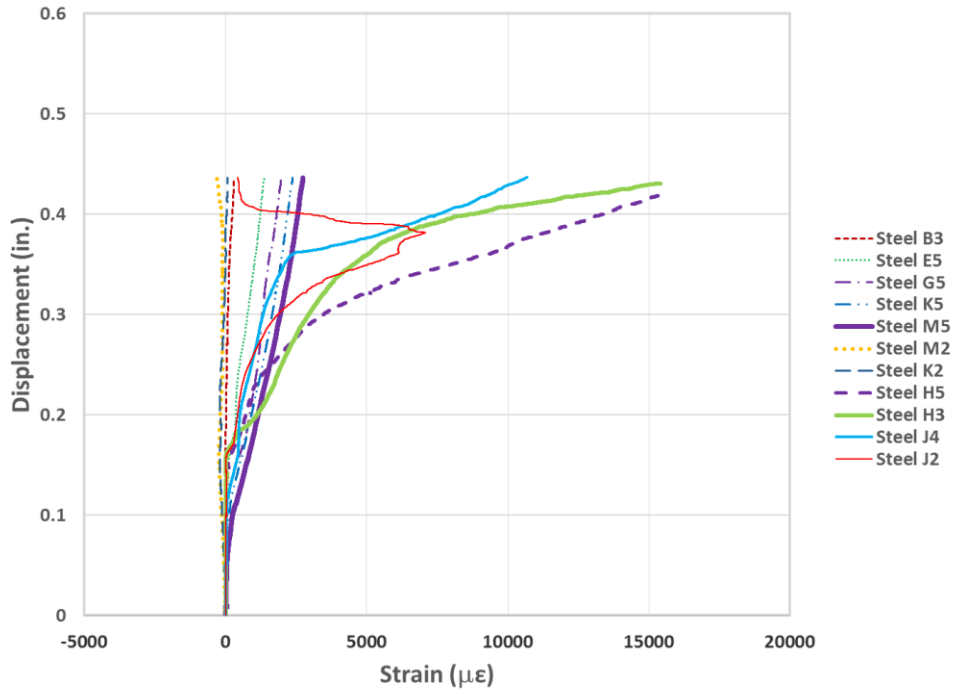

Figure 356 Displacement-strain response for RCS beam #12 subjected to 1-month aging (Phase 2)

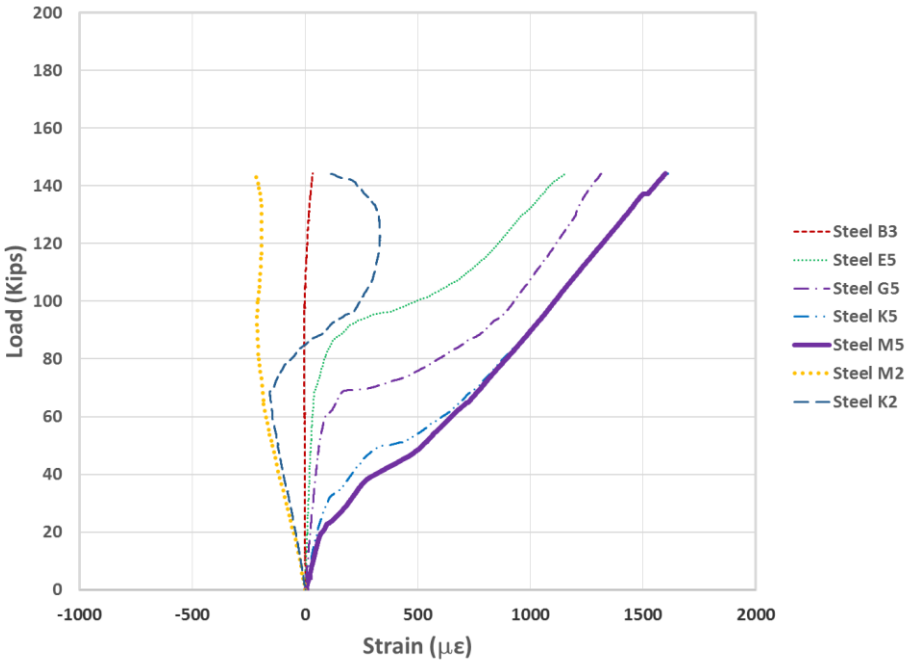

Figure 357 Load-strain response for SNFRC 0.5% beam #13 subjected to 1-month aging (Phase 2)

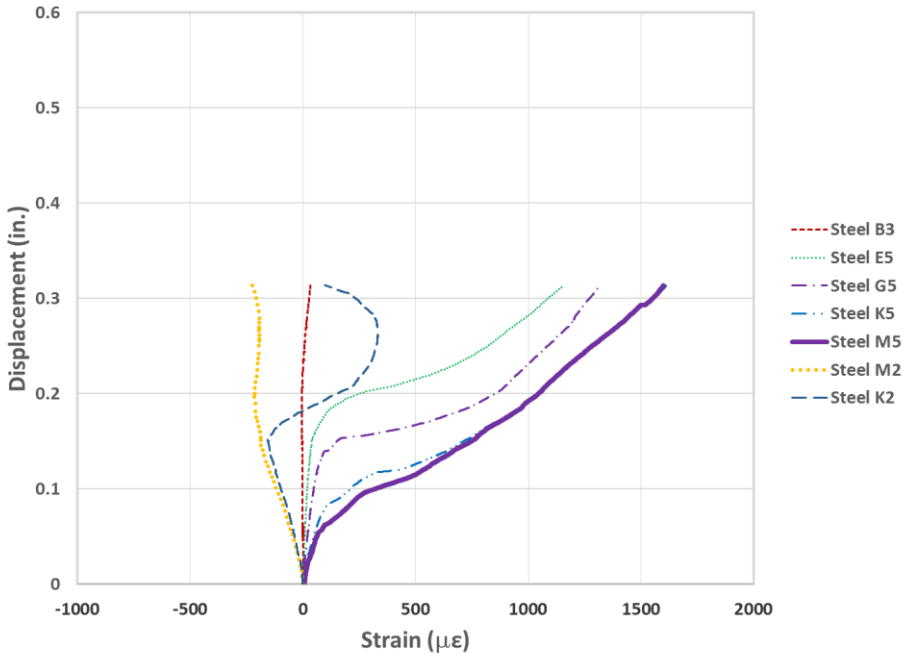

Figure 358 Displacement-strain response for SNFRC 0.5% beam #13 subjected to 1-month aging (Phase 2)

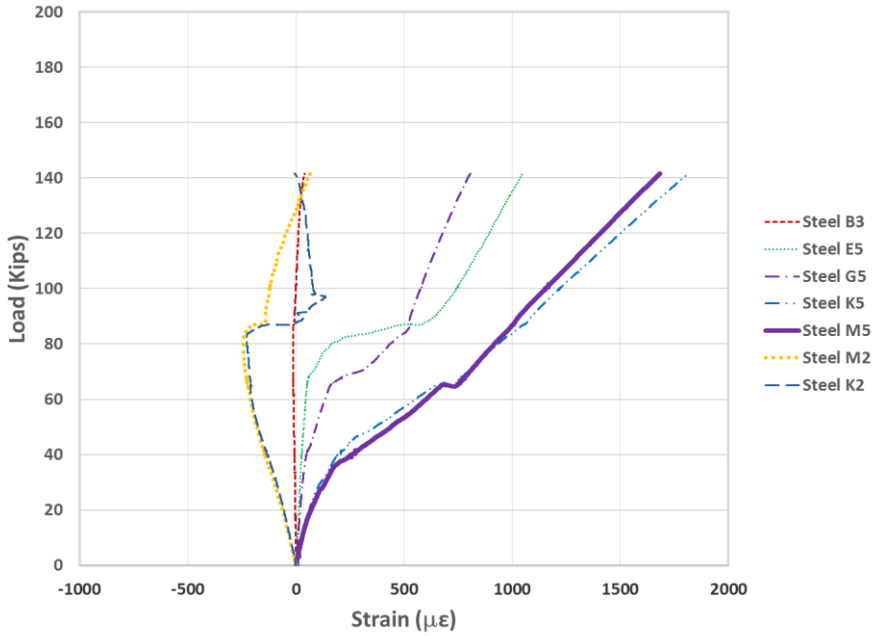

Figure 359 Load-strain response for SNFRC 0.5% beam #14 subjected to 1-month aging (Phase 2)

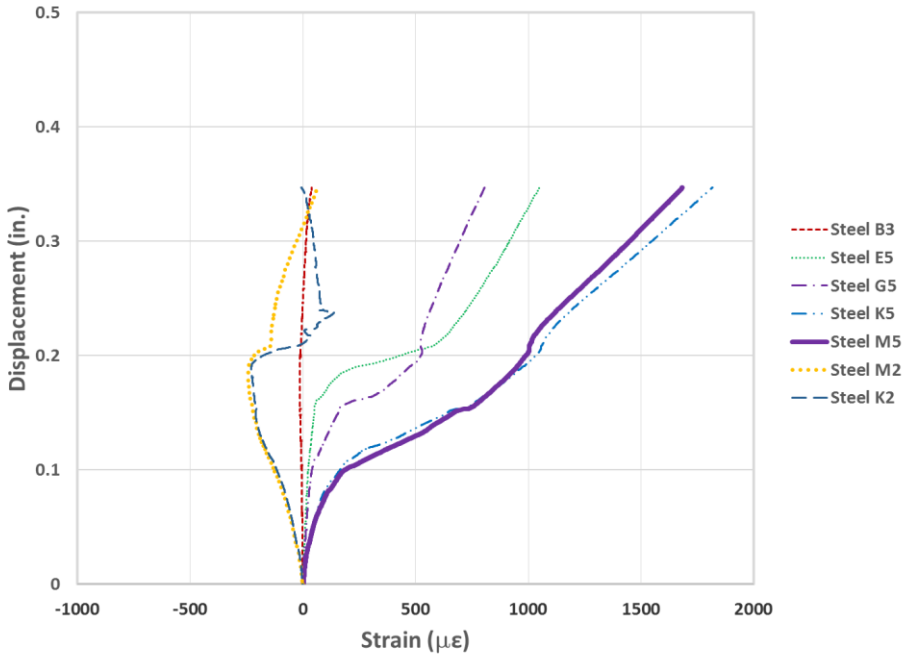

Figure 360 Displacement-strain response for SNFRC 0.5% beam #14 subjected to 1-month aging (Phase 2)

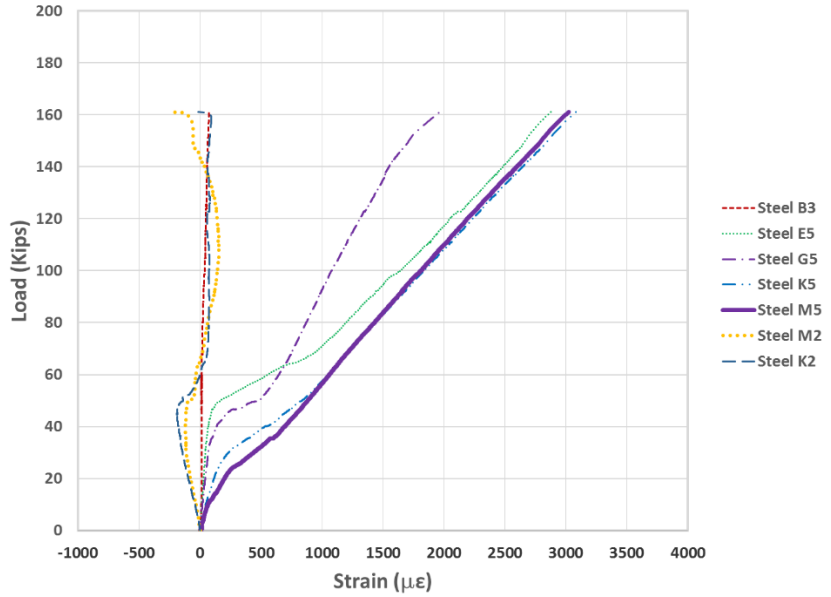

Figure 361 Load-strain response for SNFRC 0.75% beam #15 subjected to 1-month aging (Phase 2)

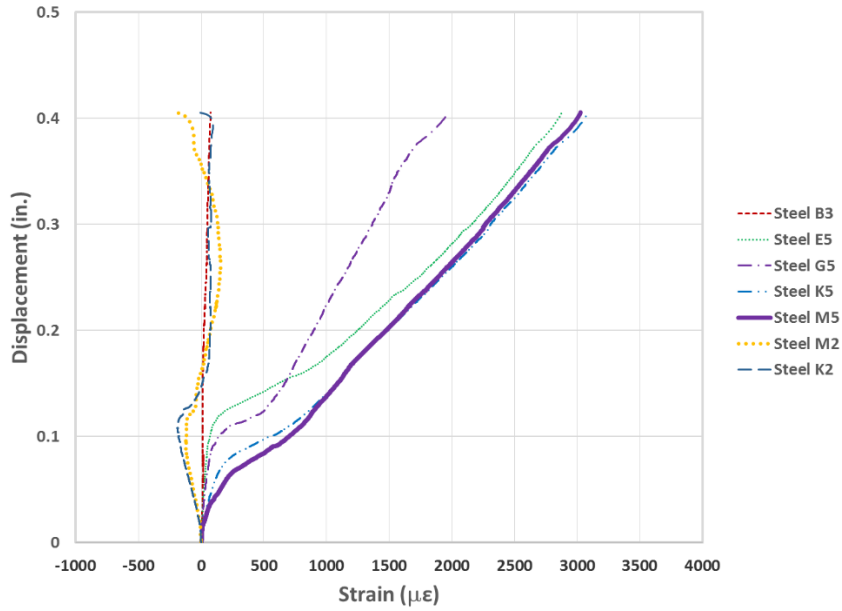

Figure 362 Displacement-strain response for SNFRC 0.75% beam #15 subjected to 1-month aging (PH. 2)

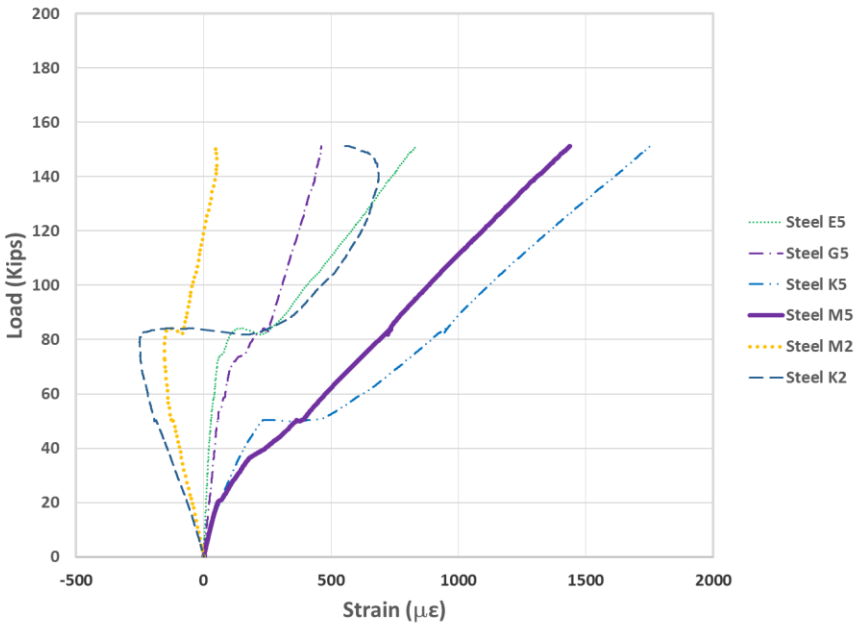

Figure 363 Load-strain response for SNFRC 0.75% beam #16 subjected to 1-month aging (Phase 2)

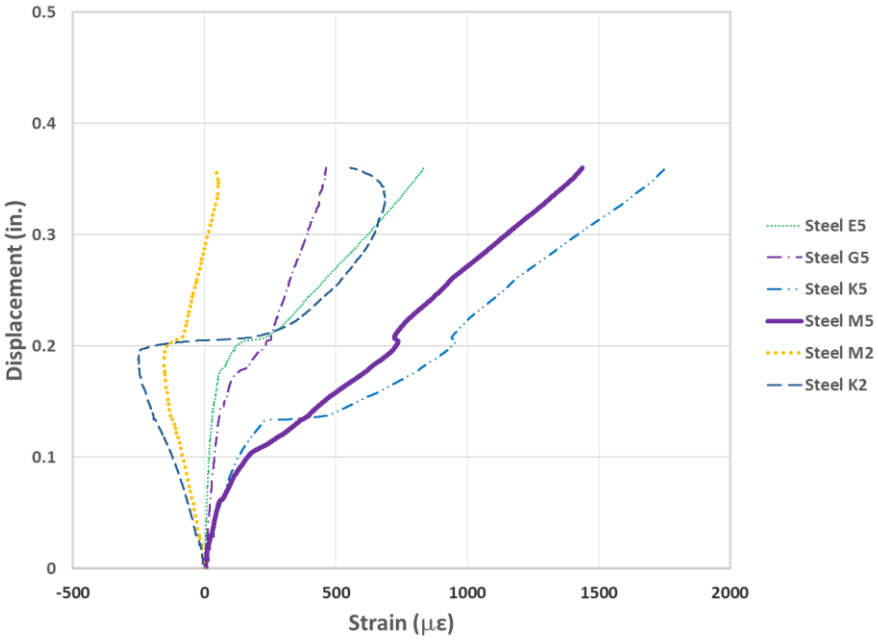

Figure 364 Displacement-strain response for SNFRC 0.75% beam #16 subjected to 1-month aging (Phase 2)

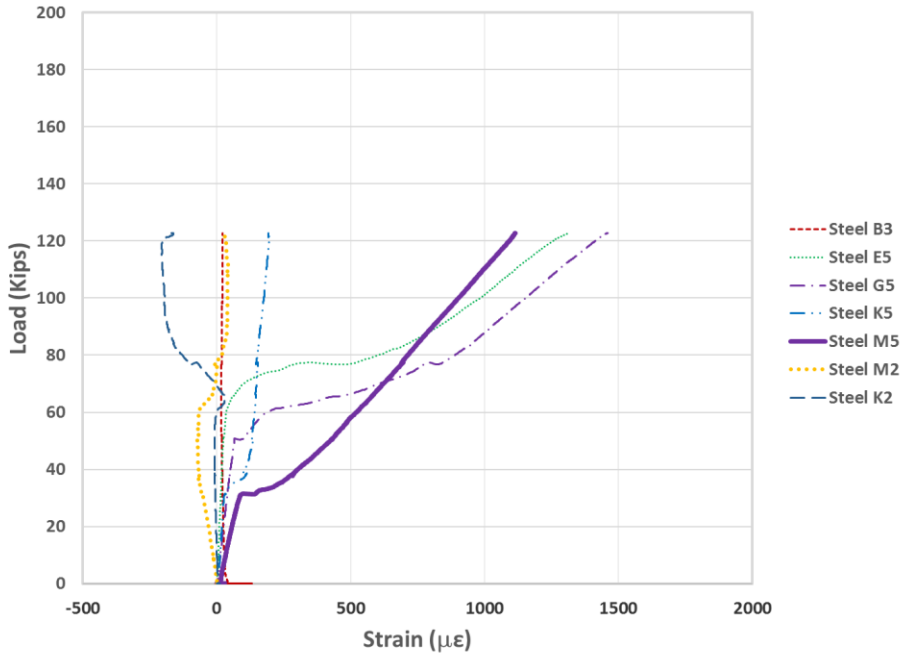

Figure 365 Load-strain response for RC control beam #17 subjected to 3-month aging (Phase 3)

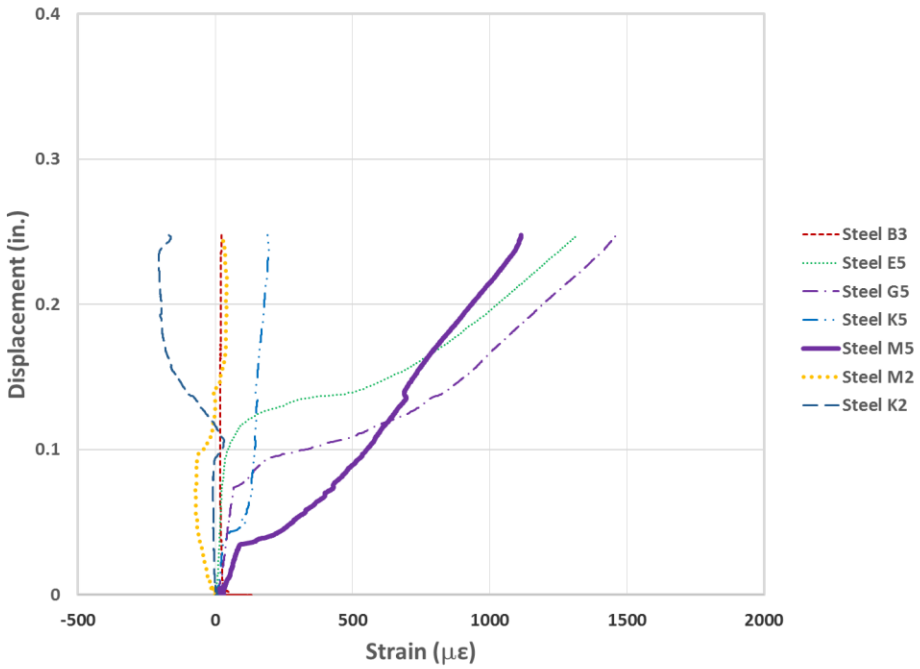

Figure 366 Displacement-strain response for RC control beam #17 subjected to 3-month aging (Phase 3)

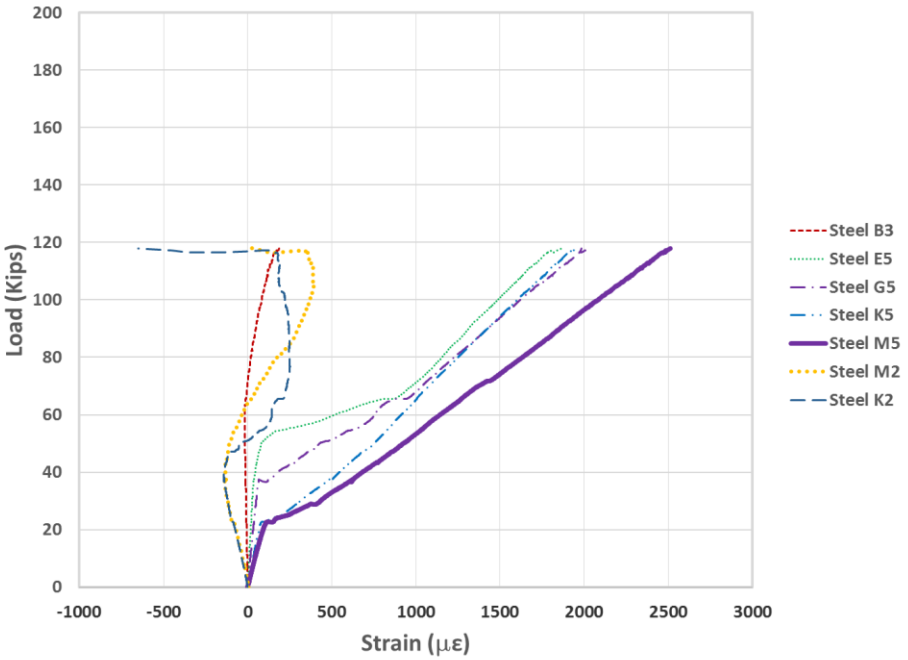

Figure 367 Load-strain response for RC control beam #18 subjected to 3-month aging (Phase 3)

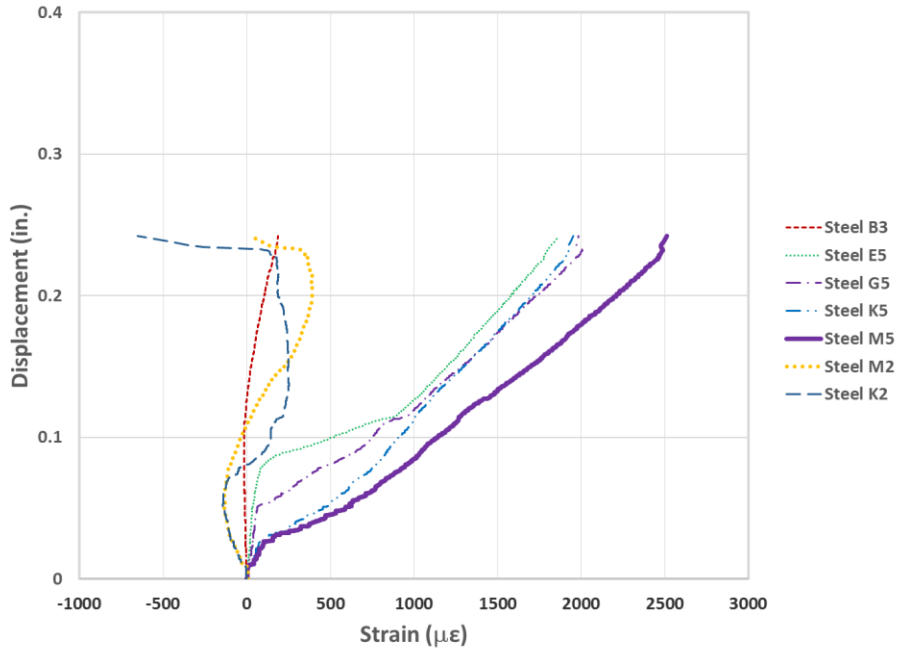

Figure 368 Displacement-strain response for RC control beam #18 subjected to 3-month aging (Phase 3)

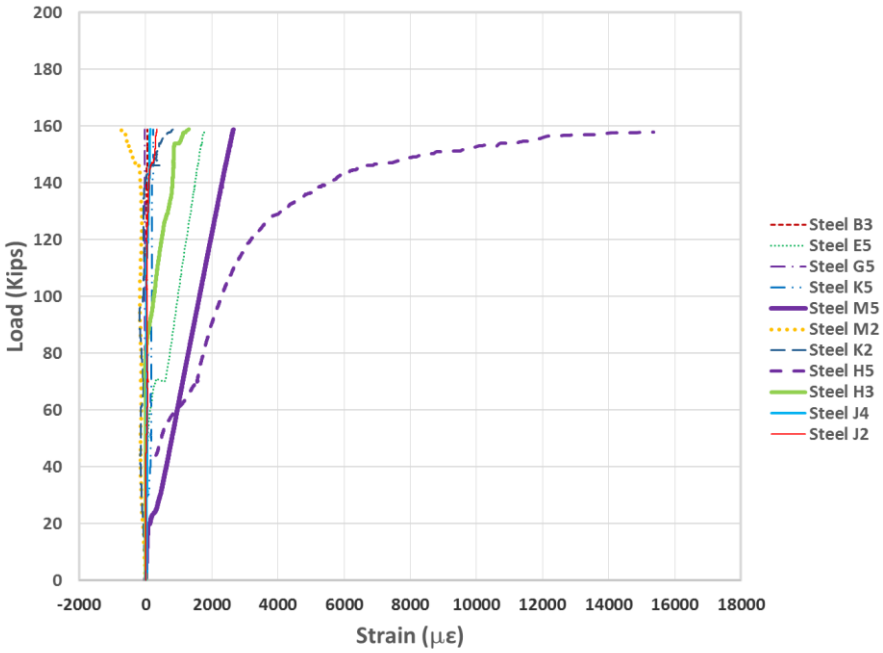

Figure 369 Load-strain response for RCS beam #19 subjected to 3-month aging (Phase 3)

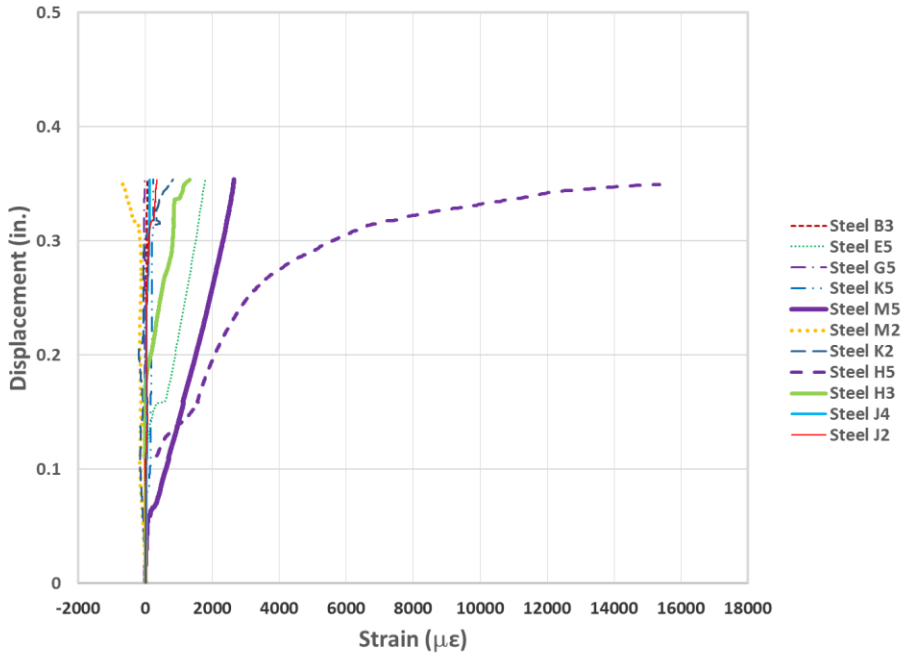

Figure 370 Displacement-strain response for RCS beam #19 subjected to 3-month aging (Phase 3)

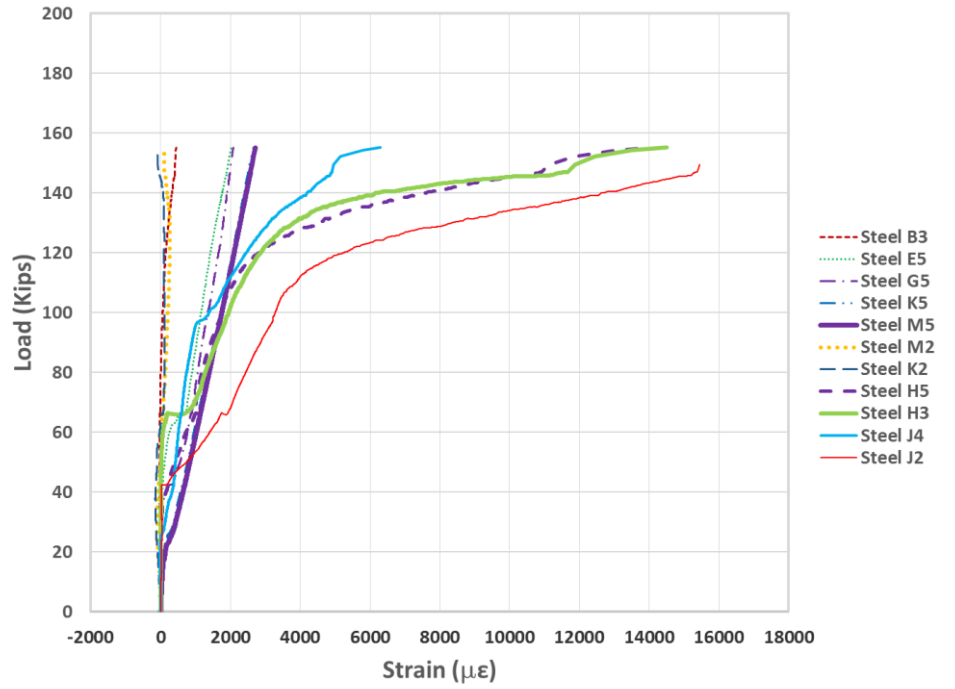

Figure 371 Load-strain response for RCS beam #20 subjected to 3-month aging (Phase 3)

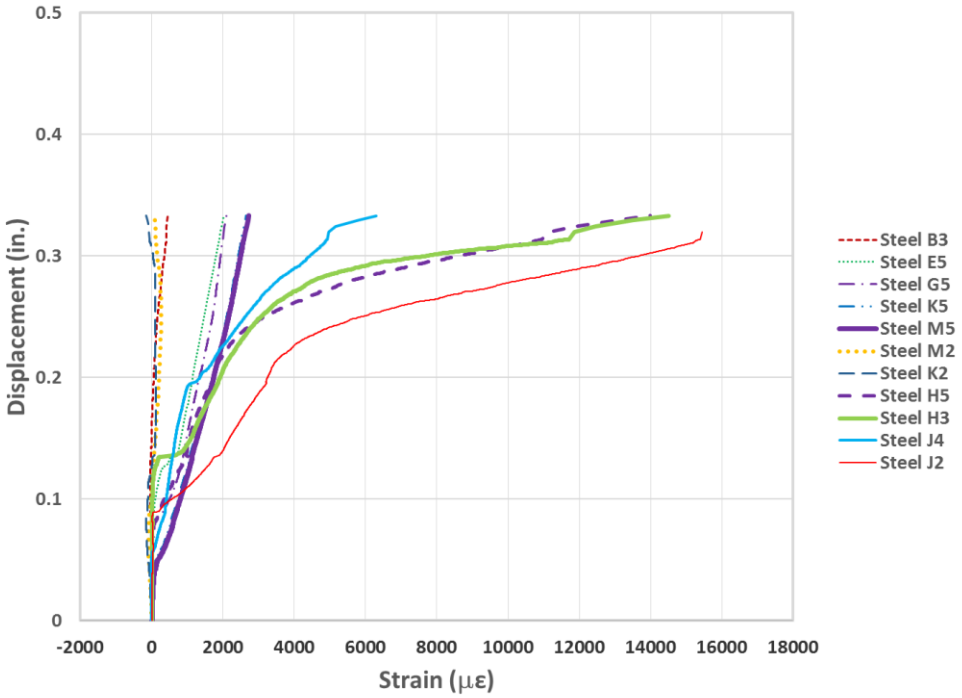

Figure 372 Displacement-strain response for RCS beam #20 subjected to 3-month aging (Phase 3)

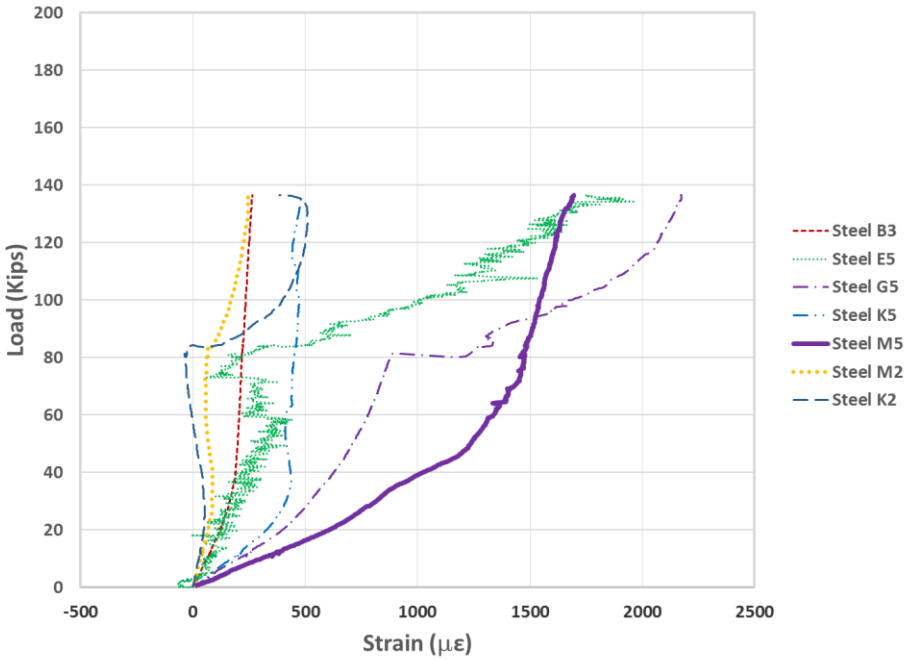

Figure 373 Load-strain response for SNFRC 0.5% beam #21 subjected to 3-month aging (Phase 3)

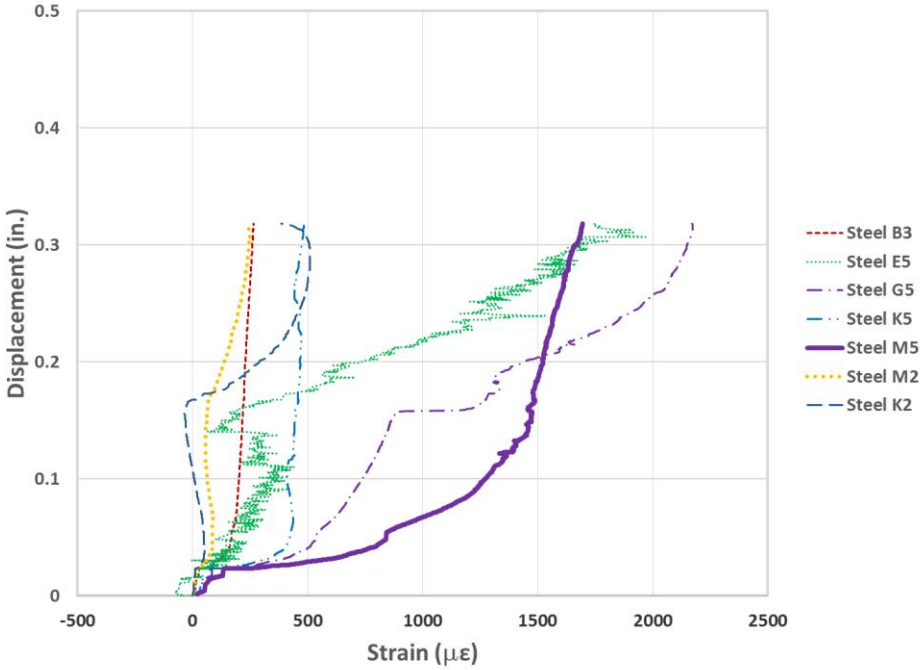

Figure 374 Displacement-strain response for SNFRC 0.5% beam #21 subjected to 3-month aging (Phase 3)

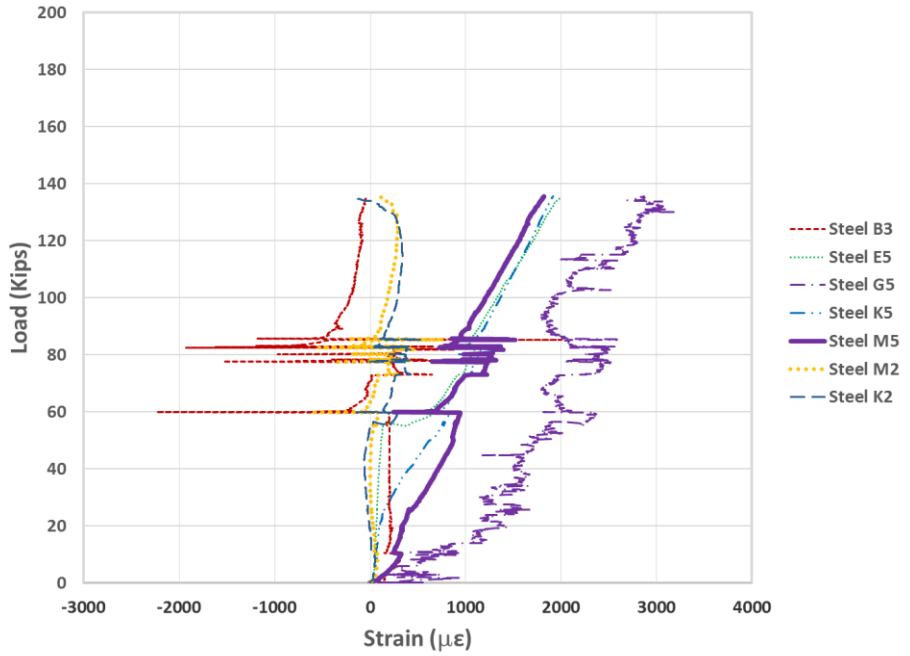

Figure 375 Load-strain response for SNFRC 0.5% beam #22 subjected to 3-month aging (Phase 3)

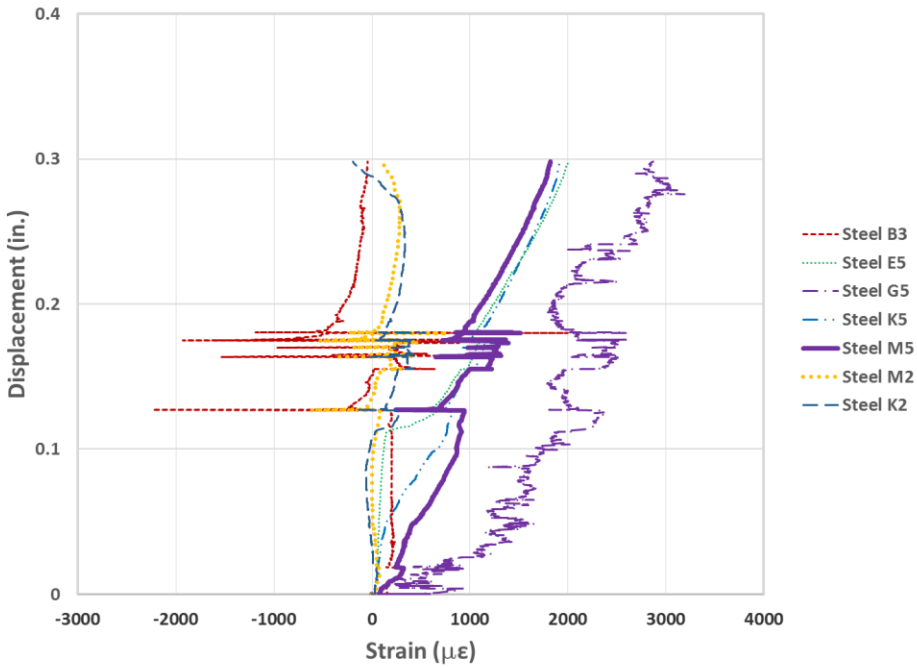

Figure 376 Displacement-strain response for SNFRC 0.5% beam #22 subjected to 3-month aging (Phase 3)

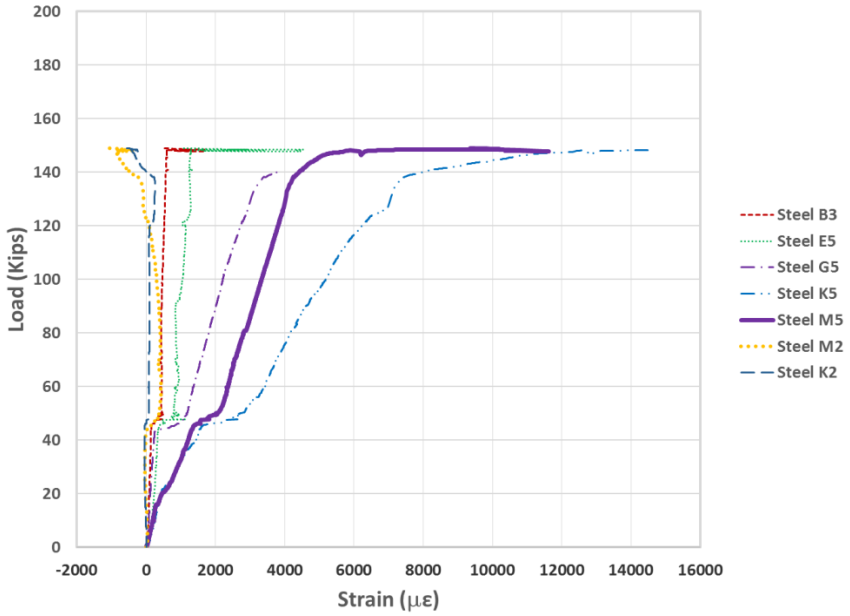

Figure 377 Load-strain response for SNFRC 0.75% beam #23 subjected to 3-month aging (Phase 3)

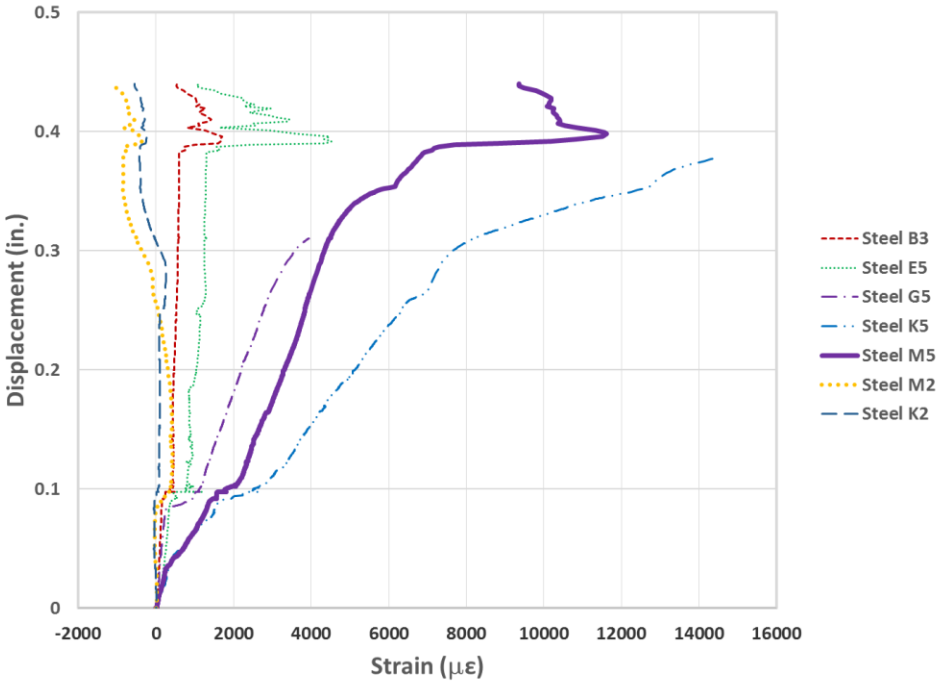

Figure 378 Displacement-strain response for SNFRC 0.5% beam #23 subjected to 3-month aging (Phase 3)

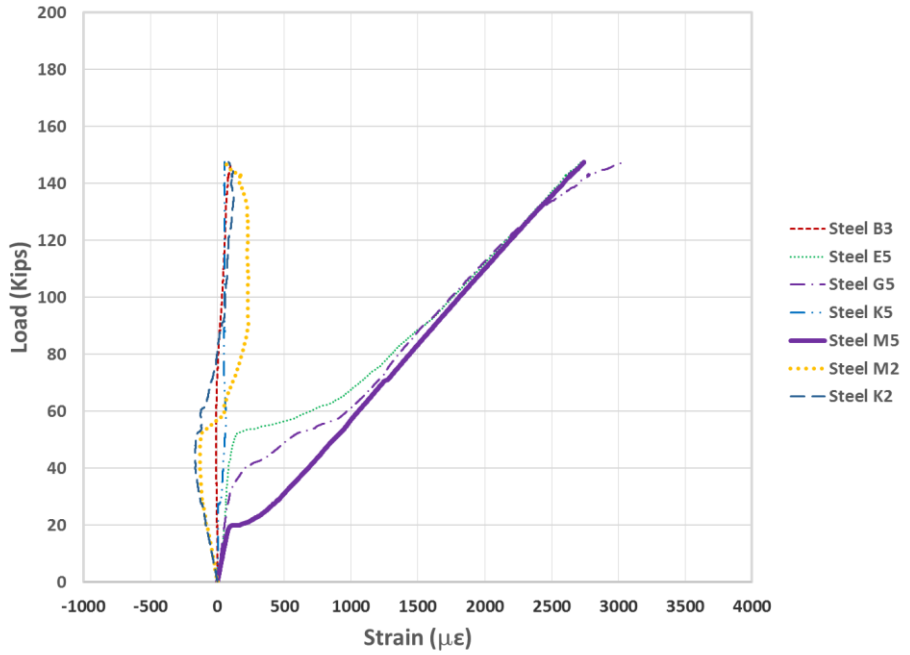

Figure 379 Load-strain response for SNFRC 0.75% beam #24 subjected to 3-month aging (Phase 3)

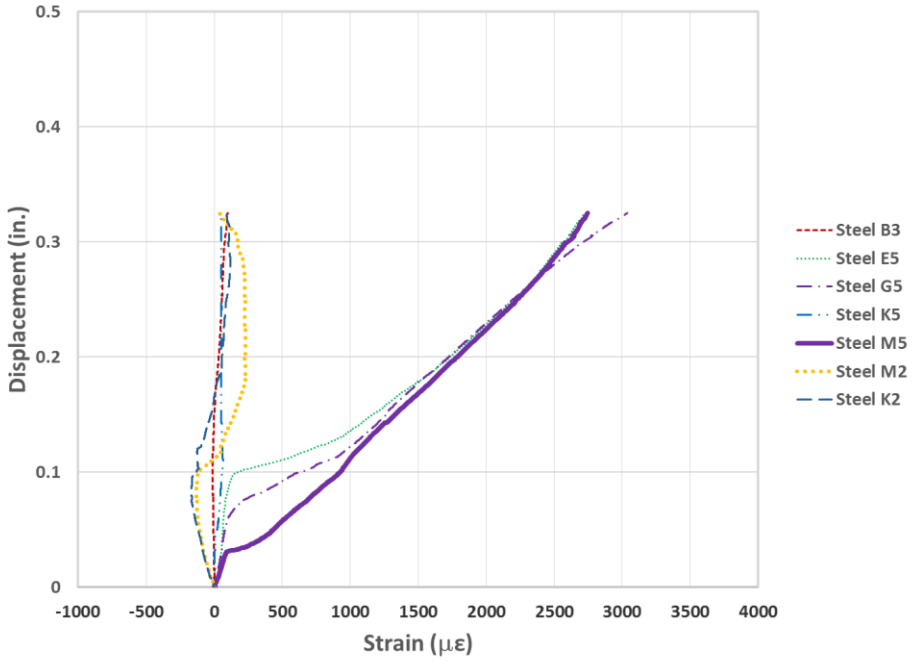

Figure 380 Displacement-strain response for SNFRC 0.75% beam #24 subjected to 3-month aging (Phase 3)

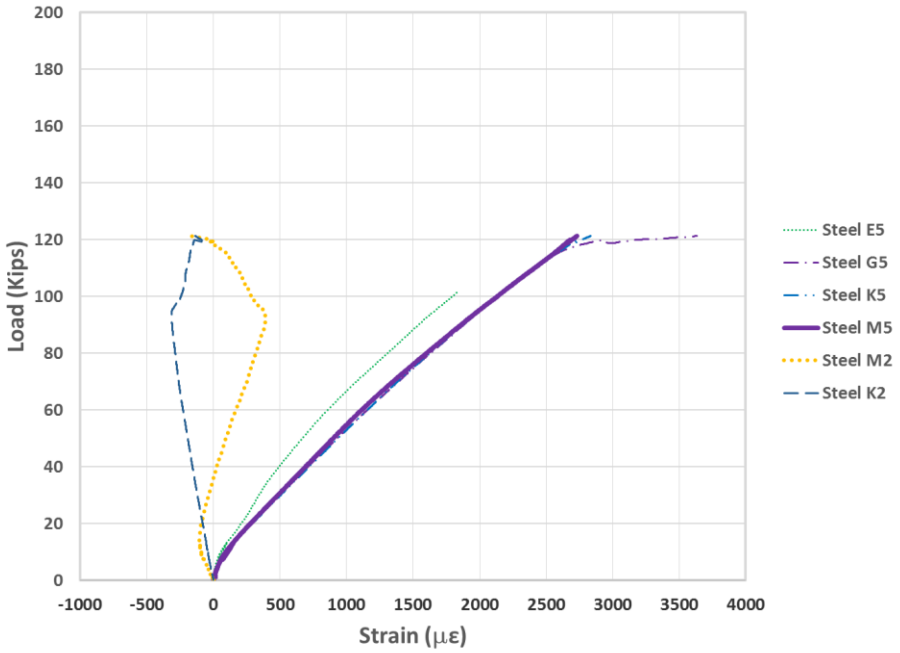

Figure 381 Load-strain response for RC control beam #25 subjected to 6-month aging

(Phase 4)

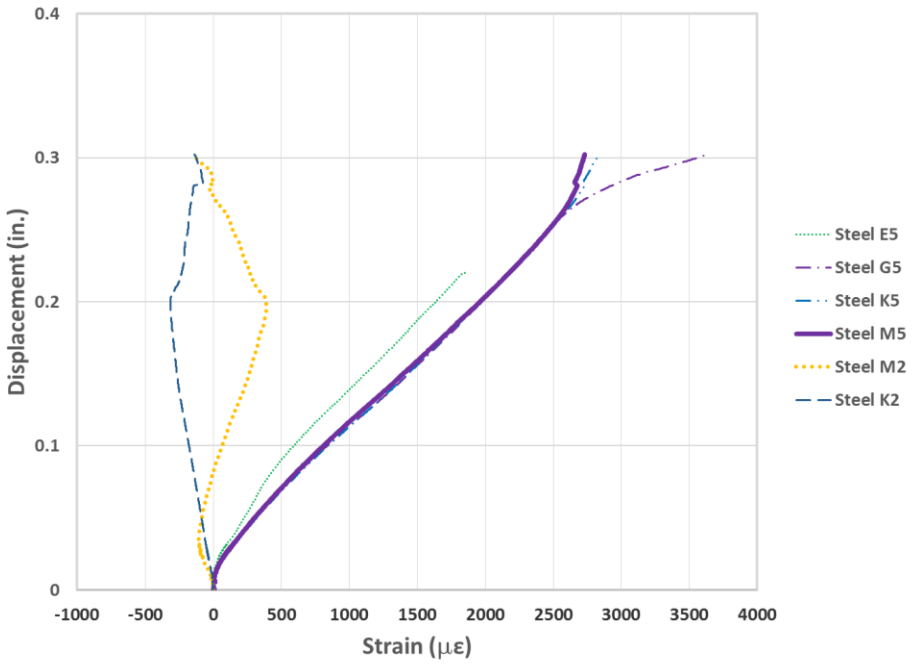

Figure 382 Displacement-strain response for RC control beam #25 subjected to 6-month aging

(Phase 4)

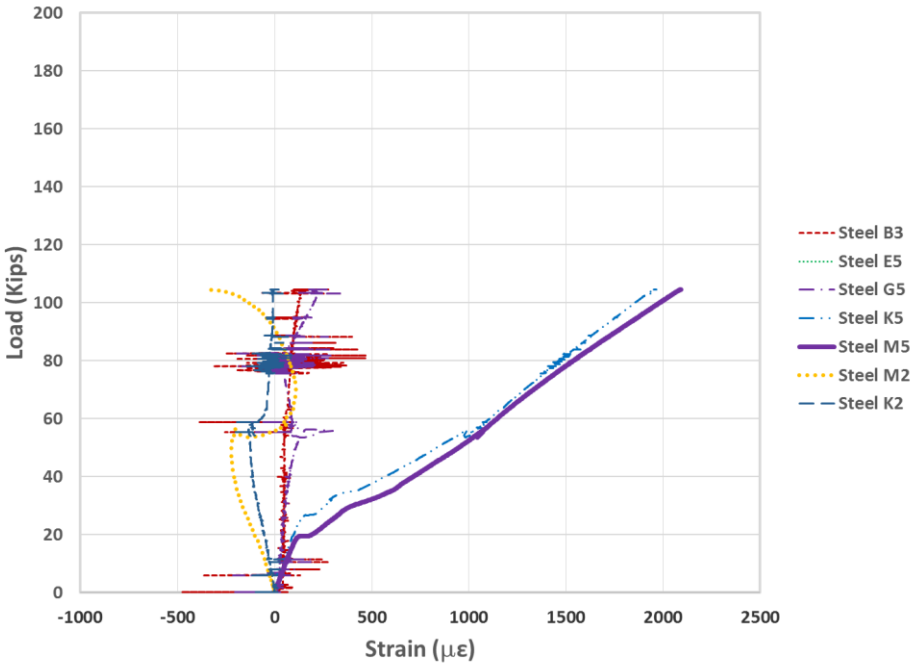

Figure 383 Load-strain response for RC control beam #26 subjected to 6-month aging (Phase 4)

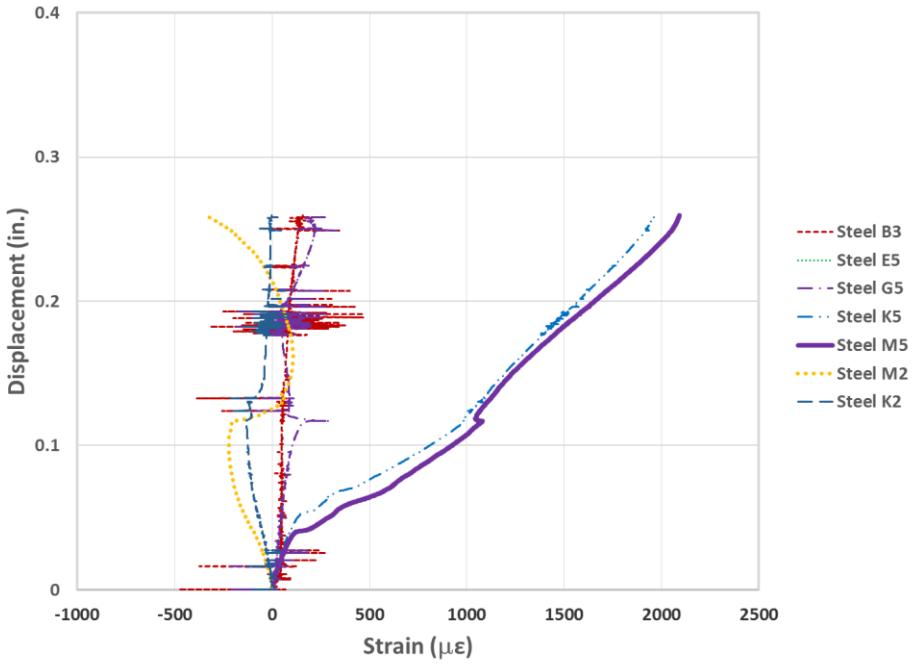

Figure 384 Displacement-strain response for RC control beam #26 subjected to 6-month aging (PH. 4)

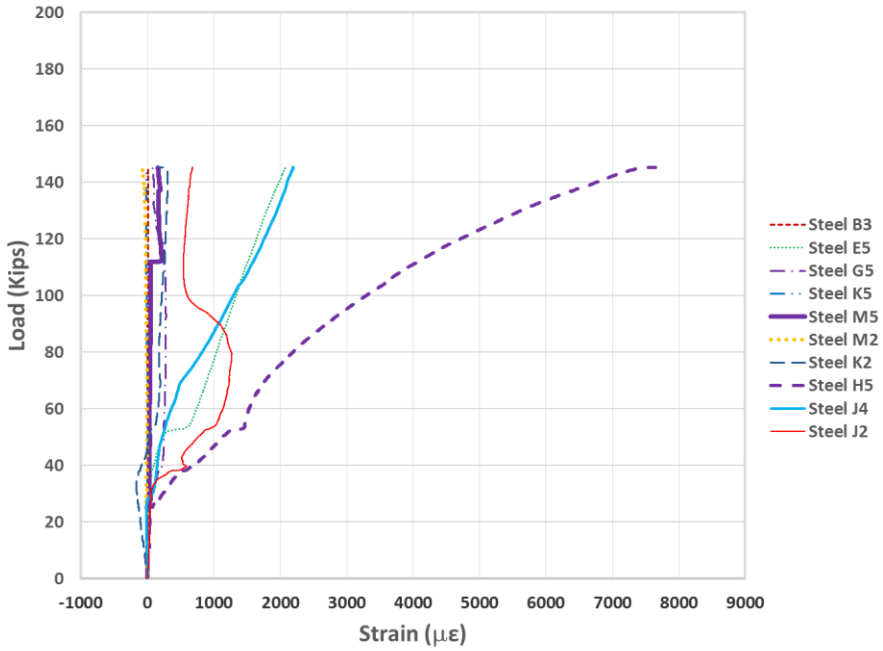

Figure 385 Load-strain response for RCS beam #27 subjected to 6-month aging (Phase 4)

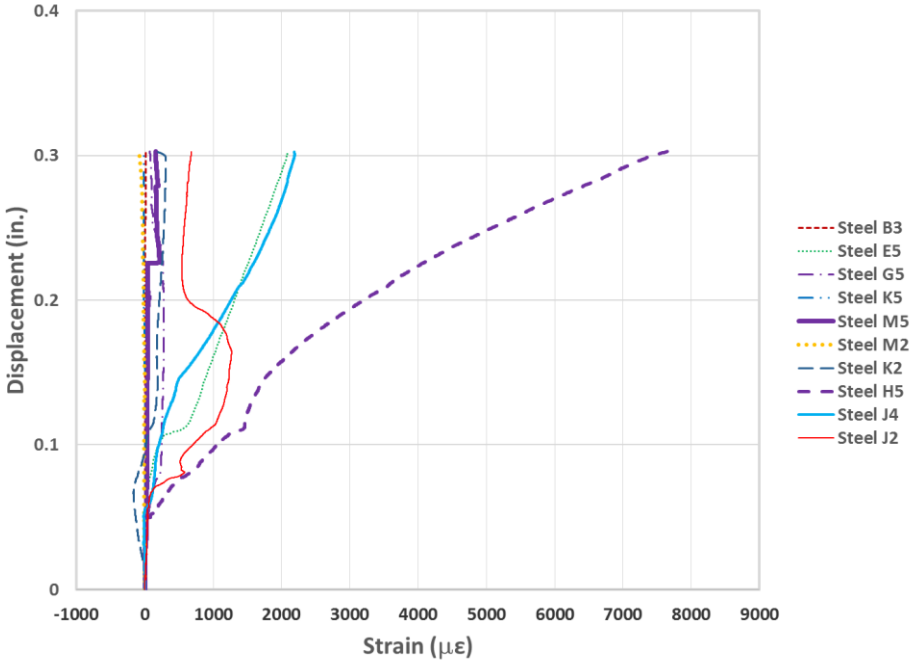

Figure 386 Displacement-strain response for RCS beam #27 subjected to 6-month aging (Phase 4)

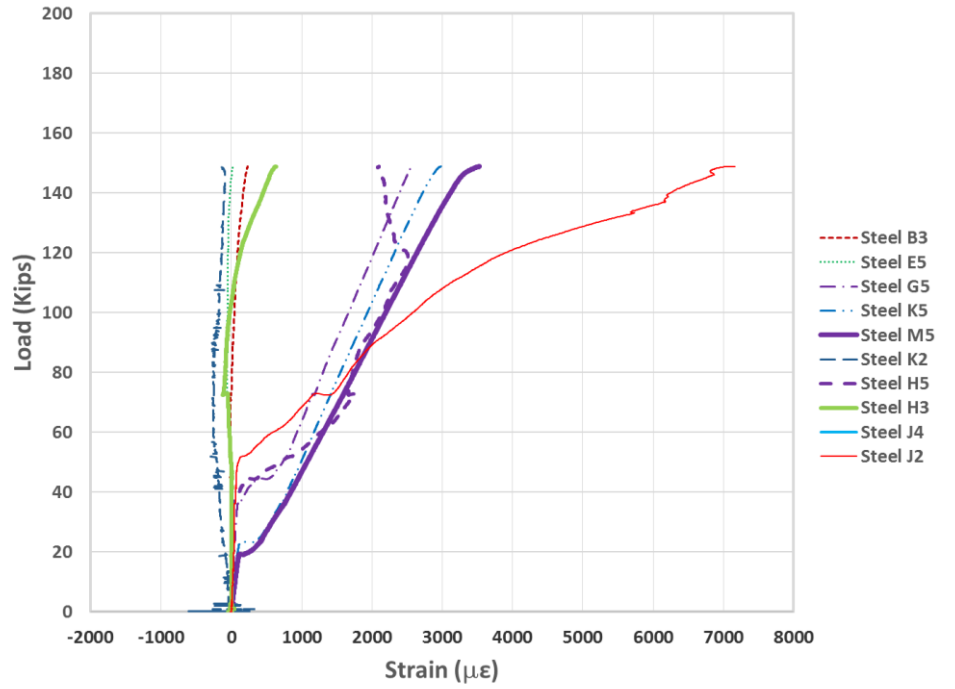

Figure 387 Load-strain response for RCS beam #28 subjected to 6-month aging (Phase 4)

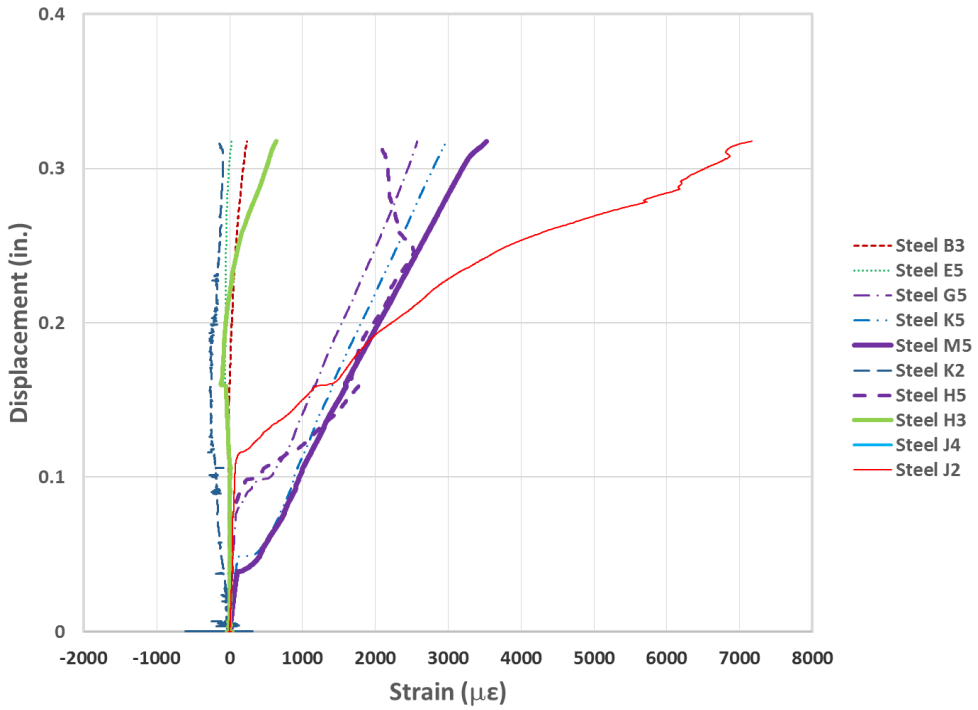

Figure 388 Displacement-strain response for RCS beam #28 subjected to 6-month aging (Phase 4)

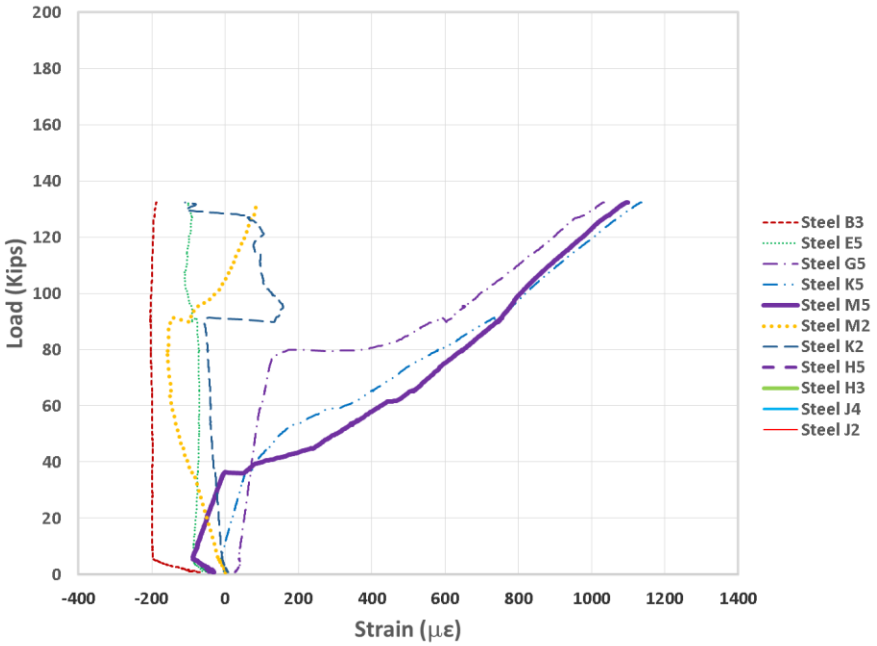

Figure 389 Load-strain response for SNFRC 0.5% beam #29 subjected to 6-month aging (Phase 4)

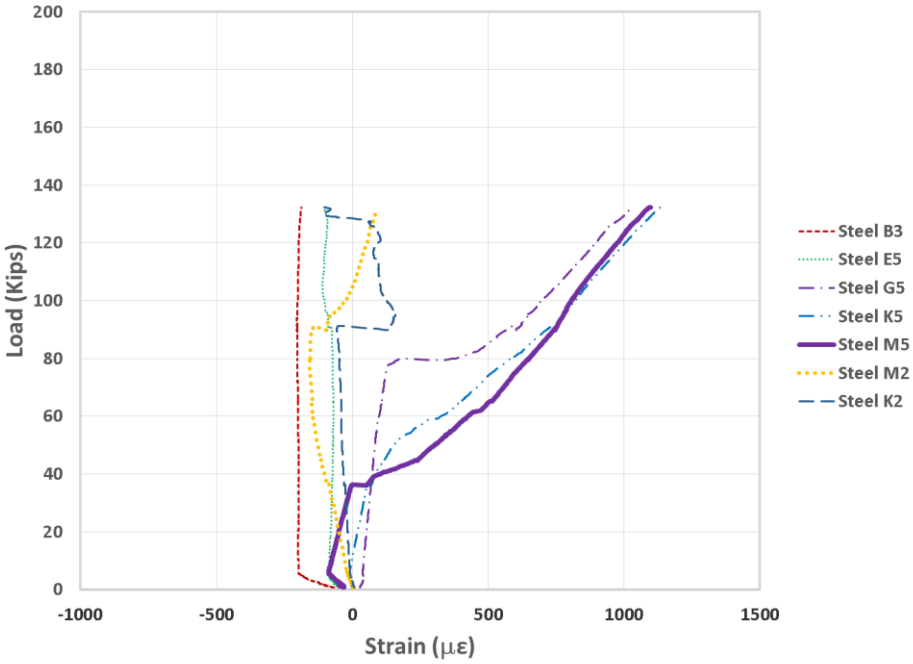

Figure 390 Displacement-strain response for SNFRC 0.5% beam #29 subjected to 6-month aging (Phase 4)

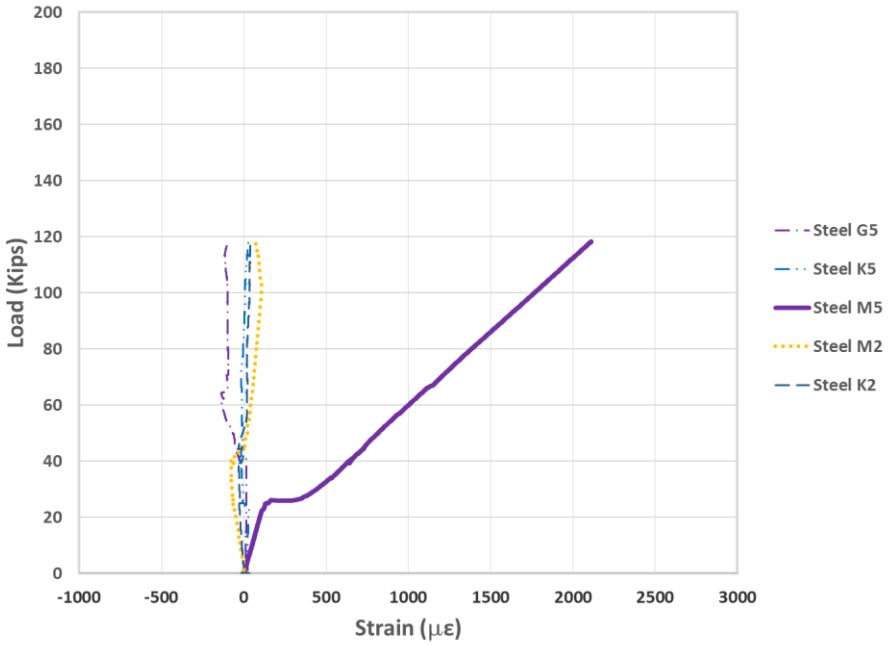

Figure 391 Load-strain response for SNFRC 0.5% beam #30 subjected to 6-month aging (Phase 4)

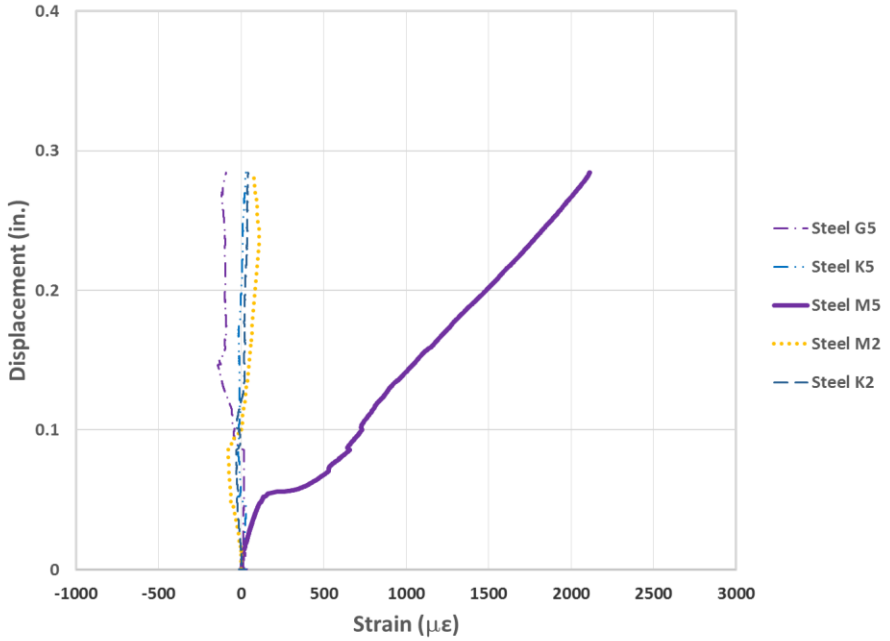

Figure 392 Displacement-strain response for SNFRC 0.5% beam #30 subjected to 6-month aging (Phase 4)

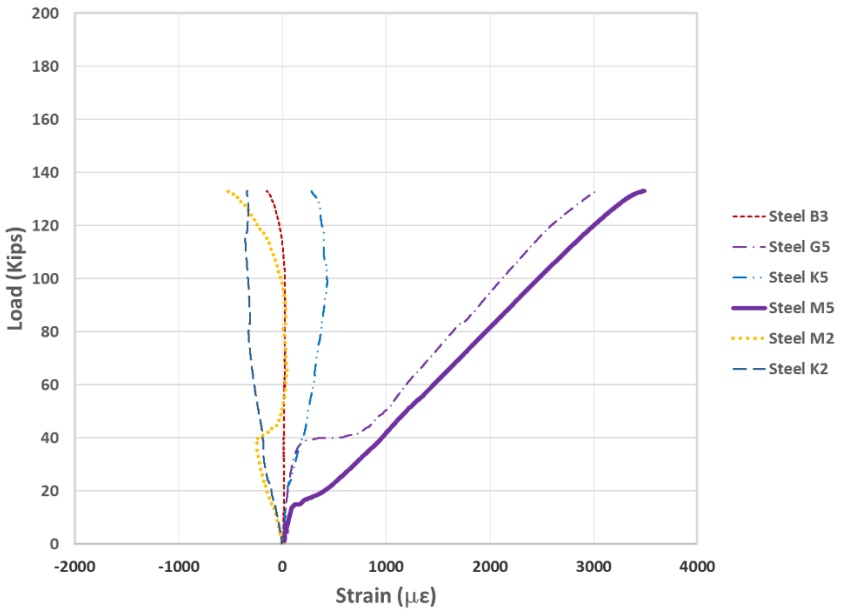

Figure 393 Load-strain response for SNFRC 0.75% beam #31 subjected to 6-month aging (Phase 4)

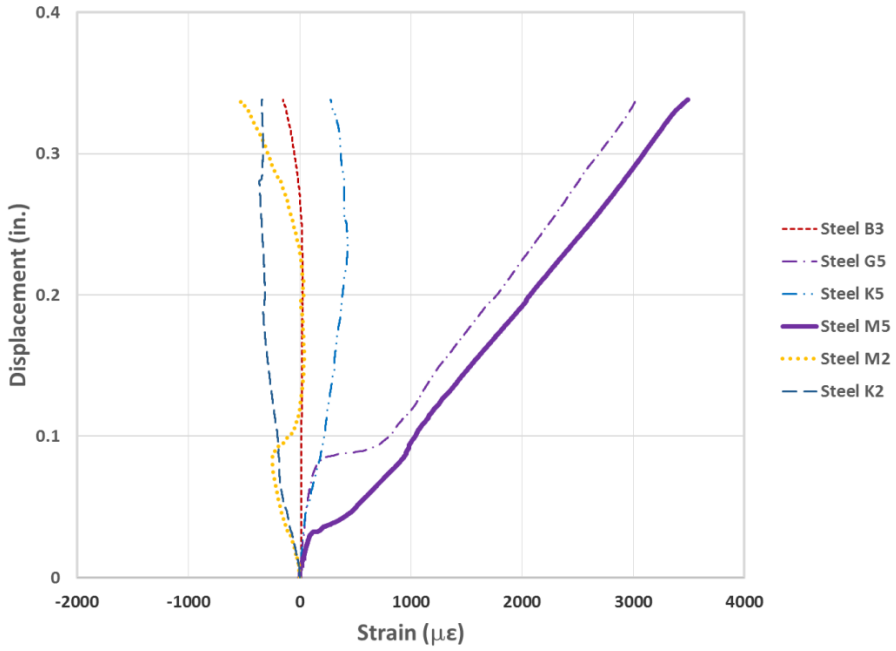

Figure 394 Displacement-strain response for SNFRC 0.75% beam #31 subjected to 6-month aging (Phase 4)

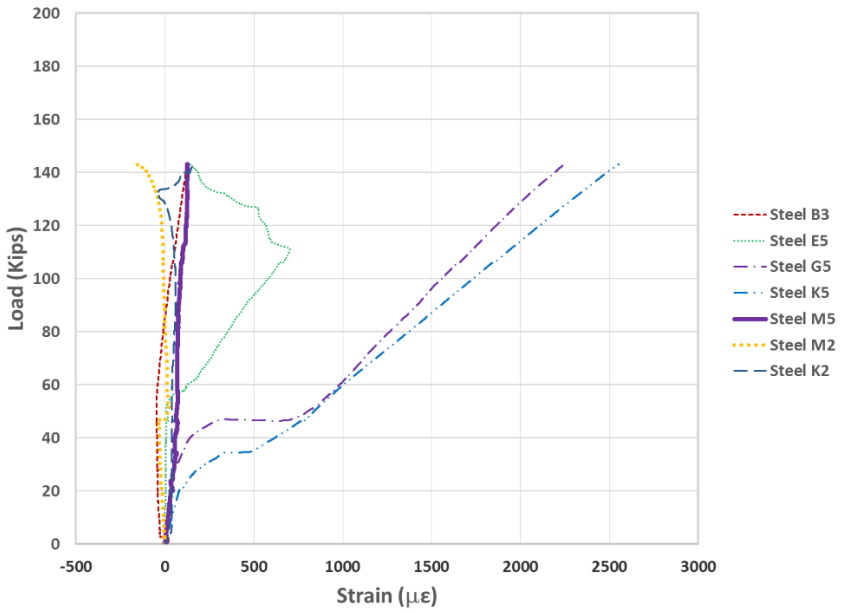

Figure 395 Load-strain response for SNFRC 0.75% beam #32 subjected to 6-month aging (Phase 4)

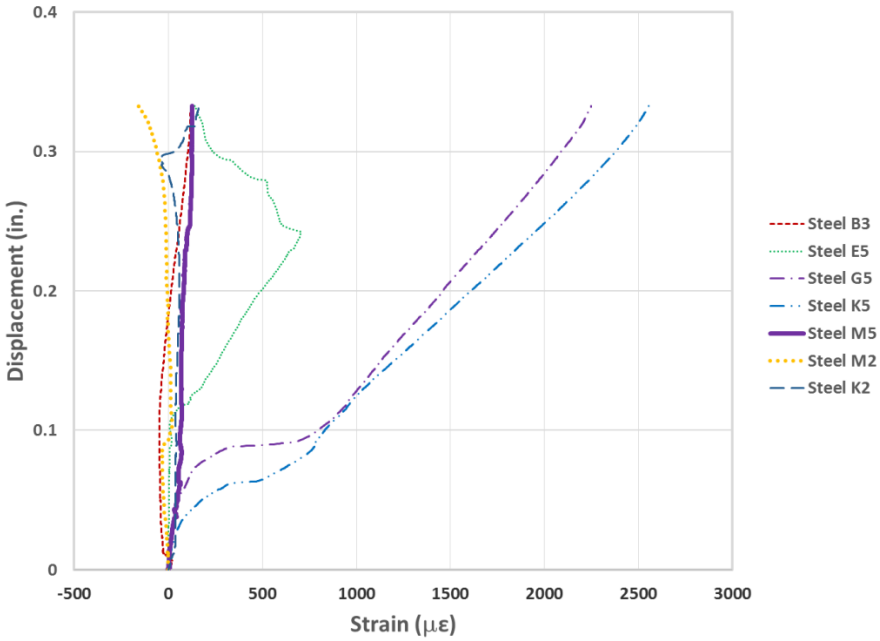

Figure 396 Displacement-strain response for SNFRC 0.75% beam #32 subjected to 6-month aging (Phase 4

Appendix I

Concrete Strain Gages

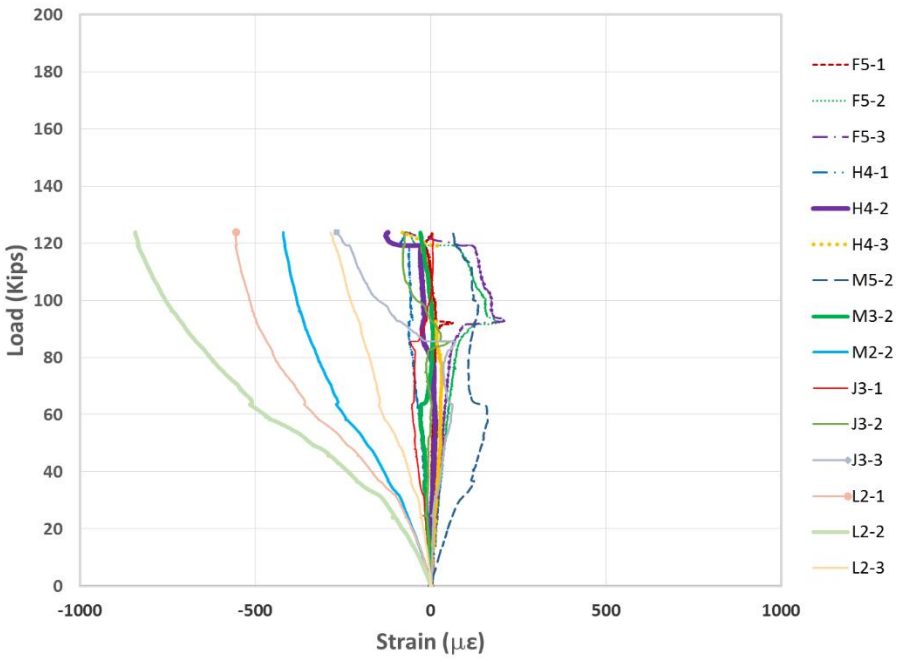

Figure 397 Load-strain response for RC beam #1 without aging

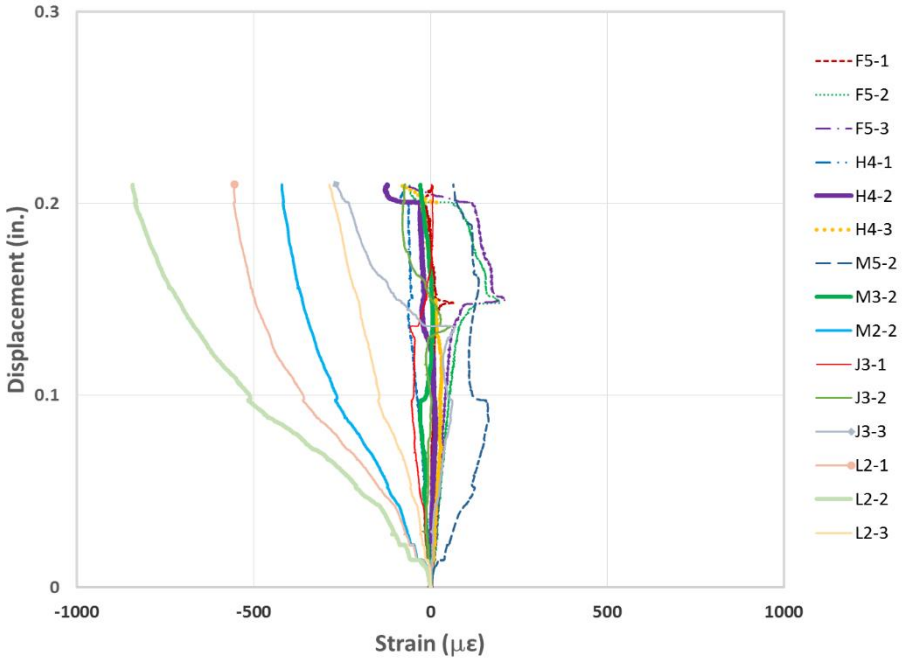

Figure 398 Displacement-strain response for RC beam #1 without aging

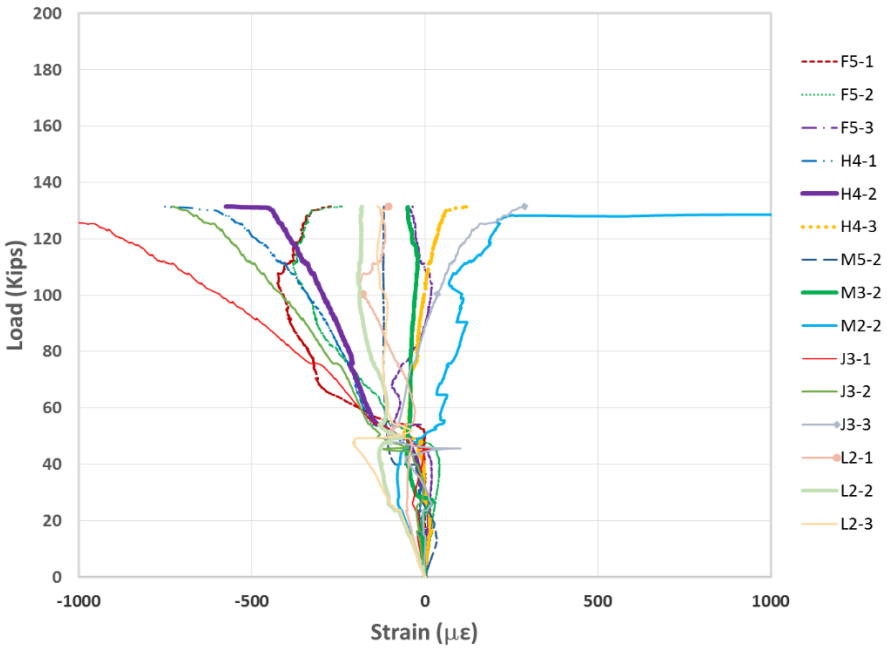

Figure 399 Load-strain response for RC beam #2 without aging

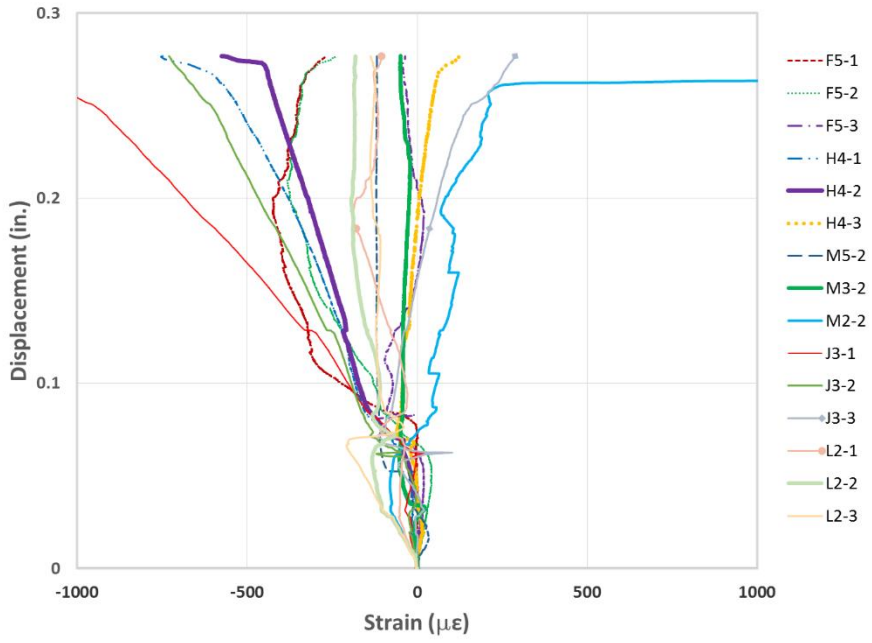

Figure 400 Displacement-strain response for RC beam #2 without aging

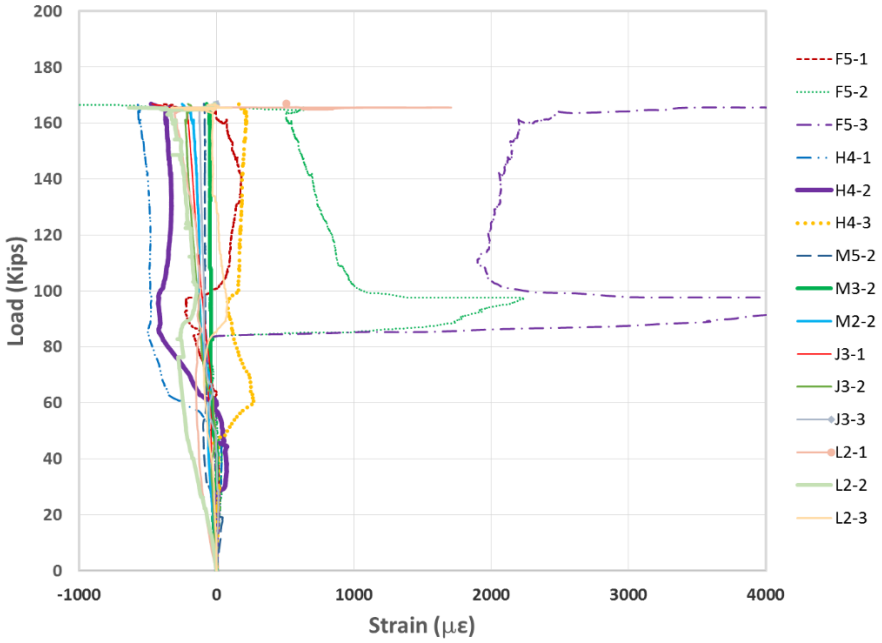

Figure 401 Load-strain response for RCS beam #3 without aging

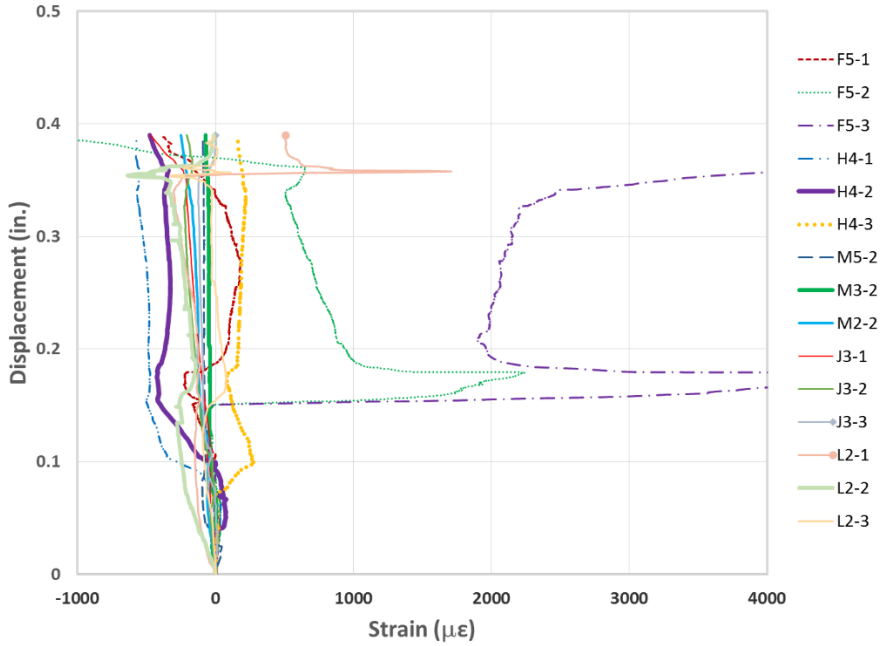

Figure 402 Displacement-strain response for RCS beam #3 without aging

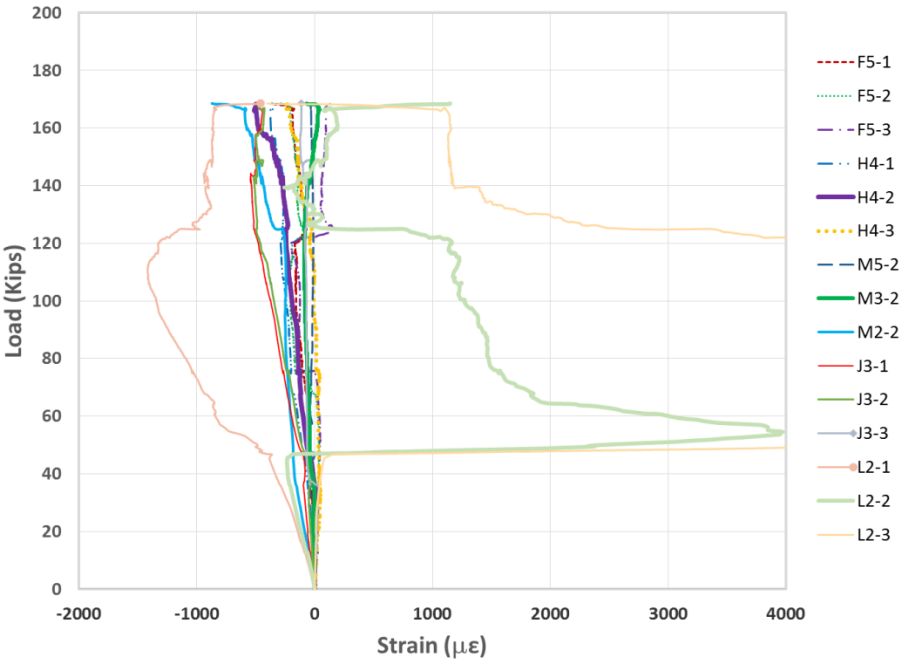

Figure 403 Load-strain response for RCS beam #4 without aging

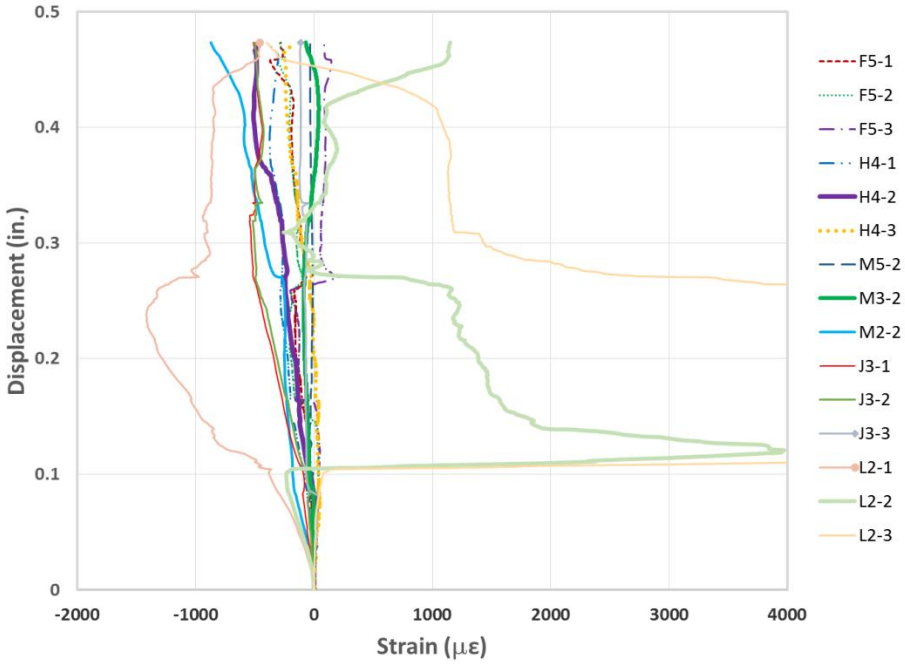

Figure 404 Displacement-strain response for RCS beam #4 without aging

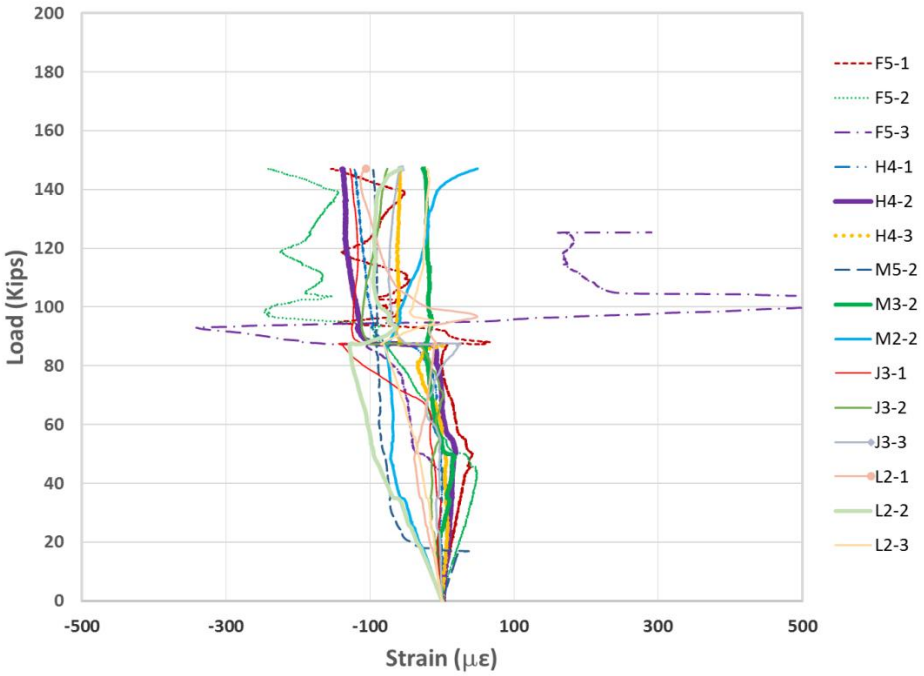

Figure 405 Load-strain response for SNFRC 0.5% beam #5 without aging

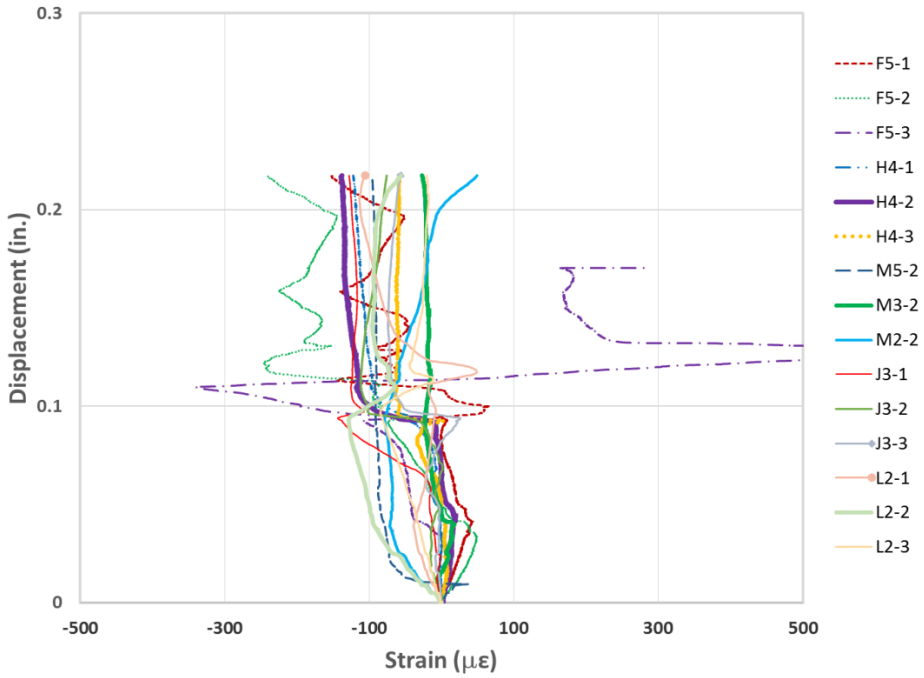

Figure 406 Displacement-strain response for SNFRC 0.5% beam #5 without aging

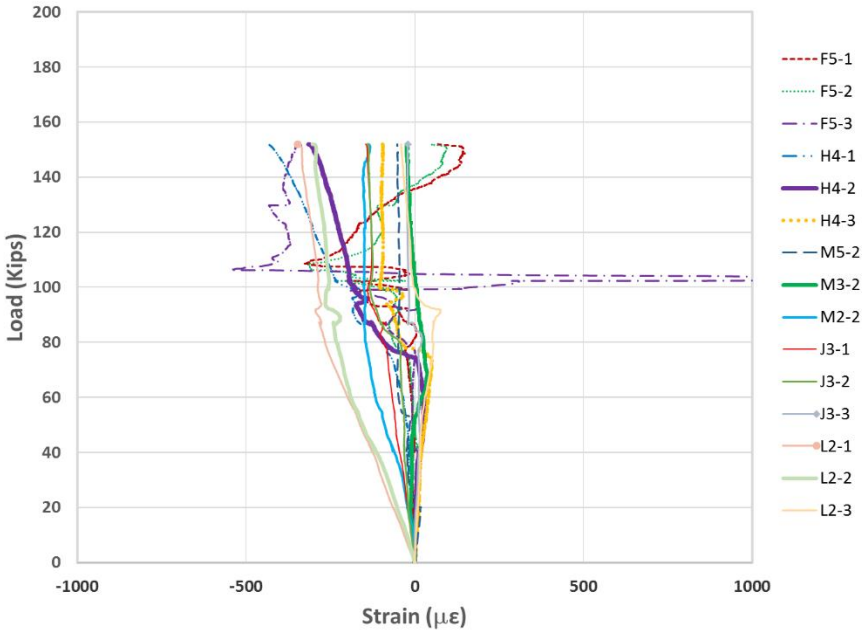

Figure 407 Load-strain response for SNFRC 0.5% beam #6 without aging

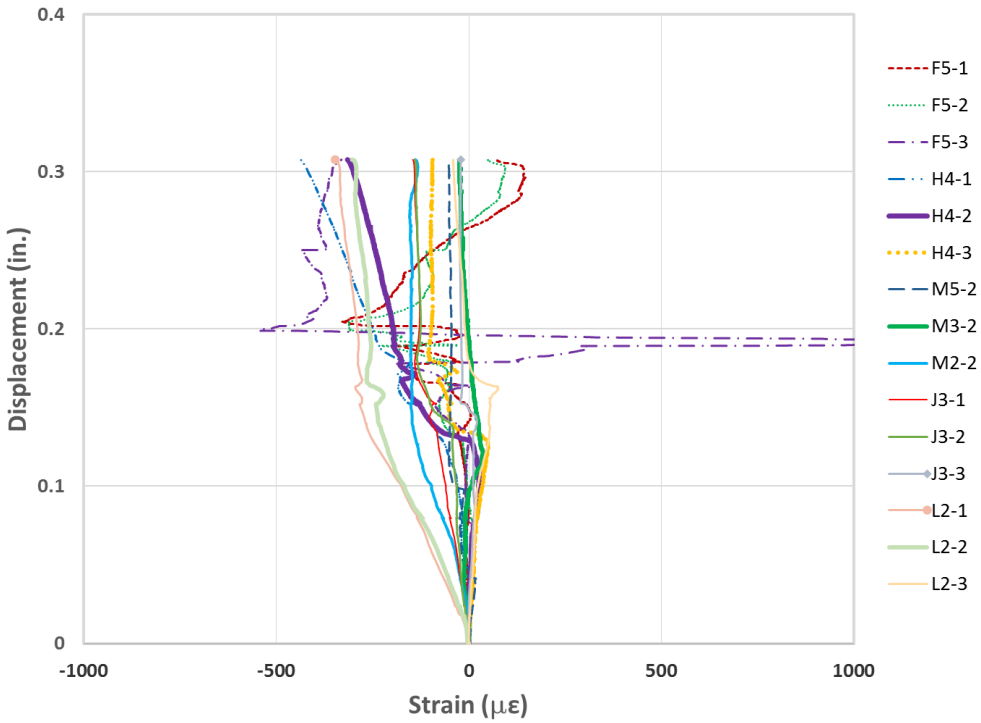

Figure 408 Displacement-strain response for SNFRC 0.5% beam #6 without aging

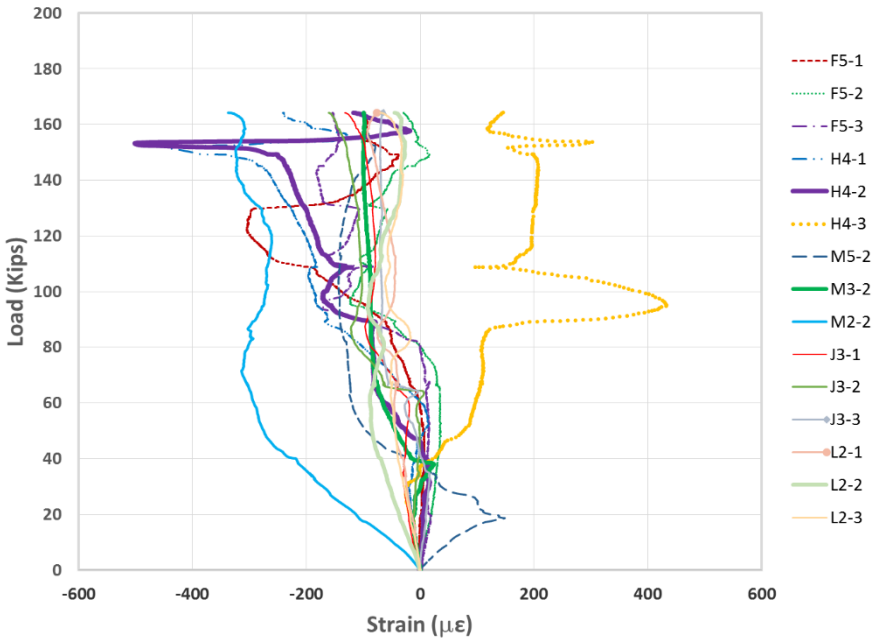

Figure 409 Load-strain response for SNFRC 0.75% beam #7 without aging

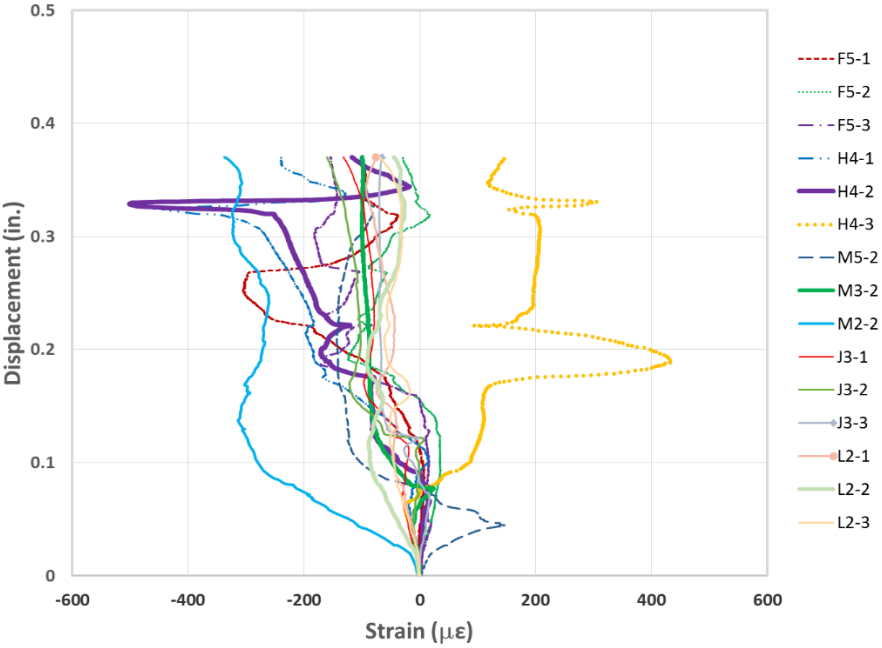

Figure 410 Displacement-strain response for SNFRC 0.75% beam #7 without aging

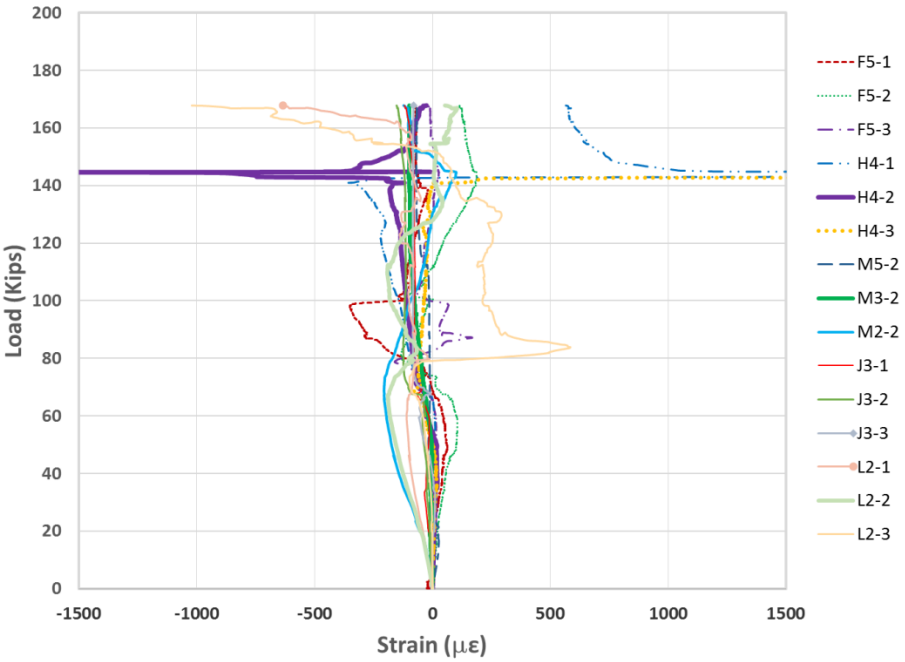

Figure 411 Load-strain response for SNFRC 0.75% beam #8 without aging

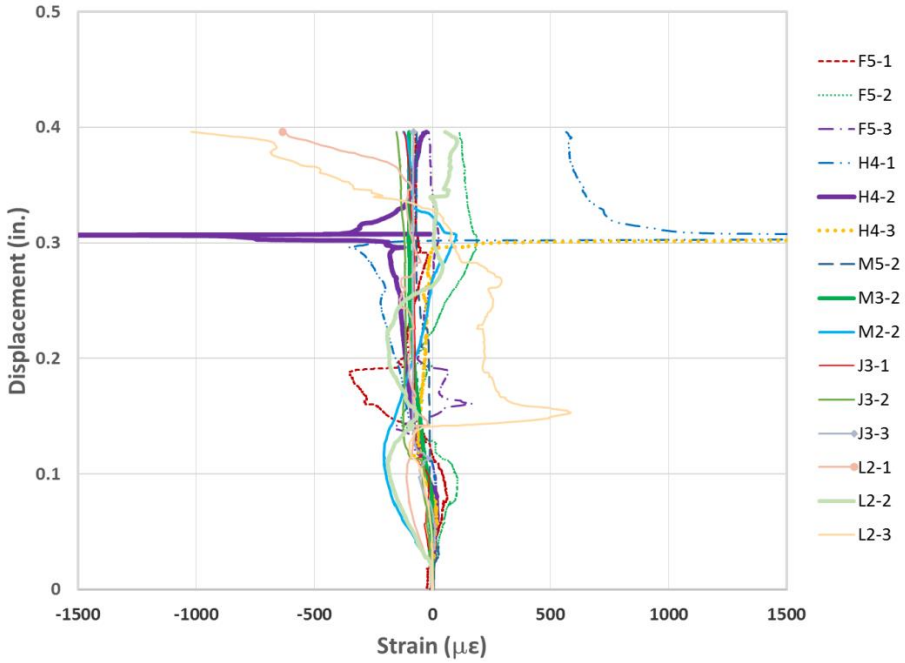

Figure 412 Displacement-strain response for SNFRC 0.75% beam #8 without aging

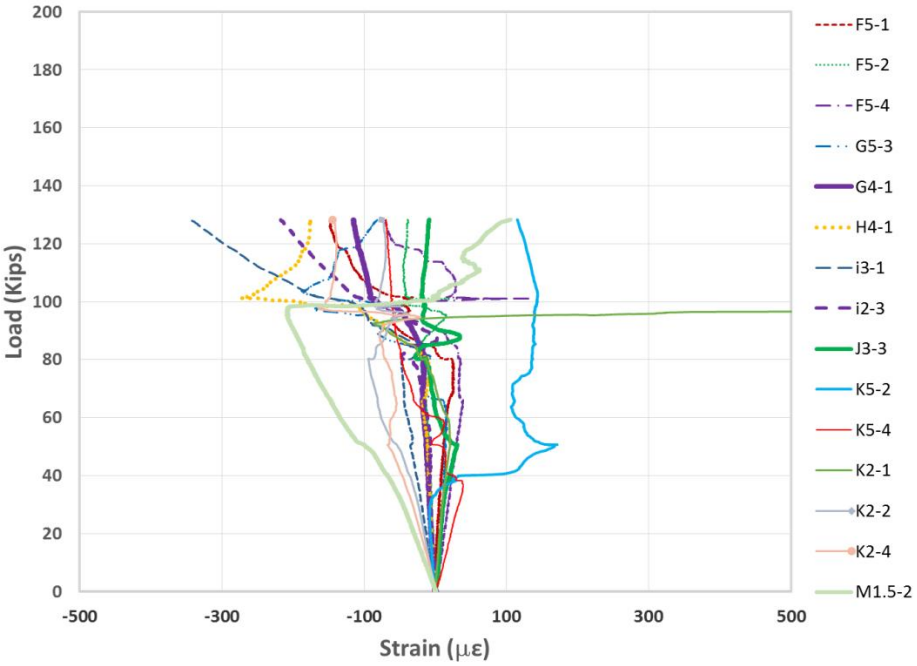

Figure 413 Load-strain response for RC beam #9 subjected to 1 month of aging (PH. 2)

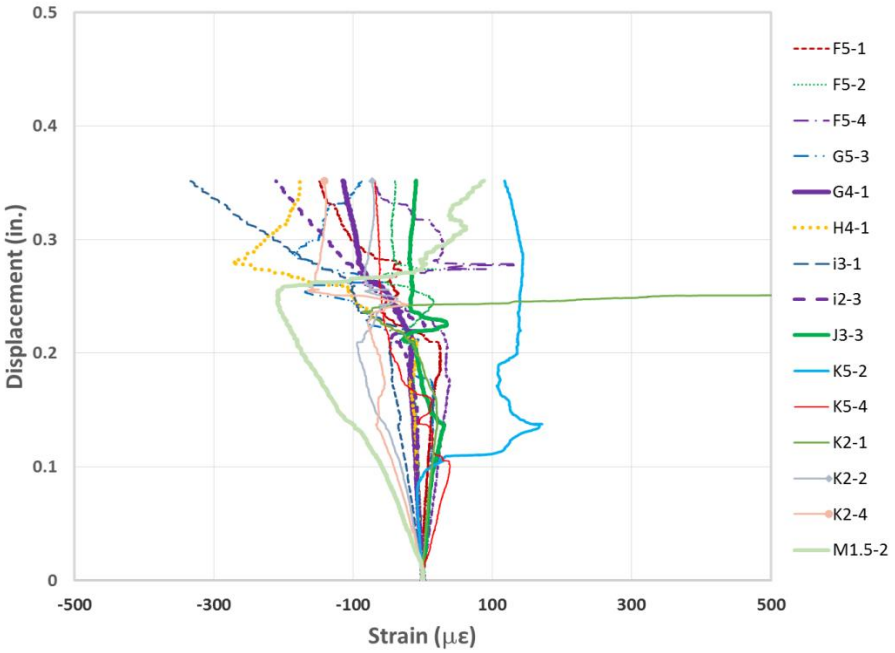

Figure 414 Displacement-strain response for RC beam #9 subjected to 1 month of aging (PH. 2)

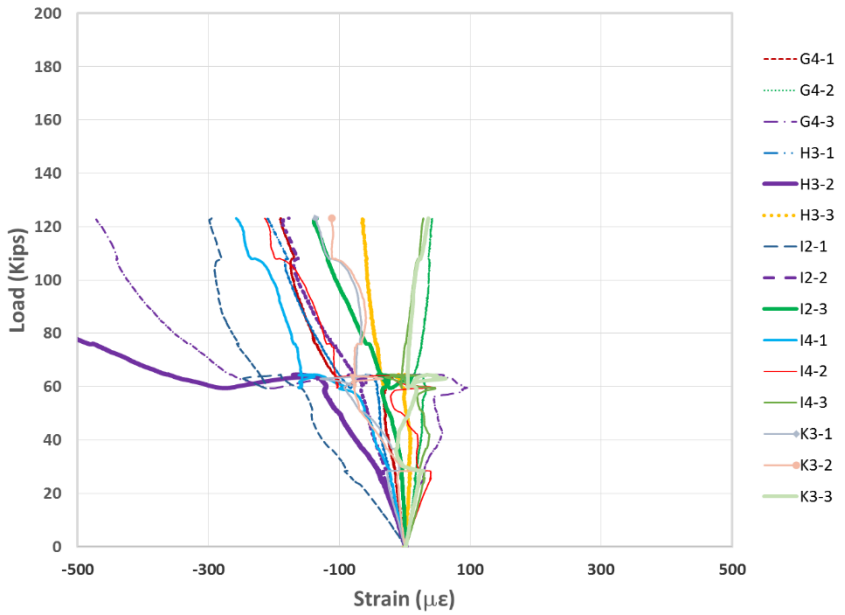

Figure 415 Load-strain response for RC beam #10 subjected to 1month aging (PH. 2)

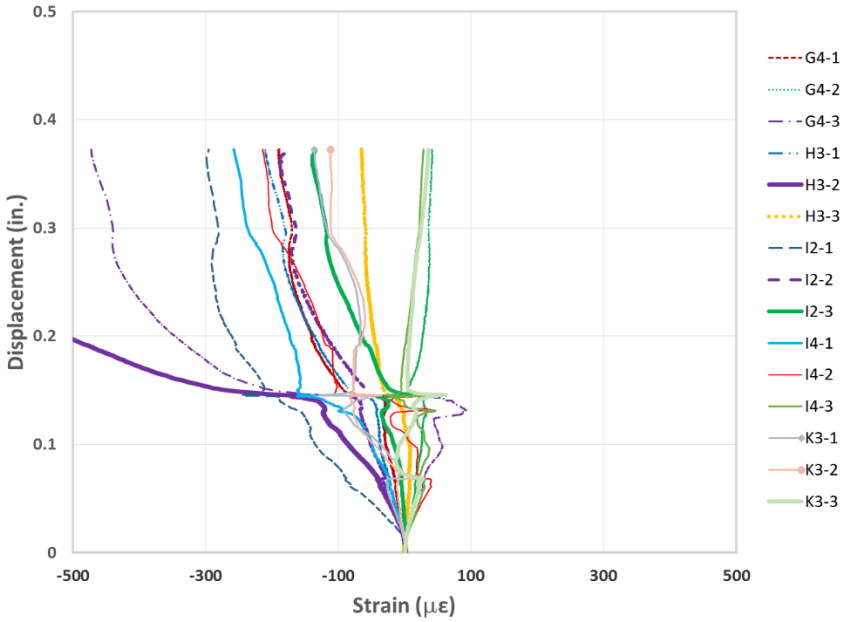

Figure 416 Displacement-strain response for RC beam #10 subjected to 1month of aging (PH. 2)

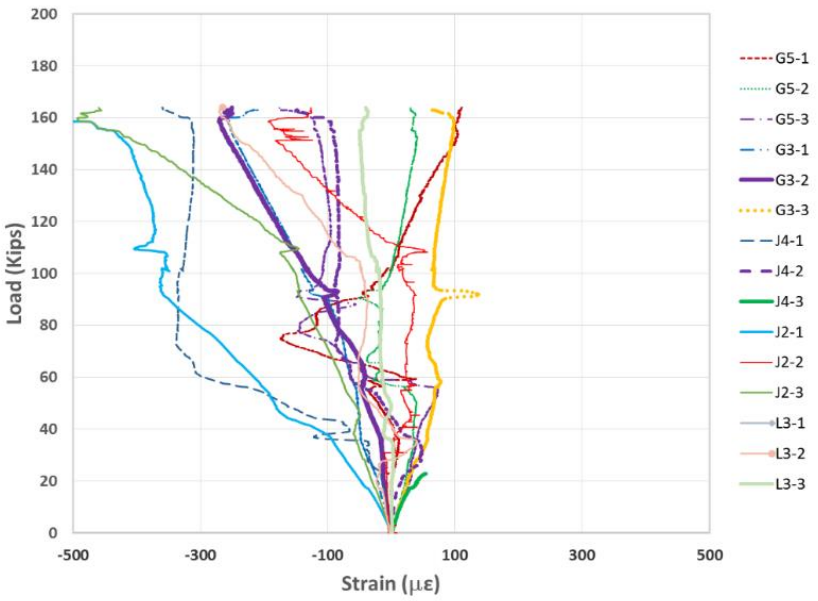

Figure 417 Load-strain response for RCS beam #11 subjected to 1 month of aging (PH. 2)

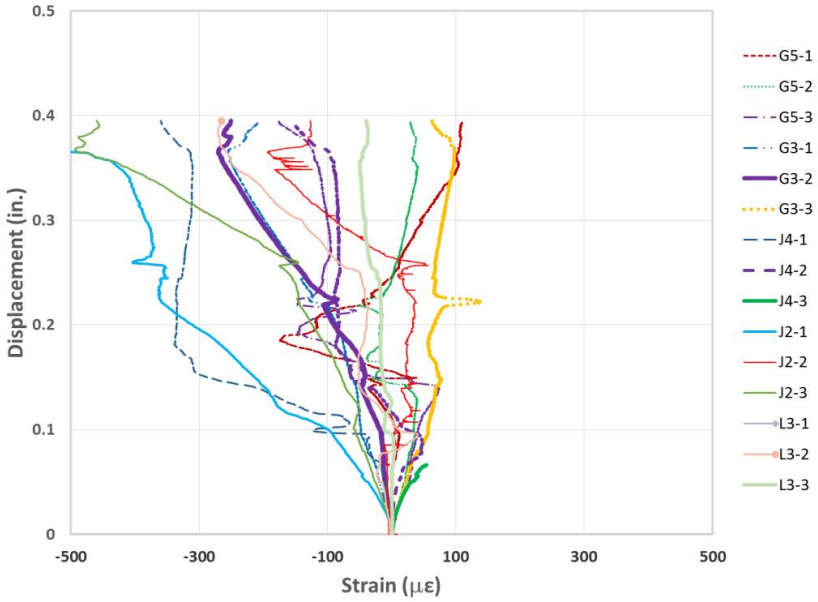

Figure 418 Displacement-strain response for RCS beam #11 subjected to 1 month of aging (PH. 2)

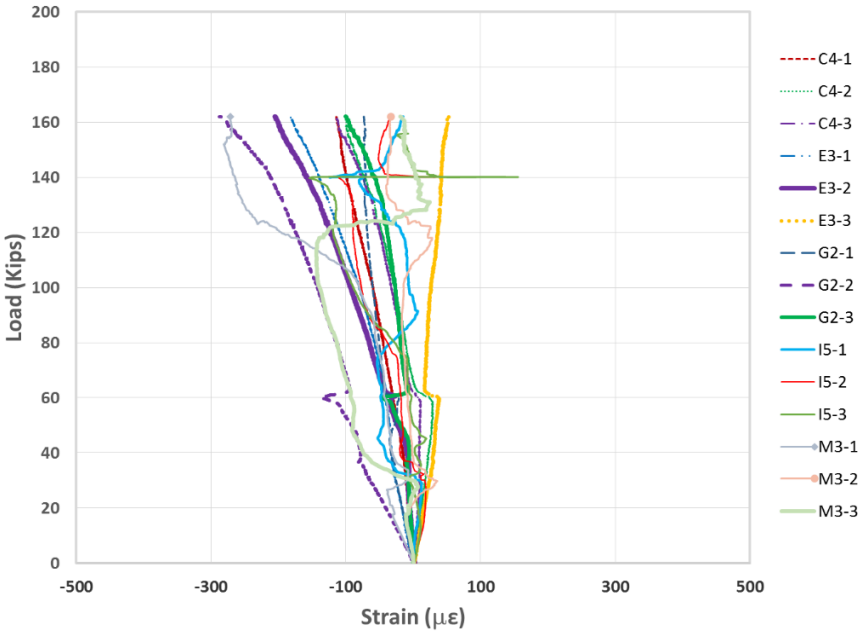

Figure 419 Load-strain response for RCS beam #12 subjected to 1 month of aging (PH. 2)

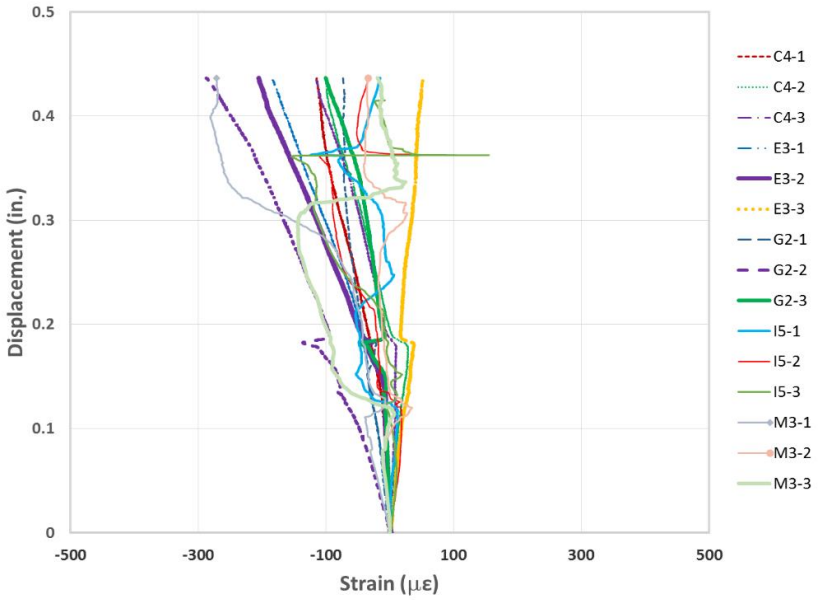

Figure 420 Displacement-strain response for RCS beam #12 subjected to 1 month of aging (PH. 2)

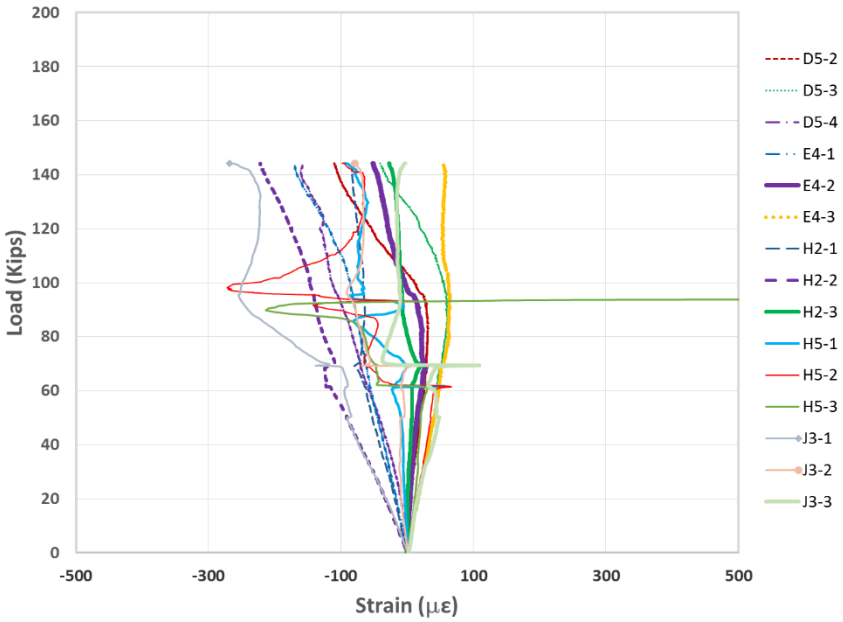

Figure 421 Load-strain response for SNFRC 0.5% beam #13 subjected to 1 month of aging (PH. 2)

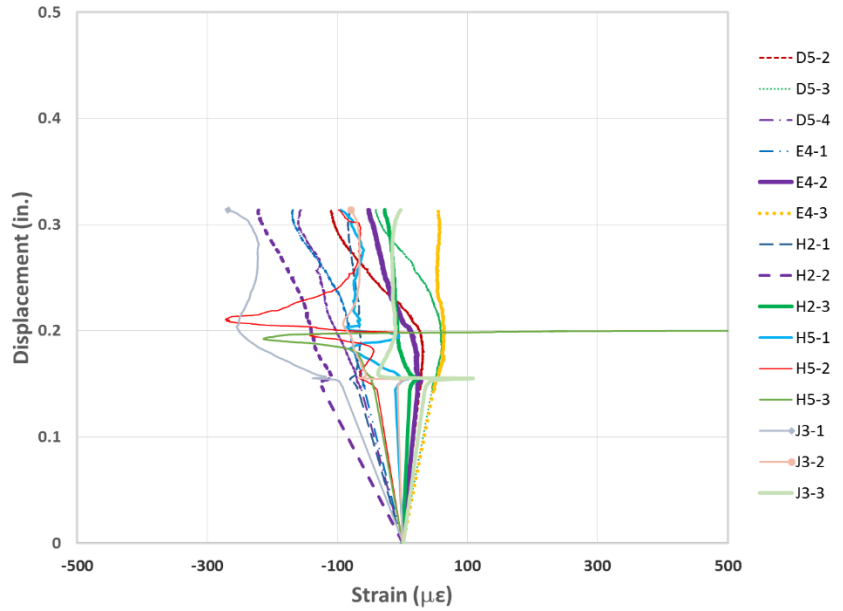

Figure 422 Displacement-strain response for SNFRC 0.5% beam #13 subjected to 1 month of aging (PH. 2)

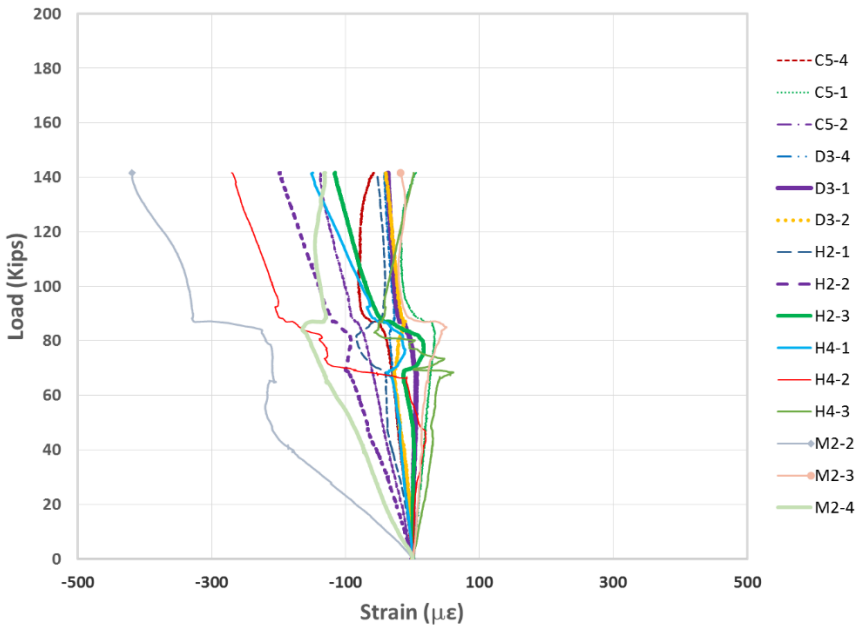

Figure 423 Load-strain response for SNFRC 0.5% beam #14 subjected to 1 month of aging (PH. 2)

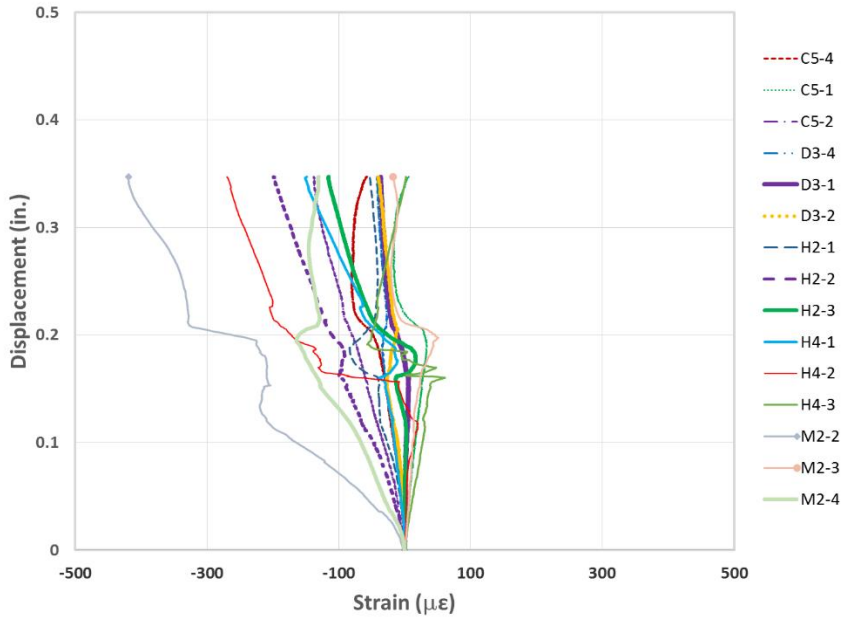

Figure 424 Displacement-strain response for SNFRC 0.5% beam #14 subjected to 1 month of aging (PH. 2)

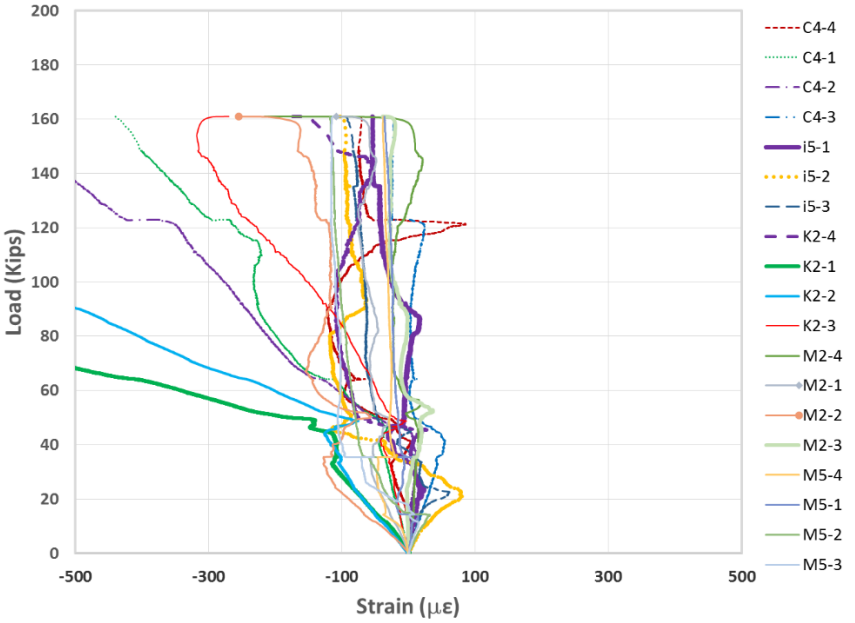

Figure 425 Load-strain response for SNFRC 0.75% beam #15 subjected to 1 month of aging (PH. 2)

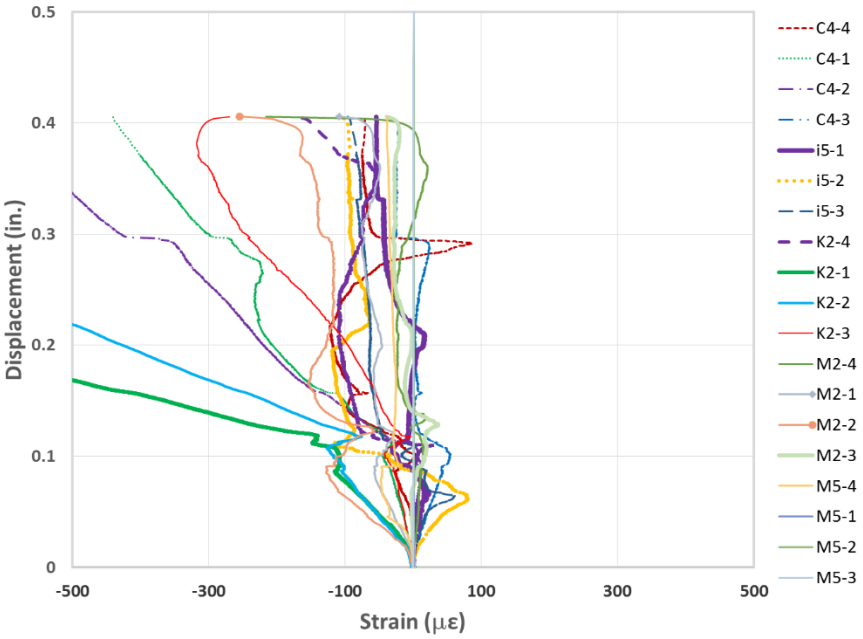

Figure 426 Displacement-strain response for SNFRC 0.75% beam #15 subjected to 1 month of aging (PH. 2)

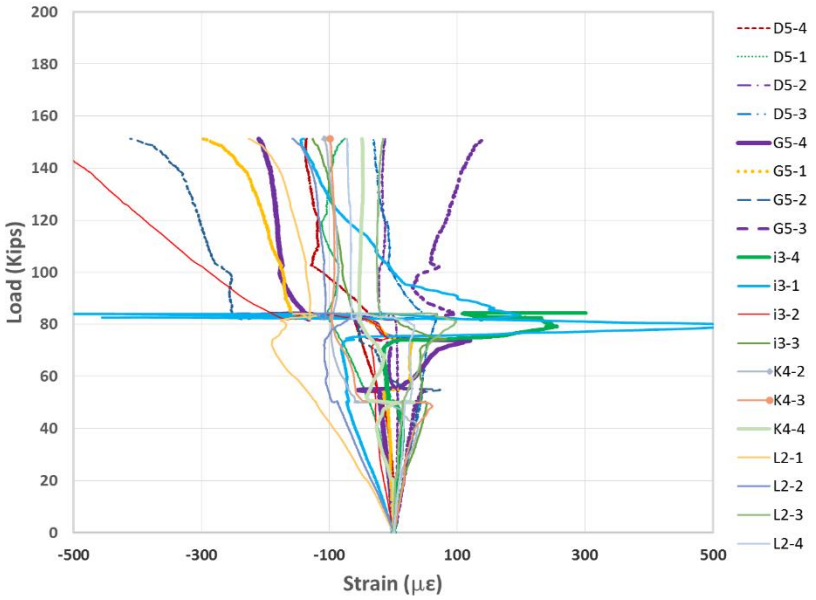

Figure 427 Load-strain response for SNFRC 0.75% beam #16 subjected to 1 month of aging (PH. 2)

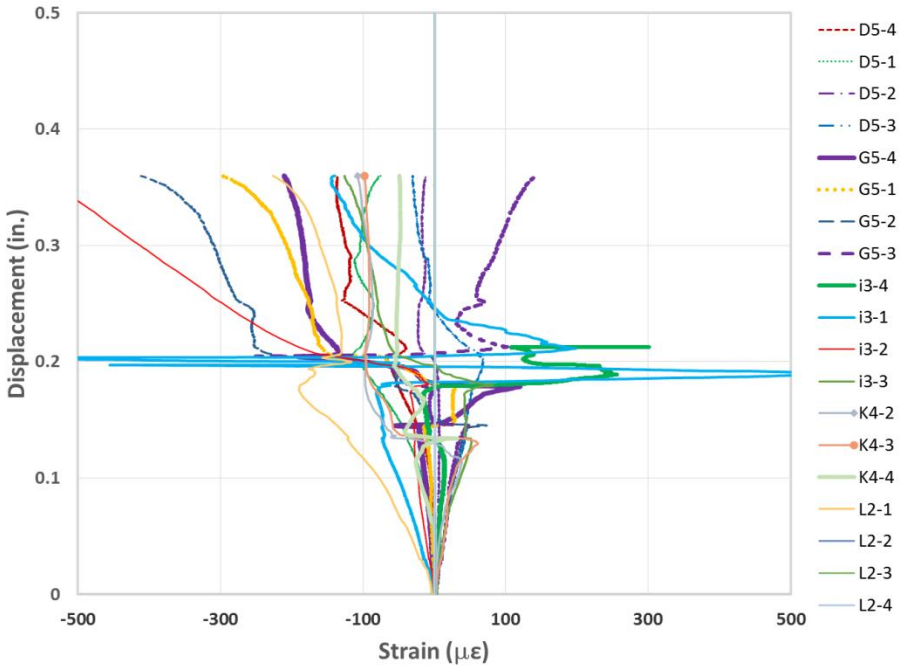

Figure 428 Displacement-strain response for SNFRC 0.75% beam #16 subjected to 1 month of aging (PH. 2)

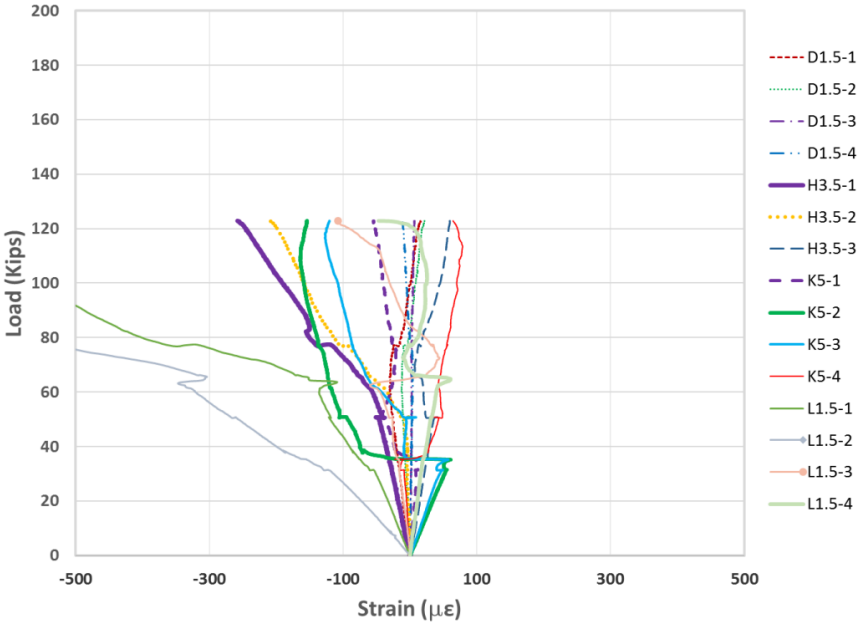

Figure 429 Load-strain response for RC beam #17 subjected to 3 months of aging (PH. 3)

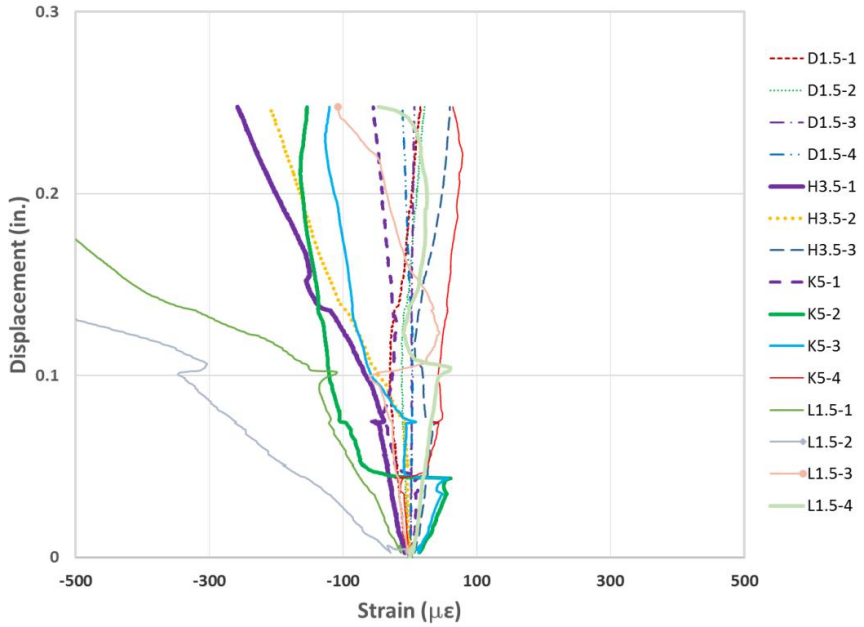

Figure 430 Displacement-strain response for RC beam #17 subjected to 3 months of aging (PH. 3

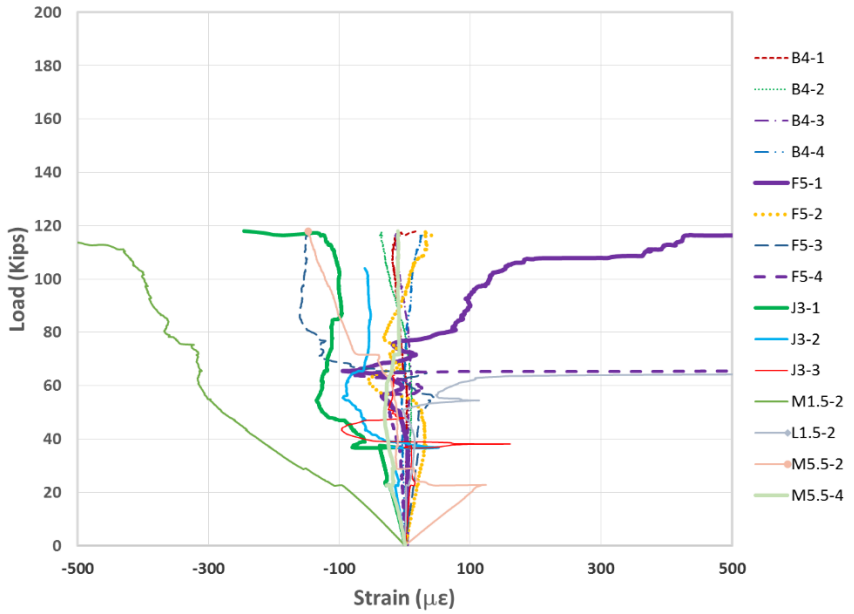

Figure 431 Load-strain response for RC beam #18 subjected to 3 months of aging (PH. 3)

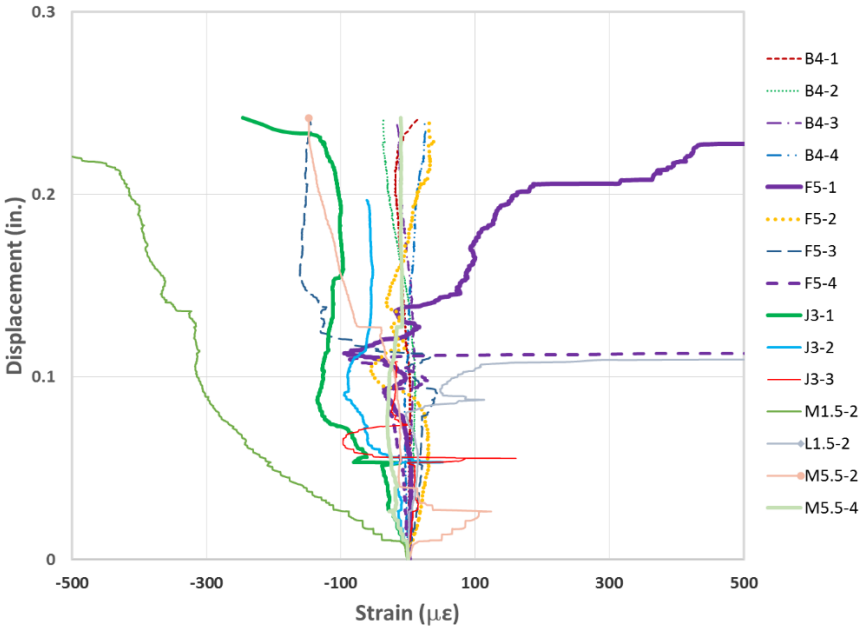

Figure 432 Displacement-strain response for RC beam #18 subjected to 3 months of aging (PH. 3)

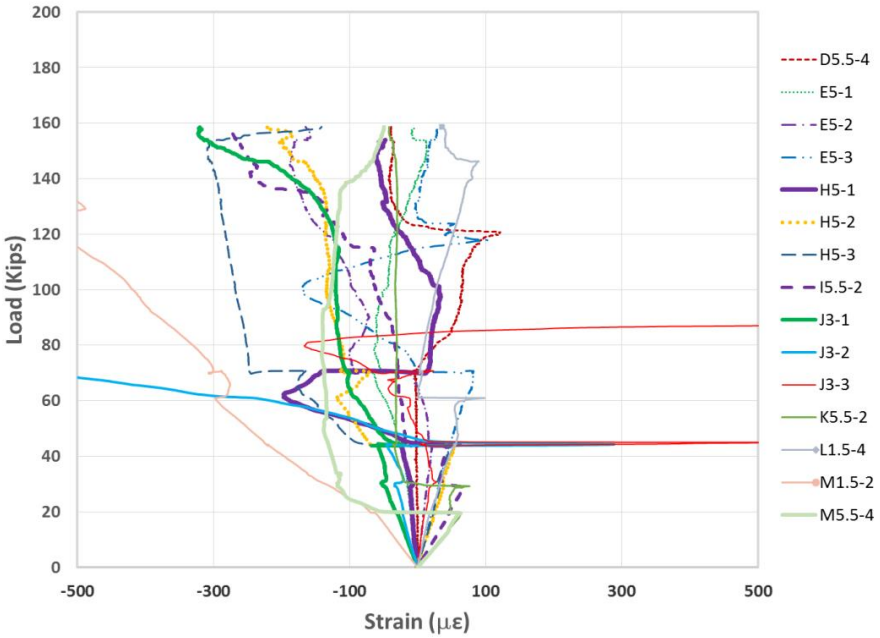

Figure 433 Load-strain response for RCS beam #19 subjected to 3 months of aging (PH. 3)

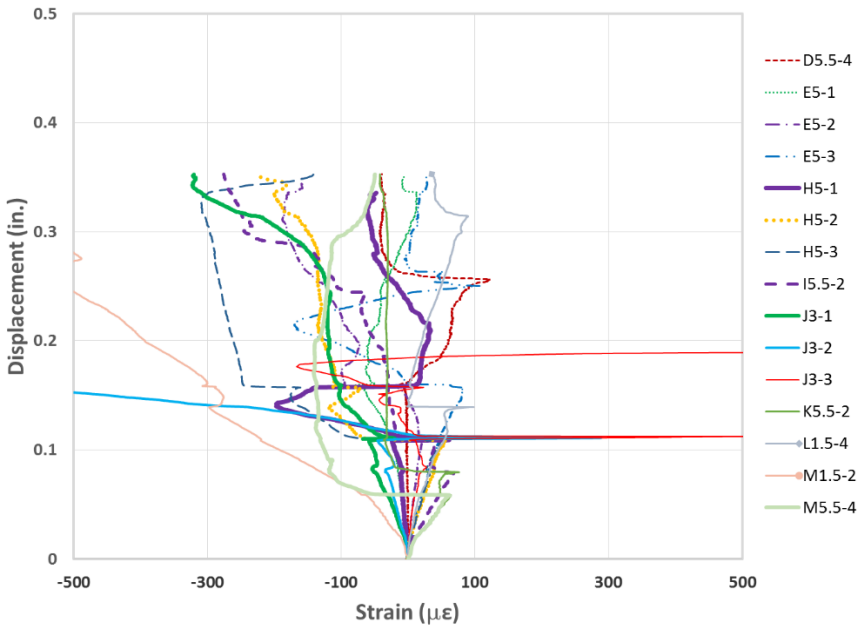

Figure 434 Displacement-strain response for RCS beam #19 subjected to 3 months of aging (PH. 3)

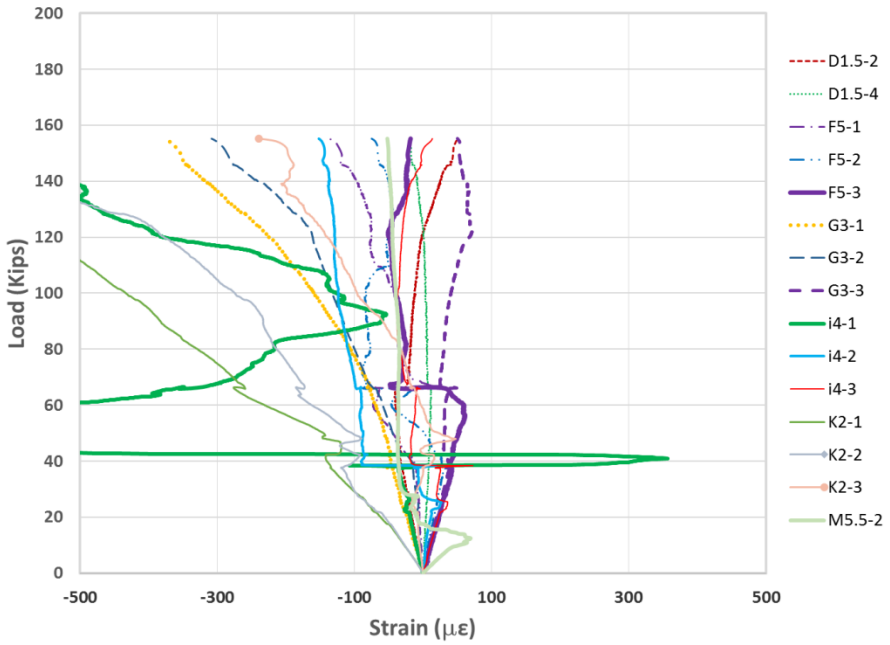

Figure 435 Load-strain response for RCS beam #20 subjected to 3 months of aging (PH. 3)

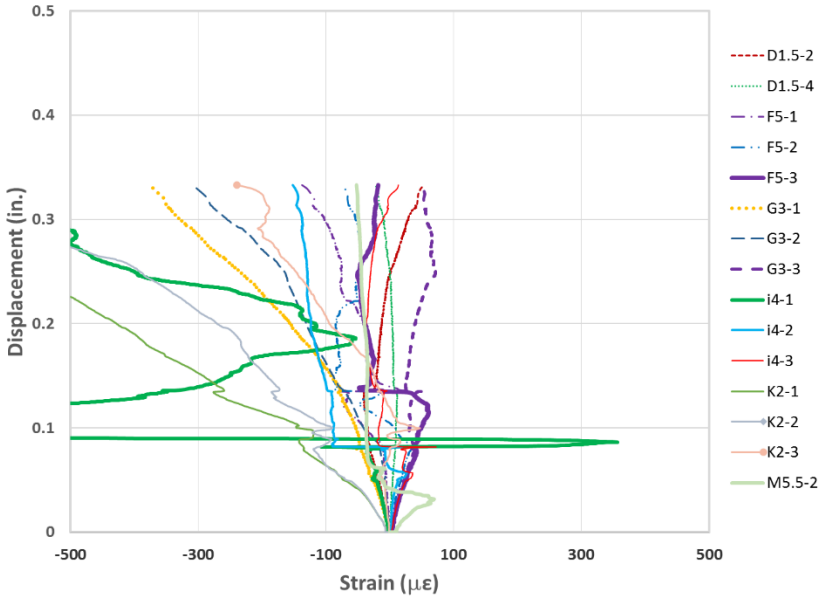

Figure 436 Displacement-strain response for RCS beam #20 subjected to 3 months of aging (PH. 3)

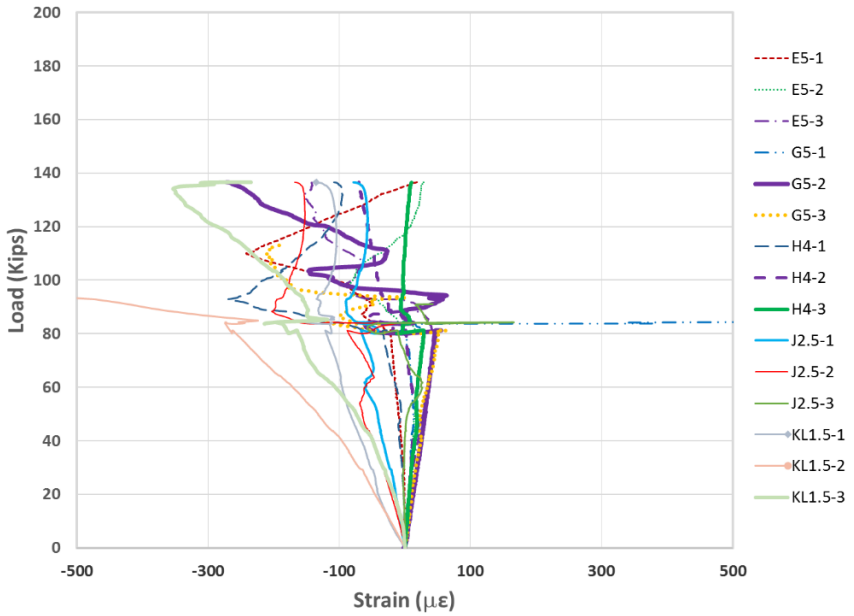

Figure 437 Load-strain response for SNFRC 0.5% beam #21 subjected to 3 months of aging (PH. 3)

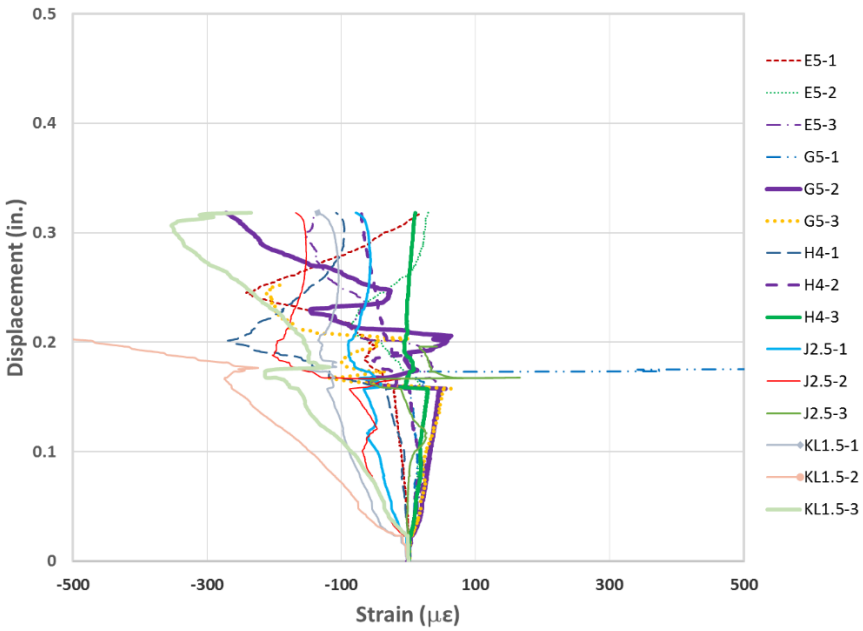

Figure 438 Displacement-strain response for SNFRC 0.5% beam #21 subjected to 3 months of aging (PH. 3)

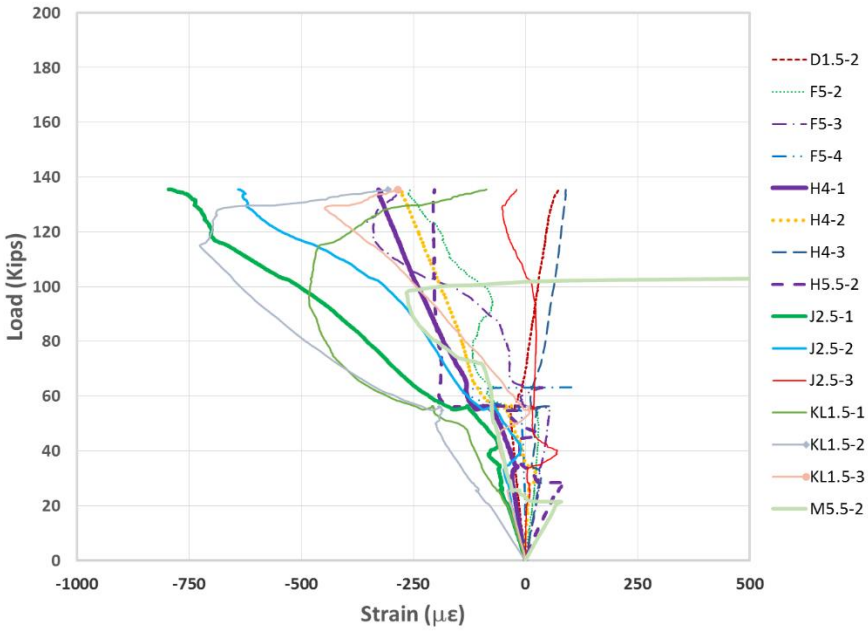

Figure 439 Load-strain response for SNFRC 0.5% beam #22 subjected to 3 months of aging (PH. 3)

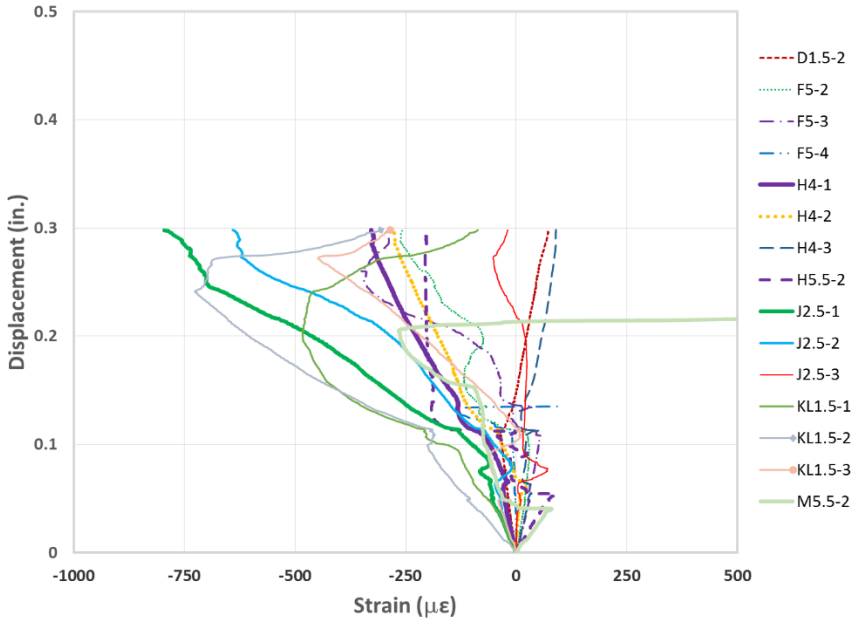

Figure 440 317 Displacement-strain response for SNFRC 0.5% beam #22 subjected to 3 months of aging (PH. 3)

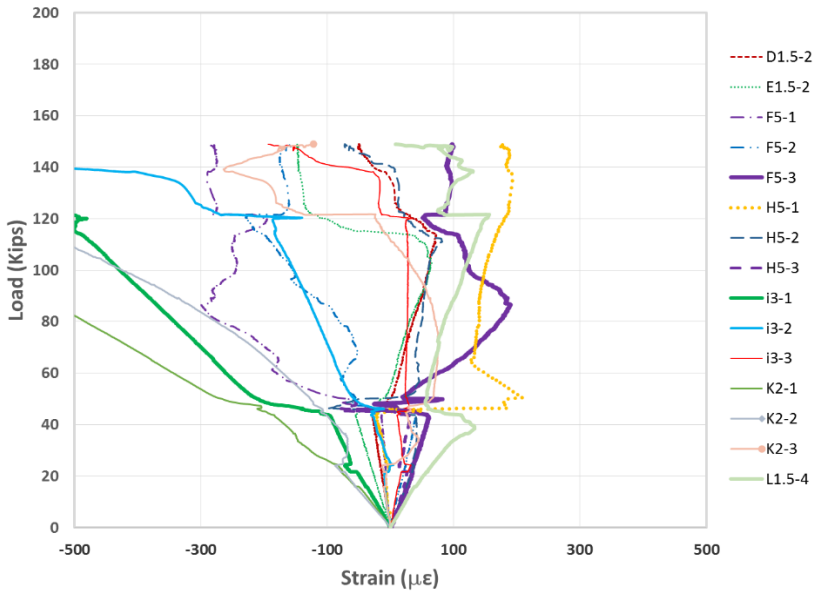

Figure 441 Load-strain response for SNFRC 0.75% beam #23 subjected to 3 months of aging (PH. 3)

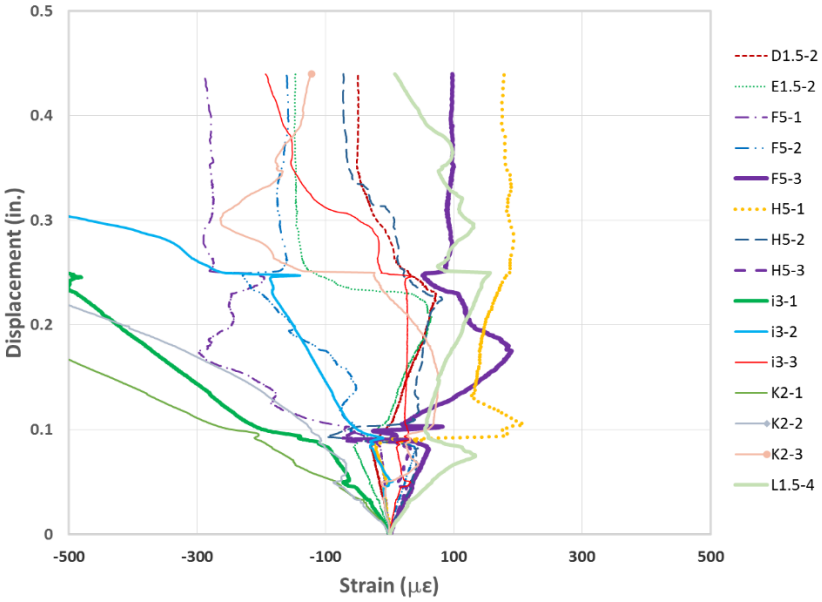

Figure 442 Displacement-strain response for SNFRC 0.75% beam #23 subjected to 3 months of aging (PH. 3)

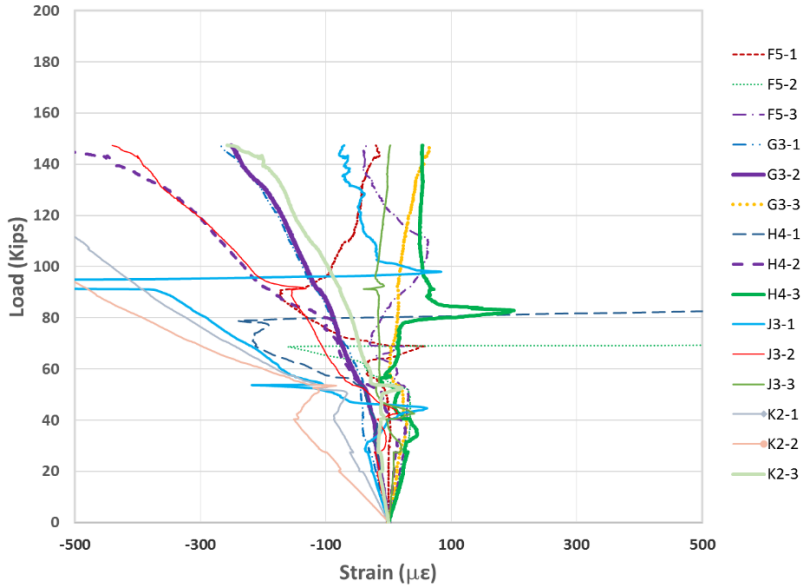

Figure 443 Load-strain response for SNFRC 0.75% beam #24 subjected to 3 months of aging (PH. 3)

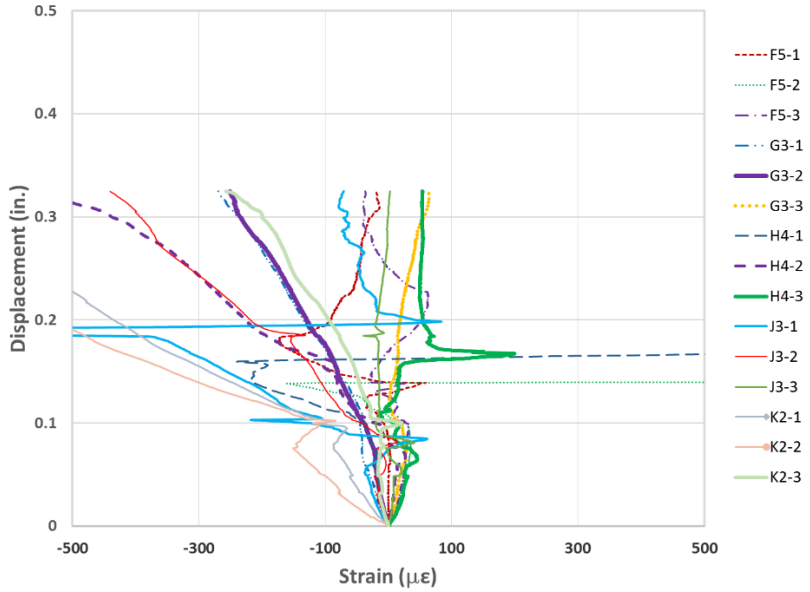

Figure 444 Displacement-strain response for SNFRC 0.75% beam #24 subjected to 3 months of aging (PH. 3)

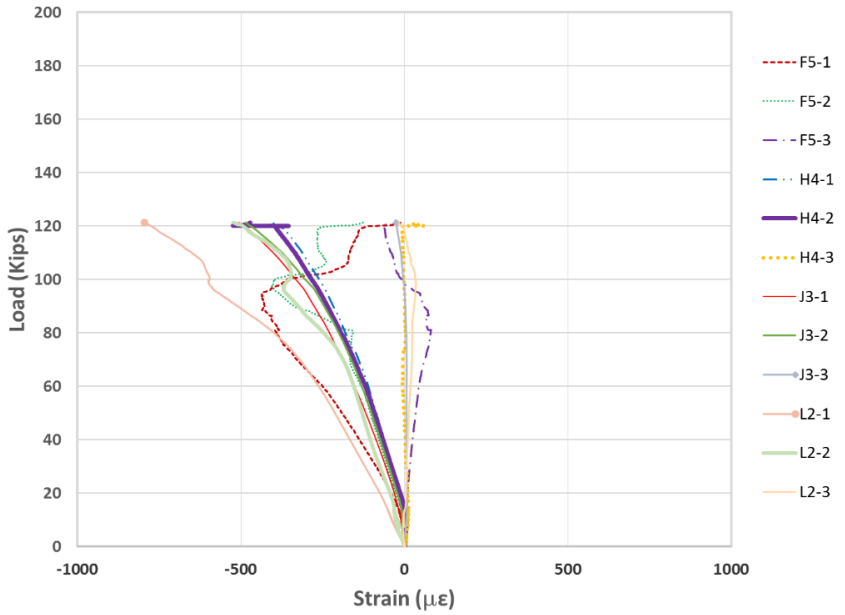

Figure 445 Load-strain response for RC beam #25 subjected to 6 months of aging (PH. 4)

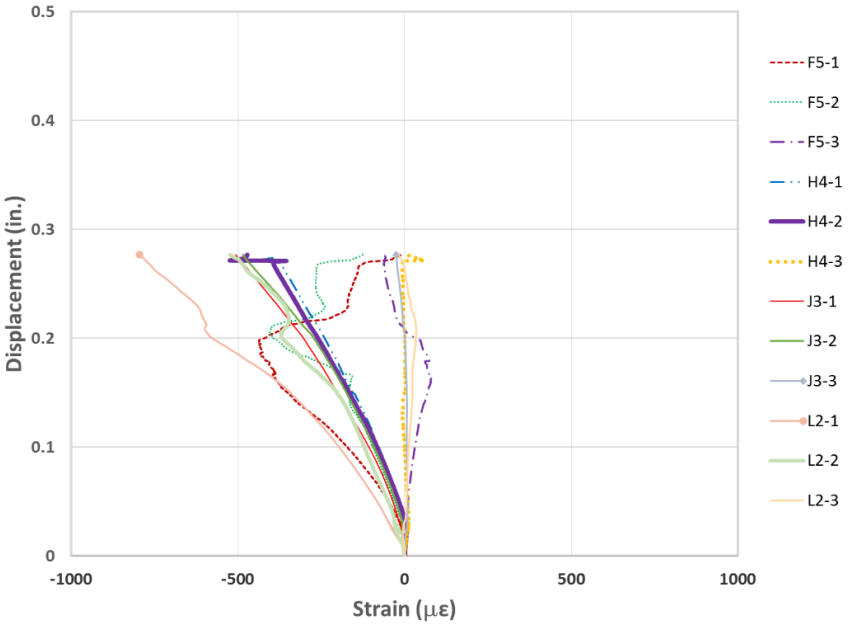

Figure 446 Displacement-strain response for RC beam #25 subjected to 6 months of aging (PH. 4)

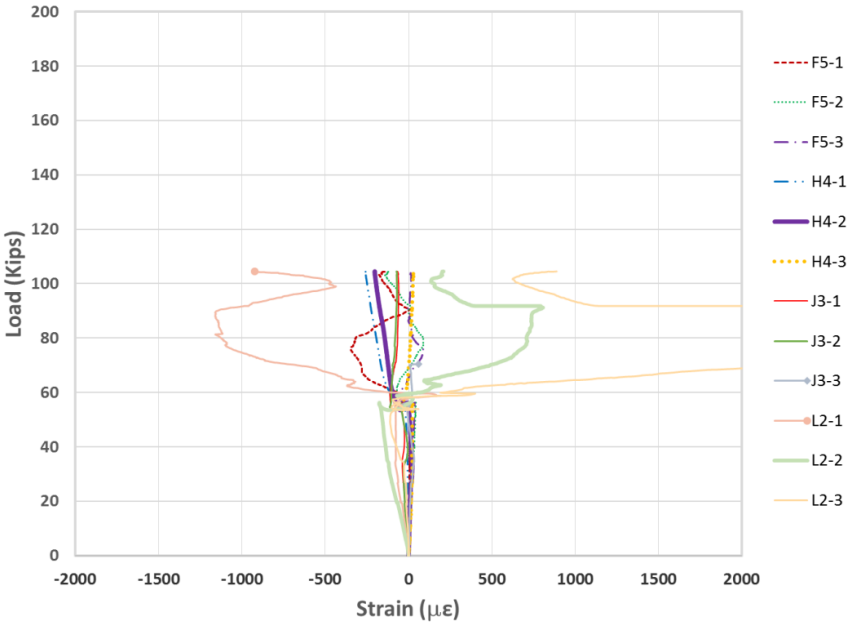

Figure 447 Load-strain response for RC beam #26 subjected to 6 months of aging (PH. 4)

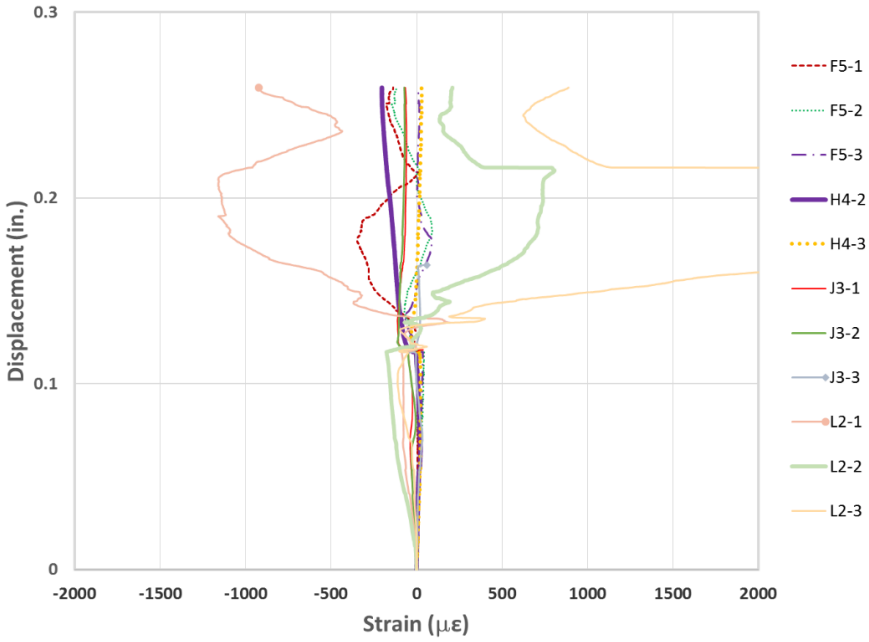

Figure 448 Displacement-strain response for RC beam #26 subjected to 6 months of aging (PH. 4)

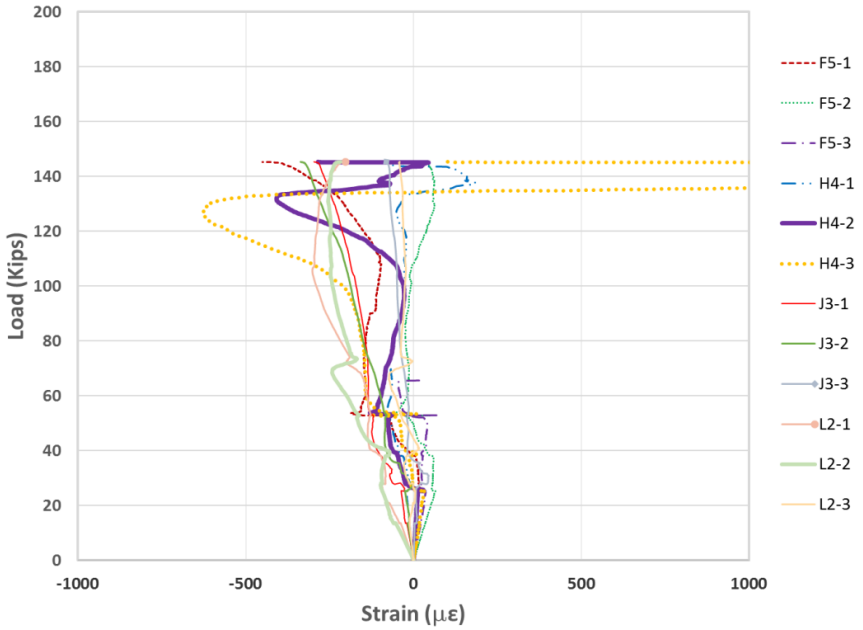

Figure 449 Load-strain response for RCS beam #27 subjected to 6 months of aging (PH. 4)

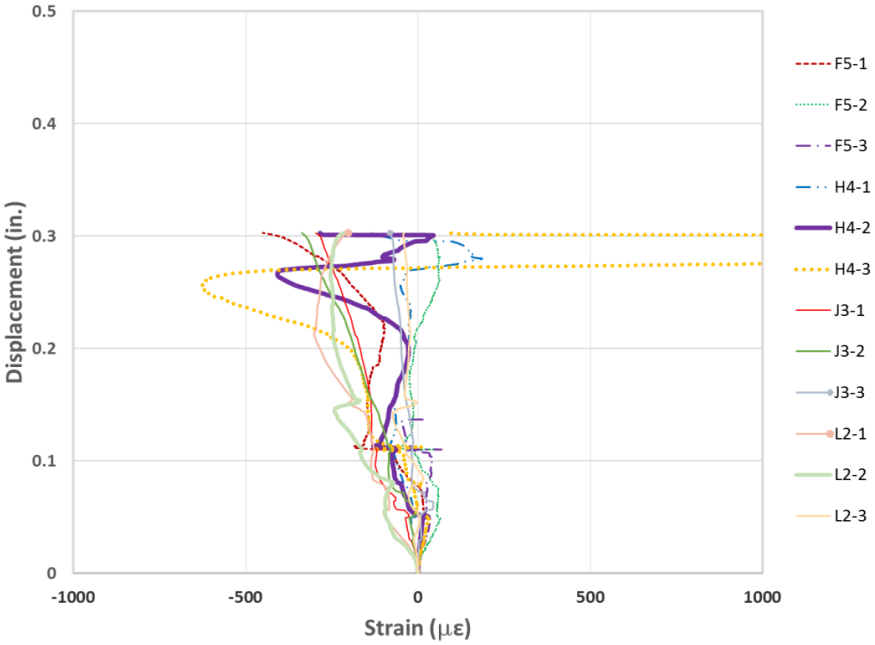

Figure 450 Displacement-strain response for RCS beam #27 subjected to 6 months of aging (PH. 4)

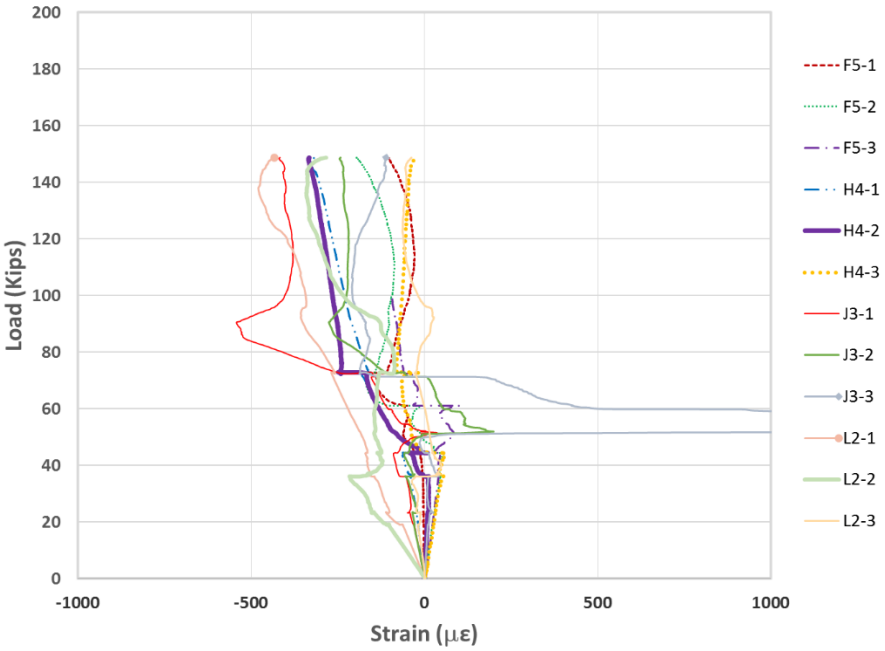

Figure 451 Load-strain response for RCS beam #28 subjected to 6 months of aging (PH. 4)

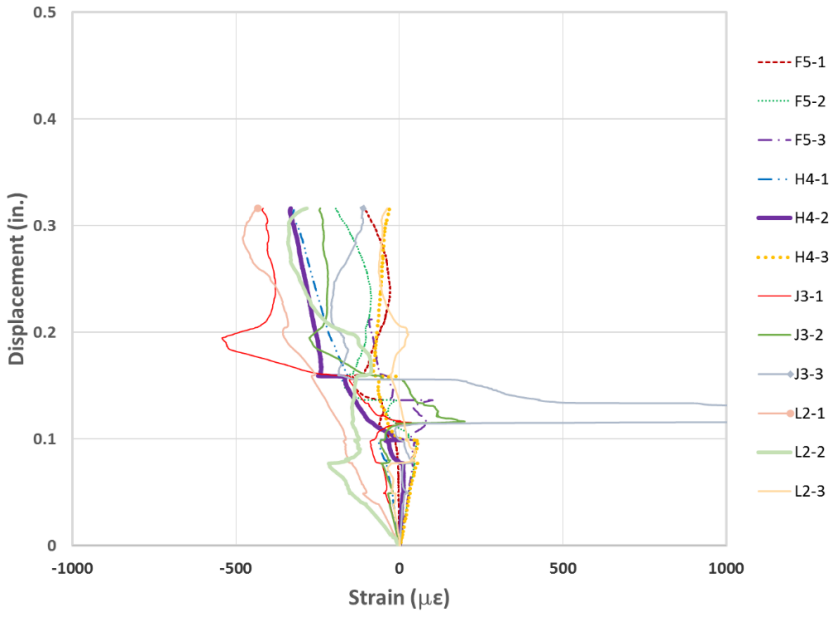

Figure 452 Displacement-strain response for RCS beam #28 subjected to 6 months of aging (PH. 4)

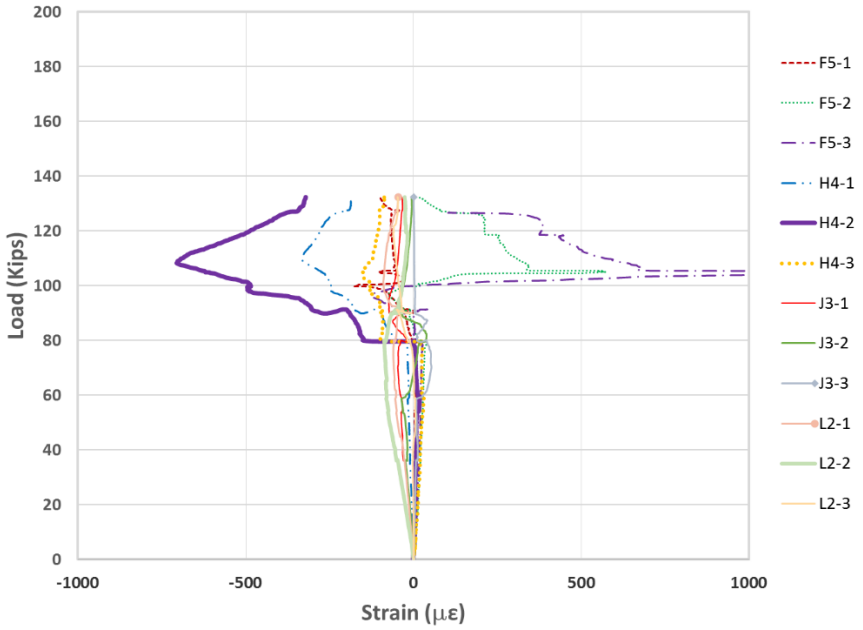

Figure 453 Load-strain response for SNFRC 0.5% beam #29 subjected to 6 months of aging (PH. 4)

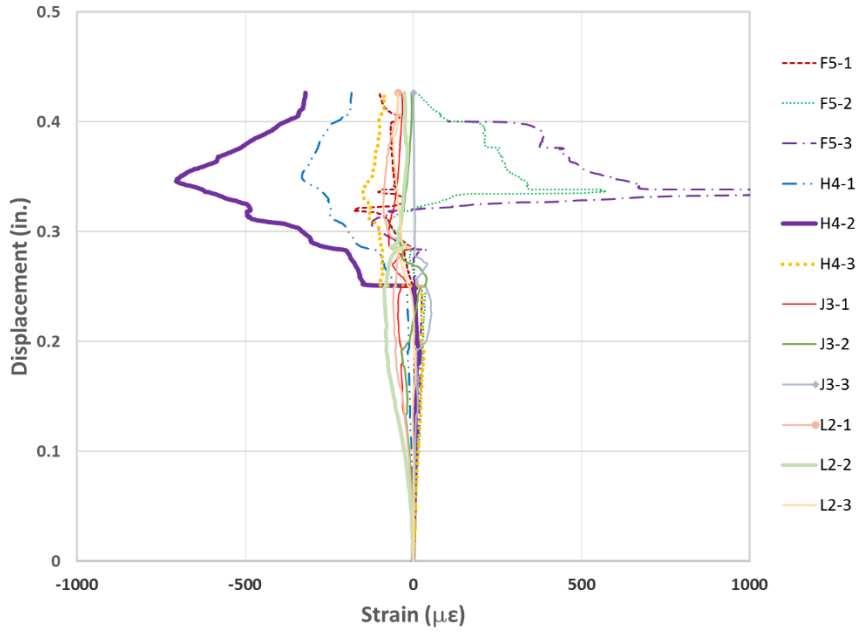

Figure 454 Displacement-strain response for SNFRC 0.5% beam #29 subjected to 6 months of aging (PH. 4)

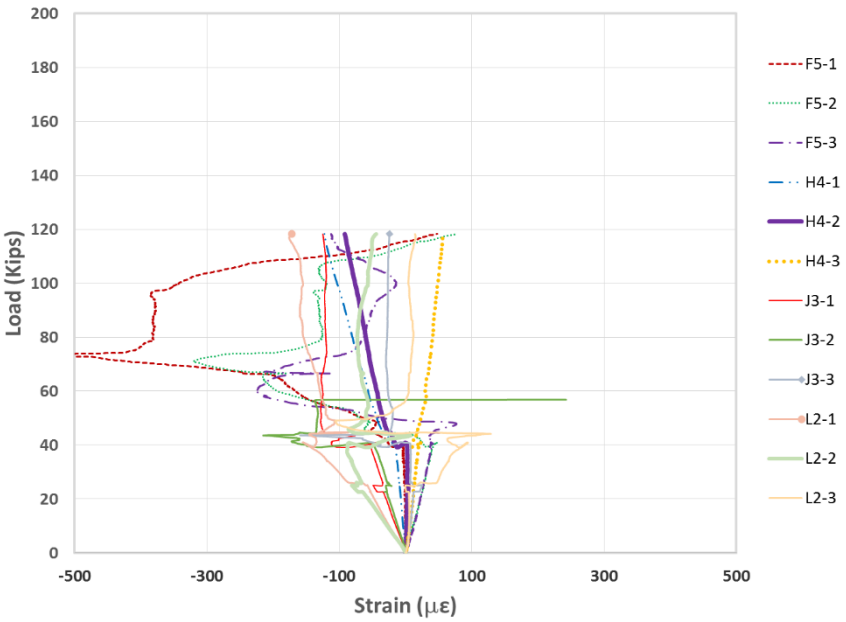

Figure 455 Load-strain response for SNFRC 0.5% beam #30 subjected to 6 months of aging (PH. 4)

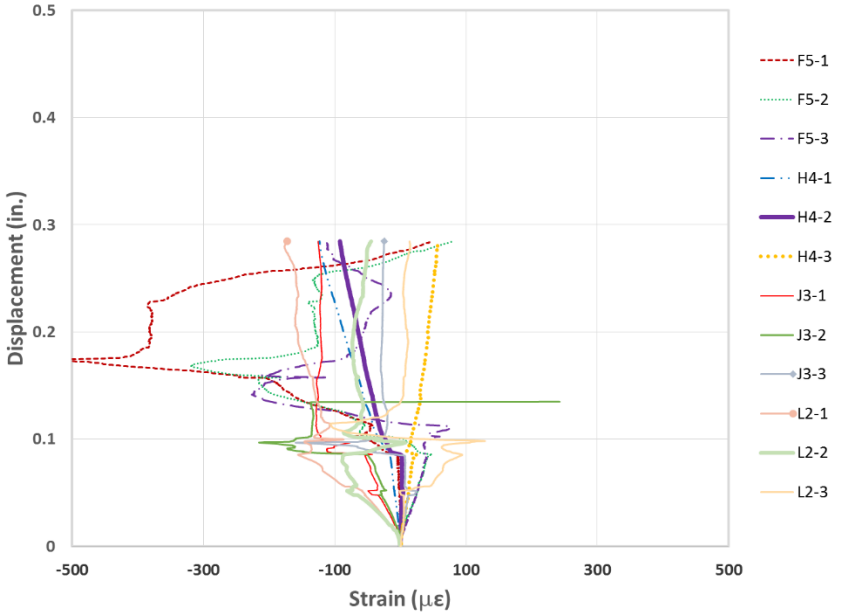

Figure 456 Displacement-strain response for SNFRC 0.5% beam #30 subjected to 6 months of aging (PH. 4)

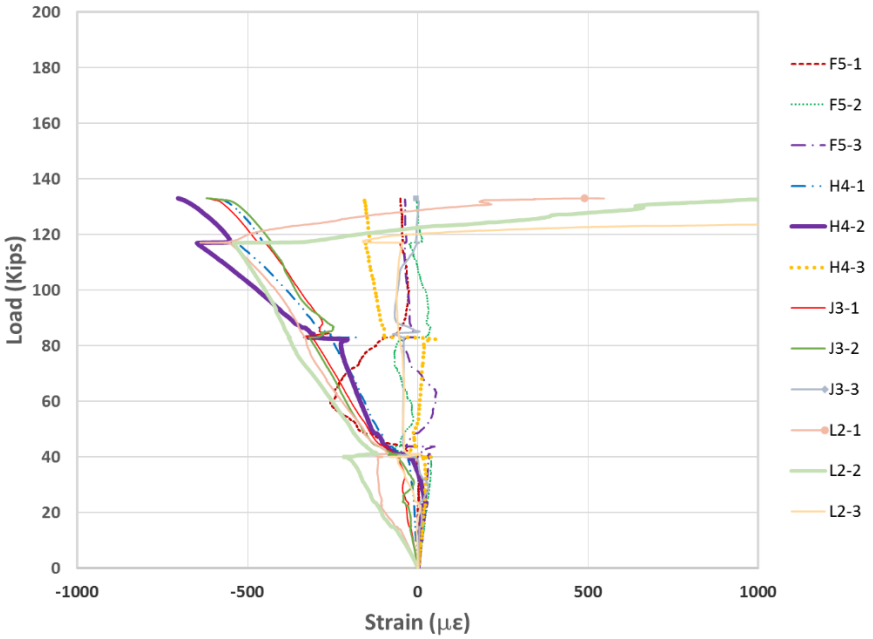

Figure 457 Load-strain response for SNFRC 0.75% beam #31 subjected to 6 months of aging (PH. 4)

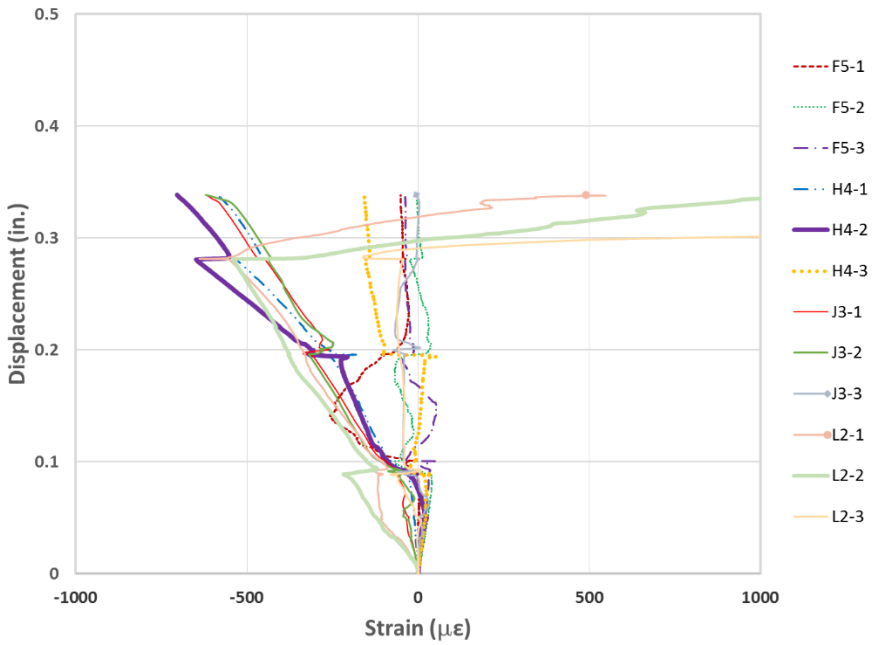

Figure 458 Displacement-strain response for SNFRC 0.75% beam #31 subjected to 6 months of aging (PH. 4)

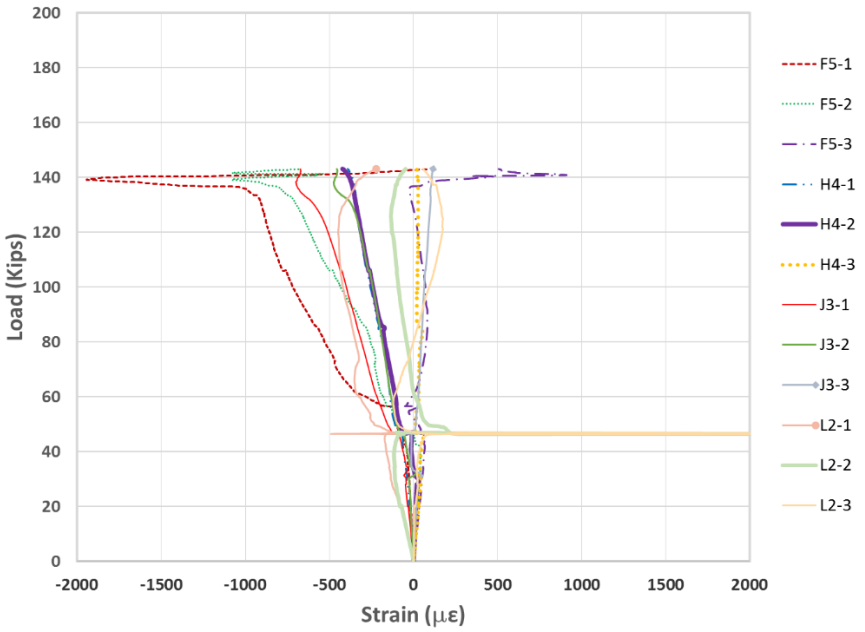

Figure 459 Load-strain response for SNFRC 0.75% beam #32 subjected to 6 months of aging (PH. 4)

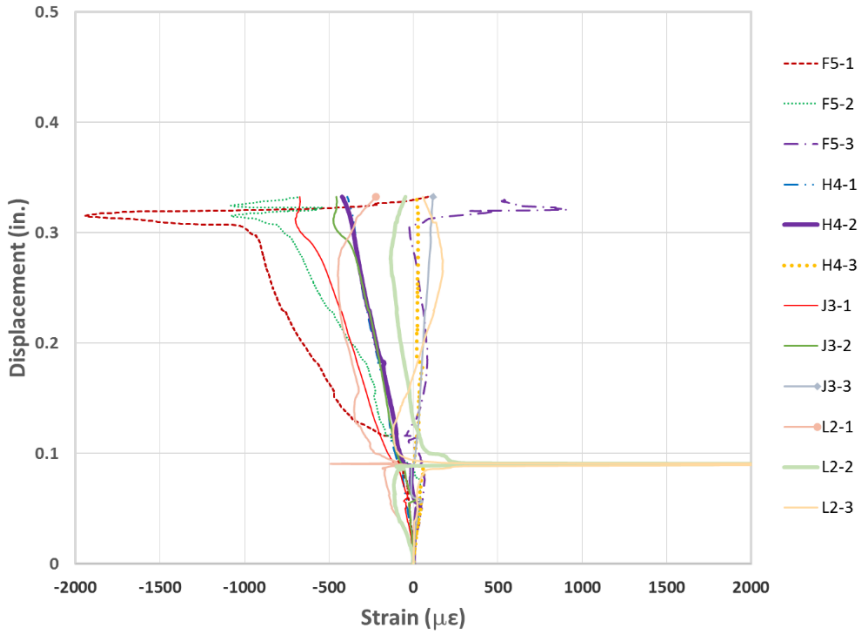

Figure 460 Displacement-strain response for SNFRC 0.75% beam #32 subjected to 6 months of aging (PH. 4)

Appendix J

Photos of Large-Scale Beams

Figure 461 RC control beam #1

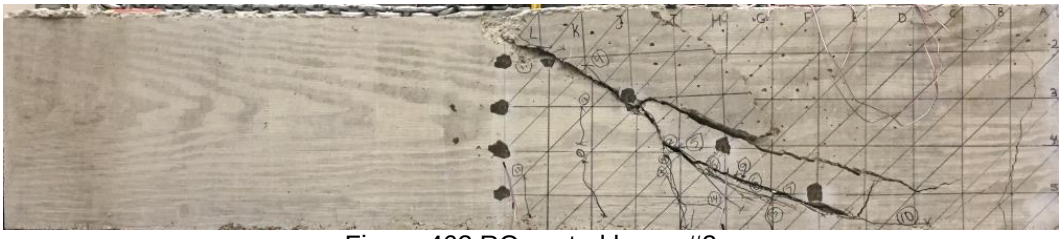

Figure 462 RC control beam #2

Figure 463 RCS beam #3

Figure 464 RCS beam #4

Figure 465 SNFRC 0.5% BM #5

Figure 466 SNFRC 0.5% BM #6

Figure 467 SNFRC 0.75% BM #7

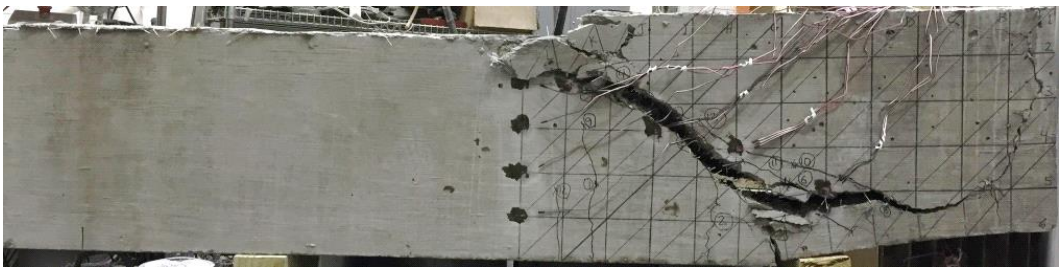

Figure 468 SNFRC 0.75% BM #8

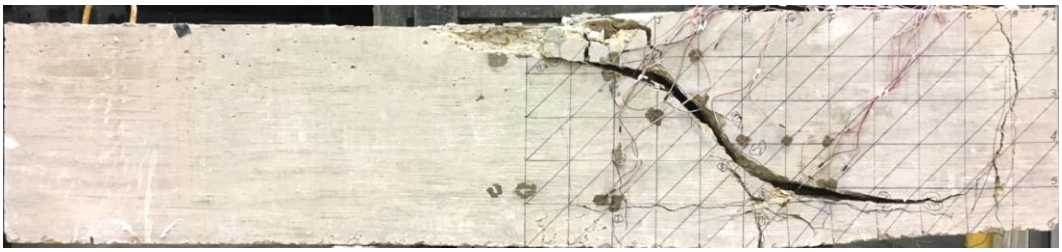

Figure 469 RC control BM #9

Figure 470 RC control BM# 10

Figure 471 RCS BM #11

Figure 472 RCS BM #12

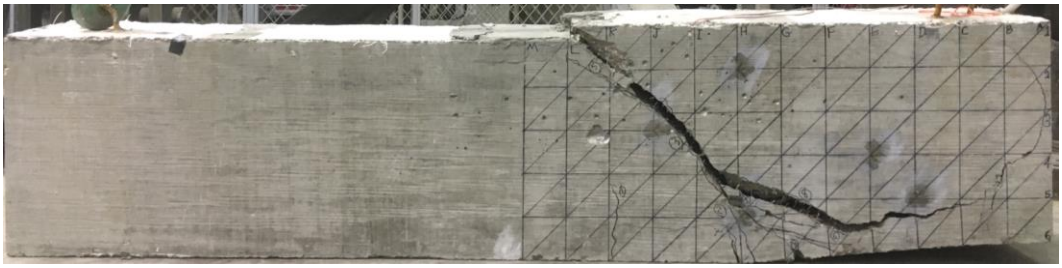

Figure 473 SNFRC 0.5% BM #13

Figure 474 SNFRC 0.5% BM #14

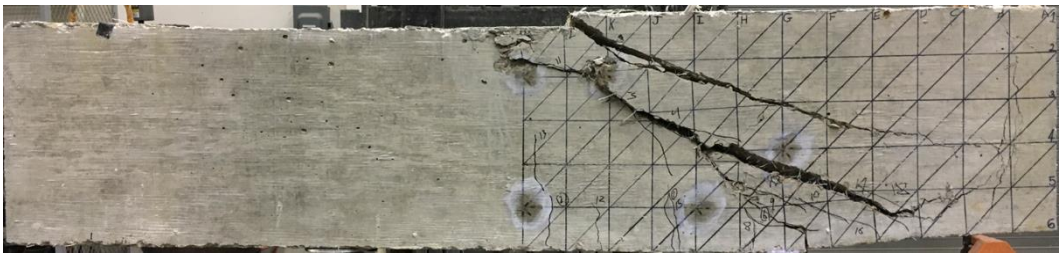

Figure 475 SNFRC 0.75% BM #15

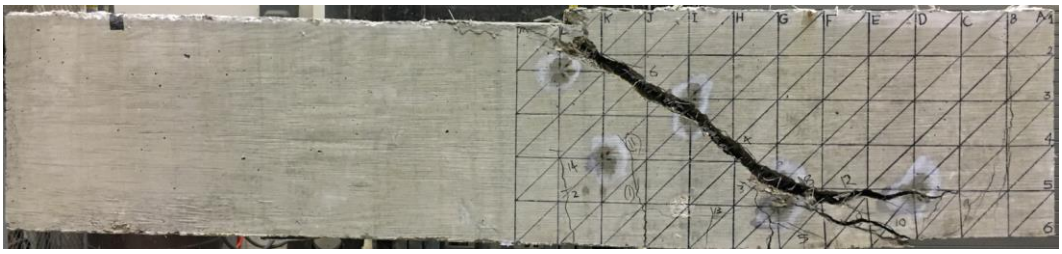

Figure 476 SNFRC 0.75% BM #16

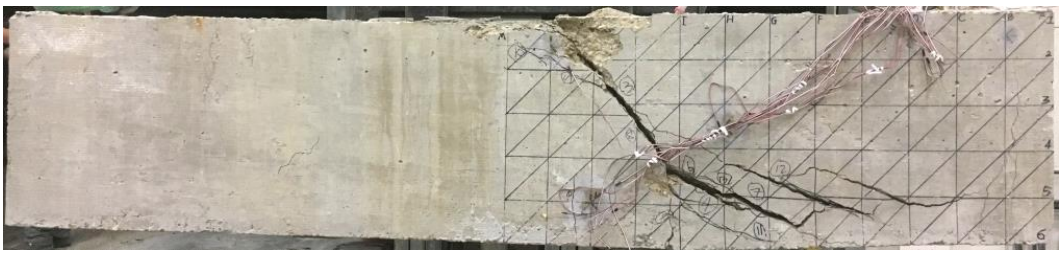

Figure 477 RC control BM# 17

Figure 478 RC control BM #18

Figure 479 RC BM #19

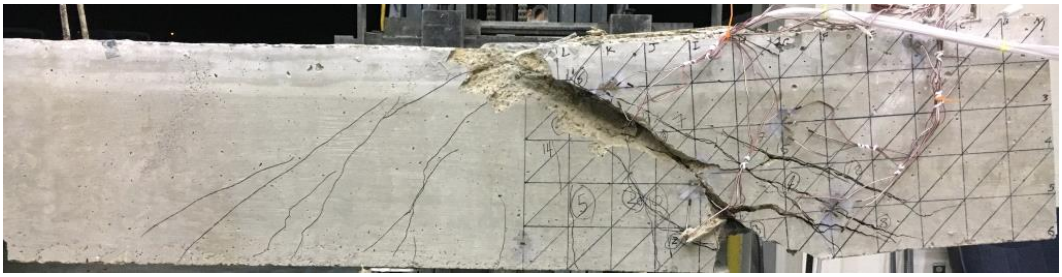

Figure 480 RC BM #20

Figure 481 SNFRC 0.5% BM #21

Figure 482 SNFRC 0.5% BM #22

Figure 483 SNFRC 0.75% BM #23

Figure 484 SNFRC 0.75% BM #24

Figure 485 RC control BM #25

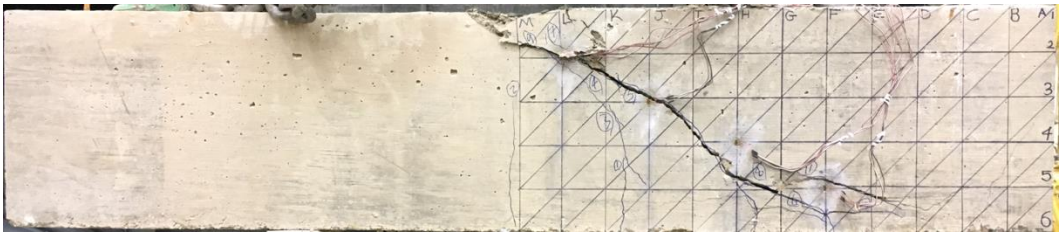

Figure 486 RC control BM #26

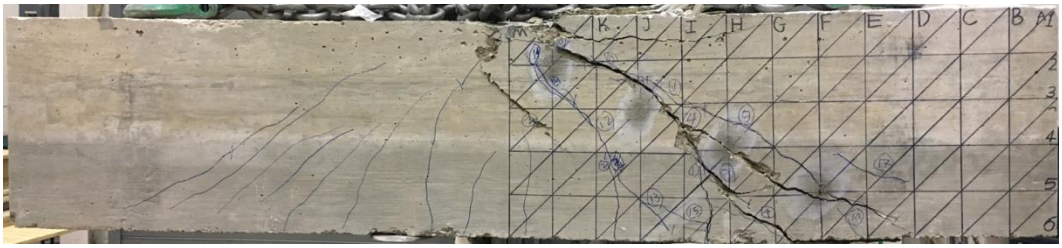

Figure 487 RCS BM #27

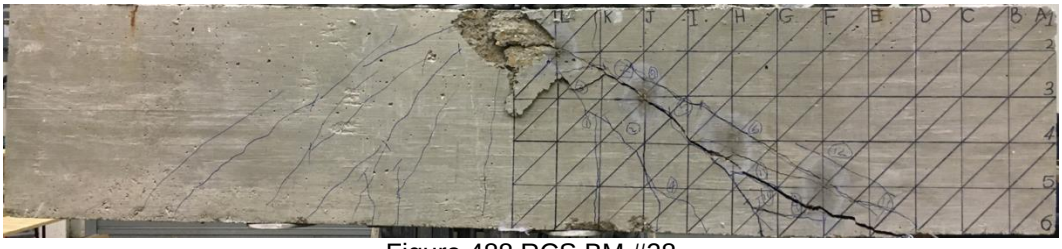

Figure 488 RCS BM #28

Figure 489 SNFRC 0.5% BM #29

Figure 490 SNFRC 0.5% BM #30

Figure 491 SNFRC 0.75% BM #31

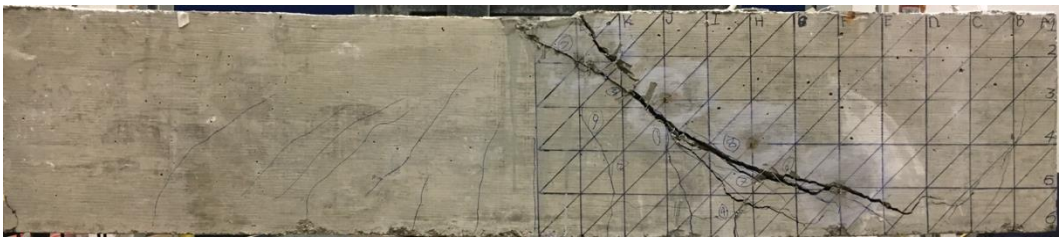

Figure 492 SNFRC 0.75% BM #32

Appendix K

Long-term prediction based on Arrhenius principle

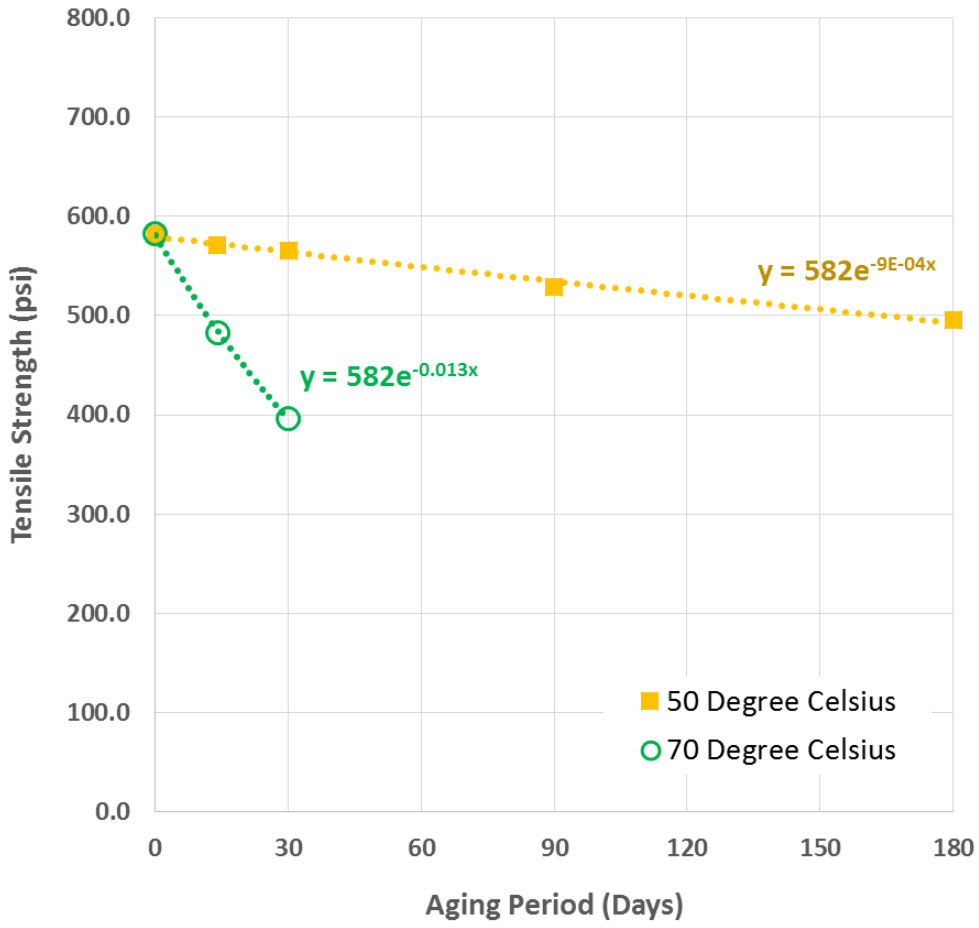

Figure 493 Tensile strength of SNFRC 0.5% cylinders subjected to accelerated aging conditions

$R = 0.008314$

$T_1 = 273 + 50 = 323$

$T_2 = 273 + 70 = 343$

$T_3 = 273 + 20 = 293$

$K_1 = \frac{-1}{180} . \ln\left(\frac{495.1}{582}\right) = 8.984 . 10^{-4}$

$$_2 = \frac{-1}{30} \cdot \ln\left(\frac{396.2}{582}\right) = 0.013$$

$$E_a = \frac{-R \cdot \ln\left(\frac{K_2}{K_1}\right)}{\frac{1}{T_2} - \frac{1}{T_1}} = 122.4 \ \frac{KJ}{Mol}$$

$$K_3 = K_2 \cdot e^{\frac{-E_a}{R} \cdot \left(\frac{1}{T_3} - \frac{1}{T_2}\right)} = 8.442 \cdot 10^{-6}$$

One day of accelarated aging at 50 degrees celsius is equivalent to $\frac{K_1}{K_3} = 106$ days at 20 degrees celsius, which is the Mean Annual Temperature (M.A.T. in Dallas).

One day of accelarated aging at 70 degrees celsius is equivalent to $\frac{K_2}{K_3} = 1518$ days at 20 degrees celsius, which is the Mean Annual Temperature (M.A.T. in Dallas).

One month of accelarated aging at 70 degrees celsius is equivalent to $\frac{30 \cdot \frac{K_2}{K_3}}{365} = 125$ years.

Tensile strength after 100 years in psi is: $F_{100years} = 582 \cdot e^{-K_3 \cdot 36500} = 427.7$

Degradation in percentage after 100 years is: $100 - \frac{F_{100years}}{582} \cdot 100 = 26.52\ \%$

$$\frac{N}{t} = e^{-\frac{E_a}{R} \cdot \left(\frac{1}{T_3} - \frac{1}{T}\right)} = e^{50.252 - \frac{14724}{T}}$$

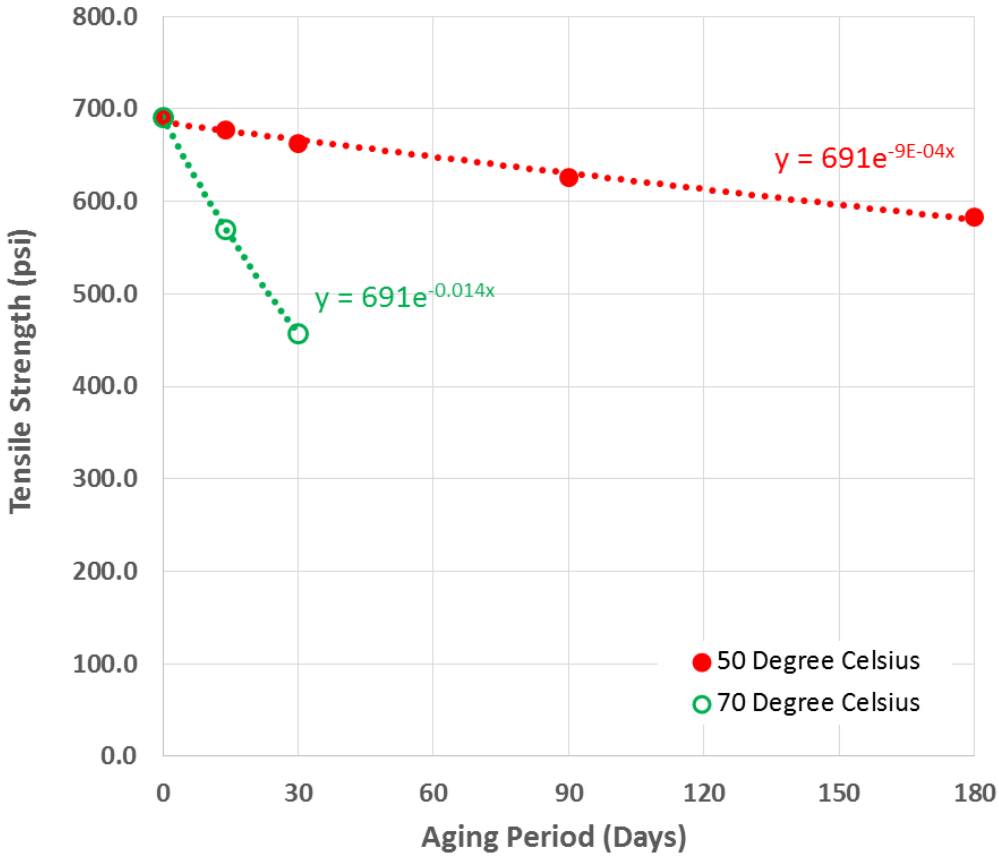

Figure 494 Tensile strength of SNFRC 0.75% cylinders subjected to accelerated aging conditions

$R = 0.008314$

$T_1 = 273 + 50 = 323$

$T_2 = 273 + 70 = 343$

$T_3 = 273 + 20 = 293$

$K_1 = \frac{-1}{180} . \ln\left(\frac{583}{691}\right) = 9.442 . 10^{-4}$

$K_2 = \frac{-1}{30} . \ln\left(\frac{457.3}{691}\right) = 0.014$

$$_a = \frac{-R \,.\ln\,(\frac{K_2}{K_1})}{\frac{1}{T_2} - \frac{1}{T_1}} = 123.4\ \frac{KJ}{Mol}$$

$$K_3 = K_2 \,. e^{\frac{-E_a}{R} \cdot \left(\frac{1}{T_3} - \frac{1}{T_2}\right)} = 8.548 \,. 10^{-6}$$

One day of accelarated aging at 50 degrees celsius is equivalent to $\frac{K_1}{K_3} = 110$ days at 20 degrees celsius, which is the Mean Annual Temperature (M.A.T. in Dallas).

One day of accelarated aging at 70 degrees celsius is equivalent to $\frac{K_2}{K_3} = 1610$ days at 20 degrees celsius, which is the Mean Annual Temperature (M.A.T. in Dallas).

One month of accelarated aging at 70 degrees celsius is equivalent to $\frac{30 \,.\, \frac{K_2}{K_3}}{365} = 132$ years.

Tensile strength after 100 years in psi is: $F_{100years} = 691 \,. e^{-K_3 \,.36500} = 505.8$

Degradation in percentage after 100 years is: $100 - \frac{F_{100years}}{582} \,.100 = 26.8\,\%$

$$\frac{N}{t} = e^{-\frac{E_a}{R} \cdot \left(\frac{1}{T_3} - \frac{1}{T}\right)} = e^{50.653 - \frac{14841}{T}}$$

Appendix L

Details of large-scale beams in parametric study

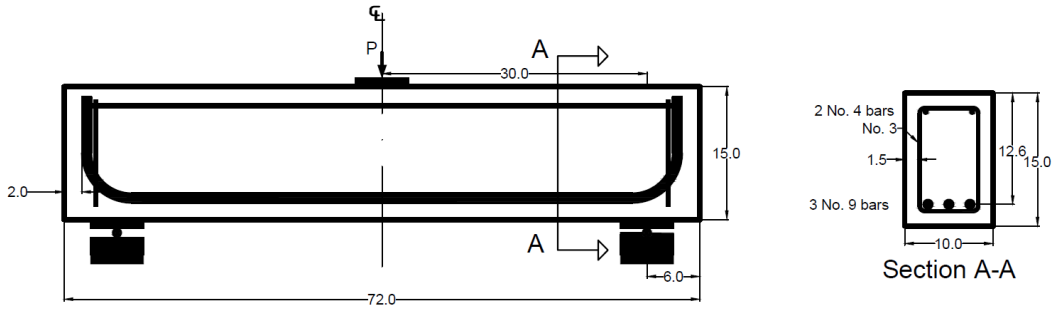

Figure 495 Configuration of large-scale beam, P1

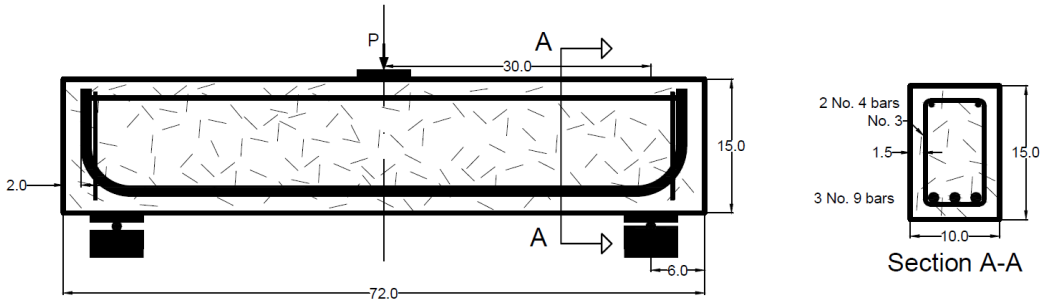

Figure 496 Configuration of large-scale beam, P2

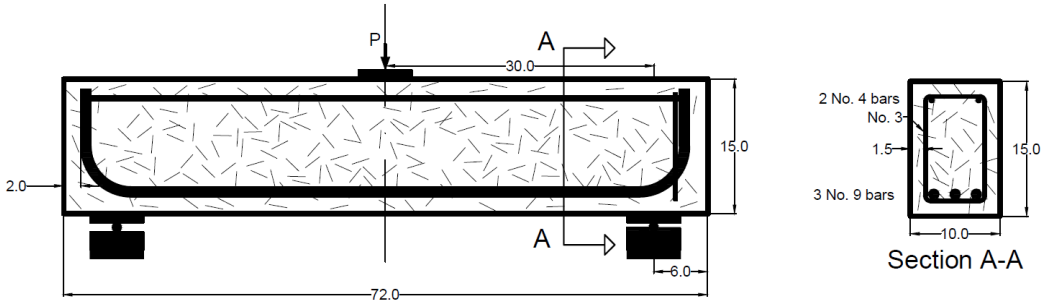

Figure 497 Configuration of large-scale beam, P3

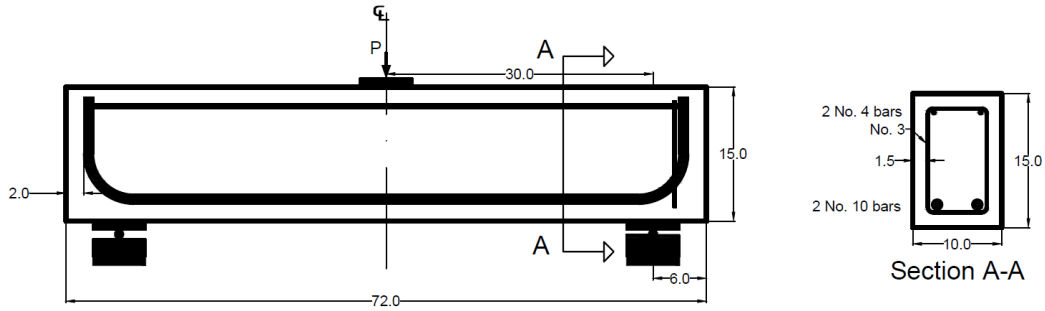

Figure 498 Configuration of large-scale beam, P4

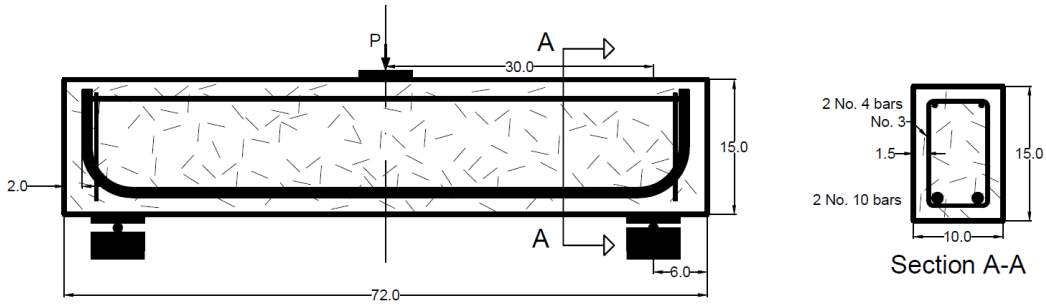

Figure 499 Configuration of large-scale beam, P5

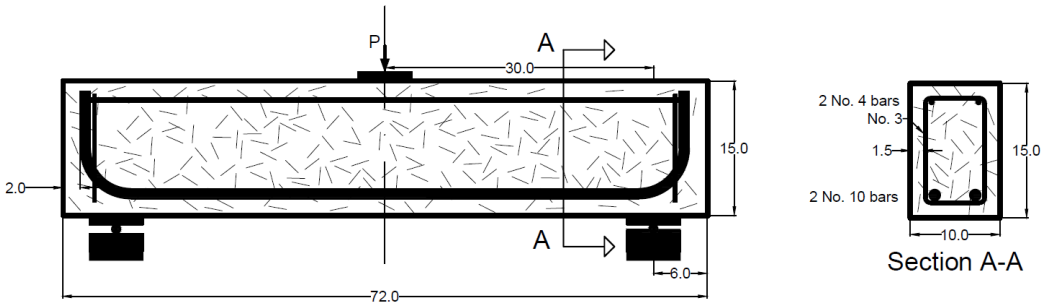

Figure 500 Configuration of large-scale beam, P6

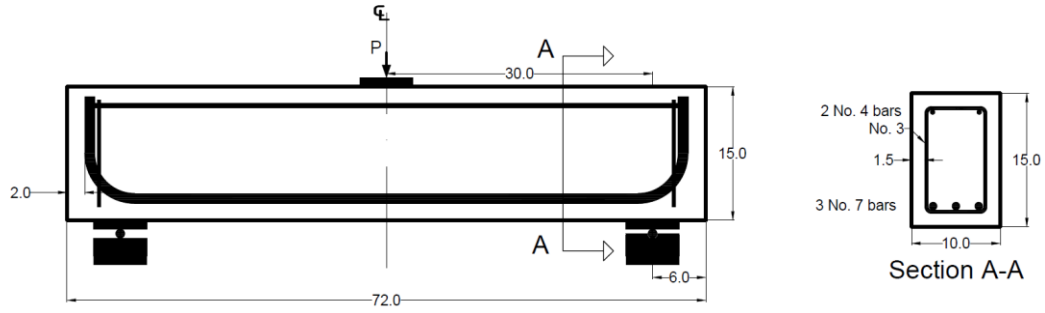

Figure 501 Configuration of large-scale beam, P7

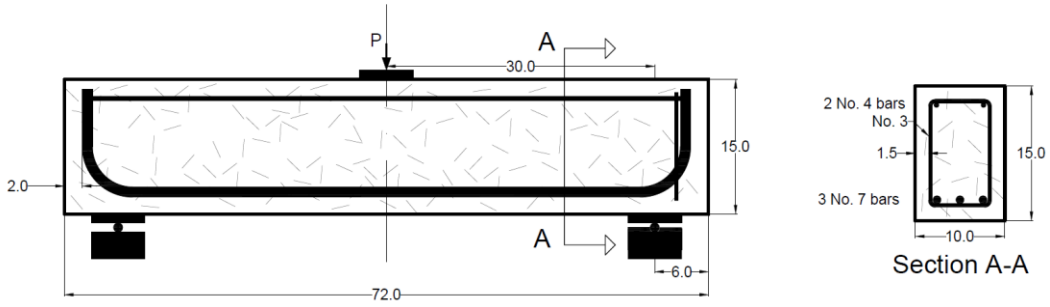

Figure 502 Configuration of large-scale beam, P8

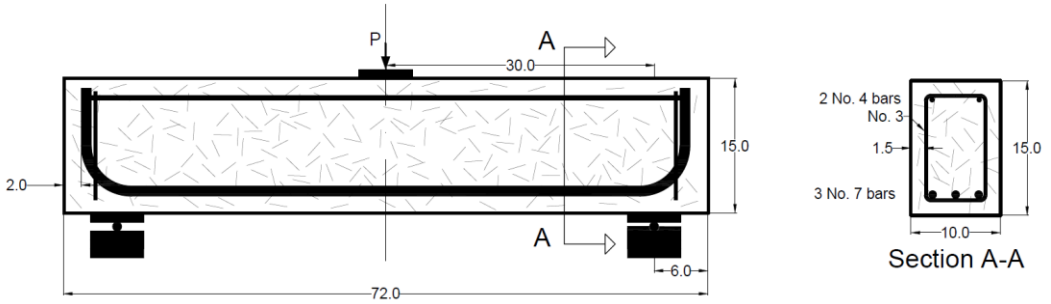

Figure 503 Configuration of large-scale beam, P9

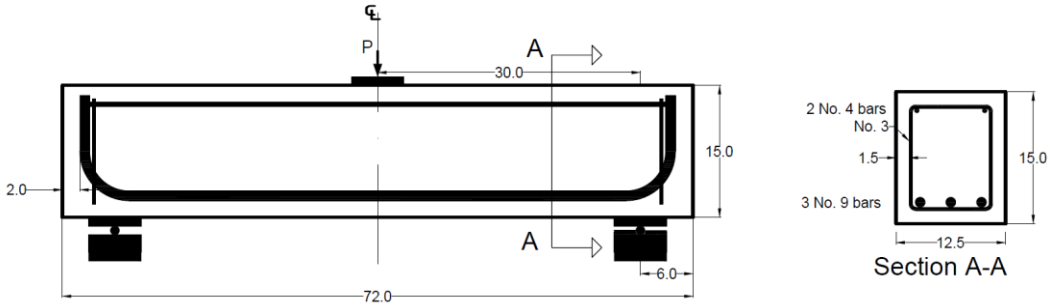

Figure 504 Configuration of large-scale beam, P10

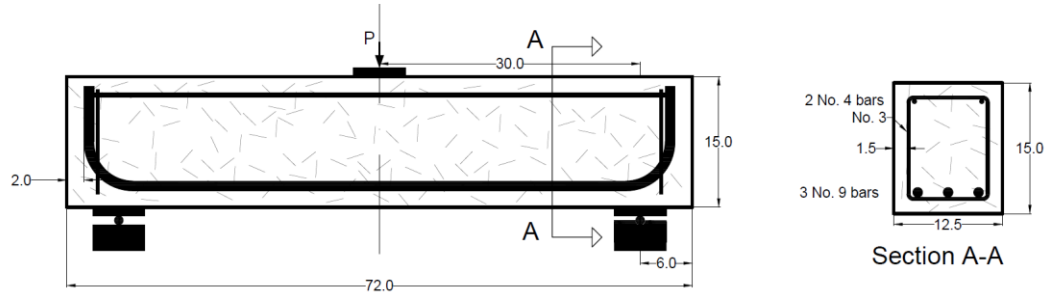

Figure 505 Configuration of large-scale beam, P11

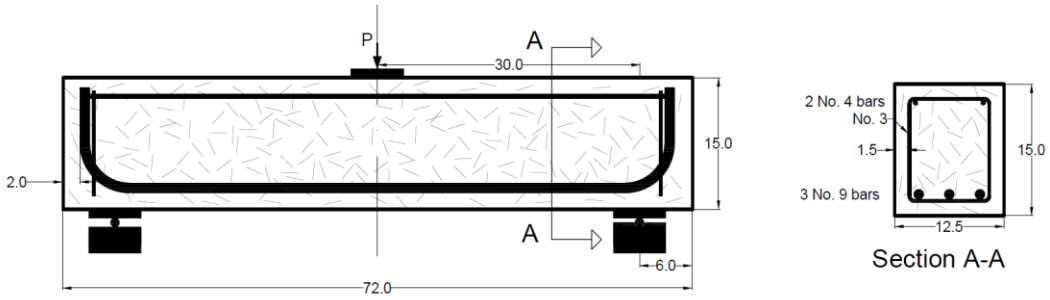

Figure 506 Configuration of large-scale beam, P12

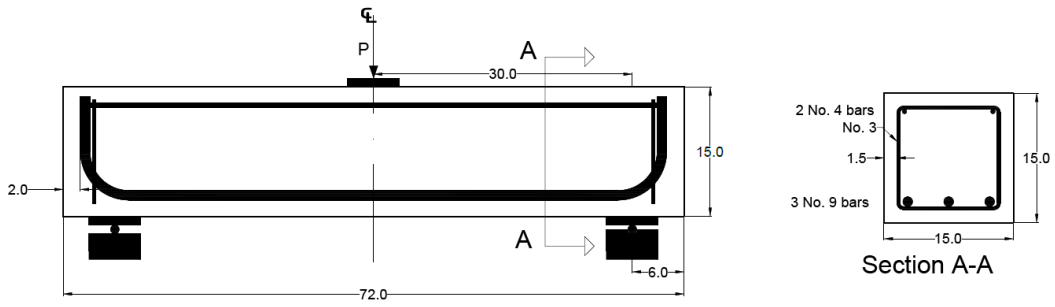

Figure 507 Configuration of large-scale beam, P13

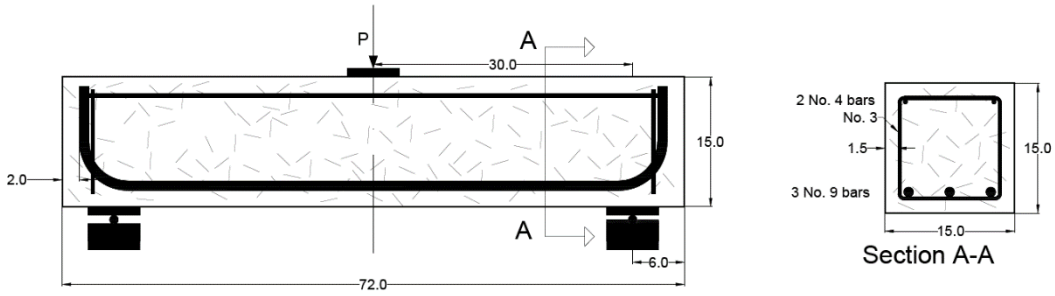

Figure 508 Configuration of large-scale beam, P14

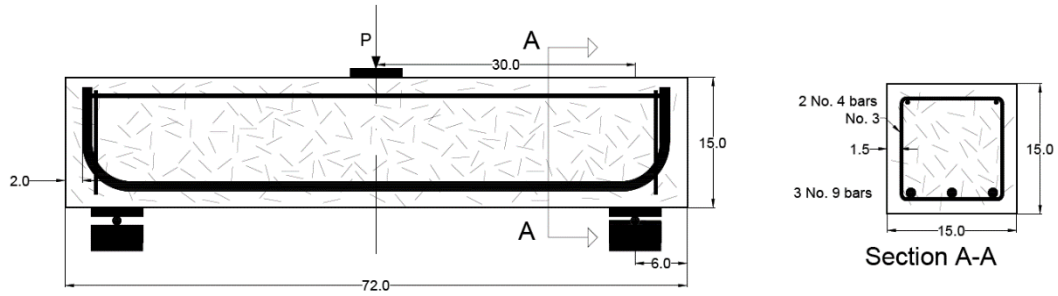

Figure 509 Configuration of large-scale beam, P15

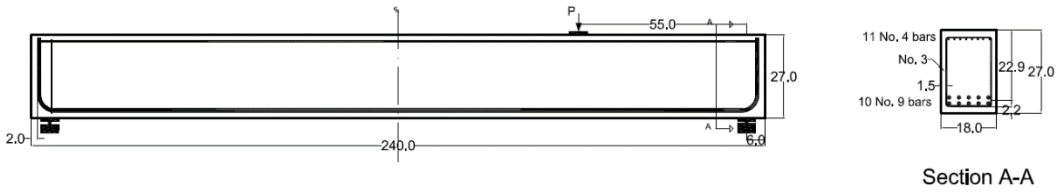

Figure 510 Configuration of large-scale beam, P16

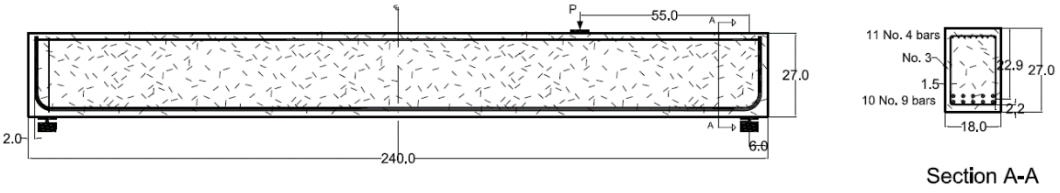

Figure 511 Configuration of large-scale beam, P17

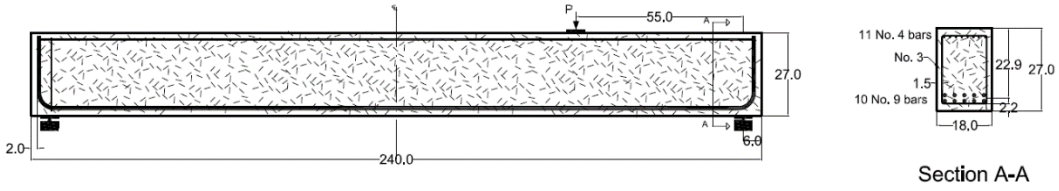

Figure 512 Configuration of large-scale beam, P18

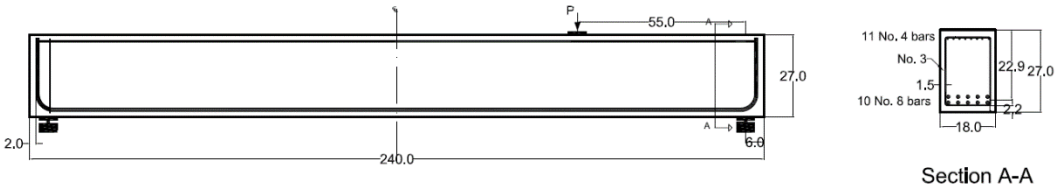

Figure 513 Configuration of large-scale beam, P19

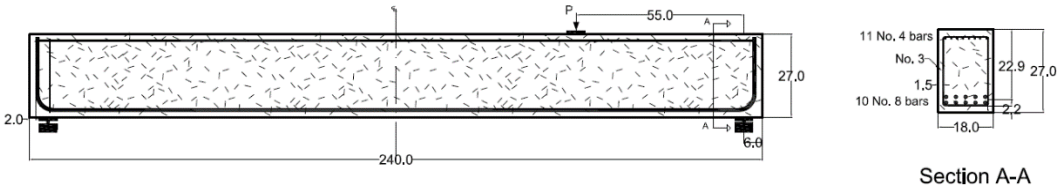

Figure 514 Configuration of large-scale beam, P20

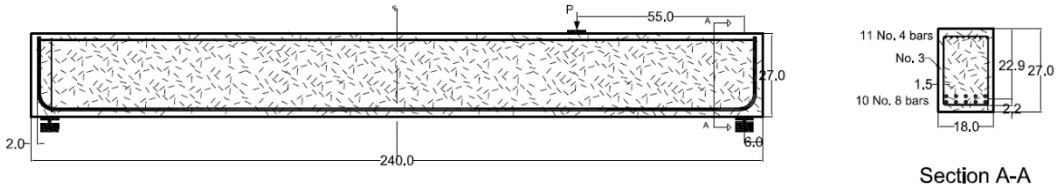

Figure 515 Configuration of large-scale beam, P21

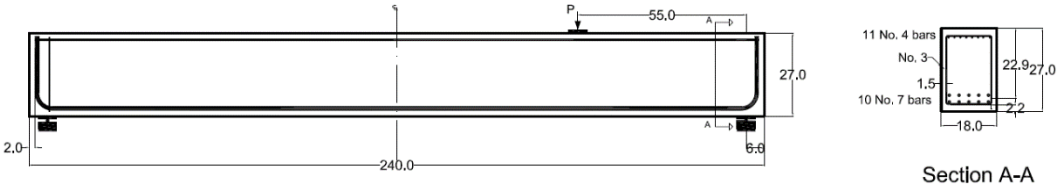

Figure 516 Configuration of large-scale beam, P22

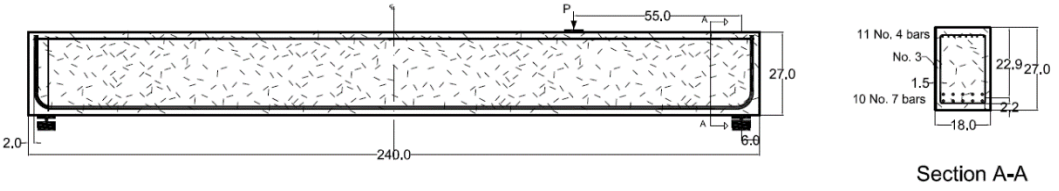

Figure 517 Configuration of large-scale beam, P23

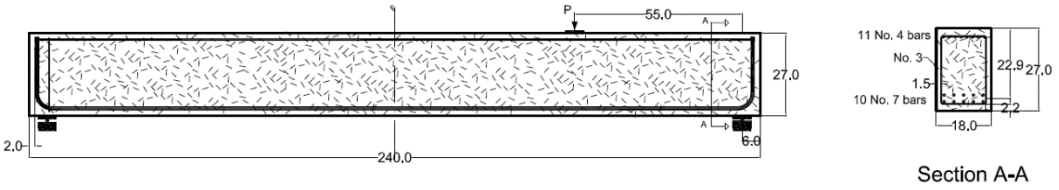

Figure 518 Configuration of large-scale beam, P24

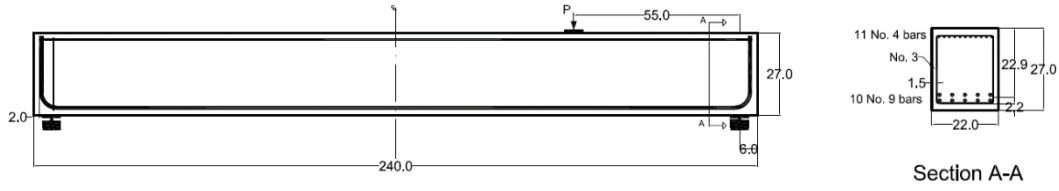

Figure 519 Configuration of large-scale beam, P25

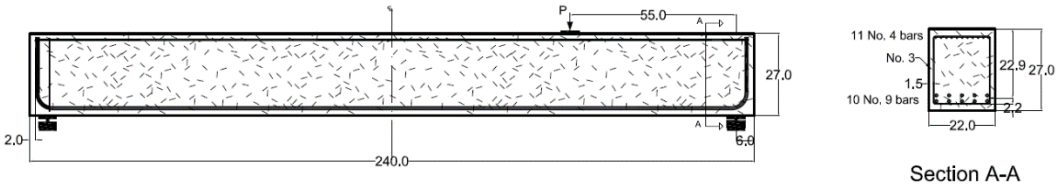

Figure 520 Configuration of large-scale beam, P26

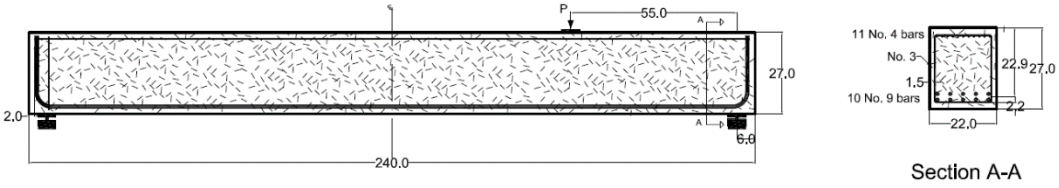

Figure 521 Configuration of large-scale beam, P27

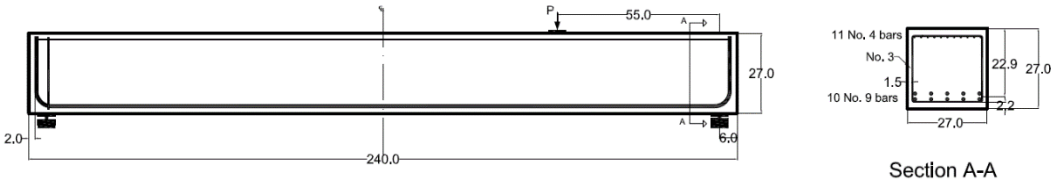

Figure 522 Configuration of large-scale beam, P28

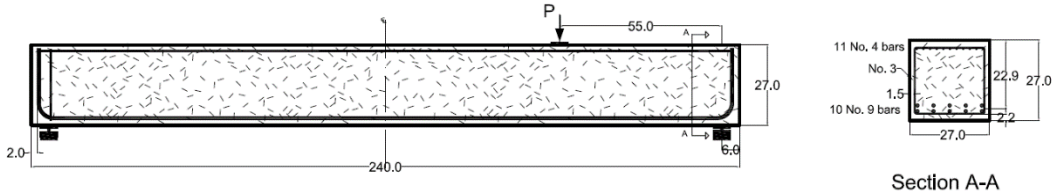

Figure 523 Configuration of large-scale beam, P29

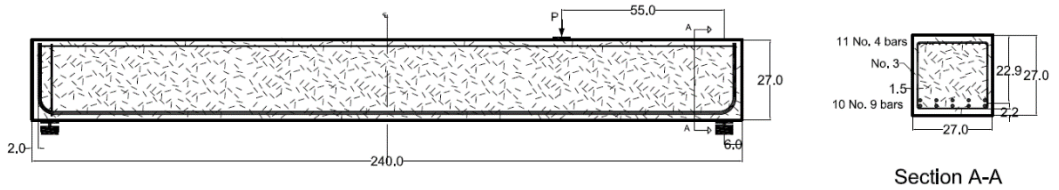

Figure 524 Configuration of large-scale beam, P30

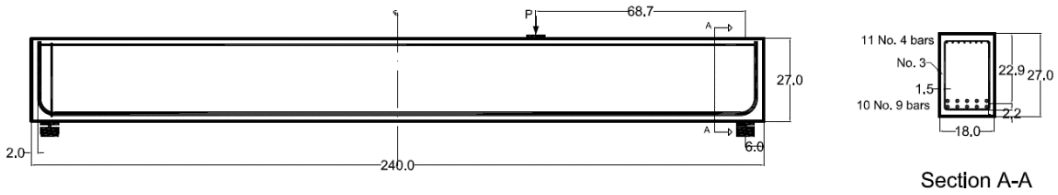

Figure 525 Configuration of large-scale beam, P31

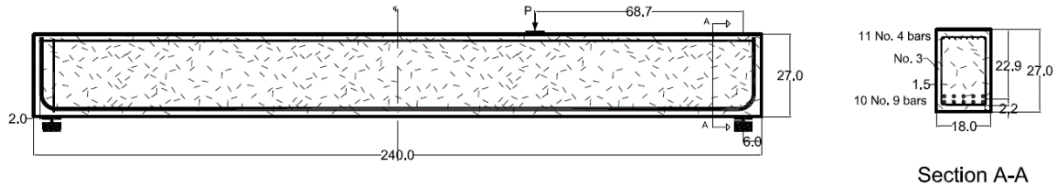

Figure 526 Configuration of large-scale beam, P32

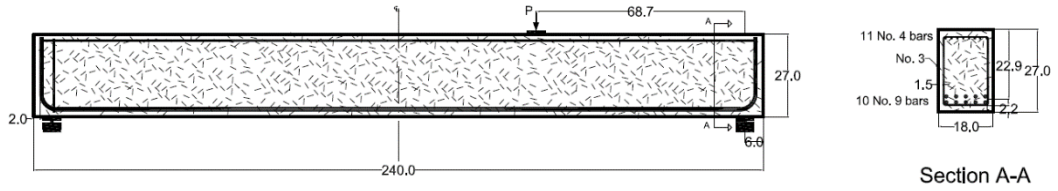

Figure 527 Configuration of large-scale beam, P33

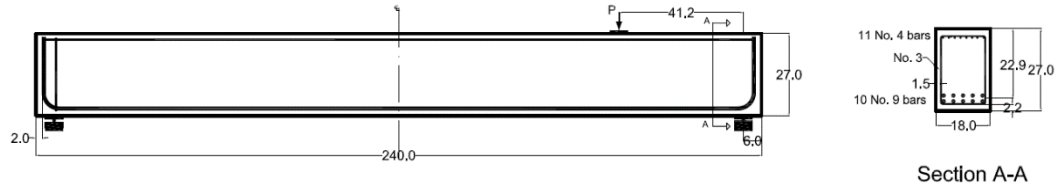

Figure 528 Configuration of large-scale beam, P34

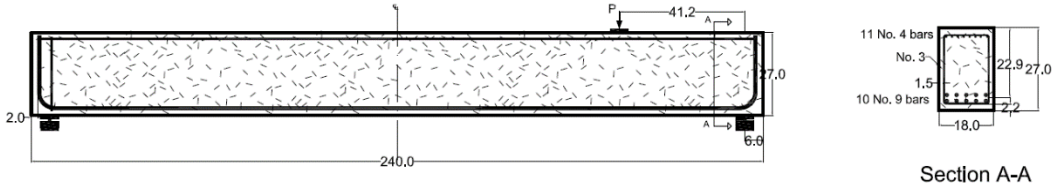

Figure 529 Configuration of large-scale beam, P35

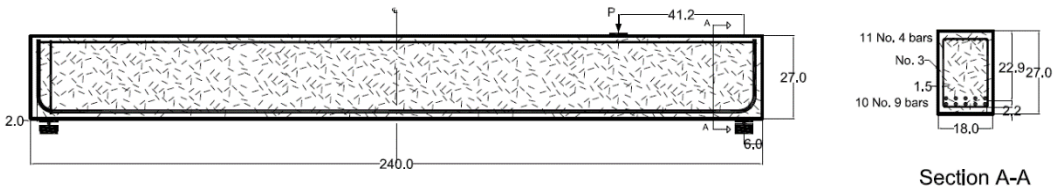

Figure 530 Configuration of large-scale beam, P36

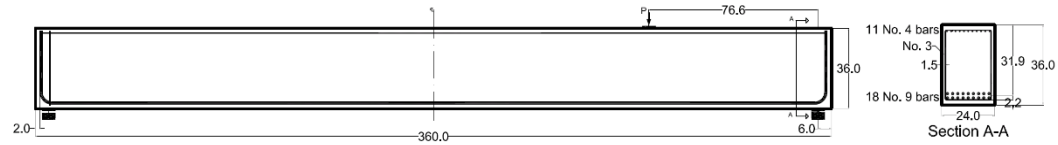

Figure 531 Configuration of large-scale beam, P37

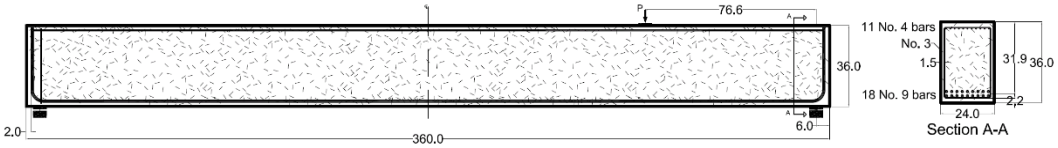

Figure 532 Configuration of large-scale beam, P38

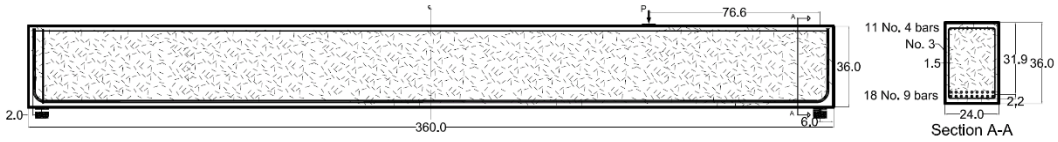

Figure Configuration of large-scale beam, P39

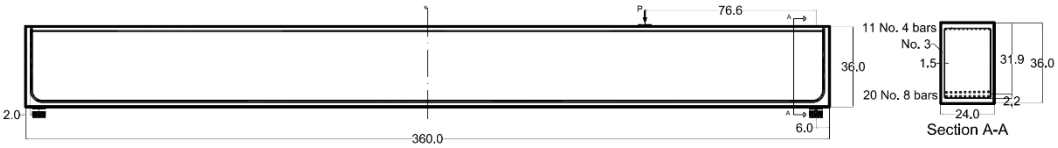

Figure Configuration of large-scale beam, P40

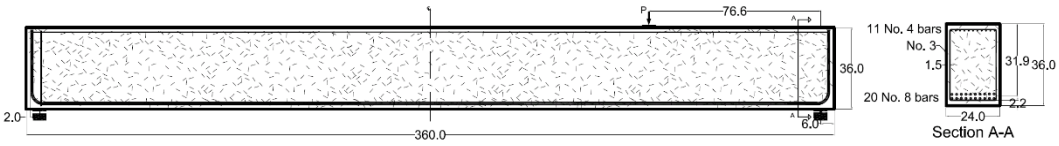

Figure 533 Configuration of large-scale beam, P41

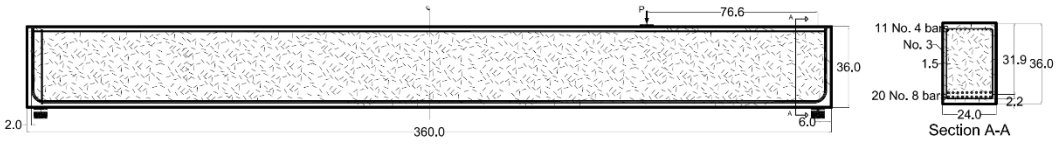

Figure 534 Configuration of large-scale beam, P42

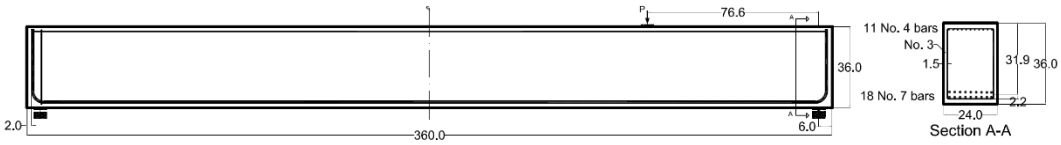

Figure 535 Configuration of large-scale beam, P43

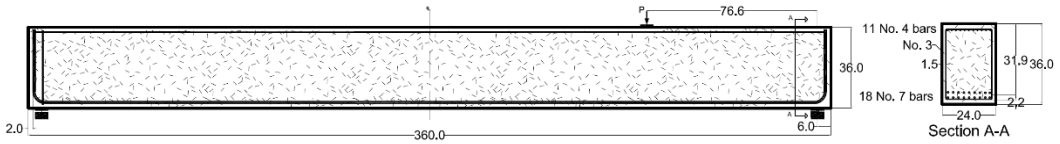

Figure 536 Configuration of large-scale beam, P44

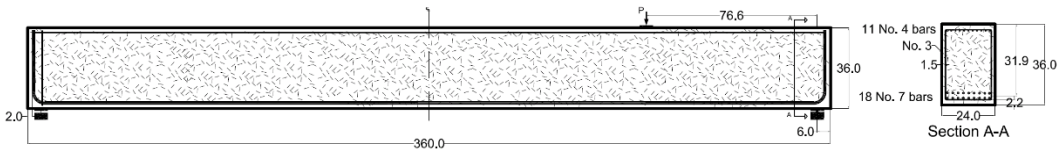

Figure 537 Configuration of large-scale beam, P45

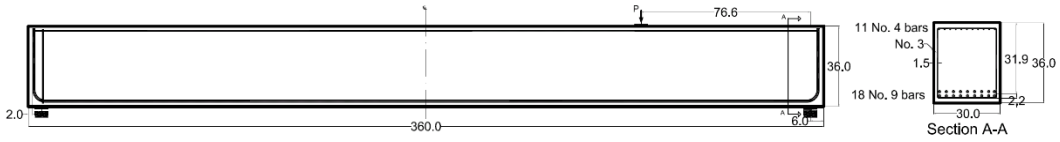

Figure 538 Configuration of large-scale beam, P46

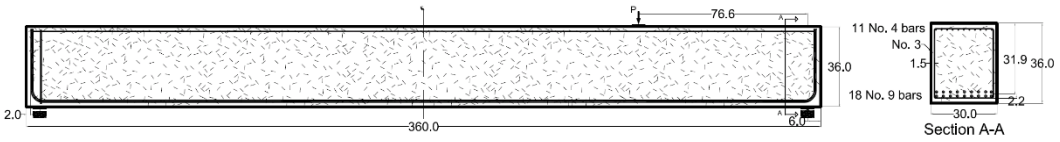

Figure 539 Configuration of large-scale beam, P47

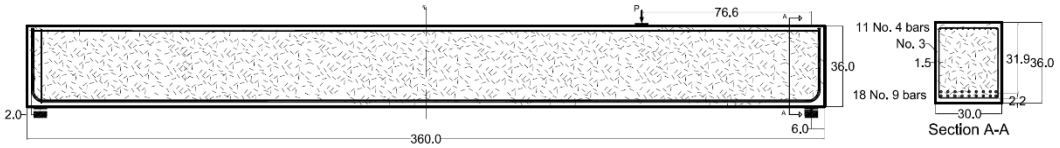

Figure Configuration of large-scale beam, P48

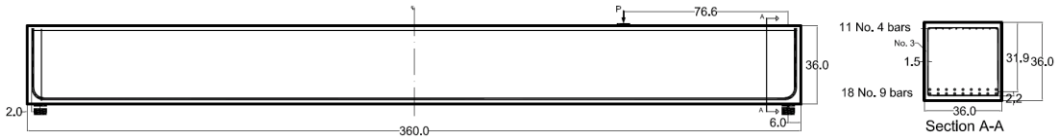

Figure 540 Configuration of large-scale beam, P49

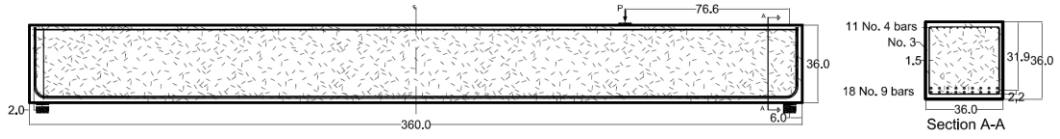

Figure 541 Configuration of large-scale beam, P50

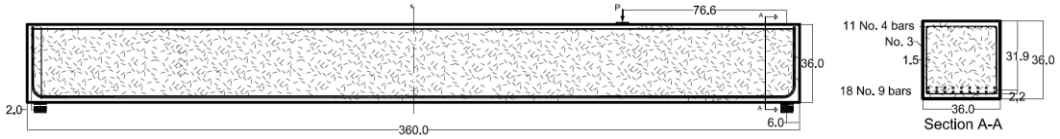

Figure 542 Configuration of large-scale beam, P51

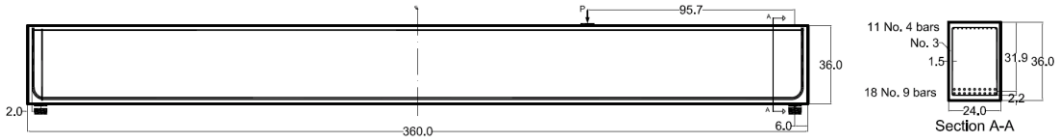

Figure 543 Configuration of large-scale beam, P52

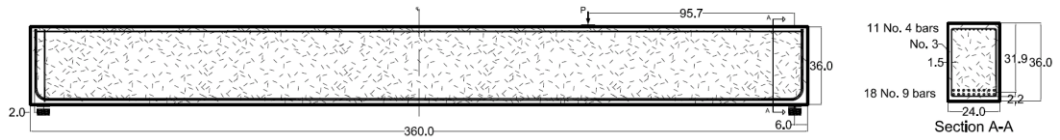

Figure 544 Configuration of large-scale beam, P53

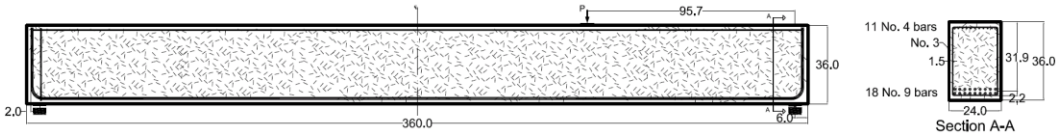

Figure 545 Configuration of large-scale beam, P54

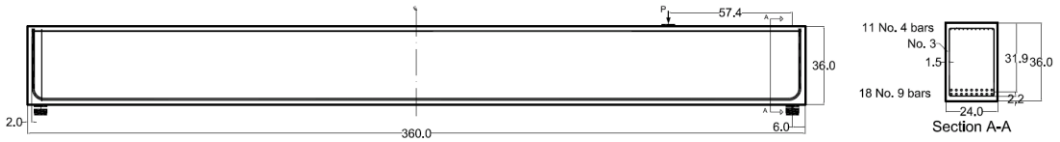

Figure 546 Configuration of large-scale beam, P55

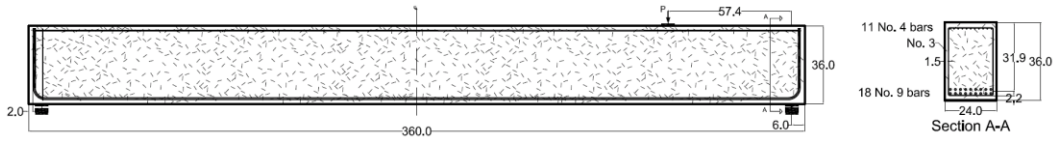

Figure 547 Configuration of large-scale beam, P56

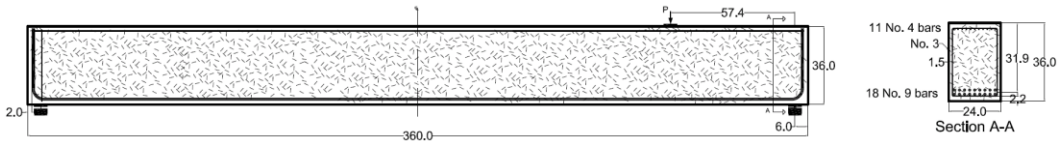

Figure Configuration of large-scale beam, P57

Appendix M

Design calculations of large-scale beams

SHEAR AND MOMENT CAPACITY OF REINFORCED CONCRETE BEAMS

$b := 10\ in$
$h := 15\ in$
$d := 12.6\ in$
$\beta := 0.8$
$f'c := 5\ ksi$
$fy := 60\ ksi$
$fyt := 60\ ksi$
$a := 2.5\ ft$

$\frac{a}{d} = 2.38$

No. 3 double-leg stirrups

$As := 3 \cdot 1.0\ in^2 = 3\ in^2$
$A's := 2 \cdot 0.2\ in^2 = 0.4\ in^2$

Note: Minimum Beam Width (in.) for 3 No. 9 bars per layer based on clear cover of 1.5in. and No3 double leg stirrup is 10in.

$Asmin := \frac{200\ psi}{fy} \cdot b \cdot d = 0.42\ in^2$

$\rho := \frac{As}{b \cdot d} = 0.02$

$Asmin < As \qquad O.K.$

$a := \frac{As \cdot fy}{0.85\ f'c \cdot b} = 4.24\ in$

$c := \frac{a}{\beta} = 5.29\ in$

$\varepsilon s := 0.003 \cdot \frac{d - c}{c} = 4.14 \cdot 10^{-3}$

$\varepsilon y < \varepsilon s < 0.005 \quad \varepsilon s - \frac{60}{29000}$

$\phi := 0.65 + .25 \cdot \frac{\varepsilon s - \frac{60}{29000}}{0.005 - \frac{60}{29000}} = 0.83$

$Mn := As \cdot fy \cdot (d - 0.5\ a) = 157.24\ ft \cdot kip$
$\phi \cdot Mn = 129.98\ ft \cdot kip$

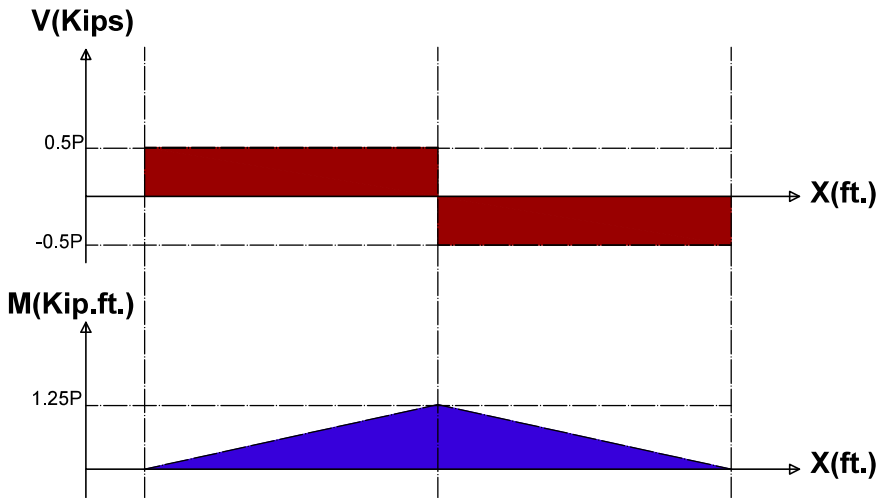
V(Kips)
0.5P
-0.5P
X(ft.)
M(Kip.ft.)
1.25P
X(ft.)

$$Pmoment := \frac{\phi \cdot Mn}{1.25\ ft} = 103.98\ kip$$

$$Vc := 2 \cdot \sqrt[2]{\frac{f'c}{psi}} \cdot b \cdot d \cdot psi = 17.82\ kip$$

$$\phi := 0.75$$

$$Av := 2 \cdot 0.11\ in^2 = 0.22\ in^2$$

$$s := 3\ in$$

$$Avmin := 0.75 \cdot \sqrt[2]{\frac{f'c}{psi}} \cdot \frac{b \cdot s}{fyt} \cdot psi = 0.03\ in^2$$

$$Smax := \frac{Av \cdot fyt}{50\ psi\ b} = 26.4\ in$$

$$Vsmax := 8 \cdot \sqrt[2]{\frac{f'c}{psi}} \cdot b \cdot d \cdot psi = 71.28\ kip$$

$$Vs := \frac{Av \cdot fyt \cdot d}{s} = 55.44\ kip$$

Vs<Vsmax O.K.

$$Pshear\_left := 2 \cdot 0.75 \cdot (Vs + Vc) = 109.89\ kip$$

$$Pshear\_right := 2 \cdot 0.75\ (0 + Vc) = 26.73\ kip$$

$$s := 6\ in$$

$$Vs := \frac{Av \cdot fyt \cdot d}{s} = 27.72\ kip$$

$$Pshear\_right\_min := 2 \cdot 0.75 \cdot (Vs + Vc) = 68.31\ kip$$

Appendix N

Compressive stress-strain response of concrete cylinders

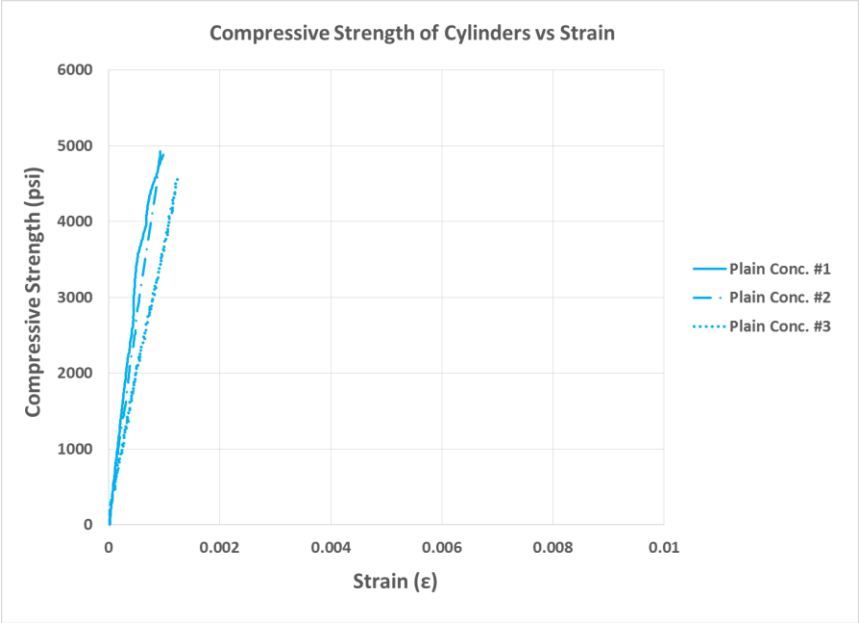

Figure 548 Compressive stress-strain curves for plain Concrete cylinders without accelerated aging (PH1)

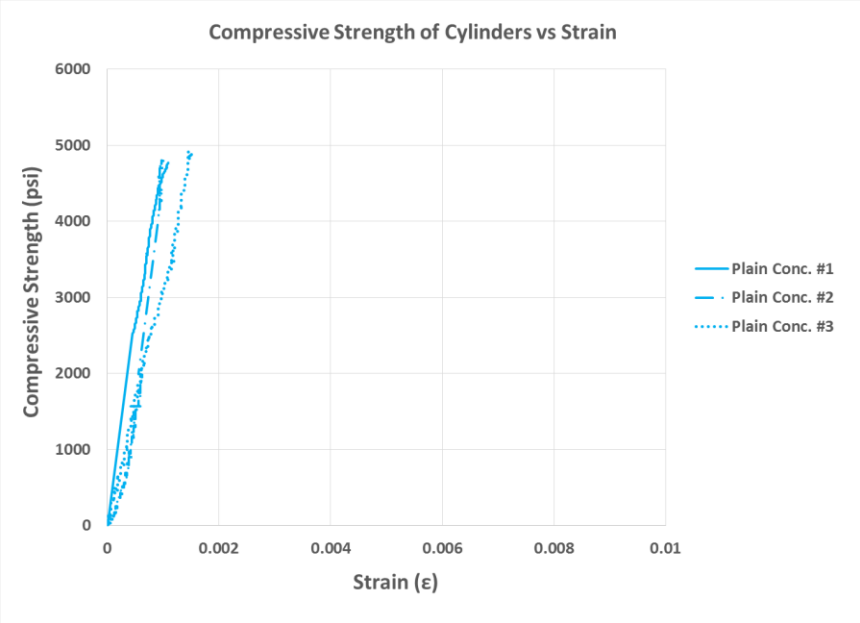

Figure 549 Compressive stress-strain curves for plain concrete cylinders subjected to 1 month of accelerated aging (PH2)

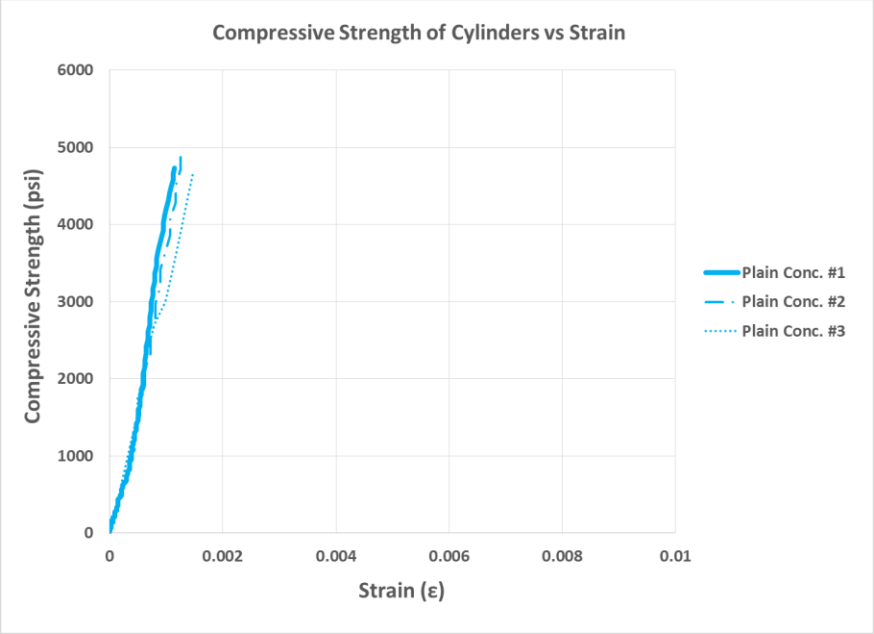

Figure 550 Compressive stress-strain curves for plain concrete cylinders subjected to 3 months of accelerated aging (PH3)

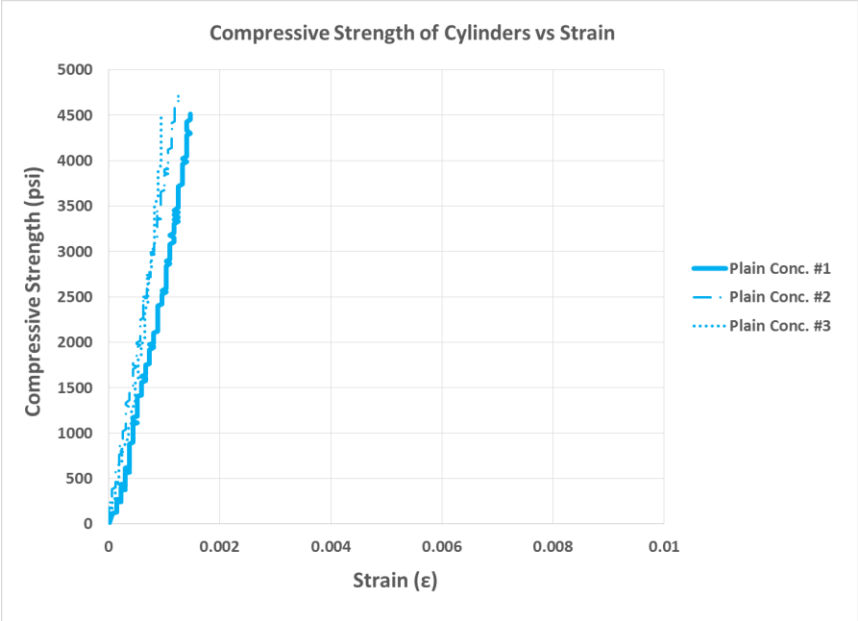

Figure 551 Compressive stress-strain curves for plain concrete cylinders subjected to 6 months of accelerated aging (PH4)

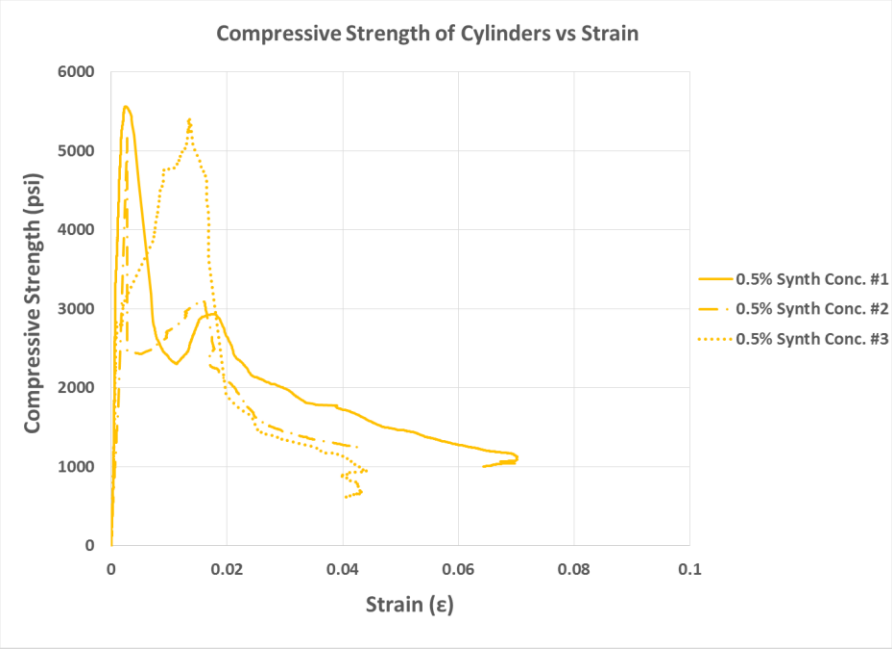

Figure 552 Compressive stress-strain curves for 0.5% synthetic fiber concrete cylinders without accelerated aging (PH1)

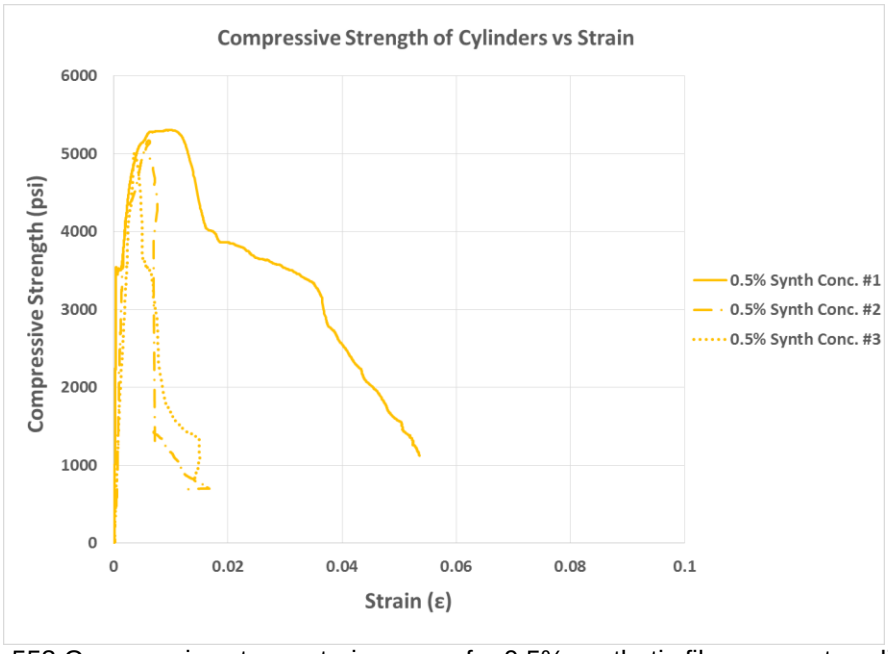

Figure 553 Compressive stress-strain curves for 0.5% synthetic fiber concrete cylinders subjected to 1month of accelerated aging (PH2)

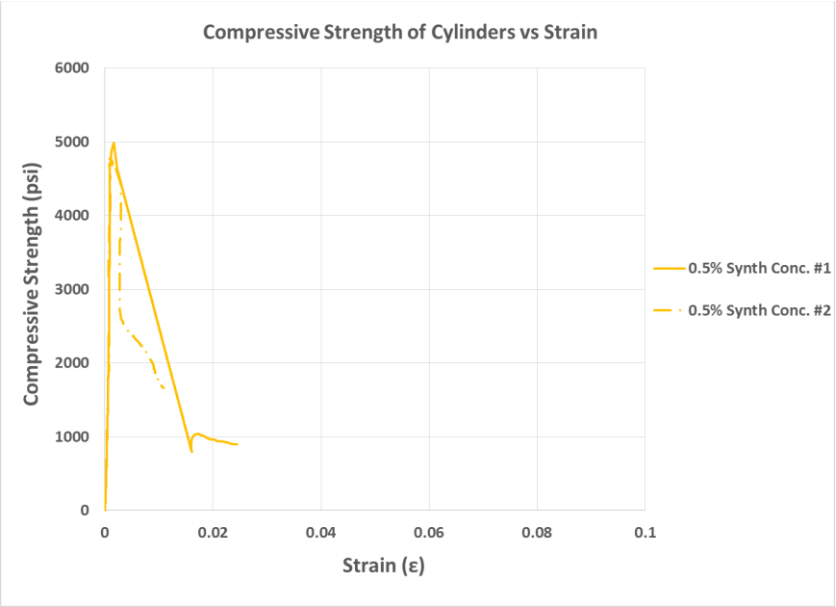

Figure 554 Compressive stress-strain curves for SNFRC 0.5% cylinders subjected to 3 months of accelerated aging (PH3)

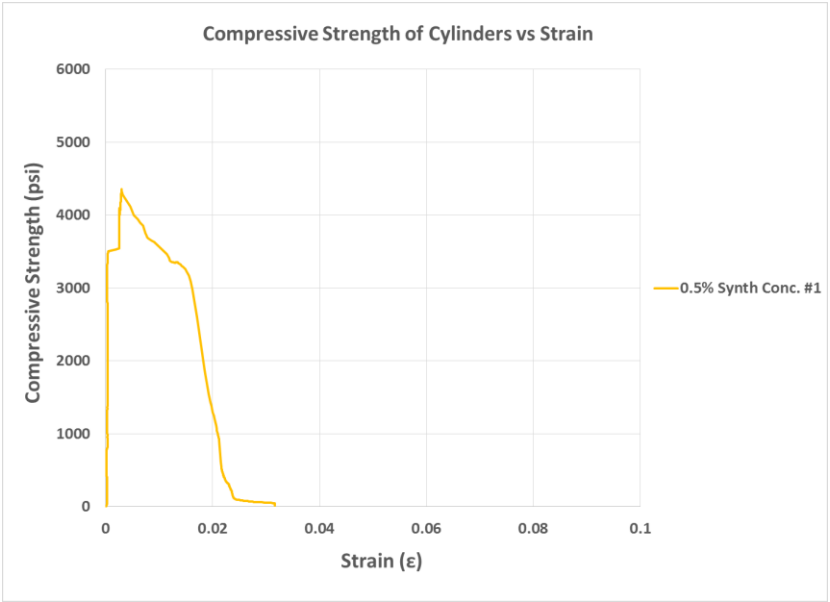

Figure 555 Compressive stress-strain curves for SNFRC 0.5% cylinders subjected to 6 months of accelerated aging (PH4)

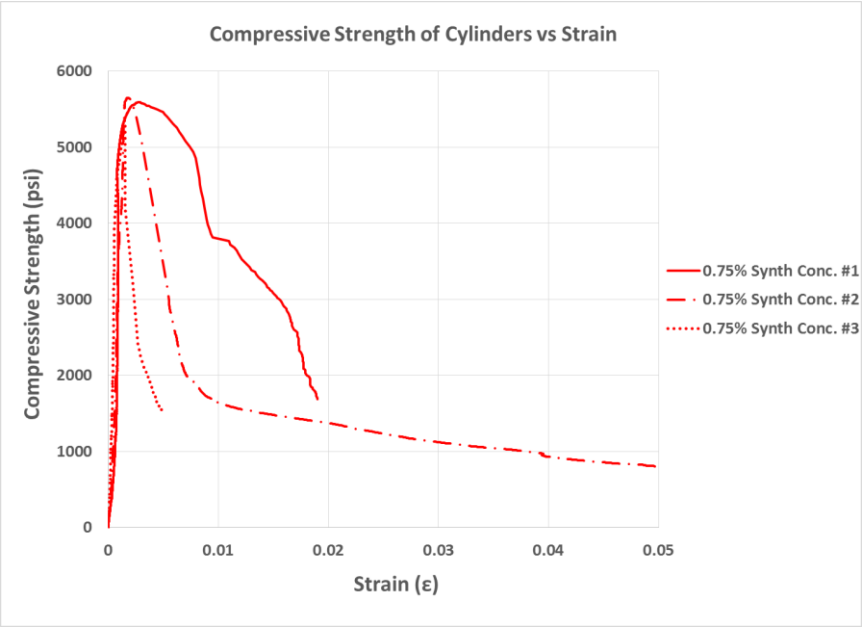

Figure 556 Compressive stress-strain curves for SNFRC 0.75% cylinders without accelerated aging (PH1)

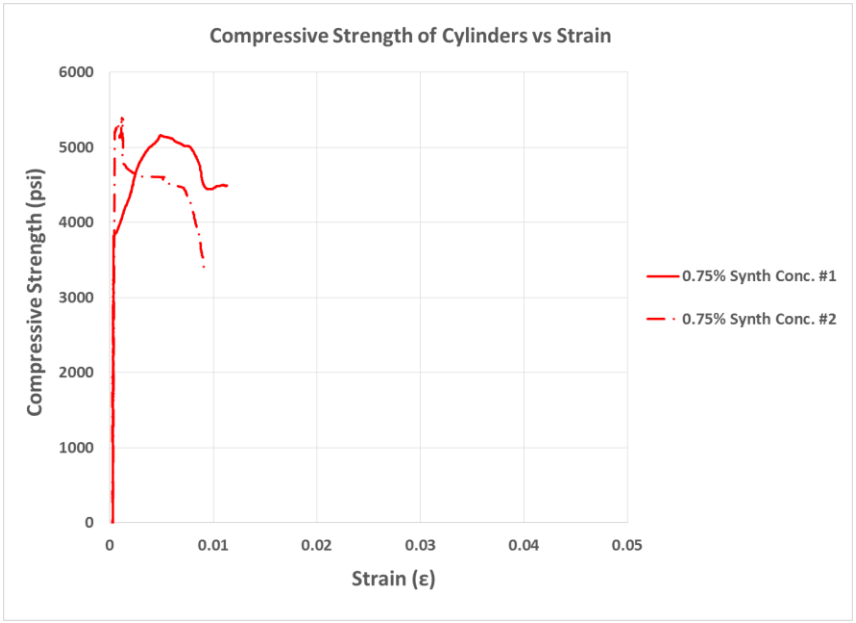

Figure 557 Compressive stress-strain curves for SNFRC 0.75% cylinders subjected to 1 month of accelerated aging (PH2)

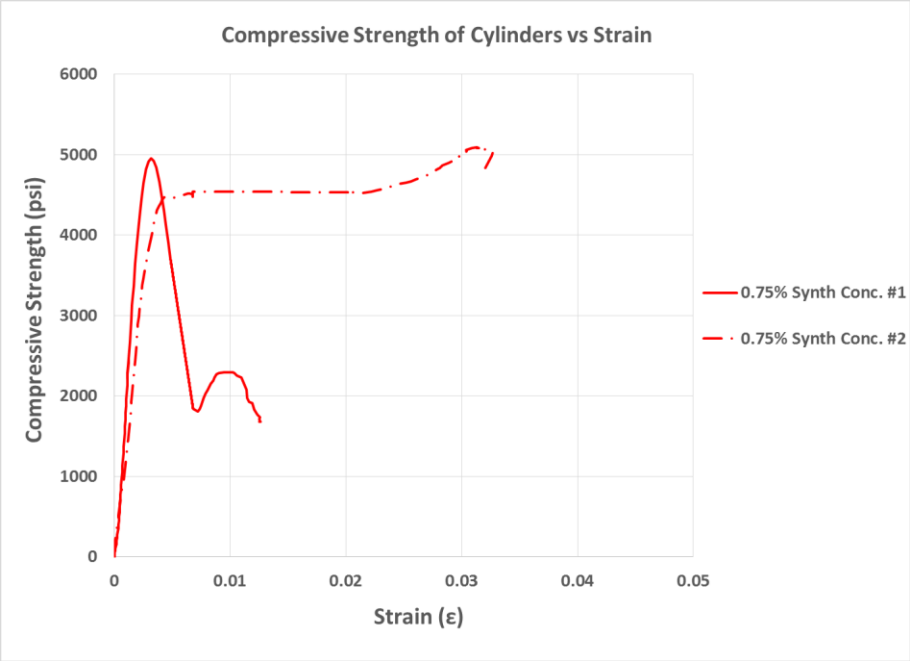

Figure 558 Compressive stress-strain curves for SNFRC 0.75% cylinders subjected to 3 months of accelerated aging (PH3)

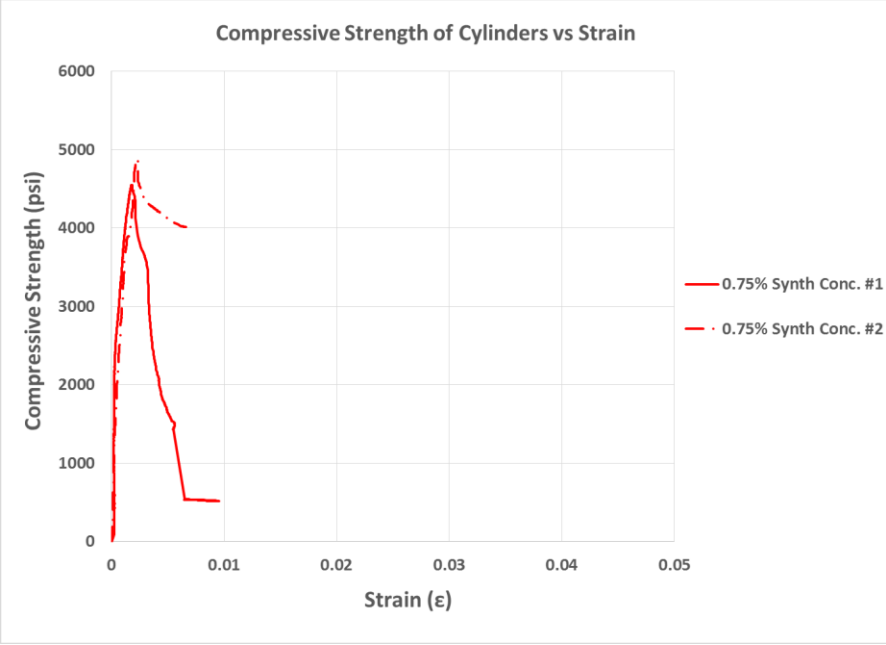

Figure 559 Compressive stress-strain curves for SNFRC 0.75% cylinders subjected to 6 months of accelerated aging (PH4)

Appendix O

Load-deflection response of concrete flexural beams

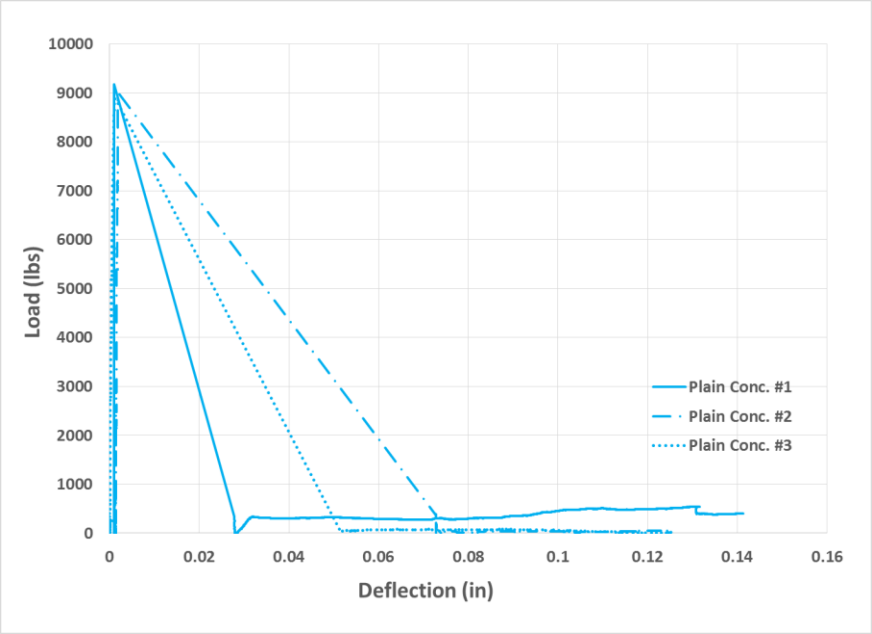

Figure 560 Load-deflection response of plain concrete flexural beams without accelerated aging (Phase 1)

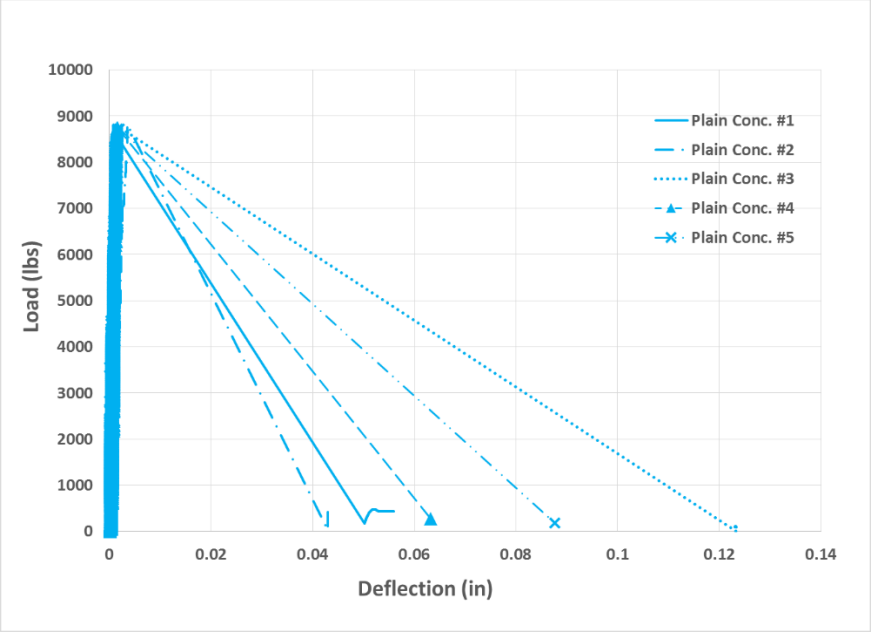

Figure 561 Load-deflection response of plain concrete flexural beams subjected to 1 month of accelerated aging (Phase 2)

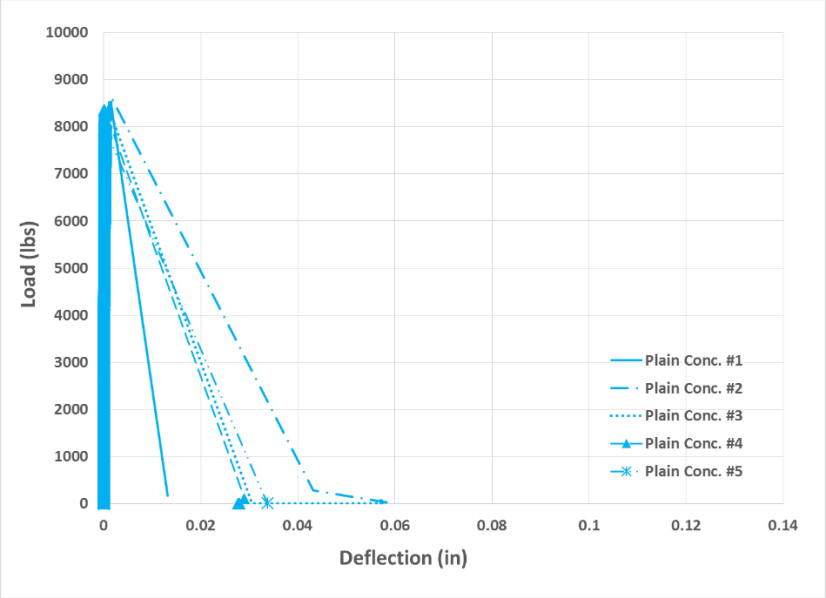

Figure 562 Load-deflection response of plain concrete flexural beams subjected to 3 months of accelerated aging (Phase 3)

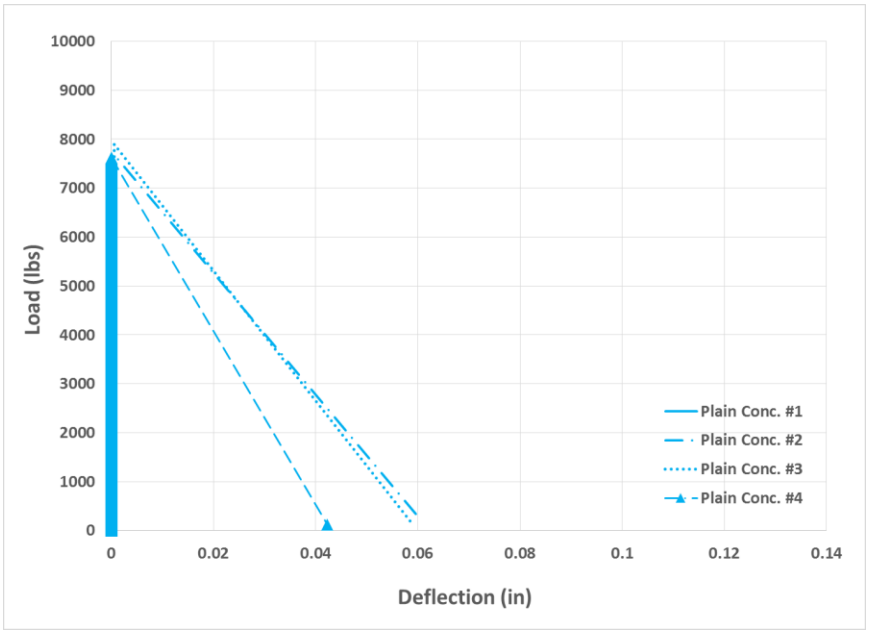

Figure 563 Load-deflection response of plain concrete beams subjected to 6 months of accelerated aging (Phase 4)

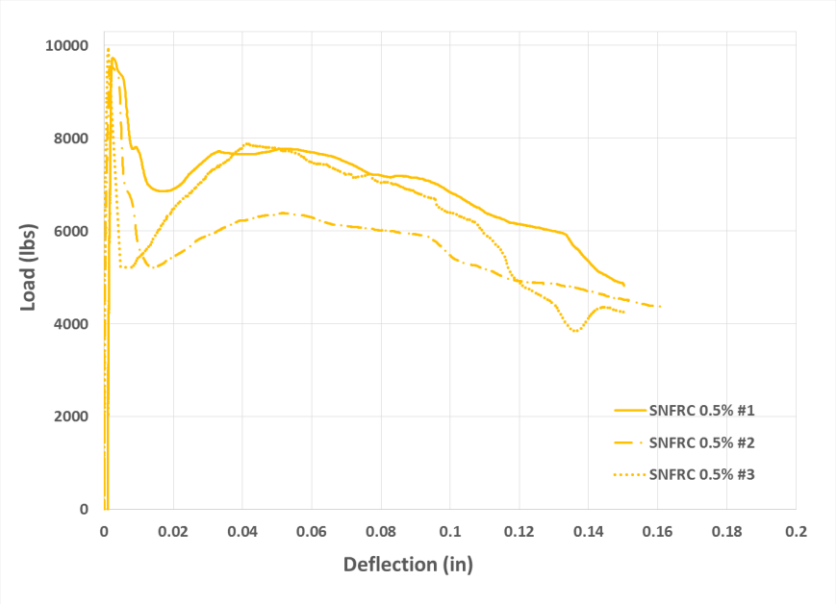

Figure 564 Load-deflection response of SNFRC 0.5% beams without accelerated aging (Phase 1)

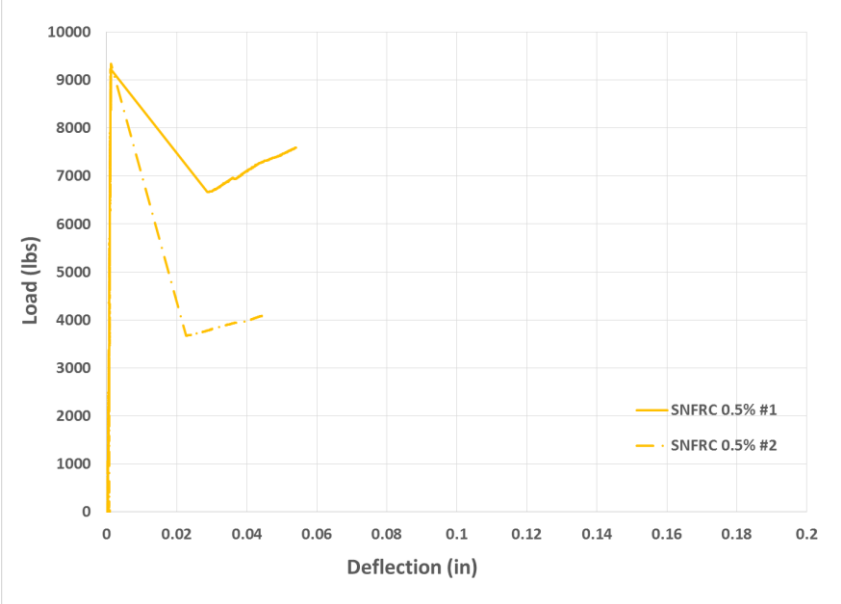

Figure 565 Load-deflection response of SNFRC 0.5% beams subjected to 1 month of accelerated aging (Phase 2)

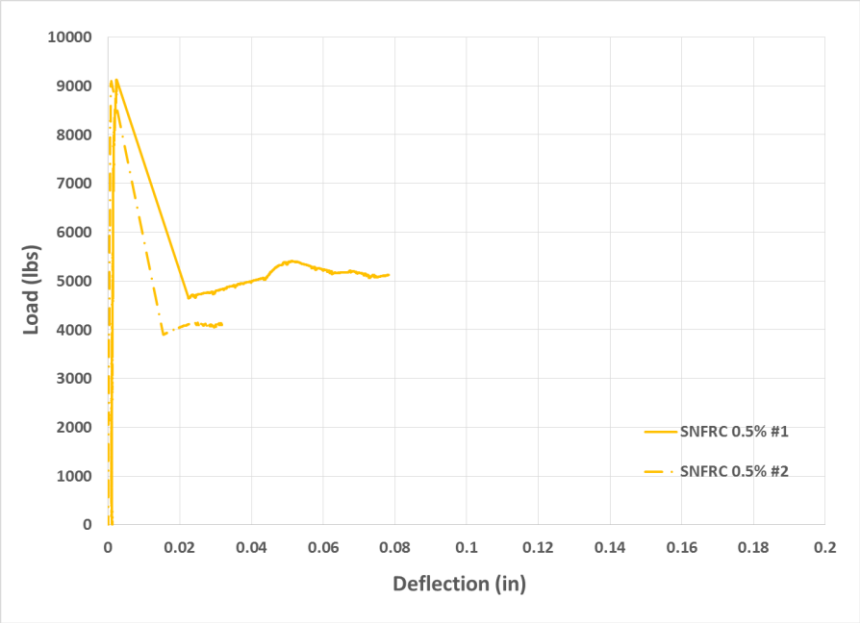

Figure 566 Load-deflection response of SNFRC 0.5% beams subjected to 3 months of accelerated aging (Phase 3)

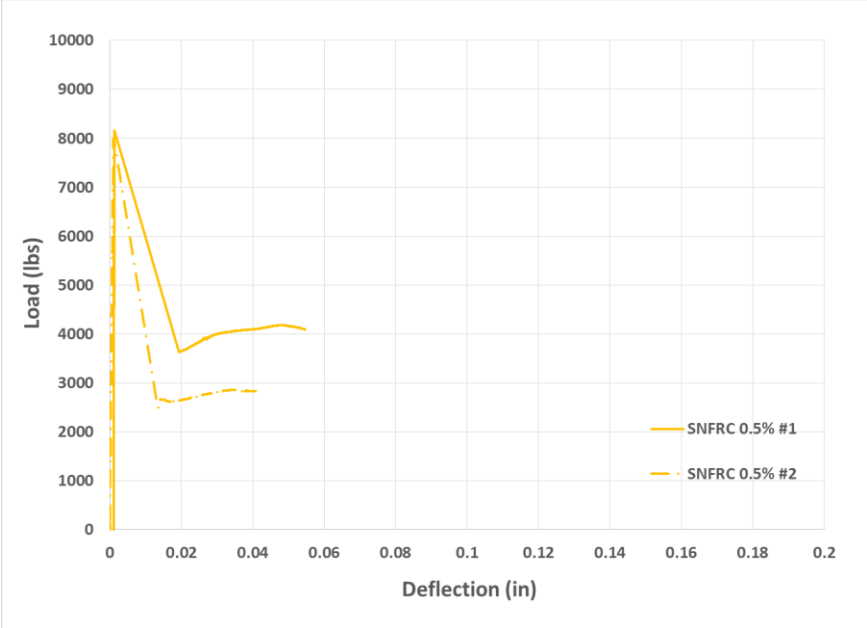

Figure 567 Load-deflection response of SNFRC 0.5% beams subjected to 6 months of accelerated aging (Phase 4)

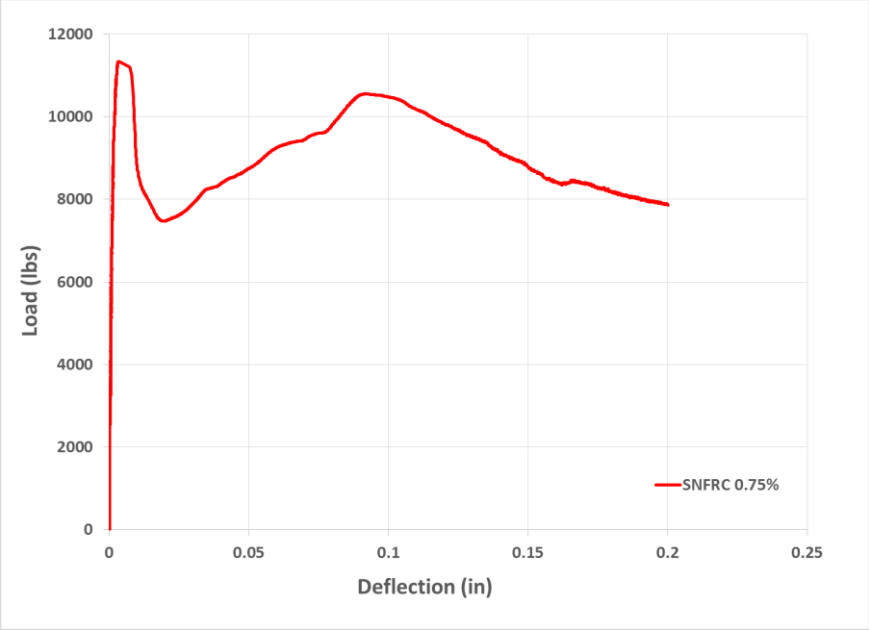

Figure 568 Load-deflection response of SNFRC 0.75% beams without accelerated aging (Phase 1)

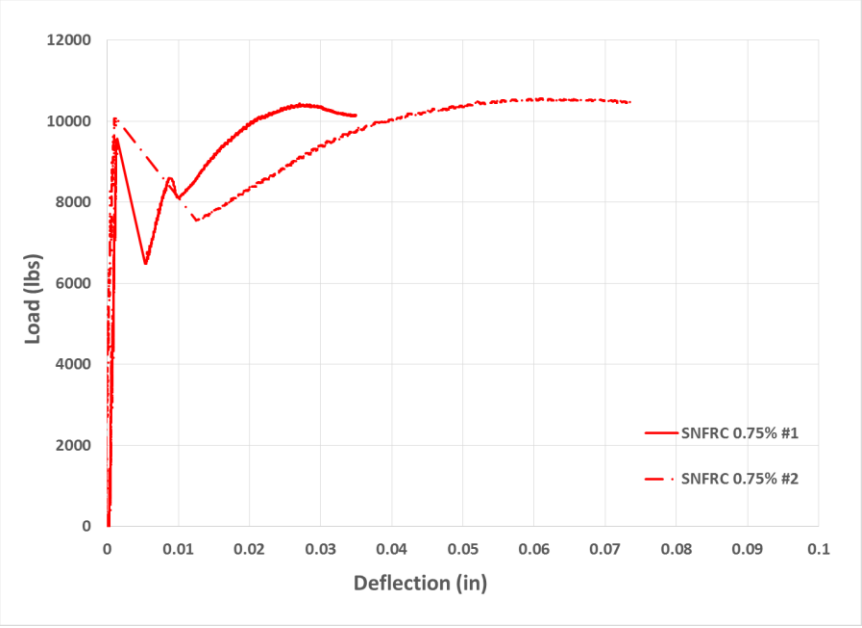

Figure 569 Load-deflection response of SNFRC 0.75% beams subjected to 1 month of accelerated aging (Phase 2)

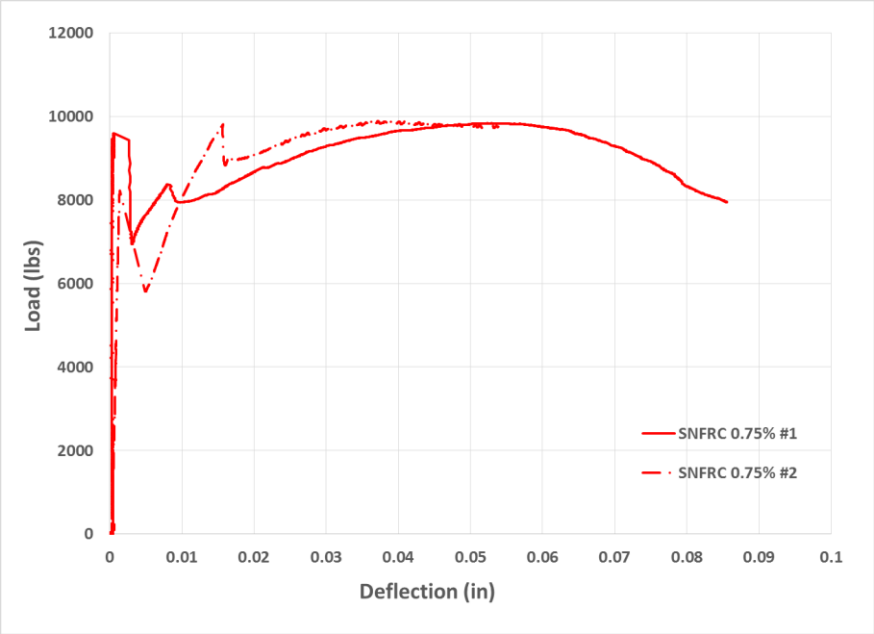

Figure 570 Load-deflection response of SNFRC 0.75% beams subjected to 3 months of accelerated aging (Phase 3)

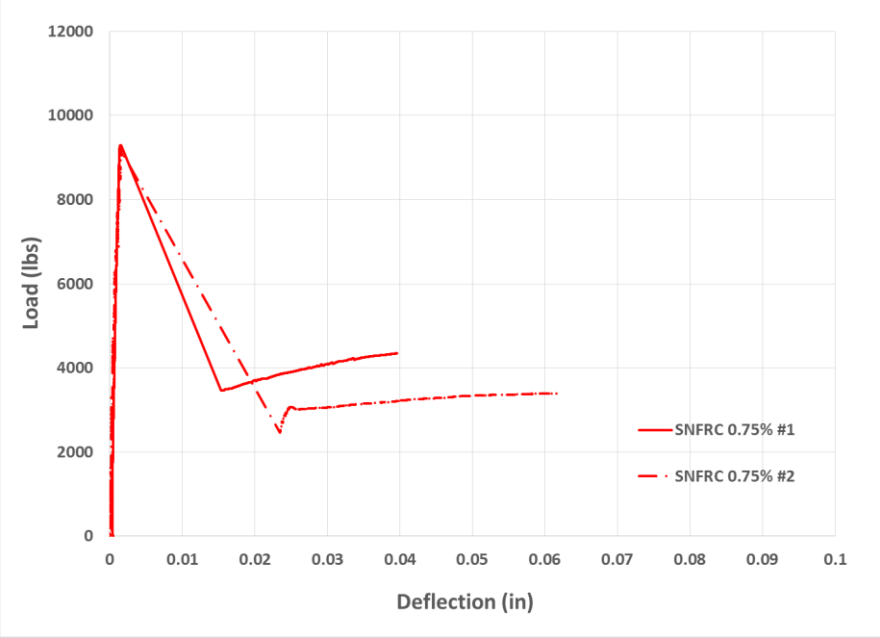

Figure 571 Load-deflection response of SNFRC 0.75% beams subjected to 6 months of accelerated aging (Phase 4)

Appendix P

Project Planning

Table 16 Schedule and sub tasks of research program

WBS	Task Description	Duration (Days)	M1	M2	M3	M4	M5	M6	M7	M8	M9	M10	M11	M12	M13	M14	M15	M16	M17	M18	M19	M20	M21	M22	M23	M24
1	**Experimental Program**	**295**																								
1.1	**Trial Large-Scale beams**	**42**																								
1.1.1	Casting	7																								
1.1.2	Curing	28																								
1.1.3	Testing	7																								
1.2	**Large-Scale Beams, flexural beams and cylinders**	**253**																								
1.2.1	Building formworks	14																								
1.2.2	Strain Gauge installation	14																								
1.2.3	Casting	7																								
1.2.4	Curing	28																								
1.2.5	Builing Tubs	10																								
1.2.6	Aging	**180**																								
	PhaseII	30																								
	PhaseIII	90																								
	PhaseIV	180																								
1.2.7	Testing	**40**																								
	PhaseI (no aging)	10																								
	PhaseII (30d aging)	10																								
	PhaseIII (90d aging)	10																								
	PhaseIV (180d aging)	10																								
2	**FEM Modeling (3D-non linear modeling) & Results Analysis**	**470**																								

References

- Balaguru, Perumalsamy N., and Surendra P. Shah. “Fiber-reinforced cement composites.” 1992.
- Naaman, A. E., “Fiber Reinforcement for Concrete.” Concrete International: - Design and Construction, Vol. 7, No. 3, Mar. 1985, pp. 21-25.
- Romualdi, J. P., and Batson, G. B., “Mechanics of Crack Arrest in Concrete.” J. Eng. Mech. Div., ASCE, Vol. 89, No. EM3, June 1963, pp. 147-168.
- ACI Committee 318, “Building Code Requirements for Structural Concrete (ACI 318-08) and Commentary.” American Concrete Institute, Farmington Hills, MI, 465 pp.
- NACE International White Paper, “NACE International White Paper Corrosion Control Plan for Bridges.” National Association of Corrosion Engineers, 2012.
- Hoff, George C. "Durability of fiber reinforced concrete in a severe marine environment." Special Publication 100 (1987): 997-1042.
- Li, Victor C., Robert Ward, and Ali M. Hamza. "Steel and synthetic fibers as shear reinforcement." ACI Materials Journal 89.5 (1992): 499-508.
- Kwak, Y. K.; Eberhard, M. O.; Kim, W.-S.; and Kim, J., “Shear Strength of Steel Fiber-Reinforced Concrete Beams without Stirrups.” ACI Structural Journal, V. 99, No. 4, July-Aug. 2002, pp. 530-538.
- Noghabai, K., “Beams of Fibrous Concrete in Shear and Bending: Experiment and Mode.” Journal of Structural Engineering, V. 126, No. 2, 2000, pp. 243-251.
- Greenough, T., and Nehdi, M., “Shear Behavior of Fiber-Reinforced Self-Consolidating Concrete Slender Beams.” ACI Materials Journal, V. 105, No. 5, Sept.-Oct. 2008, pp. 468-477.

- Hwang, Jin-Ha, et al. "Shear behavior models of steel fiber reinforced concrete beams modifying softened truss model approaches." Materials 6.10 (2013): 4847-4867.
- Kang, Thomas HK, et al. "Shear testing of steel fiber-reinforced lightweight concrete beams without web reinforcement." ACI Structural Journal 108.5 (2011): 553.
- Narayanan, R., and I. Y. S. Darvish. "Use of steel fibers as shear reinforcement." (1987): 216-227.
- Majdzadeh, Fariborz, Sayed Mohamad Soleimani, and Nemkumar Banthia. "Shear strength of reinforced concrete beams with a fiber concrete matrix." Canadian Journal of Civil Engineering 33.6 (2006): 726-734.
- Cho, Soon-Ho, and Yoon-IL Kim. "Effects of steel fibers on short beams loaded in shear." Structural Journal 100.6 (2003): 765-774.
- Cifuentes, Héctor, et al. "Influence of the properties of polypropylene fibres on the fracture behaviour of low, normal, and high-strength FRC." Construction and Building Materials 45 (2013): 130-137.
- Roesler, J. R.; Lange, D. A.; Altoubat, S. A.; Rieder, K.-A.; and Ulreich, G. R., “Fracture of Plain and Fiber-Reinforced Concrete Slabs under Monotonic Loading.” Journal of Materials in Civil Engineering, V. 16, No. 5, 2004, pp. 452-460.
- Di Maida, P., et al. "Pullout behavior of polypropylene macro-synthetic fibers treated with nano-silica." Construction and Building Materials 82 (2015): 39-44.
- Furlan, Sydney, and João Bento de Hanai. "Shear behaviour of fiber reinforced concrete beams." Cement and Concrete Composites 19.4 (1997): 359-366.

- Sahoo, Dipti Ranjan, Apekshit Solanki, and Abhimanyu Kumar. "Influence of steel and polypropylene fibers on flexural behavior of RC beams." Journal of Materials in Civil Engineering 27.8 (2014): 04014232.
- Altoubat, Salah, Ardavan Yazdanbakhsh, and Klaus-Alexander Rieder. "Shear behavior of macro-synthetic fiber-reinforced concrete beams without stirrups." ACI Materials Journal 106.4 (2009): 381-389.
- Arrhenius, Svante. Über die Dissociationswärme und den Einfluss der Temperatur auf den Dissociationsgrad der Elektrolyte. Wilhelm Engelmann, 1889.
- Abdun-Nur, Edward A. "Accelerated, early, and immediate evaluation of concrete quality." Special Publication 56 (1978): 1-14.
- Pinto, R., S. Hobbs, and K. Hover. Accelerated Aging of Concrete: A Literature Review. No. FHWA-RD-01-073,. 2002.
- Proctor, B. A., D. R. Oakley, and K. L. Litherland. "Developments in the assessment and performance of GRC over 10 years." Composites 13.2 (1982): 173-179.
- Khajuria, Anil, Kailash Bohra, and P. Balaguru. "Long term durability of synthetic fibers in concrete." Special Publication 126 (1991): 851-868.
- Fenwick, R. C., and Thomas Pauley. "Mechanism of shear resistance of concrete beams." Journal of the Structural Division 94.10 (1968): 2325-2350.
- Ashour, Samir A., Ghazil S. Hasanain, and Faisal F. Wafa. "Shear behavior of high-strength fiber reinforced concrete beams." Structural Journal 89.2 (1992): 176-184.
- Altoubat, S. A., A. Yazdanbakhsh, and K-A. Rieder. "Effect of synthetic macro-fibers on shear behavior of concrete beams." Special Publication 248 (2007): 41-52.

- Joint ACI-ASCE Committee 326 (now 426), “Shear and Diagonal Tension,” ACI JOURNAL, Proceedings V. 59, No. 1, Jan. 1962, pp. 1-30; No. 2, Feb. 1962, pp. 277-334; and No. 3, Mar. 1962, pp. 352-396.
- Abaqus manual 6.12-2 (2012)
- ACI Committee, American Concrete Institute, and International Organization for Standardization. "Building code requirements for structural concrete (ACI 318-14) and commentary." American Concrete Institute, 2014.

Biographical Information

Michael was born in Tehran, Iran, in January 1988. He received a Bachelor of Science Degree in Civil Engineering from Sharif University of Technology in February 2011. In December 2011, he moved to Texas to pursue a Master of Science degree in Civil Engineering from the University of Texas at Arlington (UTA). His area of emphasis was structures, and he worked under the supervision of Dr. Ali Abolmaali.

He graduated in August 2013 and began working as a structural project engineer at a bridge company, Ferrovial Agoman (Trinity Infrastructure, LLC) in Dallas, TX. He performed analysis and designed bridges on a 17 mile, $2.7-billion LBJ express project (IH-635) in Dallas, TX.

He started his Ph.D. program under supervision of Dr. Ali Abolmaali in August 2014, and received his Professional Engineer license in Civil/ Structural in December 2014. He is currently a licensed professional engineer in the states of California, Washington and Texas.

In August 2016, he started working as a senior project manager at Charles Gojer and Associates, Inc.